CONTROLS ON PRODUCTION IN THE CHICONTEPEC OIL-BEARING RESERVOIRS, MEXICO

By

Juan Carlos Granados Hernandez

Submitted in accordance with the requirements for the degree of

Doctor of Philosophy

The University of Leeds

School of Earth and Environment

December 2014

The candidate confirms that the work submitted is his own and that appropriate credit has been given where reference has been made to the work of others.

In memoriam:

Margarita Mendoza Olivo[†] *Alfredo Chávez Mendoza*[†]

Francisca Quintero Arzate[†] *Gregorio Rosas Hernández*[†]

Acknowledgements

I express my heartfelt and infinite gratitude towards my wife Miriam for giving me the strength, patience and courage all the way through this project. To my lovely children: Fredel, Franco and Frida, for being my inspiration.

The present research project was jointly funded by the Mexican Petroleum Oil Company (PEMEX), the Mexican Secretariat of Energy (SENER), and the National Council of Science and Technology of Mexico (CONACyT), through the CONACyT-SENER-Hidrocarburos Fund 2009-02. The author would like to thank Mr. Rafael Ramos Palmeros, Mrs. Luz Elena Aldaco Vidrio, Mrs. Maria Teresa Sanchez Serrano, Mr. Pablo Gomez Duran, Mrs. Ana Rosa Parrilla Puente, Mrs. Yanira Garcia Estrada, Mr. Leopoldo Vilchis Ramirez, Mr. Nestor Diaz Ramirez, Mrs. Rosa Maria Turriza Guzman, and Mr. Edmundo Alvarez Fernandez for their invaluable support during the development of this project.

I owe my profound gratitude to my supervisors: Prof. Quentin Fisher and Dr. Carlos Grattoni for their continuous encouraging, help, and advice throughout this research project. I appreciate their generous contribution to the critical-thinking improvement of this work, as well as their pragmatism, patience, enthusiasm, and guidance to this project. Special thanks to the transfer examiner of this study, Dr. Nigel Mountney, for his observations and enriching comments. I also thank Prof. Bill McCaffrey and Dr. David Hodgson for their valuable comments and suggestions in developing the sedimentary interpretation of this study. The author would also thank Dr. Piroska Lorinczi and Mr. Konstantin Rybalcenco for their help on the production simulation modelling. My deep and sincere gratitude goes to my external examiner, Prof. Cathy Hollis, for providing with very detailed suggestions to improve this work.

I owe my deepest gratitude to PEMEX management for their vote of confidence in this study: Mr. Antonio Escalera Alcocer, Mr. Pedro Silva Lopez, Mr. Antonio Narvaez Ramirez, Mr. Heriberto Cordova Aguayo, and Mr. Jose Guadalupe Galicia Barrios. Special appreciation must go to PEMEX internal supervisor of this project, Mr. Domingo Saavedra Torres, for his continuous advice and encouragement. The author would also thank Mr. Javier Mendez de Leon, Mr. David Lopez Garcia, Mrs. Candelaria Carral Zamudio, Mrs. Gabriela Salazar Rodriguez, Mr. Sergio ParraRodriguez, Mr. Luis Rodriguez Manzo, Mr. Victor Alvarez Maya, Mrs. Erika Carmona Castañón, Mr. Carlos Barajas Llerenas, and Mr. Jaime Barceló Duarte[†], for providing this project with information and also for the administrative support.

Special appreciation must go to Martha Mayol-Castillo for providing compositional information of a number of Chicontepec crude-oils.

The author would like to thank the London Petrophysical Society (LPS) executive committee, for awarding this project with the *Iain Hillier Academic Grant 2013*, which was employed for purchasing a number of imbibition cells used during the wettability experiments of this study. Special thanks to Mr. Mike Millar and Mr. Paul Hoddinott.

I also appreciate all the technical support from Mr. Phil Guise. Special thanks to Mr. David Lawlor for his continuous support in employing the goniometer device. Thanks to Mrs. Lesley Neve for her help in preparing samples for XRD analyses. The author would also thank Dr. Eric Condliffe and Dr. Richard Walshaw for helping me to use the scanning electron microscope. I also thank Mr. Harri Wyn Williams for his help in conditioning rock samples and preparing thin sections. I thank Mrs. Susanne Patel for her support in using the refractometer and Mrs. Rachel Gasior for running the ICP-AES tests.

Sincere thanks must go to my research office colleagues and personnel of the School of Earth and Environment of the University of Leeds for all the interesting discussions which have always been useful: Dr. Talal Al-Aulaqi, Dr. Adriana Matamoros Veloza, Dr. John Martin, Dr. Ida Shafagh, Dr. Samuel Allshorn, Mr. Javed Haneef, Mrs. Devan Hussein, Mr. Fraidon Rashid, Ms. Nichola Eardley and Mr. Majeed Shar.

Great and sincere thanks to my parents Jorge and Carmen, and my brothers Lucha and Jorge for their example, emotional support and encouragement.

Abstract

The siliciclastic, oil-bearing Chicontepec reservoirs contain 33% of Mexico's total reserves, representing the largest oil accumulation in Mexico associated with a single producing play. Oil production from these typically describes low-rates and high-declination profiles, resulting in poor-recovery efficiencies. Despite these reservoirs have been subjected to unprecedented financial inversions and an intense operative strategy, their total crude-oil output is underperforming compared to the estimated production projections. Total cumulative production (oil and gas) of Chicontepec reservoirs has only reached 0.4% of its oil originally in place (OOIP).

The principle aim of this thesis is to provide with experimental evidence and tools to increase the level of understanding of the Chicontepec reservoirs with a particular focus on their oil productivity. A study area within the Chicontepec basin was selected. This consisted of two oilfields with sufficient information to allow a comprehensive investigation. The objective has been addressed by combining descriptive, analytical, experimental and numerical approaches. The controls on oil production in the Chicontepec reservoirs have been analysed in this work by integrating: 1) descriptive studies of the reservoir rock to try to understand the origin of their low-permeability; 2) measured-rock attributes and well-log analysis to evaluate their petrophysical properties; 3) experimental tests to examine rock-fluid interactions and existence of formation damage; 4) reservoir modelling to assess heterogeneity; and 5) simulation case studies to investigate oil recovery efficiencies.

Exploiting the Chicontepec reservoirs has been challenging, particularly for their extreme-heterogeneity, their low-transmissivity capacity and the poor-recovery potential of its drive mechanism. The analytical information and experimental results reported in this work intends to contribute in improving the understanding of the variables that control the oil productivity in these reservoirs.

Table of Contents

List of Tables

CHAPTER VIII.

Illustrative Material

CHAPTER I.

CHAPTER II.

CHAPTER III.

CHAPTER IV.

CHAPTER V.

CHAPTER VI.

CHAPTER VII.

CHAPTER VIII.

CHAPTER IX.

Abbreviations

BOPD	*Barrels of Oil Per Day*
BVI	*Bulk Volume Irreducible*
BVW	*Bulk Volume Water*
BSEM	*Backscattered Scanning Electron Microscopy*
CEC	*Cation Exchange Capacity*
CSC	*Critical Salt Concentration*
CT	*Computarised Tomography*
CVT	*Critical Velocity Test*
DCM	*Dichloromethane*
DW	*De-ionised Water*
EOR	*Enhanced Oil Recovery*
F	*Formation Factor*
FFI	*Free Fluid Index*
GOR	*Gas Oil Ratio*
GR	*Gamma Ray*
ICP-AES	*Inductively Coupled Plasma by Atomic Emission Spectroscopy*
IFT	*Interfacial Tension*
IGV	*Intergranular Volume*
IOR	*Improved Oil Recovery*
MICP	*Mercury Injection Capillary Pressure*
MMBOPD	*Million Barrels of Oil Per Day*
MMMBOE	*Billion Barrels of Oil Equivalent*
MMCFD	*Million Cubic Feet Per Day*
NMR	*Nuclear Magnetic Resonance*
NTG	*Net To Gross*
OOIP	*Oil Originally In Place*
pv	*Pore volume*
PVT	*Pressure Volume Temperature*
Q_o	*Oil Flow Rate*
QXRD	*Quantitative X-Ray Diffraction*
rb/STB	*Reservoir Barrel per Stock Tank Barrel*
RI	*Refractive Index*
Rw	*Formation Water Resistivity*
Rt	*True Resistivity*

SARA	*Saturates, Aromatics, Resins, Asphaltenes*
SEM	*Scanning Electron Microscopy*
SGS	*Sequential Gaussian Simulation*
SIS	*Sequential Indicator Simulation*
S/V	*Surface to Volume*
TDS	*Total Dissolved Solids*
TVD	*True Vertical Depth*
TVDSS	*True Vertical Depth Subsea*
U	*Interstitial Velocity*
VCL	*Clay Volume*
VES	*Viscoelastic Surfactant*

k	*Permeability*
kr	*Relative Permeability*
$Ø$	*Porosity*
μ	*Viscosity*
ρ	*Density*
r	*Pore Radius*
R_s	*Gas solubility*
Sw	*Water Saturation*
Sw_i	*Irreducible Water Saturation*
So	*Oil Saturation*
So_r	*Residual Oil Saturation*
P_b	*Bubble-point pressure*

CHAPTER I.
INTRODUCTION

The state-owned Mexican petroleum company (PEMEX) provides nearly 34% of the annual federal budget (Beauregard, 2014), and has represented a major source of income to the Mexican economy for years (Fig. 1.1). Profits from crude-oil commercialisation have averaged 8% of the country's Gross Domestic Product for the last seven years (PEMEX, 2013a).

PEMEX currently has assets with total reserves of 37.4 MMMBOE (*Billion Barrels of Oil Equivalent*) and prospective resources of 113 MMMBOE; half of which is estimated to be from unconventional assets (SENER, 2014; PEMEX, 2014). PEMEX now faces the challenge of not only maintaining its base production (*i.e.* 2.3 MMBOPD, *Million Barrels of Oil Per Day*), but also increasing crude-oil and gas outputs by 3.0 MMBOPD and 5800 MMCFD (*Million Cubic Feet Per Day*) respectively by 2018 (PEMEX, 2013b).

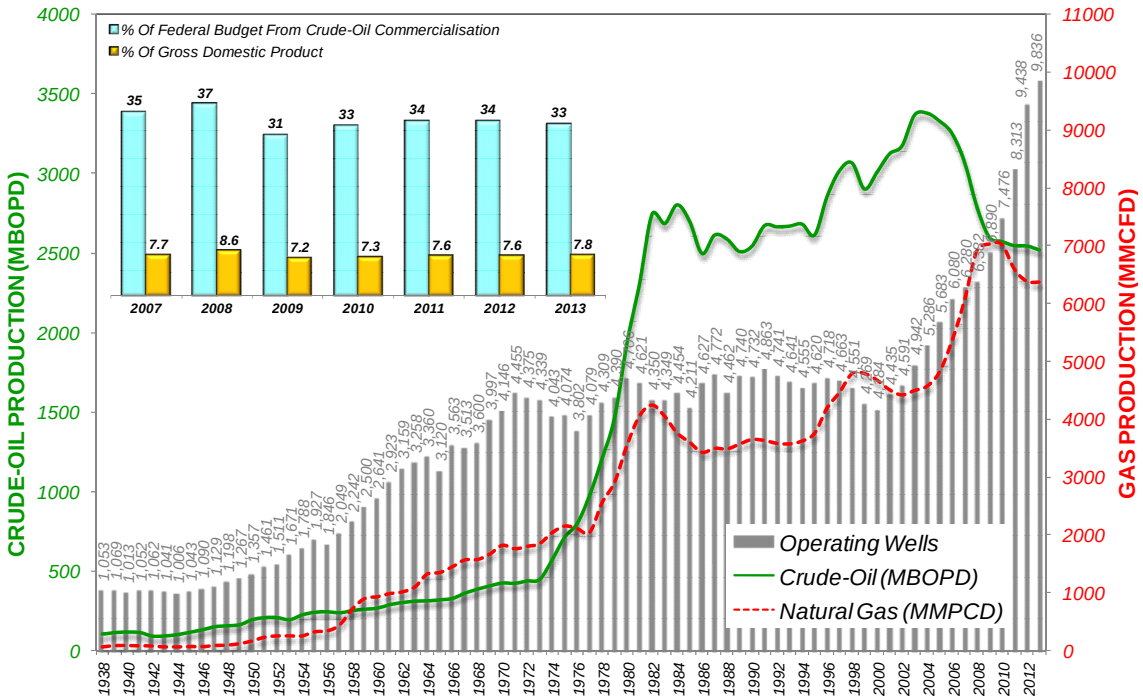

Figure 1.1 Hydrocarbon production history of Mexico as of December 2013 and the value of the crude-oil commercialisation to the Mexican economy in recent years (compiled from: CNH, 2014b; Beauregard, 2014)

Since 2005, production from the most prominent Mexican oilfields (*e.g.* Cantarell oilfield) started to decline, which represented a significant reduction of income for the Mexican government that was partially compensated with a steady increase in crude-oil prices.

In such circumstances, and with the absence of important discoveries, PEMEX choose the Chicontepec reservoirs as an emergent project for balancing the country's crude-oil output which reached a peak production of 3.4 MMBOPD in 2004 (Fig. 1.1).

The Chicontepec onshore oil project is located in the eastern portion of Mexico, about 270 km north-eastern distance from Mexico City (Fig. 1.2). The project extends 3,800 km^2 but, even though it was discovered since 1926, its total cumulative production (oil and gas) has only reached 0.41% of its oil originally in place (OOIP). As of January 2015, Chicontepec's OOIP is 87 MMMBOE, total cumulative production is 359 MMBOE and total reserves are estimated to be 12.2 MMMBOE (PEMEX, 2015).

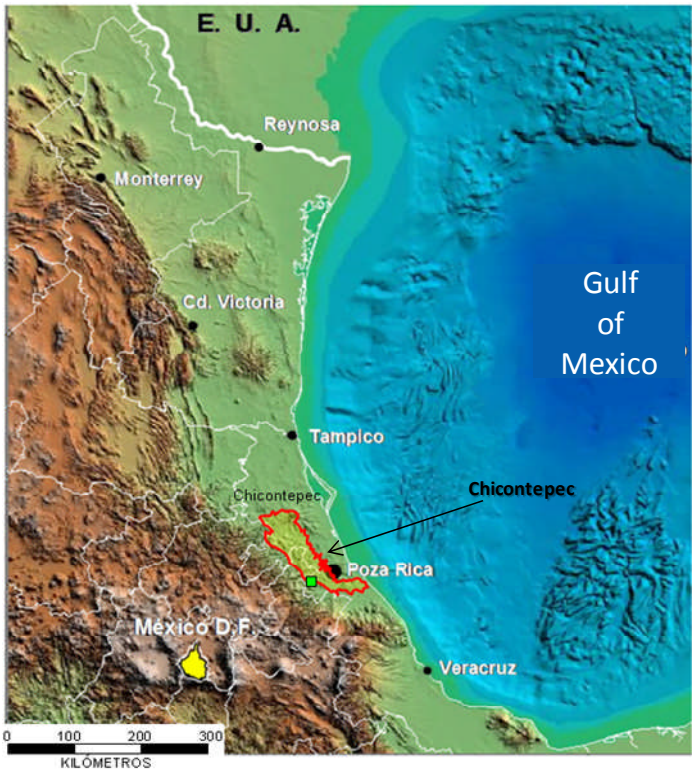

Figure 1.2 Chicontepec Project location (modified from Saavedra, 2009)

The Chicontepec reservoirs contain 33% of the country's total reserves (PEMEX, 2015), representing the largest oil accumulation in Mexico associated with a single producing play. The Chicontepec reservoirs are part of the structurally confined Tampico-Misantla foreland basin, which was developed during the Paleocene-Eocene Laramide Orogeny. These reservoirs are stratigraphically equivalent to the Wilcox Group in Texas (Tyler *et al.*, 2004) and are mainly composed by low-permeability litharenitic sandstones. The Chicontepec reservoir sandstones were deposited in variable sedimentary facies, associated with a series of submarine fan systems (Tyler *et al.*, 2004), gravity-driven deposits and mass-transport processes (PEMEX, 2009). Sand units were deposited within a tectonically-active regime (Sarkar, 2011), characterised by a

number of uplift, reworking and erosion episodes, which resulted in complex sedimentary distributions. The Chicontepec reservoir rock experienced intense calcite cementation, which significantly reduced the pore space. Reservoir units normally develop porosities between 6 to 15% and permeabilities below 10 mD (milli Darcy).

An ambitious campaign to develop the Chicontepec reservoirs started in 2006, which mainly consisted of an intense period of drilling, completion, stimulation and workover operations (Fig. 1.3). PEMEX invested unprecedented resources for drilling 3000 new wells during the following six years. Cost per well averaged USD $1.4 million (Narvaez, 2012), which illustrates the large investment made on this project. After this stage, production output averaged 66,200 BOPD in 2013; however, due to recent changes in the country's energy strategy, petroleum output has started to decline gradually (Fig. 1.4).

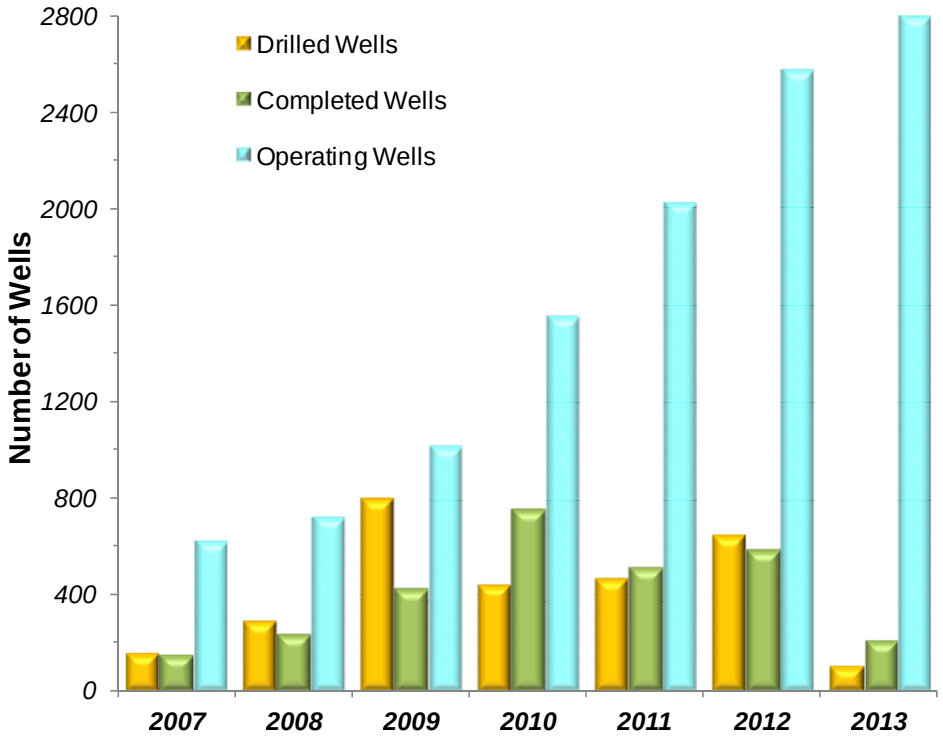

Figure 1.3 The main operational activities of Chicontepec Project in recent years (compiled from PEMEX, 2012a; 2012b)

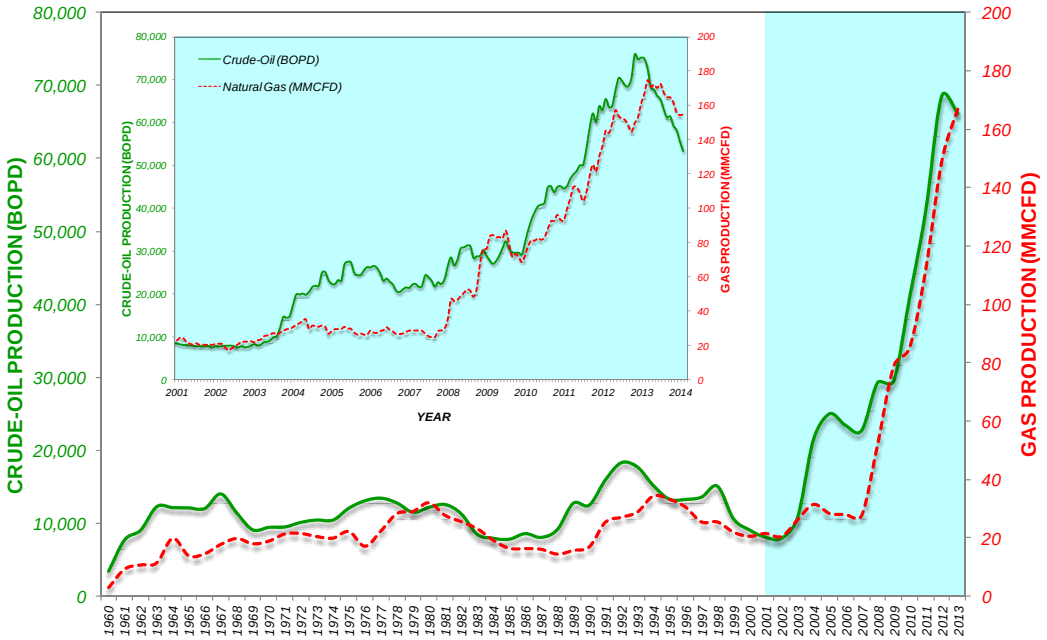

Figure 1.4 Average oil and gas production of Chicontepec Project (compiled from: CNH, 2014b)

A number of technological applications have been proved promising, but incipient, results during the development of the Chicontepec reservoirs. These have included viscous-elastic fracturing fluids (Centurion *et al.*, 2006), ultrasonic stimulation (Granados and Flores, 2013), injection pilot programmes (employing water, CO_2, steam and air), and real-time artificial lift monitoring (Narvaez *et al.*, 2011). Recently, the combination of horizontal drilling and multi-stage fracturing has given positive results to the project (Gutierrez *et al.*, 2014a, 2014b). This technique consisted of a pair of horizontal wells fractured simultaneously in multiple stages to communicate fractures along both wells. The wells produced fourteen times more oil than any vertical well at Chicontepec in similar production periods.

These reservoirs have also been subjected to a range of studies including research projects (IMP, 2001, 2009; PEMEX, 1998, 2004, 2008, 2009; Birkle *et al.*, 2006), technical opinions (Berumen *et al.*, 2004b; Tyler *et al.*, 2004; Hurtado *et al.*, 2005; Takahashi *et al.*, 2006; Abbaszadeh *et al.*, 2008; Gachuz-Muro, 2009; Luces *et al.*, 2012), consultancies (Cossey, 2007; Vessell, 2008), dissertations (Ataei, 2012; Mayol-Castillo, 2005; Sarkar, 2011), and multiple PEMEX internal reports. Despite these efforts, which have no precedent within the Mexican petroleum industry, the results have not been satisfactory, especially in terms of oil productivity and recovery.

The Chicontepec reservoirs comprise the lowest oil recovery efficiency from existing projects producing crude-oil in Mexico, despite having the largest number of operating wells (Figs. 1.5, 1.6, 1.7). Total crude-oil output of these contributes only 2% of the country's production. These

characteristics have made Chicontepec a low-profitable project and frequently centre of political debate.

The Chicontepec reservoirs are characterised by producing at low oil rates (averaging 19 BOPD per well) and high declination production profiles, which is the main reason these have been frequently referred as unconventional resources (CNH, 2010). This behaviour has generally been ascribed as the result of the tight fabric of the reservoir rock, the lack of communication between the sandstone units and the drive mechanism (*i.e.* solution gas).

Recovery factors after primary depletion in these reservoirs are under 5% (Gachuz-Muro, 2009) which would be increased after implementation of Improved and Enhanced Oil Recovery (IOR/EOR) projects. Nevertheless, little is known about the rock-fluid interaction and the spatial distribution of the sand units, as well as the architectural elements of the reservoirs and their impact on oil productivity; important input parameters to be considered. Based on experiences of secondary/tertiary pilot tests of oil recovery in this basin (*e.g.* Tyler *et al.*, 2004; Abbaszadeh *et al.*, 2008; Birkle *et al.*, 2006), a number of critical factors associated to the reservoir's compartmentalization and fluid-rock compatibility are yet uncertain.

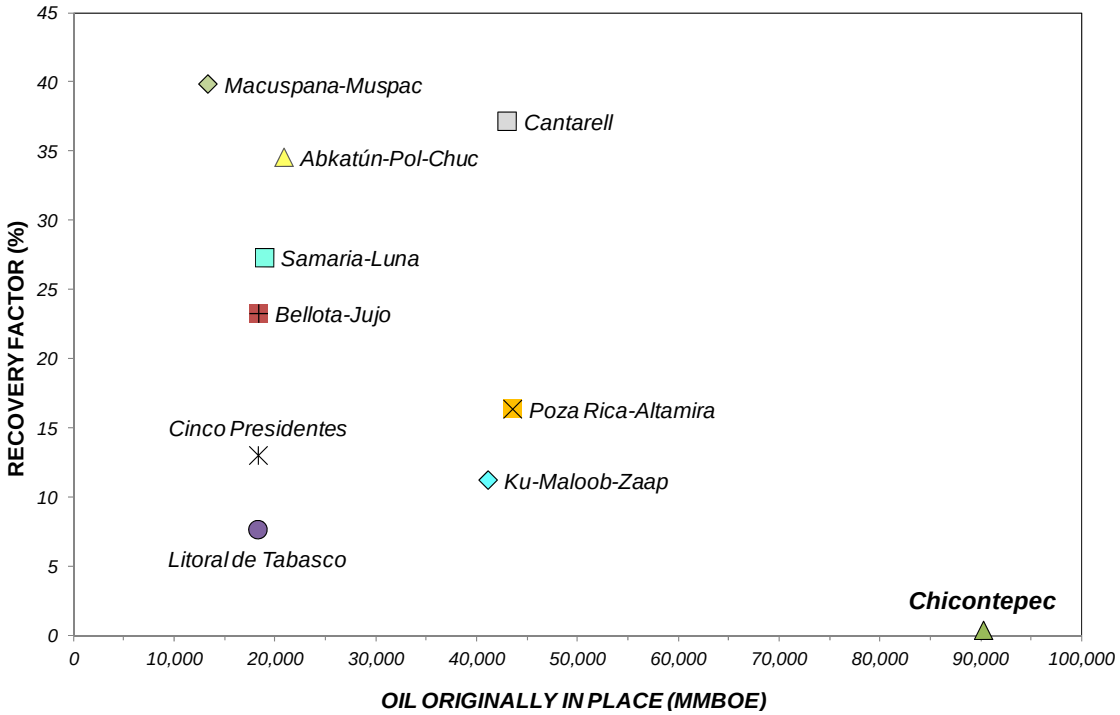

Figure 1.5 Recovery efficiencies of the Mexican petroleum projects as of January, 2014 (interpreted from reports of CNH, 2014b; SENER, 2014)

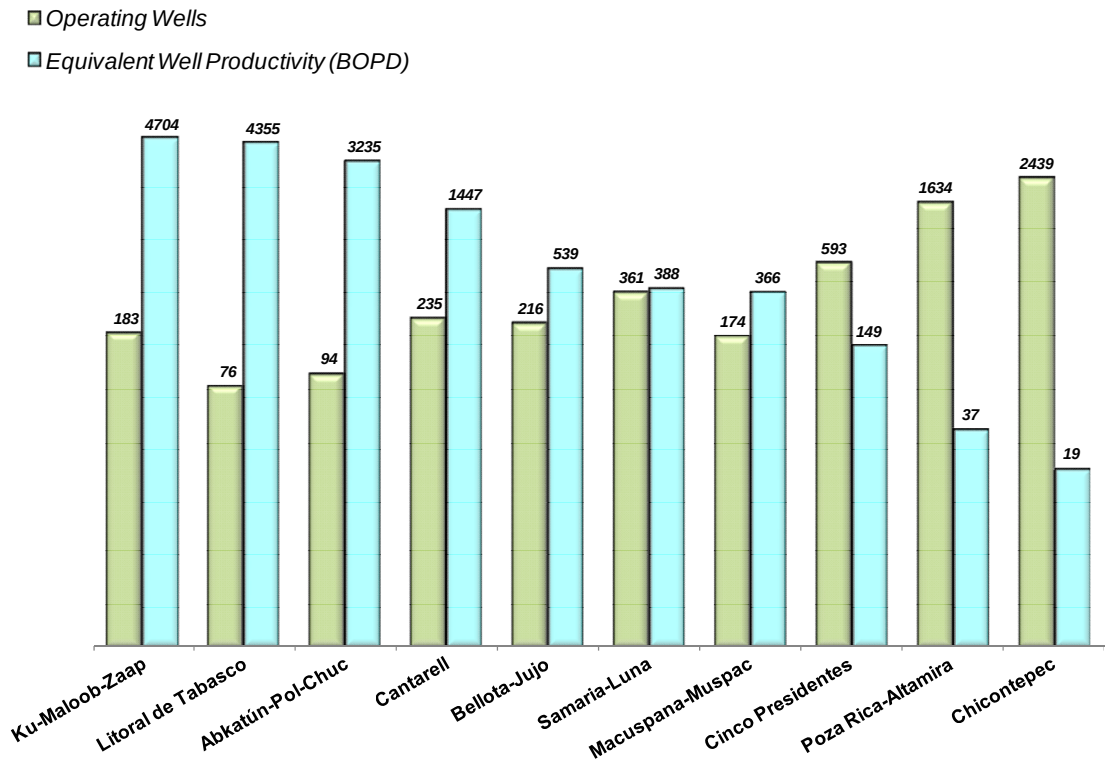

Figure 1.6 Number of operating wells and the equivalent oil productivity of petroleum projects in Mexico as of October, 2014 (interpreted from reports of CNH, 2014b; SENER, 2014)

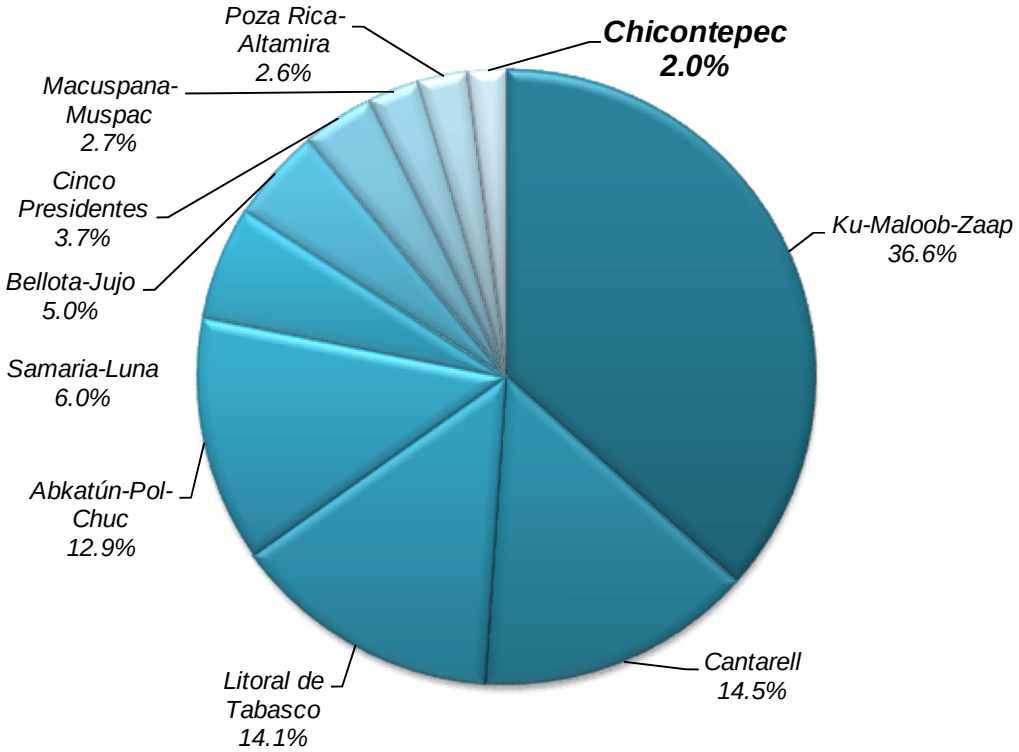

Figure 1.7 Contribution of the ten oil projects in Mexico to the total crude-oil daily output as of October, 2014 (interpreted from reports of CNH, 2014b)

Additionally, a poor performance in oil production has been observed in a number of Chicontepec wells that describes an anomalous trend compared to most production profiles observed in these reservoirs. This inconsistency is characterised by a pronounced declination in the oil rate and a sudden drop of the flowing pressure after hydraulic fracturing (*i.e.* fracking, hydrofrac) has been carried-out. It is unclear whether this performance indicates an incompatible interaction of stimulation fluids and formation (*i.e.* formation damage) or it is simply the nature of these reservoirs. It has been estimated that the flowback fracturing fluid efficiency in Chicontepec reservoirs is only 11% (Hurtado *et al.*, 2005). At present, little is known about the formulations normally prepared for stimulation treatments and their impact on productivity. Hydraulic fracturing is an indispensable technique to develop these reservoirs.

Overall, developing Chicontepec reserves has been complicated. The project has been subjected to unprecedented financial investments and an intense operative strategy. Although there have been recognized a number of technological solutions to maximise oil performance and substantial experience on developing these reservoirs has been gained, the reality is that Chicontepec is underperforming compared to the estimated production projections (CNH, 2014a). Given the complexity of such reservoirs and the high expectations associated with their development, improving understanding of oil productivity and the controls on oil recovery and production clearly becomes a matter of urgency.

PEMEX management aims to have the project producing at a plateau rate of 200,000 BOPD by 2018 (PEMEX, 2013a). This goal may potentially be accomplished by the application of an intense, organised and continuous operational strategy, with the combination of unconventional completion methods and technologically-assisted applications. The analysis of the variables that control oil production, especially those associated to rock-fluid interaction and formation damage assessment, together with the evaluation of the architectural elements of these reservoirs, will be of particular importance in developing these strategic reserves.

1.1 Project Aims

The aim of the present research project is to provide experimental evidence and tools to increase the level of understanding of the Chicontepec reservoirs with a particular focus on their productivity. The ultimate objective is to support the overall exploitation of these reservoirs.

The main objectives of this work are:

1) To examine the Chicontepec reservoir rock characteristics by a number of descriptive techniques.
2) To assess rock-fluid interaction and formation damage mechanisms in Chicontepec reservoirs by a number of experiments.
3) To evaluate oil productivity in Chicontepec reservoirs through reservoir modelling and production simulation.
4) To produce information that will assist in the development activities of Chicontepec reservoirs.

1.2 Database and Methodology

The objective of integrating the following set of data was having enough material for: (1) examining the Chicontepec reservoir rock characteristics; (2) conducting a series of experiments for assessing rock-fluid interaction and formation damage mechanisms; and (3) constructing a reservoir model for production simulation.

The selected study area (Figs. 1.8 and 1.9) appears to have sufficient information to allow a comprehensive investigation. This is located in the Occidental portion of the basin and it is composed by two of the 29 oilfields present in the Chicontepec area, named Humapa and Coyula, with 284 wells recently drilled. The oilfields in the basin have been divided by logistical reasons to facilitate exploitation. As of January 2015, only PEMEX owns complete rights to operate these fields. In general, there is no significant operational difference between reservoirs, and similar recovery efficiencies between fields are observed.

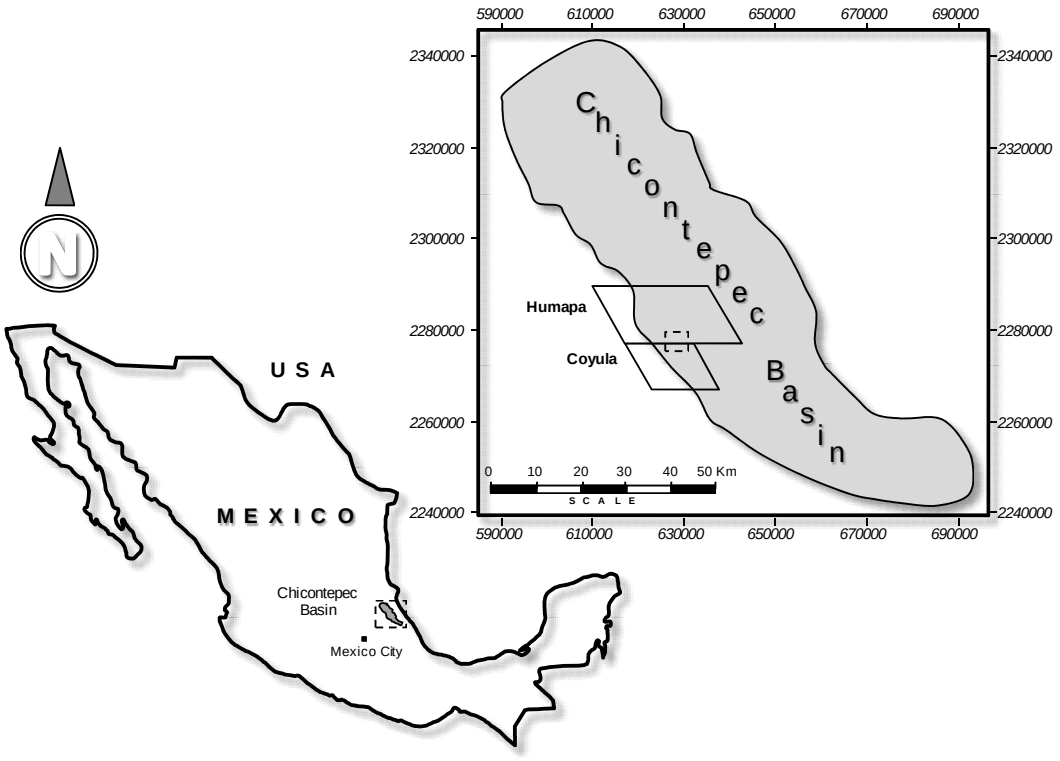

Figure 1.8 Location of the study area

It is generally accepted that the Chicontepec sand units were deposited in a deep-water environment, and during a tectonically unstable conditions. The sands generally describe discontinuous architectures separated by low and ultra-low permeability barriers, such as shales, silts and highly-cemented sandstones. Individual sands are difficult to correlate between well-to-well distances, demonstrating their erratic behaviour. However, it is more practical -and

sometimes more predictive- to follow a set of sands (*i.e.* parasequences) across oilfields. Despite their inconsistent trend, the sand-to-shale proportion intersected by most wells is normally above 50%, although the individual sands vary widely in their petrophysical properties.

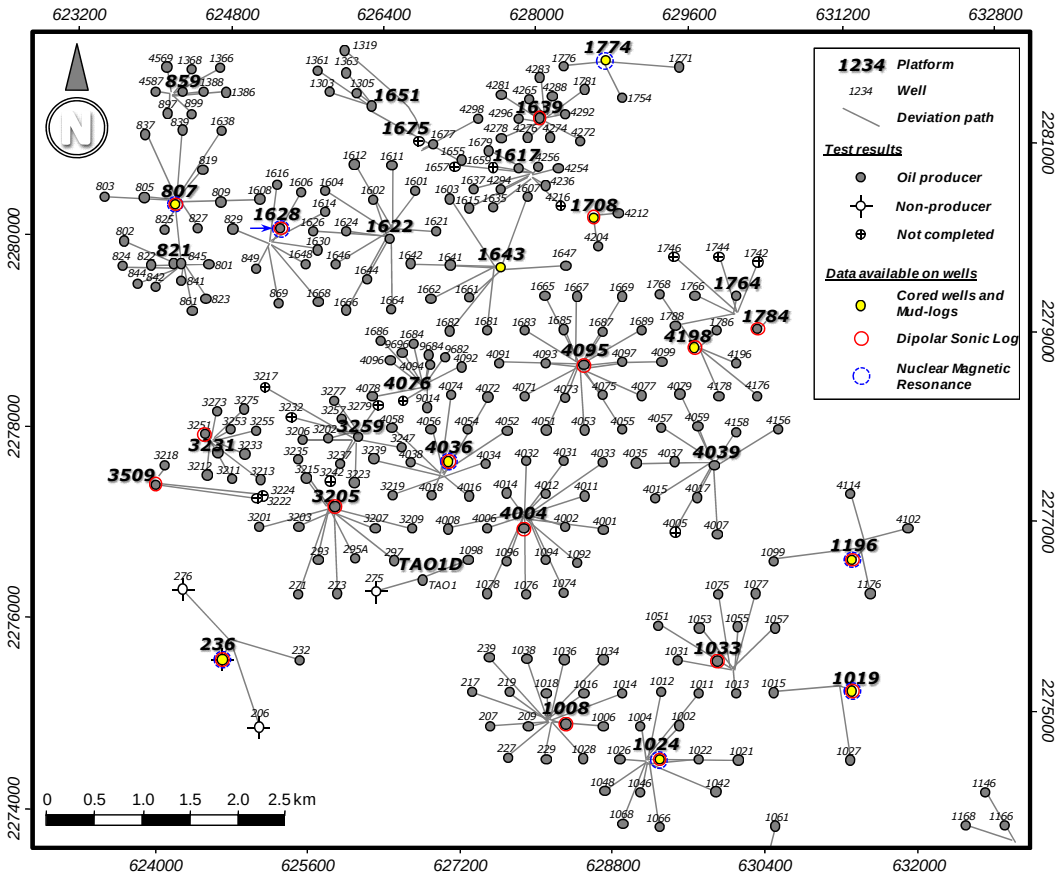

Figure 1.9 Detail of the wells used in the present research project. The figure depicts the 284 wells integrated in this study, all of them with basic well-log data available (*e.g.* gamma-ray, resistivity, neutron, density and sonic logs). Apart from the basic wireline data, eighteen of these wells had special dipolar sonic log (shown with red circle), whereas eight had nuclear magnetic resonance log (shown with dotted blue circle). The wells with core data and mudlog information are displayed in yellow

Special emphasis was given on acquiring both rock and crude-oil samples directly from producing reservoir units and general subsurface information. The data set integrated for this research project is classified into four parts: Reservoir samples, Well-logs, seismic and reports (Fig. 1.10).

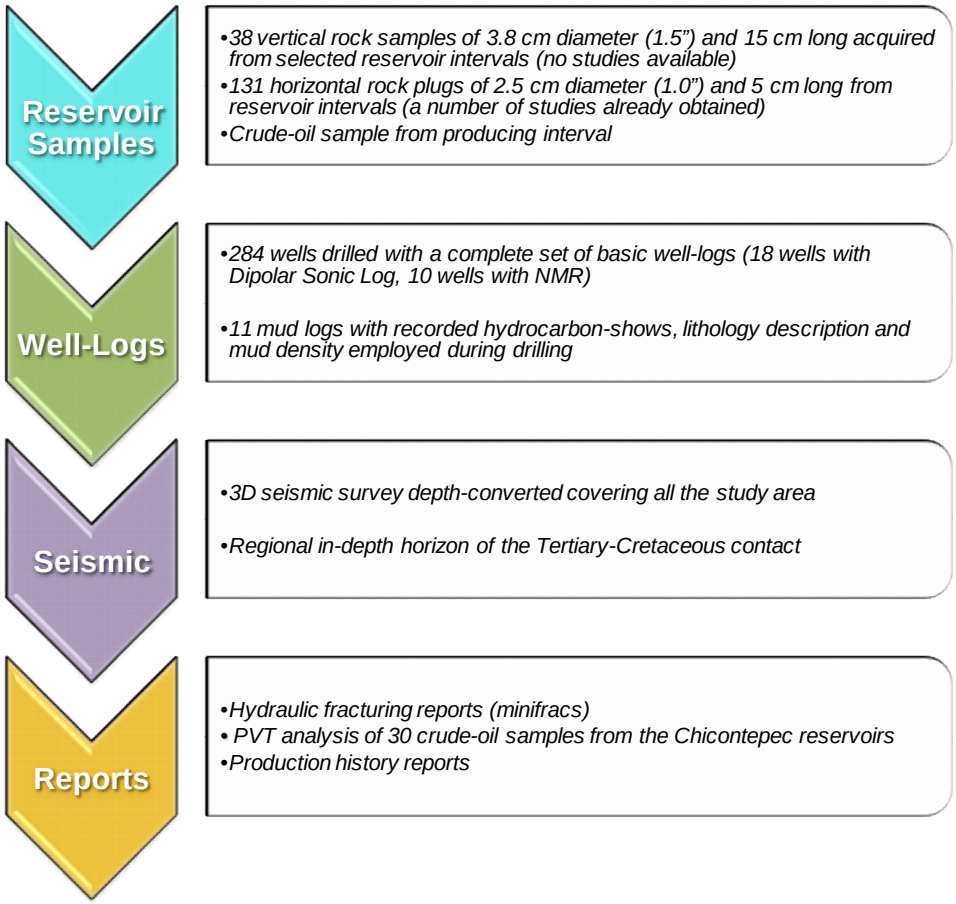

Figure 1.10 Set of information available in the research project

A number of studies were available on the core plugs provided at the start of the project (Table 1.1). The remaining samples, together with a number of these plugs, were employed to conduct complementary studies that included reservoir description and fluid flow experiments. Table 1.2 presents the studies obtained during the development of this research project.

Table 1.1 Core studies available at start up of the research project

Number of samples	Study
96	*Gas Porosity at ambient conditions*
96	*Klinkenberg's permeability* at stress conditions*
113	*Point-count description (300 points)*
113	*Quantitative X-Ray Diffraction (QXRD) mineralogy*
109	*Mercury Injection Capillary Pressure (MICP) curves*
7	*Ultrasonic Elastic Modulus*
7	*Compressibility*
5	*Electrical properties*
2	*Gas-Oil Relative Permeability*

**Instrumentation limit of 0.001 mD*

Table 1.2 Reservoir Description Studies produced in this study

Provided by PEMEX	Obtained in this project	Study
96	*46*	*Gas Porosity at ambient conditions*
96	*46*	*Klinkenberg's permeability at stress conditions*
113	*-*	*Point-count description (300 points)*
113	*33*	*Quantitative X-Ray Diffraction (QXRD) mineralogy*
-	*36*	*Backscattered Electron Microscopy (BSEM)*
109	*33*	*Mercury Injection Capillary Pressure (MICP) curves*
7	*-*	*Ultrasonic Elastic Modulus*
7	*-*	*Compressibility*
-	*35*	*Nuclear Magnetic Resonance (NMR)*
6	*6*	*Cementation Factor (m)*
5	*6*	*Saturation Exponent (n)*
-	*13*	*Surface Area to Volume Ratio (S/V)*
2	*-*	*Gas-Oil Relative Permeability*
-	*4*	*Oil-Water Continuous End-Point Relative Permeability*
-	*10*	*Brine Permeability*

An important element for analysing productivity is the integration of the reservoir geometry and its spatial distribution. This was accomplished by incorporating well-logs and the 3D seismic data. Depth-converted seismic covers the entire study. Additional information such as fracturing reports and production histories of a specific reservoir unit were also available.

Overall, the present project was divided into three workpackages: Reservoir Characterisation, Laboratory Experiments and Reservoir Modelling and Simulation (Fig. 1.11).

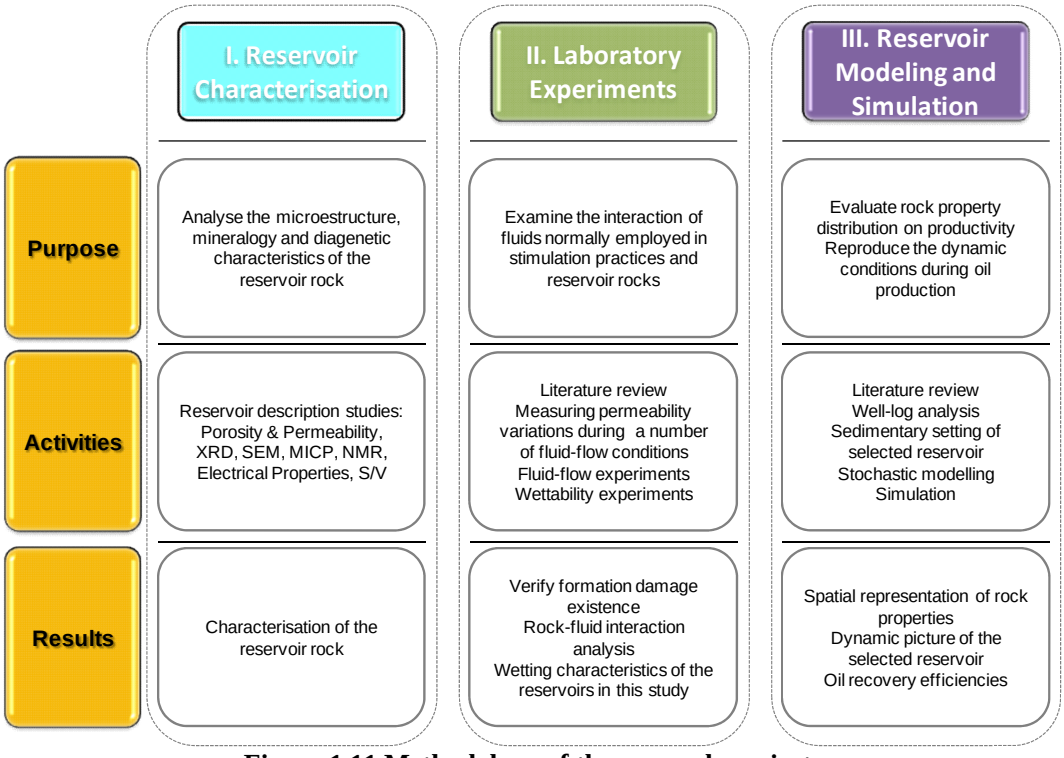

Figure 1.11 Methodology of the research project

Reservoir characterisation involved investigating the variability in the mineralogy and petrophysical properties. The purpose of this phase was to group rock types with similar characteristics. This then allowed the identification of the minerals susceptible to formation damage (*i.e.* permeability impairment), as well as the location of representative rock samples to be used in the next phase of the project.

Laboratory experiments consisted on recreating the conditions resulting from current completion treatments to assess the impact of interaction between stimulation fluids and the reservoir on production. This involved flowing a series of fluids commonly used in fracturing treatments in the study area through core plugs to assess potential formation damage mechanisms and the extent of permeability reduction. Rock-fluid interaction was also complemented with a series of experiments that evaluated the wetting characteristics of the reservoirs together with a series of tests to analyse oil recovery efficiency and asphaltene precipitation of a Chicontepec crude-oil sample.

The last stage consisted of reservoir modelling and simulation. The objective was to represent the likely distribution of rock properties and then to conduct a series of simulation exercises to reproduce the dynamic conditions that occur during petroleum production in these reservoirs (*i.e.* multiphase fluid flow through porous media). This phase was valuable in understanding the oil productivity performance of these reservoirs.

1.3 Thesis Outline

This work begins with an overview of the literature relevant to this topic, as this is concerned with productivity in petroleum reservoirs. General concepts of formation damage and hydraulic fracturing are also presented as these also show to influence productivity.

Chapter 3 looks at the detailed explanation of the descriptive techniques and experimental work conducted in this study. These include the industry standard analyses such as gas porosity, gas permeability, X-Ray Diffraction (XRD), Scanning Electron Microscopy (SEM), Mercury-Injection Capillary Pressure (MICP), Nuclear Magnetic Resonance (NMR) and electrical properties. It also describes complementary techniques that proved to be valuable in increasing the understanding of these reservoirs, such as Surface to Volume ratio (S/V), Inductively Coupled Plasma by atomic emission spectroscopy (ICP-AES), fluid-displacement experiments, and adhesion tests of crude-oil.

Chapter 4 looks at the description of the reservoirs of this study. After presenting the geological background of the Chicontepec basin and defining the stratigraphic framework of the study area, the chapter moves on to describe the main sedimentary characteristics normally observed in cores and outcrops. The reservoir rock characteristics are described separately by their depositional and authigenic features. This was done to evaluate the impact of primary and secondary characteristics of the reservoir rock on the petrophysical properties of the studied reservoirs. To examine the reservoir connectivity and its petrophysical variability, a sedimentary analysis of a selected reservoir in the study area was conducted. The resulted sedimentary interpretation was combined with a number of dynamic data (*e.g.* initial gas oil ratios, crude-oil gravities, produced oil volumes) to evaluate their grade of homogeneity (*i.e.* connectivity). An analysis of the reservoir compartmentalization and likely spatial distribution of the reservoir's architectural elements are presented.

Chapter 5 analyses the petrophysical characteristics of the reservoirs in study based on the integration of direct property measurement from rock plugs. A number of petrophysical properties were obtained from direct rock measurements, which were employed for constructing a series of correlations to help to increase the general understanding of these reservoirs, and for calibrate a number of models used in the well-log analysis. Rock typing was conducted by integrating the mineralogical, textural and petrophysical features of these reservoirs.

Chapter 6 is an extension of the precedent chapter. Petrophysical evaluation of the reservoirs in this study is conducted through the analysis of wireline data. The well-log interpretation described in this chapter was conducted to accomplish two objectives: 1) to evaluate the petrophysical characteristics of the reservoirs; and 2) to provide input data for reservoir

modelling analysis and simulation case scenarios latter described in this work. The chapter first describes the information available and explains the analytical methodology. Then the procedure to estimate the petrophysical properties is presented. These included clay content, porosity, water saturation and permeability estimations. A net-pay sensitivity analysis is also presented to evaluate the volumetric estimation of reserves in these reservoirs. Finally, an analysis of the mechanical behaviour of the reservoirs in this study is conducted. A geomechanical model was developed to improve hydro-fracturing performance in the reservoirs of this study. A correlation between mechanical rock properties and cumulative oil produced was observed in a number of wells in the study area.

Chapter 7 examines formation damage and rock-fluid interaction of the reservoirs in this study. Formation damage is evaluated by three experiments that investigate clay-swelling, particle mobilisation and polymer adhesion in rock plugs as these appear to be the key promoters to permeability reduction in these reservoirs. These experiments were designed intending to replicate the current stimulation practices. Rock-fluid interaction is assessed by a series of tests that evaluate, for example, the preference of a crude-oil sample to be adhered into a particular surface mineral. Three techniques to assess wettability of these reservoirs are also incorporated, which provide a better understanding of their non-uniform nature. Four surfactant solutions are employed to evaluate their capacity to improve oil recovery efficiency. These are assessed by a series of spontaneous imbibition tests. Finally, an experiment to analyse the onset of asphaltene precipitation of a crude-oil sample is presented which is thought to be useful for improving laboratory screening protocols of crude-oils.

Chapter 8 evaluates the impact of the rock property heterogeneity to oil productivity and recovery in a selected reservoir of the study area. Rock properties interpreted from wireline data were modelled using a series of analytical techniques to evaluate their vertical and horizontal variability. These were then upscaled and combined with the interpreted sedimentary facies to predict their likely spatial distribution. The modelled rock properties resulted from this approach were used as input to conduct a number of simulation scenarios to explain the low productivity of these reservoirs. The effect of rock property distribution together with the extension of the induced fracture on oil productivity was analysed.

The controls on production in the Chicontepec oil-bearing reservoirs are discussed in **Chapter 9**, where the descriptive, experimental, and analytical results conducted through the development of this work are integrated. A number of strategies to try to maximize oil production in these reservoirs are described.

Finally, **Chapter 10** presents conclusions from this thesis and recommendation for future work.

CHAPTER II. PRODUCTIVITY

The aim of this chapter is to provide a brief overview of productivity in petroleum reservoirs and to describe general concepts of formation damage and hydraulic fracturing as these also show to influence productivity. The chapter starts by providing basic concepts of productivity and describing some of the variables that are involved during production of hydrocarbons from a wellbore. It then makes reference to the characteristics of siliciclastic reservoirs and points out the importance of permeability as the main physical property of reservoir rocks as this exerts a significant control in fluid-flow. It describes other important variables that contribute to productivity such as the reservoir extension and heterogeneity, the fluid properties and the drive system.

This chapter includes a review of Formation Damage mechanisms and Hydraulic Fracturing; two subjects that are particularly important to understand productivity. Finally, it highlights the potential of formation damage due to hydraulic fracturing treatments.

2.1 Productivity Concepts

Petroleum reservoirs are composed of a unique combination of static (*i.e.* sedimentary geometry, texture, porosity) and dynamic (*i.e.* drive mechanism, fluid composition) properties. Productivity of hydrocarbons is the result of the combination of such characteristics together with the method of exploitation and the stimulation technique. Normally, most prolific reservoirs are composed of homogeneous highly-permeable rocks (*i.e.* permeabilities in the order of Darcies) extended over wide and hydraulically well connected areas. Examples of prolific reservoirs known by their high productivity are the Ghawar oilfield in Saudi Arabia, the Burgan oilfield in Kuwait and the Forties oilfield in the UK.

Productivity of a well is synthesised by Ahmed (2006) in Figure 2.1, which applies to vertical wells producing liquids in a radial flow pattern. This conceptual model illustrates a homogeneous reservoir composed of a single isotropic bed, although in reality, the reservoirs are constituted of multiple layers with a variety of petrophysical properties, normally interbedded with impermeable beds.

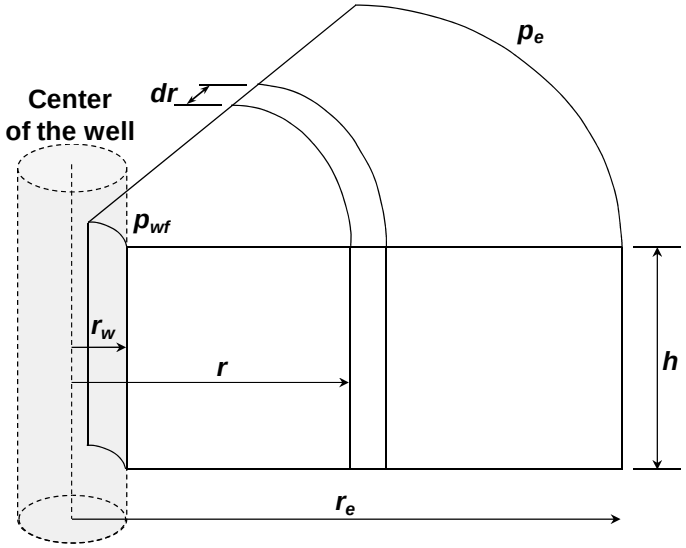

Figure 2.1 Radial flow model of oil productivity (adapted from Ahmed, 2006)

Assuming this ideal model, oil flow rate (Q_o) is defined as the relation of the reservoir rock physical properties (*e.g.* permeability, thickness), the fluid properties, and how homogeneous the rock properties are distributed (*i.e.* expressed as the extent of pressure disturbance), as:

$$Q_o = \frac{0.00708kh(p_e - p_{wf})}{\mu_o B_o ln(r_e/r_w)}$$

Drainage radius (r_e) can be expressed in terms of the area of the well spacing with that of a circle:

$$r_e^2 = \frac{43560A}{\pi}$$

And productivity index (J) is then defined as:

$$J = \frac{Q_o}{P_e - P_{wf}} = \frac{Q_o}{\Delta P}$$

where: Q_o= oil flow rate (STB/day), p_e= external pressure (psi), p_{wf}= bottom-hole flowing pressure (psi), k= permeability (mD), μ_o= oil viscosity (cP), B_o= oil formation volume factor (rb/STB), h= thickness (ft), r_e= external or drainage radius (ft), r_w= wellbore radius (ft), A= well drainage (acres).

Rewriting the flow equation incorporating the skin factor (s) that accounts for a damaged region in wells stimulated by a hydraulic fracture (Fig. 2.2), it is deducted that oil productivity is strongly controlled not only by the extent of the damaged area, but also by its reduced permeability (Ahmed, 2006):

$$Q_o = \frac{0.00708kh(p_e - p_{wf})}{\mu_o B_o \left[\ln\frac{r_e}{r_w} + s\right]}$$

where the skin factor (*s*) is defined as:

$$s = \left[\frac{k}{k_{skin}} - 1\right] \ln\left(\frac{r_{skin}}{r_w}\right)$$

where: *s* refers to the skin factor (dimensionless), k_{skin} is the permeability of the skin zone (mD), and r_{skin} is the extent of the damaged zone (ft). No damage is produced and consequently no changes in oil productivity will be observed if $k_{skin}=k$.

For wells that have been stimulated by hydraulic fracturing as of the Chicontepec wells, Cinco-Ley and Samaniego (1981) proposed the model shown in Figure 2.2. The pressure transient for a well intercepted by a finite conductivity vertical fracture (**case a** in Figure 2.2) with half-length (X_f), width (b_f), and permeability (k_f), is given by:

$$P_{wD} = f\left(\left(k_f b_f\right)_D, t_{DXf}\right)$$

where P_{wD}, $\left(k_f b_f\right)_D$, and t_{DXf} represent the dimensionless pressure, dimensionless fracture conductivity and the dimensionless fracture time, respectively.

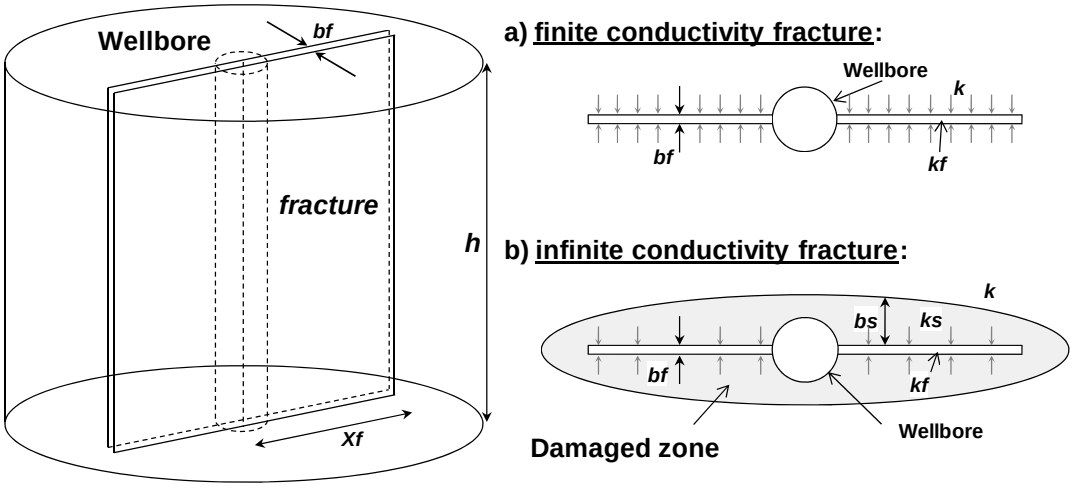

Figure 2.2 Two scenarios of a well intersected by a vertical fracture: a) finite conductivity fracture (no damage); and b) infinite conductivity damaged fracture (modified from Cinco-Ley and Samaniego, 1981)

For oil:

$$P_{wD} = \frac{0.00708khh\Delta P}{Q_o \mu_o B_o}$$

$$\left(k_f b_f\right)_D = \frac{k_f b_f}{kX_f}$$

$$t_{DXf} = \frac{2.637 \times 10^{-4} kt}{\emptyset \mu C_t X_f^2}$$

where: $\emptyset$ is the fracture porosity, k is the formation permeability, μ is the fracture fluid viscosity, t is the time, and C_t is the total compressibility.

Cinco-Ley and Samaniego (1981) assumed that any linear inflow from the formation into the fracture has to pass through this damage region. The pressure behaviour for an infinite conductivity fracture with a damaged region may be expressed as:

$$P_{wD} = f\left(t_{DXf}, S_{fs}\right)$$

where S_{fs} is the fracture face skin defined by Cinco-Ley and Samaniego (1981) as:

$$S_{fs} = \frac{\pi b_s}{2X_f}\left(\frac{k}{k_s} - 1\right)$$

where: k is the formation permeability.

It is deducted by previous equations that the oil flow rate (Q_o) is strongly influenced by the geometry of the induced fracture (X_f, b_f, h), the physical properties of formation (*e.g.* permeability, thickness), the fluid properties (B_o, μ_o), and the degree and extent of the fracture damage (k_s, b_s,).

As observed, productivity is directly proportional to permeability, thickness and pressure drop around the well. The internal reservoir framework together with its petrophysical variations are intrinsically expressed by the extension of the pressure disturbance. For example, the extension of the pressure disturbance in low-permeability reservoirs (or in reservoirs with a limited continuity due to their sedimentary architecture) will describe shorter external distances in comparison to high-permeability reservoirs. This is normally translated into the well's drainage coverage.

Permeability is possibly the most important reservoir rock physical property as oil may flow much more easily through high-permeable, low-tortuous pathways. Permeability variations (*i.e.* heterogeneity) are also important in controlling oil productivity and in siliciclastic reservoirs are

mainly controlled by the depositional system (Tyler and Finley, 1992). Permeability of clastic reservoirs is largely controlled by a combination of the depositional characteristics such as their detrital grain-size and shape, sorting, mineral fractions, burial history; and the process taking place during lithification (*i.e.* diagenesis). There is no intention to give a detailed coverage on this matter; however, it is important to mention them for understanding the permeability nature of terrigenous reservoirs.

The primary drive mechanism is also important to evaluate productivity. The drive mechanism reflects the oil recovery without the use of any process to supplement the natural energy of the reservoir. A summary of the drive mechanisms and their recovery efficiencies are presented by Ahmed (2006) in Table 2.1.

Table 2.1 Drive Mechanisms and Typical Recovery Ranges

Drive Mechanism	Oil Recovery Range (% of OOIP)
Solution Gas drive	*5 to 30%*
Gas Cap drive	*20 to 40%*
Water drive	*35 to 75%*
Gravity Drainage drive	*Up to 80%*

Tyler and Finley (1992) showed that recovery efficiencies of a number of reservoirs in Texas can be linked to their depositional system and drive energy (Fig. 2.3). This illustrates the importance of the depositional characteristics and their drive energy in clastic reservoirs.

Figure 2.3 describes an interesting relationship that demonstrates the importance of the reservoir's architectural elements and drive mechanisms on recovery efficiencies. Observe, for example, that the combination of sand-rich sedimentary systems (*e.g.* deltaic) with gravity drainage or water drive mechanisms, normally results into greater recovery efficiencies. The Chicontepec reservoir units can be fitted into the worst recovery scenario shown in Figure 2.3, as these are generally referred to as submarine fan systems with primary energy supplied by solution gas.

In the following sections, there will be described two important subjects that also contribute to productivity: formation damage and hydraulic fracturing. The increasing interest on unconventional reservoirs has permitted the development of more sophisticated techniques of completion and stimulation. Among these new practices, formation damage analysis and hydraulic fracturing treatments deserve special attention as these play an important role. These areas are described in the following paragraphs.

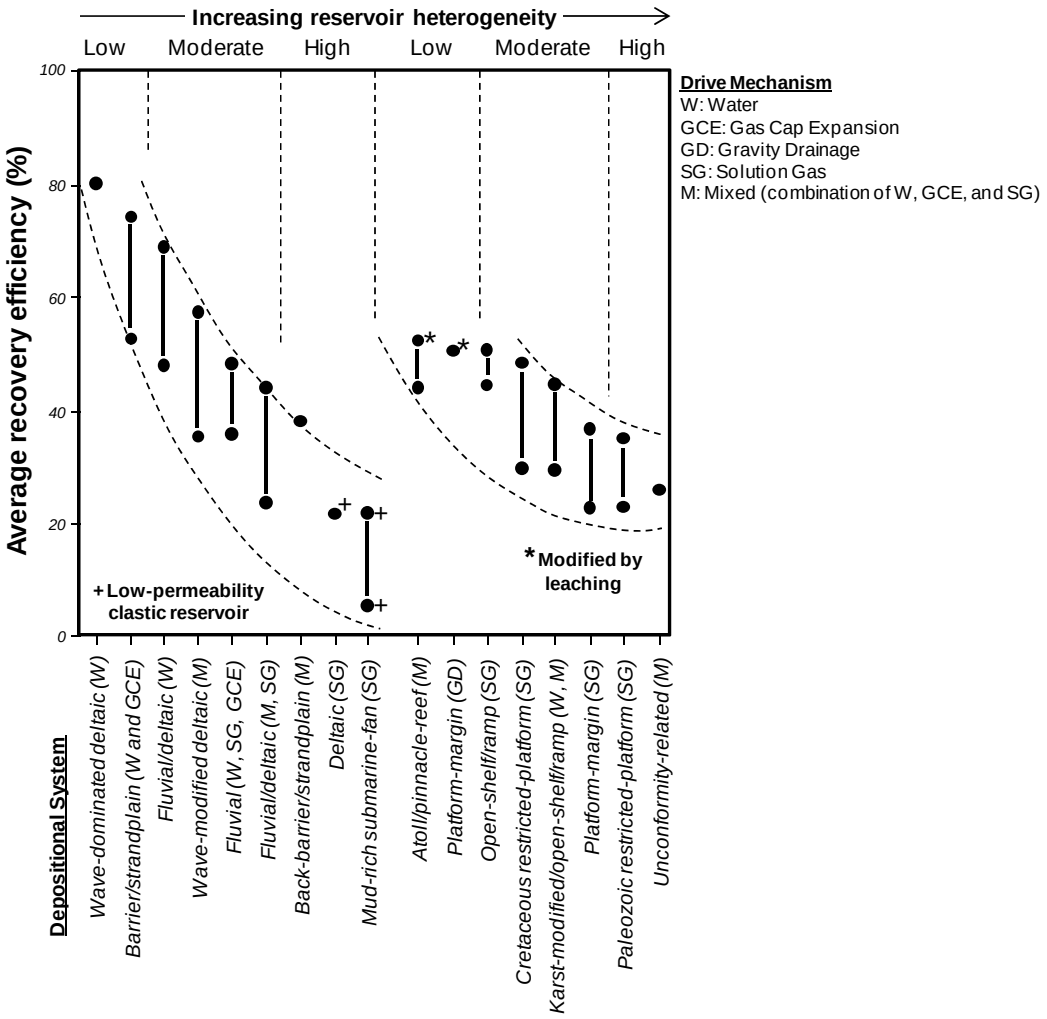

Figure 2.3 Recovery efficiencies of a number of clastic and carbonate reservoirs versus depositional system and drive mechanism (modified from Tyler and Finley, 1992)

2.2 Formation Damage

Formation damage is a broad term referred to the reduction of permeability of hydrocarbon reservoirs, as consequence of the diverse activities related to their exploitation. These include almost the entire spectrum of petroleum development operations: drilling, cementing, perforating, completion, stimulating, production and EOR practises (*e.g.* chemical, steam injection). Bennion (2002) described formation damage as: "*...any process that causes a reduction in the natural inherent productivity of an oil or gas producing formation; or a reduction in the injectivity of a water or gas injection well...*"

Formation damage has been recognized as a significant, probably unavoidable, problem in most reservoirs, affecting the ultimate oil recovery and consequently, reducing the profitability of petroleum development projects. It has been argued that any foreign fluid injected into a formation will do some damage (MacDonald and Chenery, 1988) and even the natural reservoir depletion during oil production is prone to reduce permeability in certain formations (Soares *et al.*, 2003).

The causes of permeability impairment have been described by many authors (*e.g.* Keelan and Koepf, 1977; Porter, 1989; Masikewich and Bennion, 1999; Doane *et al.*, 1999; Bennion *et al.*, 1998; Bennion, 2002; Bishop, 1997; Bennion *et al.*, 1995; Bennion and Thomas, 1994; Civan, 2007). These, are generically classified by Civan (1996) according to their physico-chemical, chemical, hydrodynamic, thermal, mechanical and biological interactions among native and foreign substances.

Bennion (2002) presents what is possibly the most comprehensive classification of formation damage (Figure 2.4). Each mechanism impacts permeability in a different manner, with certain mechanisms having more severe effects than others depending on the particular reservoir conditions and the method of exploitation (*i.e.* drilling mud type, completion fluids, stimulation method). In general, the effects of formation damage are particularly drastic in low-permeability formations, as capillary forces are stronger and the damaging fluids are more difficult to remove (Ding *et al.*, 2012).

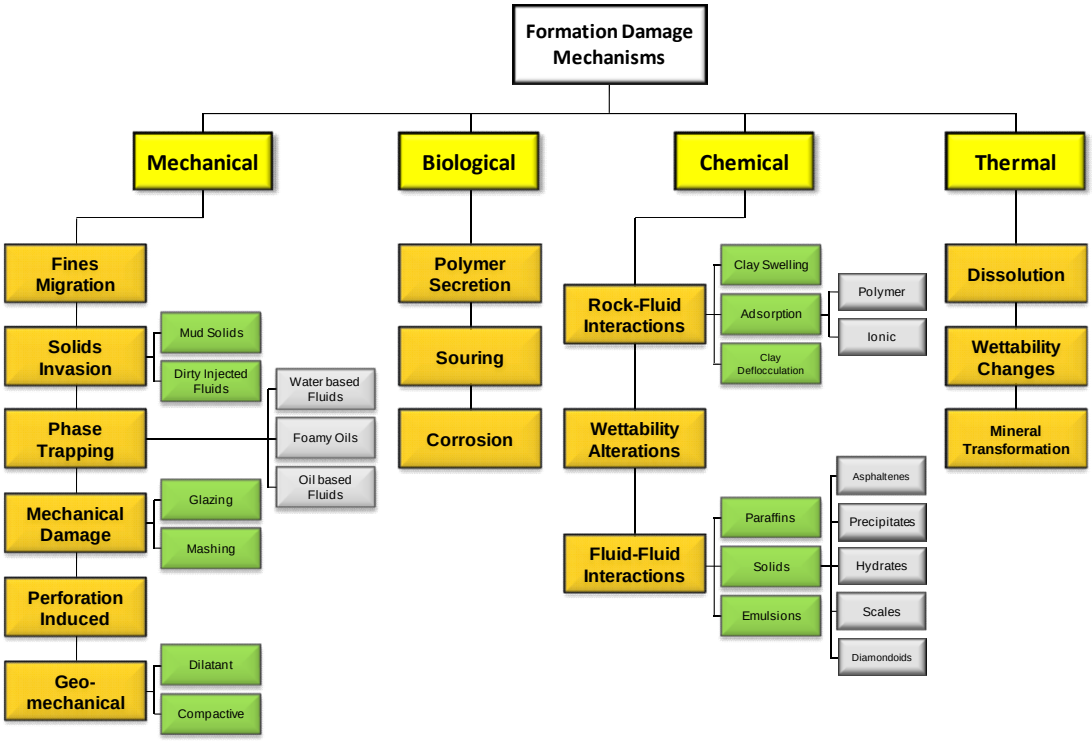

Figure 2.4 Common Formation Damage mechanisms (modified from Bennion, 2002)

There is certain tendency to refer to formation damage as occurring exclusively in the near wellbore region as a result of drilling fluid invasion (Al-Marhoon *et al.*, 1998; Audibert *et al.*, 1999; Byrne *et al.*, 2007; Ding, 2010). The damaged area may be reduced by underbalanced drilling or bypassing the invaded zone using deep-penetration perforations or hydraulic fracturing. Nevertheless, it has been shown that underbalanced drilling is also capable of promoting damage (Ding *et al.*, 2004; Moghadasi *et al.*, 2010); while Volk *et al.*, (1983) and Chen *et al.*, (2006) demonstrated that fracturing fluids may also incur in permeability impairment.

In this way, formation damage is a phenomenon that depends on the specific reservoir characteristics and the development method. Amaefule *et al.*, (1987) and Porter (1989) stated that formation damage analysis should be addressed using a multi-disciplinary and integrated view to produce a proper customized solution for the reservoir in study.

Formation Damage has been a recurring subject that has been mentioned in the literature as: “geochemical formation damage” (Riese and Riese, 1968), “storage formation damage” (Bomar and Dereniewski, 1997), “clay damage” (Da Motta and Dos Santos, 1999), “organic skin damage” (Newberry and Barker, 2000), “mechanical formation damage” (Soares and Ferreira, 2002; Soares *et al.*, 2002.), “brine imbibition damage” (Erwin *et al.*, 2006), “permeability damage” (Ali and Currie, 2005; Andesina *et al.*, 2010) and more recently “hydraulic damage” (Ding *et al.*, 2012). All of these referring to either permeability reduction or hydrocarbon

production decrease. There is no a unified classification of formation damage, as new mechanisms are continuously recognised. The classification from Bennion (2002) offers a generic approach, allowing the incorporation of new mechanisms into this categorization.

In the following sections, the mechanisms of formation damage will be described according to the categories presented by Bennion (2002).

2.2.1 Mechanical

Mechanical formation damage refers to the direct, non-chemical interaction between native and foreign materials. This is subdivided according to physical interrelations (Fig. 2.4).

Fines migration is associated to the motion of naturally existing particles in the pore system caused by high fluid shear rates (Bennion, 2002). These particles are frequently loosely attached to formation and may include detrital rock fragments, unconsolidated grains and authigenic minerals. Kaolinite is usually identified as the main migratory clay, although illite clay may also be subjected to mobilization (Mohan and Fogler, 1997). Permeability reduction caused by fines migration is associated with the gradual blocking effect, which tends to plug pore throats resulting in a reduction of permeability. Since fines generally tend to migrate fairly exclusively in the phase that wets the rock (Bennion *et al.,* 1995), fines migration is strongly dependant on reservoir wettability. Fines migration (also known as velocity-induced damage) is usually considered as near wellbore effect in vertical producing wells (Huang *et al.,* 2010) as interstitial velocity is more severe in this region. Yang and Sharma (1991) demonstrated that the alkaline nature of cement filtrates tends to release fines.

Solids invasion occurs by the incursion of external solids into formation pore space, particularly from drilling mud. Weighting agents, fluid additives, lost circulation materials and fluid control substances are the common suspended particles in drilling fluids prone to develop solids invasion (Bennion *et al.,* 2002). This process is frequently originated by overbalanced drilling and it is generally confined to short distances from the wellbore. In some cases where permeability is extremely high, or in a pressure depleted reservoirs; the extent of solids invasion describes greater distances (Bennion *et al.,* 1995).

Water injection, employed either for completion, stimulation or waterflooding, may transport either colloidal (*i.e.* less than 1µm) or suspended solids prone to plug the near injection face region (Bennion *et al.,* 1998). Formation fines and clays from previously produced water, suspended sand, silt, carbonate fines, corrosion products, and even bacteria, would be some examples of the solid particles suspended in water. The mechanism is mitigated by filtrating or centrifuging the fluids prior to be employed for injection.

Phase trapping is defined by Bennion *et al.,* (2006) as: "*...the temporary or permanent trapping of oil- or water-based fluids introduced into a porous media which result in a reduction in the effective permeability to the desired producing or injected phase...*" It is the result of the invasion and retention of high oil, gas or water saturation in the near wellbore region, reducing productivity. Phase trapping is especially important in low permeability reservoirs, since capillary forces are stronger. Phase trapping is caused by the interaction of capillary pressure and relative permeability phenomena (Bennion *et al.,* 2006) and it has been mentioned as one of the few types of damage that is able to cause total occlusion of permeability (Bennion, 2002).

An example of phase trapping would be in a gas-producing formation in which water may be trapped in the near wellbore region as consequence of the employment of water-based drilling fluids. The increase of water saturation in the vicinity of the wellbore may reduce the relative permeability to gas, which ultimately reduced gas production rates.

Similarly, in an oil-producing formation, gas may be trapped as a consequence of the employment of aerated fluids, foams or nitrogen energized fluids (Bennion, 2002). The natural gas liberation during sub-bubble point production may also result in the creation of trapped gas saturation.

The employment of surface tension reducer agents (*e.g.* surfactants, alcohols, energized gases) to lower capillary pressure is a commonly used technique to reduce the effects of phase trapping. Other alternatives include performing high drawdown pressures to recover the trapped fluid; increasing the reservoir's pressure, or using wettability modifiers (Bennion *et al.,* 2006).

Mechanical formation damage by **glazing** process refers to the direct damage of the wellbore face as consequence of the heat generated by the bit during drilling, which results in the creation of a thin, usually impermeable film (glazing) of ceramic-like material. This can occur when drilling mud has insufficient heat capacity to cool and lubricate the bit-rock interface, particularly in air-drilled wells and in open-hole completions (Bennion and Thomas, 1994; Bennion *et al.,* 2000). It only affects the rock very close to the wellbore so may be bypassed by conventional perforations in cased-holes. Glazing is avoided by the use of drilling mud lubricants or increasing the mud's pumping rate, to favour circulation and diminish bit/rock temperature. **Mashing** is produced by small drill cuttings and fines attached to the formation face as consequence of a sliding drill pipe or poor drill string centralization (Bennion *et al.,* 2000). As similar to glazing, mashing is reduced by efficient cleaning and conditioning to avoid large amounts of solids in the wellbore (Bennion, 1999).

The detonation of **perforation** charges may result in the creation of a crushed zone that generates mobile fines adjacent to the perforation tunnel (Bennion, 2002), which may reduce well productivity. Nabipour *et al.,* (2010) demonstrated that the extent of the damaged zone in perforated sandstone samples is influenced by particle size distribution, porosity, and magnitude of in-situ stress. Its effect is partially controlled by employing high-penetration, low-residue charges.

Geomechanical induced formation damage refers to the distortion of the stress regime caused by drilling, completion and production operations. This alteration causes irreversible reduction of rock strength which may reduce the rock flow properties (Thallak *et al.,* 1993). Tensile or compressive stress fields can be induced in the near wellbore region, depending on well orientation relative to the *in situ* tensor (Bennion, 2002). Examples of geomechanical damage include the deformation of casings (Bruno, 2002) and pore collapse as a result of pressure depletion (Soares *et al.*, 2003). In hydraulically fractured reservoirs, proppant may be crushed and form fines as consequence of the increasing effective stress during production (*i.e.* pore-pressure depletion). This type of damage has been referred as mechanically induced fracture face skin (Reinicke *et al.,* 2011) and is becoming particularly important in unconventional reservoirs.

2.2.2 Biological

Formation damage by biological processes is almost entirely as a result of bacterial growth. This may promote plugging, corrosion or souring in reservoirs. Most bacteria secrete polymeric compounds naturally that potentially can be attached to the rock surface and plug the formation. Similarly, some types of bacteria set up an electro-kinetic hydrogen reduction reaction, which may create corrosion in metallic surfaces (pipes or surface facilities). Other bacteria groups known as sulphate reducing bacteria are able to reduce sulphate present in both formation and injection waters resulting in H_2S generation, which increases the fluid toxicity and can lead to scaling and corrosion.

Bacterial growth is a function of temperature and nutrients supply (Bennion, 2002). Hayatdavoudi and Ghalambor (1996a) demonstrated that certain minerals, like calcite and olivine, may provide enough nutrients for bacteria proliferation.

2.2.3 Chemical

Chemical formation damage refers to the molecular interaction of native formation components and foreign materials. Three associated mechanisms of chemical formation damage are

recognised (Bennion, 2002): rock-fluid interaction, rock-rock interaction and wettability alteration.

Clay swelling is probably one of the most referred formation damage by **rock-fluid interaction** in the literature, apart from fines migration. It consists of the hydration of certain clay minerals such as smectite (*e.g.* montmorillonite, saponite) and mixed-layer groups. The negative charge of smectite platelets is balanced by means of the positive charge of K^+, Na^+, Ca^{2+} and Mg^{2+} cations, keeping platelets dehydrated. When exposed to low-ionic strength aqueous solutions (*i.e.* low-salinity or fresh fluids), the interlayer cations adsorb water molecules resulting in swelling (Fig. 2.5). Hydratated smectites can expand as much as 1000% of their volume (Davies, 1980).

Clay swelling, also referred as "water sensitive" formations, may be prevented by maintaining high concentrations of the K^+ cation in aqueous solutions, which maintains clay platelets in a dehydrated state. The relative small size of K^+ compared to larger molecular cations such as Na^+, Li^+, Ca^{+2} and Mg^{+2}; permits a better fitting into the clay flakes. Bennion (2002) states that using high salinity fluids, glycols, cationic polymers and amines, are useful to maintain clays stabilized. Hydration of clays is also controlled using hydroxyl-aluminium solutions (Reed, 1972, 1974).

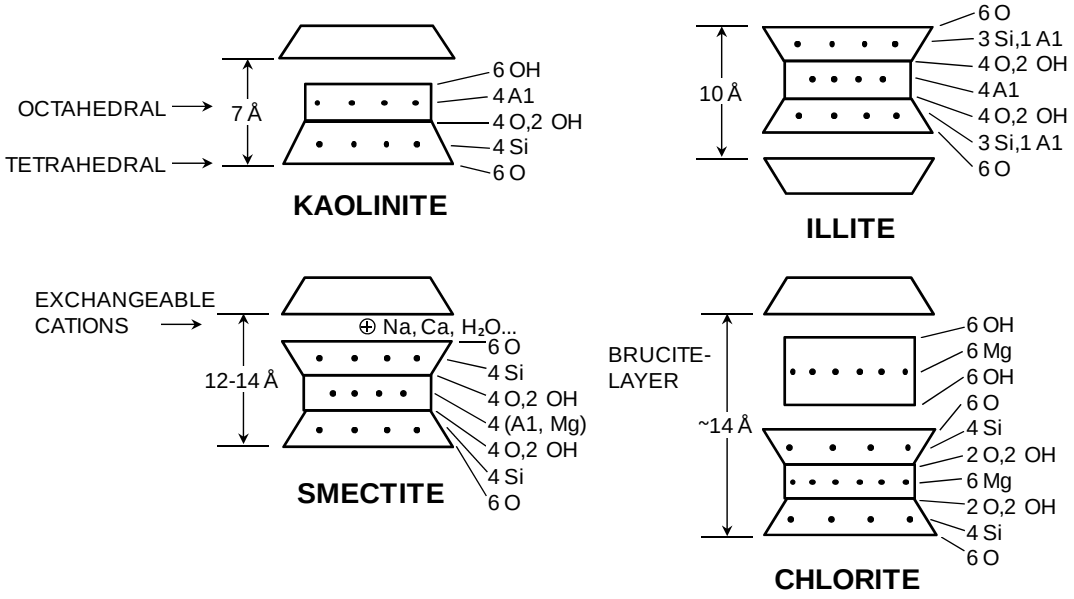

Figure 2.5 Structural components of clay minerals (modified from Pittman, 1989)

Adsorption is associated to the occurrence of polymers and other high molecular weight materials in treatment fluids, which tend to be physically adsorbed by formation minerals. As a consequence of their large molecular size, they may reduce pore space affecting permeability. Another documented effect is the alteration of wettability, generally to a more oil-wet state

(Bennion *et al.*, 1998). Common materials used in the industry prone to be adsorbed are: de-emulsifiers, surfactants, corrosion inhibitors, fluid thickeners and scale inhibitors.

Wettability alteration has also been associated to the adsorption of polar organic components such as resins and asphaltenes (Bennett *et al.*, 2004). Durand and Rosenberg (1998) reported that wettability is also influenced by the type, morphology, quantity, and distribution of clay minerals in clay-bearing reservoirs. Buckley and Liu (1998) demonstrated the relative dependence of water salinity, crude-oil's asphaltene content and temperature on wettability alteration. Wettability alteration from a water-wet to oil-wet conditions, may lead to a significant reduction in the relative permeability to oil, which is translated into higher residual-oil saturations and lower oil recoveries.

Clay deflocculation is referred to the disturbance of electrostatic forces that are responsible for the attachment of clays to pore walls. An abrupt change in divalent ion concentration from high to low (*i.e.* low salinity water) or a rapid transition of pH (generally to a more caustic state) can induce deflocculation, which can be even as severe as clay swelling (Bennion, 2002). Kaolinite, which forms as booklets or stacks of pseudo-hexagonal crystals (Fig. 2.6), is an example of non-water sensitive clay that may deflocculate (Mungan, 1965).

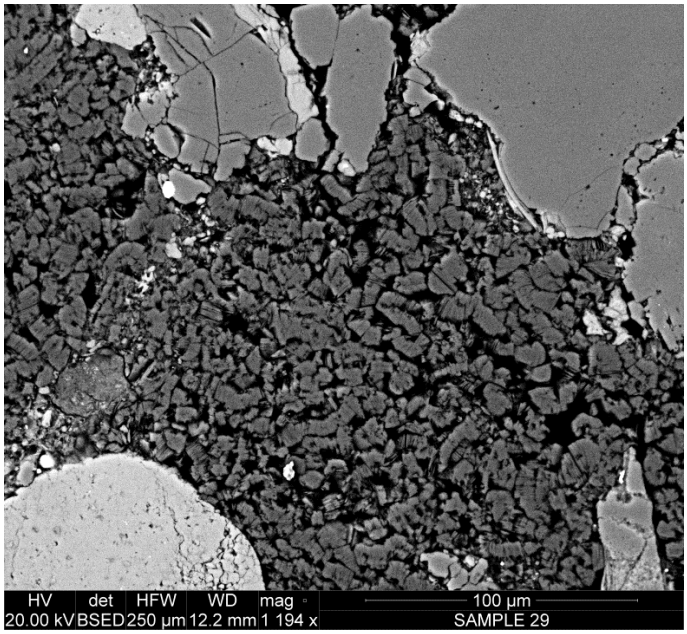

Figure 2.6 Pore-filling kaolinite booklets in a Chicontepec reservoir rock

Bennion *et al.* (1998) states that the water salinity required to maintain aggregated clays (*i.e.* flocculated) increases with increasing cation exchange capacity (CEC). However, examples of formation damage induced by high-salinity brines are also documented (Cikes *et al.*, 1990; Bishop, 1997). This exemplifies the importance of employing the proper fluid salinity according to the specific reservoir conditions.

In general, avoiding pH shocks may reduce the effects of this mechanism. The employment of KCl or NH_4Cl as additives in the treatment water is a common practice in the industry. However, even when KCl solutions are effective in eliminating damage in the pH range of 3 to 7, they do damage at pH values of 9 or greater (Keelan and Koepf, 1977).

Morphology and distribution of clay minerals is of particular importance in the analysis of formation damage. Many types of clay in siliciclastic reservoirs are authigenic (Pittman, 1989), which means that they grow in or around existent grains within the pore space. Authigenic clay minerals are generally loosely attached to detrital fragments as grain-coating, pore-lining, pore-bridging or pore-filling morphologies (Neasham, 1977).

Formation damage by **fluid-fluid interaction** refers to the precipitation of hydrocarbon scales, particularly in the perforation region, wellbore or surface facilities. These include the deposition of paraffin and waxes from producing crude oils. Asphaltene and diamondoids may also precipitate from reservoir fluids and cause plugging. The application of both heat and chemical solvents is routinely used to mitigate the effects of this mechanism.

2.2.4 Thermal

Thermal formation damage refers to permeability reduction through the increase of temperature. This process applies almost exclusively to steam injection or in-situ combustion, performed to enhance oil recovery. The sudden temperature increase as result of steam injection may alter permeability by either expansion or contraction of grains (Civan, 2008). The increase in temperature has also been documented as responsible of creating fines mobilization (Gunter *et al.*, 1994; Hayatdavoudi and Ghalambor, 1996a, 1998) and inducing wettability changes (Schembre and Kovscek, 2004; Bennion and Thomas, 1992; Bennion, 2002). Thermal damage may also cause mineral transformations and mineral dissolution (Bennion and Thomas, 1992).

2.3 Hydraulic Fracturing

Hydraulic fracturing (*i.e.* fracturing, hydrofrac, frac or fracking) is a widely used technique, usually applied in low-permeability rocks, that aims to increase conductive paths between the formation and wellbore (Fig. 2.7). A fracture is artificially created by pumping fluids into rock, which is then often propped with ceramic or silica sand grains to prevent fracture closure as the well is put on production. Hydraulic fracturing increases the wellbore drainage coverage, which enhances productivity and ultimate hydrocarbon recovery. This technology has been used for over 60 years in more than one million wells (Sun *et al.,* 2011) and its application is under continuous development.

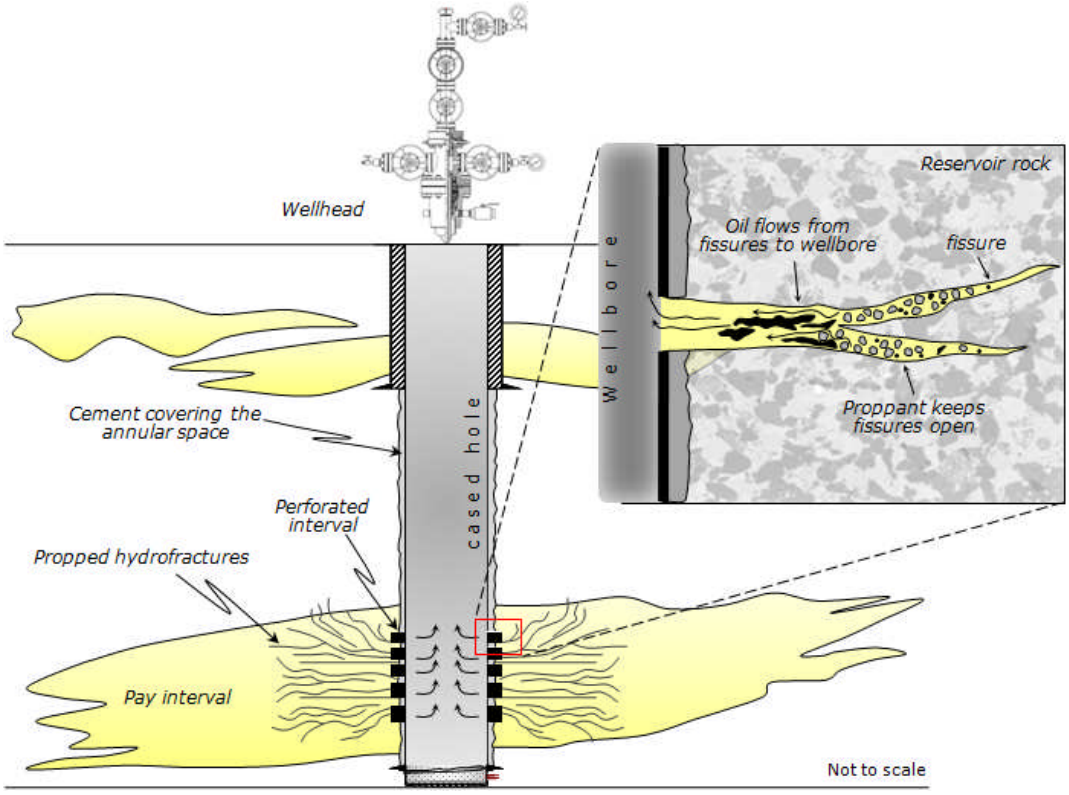

Figure 2.7 Diagram of the completion design in the study area

Hydraulic fracturing technology has significantly improved the development of unconventional resources, and its employment has changed radically the world's energy picture. King (2012) shows how the development and application of technologies have increased the gas recoveries in US unconventional reservoirs (Table 2.2).

Different strategies are used for fracturing depending on the type of reservoir to be stimulated. For example, massive hydraulic fractures are formed using in the order of million gallons of water and up to 5 million pounds of proppant (EPA, 2011). On the other hand, most fracturing

treatments average 60,000 gallons of fluid and 100,000 pounds of proppant (Montgomery and Smith, 2010).

Table 2.2 Technology Development Impact on Gas recovery in Shale Gas Reservoirs

Year	Technology applied	%OGIP* Recovery
1980's	*Vertical wells, low rate gel fracs*	*1%*
1990's	*Foam fracs, 1st slickwater in shale*	*1.5 to 2%*
2001	*High rate slickwater fracs*	*2 to 4%*
2004	*Horizontal well dominant, 2 to 4 fracs*	*5 to 8%*
2006	*Horizontal wells, 6 to 8 fracs, water recycle trial*	*8 to 12%*
2008	*+16 fracs per well*	*12 to 30%*
2010	*Technology to flatten decline curve, feeling pinch for frac water*	*30 to 40%*
2011	*Pad development drains 5000 acres, salt water displacing fresh for fracs*	*+45%*
Future	*Green chemicals, salt water fracs, low disposal volume, reduced truck traffic, pad drilling, electric rigs and pumps*	*project 45 to 55%*

**OGIP: Original Gas in Place*

The mixture of materials employed during fracturing has varied substantially since the technique was experimentally applied in a gas reservoir in Kansas (USA) in 1947 (Montgomery and Smith, 2010). Initially, oil-based treatment fluids were employed (*e.g.* gelled-crude, kerosene, crude-oil and even napalm were used), progressively changing to water-base fluids, widely used today.

A variety of fluid mixtures are employed for hydraulic fracturing, such as water, foam, oil, acid, alcohol, emulsion and cryogenic gases (Gandossi, 2013). Water-based fluids are now most commonly used as they show better cost-effective solutions in comparison to the rest. However, a growing interest exists to employ non water-based fluids due to environmental concerns and formation damage prevention. Ribeiro and Sharma (2013) presented a comprehensive analysis for selecting fracturing fluids.

In general, the greater and more complex the fracture geometry is, the better the productivity (Mayerhofer *et al.*, 2010). To achieve this, water-based fracturing fluids are prepared employing a number of formulations, namely slickwater, linear fluids, crosslinked fluids and viscoelastic surfactant fluids (VES).

Slickwater (sometimes referred to as a waterfrac or riverfrac) is basically water combined with a friction reducer for maximising fluid pumping. Slickwater is a low-viscosity fluid and thus a poor proppant carrier. Waterfracs are usually employed in areas with low-stress anisotropy and normally develop complex fracture geometries resulting in greater stimulated volumes (Warpinski *et al.*, 2005) in comparison to gel-based fractures. As slickwater is gel-free, formation damage by polymer adsorption is avoided (Palisch *et al.*, 2008).

For keeping proppant suspended and also to increase proppant placement, the fracturing fluids are thickened by a wide range of polymers. These polymers are dry powders that swell when mixed in aqueous solutions forming a viscous gel. Polymer-based fluids are generically named as linear or conventional gels. Polymers employed in these formulations are generally cellulose or guar derivatives: guar, hydroxypropyl guar (HPG), carboxymethyl hydroxypropyl guar (CMHPG), hydroxyethyl cellulose (HEC), carboxymethyl cellulose (CMC), carboxymethyl hydroxyethyl cellulose (CMHEC).

Linear gel performance is improved by employing crosslinkers that increase fluid viscosity without increasing polymer concentration. Borate is a widely used crosslinker used to prepare more viscous formulations for better transporting capabilities. Zirconium (Zr), titanium (Ti) and aluminium (Al) are also employed. Crosslinking is reversible and controlled by pH changes, which helps the flowback and cleanup process. Crosslinked fluids are employed in a wide range of operating conditions; apart from provide a stable rheology and efficient proppant suspension.

VES is a different family of fluids that have been used for hydraulic fracturing and matrix acidizing treatments. VES is a surfactant combined with inorganic salts that create entangled structures to form networks that exhibit viscoelastic behaviour (Yu and Nasr-El-Din, 2009). VES improves the management of suspension properties at lower viscosities and reduced interfacial tensions than polymer-based formulations (Samuel *et al.,* 2000). VES fluids prevent formation damage by polymer adsorption or biological secretion as they do not contain organic polymers.

Table 2.3 shows the different fluids employed for hydraulic fracturing (adapted from EPA, 2011; Gandossi, 2013).

Table 2.3 Types of fluid employed for hydraulic fracturing

Base Fluid	Fluid Type	Main Composition
Water	*Slickwater*	*water + sand + chemical additives*
	Linear	*gelled water, GUAR<HPG, HEC, CMHPG*
	Crosslinked	*crosslinker + GUAR, HPG, CMHPG,*
	Viscoelastic	*CMHEC*
	surfactant	*electrolyte + surfactant*
Foam	*Water-based*	*water and foamer +N_2 or CO_2*
	Acid-based	*acid and foamer +N_2*
	Alcohol-based	*methanol and foamer +N_2*
Oil	*Linear*	*oil, gelled oil*
	Crosslinked	*phosphate ester gels*
	Water Emulsion	*water + oil + emulsifiers*
Acid	*Linear*	-
	Crosslinked	-
	Oil Emulsion	-
Alcohol	*Methanol/water*	*methanol + water*
	Only Methanol	
Emulsion	*Water-oil*	*water + oil*
	CO_2-methanol	*CO_2 + water + methanol*
Cryogenic	*Liquid CO_2*	*CO_2*
	Liquid N2	*N_2*
	Liquid He	*He*
	Liquid natural gas	*LPG (butane or propane)*

Fracturing design requires from the knowledge of the *in situ* stress, the rock's mechanical properties (*i.e.* Young's modulus, Poisson's ratio) and its fracture transmissibility capacity (*i.e.* permeability, porosity, reservoir pressure). A prior estimation of such properties is conducted to adjust the volume of fluids, pumping rates, and proppant loads to be employed during the treatment (Barree *et al.*, 2002). Proppants, which started to be simply river sand, were gradually modified through the years, employing different materials (*e.g.* plastic, steel, glass and aluminium). The fabric utilized for the construction of most proppants nowadays is sintered bauxite and ceramic, which may occasionally be coated by either resins or fibres as flowback control agents (England, 2004). Proppants are designed to resist high effective stress and shaped as uniform ball-sizes to favour high conductivity. The tendency in increasing proppant efficiency today is via developing lighter, better-sorted, and more resistant microscopic spheres (Durham, 2011; Bhatia and Chacko, 2011). The world's attention to the fracturing-fluids composition began with the growing interest in unconventional reservoirs and their potential risk on subsurface water reservoirs (Committee on Energy and Commerce, 2011). The components that are commonly employed in fracturing fluids are detailed in Table 2.4. This was compiled employing information obtained from: the American Petroleum Institute (2010); the EPA (2011); the Division of Mineral Resources, USA (2009); the Committee on Energy and Commerce, USA (2011); Arthur *et al.* (2008); Chesapeake Energy (2011); Gandossi (2013) and from fracfocus.org/chemical-use; www.epa.gov; www.hydraulicfracturing.com websites. The type and quantity of the components very substantially depending on the treatment and the reservoir characteristics.

Table 2.4 Common chemical compounds employed in most world's hydraulic fractures*

Product	Chemical	Purpose	%
Base Fluid	Water, Oil	Treatment fluid for breaking formation and transporting proppant	~98
Proppant	Sintered bauxite Ceramic Silica	Keeps fracture path open and permits fluid flow	
Acid	Hydrochloric acid Muriatic acid	Dissolves minerals partially in order to favour the creation of cracks Weakens rock	~2
Anti-Bacterial	Glutaraldehyde Ammonium chloride Tetrakis hydroxymethyl-Phosphonium sulphate	Eliminates bacteria in the water that produces corrosive products	
Breaker	Sodium chloride Ammonium persulphate Magnesium peroxide Calcium chloride	Delays the gel's breakdown	
Clay Stabilizer	Sodium chloride Potassium chloride Choline chloride Tetramethyl ammonium chloride	Prevents clay minerals from swelling or mobilizing (react as sodium-potassium ion exchange)	
Corrosion Inhibitor	Isopropanol Methanol Formic acid Acetaldehyde N, n-dimethyl formamide	Prevents pipe corrosion	
Crosslinker	Petroleum distillate Potassium metaborate Triethanolamine zirconate Sodium tetraborate Boric acid Ethylene glycol Methanol	Maintains fluid viscosity	
Friction Reducer	Polyacrylamide Mineral oil Petroleum distillate Methanol Ethylene glycol	Minimize friction between treatment fluid and the pipe	
Gelling Agent	Guar gum (or HEC: hydroxyethyl cellulose) Petroleum distillate Methanol Polysaccharide blend Ethylene glycol	Thinckens the treatment fluid for suspend the proppant	
Iron Control	Citric acid Acetic acid Thioglycolic acid Sodium Erythorbate	Prevents precipitation of metals in the pipe	
Non-Emulsifier	Lauryl sulphate Isopropanol Ethylene glycol	Avoids the formation of emulsions in the treatment fluid	
pH Adjusting Agent	Sodium hydroxide Potassium hydroxide Acetic acid Sodium carbonate Potassium carbonate	Maintains the pH of treatment fluid in order to keep effectiveness of other components	
Scale Inhibitor	Ethylene glycol Copolymer of acrylamide and sodium acrylate Sodium polycarboxylate Phosphonic acid salt	Prevents scale deposits both in the pipe and equipment	
Surfactant	Isopropanol Lauryl sulphate Ethanol Naphtalene Methanol	Increases viscosity of the treatment fluid	

*Compilation from: American Petroleum Institute (2010); EPA (2011); Division of Mineral Resources, USA (2009); Committee on Energy and Commerce, USA (2011); Arthur *et al.* (2008); Chesapeake Energy (2011); Gandossi (2013); fracfocus.org/chemical-use; www.epa.gov; www.hydraulicfracturing.com

2.3.1 Formation Damage from Hydraulic Fracturing

Although hydraulic fracture treatments are aimed at increasing production, there is also the risk that the process could damage the reservoir and reduce production rates (*e.g.* Volk *et al.*, 1983; Thompson and CeVine, 1995; Jiang *et al.*, 2005; Chen *et al.*, 2006; Ribeiro and Sharma, 2011; Ning and Olsen, 1995; Yu and Guo, 2010; Agrawal *et al.*, 2011; Bottero *et al.*, 2010; Terracina *et al.*, 2010).

Fracturing fluids are deliberately placed in contact with large areas of reservoir rock by forced invasion, potentially resulting in the forced imbibition of treatment fluids into the reservoir. Formation damage by hydraulic fracturing treatments may mainly be caused by mechanical and chemical processes. As explained previously, injected water and gas may favour phase trapping effects into the wellbore region, in situations when reservoir's drawdown pressure is not enough for removing completely fracturing fluids. Phase trapping has important implications for low-permeability reservoirs, since tight formations develop higher capillary forces that make flowback and cleanup difficult. Additionally, the gas liberated during sub-bubble pressure production in solution gas drive reservoirs may also favour gas-trapping. Table 2.5 summarises the potential mechanisms of formation damage by hydraulic fracturing fluids. Figure 2.8 illustrates these mechanisms.

Table 2.5 Formation Damage Potential from fracturing fluids

Element	Interaction level	Mechanism
Fracturing Fluids	*Mechanical*	*Phase Trapping (Water, Gas)*
		Fines Migration
		Solids Invasion
	Chemical	*Clay Deflocculation*
		Polymer Adsorption
		Wettability Alteration

Fines migration and clay deflocculation can be triggered if stimulation fluids are not pre-conditioned. Kaolinite booklets may be dislodged and trapped into pore space and reduce permeability. Smectitic clay can also reduce permeability by swelling as previously explained.

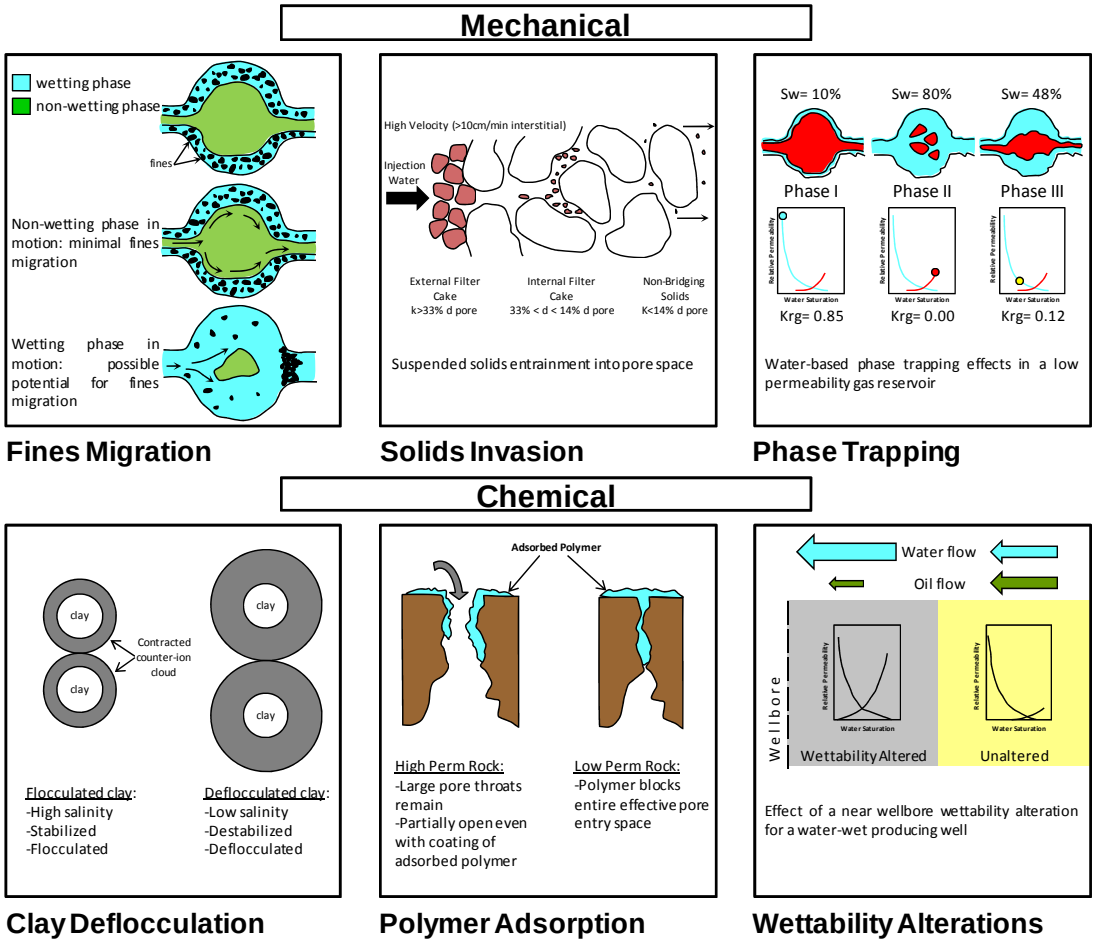

Figure 2.8 Potential formation damage mechanisms from fracturing fluids (modified from Bennion, 2002)

Wettability alteration may potentially be produced from two mechanisms: polymer adsorption or asphaltene precipitation. The first may be sourced from the guar-based polymer routinely employed as gelling agent. Diverse published examples demonstrate the importance of employing polymer-free solutions for fracturing purposes (Wang, 2003; Sun *et al.*, 2010, 2011). Polymer may also lead to permeability reduction by inadequate breaking of the fracturing fluid polymer.

Wettability alteration from polar organic compounds deposition may also represent a mechanism for permeability reductions, which has been documented in the literature (Leontaritis *et al.*, 1994; Piro *et al.*, 1996; Sim *et al.*, 2005; Gholami *et al.*, 2008; Rezaian *et al.*, 2010).

CHAPTER III.
EXPERIMENTAL PROCEDURES

This chapter describes the experimental procedures used during this research project. These were designed for analysing the reservoir-rock characteristics, the formation damage potential and rock-fluid interactions in the reservoirs of this study. Most of the experiments were conducted by the author at the University of Leeds facilities. Some other were provided by PEMEX contractors and/or developed by laboratories specified in the text. The aim of this chapter is to show the detail of the experimental techniques so that these can be repeated in further work. The analytical procedure is also defined so that the results obtained in this study can be compared to other datasets.

The chapter starts with a general explanation of the workflow, illustrating the different techniques applied to rock and fluid samples. The tests applied to rock plugs are first defined, which include the descriptive studies and fluid-displacement procedures. The experimental techniques applied to fluids (brine and oil) are then described.

3.1 Introduction

Figure 3.1 illustrates the experimental techniques applied to rock and fluid samples conducted in this study.

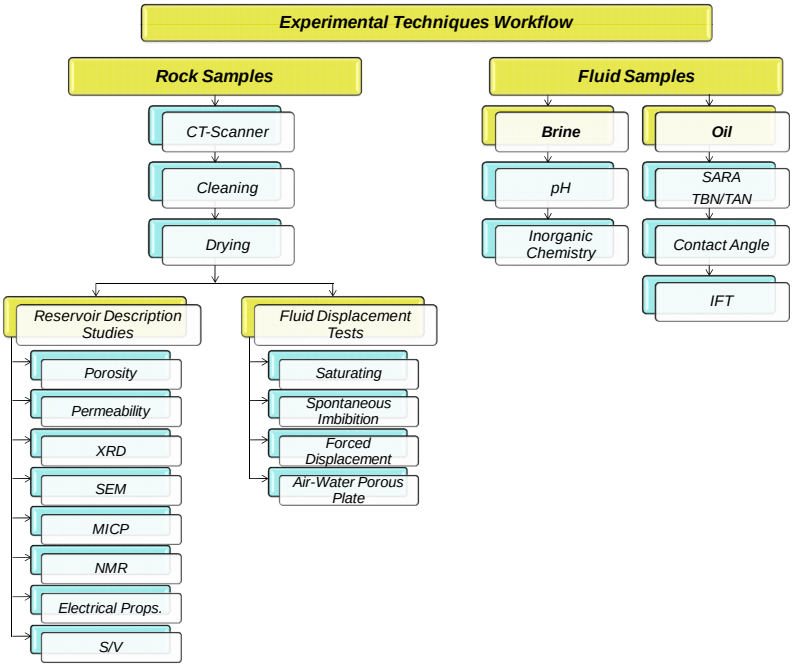

Figure 3.1 Workflow of experimental techniques applied to rock and fluid samples in this study

As explained previously, diverse studies were available on a number of core samples at the start of the project (see Table 1.1 in Chapter 1). These consisted of reservoir description studies (*e.g.* porosity/permeability, XRD, SEM, MICP and electrical properties) and are referred here as "studied" samples. Thirty-eight new rock samples were provided by PEMEX at the start of the study; these had not previously been analysed. These new plugs together with a number of the "studied" samples were used for conducting diverse experiments to try to fill gaps in the knowledge of these reservoirs. Table 3.1 shows the summary of the descriptive studies conducted during this project.

Table 3.1 Reservoir Description Studies produced in this study

Number of samples	Study
46	*Gas Porosity at ambient conditions*
46	*Klinkenberg-corrected permeability at stress conditions*
33	*Quantitative X-Ray Diffraction (QXRD) mineralogy*
36	*Backscattered Electron Microscopy (BSEM)*
33	*Mercury Injection Capillary Pressure (MICP) curves*
35	*Nuclear Magnetic Resonance (NMR)*
6	*Cementation Factor (m)*
6	*Saturation Exponent (n)*
4	*Oil-water continuous end-point relative permeability*
10	*Brine permeability*
13	*Surface Area to Volume Ratio (S/V)*

A number of experimental techniques that has not been used in the past in these reservoirs and that provide with additional information for their understanding were conducted in this project. These consisted of a series of tests to evaluate formation damage, the reservoir's wetting characteristics, the asphaltene precipitation and the efficiency of a series of surfactants to improve oil recovery.

The experiments applied to rock samples are divided into two groups (Fig. 3.1): the reservoir description studies and the fluid-displacement tests. The descriptive studies were conducted for characterising the reservoir rock in terms of its texture, mineralogy, pore-size variations and petrophysical characteristics. This allowed the identification of the minerals susceptible to formation damage, as well as the location of representative rock samples to be used for fluid-displacement tests. The displacement tests were designed to evaluate the potential of formation damage, wettability and rock-fluid interactions.

The experiments conducted on fluid samples are divided in two groups: brine and crude-oil samples (Fig. 3.1). The analysis of brine samples mainly consisted of quantifying trace-elements through the inductively couple plasma by atomic emission spectroscopy (ICP-AES) technique. Similarly, the tests performed in crude-oil samples were conducted to characterise their major components and in this way make further comparisons to other crude-oils.

3.2 Rock Samples

In the following paragraphs there will be described the experiments conducted on rock samples. The general conditioning procedure (*i.e.* analysis of the internal structure, cleaning and drying) on these samples is first described, followed by the explanation of the techniques and the fluid-displacement tests.

3.2.1 CT-Scanning

The internal structure of the rock samples employed in this study was evaluated using a medical-type CT-scanner at the Wolfson Multiphase Flow laboratory of the University of Leeds to assess the level of heterogeneity and core damage (Fig. 3.2). Seven naturally-fractured and highly-laminated samples (typically with unusual high-permeability values) were discarded from this study as these do not follow the general petrophysical behaviour of most samples observed in the Chicontepec reservoirs. Luces *et al.* (2012) points out that natural fractures, frequently observed in Chicontepec subsurface data and in outcrop samples, do not seem to be interconnected and their influence on fluid-flow is thus neglected in this study.

a) **b)**

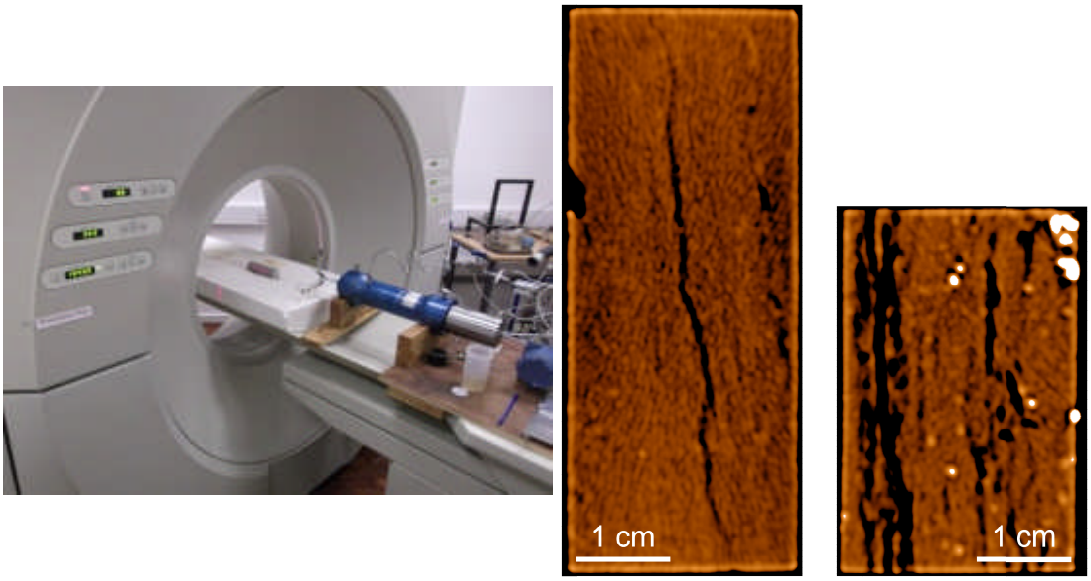

Figure 3.2 a) Medical-type CT-scanner; b) two highly-laminated and fractured samples

3.2.2 Sample Cleaning and Drying

All samples were cleaned in a Soxhlet extractor with dichloromethane (DCM) and dried to constant weight in a convection oven at 60°C. The sample cleaning and drying was performed by the author at the Wolfson Multiphase Flow laboratory of the School of Earth and

Environment. DCM allows the samples to be cleaned at lower temperatures (*i.e.* DCM boils at 40°C) than industry standard solvents such as toluene and methanol. In this way the exposure to damage was minimised.

3.2.3 Reservoir Description Techniques

The entire set of experiments described in the following paragraphs was conducted at the University of Leeds facilities. Some other were provided by PEMEX contractors and/or developed by laboratories specified in the text.

A number of measurements (*e.g.* porosity, permeability) in selected samples were repeated to ensure confidence in the results. In some cases, diverse methods were used to estimate the rock property. For example, the porosity of a number of samples was estimated using three techniques: a gas pycnometer device, the Archimedes principle of mass displacement and mercury injection. Determination of porosity, permeability and fluid saturations were performed by the author at the Wolfson Multiphase Flow laboratory of the School of Earth and Environment.

3.2.3.1 Porosity

Porosity (Ø) is the measure of the void spaces in a rock. Porosity can be determined from the following equation:

$$\emptyset = \frac{P_v}{B_v} = \frac{B_v - G_v}{P_v + G_v}$$

where: P_v is the pore volume (*i.e.* the total volume of void space in the sample), B_v is the bulk volume (the volume of the solid rock components plus void spaces), and G_v is the grain volume (the total volume of solid rock components).

A gas pycnometer device (Fig. 3.3) was used to determine the grain volume of dry rock samples. The core plug is placed into a reference chamber with known volume. Helium gas is admitted into the reference chamber at predetermined pressure, typically 100 to 200 psig. After equilibrium, the gas is allowed to expand resulting in lower pressure. The sample's grain volume (G_v) is calculated using the Boyle's Law ($P_1V_1=P_2V_2$). The sample's bulk volume (B_v) is determined by measuring the sample dimensions by a manual caliper. The pycnometer device is calibrated with known volumes and in this way the quality control on the measurements was ensured. Porosity is then calculated from the grain volume (G_v) and bulk volume (B_v):

$$\emptyset = \frac{B_v - G_v}{B_v}$$

Other techniques were used to verify the pore volume and bulk volume measurements. Using the Archimedes principle of mass displacement, the sample's weight is first measured dry (W_d). The dry weight is then compared to the weight of the fully-saturated conditions using brine (W_b). Weight difference results into the mass of fluid occupying the pore space. Assuming a brine density (ρ_b) of 1.024 g/cm^3, corresponding to 3.5% NaCl brine at 21°C, pore volume is estimated by:

$$P_v = \frac{W_b - W_d}{\rho_b}$$

The bulk volume of the sample is estimated by measuring the dimensions of the cylindrical shape of the plug by a precision calliper (B_v). The porosity of the sample when brine is the saturating fluid is then calculated as:

$$\emptyset = \frac{P_v}{B_v}$$

Porosity was also estimated using mercury injection data. This was conducted by recording the total volume of mercury injected to the sample (V_{Hg}) and the sample's weight differences (*i.e.* the dry and fully-saturated with mercury; W_d and W_{Hg}, respectively). The sample's bulk density (ρ_{bulk}) is determined using the mercury density (ρ_{Hg}) of 13.59 g/cm^3 as:

$$\rho_{bulk} = \frac{W_d}{\left(V_{Hg} - \left(\frac{W_{Hg} - W_d}{\rho_{Hg}}\right)\right)}$$

Assuming a grain density (ρ_{grain}) of the sample (approximately 2.68 g/cm^3 in the rock samples of this study), then the porosity is obtained by:

$$\emptyset = 1 - \frac{\rho_{bulk}}{\rho_{grain}}$$

Figure 3.3 Helium-pycnometer device

3.2.3.2 Saturation

Saturation is defined as the fraction of the pore volume occupied by a particular fluid (oil, gas, or water). For samples saturated with water, saturation (*Sw*) is normally expressed as the ratio of the total volume of water (B_w) and the pore volume (P_v):

$$Sw = \frac{B_w}{P_v}$$

During the development of this study, three techniques were used for estimating the sample's water saturation (*Sw*) to ensure consistency on the measurements. The first, when water was used as single-phase in the sample, the Archimedes principle was used, as:

$$Sw = \frac{W_b - W_d}{\rho_b \cdot P_v}$$

The second technique, when two-phases are present into pore space; in this case oil and water:

$$Sw = \frac{[M - W_d - (P_v \cdot \rho_o)]}{[P_v \cdot (\rho_b - \rho_o)]}$$

where: M is total mass of the core and fluids, W_d is the dry mass of the core, P_v is the pore volume, and ρ is the fluid densities (brine, oil). During the two-phase (*e.g.* oil and water) displacement experiments conducted in the rock plugs, effluent fluids were continuously collected and later separated using a centrifuge for quantification. The average water saturation (Sw_{av}) of the sample was estimated by:

$$Sw = \frac{V_{oil\ (effluent)}}{P_v} + Sw_i$$

where: Sw_i is the sample's water saturation at the start of the experiment, and V_{oil} is the effluent oil phase (*i.e.* produced). Generally, no significant differences were observed when these three methods were compared.

Synthetic brine was employed for saturating core samples. The brine was prepared employing de-ionised water and pure salts. The brine was then filtered through a 0.45 μm cellulose nitrate filter paper and degassed. Saturation was achieved by immersing the core plugs in the saturating brine which was evacuated in a suction chamber. The samples and brine were then placed overnight in a pressure vessel at 1000 psi to ensure complete saturation.

3.2.3.3 Permeability

Permeability (k) is the measure of the ability of a porous material to allow fluids to pass through it. Henry Darcy developed in 1856 a mathematical equation to define the flow of water passing through sand filters. This formula is known as Darcy's Law and is expressed as:

$$q = \frac{kA}{\mu}\frac{\Delta P}{L}$$

where: q is the rate of fluid-flow (cm^3/sec), A is the cross-sectional area of the sample (cm^2), μ is the viscosity of the flowing fluid (cP), ΔP is the pressure drop along the sample (atm), L is the length of the sample (cm), and k is permeability (Darcy). A number of conditions must exist during the measuring of a single-phase permeability: 1) laminar, steady-state (*i.e.* not turbulent) flow is achieved; 2) no fluid-rock interactions; 3) pore space must be fully-saturated with an incompressible, Newtonian fluid.

Different permeability measurements were conducted in this work, using a variety of rock samples and fluids. The methods are described below.

3.2.3.3.1 Single-Phase Permeability

Steady-State Method

The setup of single-phase axial flow of fluid (gas or liquid) is illustrated in Figure 3.4.

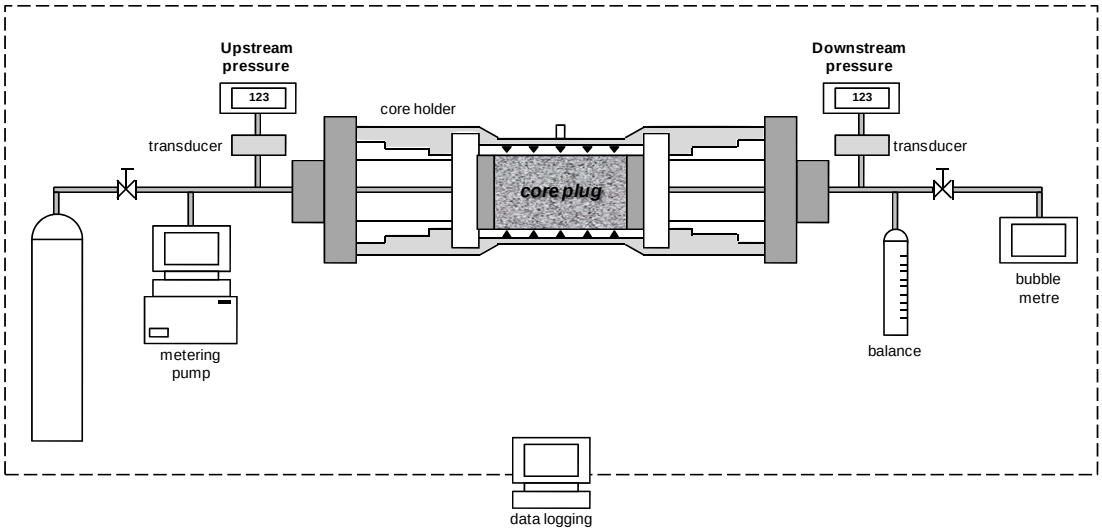

Figure 3.4 Steady-state permeability setup

A cleaned and dried cylindrical core sample (or fully-saturated sample if liquids are used) was placed into a Hassler-type core holder within a flexible sleeve to maintain a constant radial confining stress during the test. Both ends of the core are connected to a port for monitoring inlet and outlet pressures, and the outflow line is attached to a flow-rate measuring device. Steady-state is reached when both end-pressures and flow-rate throughout the sample become constant with time, meeting the Darcy's Law principles. The measurements were obtained at constant temperature of 23.5°C and atmospheric pressure. Helium and synthetic brine at 3.5% NaCl concentration were used.

Diverse effects must be taken into account when permeability is determined using gas. These include gas slippage and inertial effects. Klinkenberg (1941) founded that the permeability of a core sample was not constant, but varied with the gas used to make the measurement, as well as the mean pressure existing in the core sample at the time of measurement. His investigations indicated that at low-mean pressures the gas molecules are far apart and they slip through the pore spaces with little friction loss, and yield a higher value of permeability. This is known as the slippage effect. At higher mean pressures the gas molecules are closer together and experience a friction drag at the side of the pore walls. Repeated measurements of gas permeability at different mean pressures can be extrapolated to infinite pore pressure where the gas behaves as a liquid (*i.e.* incompressible fluid). This was performed to correct permeability for gas slippage and the Klinkenberg-corrected permeability was determined. An example of

how the Klinkenberg-corrected permeability is shown in figure 3.5. Permeability is measured at different gas mean pressures (*Pm*) to construct a linear tendency. The resulted trend is then extrapolated to simulate as if a liquid is being used (*i.e.* no compressibility or 1/Pm= 0). The Klinkenberg-corrected permeability is then obtained.

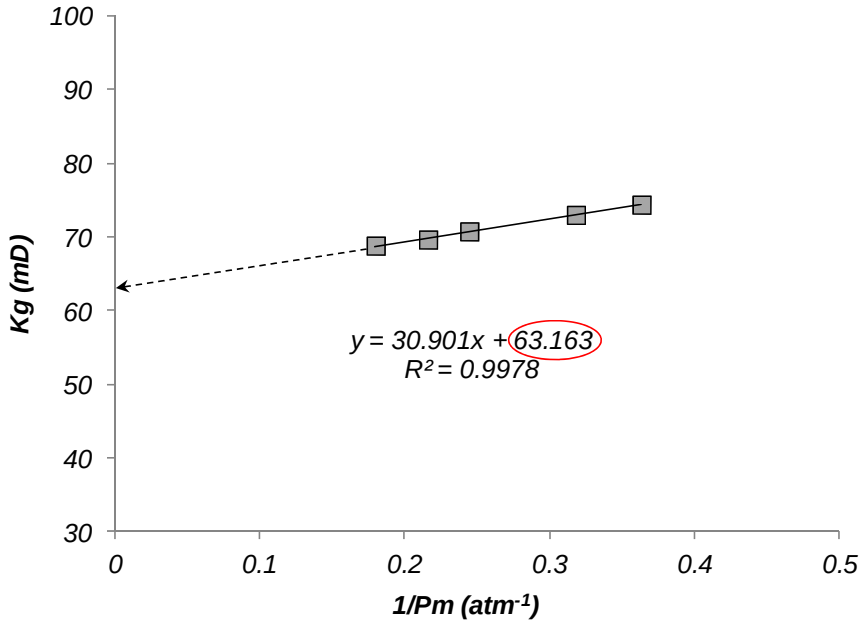

Figure 3.5 Determination of Klinkenberg-corrected permeability in one rock sample of this study. In this case, the corrected-permeability resulted of 63 mD

The flow changes from laminar to turbulent regime when the gas- or liquid-flow velocity increases. This means that the fluid molecules are not all moving parallel in the same linear direction but following irregular trajectories. The pressure differential along the core sample will not only express the movement of the fluid as a whole, but also the movement spent internally. This is known as the Forchheimer inertial resistance. The Darcy equation is then adapted considering the Forchheimer factor (β) and mean flow velocity ($\bar{v}^2$), as follows:

$$\frac{\Delta P}{\Delta x} = \frac{\mu}{k}\bar{v} + \beta\bar{v}^2$$

Unsteady-State Method

Steady-state method is a commonly used technique for determining the rock's permeability in the laboratory. For low-permeability samples (*e.g.* lower than 0.1 mD), this method is impractical since long periods of time are required for achieving steady-flow conditions.

The transient-flow method for measuring permeability was introduced by Brace *et al.* (1968). This technique consisted of a cylindrical core sample which is connected to two fluid reservoirs. The fluid pressure is suddenly increased in the upstream end. The upstream pressure decays as

the fluid travels from the upstream reservoir across the sample to the downstream reservoir. The permeability of the sample is determined from the pressure decay in the upstream reservoir.

Jones (1997) proposed a new method for pulse-decay technique that is able to reduce the analytical time required to determine permeability. The pulse-decay setup is shown in Figure 3.6.

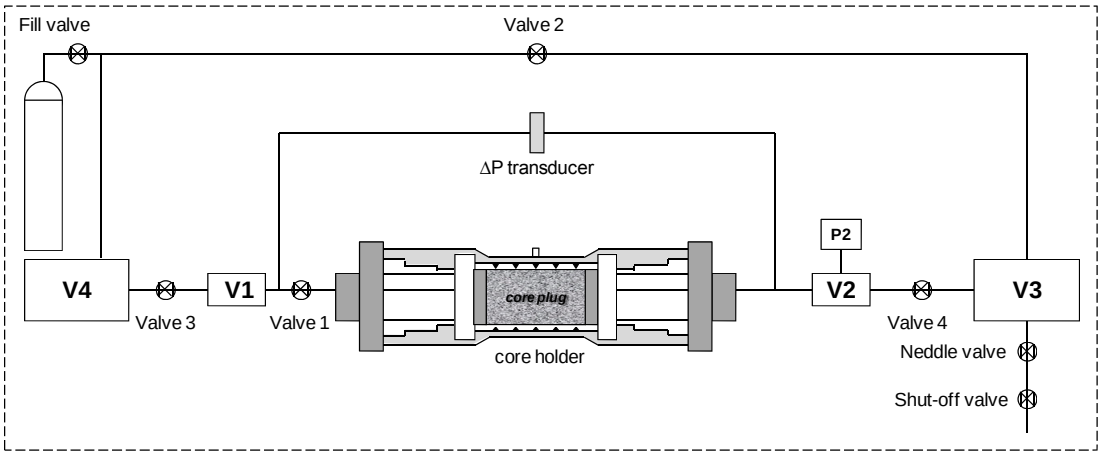

Figure 3.6 Pulse-decay permeability setup (based on Jones, 1997)

In the Jones model (Fig. 3.6), the pore volume of the sample must be determined separately. The setup includes four reservoirs (two large and two small) of known volumes. All reservoirs all filled at desired pressure by opening valves 1 and 4. After a few minutes of equilibration, the fill valve is closed and the pressure transducer zeroes. Valve 2 is also closed. With the needle valve almost closed, the shut-off valve is opened to allow the downstream pressure in volumes 2 and 3 to decrease until the pressure difference reads the pre-set value. Then the shut-off valve is closed and both the differential pressure (ΔP) and the downstream pressure (P2) are monitored until the mean pressure becomes constant with time. Pressure difference should not exceed 10 psi to minimise inertial gas resistance.

The pulse-decay technique was employed for single-phase gas-permeability measurements in this study. These experiments were conducted at the Wolfson Multiphase Flow laboratory of the University of Leeds. The gas-permeability measurements from the studied rock samples provided at the start of the study were constrained to a minimum value of 0.001 mD. This was due to instrumentation limits of the PEMEX's contractor. A number of new and studied samples were employed for determining gas-permeability below this frontier. This permitted to populate more representatively the pore-perm association of these reservoirs and to construct more predictable correlations.

3.2.3.3.2 Relative Permeability

Relative permeability (k_r) is defined as the ratio of effective permeability (k_e) of a specific fluid to absolute permeability (k_a). For a three-phase system (water-oil-gas):

$$k_{rw} = \frac{k_{ew}}{k_a} \qquad k_{ro} = \frac{k_{eo}}{k_a} \qquad k_{rg} = \frac{k_{eg}}{k_a}$$

where: $kr_{w,o,g}$ is the relative permeability to water, oil and gas respectively; $ke_{w,o,g}$ is the effective permeability to water, oil and gas, respectively, for a given saturation.

In this study, the relative permeability was determined using high-permeable samples (*i.e.* greater than 1 mD), and the steady-state regime was employed. Relative permeability reflects the rock and fluid chemical and physical properties, therefore is sensitive to the relative wetting characteristics of the rock and fluids (Tiab and Donaldson, 2012). Special attention was applied in restoring the wetting state of the samples to produce what it is generally accepted the representative reservoir condition. Although the restoring procedure may be inaccurate by definition (*i.e.* the sample is subjected to a series of conditions different from its natural state), it is generally accepted that the procedure is a close replica of the natural reservoir state. The restoring procedure (*i.e.* aging) is described below.

At fully saturated conditions with synthetic brine, the core sample was placed into a Hassler-type core holder at *in situ* stress conditions. Absolute brine permeability was determined using the steady-state method (k_w) as described in Figure 3.4. Crude-oil was then injected into the sample at variable rate until no further brine was produced (*i.e.* primary drainage cycle), achieving irreducible water saturation (Sw_i). Irreducible water saturation is defined as the maximum water saturation that a formation with a given porosity and permeability can retain without producing water. Effluent fluids, oil and brine, were continuously collected and later separated using a centrifuge. Water saturation was estimated by weight differences and material balance.

The sample was then removed from the core holder and placed into a glass-sealed container filled with oil. The aging process was carried out employing a water bath device at 65°C for 72 hours, following aging preparation from Rühl *et al.* (1963), Salathiel (1973) and Cuiec *et al.* (1979); although different authors advise greater restoration times (Mungan, 1972; Anderson, 1986a).

After aging, the sample is placed in the core holder and two pore volumes of Decalin were pumped through each sample to displace crude-oil, thus avoiding the precipitation of crude-oil residues during further measurements. Decalin is an intermediate solvent which proved to retain wettability in previously-aged surface minerals during adhesion tests. Decalin was later

removed by flowing synthetic brine until reaching residual oil saturation (So_r). So_r is defined as the fraction of oil that remains in the pores after the sample has been subjected to waterflooding (*i.e.* displacement process of the oil by brine).

At aged state, the sample was placed in a core holder as illustrated in Figure 3.7. This setup was fitted with a pressure transducer connected to the inlet and a back pressure regulator to maintain pore pressure. Outlet pressure was assumed to be atmospheric. A metering pump was employed for injecting fluids (brine or oil) at steady flow-rates. Measurements were obtained at constant room temperature of 21°C.

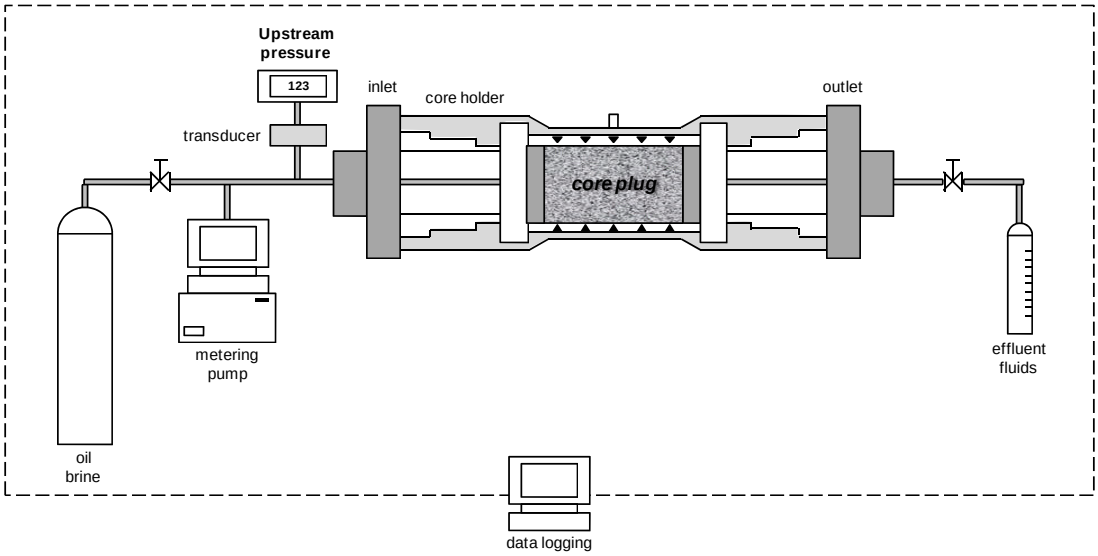

Figure 3.7 Steady-state setup for determining relative permeability

At So_r conditions, paraffinic oil was injected into the sample at increasing flow-rates until pressure equilibrium was achieved through the core on each rate point and brine was no longer produced (*i.e.* stepped end-point saturation). The paraffinic oil was bought from ExxonMobil Chemical laboratory. It consists of linear saturated hydrocarbon (Isopar-V) with similar physical properties as the crude-oil. Different oil rates were applied to describe the effective permeability curve (k_{eo}) for a wide range of saturation until reaching the irreducible water saturation condition.

Similarly, at Sw_i conditions, brine was injected to displace oil at increasing flow-rate stages (*i.e.* secondary drainage cycle). The obtained effective permeabilities to oil and water (k_{eo}, k_{ew}) at a range of water saturations, were scaled with the oil effective permeability at irreducible water conditions ($k_o@Sw_i$), thus continuous end-point relative permeability curves to oil and water were estimated.

A limitation of this method was the estimation of the sample's water saturation. Disassembly of the core after each saturation step can cause loss of the fluid, which may introduce errors in

saturation measurements. Additionally, physicochemical changes of crude-oil (*e.g.* precipitation of asphaltenes) may also lead to inaccuracies in saturation estimations. Alternate methods to estimate water saturation, as described earlier, were used to ensure consistency in the measurements.

Estimation of the error in permeability measurements was conducted during the development of this study. Figure 3.8 illustrates the differences in single-phase permeability using gas in a number of samples used in this project. Three permeability measurements were acquired on each sample maintaining the same conditions (*e.g.* mean pressure, *in situ* stress and flow rate). As observed, no significant differences were obtained and the error was considered acceptable. Note in the Figure 3.8 that the largest variation was obtained at lower permeabilities.

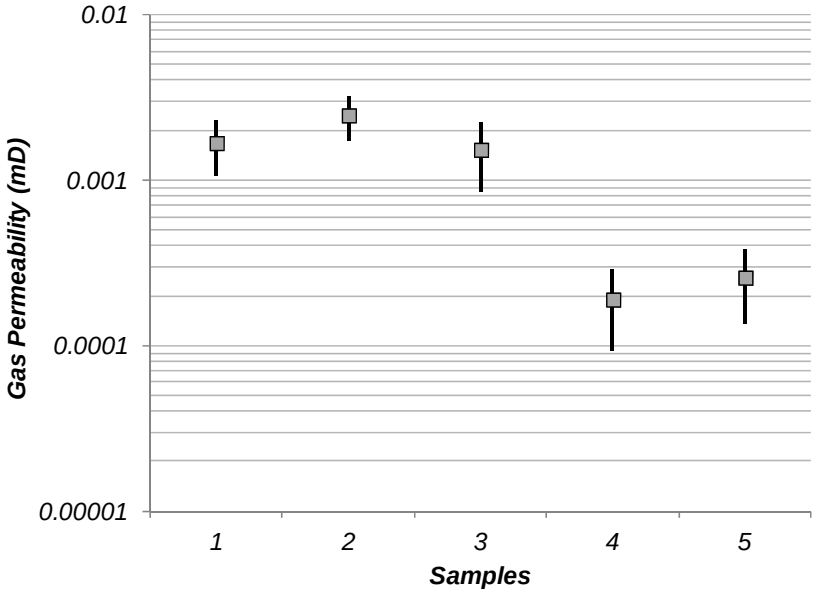

Figure 3.8 Differences in single-phase permeability determination in a number of rock samples used in this study. No significant variation was observed

3.2.3.4 X-Ray Diffraction

The mineralogy of powdered rock samples was determined using X-Ray Diffraction (XRD) using the XRD laboratory of the School of Earth and Environment of the University of Leeds. A number of rock samples were disaggregated and mixed with 20% corundum, which is used as spike reference. The samples were spray dried to produce completely random mineral orientations. A focused X-ray beam interacts with planes of atoms that form crystal lattices. Portions of the beam are transmitted, absorbed, refracted and scattered, and a part is diffracted. X-rays are diffracted by each mineral differently, depending on the type of atoms forming the crystal lattice and how these atoms are arranged.

The prepared sample is placed in a holder which is illuminated with x-rays of a fixed wave-length (λ) and the intensity of the reflected radiation is recorded using a goniometer. The data is analysed for the reflection angle to calculate the inter-atomic spacing (d), according to the Bragg's Law:

$$2d(\sin\theta) = \lambda$$

where: θ is the X-ray incidence angle. Plotting the angular positions and intensities of the diffracted peaks produces a characteristic pattern which is matched against databases of recorded phases to identify mineral fractions.

Mineral quantification was conducted using the reference intensity ratio (RIR) method using corundum as standard phase. The equation to estimate RIR factors that use corundum as the standard phase is:

$$RIR_{cor} = \left(\frac{X_s}{X_i}\right)\left(\frac{I_{(hkl)i}}{I_{(hkl)s}}\right)\left(\frac{I^{rel}_{(hkl)s}}{I^{rel}_{(hkl)i}}\right)$$

where: X is the weight fraction, I is the intensity, I^{rel} is the relative intensity, i is the phase of interest and s is the standard phase. As a known amount of corundum is added to the sample (20% in these samples), it is possible to obtain the concentration of a phase as:

$$X_i = \left(\frac{X_{cor}}{RIR_{cor}}\right)\left(\frac{I_{(hkl)i}}{I_{(113)cor}}\right)$$

The X-ray diffraction data was collected using a Phillips PW1050 diffractometer employing CuKα radiation, powered to 50kV/40mA and fitted with a secondary graphite monochromator. The data was collected over a range of 3-70° 2θ with a step size of 0.01° and speed of 0.6°/min. The phases were interpreted by Lesley Neve, from the University of Leeds, using BrunkerEva and MacDiff software.

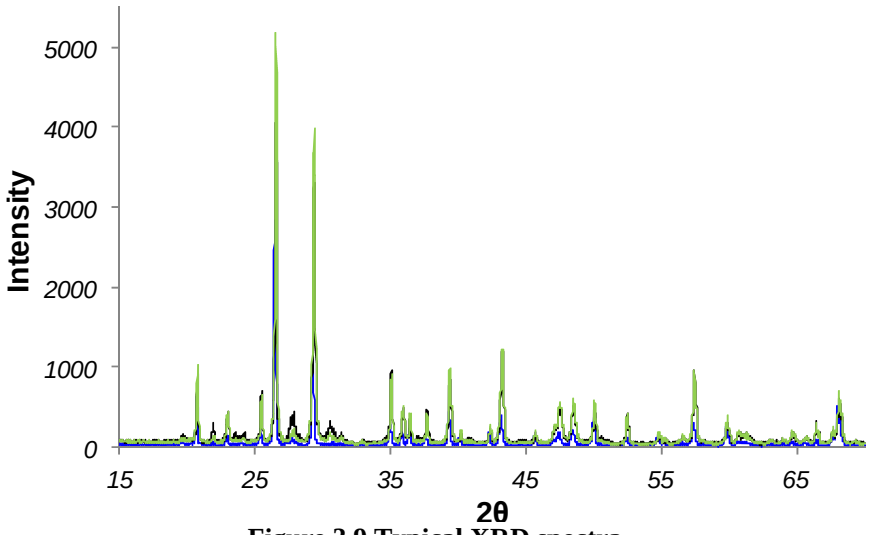

Figure 3.9 Typical XRD spectra

3.2.3.5 Scanning Electron Microscopy (SEM)

The microstructure characteristics of selected samples were analysed using SEM. Generally, polished blocks were analysed using back-scattered electron microscopy (BSEM). Samples for BSEM were first cut with a diamond saw into blocks of 1.5x1.5x0.5 cm. These were then cleaned with DCM and dried to constant weight, before being impregnated with a low viscosity resin. The samples were polished with successively finer grades of diamond paste to obtain flat surfaces. Finally, the samples were carbon-coated to prevent them charging during examination using the SEM.

Sample analysis was conducted at the Faculty of Engineering of the University of Leeds using a Quanta^{TM} 650 SEM manufactured by FEI (Fig. 3.10). This has a hot field emission electron source and is fitted with secondary electron (SE), backscattered electron (BSE), cathode luminescence (CL) and energy dispersive X-ray (EDX) detectors. The EDX detector was linked to the INCA350^{TM} software for identification and quantification of the chemical composition of minerals.

Figure 3.10 The Quanta™ 650 SEM used during this study

3.2.3.6 Capillary Pressure

Capillary pressure is the pressure difference that exists across the interface of two immiscible fluids in a capillary (porous) system. Two approaches were used for determining capillary pressure: the injection of mercury at high pressures and the air-water system using an air-water porous-plate. Both experiments were performed by the author at the Wolfson Multiphase Flow laboratory of the School of Earth and Environment of the University of Leeds.

Mercury Injection Capillary Pressure (MICP)

Mercury injection involves forcing mercury under pressure into evacuated pores of a sample, previously cleaned and dried. As injection pressure increases, the mercury enters progressively into smaller pore throats. Mercury injection profiles provide with significant insight into the nature of pore geometry and distribution. Maximum injection pressure was of 60,000 psi at constant stepped increments. Converting laboratory (*i.e.* air-mercury) capillary pressure to reservoir (*i.e.* oil-brine) conditions:

$$Pc_{oil-brine} = Pc_{air-mercury} \frac{\sigma \cos \theta_{oil-brine}}{\sigma \cos \theta_{air-mercury}}$$

where: σ is the interfacial tension (Dynes/cm), θ is the contact angle (degrees), and *Pc* is the capillary pressure (air-mercury, oil-brine systems). For estimating pore radius (R):

$$R = \frac{2\sigma \cos \theta_{oil-brine}}{Pc_{oil-brine}} \cdot 0.145$$

Estimations were obtained employing the following parameters:

Table 3.2 Mercury injection parameters

Parameter	Laboratory (air-mercury)	Reservoir (oil-brine)
θ (degrees)	*140*	*30*
σ (Dynes/cm)	*480*	*31*
σcosθ	*367.7*	*41.5*

Porous-Plate Method

Air-water capillary pressure was determined by the porous plate method. Figure 3.11 shows the porous-plate apparatus at the Wolfson Multiphase Flow laboratory. The technique consists of placing one end of a fully-saturated sample against a porous membrane, within a pressurised chamber filled with air. A moist mixture is placed between the sample and the membrane for maximising capillary contact. De-saturation of the core is achieved by increasing pressures in the chamber in a step wise manner, forcing air to displace water. Effluent fluid is collected in a graduated burette for monitoring the volume of produced water; capillary equilibrium is attained when water is no longer produced. The samples are then removed from the chamber and their saturation is obtained by weight differences on each pressure stage.

The samples are then placed back in the chamber and the pressure is increased displacing more water gradually. The capillary pressure curve is determined by plotting the step-increasing pressures and corresponding water saturations.

Figure 3.11 Air-Water porous plate apparatus

3.2.3.7 Nuclear Magnetic Resonance (NMR)

NMR measures the magnetic signal emitted by spinning protons (hydrogen nuclei) as they return to their original state following stimulation by an applied magnetic field. The signals are expressed as time constants that are plotted as the decay of magnetization (T2 relaxation). NMR T2 relaxation in fully-saturated rock samples can be used to estimate porosity, permeability, irreducible water saturation, and pore-size distribution.

NMR measurements were performed using an Oxford Instruments™ MARAN Ultra™ spectrometer (Fig. 3.12) at 2MHz frequency, at ambient pressure and operating temperature of 35°C. No NMR studies have previously been conducted in the study area, and these were then acquired in the Wolfson Multiphase Flow laboratory of the University of Leeds. The spin echo train was generated with a Carr-Purcell-Meiboom-Gill (CPMG) pulse sequence for removing external magnetisation. Around 100 scans, 100 for core plugs with a 1.5” diameter and 200 scans for 1” diameter samples were used.

Figure 3.12 NMR spectrometer

The average T2 distribution was calculated as:

$$T2_{LM} = exp\left(\frac{\sum_i (S_{ai} log T2_i)}{\sum_i S_{ai}}\right)$$

where: *T2* is the relaxation time, *Sa* is the signal amplitude, and $T2_{LM}$ is the log mean T2 distribution. The area under the T2 distribution curve obtained at *Sw*=100% is proportional to total porosity.

3.2.3.8 Electrical Properties

Electrical properties were measured to core samples at different saturating conditions. These were acquired at the Wolfson Multiphase Flow laboratory of the University of Leeds by a LCR meter model QuadTech 7600 Plus Precision manufactured by IET Labs Inc. (Fig. 3.13). Core samples were placed into a Hassler-type core holder at stress conditions fitted with two electrodes Measurements were made at a constant frequency of 2 KHz.

True resistivity (*Rt*) was estimated comparing electrical resistance (*R*) and the sample dimensions:

$$R_t = R \cdot \frac{L}{A}$$

where: *L* is the sample's length (cm), and *A* is the sample's sectional area (cm^2).

Resistivity Index ($IR = R_t/R_o$) was calculated comparing the true resistivity ($R_t = R \cdot (L/A)$) at the adjusted saturation and the sample's resistivity fully saturated with brine (R_o). Archie's saturation exponent, *n* (Archie, 1941) is determined from the slope of a line fitted to the *log*IR versus *log*Sw:

$$n = \frac{logRI}{logSw}$$

Archie's cementation exponent, *m* (Archie, 1941) was calculated as:

$$m = \frac{logF}{log\emptyset}$$

where: *F* is the formation factor and is expressed as: $F = R_o/R_w$, *Rw* is the formation water resistivity at room temperature (*Rw*= 0.195 Ω·m @ 20°C, equivalent to 35, 000 ppm of NaCl brine), and *Ø* is the porosity obtained by weight differences (fraction).

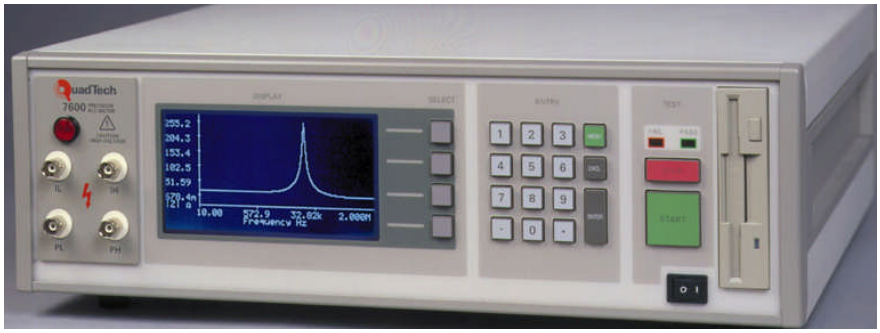

Figure 3.13 LCR meter for electrical resistance measurements

3.2.3.9 Surface Area to Volume Ratio (S/V)

Grain surface area (or specific grain surface) by multipoint BET (Brunauer-Emmett-Teller theory) nitrogen adsorption method was determined by Micromeritics® in a number of disaggregated samples. The method involves determining the quantity of nitrogen required to form a layer one molecule thick on the surface of a sample. Results are expressed as square meters of surface per gram of solid (m^2/g). Surface to volume ratios is an important parameter to estimate immobile water volumes and permeability.

Conversion from specific grain surface per gram of solid (S_g) to specific surface area per unit grain volume (SV_{gr}) was derived from:

$$SV_{gr} = S_g \cdot \rho_g$$

Conversion of SV_{gr} to specific pore surface (S_p) was derived from:

$$S_p = SV_{gr}\left(\frac{1-\emptyset}{\emptyset}\right)$$

where: ρ_g is the sample's grain density, and *Ø* is the gas-porosity.

Pore surface was combined with NMR measurements to estimate the surface relaxivity (ρ). Surface relaxivity is defined as the ability of a surface to relax the spinning protons (Schön, 2011) and it was determined as:

$$\frac{1}{T2_{LM}} = \rho S_p$$

3.2.4 Fluid Displacement Tests

3.2.4.1 Spontaneous Imbibition

Spontaneous imbibition of oil and brine were conducted in this study. The experiments were performed using Amott imbibition cells as shown in Figure 3.14, which were designed for immiscible oil-brine systems, at room temperature and atmospheric conditions. These experiments were performed by the author at the Wolfson Multiphase Flow laboratory of the University of Leeds.

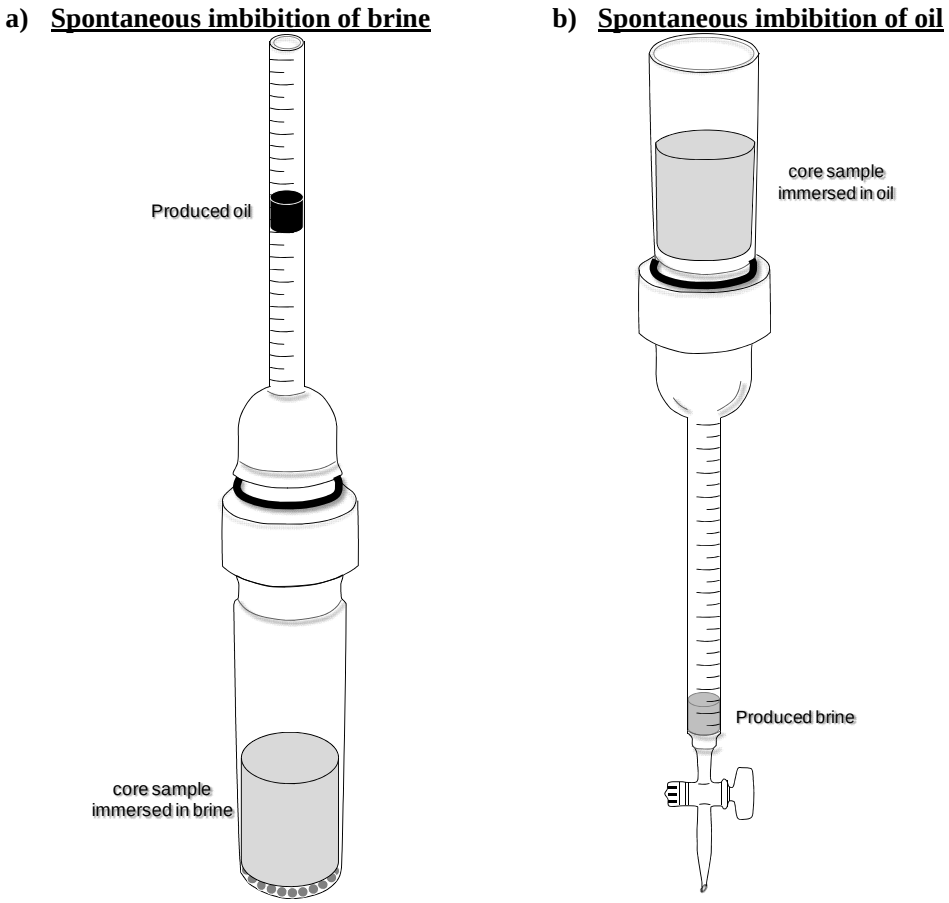

Figure 3.14 Amott imbibition cells

The imbibition experiment refers to the amount of brine and oil that naturally is imbibed by a rock sample. The plug is saturated with synthetic brine at 3.5% NaCl concentration, which is then displaced by crude-oil until irreducible conditions (Sw_i) are reached. The sample is aged by crude-oil as explained in the *relative permeability* section and then immersed into synthetic brine in the Amott cell, leaving the buoyancy forces and the sample's preference to fluids (*i.e.* wettability) to act.

Spontaneous imbibition of brine is determined as the amount of oil that is expelled (*i.e.* displaced) from the sample. The produced oil is monitored by a graduated burette as shown in Figure 3.14a. The average water saturation of the sample (*Sw*) is determined as:

$$Sw = \frac{V_{oil\ (expelled)}}{P_v} + Sw_i$$

where: $V_{oil\ (expelled)}$ is the oil produced by spontaneous imbibition of brine, Sw_i is the irreducible water saturation and P_v is the sample's pore volume. Similarly, spontaneous imbibition of oil is obtained by monitoring the amount of brine driven out from the sample (Fig. 3.14b). Separation and quantification of the immiscible phases is resulted from their density differences. According to Amott methodology (Amott, 1959), the fluid that spontaneously imbibes most into the sample is normally ascribed as the wetting fluid.

The rate at which brine imbibes spontaneously into core can also be monitored, which is used as additional data for assessing the sample's wetting characteristics (Tang and Morrow, 1999 and 2005; Nasiri and Skauge, 2009; Ma *et al.*, 1999). If we assume that the pore volume (P_v) of the sample is entirely occupied by water and oil at different immiscible phase proportions during the experiment:

$$P_v = V_{water} + V_{oil}$$

The volume of oil in the sample is expressed as:

$$V_{oil} = \frac{[P_v * (100 - Sw)]}{100}$$

The volume of oil naturally produced from the sample ($V_{oil\ (expelled)}$) is then expressed as the percent of oil in place recovered (%OOIP):

$$OOIP = \frac{V_{oil\ (expelled)}}{V_{oil\ (initial)}} \cdot 100$$

where: $V_{oil\ (initial)}$ is the volume of oil in the sample at the start of the experiment (*i.e.* at Sw_i conditions). For comparing different plug's dimensions and diverse fluid systems, the produced oil is plotted against dimensionless time (*td*) (Ma *et al.*, 1999):

$$t_d = C\sqrt{\frac{k}{\emptyset}} \cdot \frac{\sigma}{\sqrt{\mu_o \mu_w}} \cdot \frac{t}{L_c^2}$$

where: C is a constant unit conversion (0.018849), k is the absolute permeability (mD), $\emptyset$ is the porosity (fraction), σ is the interfacial tension (dyne/cm); $\mu_{o,w}$ is the fluid viscosity (oil and water, cP), t is the imbibition time (min) and L_c is the plug's length (cm).

3.2.4.2 Forced Displacement

Forced displacement experiments were conducted employing the set-up shown in Figure 3.7. The core holder consists of a pressure transducer connected to the upstream and a back pressure regulator to maintain pore pressure. The sample is contained within a flexible sleeve to mimic the reservoir's *in situ* stress conditions. A metering pump was used for injecting fluids (brine or oil) at controlled flow-rates. Measurements where conducted at constant room temperature of 21°C and atmospheric conditions at the Wolfson Multiphase Flow laboratory of the University of Leeds. Effluent fluids were continuously collected and later separated using a centrifuge. In this way it was possible to determine the sample's average water saturation by material balance. Water saturation was also estimated by weight differences.

Forced displacement procedure was mainly used for achieving end-point saturations (*i.e.* Sw_i and So_r). Sw_i is reached by injecting oil into a fully-saturated sample until no further brine is produced (*i.e.* drainage). Similarly, during the displacement process of the oil by brine (*i.e.* forced imbibition or waterflooding), there is a volume of oil remaining in the sample that is characterised by a residual oil saturation (So_r). Figure 3.15 describes the concept of the end-point saturations for strongly-wetted samples (Donaldson *et al.*, 1969).

Forced displacement experiments were performed using cylindrical core samples of approximately 5 cm long and 3.8 cm diameter. The flow-rates employed for displacing immiscible phases varied from 0.2 to 3 ml/min. The injected fluid pressure remained below the sample's stress conditions to avoid leaks or pore collapse. This was monitored by the inlet pressure transducer which was fixed by controlling the flow rate.

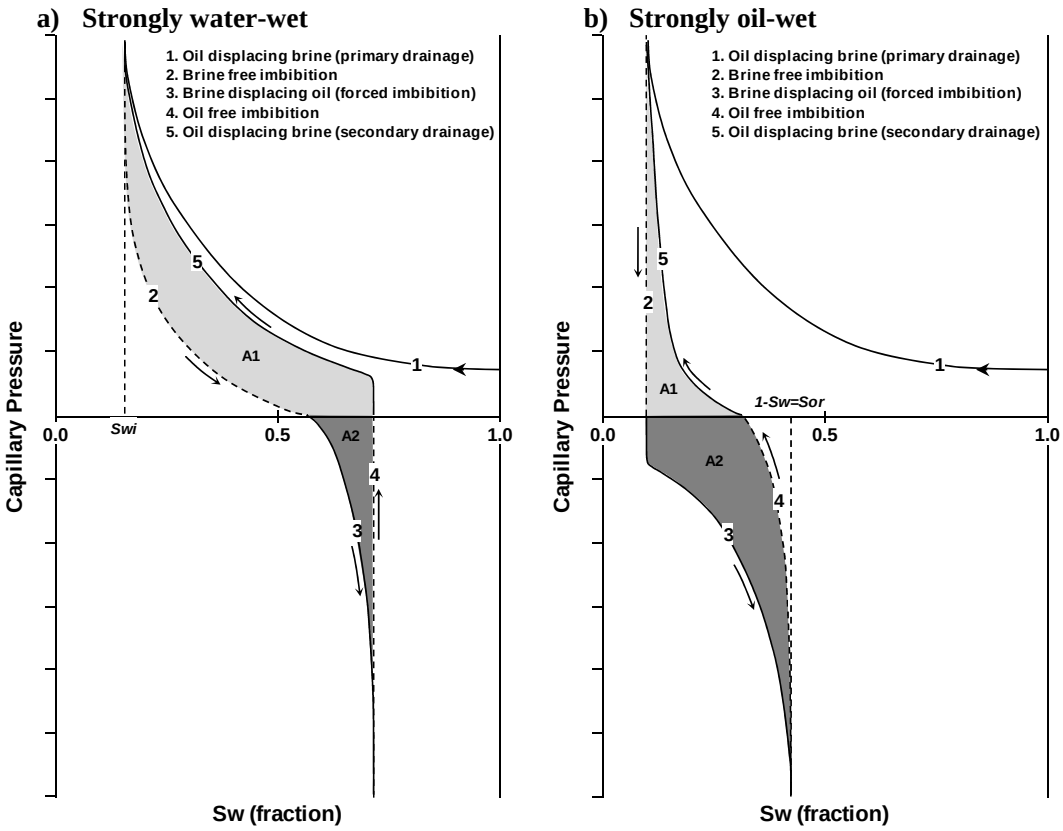

Figure 3.15 Drainage and imbibition capillary pressure curves for strongly wetted reservoirs (modified from Donaldson *et al.*, 1969)

3.3 Fluid Samples

The following paragraphs describe the analytical procedures conducted in fluid samples. The fluids used in this project were mainly of two types: brine and crude-oil. Brine samples were analysed through the examination of their inorganic chemistry. These samples were collected from a number of fluid displacement tests and then analysed using a plasma source apparatus. The analyses conducted in the crude-oil samples were mainly descriptive and used to characterise crude-oil phases for further comparative analyses with other crude-oil systems.

3.3.1 Brine

3.3.1.1 Inorganic Chemistry Analysis

Permeability impairment experiments were conducted using a number of brine samples. The brine was injected through a core sample and the permeability variation was analysed by changing the type and concentration of brine. The brine concentration varied from 0.5 to 3.5% of NaCl. The effluent fluids were collected and stored for further analysis.

The collected fluids were diluted with de-ionised water (DW) to produce approximately 20 ml of solution at 1.5% NaCl concentration. The elements tested were Al, Ca, Fe, K, and Mg, as these were suspected to be lixiviated from the core sample. Blank solutions of each brine concentration used for conducting the experiments were also analysed by the ICP-AES. This was performed for validating the results.

Inductively coupled plasma by atomic emission spectroscopy (ICP-AES) was employed for the chemical quantification of selected inorganic components. ICP-AES permits the identification of trace elements in concentrations as low as one part in trillion (1×10^{12} ppt). The technique combines a high temperature plasma source with an atomic emission spectrometer. The ICP source converts the atoms of the elements in the sample to ions. These ions are detected by mass spectrometer and expressed as mg of the trace-element per litre of solution. The ICP-AES instrument used in these analyses is a Perkin Elmer Optima 5300DV ICP-OES located at the School of Geography. The tests were run by Rachel Gasior from the University of Leeds.

3.3.2 Crude-Oil

3.3.2.1 SARA Analysis

SARA (Saturates, Aromatics, Resins, Asphaltenes) test measures major crude-oil components and is a standard technique for comparing crude-oil compositions. Three methods are used for separating oil components in SARA test (Fan and Buckley, 2002): 1) clay-gel adsorption

chromatography, 2) high-pressure liquid chromatography (HPLC), and 3) thin-layer chromatography (TLC). Here the TLC method was used, which was conducted by Intertek Services, UK. The method is commercially known as latroscan TLC-FID and determines all four compound classes by adsorption chromatography (IP-469), presented as % mass.

3.3.2.2 Base and Acid Numbers

Total base and acid numbers (TBN and TAN, respectively) were determined from crude-oil samples. These numbers illustrate how alkaline or acidic a crude-oil may be. The numbers are determined by standard procedures (IP-276). Total acid number express the amount of potassium hydroxide (KOH) needed to neutralise the acids in one gram of oil. Similarly, TBN illustrate the level of base in the oil and is determined by measuring the amount of acid required to neutralize the base. The results are expressed as an equivalent amount of potassium hydroxide in one gram of oil (mgKOH/g). Total numbers were conducted by Intertek Services, UK.

3.3.2.3 Contact Angle and Interfacial Tension

Diverse techniques were used in this study for assessing wettability in the Chicontepec reservoirs. One of these techniques was analysing the adhesion of a crude-oil sample obtained from a producing sand unit into quartz and calcite flat surfaces. Quartz and calcite are the main mineral fractions in these reservoirs.

Pure quartz and calcite crystals were impregnated with a low viscosity resin to produce blocks of 1.5x1.5x1.0 cm. Flat mineral surfaces were produced by polishing these blocks with successively finer grades of diamond paste. The blocks were cleaned with acetone and DCM, and then immersed in a 3.5% NaCl brine for a week in closed flasks to establish ionic equilibrium. Pairs of these samples were then immersed directly into a crude-oil sample in closed glass containers. Aging process was carried out employing a water bath device at 65°C for 72 hrs. After aging, the blocks were rinsed with Decalin which is an intermediate solvent that has been reported to preserve the wettability state of previously-aged surfaces (Tong *et al.*, 2002). The blocks were dried at ambient temperature in closed containers.

The prepared surfaces were immersed into a variety of NaCl brines and at different temperatures. A drop of oil is forced to contact the mineral surface for five minutes in which adhesion or repulsion of oil is established. The aim of the experiment is to evaluate the preference of quartz and calcite to oil, as a manner to mimic the reservoir's wettability. When adhesion occurs, the static contact angle of the drop of oil is measured as follows.

Contact angles of the crude-oil phase were measured employing the sessile-drop technique in a Krüss Easy Drop goniometer apparatus (Fig. 3.16). The device consists of a vibration isolation table, an adjustable drop dispenser and a high resolution video camera where the shape of the drop is analysed. The device is equipped with Drop Shape Analysis (DSA) software which captures the drop's geometry and dimensions. The DSA determines the drop edge coordinates, height and diameter, and the profile of the drop is extracted to estimate contact angle (Fig. 3.17a) by fitting the Young-Laplace equation. Static and advancing contact angles of oil through the brine phase were measured. These tests were run at the Faculty of Engineering of the University of Leeds.

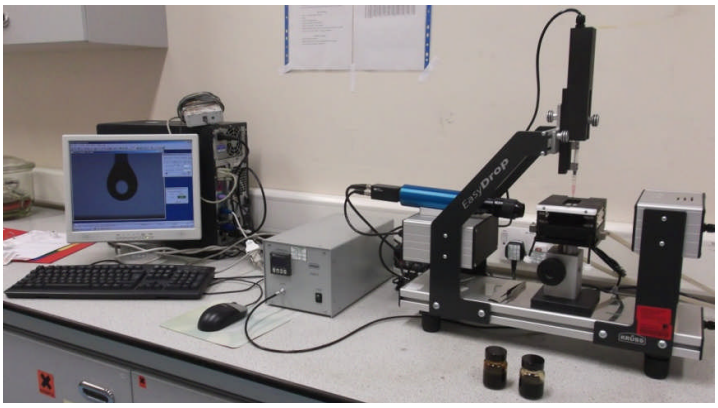

Figure 3.16 Krüss Easy Drop goniometer

Oil-brine interfacial tension was also measured employing the axisymmetric drop shape analysis (ADSA) technique. A profile of an inverted drop of oil is formed (Fig. 3.17b) and analysed by the DSA software. Interfacial tension is determined by solving Young-Laplace equation as:

$$\frac{\partial \emptyset}{\partial s} = 2 + \frac{\Delta \rho g R_0^2}{\gamma} \cdot z - \frac{\sin \emptyset}{R}$$

where: ∂s is the differential arc length (cm), $\emptyset$ is the tangent angle to surface (degrees), $\Delta\rho$ is the oil-brine density difference (g/cm^3), R_0 is the radius of the drop (cm), and γ is interfacial tension (mN/m).

a) **b)**

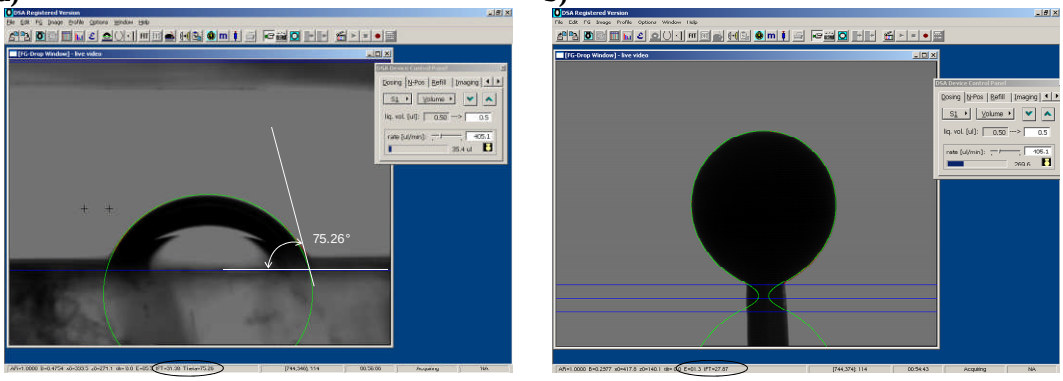

Figure 3.17 a) contact angle and b) interfacial tension determination

CHAPTER IV.
RESERVOIR DESCRIPTION

This chapter describes the main textural, mineralogical, and petrographic characteristics of the reservoirs in this study as well as the general sedimentary features of the S4 reservoir. The description is based on petrographic analysis obtained from environmental and backscattered electron microscopy (SEM, BSEM), and mineral quantification from XRD analyses.

The aim of this chapter is to describe the main geological and sedimentary characteristics of the sand units in the study area, as well as their interrelationship to their detrital and authigenic components. A more detailed description is conducted in the S4 sequence, which is used in conjunction with production data to evaluate the reservoir's spatial distribution and connectivity.

4.1 Introduction

A number of petrographic descriptions of thin-sections were provided by PEMEX from reservoir samples in the study area. These consisted of 113 samples that were analysed by the point-count method. The point-count technique quantifies the main depositional and authigenic constituents based on the statistical analysis of 300 points observed in thin section. Additionally, PEMEX provided XRD results from 113 samples and a number of environmental scanning electron microscopy (SEM) images from these plugs.

During the current project, backscattered electron microscopy (BSEM) images and XRD analyses were obtained from new rock plugs as explained in chapter one. The new XRD data was comparable with the dataset provided by PEMEX, as both methods were equivalent. The interpreted mineral types and proportions in both cases resulted very similar.

All this information (*i.e.* the provided by PEMEX and the produced in this study) was integrated and interpreted to describe the main textural and mineralogical characteristics of these reservoirs. The crossplots and images shown in this chapter were produced by combining both datasets.

Additionally to this, Mayol-Castillo (2005) provided substantial information regarding composition of Chicontepec crude-oils. These are shown in a number of figures in this chapter to illustrate their variability. Similarly, a number of PVT analyses from Chicontepec crude-oils were used to show the low primary energy of the solution gas drive mechanism. The information was provided by PEMEX.

The sedimentary interpretation described below was conducted using a number of approaches. First, all the existent wells in the study area (*i.e.* 284 wells) were incorporated into *Interactive Petrophysics*® software in which these were edited and interpreted (Fig. 4.1). A more detailed explanation of the well-log analysis is described in chapter six. The processed well-logs were then uploaded into *Petrel*® software for further geological interpretation. In this platform a well-to-well correlation was conducted using depth-converted seismic data and the regional stratigraphic framework of the study area was produced. A more detailed analysis was conducted in the S4 reservoir that included geological modelling and simulation which is reported in chapter eight.

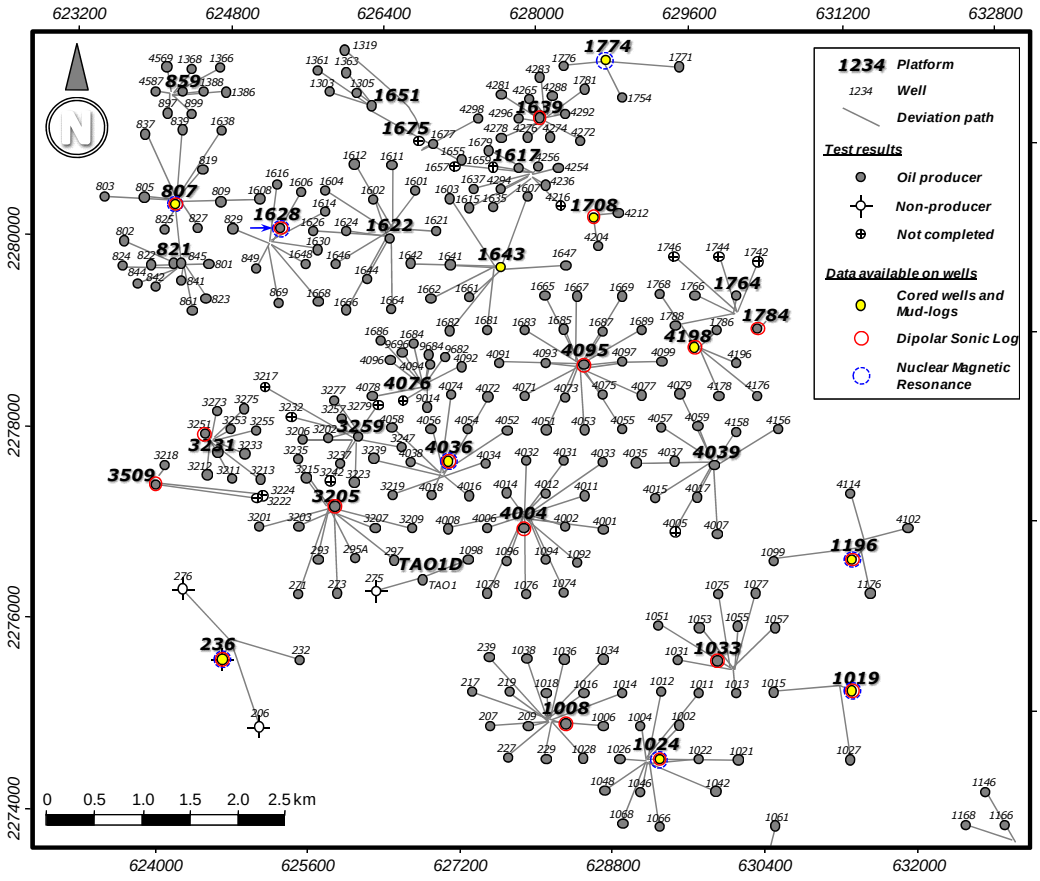

Figure 4.1 Location map of the wells used in the present research project

The interpreted well-logs were used to construct net-sand and net-to-gross (NTG) maps to illustrate the variation of the sand distribution and to support the sedimentary interpretation.

Production data (*e.g.* oil rates and produced oil properties) was also provided by PEMEX and this is displayed in the following paragraphs as bubble maps for comparing well-to-well differences in the S4 reservoir. The integration of the interpreted thickness maps, together with

the structure of the S4 reservoir and production data, was used to evaluate the reservoir's heterogeneity.

4.2 Geological Background

Chicontepec is part of a structurally confined foreland basin (Fig. 4.2), which was formed within a tectonically active regime (Sarkar, 2011) during the Paleocene-Eocene Laramide orogeny. Frequently referred as a paleocanyon or a paleochannel (Tyler *et al.,* 2004; Estrada *et al.,* 2010; Gachuz-Muro, 2009; Cheatwood and Guzman, 2002), the Chicontepec basin was subjected to a number of deposition, reworking and erosion episodes, which resulted complex sedimentary distributions and limited reservoir continuity. Reservoir sandstones were deposited in a range of sedimentary environments, associated with submarine fan systems (Tyler *et al.*, 2004), gravity-driven deposits and mass-transport processes (PEMEX, 2009). Sediments that filled the basin were supplied from both the carbonate-rich western mountains and from north-western sources (PEMEX, 2009; Cantu-Chapa, 2001). Deposition was primarily developed within a deep-water setting according to the biostratigraphic record (PEMEX, 2008; Busch and Govela, 1978).

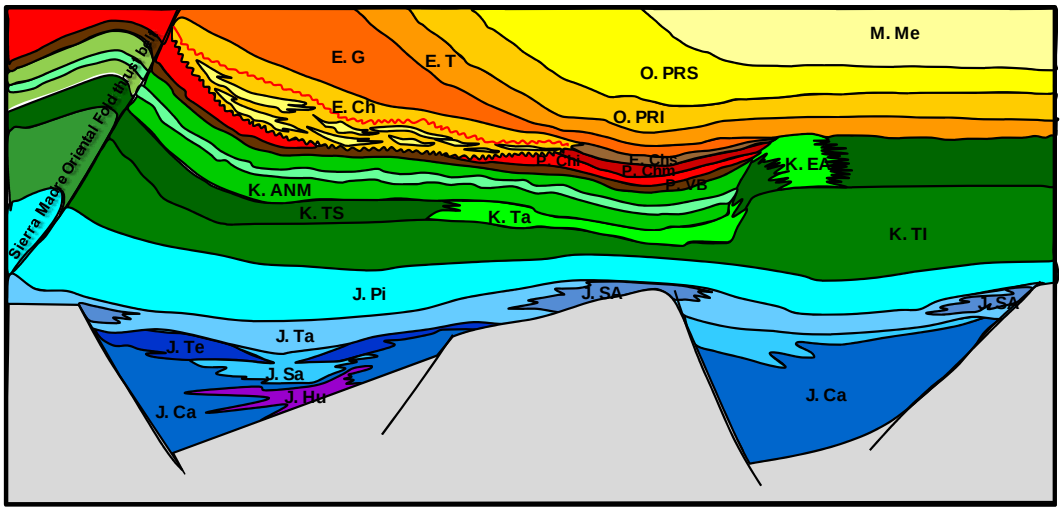

M. Me – Miocene *Meson Fm.*
O. PRS – Oligocene *Palma Real Superior Fm.*
O. PRI – Oligocene *Palma Real Inferior Fm.*
E. T – Eocene *Tantoyuca Fm.*
E. G – Eocene *Guayabal Fm.*
E. Ch – Eocene *Chicontepec Fm. (this study)*
E. Chs – Eocene *Chicontepec Superior Fm.*
P. Chm – Paleocene *Chicontepec Medio Fm.*
P. Chi – Paleocene *Chicontepec Inferior Fm.*
P. VB – Paleocene *Velasco Basal Fm.*
K. ANM – Cretaceous *Agua Nueva Mendez Fm.*
K. TS – Cretaceous *Tamaulipas Superior Fm.*
K. Ta – Cretaceous *Tamabra Fm.*
K. EA – Cretaceous *El Abra Fm.*
K. TI – Cretaceous *Tamaulipas Inferior Fm.*
J. Pi – Jurassic *Pimienta Fm.*
J. Ta – Jurassic *Taman Fm.*
J. SA – Jurassic *San Andres Fm.*
J. Te – Jurassic *Tepexic Fm.*
J. Sa – Jurassic *Santiago Fm.*
J. Ca – Jurassic *Cahuasas Fm.*
J. Hu – Jurassic *Huehuetepec Fm.*

Figure 4.2 Regional cross-section of the Tampico-Misantla basin (modified from PEMEX, 2008)

The Chicontepec paleocanyon was formed during the development of the Sierra Madre Oriental thrust belt in a series of sedimentary cycles, deposited erratically within a confined and tectonically-active regime (Tyler *et al.*, 2004; PEMEX, 2009; PEMEX, 2008; Busch and Govela, 1978). Sandstone successions are frequently incomplete due to reworking and delineation of reservoir distribution is only possible through combination of well data and seismic information. Sand thickness and petrophysical properties vary considerably, even in inter-well distances.

As part of this study, ten sedimentary sequences were recognised within the study area, six of them currently producing (Fig. 4.3). Sequence definition was carried out correlating well-log data from 284 wells and employing depth-converted 3D seismic information. Core data was available in sequences 3, 4, 6, 7, 8 and 9. Sedimentological characteristics of Sequences 2 and 5 do not represent prospective interest. The core samples available in this study were positioned into the interpreted stratigraphic setting for comparison purposes. Fig. 4.3 illustrates the delineation of the stratigraphic framework.

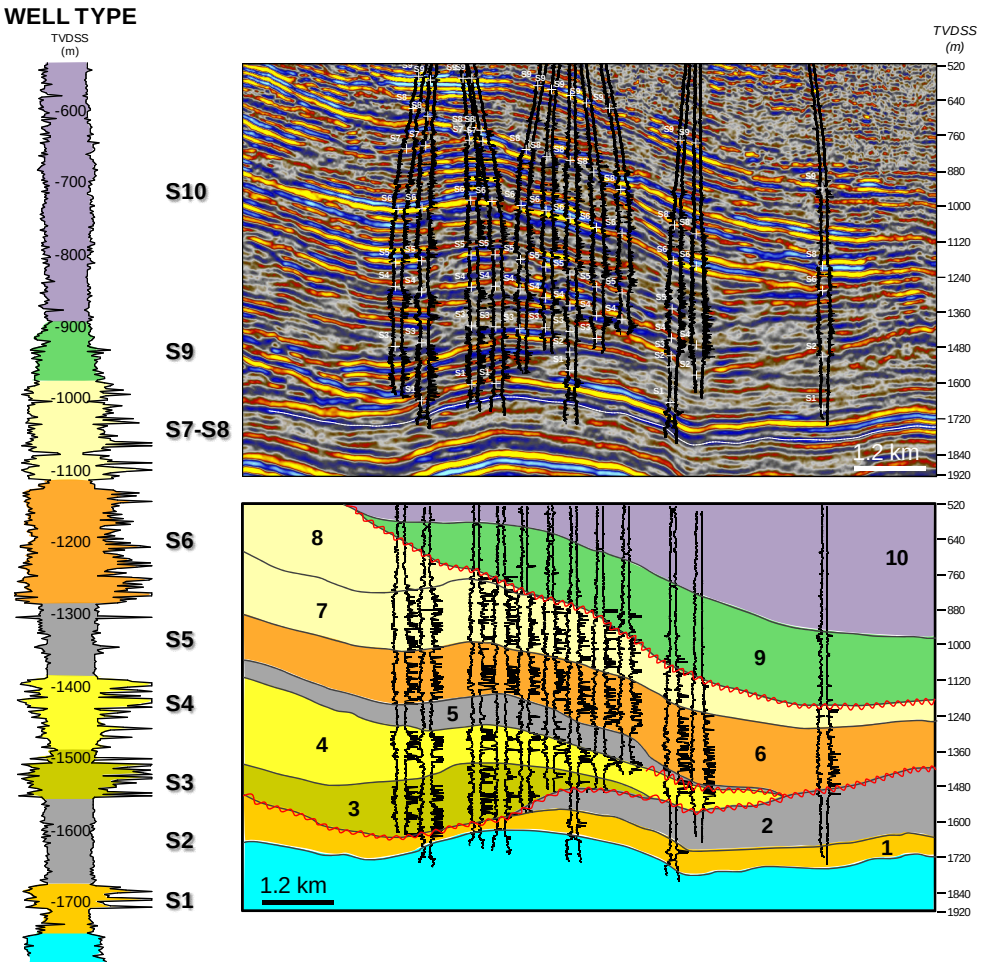

Figure 4.3 Stratigraphic definition of the study area. It is a cross section showing depth converted impedance contrasts

4.3 Regional sedimentary features

Reservoir sandstones, as observed in slabbed core information, display a wide range of sedimentary characteristics, which results into different well-log motifs. Sedimentary features frequently observed in these reservoirs along the entire stratigraphic column are:

1) **Sand-shale intercalation**, typically forming fining-upward successions. Intercalated beds vary from millimetres to centimetres and are frequently bioturbated. Grain sizes of sandstone beds vary from fine to medium and their prospective characteristics depend upon the sand/shale ratio and the sandstone quality. Sandstone beds are occasionally oil-stained and despite their thickness they may preserve exceptional petrophysical properties. Fining-upward responses are seen in the well-log character (Fig. 4.4).

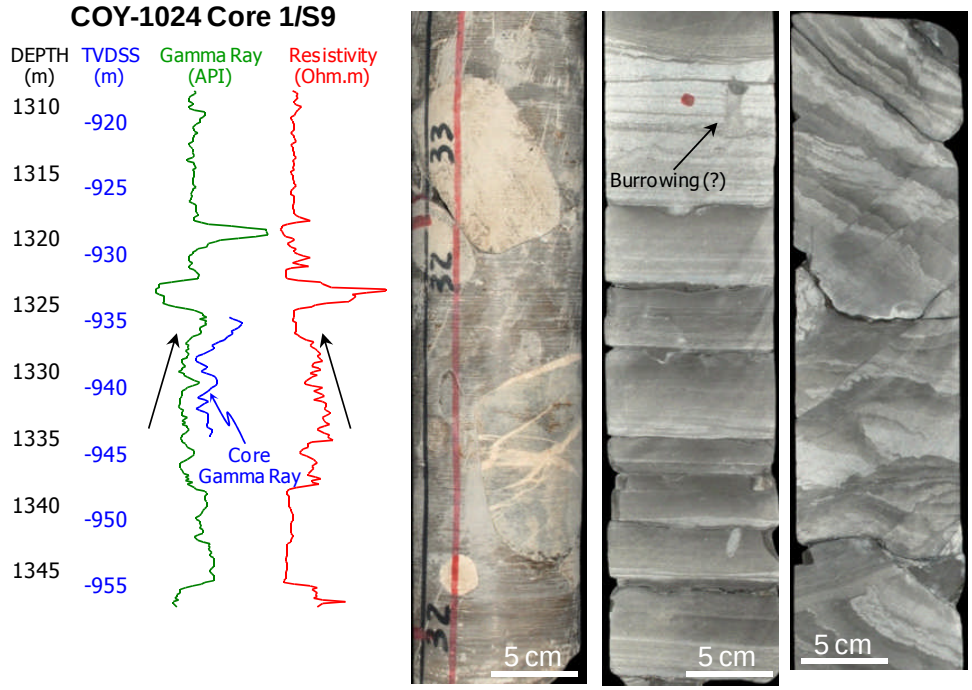

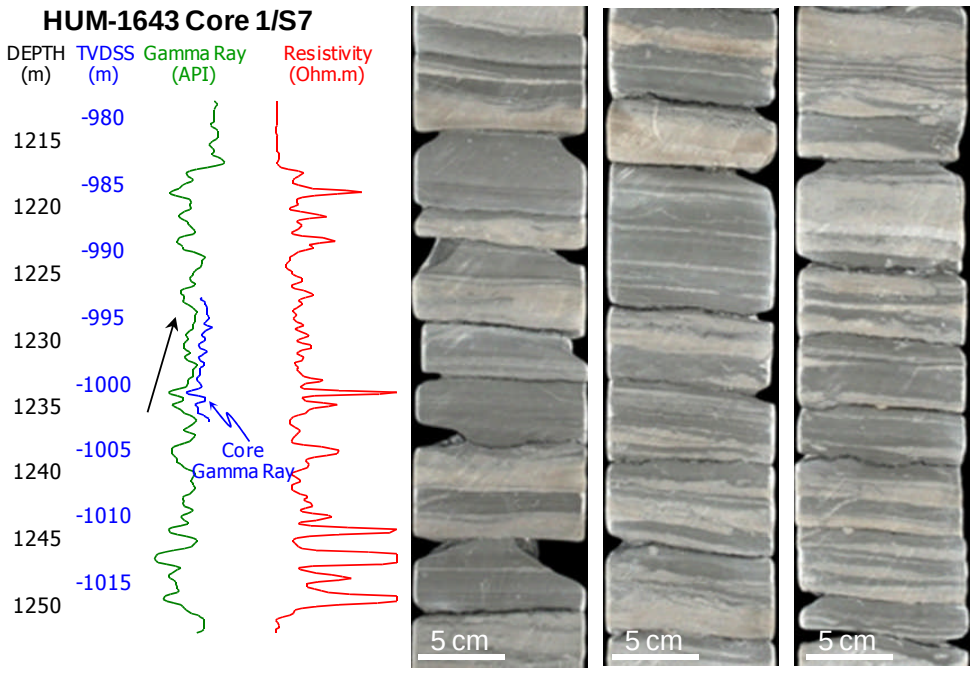

Figure 4.4 Sandstone/shale intercalation and its well-log signature. Note the alternating character of sandstone/shale beds that results into fining upward motifs in their well-log response

2) **Medium to coarse-grained, gray-coloured sandstone, generally resting over sharp contacts.** These are normally structureless (massive) and sometimes composed by floating grains (cobble and gravel-size). Porosity varies depending upon grain sorting and calcite cementation, although these generally describe porosities greater than 6%. Thickness varies considerably and the beds are normally confined between thick shale packages. Oil-stained intervals are seen frequently in these bedforms. Blocky-type motifs are recognized in the well-log response (Fig. 4.5).

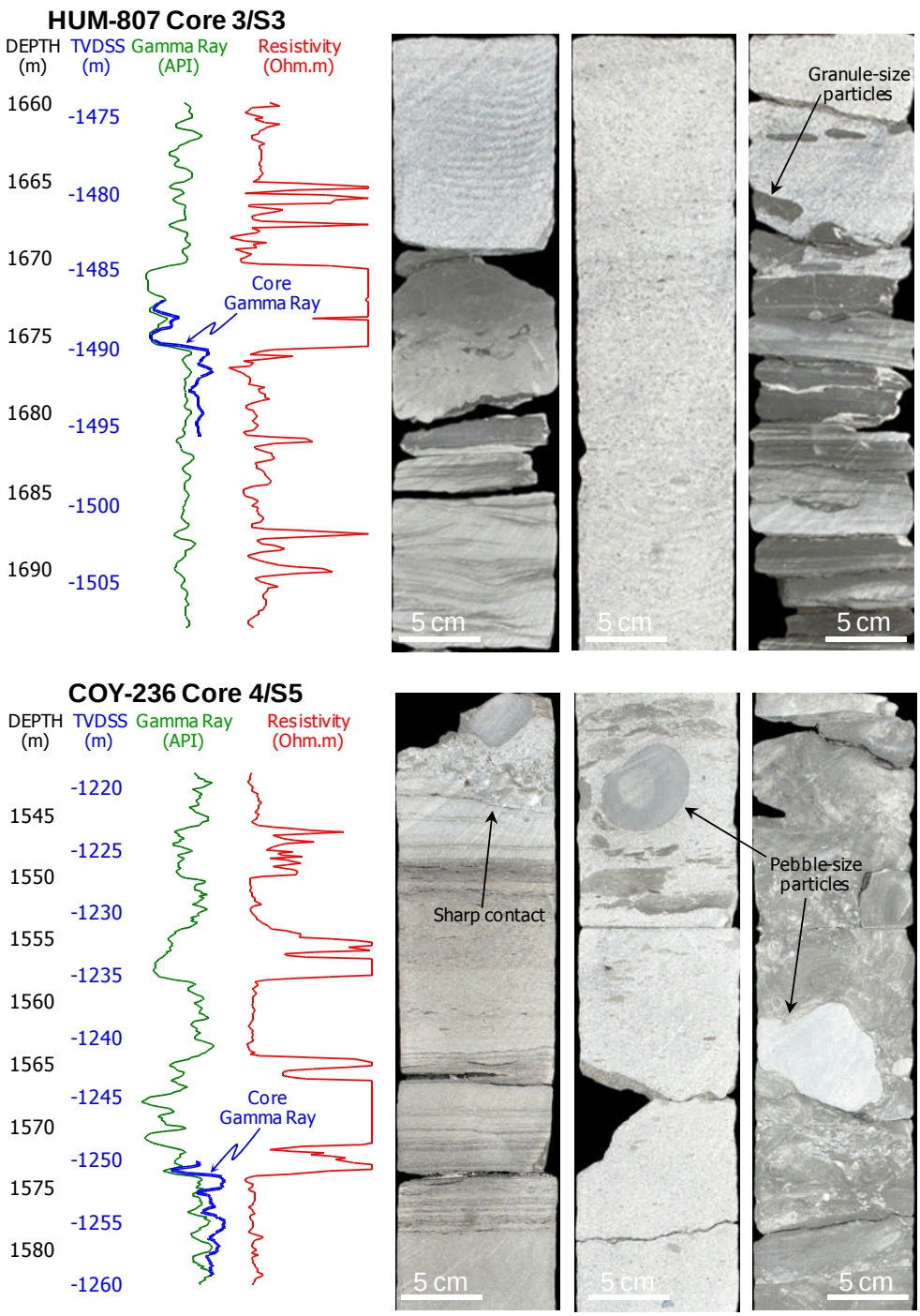

Figure 4.5 Massive sandstone. Blocky-shaped motifs are normally generated in well-logs. The bright colours are generated by the intense calcite cementation. Note that the thick sandstone beds are resting over sharp contacts

3) **Convolute beds** are frequently observed and are usually composed of silt and shale lithologies. This feature is frequently observed in younger sequences and normally do not develop prospective interest (Fig. 4.6).

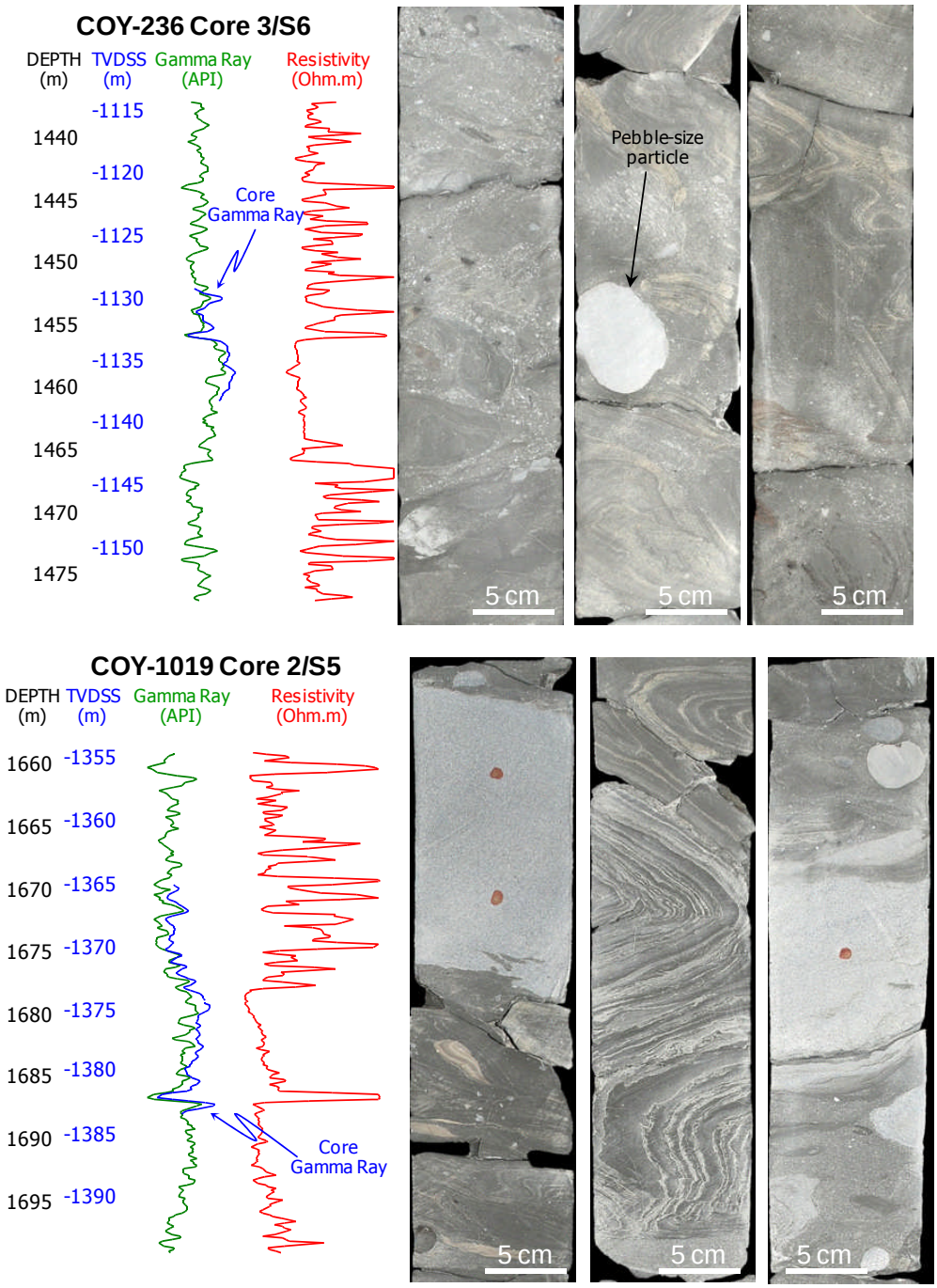

Figure 4.6 Convoluted beds. Note the overturned character of the beds suggesting syn-sedimentary processes. Generally, this bedform are accompanied by granule and pebble-sized particles

Components in the reservoirs in this study were described according to their origin (*i.e.* detritic and authigenic) to analyse the individual contribution of primary and secondary processes in rock-quality. In the following sections, both depositional and secondary characteristics of the reservoir rock are described.

4.4 Reservoir Rock

4.4.1 Depositional Characteristics

Reservoir rock in the study area is an immature litharenite and sublitharenite (Folk, 1974) with an average composition of $Q_{45}F_3L_{52}$ (Fig. 4.7). The lithic fraction, which is the most abundant component, consists of limestone (23%), plutonic (18%), volcanic (5%), and metamorphic (4%) fragments as the most frequent constituents (Granados-Hernandez and Fisher, 2014). Variable amounts of shale, sandstone and dolomite rock fragments were also recognised but in minor proportions (*i.e.* up to a total of 2%). The quartz fraction represents the second most abundant detrital component. It is usually present in two forms: as individual grains (monocrystalline, 41%) or as plutonic fragments (polycrystalline, 4%). Feldspar grains are consistently the least abundant fraction in these rocks. Sodium feldspar (*i.e.* plagioclase) is the most common (2%), although alkali-feldspar grains are also founded in minor quantities (1%).

The average detrital grain sizes typically vary from 0.07 mm (very fine sand) to 0.87 mm (coarse sand); 0.1 mm (very fine sand) is the most common (Fig. 4.7b). Gravel and boulder grain sizes are frequently observed in slabbed full-diameter cores, usually associated with erosive contacts. The broad range in detrital grain-sizes observed in these rocks result in different packing arrangement during burial, which has an effect on porosity variation.

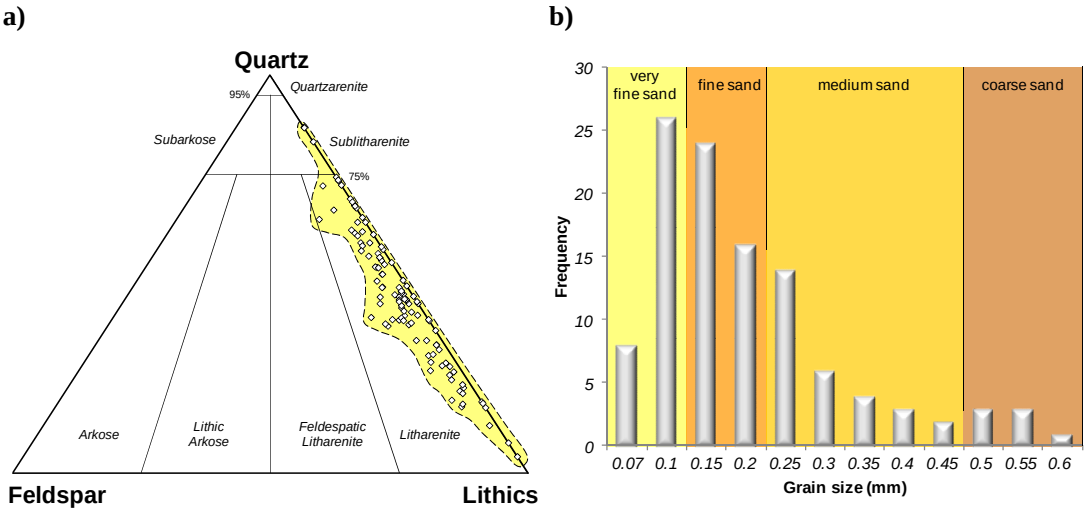

Figure 4.7 a) Sandstone rock classification (Folk, 1974); b) frequency histogram of average grain size in reservoir sandstone samples (crossplots constructed using point-count petrographic studies provided by PEMEX)

Detrital grain shapes fluctuate from subangular to subrounded and their sizes are normally variable, resulting into a moderate to poor-sorted textures. Well-sorted rocks with grains larger than 0.2 mm generally are associated with better porosity/permeability (k/Ø) ratios (Fig. 4.8).

Nevertheless, large grain sizes do not seem to be sufficient for controlling rock quality. Grain sorting appears to be a key element for developing prospective rock characteristics.

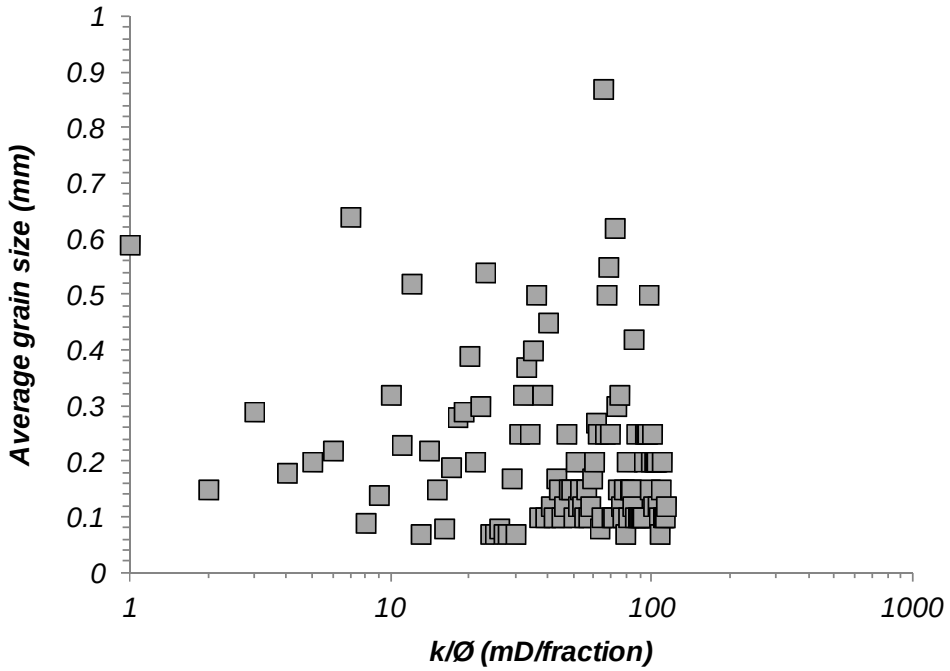

Figure 4.8 Crossplot of the k/Ø ratios and the average grain size. No tendency is observed; however, this can be resulted by the intense calcite cementation and the variable grain sizes (sorting) of these reservoirs. Well-sorted textures generally produce better petrophysical properties (crossplot constructed using point-count petrographic studies provided by PEMEX and data generated in this study)

The relative abundance of detrital quartz and limestone fragments (Fig. 4.9b), the most abundant detrital components in these reservoirs, also seems to control rock quality. Greater porosities and permeabilities are associated with greater detrital quartz to limestone fragment ratios (*e.g.* sequences 4, 6 and 8). This appears to be reasonable as quartz is chemically more stable than calcite, and porosity is better preserved when the rock contains more quartz than calcite. Most of the tightest samples (less than ~4% porosity) have low detrital quartz to limestone ratios.

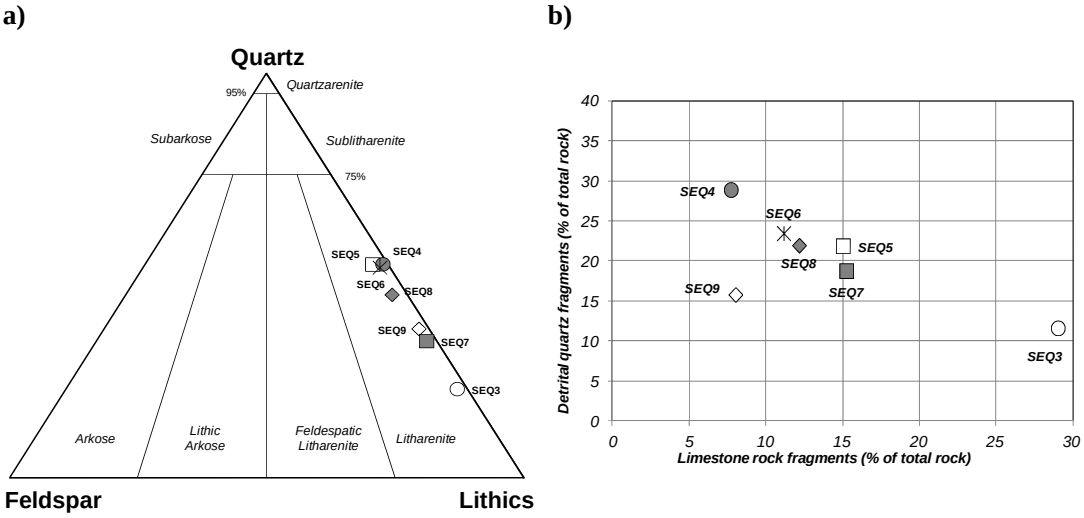

Figure 4.9 a) average rock classification (Folk, 1974); b) detritic quartz/limestone relationship (crossplots constructed using point-count petrographic studies provided by PEMEX)

The quartz-to-limestone variation also evidences the series of fluctuations in the sedimentary supply, which is in part resulted from the active tectonic regime. The most significant change in such variation is observed in Sequence 3 (carbonate-rich) to Sequence 4 (quartz-rich), as it is shown in Fig. 4.9b.

4.4.2 Authigenic Mineralogy Characteristics

Diagenetic minerals typically found in these rocks are: calcite (30%), dolomite (0.4%) and pyrite (0.05%). The reservoir rock experienced intense calcite cementation as consequence of the high detrital carbonate content, which significantly reduced the pore space. Calcite cement occludes the rock's intergranular volume (IGV) in variable ranges, depending on the depositional porosity and the burial history. IGV expresses the effects of compaction and cementation and is determined by the sum of intergranular pore space, integranular cement, and depositional matrix (Paxton *et al.*, 2002).

On average, authigenic calcite occupies 30% of the IGV in most samples (Fig. 4.10a), but it can also occupy up to 50% of the IGV in the tightest rocks. Porosity reduction caused by cementation seems to have been more important than by compaction in these samples (Fig. 4.10). Porosity has also been reduced by the immature character of the rock, which in conjunction with the subangular detrital grains, tend to be less favourable for preserving depositional porosities during burial. The large number of point-to-point grain contacts seen in thin sections, indicates that compaction was not pervasive. Porosity is approximately reduced by 1% for every 2.5% increment in calcite cement (by total rock volume) in most samples (Fig. 4.10b); although this varies widely.

Despite the abundance of calcite, the porosity observed in the majority of the samples is intergranular; secondary porosity by grain dissolution (*e.g.* feldspars) is rarely observed. When present, secondary pores are normally distributed as oversized pores compared to the integranular matrix, however these do not seem to be interconnected and their influence to fluid-flow is neglected in this study. Mercury injection data normally describe uni-modal curve shapes, suggesting that a single pore family controls fluid-flow. Examples of these modal curves are shown in Chapter 5, where the petrophysical analysis of the reservoirs in this study is examined.

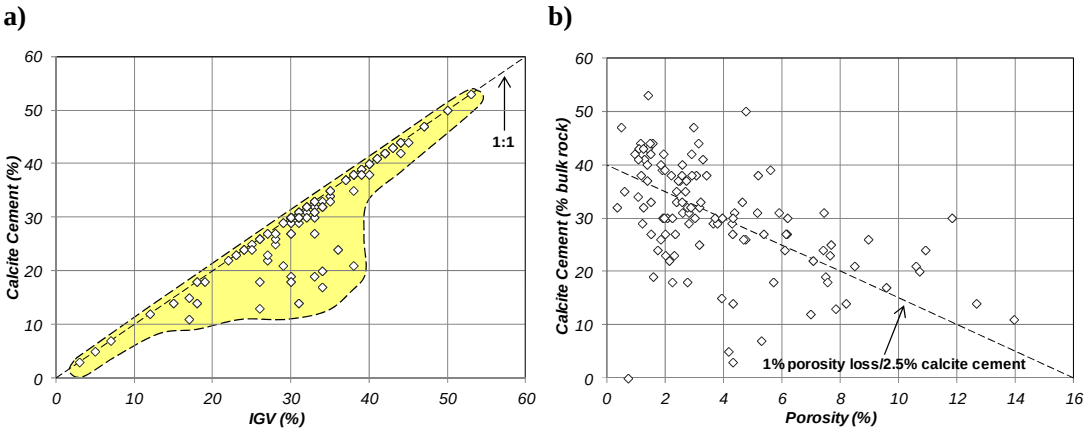

Figure 4.10 Calcite cementation relationship in these reservoirs: a) most of the IGV is filled by calcite; b) porosity reduction by calcite cementation (crossplots constructed using point-count petrographic studies provided by PEMEX)

Authigenic clay minerals (Fig. 4.11) are irregularly distributed in most of the samples, usually present in proportions <10% of the total rock composition. These normally consist of pore-lining and pore-bridging illite/smectite clay (6%), and pore-filling kaolinite booklets (3%). Chlorite is consistently the least abundant clay mineral (1%). Clay minerals were quantified by the XRD analyses conducted in this study and provided by PEMEX contractors.

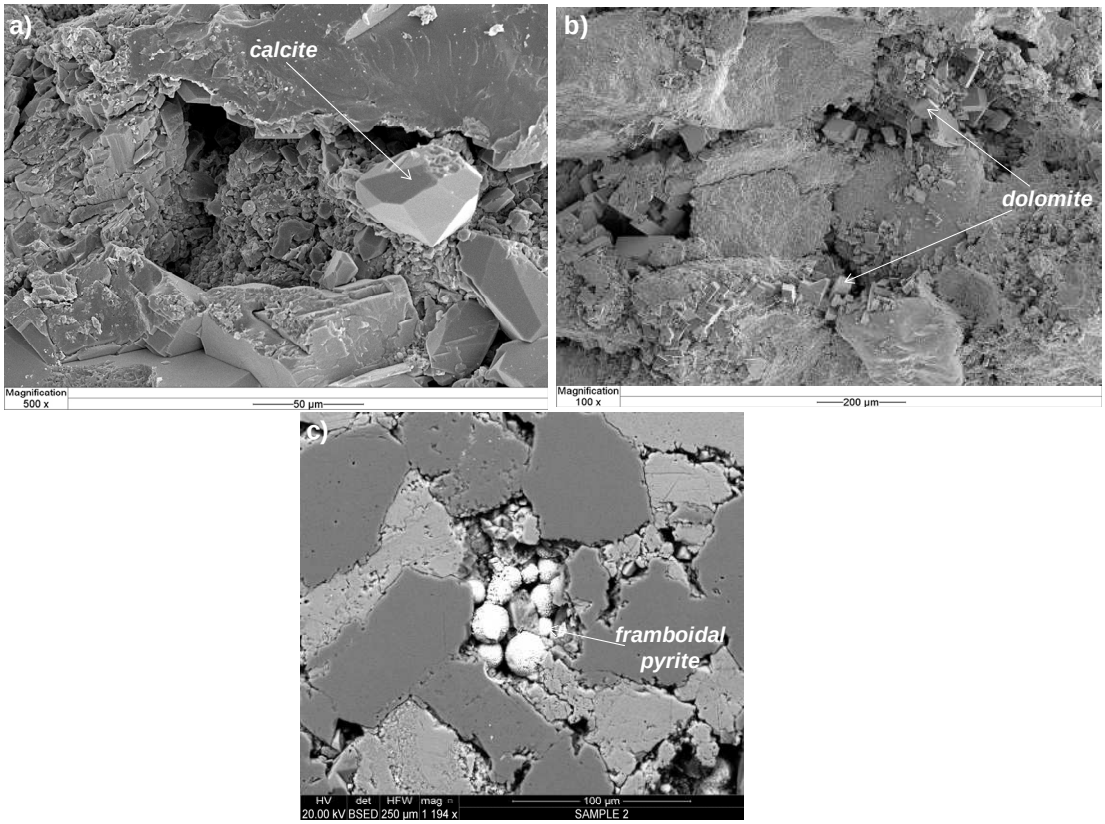

Figure 4.11 Common authigenic minerals in pore space: a) calcite, b) dolomite, c) framboidal pyrite (images a and b provided by PEMEX)

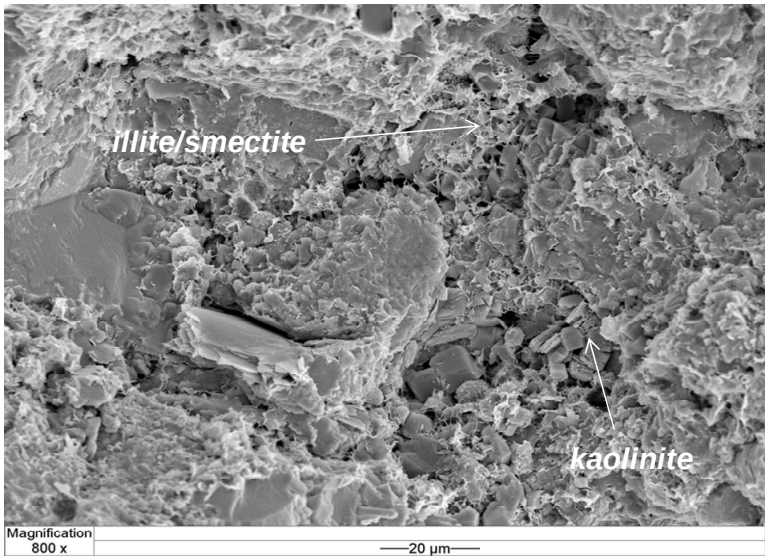

Figure 4.12 Common clay minerals into pore space (image provided by PEMEX)

The samples with the highest permeability (>1mD permeability) are characterised by their low clay and authigenic calcite content (Fig. 4.13). Their detrital grain sizes are normally larger than 0.2 mm and generally display well-sorted textures. Mixed-layer illite/smectite and kaolinite clays are also present in the pore space but randomly distributed and in much lower proportions

than lower quality samples. On the contrary, tight samples are normally associated to poor-sorted textures and high authigenic calcite cement (Fig. 4.14).

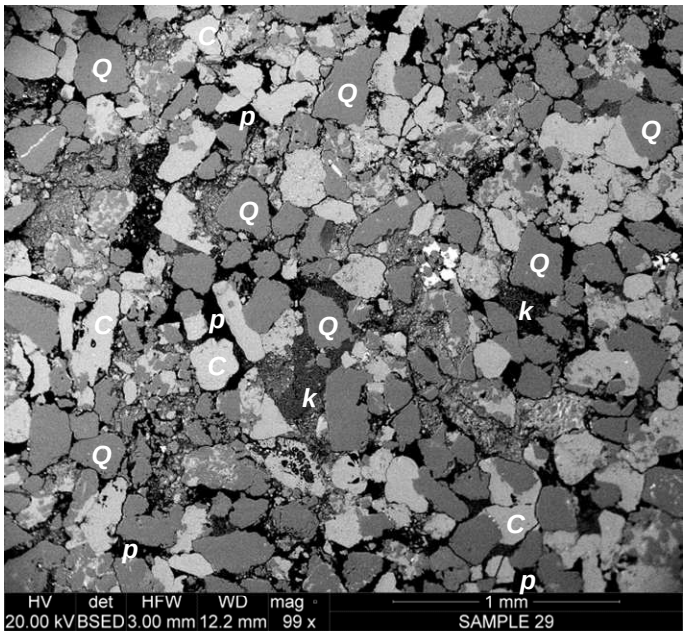

Figure 4.13 BSEM image of one of the best samples (k= 10 mD; Ø= 15%). Note the absence of authigenic calcite cement (Q:quartz, C:calcite, p:pore, k:kaolinite)

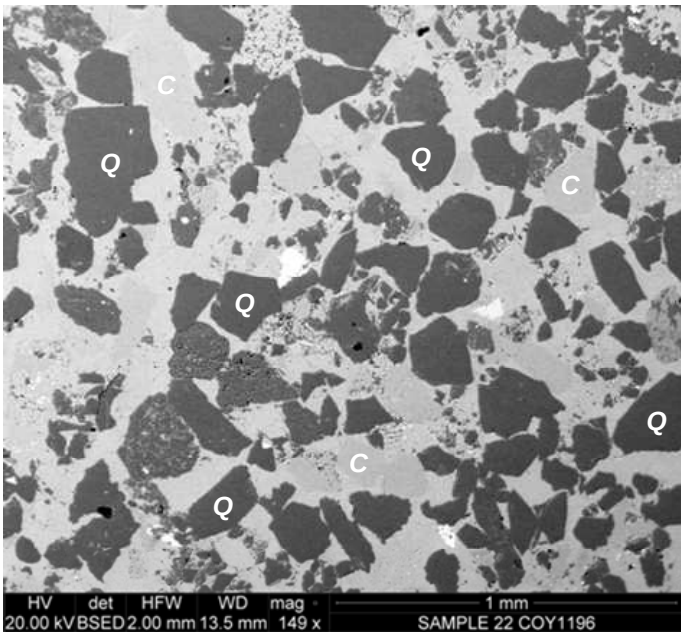

Figure 4.14 BSEM image of a low quality sample (k= 0.0003 mD; Ø= 2%). Authigenic calcite is filling almost the entire pore space (Q:quartz, C:calcite)

4.5 Reservoir Fluids

The Chicontepec crude-oils exhibit high variability in their composition (Fig. 4.15). This is thought to be the result of the complex tectono-sedimentary history of the basin, which was subjected to a number of deposition and uplift episodes that may have impacted on the crude-oil genesis (*i.e.* maturation of the Upper Jurassic source-rock and degradation of the migrated oil). Studies conducted in Chicontepec crude-oils (*e.g.* Abbaszadeh *et al.*, 2008) show wide variations in their composition, bubble-point pressure (P_b) and gas solubility (R_s).

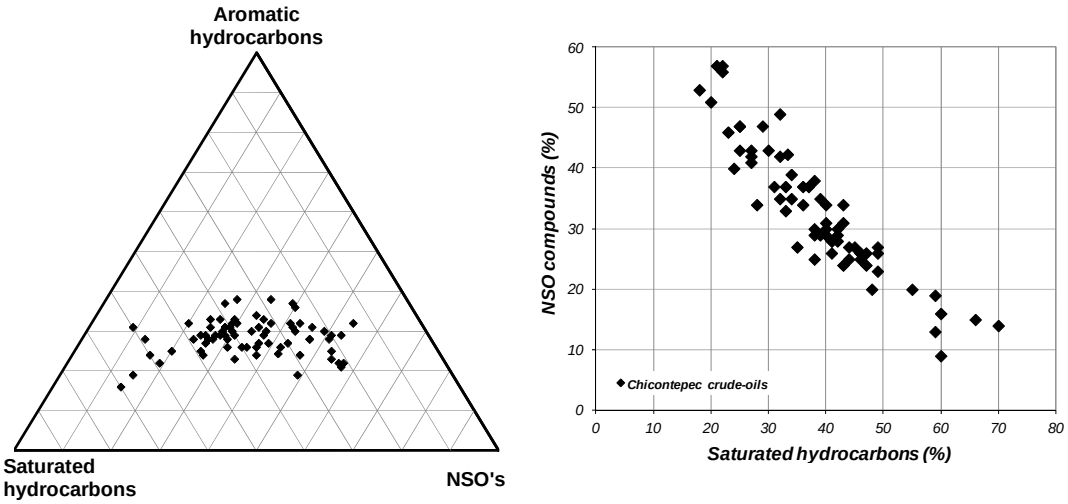

Figure 4.15 Composition of a number of Chicontepec crude-oils (data courtesy of Mayol-Castillo, 2005; ternary diagram modified from Tissot and Welte, 1985)

It is generally accepted that most of these reservoirs were initially undersaturated. However, bubble-point pressure is normally reached just after a few months of production. In most cases, less than 800 psi drawdown is required to reach bubble pressure (Fig. 4.16b). Artificial lift systems are widely applied in these reservoirs to improve primary production. Primary oil recovery by solution-gas normally accounts for less than 5% of the oil-in-place in most reservoirs (Gachuz-Muro, 2009).

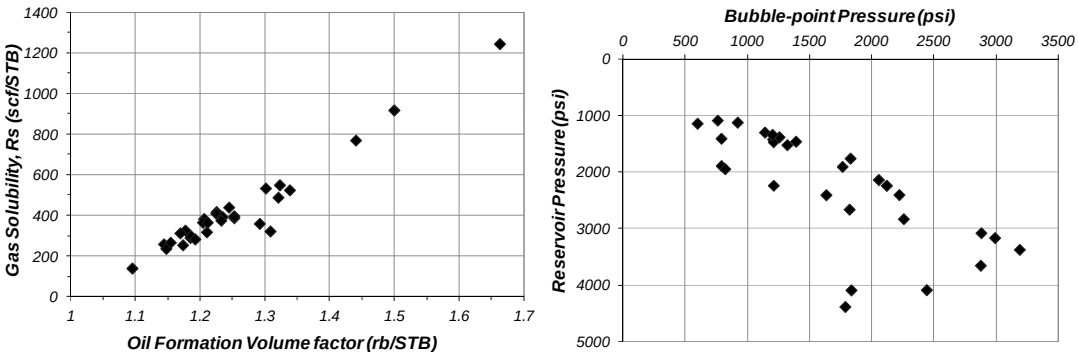

Figure 4.16 Correlations of a number of Chicontepec crude-oils (data obtained from PVT analysis provided by PEMEX)

Brine salinity is generally of 35,000 ppm of TDS (3.5%, 35 g/l) in most reservoirs and no significant variations are observed within the entire stratigraphic column. Table 4.1 illustrates the typical composition of produced Chicontepec waters.

Table 4.1 Reservoir's brine composition

Component		Concentration (mg/l)
Cations:		
	Sodium, Na^{+}	*12432.1*
	Calcium, Ca^{2+}	*835.4*
	Magnesium, Mg^{2+}	*184.9*
	Iron, Fe^{2+}	*44.5*
Anions:		
	Chloride, Cl^{-}	*20080*
	Bicarbonate, HCO_3^{-}	*1745.36*
	Sulfate, SO^{2-}_4	*200*
	Total Dissolved Solids (ppm):	***35,522***
	Equivalent salinity (in ppm of NaCl):	***32,566***

4.6 Sedimentary Interpretation of the S4 Reservoir

The S4 reservoir is the most prolific within the study area. Further PEMEX's development strategy is focused on this unit. A submarine fan system is proposed as the main depositional environment in this level, which has also been recognised in southern adjacent oilfields at similar stratigraphic conditions (Berumen *et al.*, 2004b; Tyler *et al.*, 2004; Gachuz-Muro, 2009). The complete submarine fan system is expected to envelop a larger extension than the scale of this study would be able to resolve. Unlike most submarine fans described in the literature (*e.g.* Howell and Normark, 1982; Walker, 1978), this is assumed to have developed within structurally confined conditions (Sarkar, 2011), distributing into an elongate shape following the foredeep structure parallel to the Sierra Madre Oriental.

Well-to-well correlation was conducted employing depth-converted seismic information, following the regional shale sequence superimposed to the S4 reservoir as reference (Fig. 4.17), which assured the correlation of equivalent sand bodies. Sand thickness is beneath seismic resolution and, due to the prograding and mounded pattern of the sand bodies, the complete S4 reservoir is associated with discontinuous seismic responses, which prevent the use of seismic attributes or geobody extraction to assess reservoir distribution (see the seismic discontinuous character in Fig. 4.17).

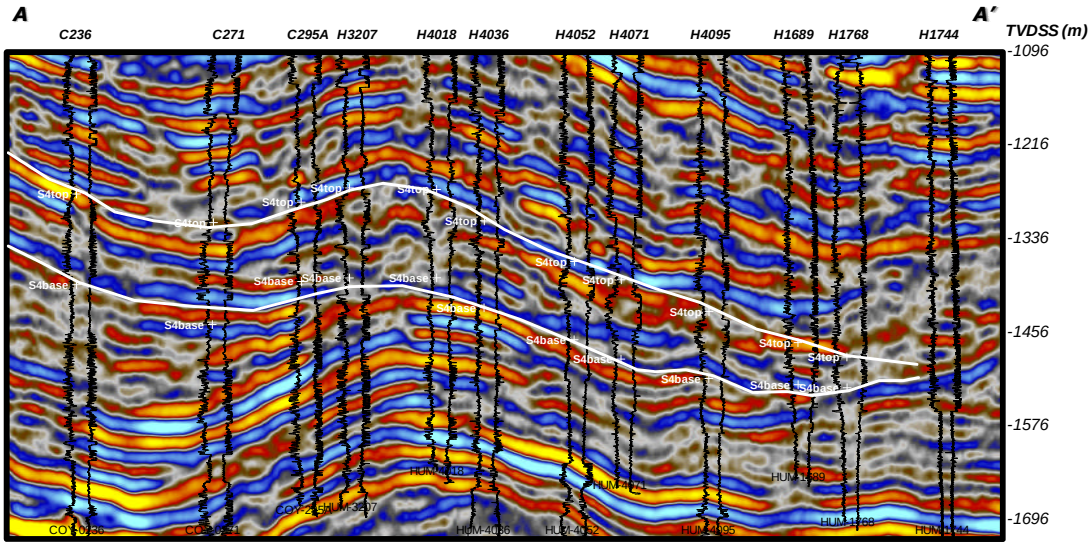

Figure 4.17 Arbitrary cross section showing the detail of the seismic impedance contrasts and the interpreted geological top and base of the S4 reservoir. Note the discontinuous character of the sand bodies and the erratic seismic response. Location of section is shown in Fig. 4.19

Sedimentary interpretation was based on the integration of sedimentary descriptions (*i.e.* HUM-1708 core; Fig. 4.18), well-log motifs, net-sand thickness distribution and production performances. Sedimentary supply by analysis of the sand thickness variations was interpreted to originate from northern portions, and it is probable that a number of supply points were active. This presumption is in agreement with information published by Vasquez *et al.* (2014).

The folds in the study area, together with the recognition of eroded intervals, indicate that basin's deformation progressed intensively after deposition. The criterion for estimating the net-sand thickness (*i.e.* the meters of sand in the entire sequence) was by application of a cut-off value of 50% in the interpreted clay volume (VCL). This value is normally established by PEMEX and generally provides with a close estimation of the amount of sand in the sequence. The cut-off has been extensively calibrated with core and outcrop data. Net-sand thickness (Fig. 4.19) was corrected by borehole deviation. The net-sand thickness map was produced in *Petrel*®. The map was produced by interpolating (*i.e.* convergent interpolation) the net-sand thickness values of each well, resulted from the well-log analysis. This method ensures honouring the control data observed in wells. The data is displayed in colour-codes to analyse the thickness variation between wells (Fig. 4.19).

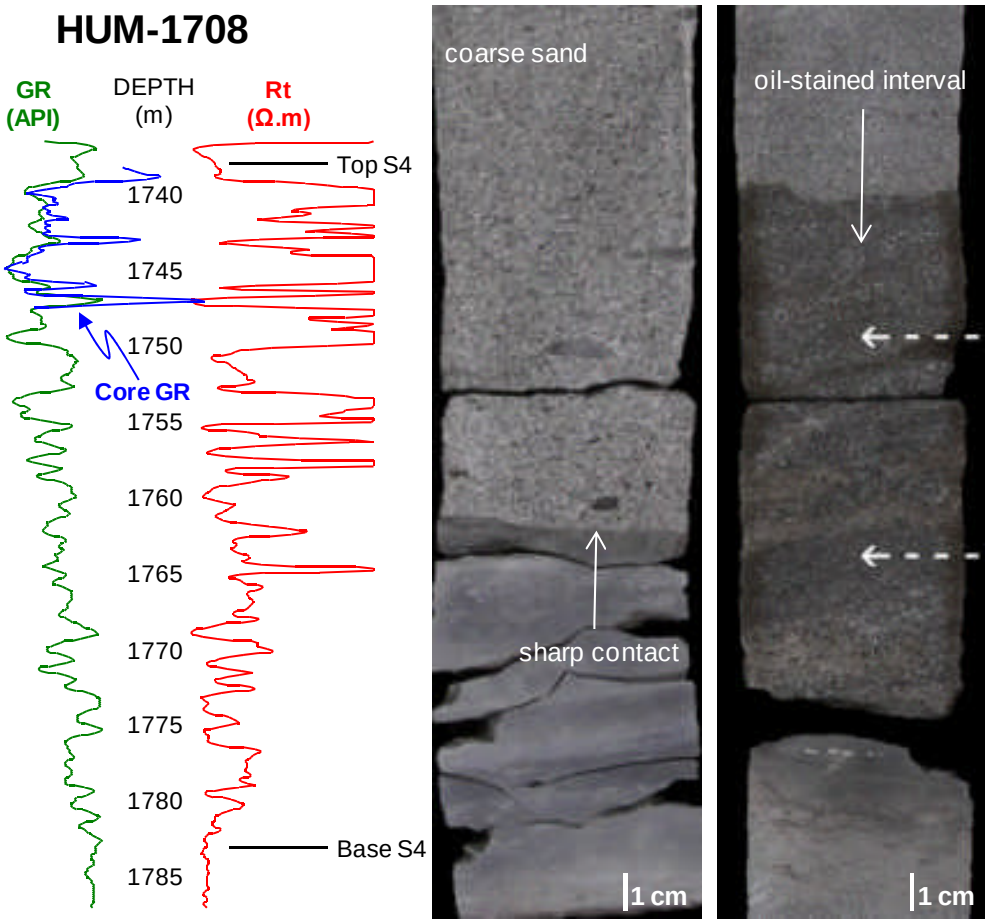

Figure 4.18 Conventional core obtained from S4 reservoir and slabbed core images. Observe that the complete sequence describes a coarsening upward pattern and that the core was acquired at the top of the succession. Medium to coarse-grained sands are oil-stained. Arrow shows places where plugs were acquired

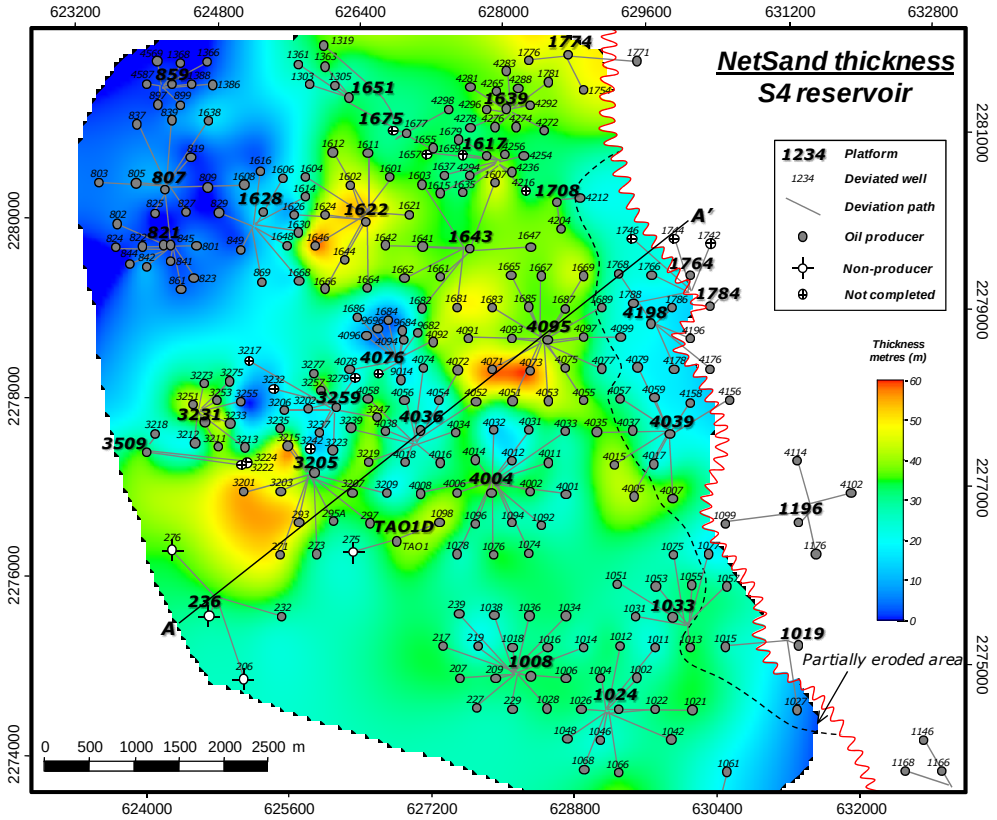

Figure 4.19 Net-sand thickness map of S4 reservoir. Note that the reservoir is partially eroded towards the eastern portion of the study area. Map constructed using a simple convergent interpolation between wells. Thick concentrated zones are observed and were corroborated to be a genuine representation of the thickness variation. Note that the sand distribution tends to follow erratic patterns with a general thinning tendency to the south

S4 reservoir generally describes a coarsening-upward sequence (Fig. 4.20) that is composed by stacked lobes and channel complexes that grade laterally from proximal to distal fan deposits. Lobes are defined in this work as the composite of overbank-levee deposits, which are mainly consistent of sand-shale intercalations at different proportions. Figure 4.20 illustrates the conceptual stratigraphic sequence of a prograding submarine fan system as depicted by Walker (1978), which seems to be in close agreement with the reservoir in this study. As comparison, the HUM-1624 well was plotted against Walker's model. Better reservoir quality is typically developed in the coarser-grained mid- to upper-fan facies. Lobe successions vary in thickness, net-to-gross (NTG) ratios and quality. Lateral variability by well-to-well evaluation is remarkably high and individual identification of lobes is difficult due to seismic resolution, deformation and partial erosion of the sand bodies. Lobes were thought to be fed by channel complexes mainly distributed along the central portion of the study area.

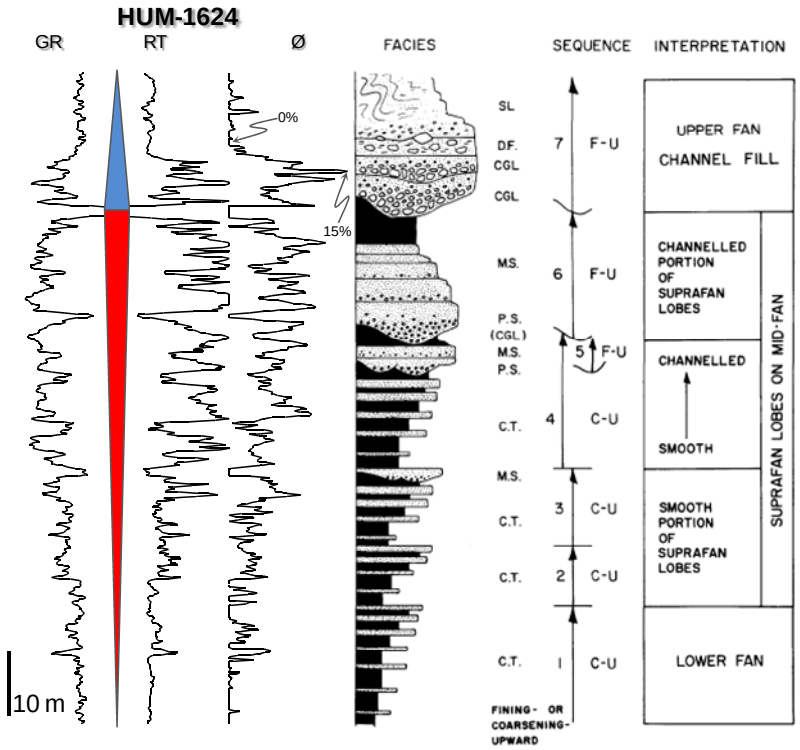

Figure 4.20 Stratigraphic succession of submarine fan system (Walker, 1978). Note that porosity variations follow the coarsening-upward trend (porosity in linear scale)

Analysis of the well-log motifs and making comparisons to outcrop and published examples (*e.g.* Beaubouef *et al.*, 1999; Howell and Normark, 1982), revealed the presence of three main sedimentary elements: channel, lobe, and mud (*i.e.* non-reservoir). Differentiation of facies is important as they generally imprint an important control on rock quality in this reservoir. In general, channel facies (Fig. 4.21) offer the most attractive prospectivity as they frequently develop porosities greater than 9% and low clay contents. Lobes (*i.e.* overbank and levee deposits) are also attractive as they usually develop high NTG ratios and a wide range of porosities (Fig. 4.22).

Channels were interpreted to express blocky-shaped signatures with sharp contacts in well-logs. This response has been observed in conventional core information calibrated with gamma ray logs in this study and in published examples (Shepherd, 2009). Two wells in the study area intersect a channel axis that locally corresponds to a high amplitude channel-like geometry. Assuming that these wells actually intersect the complete channel section and that the seismic amplitude characterises the channel geometry, an aspect ratio (*i.e.* width-to-thickness) of approximately 5:1 was estimated. This low aspect ratio is consistent with the deposits being either structurally-controlled (Cronin, 1995) or proximal submarine-fan channels (Beaubouef *et al.*, 1999); although Weimer and Slatt (2004) suggest a ratio varying from 10:1 to 300:1 for deep-water channels. Diagnostic characteristics of channelized facies include high variation on

the NTG and uncorrelatable characteristics of well-log expressions over inter-well distances (Weimer and Slatt, 2004).

High uncertainty is associated to the analysis of the channel's shape, frequency and spatial distribution. This is due to the lack of outcrop data and sub-seismic resolution. However, by observing the allocation of channels intersected by wells, together with literature examples (Beaubouef *et al.,* 1999), it was possible to delineate the channel's apparent geometry, orientation and frequency (*i.e.* amalgamation). Channelized facies seem to follow a -20° orientation, have a moderate sinuosity and poor amalgamation.

Lobe facies develop a wide range of well-log geometries which generally consist of coarsening-upward successions. Variability in their well-log shapes is the result of the mounded nature of the multiple sand deposits. Thickness, petrophysical characteristics and net-to-gross ratios vary widely, even at inter-well scale.

Mud facies (Fig. 4.23) was considered as non-reservoir and included both interlobe and shale-rich intervals. Their well-log motifs were generally associated to a straight response, typically with high gamma-ray and low resistivity values.

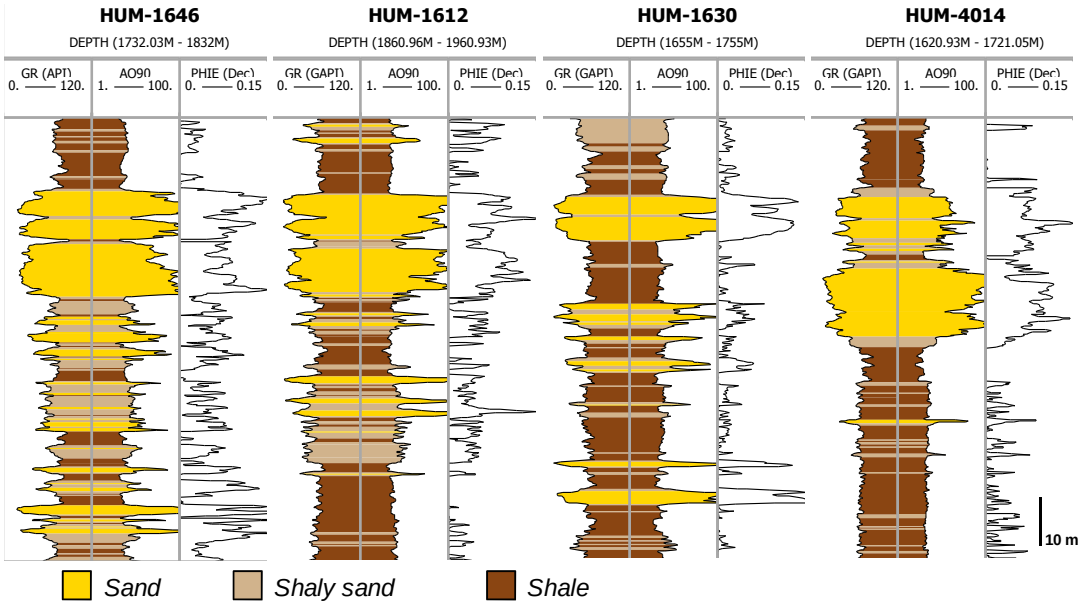

Figure 4.21 Channel facies. Observe the sharp basal contacts and blocky-shaped signatures; porosities are normally greater than 9%. The figure shows four wells located randomly in the study area; no constant spacing exists between them

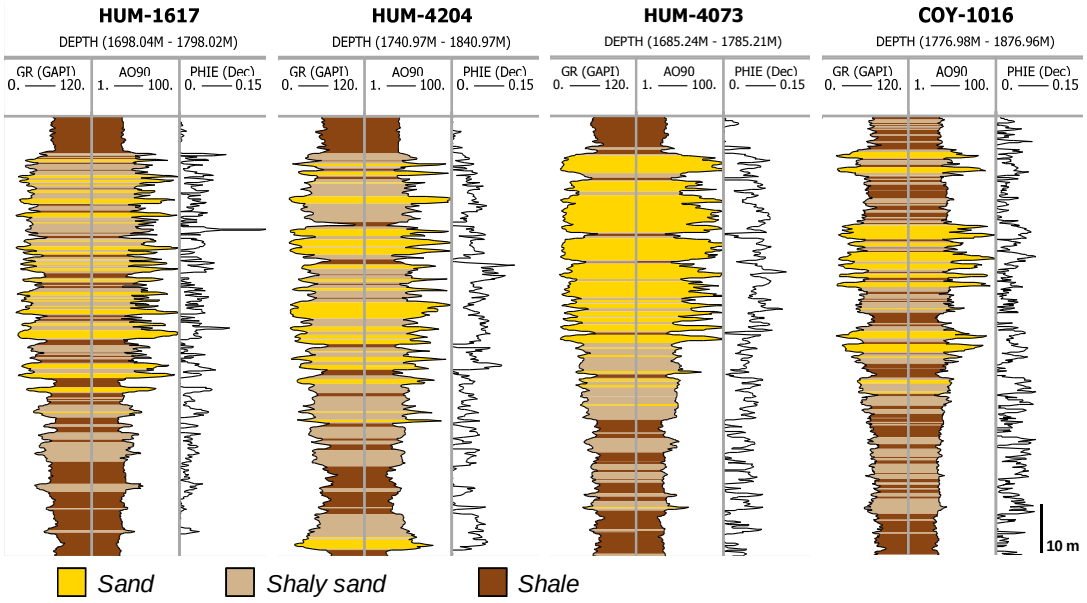

Figure 4.22 Lobe facies. Note the high variation in sand thickness and rock quality; coarsening-upward successions are normally developed. The wells are located randomly in the study area; no constant spacing exists between them

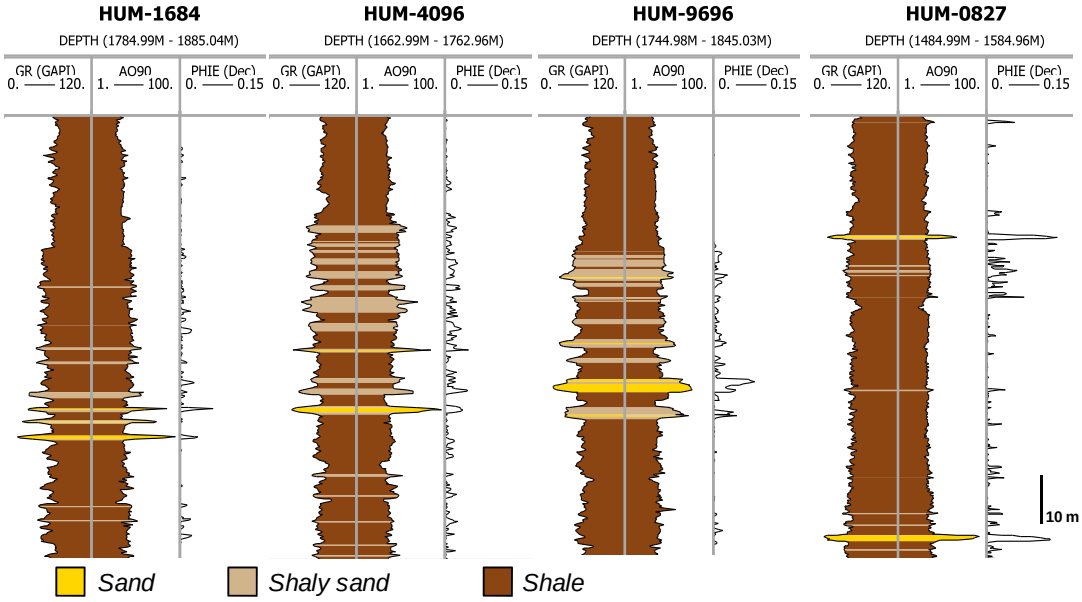

Figure 4.23 Mud facies. No prospective interest is observed due to very low net-to-gross ratios. No constant space exists between the wells shown

A facies map was constructed based on individual well-log responses and the interpreted sedimentary element for each well (Fig. 4.24). Channalized facies were sketched following their interpreted depositional dip.

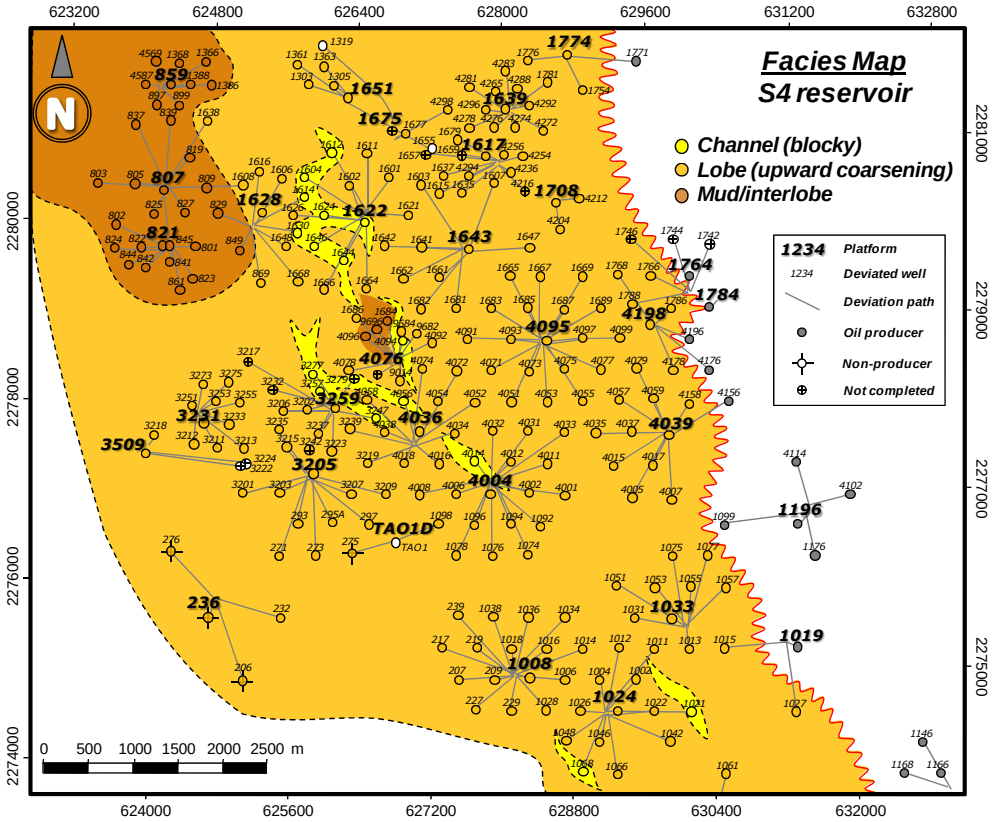

Figure 4.24 Facies Map of S4 reservoir. The figure displays the wells that according to their well-log motif were interpreted as channel, lobe or mud facies

Despite the effects of the intense diagenetic alteration, which sometimes masks the depositional characteristics, sedimentary facies generally exert a significant control on petrophysical properties. Figure 4.25 illustrates the distribution of porosity and permeability on the interpreted sedimentary facies, in which channels seem to proffer the most attractive character.

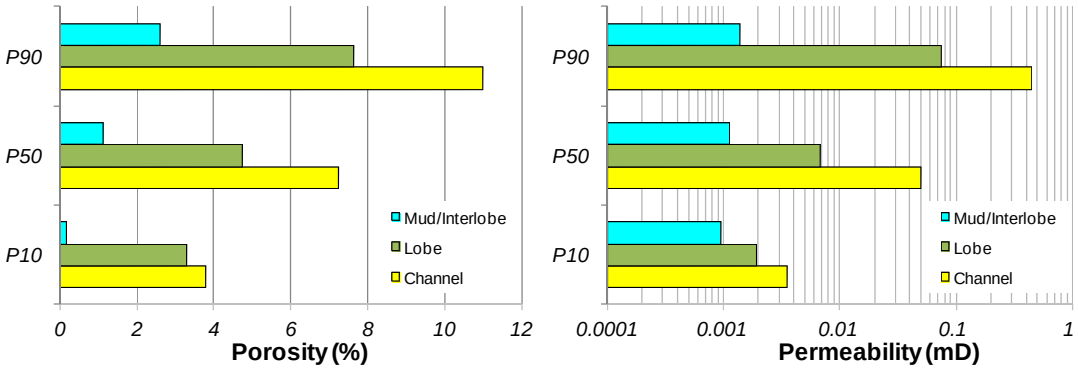

Figure 4.25 Porosity and permeability distributions by the recognised sedimentary facies at S4 reservoir. The plot was constructed averaging porosity and permeability values for each sedimentary facies of the 263 wells

4.6.1 Reservoir Connectivity and Spatial Distribution

While S4 reservoir is generally composed of multiple sand units and these frequently seem to show continuity in their well-log expression, lateral hydraulic communication between lobes may be low due to permeability barriers created by the combination of the reservoir's sedimentary characteristics and the tight rock nature. The latter is illustrated in Figure 4.26 where three wells intersect what appears to be the same sand unit as well-logs show similar character. By observing the seismic data in more detail it becomes clear that the reservoir is rather composed by three stacked bodies indicated by truncation of seismic reflectors. Porosity distribution for each well (Fig. 4.26) expresses uncorrelatable characteristics even within equivalent sand bodies.

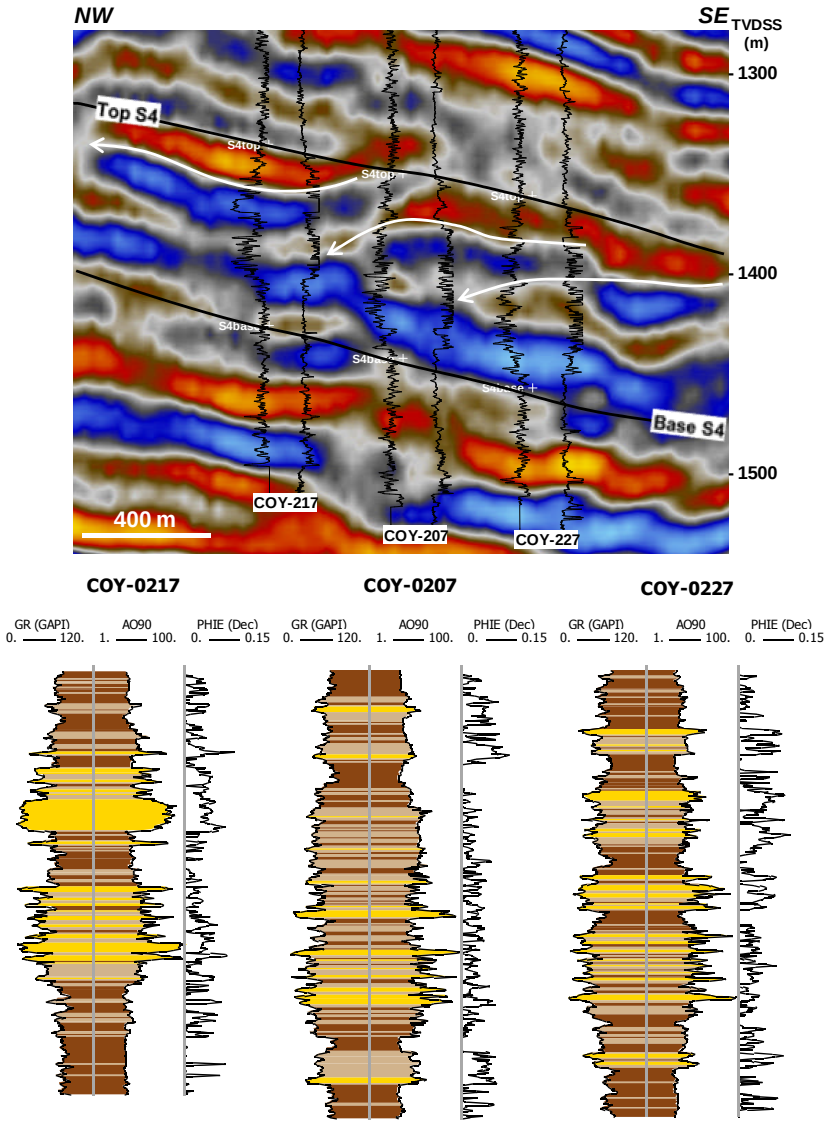

Figure 4.26 Mounded expression of stacked lobes in S4 reservoir and their dissimilar porosity values (wells are 400 m apart). The upper figure displays seismic impedance data

This feature is systematically consistent in almost the entire study area and marks a characteristic attribute not only on this unit but perhaps in the majority of Chicontepec reservoirs.

The following figures (4.27 trough 4.32) illustrate the non-homogeneous behaviour resulted from what it is seems the poor connectivity of sand units at S4 reservoir. High variation is observed in both initial oil-rates (Fig. 4.27) and cumulative oil volumes (Fig. 4.28) in both similar completion and production conditions. Six-month cumulative volume was selected as comparable data due to most reservoirs generally deplete within six-month of primary production. For comparison reasons, cumulative production data was used only for those wells completed in a single interval due to it is a common practice in the studied oilfields to set on production multiple zones (*i.e.* commingled).

High deviation is observed in initial gas-to-oil ratios (GOR) and produced oil gravities that vary from light to heavy crudes (Figs. 4.29 and 4.30). No correlation is found between these and their structural position, confirming the highly segregated pattern of this reservoir. Normally, greater initial oil rates produce greater cumulative volumes, although this is not strictly proportional. No connection is observed between initial GOR and the produced oil.

The structure map shown in Figures 4.29, 4.30 and 4.32 was produced by interpolating the interpreted well tops of S4 reservoir resulted from the well-to-well correlation. These tops were adjusted by seismic data. Kriging interpolation was used and the resulted map fitted well to the interpreted well-tops. Kriging is a non-linear Gaussian process regression that honours the given data points.

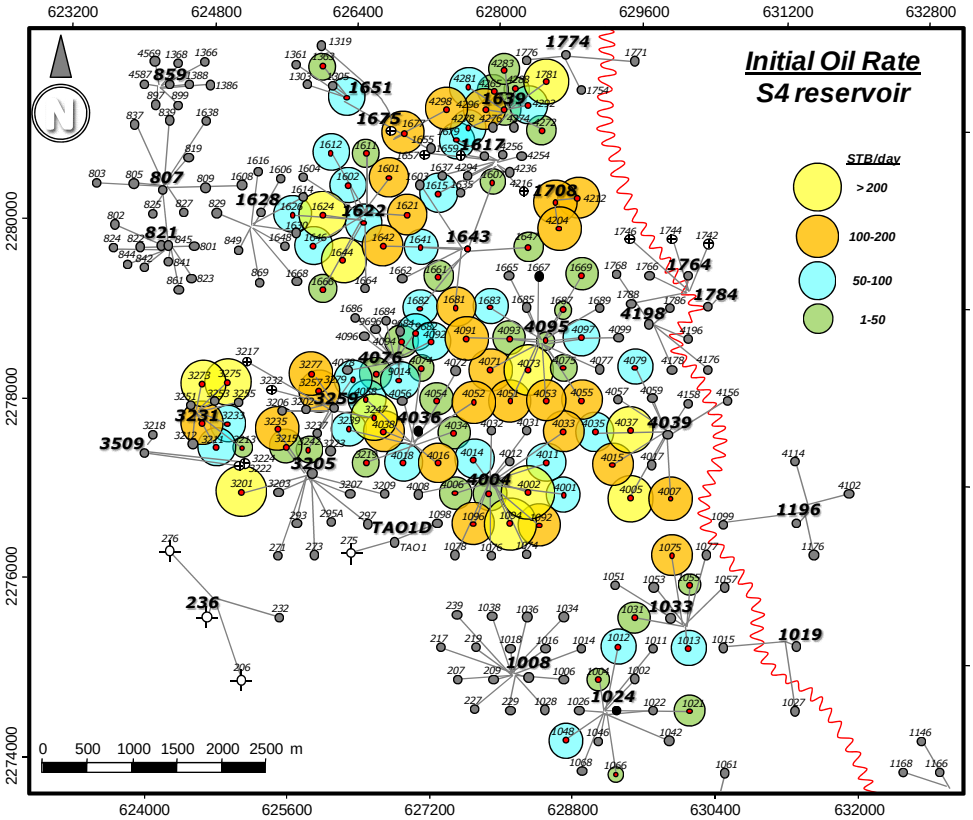

Figure 4.27 Initial oil rate

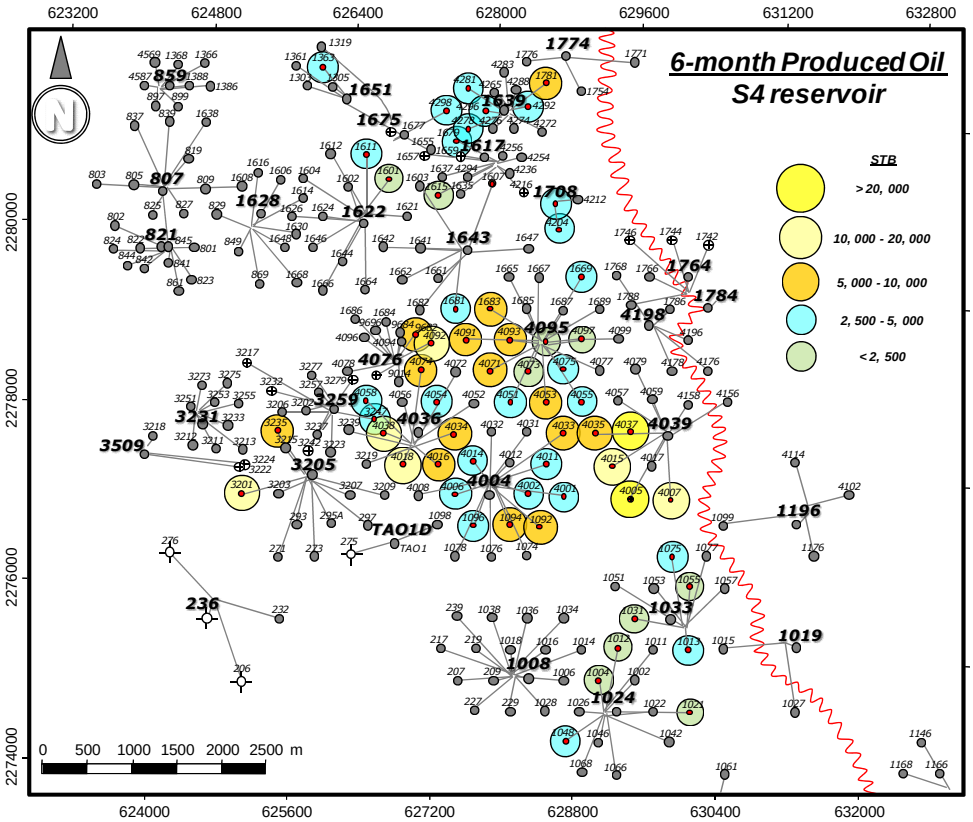

Figure 4.28 Produced oil after six-month

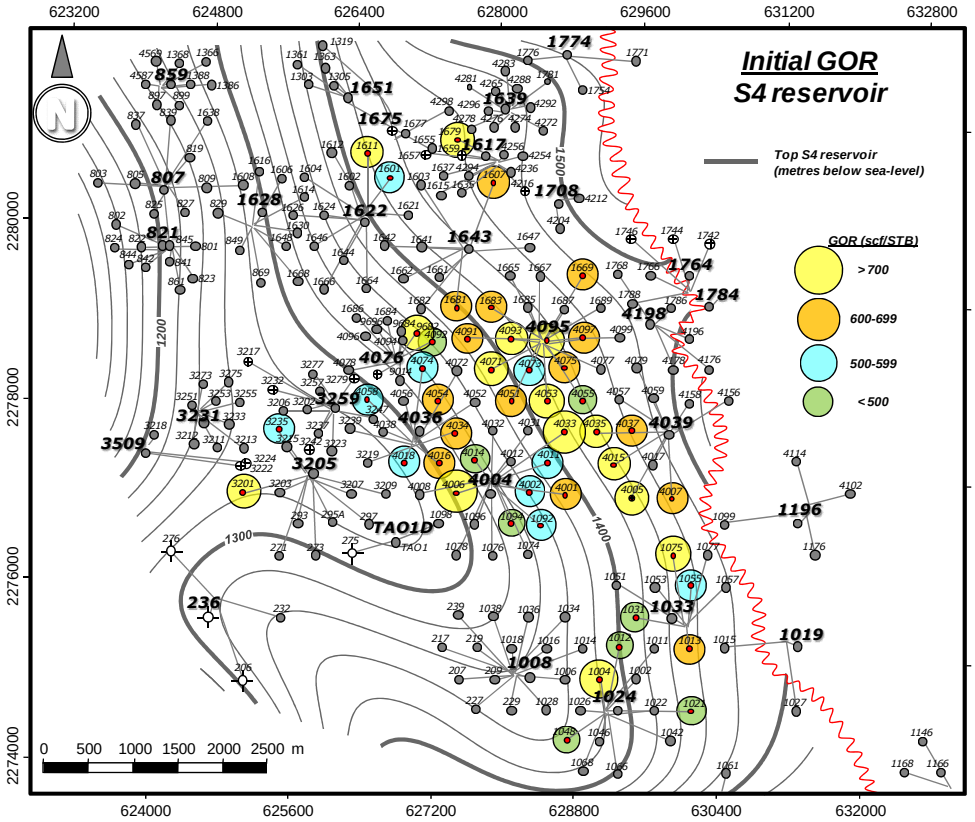

Figure 4.29 Initial gas/oil ratios

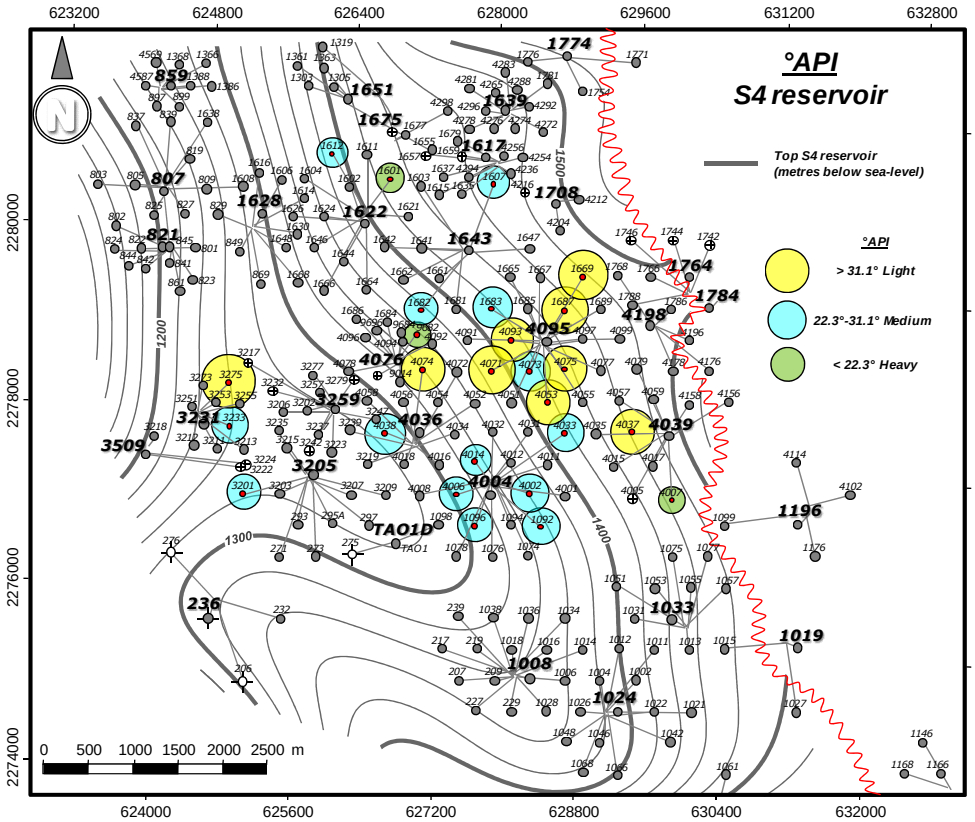

Figure 4.30 Oil gravities of produced crude-oils

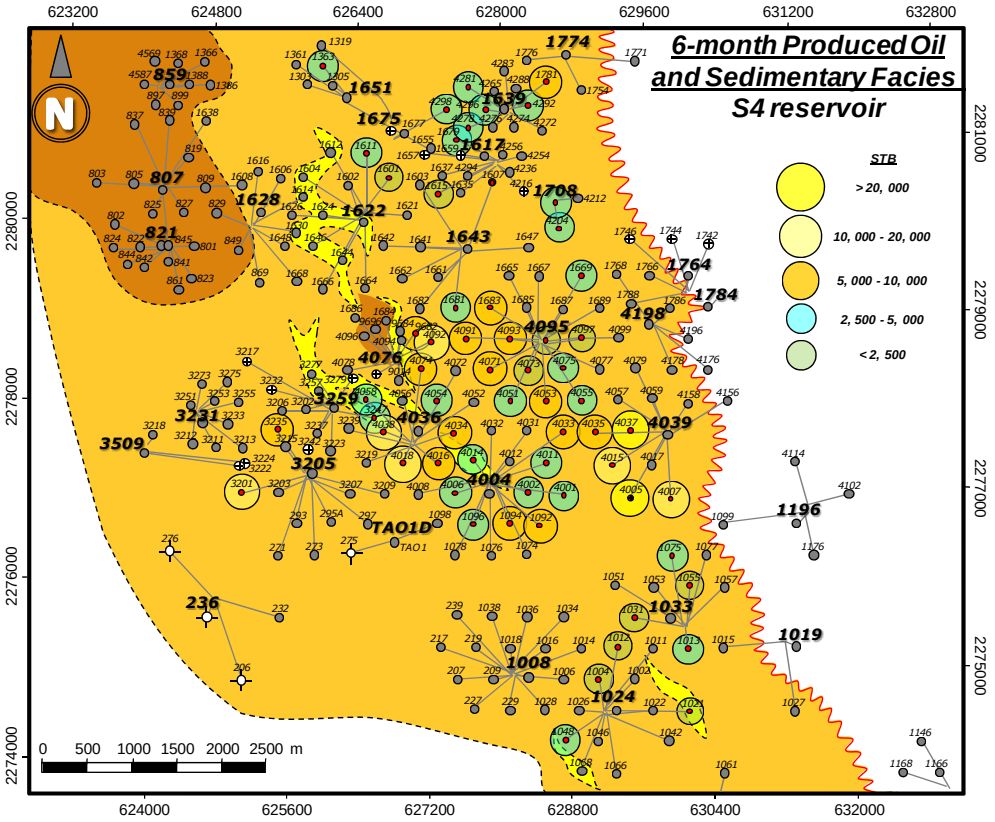

Figure 4.31 Produced oil after six-months superimposed on the sedimentary facies map

S4 reservoir behaves as highly compartmentalized units, which is evidenced by its segregated pattern of their fluid compositions and production performances. This means that sandstone bodies do not form a continuous medium to allow fluids to describe uniform flow patterns due to these have low-permeability and are frequently divided by ultralow permeability barriers. Jolley *et al.* (2010) integrate a comprehensive work for detecting and monitoring reservoir compartmentalization and explain that these permeability boundaries act as fluid-flow seals over production time-scales. Even at initial stages, where it is assumed that fluid/pressure is under equilibrated conditions, crude-oil gravities and GOR's show a strong variability between wells.

Despite having attractive petrophysical properties, the volume of oil produced in channel facies is generally lower compared to lobe facies (see Fig. 4.31). Three wells that intersect channelized facies (*e.g.* HUM-4014, HUM-3247, COY-1021) produce lower oil than the surrounding wells at same time-periods. This can probably be explained by the highly variable spatial distribution and apparent poor amalgamation of channels. It appears that channels, despite of having attractive petrophysical properties, are spatially isolated around their adjacent facies associations.

Unlike channels, lobes are composed by a number of stacked sands which are frequently distributed adjacent to each other, developing more continuous sand bodies. Cumulative

volumes in lobe facies normally develop more uniform performances, although significant deviations are sometimes observed. This can be the result of the variable NTG ratios of lobe units which impact on connectivity and consequently in produced volumes. Dynamic characteristics, such as crude-oil composition, gas solubility, and bubble-pressure, also influence flow performances and are neglected in connectivity analysis. Hydraulic fracturing performance in these reservoirs also plays an important role which is analysed in chapter eight.

Hovadik and Larue (2010) explain that a threshold in the NTG ratio should be achieved to determine whether a reservoir is highly or poorly connected. In general, increases in NTG resulting in increased likelihood of sands being interconnected. Four wells (*e.g.* HUM-4005, HUM-4037, HUM-4015 and HUM-4007) produce together the 22% of the cumulative volume after 6-month primary production. Their petrophysical properties are not significantly different from other areas; however these seem to fall into uniform alignment of NTG ratios. NTG ratios tend to be greater in the structurally downdip direction (Fig. 4.32) as S4 sequence thins. The partially eroded interval in the downdip portion also computes greater NTG ratios. At this portion, it is more likely to the sands to be interconnected, potentially developing sheet-sand geometries.

NTG represents the portion of the S4 sequence that is composed by sand and was estimated by the ratio of the Net-sand to gross thickness. The variations in NTG values seem to be the result of the series of deposition, reworking and erosion episodes typically observed in these reservoirs. This may cause the deposition of sand bodies of high-variation in both their thickness and their aerial distribution. The sedimentary character of this reservoir, together with the intense diagenetic alteration, may be the main cause of their apparent low connectivity.

NTG map (Fig. 4.32) was produced in *Petrel*® using the convergent interpolation method and employing data of 263 wells.

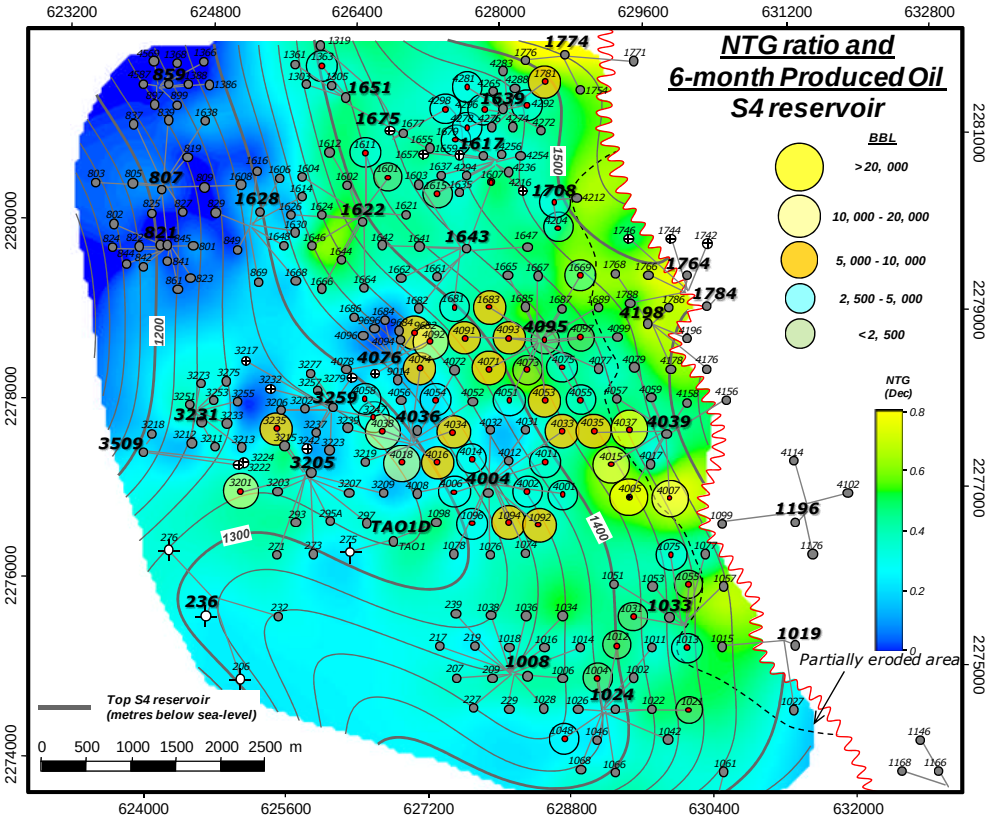

Figure 4.32 NTG ratios and produced crude-oil volumes of S4 reservoir

Weimer and Slatt (2004) describe sheet-sands to be some of the best high-ultimate recoveries within deepwater reservoirs. Sheet-sands are deposited at the termini of channels and characterised by having high NTG ratios and few erosional features, which results into good lateral continuity and potentially good vertical connectivity. Sheet-sands in the Brushy Canyon Formation of West Texas are described by Beaubouef *et al.* (1999) as highly amalgamated sands of uniform grain-size (*i.e.* massive).

Although reservoir connectivity is a difficult task to evaluate, due in part that it should involve both static and dynamic approaches, the results show that S4 reservoir is highly compartmentalized. The latter is a significant input parameter to be considered in secondary and tertiary recovery projects. Tyler and Finley (1992) proposed a mechanism to evaluate recovery efficiency by combining facies relations and drive mechanisms. Among the studied reservoirs, submarine fan systems driven by solution-gas primary production mechanism (as of S4 reservoir) are normally able to recover less that their 20% of OOIP. This is due to their high lateral and vertical heterogeneity and the limited oil recoveries by solution-gas drive mechanism.

4.7 Conclusions

The depositional and authigenic characteristics of the reservoirs in the study area were described. Reservoir rock consists of an immature litharenite with large proportion of quartz and limestone fragments. Extensive diagenesis produced a significant reduction in porosity. Generally, quartz to limestone (or calcite) ratios can be used to determine the rock quality in these reservoirs.

The sedimentary environment of the S4 reservoir was interpreted. This seems to be fit to a submarine fan system in which there were recognised three main sedimentary elements: channel, lobe and mud (or interlobe). The variations in sand distribution as well as their petrophysical properties are partially produced by the series of deposition, reworking and erosion episodes together with the intense diagenetic alteration.

S4 reservoir performs in a highly compartmentalised mode, according to their production data and produced oil properties. This behaviour seems to be consistent in most Chicontepec sand units, and establishes an important feature of these reservoirs, not only to be considered for secondary/tertiary applications to oil recovery, but also for selecting the proper parameters in forecast projections, development plans, as well as in modelling and simulation studies.

CHAPTER V.
PETROPHYSICAL ANALYSIS

The purpose of this chapter is to analyse the petrophysical properties of the reservoirs in this study. Two approaches were conducted for evaluating this: through the direct measurement of rock properties and by well-log analysis. The measured properties are reported in this chapter whereas the well-log analyses are described in chapter six. The rock tests were used for developing a number of petrophysical correlations to calibrate some of the parameters in the well-log evaluation which then were used for building a simulation model to explain variations in production between the wells.

Analysis of porosity (*Ø*), permeability (*k*), pore radius (*r*), and irreducible water saturation (*Swi*) in rock samples obtained from reservoirs of this study are evaluated. The petrophysical interpretations described in this chapter provide additional information and tools to improve the petrophysical understanding of these reservoirs.

5.1 Introduction

Diverse studies provided by PEMEX were available on a number of rock samples of the reservoirs in this study (*i.e.* Humapa and Coyula oilfields). These mainly consisted on reservoir description studies. To complement the petrophysical understanding of these reservoirs, new data was obtained during the development of this research project. This new data consisted of previously-obtained properties as well as new rock tests that had not been acquired before not only in these reservoirs but in the entire Chicontepec sand units (*e.g.* BSEM, NMR, and S/V). Table 5.1 describes both the data provided by PEMEX and the core tests produced during this study. As observed, there are six attributes (*i.e.* porosity, Klinkenberg-corrected gas permeability, XRD, MICP, cementation factor, and saturation exponent) that were obtained by two approaches.

Overall, the methodology and analytical procedures conducted in determining rock-properties in this study, specially the properties used to develop petrophysical correlations, were equivalent to those used by PEMEX. This permitted to integrate both datasets and treat them as one when correlations were developed.

Table 5.1 Reservoir Description Studies produced in this study		
Provided by PEMEX	**Obtained in this project**	**Study**
96	*46*	*Gas Porosity at ambient conditions*
96	*46*	*Klinkenberg's permeability at stress conditions*
113	*-*	*Point-count description (300 points)*
113	*33*	*Quantitative X-Ray Diffraction (QXRD) mineralogy*
-	*36*	*Backscattered Electron Microscopy (BSEM)*
109	*33*	*Mercury Injection Capillary Pressure (MICP) curves*
7	*-*	*Ultrasonic Elastic Modulus*
7	*-*	*Compressibility*
-	*35*	*Nuclear Magnetic Resonance (NMR)*
6	*6*	*Cementation Factor (m)*
5	*6*	*Saturation Exponent (n)*
-	*13*	*Surface Area to Volume Ratio (S/V)*
2	*-*	*Gas-Oil Relative Permeability*
-	*4*	*Oil-Water Continuous End-Point Relative Permeability*
-	*10*	*Brine Permeability*

Porosity data provided by PEMEX was obtained using a helium pycnometer device at ambient conditions, similarly to the gas porosities determined in this study. Permeability measurements provided by PEMEX, by the contrary, were restricted to a minimum value of 0.001 mD. This was due to an instrumentation limit of the contractor. A number of plugs provided by PEMEX plus new rock samples were employed for permeability determination to achieve a better and more representative distribution of permeability in the reservoirs of this study. This allowed construction of more predictable correlations. The entire permeability data was obtained at *in situ* stress conditions and corrected by gas-slippage (Klinkenberg's corrected). Figure 5.1 shows the comparison of porosity and permeability of both datasets.

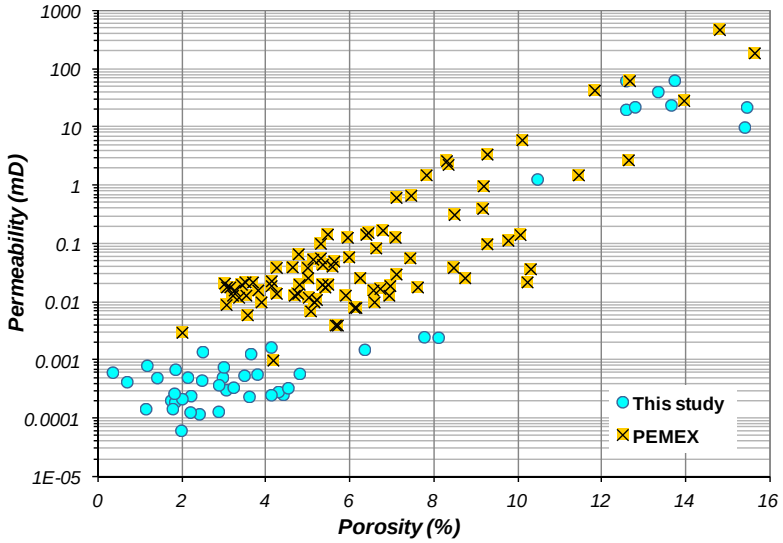

Figure 5.1 Porosity vs permeability crossplot of the datasets in this study. Note that permeability determination conducted in this project was mainly focused on low-permeable samples. This permitted to develop a better evaluation of permeability distribution in these reservoirs

Even though permeability determination in both datasets used different methods (*i.e.* steady- and unsteady-state), no significant variations were observed as these follow the same permeability trend. Porosity and permeability measurements were conducted on a number of PEMEX plugs to corroborate consistency in both methods. No significant differences were observed. Permeability was also assessed using alternate approaches such as mercury injection data and nuclear magnetic resonance. These methods are examined further in this Chapter.

XRD data given by PEMEX was obtained from powdered-samples and using a X-ray diffractometer, which is equivalent to the instrument used in this study. The data of both sources was collected in similar scanning ranges and using equivalent acquisition procedures, although these were interpreted by different specialists. The proportion of quartz, calcite and clay minerals were contrasted in both dataset and the differences are shown in Figure 5.2. The minerals showed in the ternary diagram constitute together approximately 90% of the total mineral fraction in most of these samples. No significant differences in mineral type and proportions were observed.

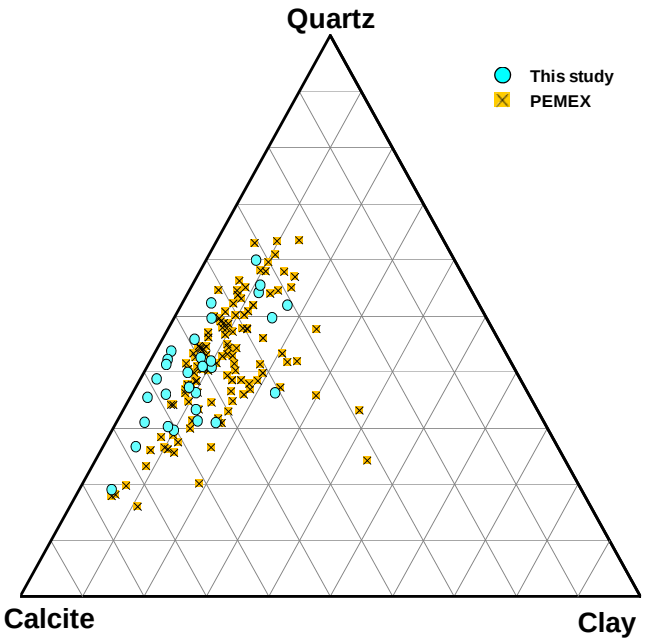

Figure 5.2 Differences of interpreted mineral proportions in both datasets. These three mineral fractions normally integrate 90% of total mineral content in the reservoirs of this study

Mercury injection data was obtained using comparable mercury porosimeters. Although both datasets were determined at same ultimate injection pressure (*i.e.* 60, 000 psia), significant differences were observed in the quantity of the data collected. Approximately, 40 data-points were used to describe the capillary curves in this study, in comparison to the data provided by PEMEX that define this curve with better resolution employing approximately 120 data-points. Figure 5.3 shows the comparison of two capillary pressure curves in both datasets.

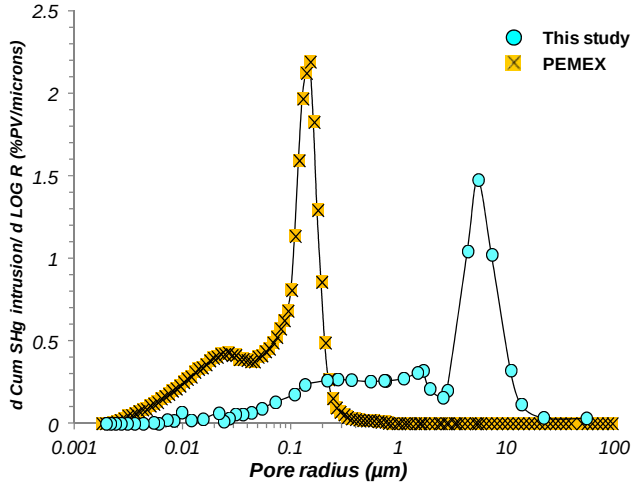

Figure 5.3 Differences in resolution of both MICP datasets. Observe the number of data-points to describe the capillary curve in each case

The lack of data-points for the samples in this study prevented them being used to define a high resolution capillary pressure curve (and the characteristic pore radius). In a number of samples, the determination of the pore radius was too uncertain that the data were discarded. It was assumed that the MICP curves used to develop petrophysical correlations were clearly defined.

Archie's cementation factor (m) and saturation exponent (n) were obtained by the two-electrode method, at *in situ* stress conditions and ambient temperature in both datasets. The saturating brine was also equivalent (*i.e.* 3.5% NaCl) although the PEMEX sample's conditioning and preparation (*e.g.* the method for saturating samples or the electrical frequency at which the PEMEX data was obtained) was unknown. Resistivity index in both cases was determined using air-brine system. Figure 5.4 shows the comparison of both datasets, no significant divergence is generally observed.

a) cementation factor (m) **b) saturation exponent (n)**

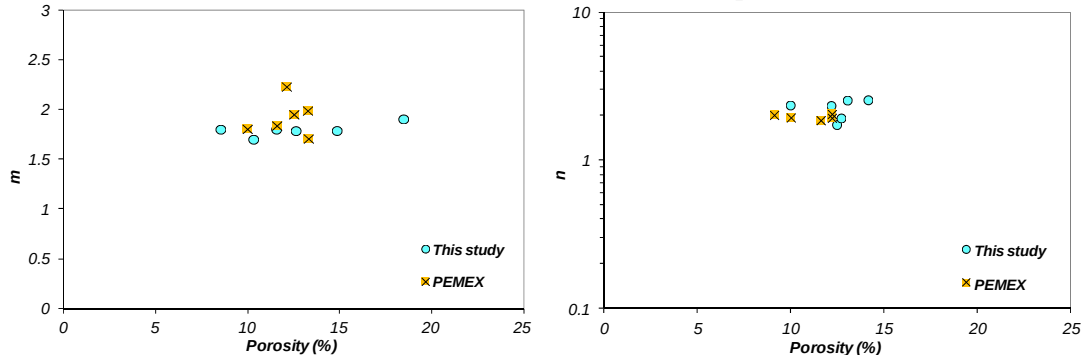

Figure 5.4 Comparison of electrical properties of both datasets

Additionally to the data described above, substantial petrophysical information was also used from two main resources. First, from descriptive core studies conducted by PEMEX in the rest of the oilfields beyond the study area (Chicontepec is integrated by 29 oilfields). Second, from

extensive petrophysical core analyses of the Mesaverde tight-gas reservoirs and published by the University of Kansas (http://www.kgs.ku.edu/mesaverde/index.html). Both resources were used to observe tendencies and sometimes this data was plotted against the obtained in this study for comparison purposes.

5.2 Measured rock properties

Diverse analyses were conducted employing rock-measured properties to assess porosity (*Ø*), permeability (*k*), pore radius (*r*), and irreducible water saturation (Sw_i) in the reservoirs of this study. Archie's-based parameters, m and n, used in well-log analysis for estimation of water saturation (*Sw*) were also determined.

As result of this approach, a number of petrophysical correlations were developed and a rock-typing model was produced that was integrated with the textural and mineralogical characteristics of these reservoirs. The observations conducted in this section were used to calibrate and adequate petrophysical models to the reservoirs of this study.

5.2.1 Porosity

A range of measured-rock tests were used to assess porosity in the reservoirs of this study. The first, involved the determination of the grain volume using a gas pycnometer device (helium Ø). This was compared to the porosity obtained by weight differences of samples saturated with brine (brine Ø) and mercury (MICP Ø), and determined from NMR measurements (NMR Ø). Figure 5.5 is the frequency histogram of helium-Ø data obtained from 142 samples.

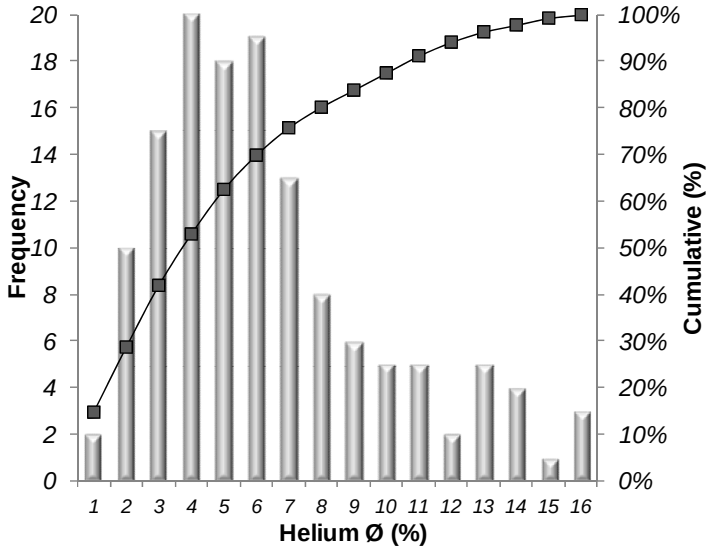

Figure 5.5 Frequency histogram of helium-porosity measurements of the samples used in this study

A maximum porosity of 16% was observed which illustrates the low-storage capacity of these reservoirs. The bimodal distribution in the histogram results from two porosity families in the dataset. Most of the samples in this study have porosities ranging from 1 to 9%, whereas approximately 15 samples have porosities greater than 12%. This low-porosity trend is mainly resulted from the high-cemented nature and the poor-sorted textures (*i.e.* the high variability in their grain-sizes) normally observed in these rocks. According to petrographic observations, the calcite cementation in most of the samples in this study seems sometimes to be more drastic in reducing the porosity than the effects caused by compaction.

Helium-porosity was compared to brine, mercury and NMR porosities determined in a number of samples in this study (Figs. 5.6 and 5.7). In general, gas pycnometry produced higher porosity values than the obtained from the other methods. This probably may be due to the small molecular size of helium that permits a better penetration of smaller pore sizes allowing superior quantification of pores, compared to water or mercury. The porosity determined by weight differences (*e.g.* brine and mercury porosities) and from NMR strongly depends on ensuring the complete pore volume saturation.

In general, when are compared to helium technique, the NMR porosity shows less deviation than brine porosity. Differences of porosity values vary from 0 to 4.4% in both methods.

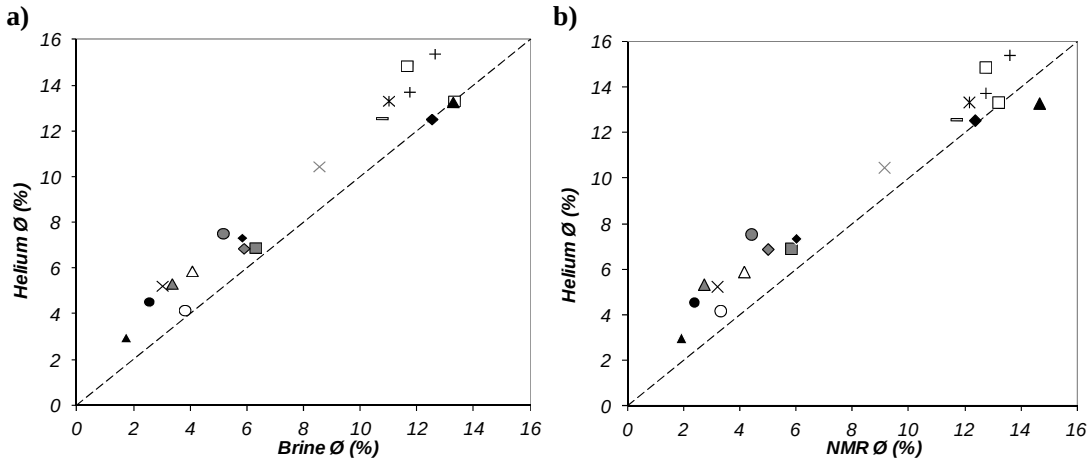

Figure 5.6 Comparison of helium-porosity to brine and NMR porosities

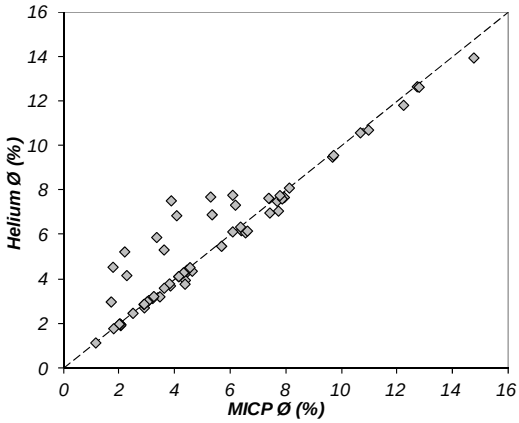

Figure 5.7 Comparison of helium-porosity to MICP porosity. Observe the numerical deviation in low porosity values (*i.e.* below 9%)

The porosity determined by mercury injection data seems to fit better with helium-porosity (Fig. 5.7), possibly because the greater injection pressures used in this method are able to invade smaller pore sizes. Differences of up to 3.6% are observed in low-porosity samples (*i.e.* below 9% Ø). Above 9% cut-off, an acceptable agreement between helium and MICP porosities is observed.

Bulk compressibility in samples of this study is normally low and varies from 1 to 6×10^{-6} psi^{-1} in the 1000 to 4000 psi net stress range. This is mainly ascribed as the result of the well-cemented nature of these samples that prevent significant pore volume changes at increasing stress (Fig. 5.8). During simulated drawdown (*i.e.* by increasing the net stress), the pore volume in most of the samples is only reduced by 20% at maximum stress of 4000 psi. Porosity reduction at maximum confining stress in most rock plugs is normally less than 2 porosity units (Fig. 5.8b). The average rate of porosity reduction by applied stress is approximately -1%/2500 psi.

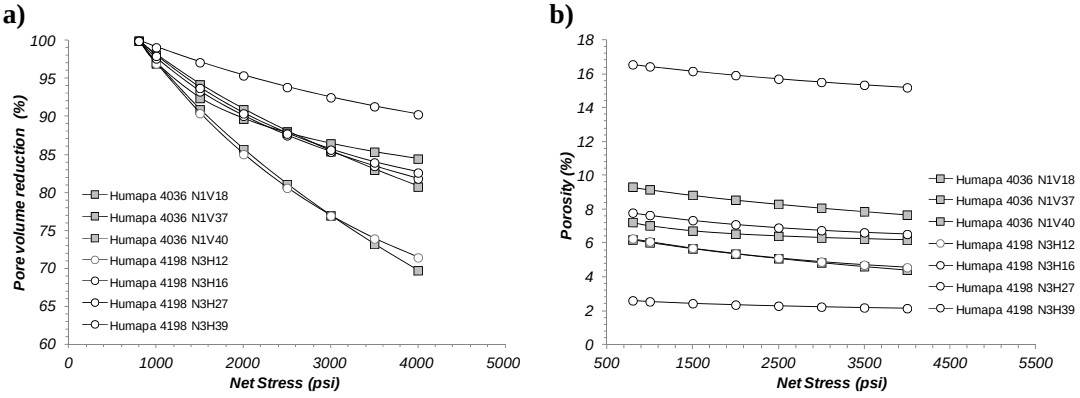

Figure 5.8 Pore volume and porosity variations by increasing net stress pressures

Overall, porosity variations in the reservoirs of this study -as observed from a number of approaches- show similar low values although there are minor numerical differences between

the methods used. Porosity of these reservoirs vary from poor to moderate when is compared to the porosities observed in other sandstone reservoirs. For example, Ehrenberg and Nadeau (2005) published an extensive porosity and permeability database from over 30 thousand siliciclastic petroleum reservoirs. According to this data, porosity in most terrigenous reservoirs varies from 13 to 28% at equivalent burial depths of the reservoirs in this study. This illustrates the limited storage efficiency of Chicontepec reservoirs.

5.2.2 Permeability

A number of unusual high-permeability samples were discarded from this study as these were highly-laminated and show natural-fractures. Although it was difficult to distinguish whether these fractures were natural or caused by coring, they show a clear deviation in the general porosity-permeability trend observed in the database. Luces *et al*. (2012), points out that natural fractures in the Chicontepec reservoirs do not seem to provide significant control in fluid flow efficiencies and their effect on hydrocarbon recovery and productivity is neglected in this study. Further analysis on this matter should be conducted, particularly because natural-fractures are frequently observed in subsurface data (*e.g.* well-logs, cores) and outcrops in these reservoirs.

Gas-permeability

Permeability of the reservoirs in this study was assessed using a number of techniques. Figure 5.9 shows the frequency histogram of Klinkenberg's permeabilities at *in situ* stress conditions. These measurements are frequently mentioned in this chapter as "gas-permeability".

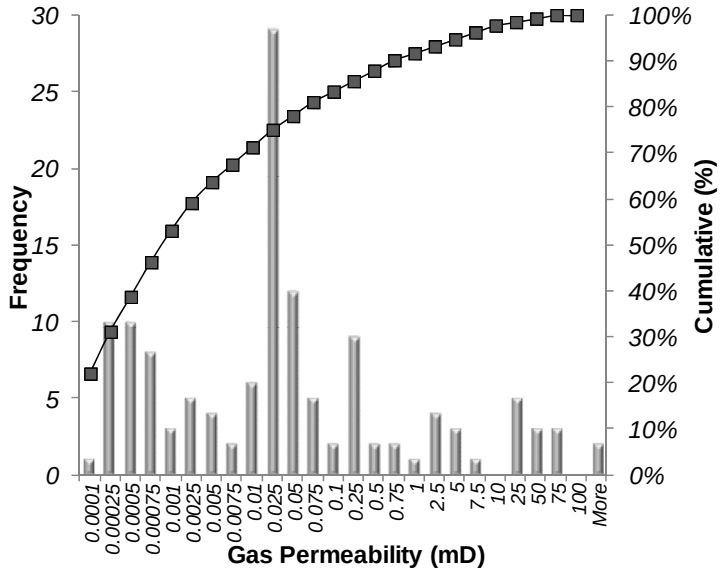

Figure 5.9 Frequency histogram of gas-permeability measurements corrected by gas-slippage used in this study

Most of the samples in Figure 5.9 describe permeabilities lower than 0.1 mD and maximum values are under 500 mD. The low permeability is mainly resulted from the combination of the fine-grained textures and the extensive diagenetic processes experienced in these rocks (*i.e.* calcite cementation). Small and tortuous integranular conducts are frequently observed in microscopic images, which are normally regarded to make fluid-flow difficult. Samples with permeabilities greater than 1 mD are normally associated to well-sorted textures with low clay and authigenic calcite content.

Despite that the intergranular volume has been significantly reduced mainly due to calcite precipitation in the reservoirs of this study, most of the porosity observed in thin sections is found to be primary (*i.e.* intergranular). Only a small portion of the reservoir porosity is from secondary processes. The secondary pores observed in thin sections do not seem to be interconnected and even their relative large size compared to the matrix, these appear to be isolated. This signifies that the grade of connectivity between pores is mostly controlled by the extent of the authigenic calcite and the textural (*i.e.* depositional) characteristics. This is exemplified in Figures 5.10 and 5.11, in which permeability appears to be function of the detrital grain-size (which impacts on pore-size) and the calcite cement. Observe that larger -and better-sorted- grain-sizes tend to produce larger pores, and that larger pores are more likely to be interconnected. This simple although meaningful observation permits to presume that permeability in these reservoirs is strongly linked to the rock's depositional characteristics and the degree of diagenesis.

Figure 5.10 illustrates the correlation between porosity and permeability in the reservoirs of this study. Observe that for a single porosity value there is a corresponding range of permeability that can vary within two orders of magnitude. This seems to be consistent even at high porosities (*e.g.* greater than 12%). The wide deviation of permeability appears to be linked to the extent of calcite precipitation and the primary characteristics in these rocks. Although the resulting correlation in Figure 5.10 is prone to significant error due to the wide permeability variations, this correlation provides a practical approach that is especially useful for well-logging interpretation purposes. A high variation in permeability is also observed in the Mesaverde tight-gas samples plotted in the same figure. Note that Mesaverde reservoirs develop lower permeabilities than the reservoirs of this study.

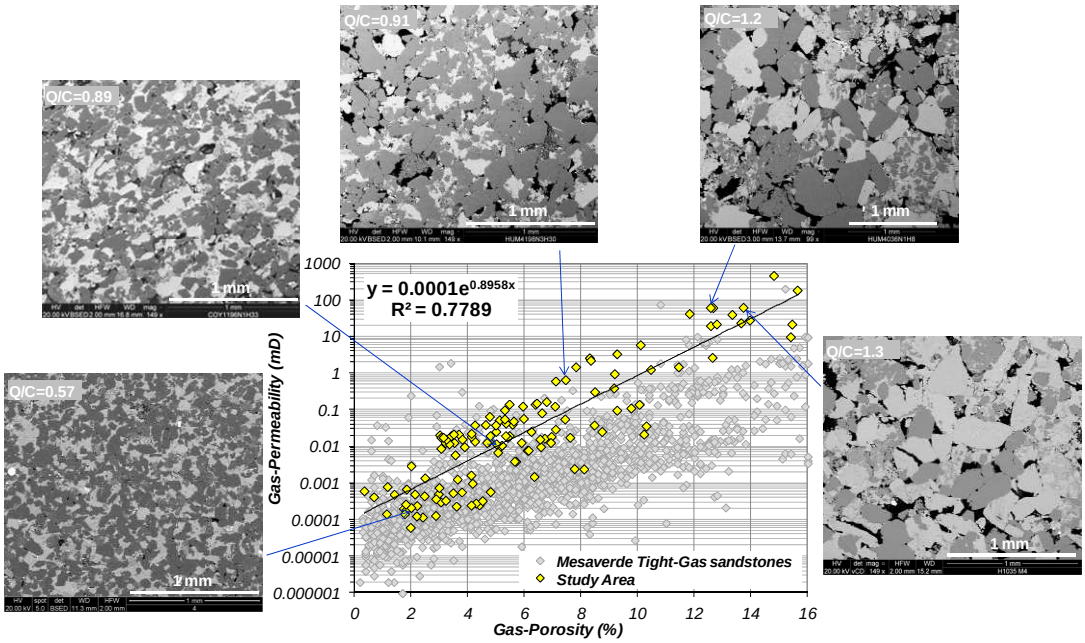

Figure 5.10 Gas porosity/permeability relationships. The Mesaverde tight-gas samples are plotted for comparison purposes. Note the relative influence of grain-size and calcite cement to rock quality. The quartz to calcite ratio (Q/C) is also plotted in each sample. Note the relative influence of the Q/C over rock quality

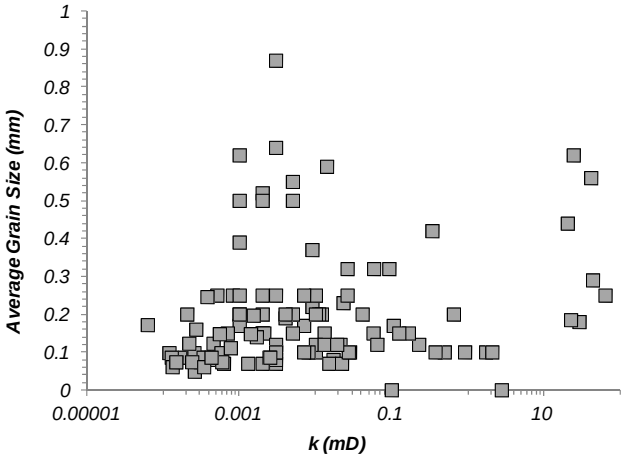

Figure 5.11 Permeability versus the average grain size. Observe the relative control of the grain size over permeability. The diverse trends observed may be produced by the wide grain-size variation and diagenetical alteration

Brine-permeability

When it is compared to gas (*kg*), the brine-permeability (*kb*) is normally reduced within an order of magnitude (Fig. 5.12). Brine permeability was obtained using synthetic brines and at *in situ* stress conditions. Average *kg/kb* ratios is 2.53 (st.dev.= 0.92). Figure 5.12 displays a number of samples in this study together with published correlations (Jones and Owens, 1980; Chowdiah, 1987).

Although the dataset shown in Figure 5.12 is restricted to permeabilities greater than 0.1 mD and are limited to small amount of samples, the correlation obtained from this approach is:

$$k_b = 0.2874 k_g^{1.1321}$$

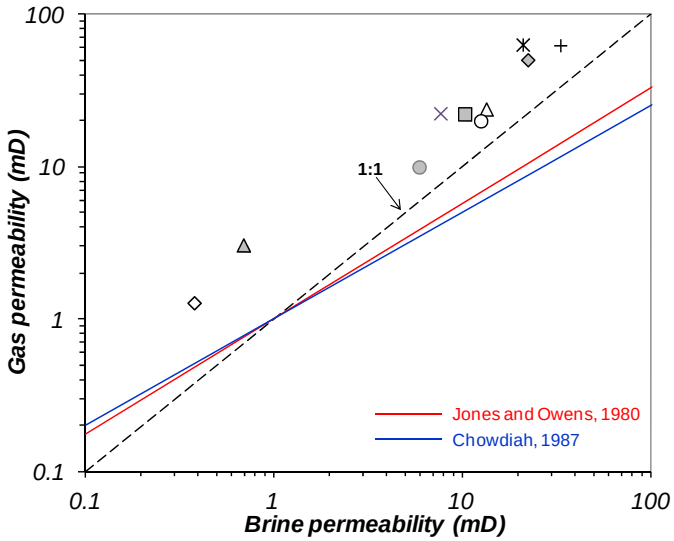

Figure 5.12 Comparison of k_g and k_b data obtained in this study

The deviation of *kg/kb* ratios seems to increase in low-permeable samples (*i.e.* lower than 1 mD). Further investigation was conducted on explaining the *kg/kb* differences and is described in chapter seven. These results show that Chicontepec samples are highly reactive to the type and concentration of the brine used, which is mainly controlled by clay swelling and particle mobilisation.

MICP-based permeability

Mercury injection data was also used for assessing permeability in these reservoirs. Based on previous work of Purcell (1949) and Thomeer (1960); Swanson (1981) developed a correlation between mercury injection capillary pressure (MICP) and permeability. He defined the term *apex* in the capillary pressure curve in which most of the interconnected pores that dominate fluid-flow are filled with mercury.

Apex point is normally recognised as the maximum ratio of mercury saturation to capillary pressure (*Sb/Pc*) as shown in Figure 5.13. By comparing *Sb/Pc apex* ratios and permeability from a number of sandstone and carbonate rock samples, Swanson established the following correlation:

$$k_a = 399 \left(\frac{S_b}{P_c}\right)_A^{1.691}$$

where: k_a is the air-permeability (mD) and *A* refers to the apex point determined in the capillary pressure curve.

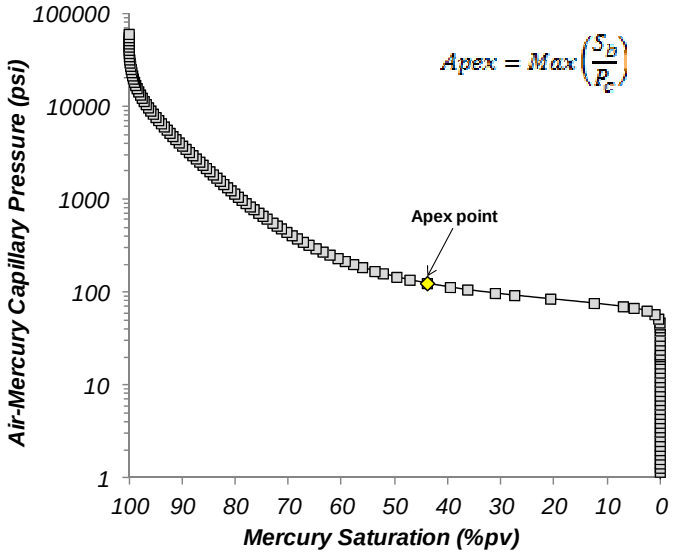

Figure 5.13 Definition of Apex point according to Swanson (1981)

Similarly to the methodology of Swanson (1981), a number of mercury injection data in this study (Fig. 5.14) was compared to gas-permeability. The gas-permeability data was corrected by slippage and determined at *in situ* stress conditions. Most of the capillary pressure curves have uni-modal pore-size distributions, suggesting the existence of single pore-radius family. This allowed a better recognition of *apex* points. Bi-modal populations in these curves are rarely observed and excluded from further analysis.

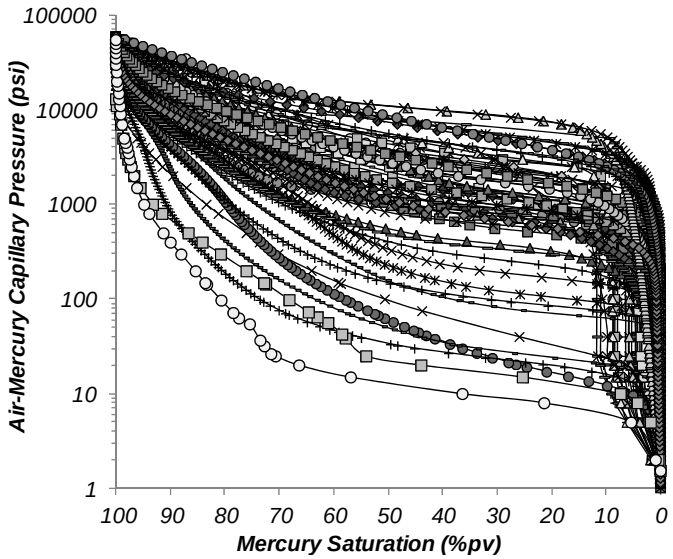

Figure 5.14 MICP data used in this study

The mercury data at *apex* point was plotted against gas-permeability (Fig. 5.15). The *apex* point was determined between mercury saturations ranging from 13 to 82% (av. 34%) and from 10 to 11, 000 psi (av. 2250 psi) air-mercury capillary pressure. Figure 5.15 illustrates the obtained correlation. Observe the dispersion of data towards decreasing permeabilities (*i.e.* below 0.1 mD). In this portion, the *apex* point is difficult to recognize as *Sb/Pc* ratios tend to be fairly constant. Overall, an acceptable agreement is observed. Note that the area below 0.001 mD, which was populated as part of this study, allowed a better evaluation of permeability distribution in the reservoirs of this study.

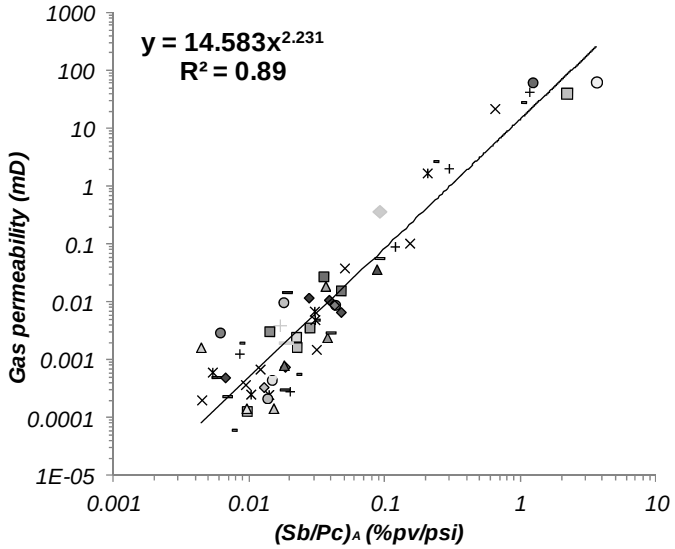

Figure 5.15 Correlation of MICP data at *apex* points and permeability in samples from this study

The permeability correlation obtained in Figure 5.15 was evaluated in Figure 5.16. A comparison of permeability estimated by this model *versus* gas-permeability determined from core plugs was plotted. The model developed by Swanson was also displayed. Observe that Swanson's model overestimates permeability over an order of magnitude in these samples. A larger deviation is observed below 0.1 mD. This illustrates the importance of adequate petrophysical models to the specific reservoir characteristics.

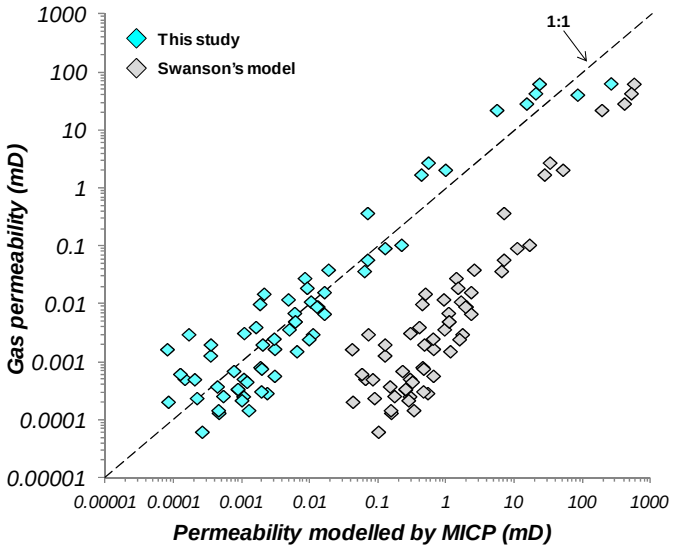

Figure 5.16 Evaluation of the permeability model determined by MICP data. Observe the high deviations of the Swanson's model compared to the obtained in this study. The disagreement is consequence of the different rock types used for calibration

NMR-based permeability

Nuclear magnetic resonance (NMR) was also used to evaluate permeability in the reservoirs of this study. NMR T2 relaxation distribution was acquired in a number of fully-saturated samples with synthetic brine. Figure 5.16 shows the samples used in this study.

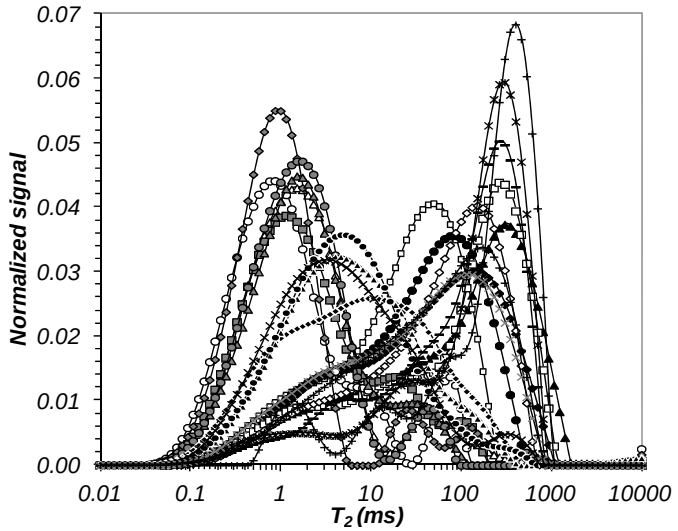

Figure 5.17 NMR T2 relaxation distributions employed in this study

As most of these curves described uni-modal relaxation distributions (*i.e.* have single peak as also was observed in MICP curves), the logarithmic mean of the relaxation distribution ($T2_{LM}$) was used to characterise each sample. $T2_{LM}$ was estimated by:

$$T2_{LM} = exp\left(\frac{\sum_i (S_{ai} log T2_i)}{\sum_i S_{ai}}\right)$$

where: *T2* is the relaxation time, and *Sa* is the signal amplitude.

The $T2_{LM}$ was compared to gas-permeability data and the resulted correlation is shown in Figure 5.18. The gas-permeability was corrected by slippage and at *in situ* stress.

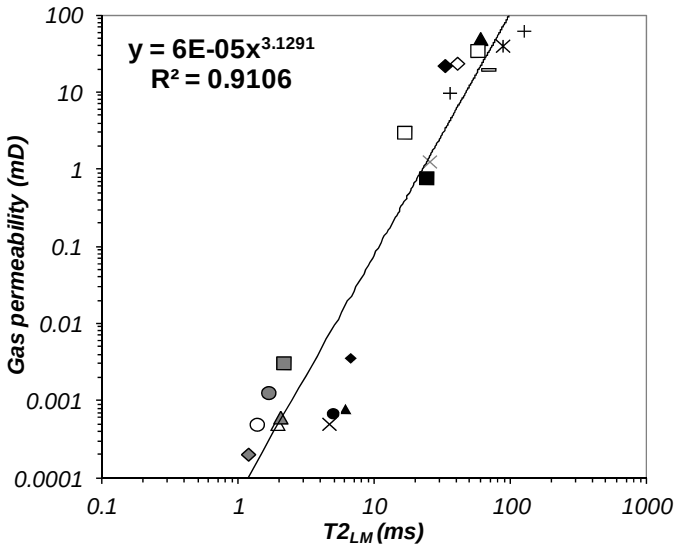

Figure 5.18 Correlation of $T2_{LM}$ of fully-saturated samples and gas-permeability

Figure 5.19 shows the evaluation of this model by comparing it to core derived gas-permeability measurements. As for the model determined by mercury injection data, a larger dispersion is observed at decreasing permeabilities (*i.e.* lower than 0.1 mD). This variation is produced by the wide range of T2 relaxation distributions observed in Figure 5.18, which may result from uncertainties in the determination of the characteristic T2 value. In this model it was assumed that the logarithmic mean of the T2 distribution characterises each sample well. However, other central tendency averages can also be used to characterise the T2 curves. A number of average techniques were used to determine a representative T2 relaxation value that included median, geometric and harmonic means. No significant improvements on permeability determination were observed.

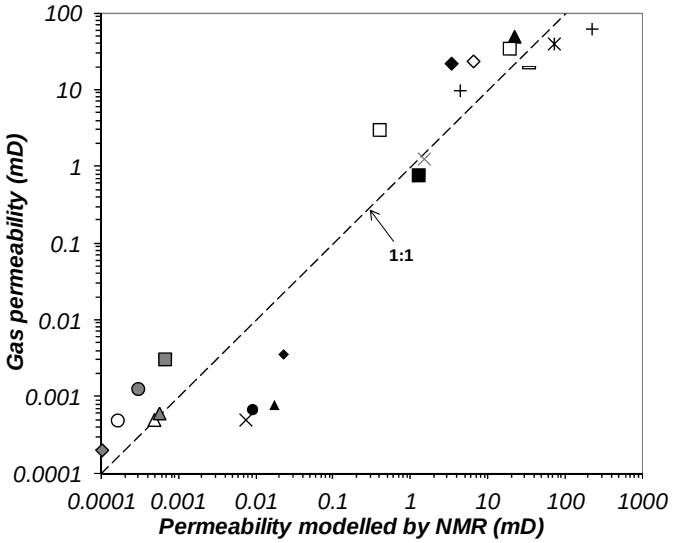

Figure 5.19 Evaluation of the modelled permeability using NMR T2 of fully-saturated samples

Permeability in these reservoirs was also assessed using the free-fluid model (Coates and Denoo, 1981). This permeability model is based on the determination of the free-fluid (FFI) and irreducible water (BVI) volumes using NMR T2 relaxation distributions. Coates and Denoo (1981) model is expressed as:

$$k = \left[c \cdot \emptyset_{NMR}^{m} \left(\frac{FFI}{BVI}\right)\right]^{n}$$

where: k is the permeability in mD, FFI is the free-fluid index, BVI is the irreducible water volume, $\emptyset_{NMR}$ is the total porosity determined by NMR and c, m and n are empirically determined constants (default values are 10, 2 and 2, respectively).

Figure 5.20 illustrates the definition of FFI and BVI using NMR T2 distributions obtained at two saturating sates. The sample is fully saturated with synthetic brine and the T2 relaxation is acquired. Then the sample is desaturated until reaching irreducible saturation (*Swi*) and the T2 curve is acquired for second time. The two curves are compared and expressed in terms of their cumulative signal (or cumulative total porosity). In this way FFI, BVI and the characteristic T2 cut-off are determined. T2 cut-off is used to partition free (*i.e.* mobile) and bound (*i.e.* immobile) fractions, and the industry standard value is 33 ms.

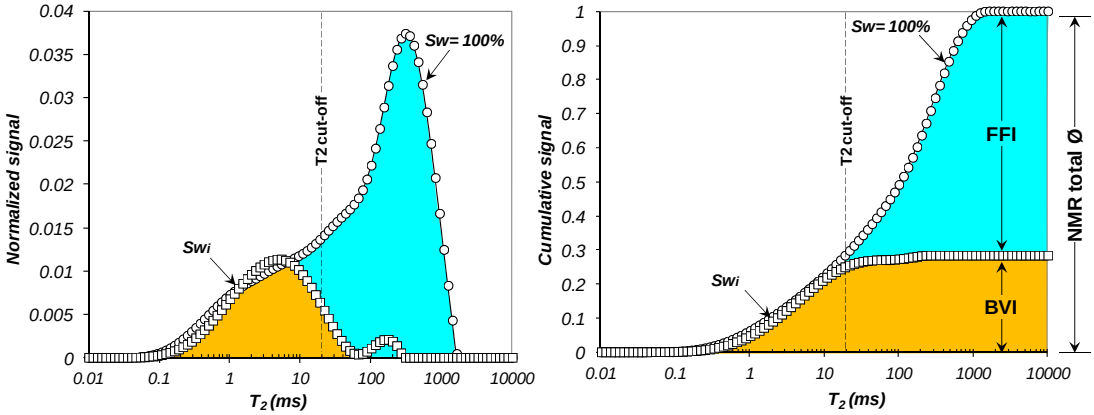

Figure 5.20 T2 distributions at fully saturated (blue) and when it is desaturated at irreducible water condition (orange). Observe that in this example a T2 cut-off of 20 ms was determined

Total porosity of the sample is proportional to the area under the T2 distribution curve at Sw=100%. Similarly, the area under the T2 distribution curve obtained at irreducible condition expresses the fraction of immobile fluid that is in the pore system as capillary- or clay-bound. FFI is then estimated by subtracting BVI from total NMR porosity.

Figure 5.21 shows the NMR T2 distributions obtained at fully-saturated and irreducible conditions. The samples were desaturated using a porous-plate device. Irreducible water saturation was reached at 40 psi air-brine capillary pressure. The T2 cut-off for discriminating capillary-bound and mobile fluids varied from 10 to 28 ms. Diverse averaging techniques such as arithmetic (24 ms), geometric (23 ms) and harmonic (21 ms) were employed to determine a single representative T2 cut-off value for subsequent well-logging interpretation purposes. T2 cut-off of 20 ms was selected to differentiate free and capillary-bound volumes.

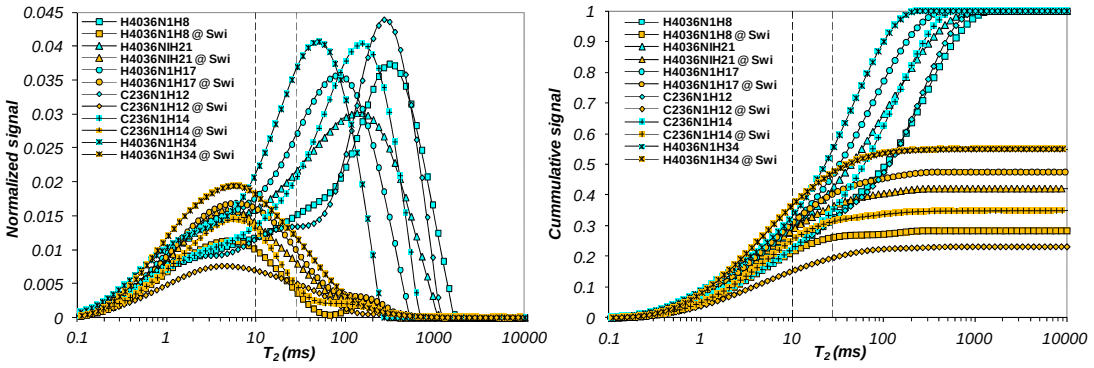

Figure 5.21 T2 distributions at fully saturated (blue) and at irreducible conditions (orange) in samples of this study. Observe the T2 cut-offs variations indicated by the two vertical dashed lines

Table 5.2 shows the observed T2 cut-offs obtained on each sample and the FFI and BVI estimations. The values are expressed based on the total NMR porosity.

Table 5.2 NMR Results

Sample	NMR Ø (%)	Klinkenberg's permeability (mD)	Swi (%pv)	Individual T2 cut-off (ms)	FFI (%)	BVI (%)
H4036N1H8	*14.7*	*50.7*	*26*	*18.7*	*10.5*	*4.2*
C236N1H12	*12.7*	*35.4*	*20*	*10.7*	*9.8*	*2.9*
C236N1H14	*14.6*	*24.2*	*26*	*28.5*	*9.4*	*5.2*
H4036N1H34	*13.2*	*3.1*	*42*	*28.5*	*5.8*	*7.4*
H4036N1H21	*12.4*	*22.6*	*35*	*28.5*	*7.1*	*5.3*
H4036N1H17	*9.8*	*0.79*	*39*	*28.5*	*5.2*	*4.6*

The constant "c" value in the Coates and Denoo (1981) model was statistically determined based on plotting $(k_{core}/\emptyset_{NMR}^4)$ versus $(FFI/BVI)^2$ using individual T2 cut-offs observed on each sample and gas-permeability data obtained in cores (Fig. 5.22). The constant *c* is $c = \sqrt[4]{16990} = 11.41$.

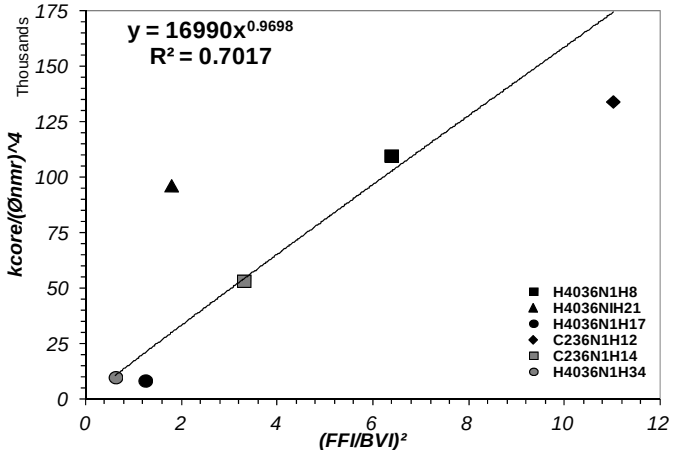

Figure 5.22 Determination of constant "c" in the Coates-Denoo equation

Constants *m* and *n* are assumed to be 2. The free-fluid model for permeability estimation in this study was rewritten as:

$$k = \left[(11.41 \cdot \emptyset_{NMR})^2 \left(\frac{FFI}{BVI}\right)\right]^2$$

Figure 5.23 illustrates the comparison of modelled permeability using the calibrated Coates-Denoo equation compared to core data. FFI and BVI were determined by applying a T2 cut-off of 20 ms. Observe the relative dispersion of datapoints towards low-permeable samples, approximately at lower permeabilities than 1 mD. The scattering is associated to wide shapes in the T2 distributions in which free and capillary fractions are difficult to differentiate.

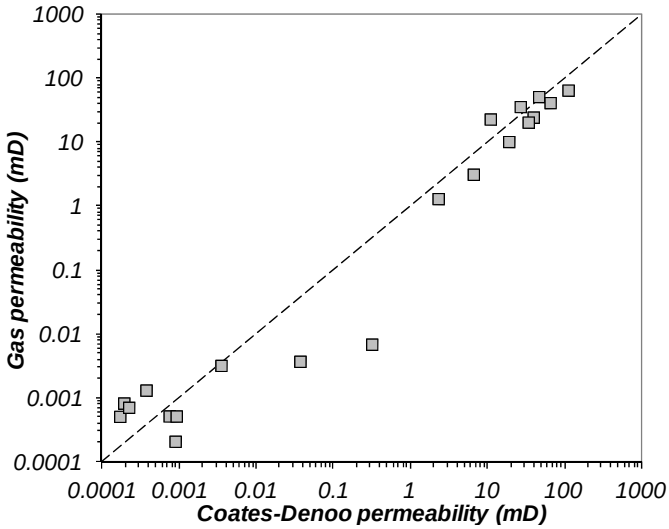

Figure 5.23 Comparison of modelled and measured permeabilities based on the calibrated free-fluid model

Overall, the reservoir-rock permeability analysed through a series of techniques shows a wide range of variation, from 0.0001 to almost 500 mD. Compared to the data published by Ehrenberg and Nadeau (2005), the permeability of the reservoirs in this study is low. The methods used to evaluate permeability in these reservoirs show numerical discrepancies mainly due to their inherent experimental and analytical procedures. The calibrated free-fluid permeability model seems to be useful, especially for wireline applications, although it requires the acquisition of NMR log to estimate FFI and BVI fractions. Even when a limited number of samples was used for calibration, more data can eventually be integrated to reduce uncertainty.

A more practical permeability correlation was obtained from porosity (Fig. 5.10). This can be applied to well-log analyses in wells with no core or NMR information exists. Although this correlation shows high variation, it can be a useful tool to conduct qualitative comparisons of permeability between wells.

Gas-permeability information below the 0.001 mD, which was populated during this study, helped to evaluate permeability in these reservoirs.

5.2.3 Pore Size Distribution

The pore-size evaluation in the reservoirs of this study was based on the analysis of mercury injection, k/Ø ratios and NMR T2 distributions. Different correlations were obtained to estimate pore sizes.

The MICP data shown previously in Figure 5.14 was converted from laboratory (*i.e.* air-mercury) to equivalent reservoir conditions (*i.e.* oil-brine). This was essentially conducted by dividing air-mercury pressure by 14 ($\theta cos\sigma_{air\text{-}mercury}$= 368 Dyne/cm; $\theta cos\sigma_{oil\text{-}brine}$= 27 Dyne/cm). Pore radius (R) was determined by:

$$R = \frac{2\sigma \cos\theta_{oil-brine}}{Pc_{oil-brine}} \cdot 0.145$$

where: R is the pore-radius (μm), σ is the interfacial tension (Dynes/cm), θ is the contact angle (degrees), and Pc is the capillary pressure at reservoir conditions (oil-brine system). Characteristic pore-radius of each sample was obtained at *apex* point as discussed previously. Figure 5.24 shows the distribution of pore-radius in these reservoirs. Observe that pore sizes vary from 0.005 to 10 μm. This range agrees to the pore sizes characteristic of unconventional tight reservoirs, according to the data reported by Nelson (2009).

Most of the curves observed in Figure 5.24, describe single-pore systems as these show uni-modal shapes (*i.e.* single peaks). This is in agreement what it has been observed at microscopic level, in which most of the pores in reservoir-rock samples are primary (*i.e.* intergranular). Secondary pores associated to grain dissolution were also observed but in minor proportion.

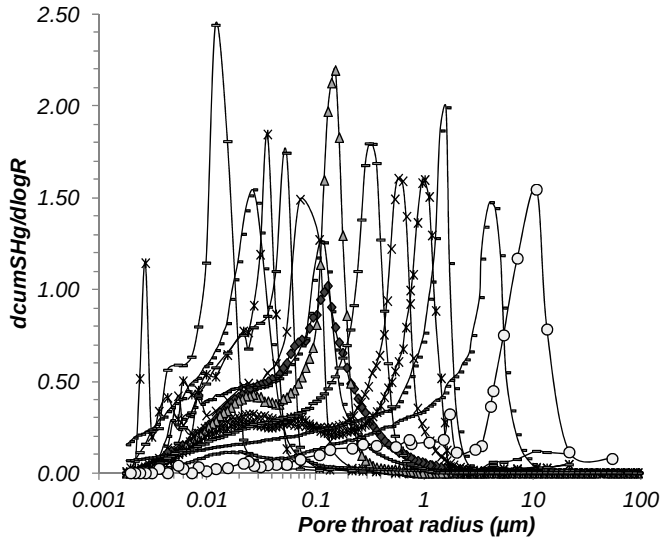

Figure 5.24 Pore throat radius distribution based on MICP data of a number of samples used in this study

A number of published correlations (*e.g.* Pittman, 1992; Winland, 1980 *in* Kolodzie, 1980; Aguilera, 2013) relate porosity and permeability to estimate pore radius. These have been developed using mercury injection and uncorrected air permeability data from a variety of sandstone and carbonate samples. The model developed by Winland is:

$$R = 5.395\left(\frac{k^{0.588}}{\emptyset}\right)^{0.864}$$

Whereas the Aguilera's equation is:

$$R = 2.665\left(\frac{k}{\emptyset}\right)^{0.45}$$

where: R is the pore-size (μm), k is permeability (mD) and $Ø$ is porosity (%).

By comparing the pore radius obtained from MICP curves at the *apex* inflection point with their porosity/permeability ratios, a correlation to estimate pore radius in the reservoirs of this study was obtained. The outcome of this comparison is shown in Figure 5.25 and is expressed as:

$$R = 2.762\left(\frac{k}{\emptyset}\right)^{0.4941}$$

where: R is the pore-size (μm), k is the Klinkenberg's permeability (mD) and $Ø$ is the helium-porosity (%). Note that in Figure 5.25 the k/Ø ratio is expressed as the square root.

As observed, the model is not significantly different from Winland or Aguilera's, as the modelled pore-sizes resulted very similar. Numerical deviations between the three equations are within an order of magnitude. Figure 5.26 evaluates the obtained correlation in predicting pore sizes.

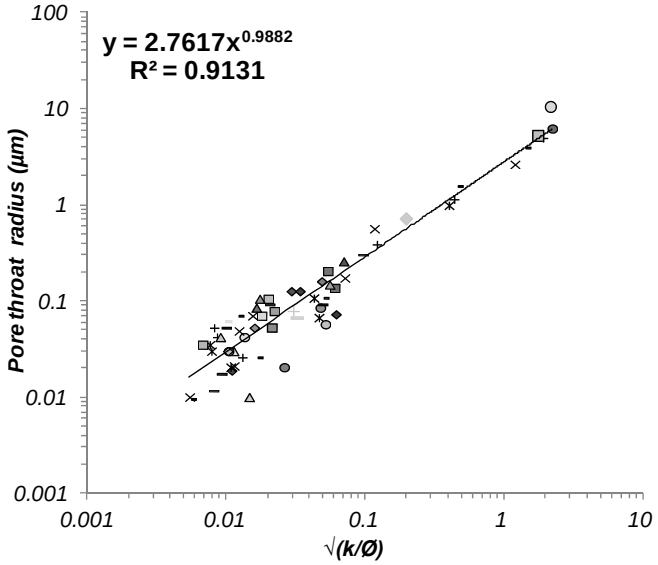

Figure 5.25 Correlation of k/phi ratios and characteristic pore sizes in the reservoirs of this study

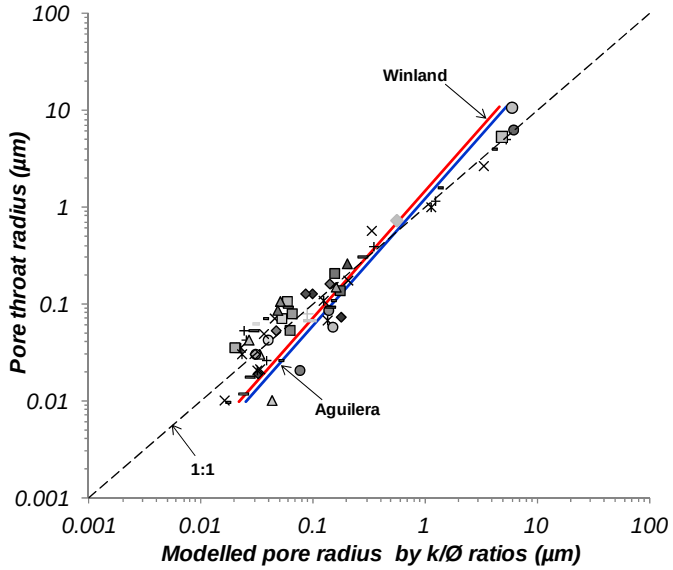

Figure 5.26 Comparison of measured and modelled pore sizes in the reservoirs of this study using the correlation shown in Figure 5.24. Aguilera and Winland models are also shown

As previously explained, most of the rock samples used in this study describe intergranular porosities. Single-pore systems are observed in both their mercury injection curves and NMR T2 distributions. A correlation exists between the logarithmic mean of T2 relaxations and the pore sizes at *apex* point obtained by MICP (Fig. 5.27). The T2 distributions were obtained from fully-saturated samples. An acceptable correlation is developed between the modelled and measured pore sizes using the model based on NMR T2 distributions (Fig. 5.28).

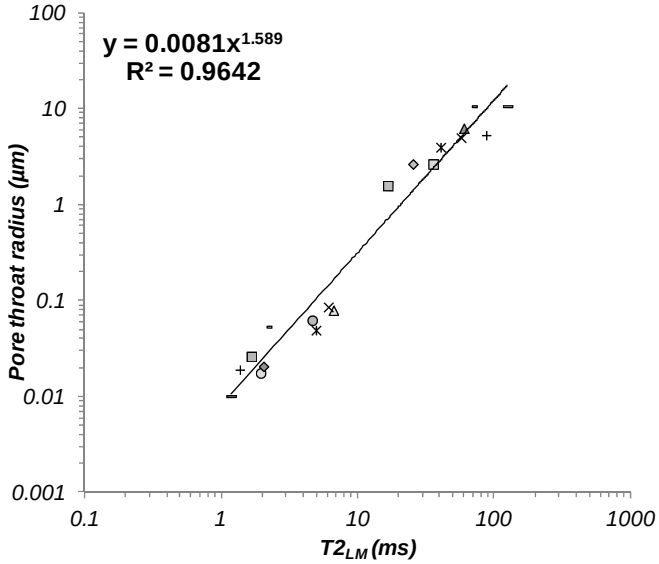

Figure 5.27 Correlation obtained by comparing the logarithmic mean of T2 distributions of fully-saturated samples and pore sizes obtained from MICP

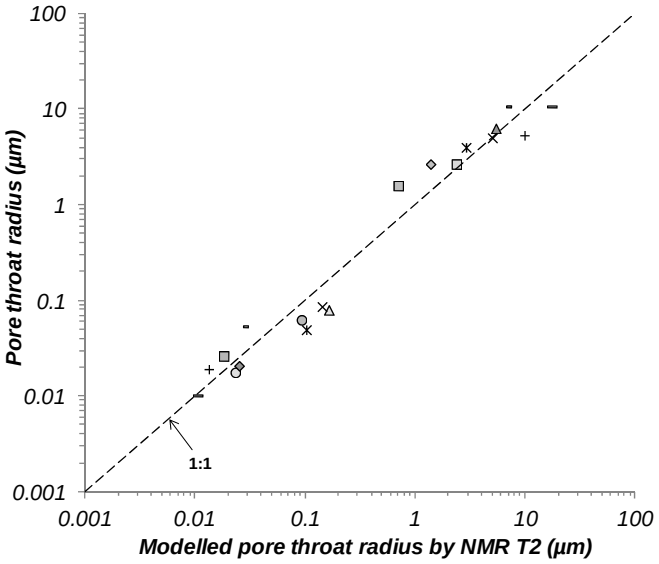

Figure 5.28 Comparison of modelled and measured pore radius based on the model of NMR T2 logarithmic mean distributions

5.2.3.1 Irreducible Water Saturation

Irreducible water saturation (Sw_i) is defined as the maximum water saturation that a rock with a given porosity and permeability can retain without producing water. Estimation of Sw_i provides important information related to the reservoir production performance, fluid sweep capacity and permeability.

Previously, irreducible conditions were achieved in a number of samples during calibration of the NMR T2 cut-off by applying 40 psi air-brine capillary pressure. This value is approximately equivalent to 200 psi air-mercury pressure system, which was applied to the MICP data to estimate the irreducible saturation of the wetting fluid. Above this pressure, pore throat sizes are approximately smaller than 0.5 µm and most of the fluid in these pores remains immobile by capillary forces or clay-bound (*i.e.* irreducible). Figure 5.29 illustrates how this process was conducted.

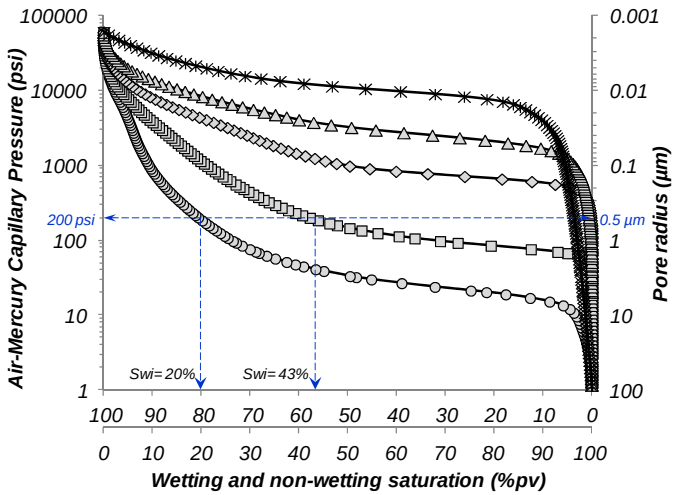

Figure 5.29 Determination of irreducible saturation. Observe that 200 psi air-mercury was used as cut-off, corresponding approximately to 0.5 µm pore radius

Although this procedure appears to be sensitive, especially because a range of saturations can be obtained at different pressure cut-offs, it provides an estimation of the water saturation that may remains immobile in the reservoirs of this study (Sw_i). Figure 5.30a shows the obtained irreducible water saturations at 200 psi air-mercury threshold. When a 1000 psi air-mercury cut-off is used instead (*i.e.* approximately 0.1 µm pore-size), the regression coefficient improves up to 0.89 (Fig. 5.31a). The threshold pressure should be specific for each sample, based on its pore throat size and equivalent irreducible volume. The selected cut-offs were used to illustrate comparisons. Figures 5.30b and 5.31a are two models at 200 and 1000 psi thresholds to estimate irreducible water saturations based on k/Ø ratios.

If it is assumed that a particular reservoir in the study area is at irreducible conditions (*i.e.* no water will be produced), and that the oil phase in the reservoir is undersaturated (*i.e.* no other phases than just oil and connate water exist), the generalised curves shown in Figure 5.30 and 5.31 can be a practical tool to estimate saturation profiles. These charts assume that a rock type with a given pore-size distribution develop characteristic saturation profiles.

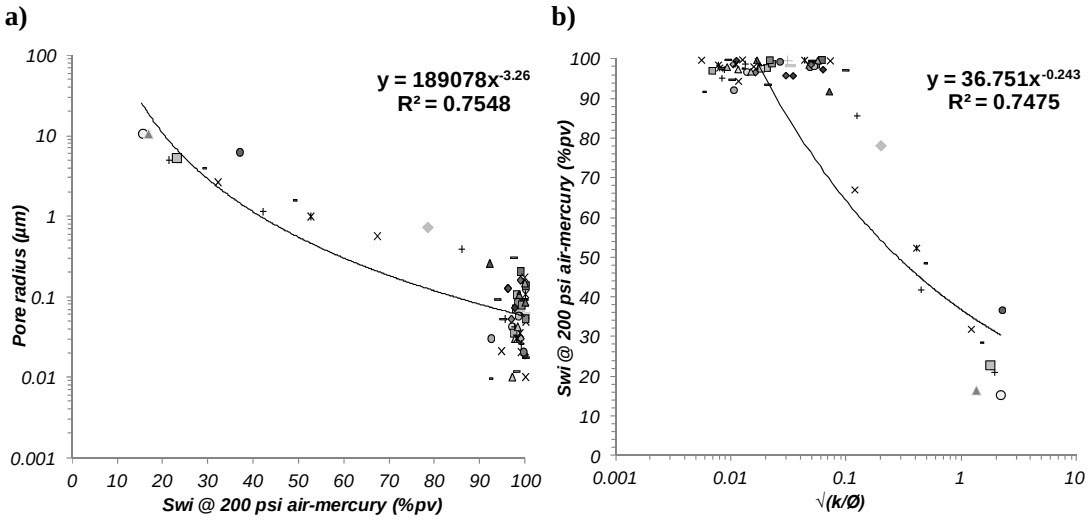

Figure 5.30 Irreducible water saturations obtained at 200 psi air-mercury capillary pressure and estimation of Swi based on k/Ø ratios. Observe that lower irreducible saturations are developed in larger pores

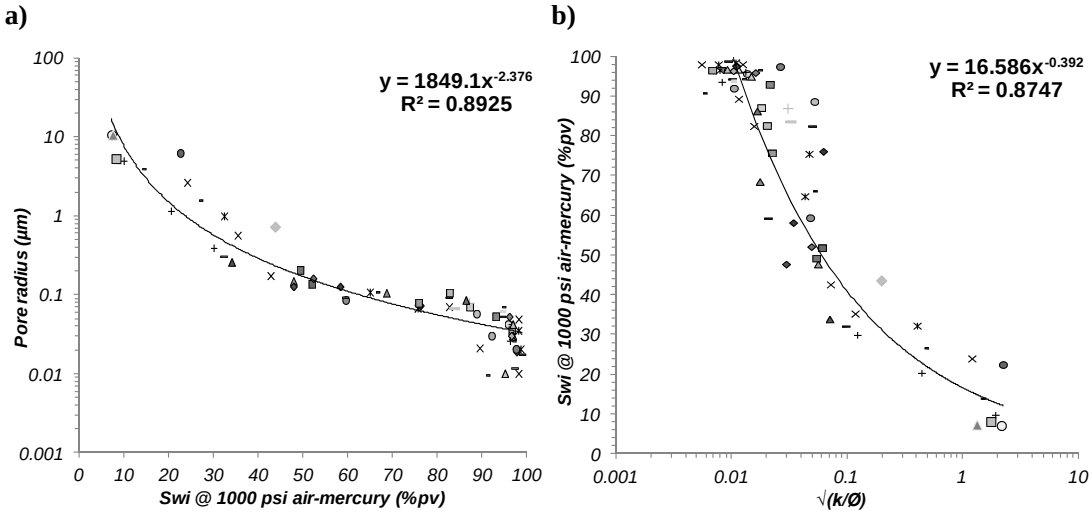

Figure 5.31 Irreducible water saturations obtained at 1000 psi air-mercury threshold. Observe differences with previous figure

5.2.3.2 Surface Area to Volume Ratio

Grain surface area by multipoint BET (Brunauer-Emmett-Teller theory) nitrogen adsorption method was obtained from 13 samples. Conversion from specific grain surface per gram of solid (S_g) to specific surface area per unit grain volume (SV_{gr}) was derived from:

$$SV_{gr} = S_g \cdot \rho_g$$

Conversion of SV_{gr} to specific pore surface (S_p) was derived from:

$$S_p = SV_{gr}\left(\frac{1-\emptyset}{\emptyset}\right)$$

where: ρ_g is the sample's grain density, and $\emptyset$ is the gas-porosity.

Specific surface area of pores (S_p) expresses the total area exposed within the pore space and is an important property of siliciclastic rocks. Specific surface area can sometimes linked to irreducible water saturation and permeability in intergranular porosity textures. Large specific surface areas tend to be developed in fine-grained textures. By contrast, small surface areas per pore unit are normally produced in coarser-grained textures. In this context, the specific surface areas can sometimes be linked to other parameters such as permeability and irreducible water saturation. Figures 5.32 and 5.33 show a number of correlations of the specific surface area of pores (S_p) with irreducible water saturation and permeability. These were obtained using pairs of rock samples which were used to obtain gas permeability, mercury injection and grain surface area by multipoint BET.

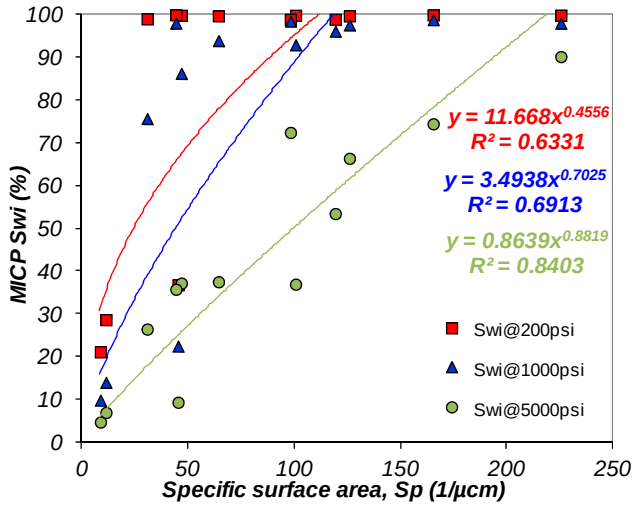

Figure 5.32 Comparison of specific surface area per pore unit (*Sp*) and irreducible water saturation obtained at different capillary pressure thresholds

Figure 5.32 compare the specific surface area of pores (S_p) versus irreducible water saturations obtained at different air-mercury thresholds. Similarly, a comparison of specific surface areas and permeability is shown in Figure 5.33.

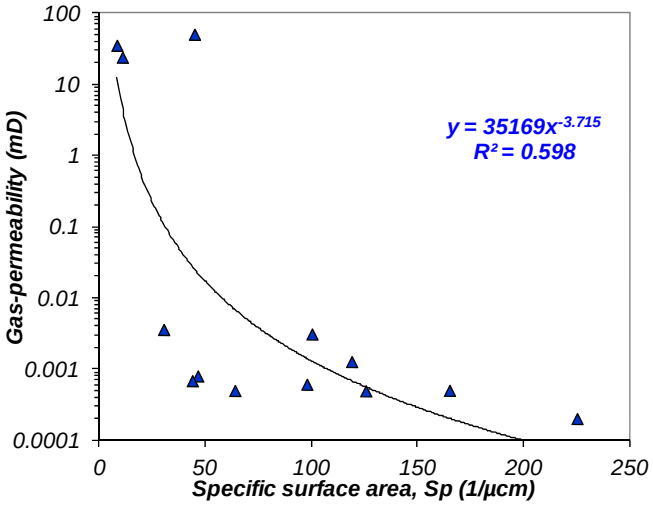

Figure 5.33 Correlation of specific surface area and Klinkenberg's permeability

Irreducible water saturations and permeability seem to be related to specific surface area of pores (S_p) in the reservoirs of this study. Greater surface areas tend to produce greater irreducible saturations and consequently low-permeabilities as normally occur in terrigenous reservoirs. However, deviations are observed possibly due to the non-uniform shape of detrital grains and the poor-sorted textures.

Pore surface was combined with NMR measurements to estimate the surface relaxivity (ρ). Surface relaxivity is defined as the ability of a surface to relax the spinning protons (Schön, 2011) and it was determined as:

$$\frac{1}{T2_{LM}} = \rho S_p$$

Figure 5.34 show the comparison of surface relaxivity with T2 logarithmic mean and pore size obtained from mercury injection.

The overall correlation observed in Figure 5.34 is that smaller pores tend to relax the spinning protons more effectively than larger pores, although moderate to high dispersion is observed. This may be produced by the wide range of grain sizes (*i.e.* poor-sorted textures) and the irregular shapes of detrital components in these samples. Surface relaxation mechanism should dominate the NMR T2 relaxation in water-wet and fully-saturated samples (Coates *et al.*, 1999). A more detailed discussion of the wetting characteristics of the samples and their effect on the NMR T2 relaxivity is showed in Chapter 7.

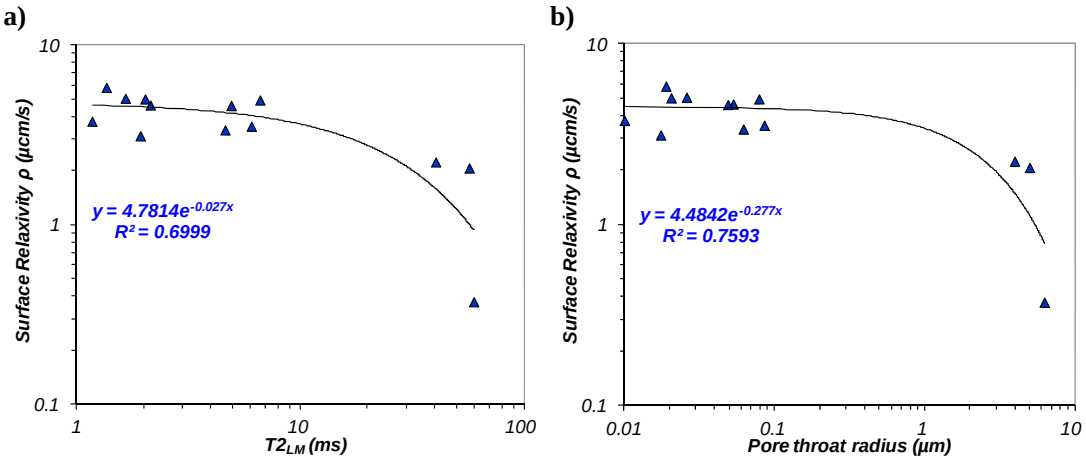

Figure 5.34 Comparison of surface relaxivity with logarithmic mean T2 and pore size

The surface area determined by the adsorption method was conducted using disaggregated rock samples. This method may be biased by the degree of pulverisation of the sample, in the sense that higher surface areas would be artificially produced as the sample is continuously pulverised. Tiab and Donaldson (2012) point out that specific surface area should be limited to porous media that do not have large specific surfaces (*e.g.* clay-size particles), and in rocks with well-sorted textures.

5.2.4 Saturation Exponent (n) and Cementation Factor (m)

A number of samples of this study were used to obtain the saturation exponent (n) and cementation factor (m) coefficients necessary to estimate water saturations using Archie-based equations. The effect of clays in the determination of the water saturation is discussed in Chapter 6. The electrical resistance (*R*) was obtained using a two-electrode device at constant frequency of 2 KHz and at different saturation stages.

Desaturation process was carried out using an air-water porous plate device applying six capillary pressure thresholds to describe with precision the desaturation process. Resistivity Index ($IR = R_t/R_o$) was calculated comparing the true resistivity ($R_t = R \cdot (L/A)$) at the adjusted saturation and the sample's resistivity when fully saturated with brine (R_o). Archie's saturation exponent, *n* (Archie, 1942) is determined from the slope of a line fitted to the *log*IR versus *log*Sw:

$$n = \frac{logIR}{logSw}$$

Similarly, electrical resistance (*R*) was acquired from a number of fully saturated samples. Archie's cementation exponent, *m* (Archie, 1942) was estimated by:

$$m = \frac{logF}{log\emptyset}$$

where: Archie's Formation Factor $F = R_o/R_w$; *Rw* is the formation water resistivity at room temperature (*Rw*= 0.195 Ω·m @ 20°C, equivalent to 35, 000 ppm of NaCl brine); and Ø is the porosity obtained by weight differences (*i.e.* brine porosity). The results from this approach are shown in Fig. 5.35.

For comparison purposes, cementation factors of Mesaverde tight-gas reservoirs are also plotted to observe tendencies in the following figures. Electrical properties of Chicontepec reservoirs acquired from oilfields beyond the study area are also displayed to compare estimations.

As observed in Figure 5.35, average cementation factors of all datasets are around 1.8 to 2.2, but reduce to 1.0-1.7 at porosities lower than 10% approximately. The effect of computing water saturations by varying *m* from 1.9 to 1.3 and maintaining constant the rest of the parameters in the Archie equation is significant. It cans even double the estimated hydrocarbon pore volume in a particular reservoir.

This behaviour is inconsistent with published models in the literature (Neustaedter, 1968, *i.e.* Shell's model), possibly because these rocks should be considered as non-Archie reservoirs. The model proposed by Neustaedter (1968) is also plotted in Figure 5.35.

Cementation Factor (m)

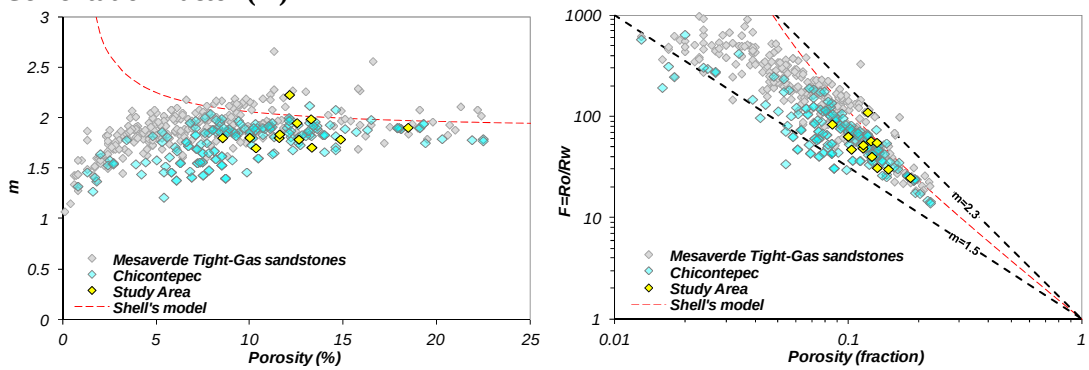

Figure 5.35 Archie's cementation factor measured from plugs. As reference, a number of Mesaverde tigh-gas and Chicontepec samples are plotted. Observe that cementation factor decreases at low porosities (*i.e.* lower than 10%)

Archie rocks as described by Archie (1942) have intergranular pores and the electrical conduction is exclusively through the brine in the intergranular, water-wet, isotropic pore spaces. In these rocks, the model of Neustaedter (1968) is justified, since porosity presumably becomes more isolated at low values (*e.g.* lower than 10%). The bulk resistivity of these rocks would describe greater resistance to the flow of electrical current than that at high porosities (*e.g.* greater than 10%). The effect of this behaviour is the increase of computed cementation factors at low-porosities, as described by the Neustaedter (1968) model in Fig. 5.35.

The opposite is observed in Chicontepec and Mesaverde samples. Electrical conduction at low porosities seems to be more efficient (or less resistance to electrical conduction is observed) compared with Archie type rocks. Observe that lower cementation factors seem to be developed at lower porosities (Fig. 5.35). This can possibly be due to micropores and microcracks that may improve electrical conduction even at low porosities. The latter is exemplified in Figure 5.36, where two BSEM images of samples of this study are shown.

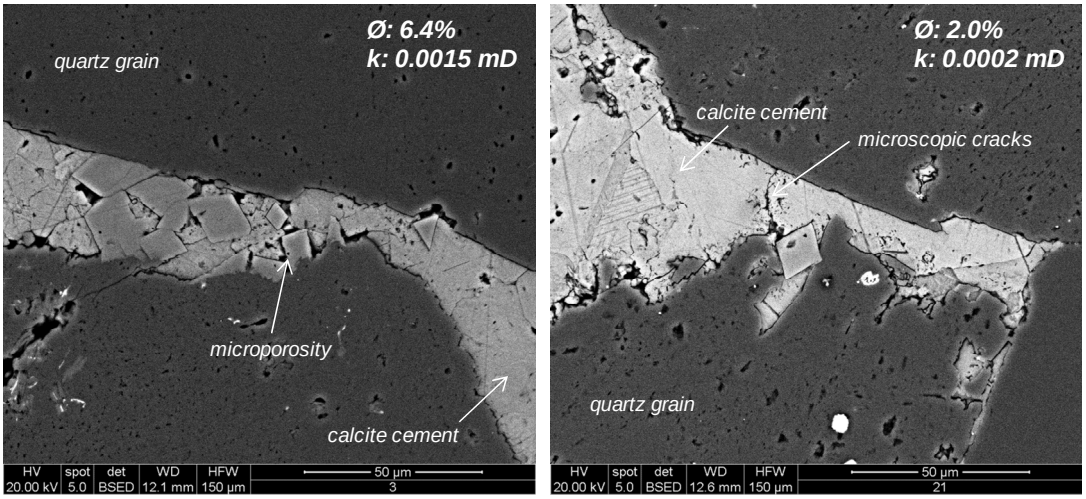

Figure 5.36 Two low-porosity samples of reservoirs in this study. Observe the presence of what it seems micropores and microcracks within authigenic calcite cement

The authigenic cement was observed to partially filling the space between quartz grains (Fig. 5.36). A more detailed observation reveals the presence of micropores and microscopic cracks within the calcite cement. Although is difficult to appraise the distribution of these micropores by just observing a two dimensional image, it is thought that despite their size, these may be well developed throughout authigenic cement and possibly this may be the cause of low cementation factors computed in well-cemented, low-porous samples. Herrick and Kennedy (1996) argue that in a dual-porosity system (in which large pores are oil-filled and micropores filled with brine), the continuous extension of micropores in the sample controls the flow of electric current, and even when the rock is completely filled with oil, the overall electrical output of the sample behaves as a highly conductive medium (or low-resistivity, low-contrast pay).

An increase of cementation exponent at high porosities (*e.g.* greater than 10% Ø) is also observed in Chicontepec and Mesaverde samples (Fig. 5.35). This implies that greater electrical resistance takes place at increasing porosities. This may possibly be due to the presence of secondary pores. The secondary pores observed in thin sections are rare in Chicontepec reservoirs. However, when these occur, they do not seem to be interconnected and although they tend to increase the total porosity of the sample, their influence to fluid-flow (and also to the flow of electrical current) appears to be null.

A similar tendency is found in saturation exponent estimations (Fig. 5.37). A threshold of 6% porosity is determined, above which *n* values follow a fairly constant trend of approximately 1.9. At lower porosities, *n* approaches unity. As described above, continuous micropores seem to develop a highly efficient electrical pathway through the rock. It is estimated that between 1 to 3% is associated to microporosity in most studied samples. At decreasing water saturations,

where one would expect greater electrical resistance and consequently high *n* computations; the result is the opposite.

Slight greater *n* values are observed in samples from this study compared to other areas of Chicontepec. This may be produced by differences in the plug's cleaning/drying process or dissimilar instrumentation characteristics. All Chicontepec plugs were cleaned with toluene and dried at high temperatures, whereas study area samples with DCM.

Saturation Exponent (n)

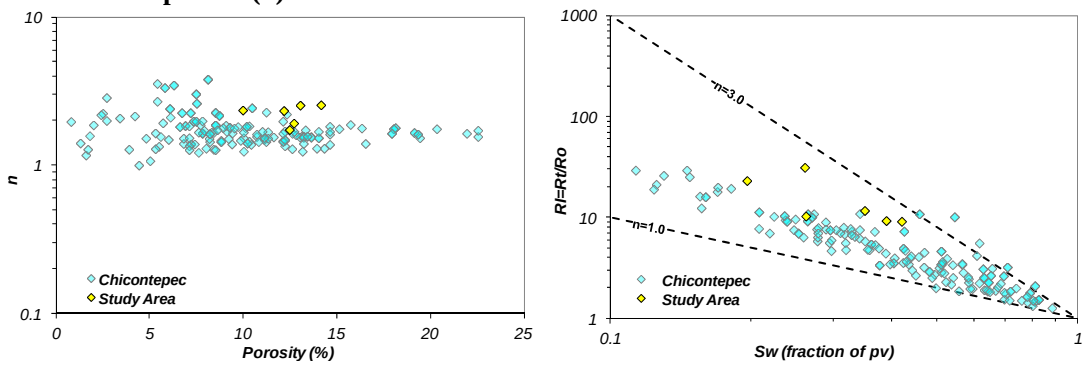

Figure 5.37 Archie's saturation exponent. A number of Chicontepec samples are plotted to compare them with the obtained in this study

Although low *m* and *n* values at low porosities seem to be required to honour the observations seen in Chicontepec samples (Figs. 5.35, 5.37), thin section microscopy provided by PEMEX, suggest that most micropores (*i.e.* microporosity and micro-cracks in the calcite cement) may provide no influence to fluid-flow, despite their apparent continuity. If low *m* and *n* values were used in well-log analysis (*e.g.* m= 1.3 and n= 1.5), inconsistent high hydrocarbon saturations would be computed at low-porosities in which it is known that most of the fluid in these pore systems will remain immobile by capillarity. Moreover, additional hydrocarbon pore volumes would be estimated and accounted as reserve with no apparent commercial interest.

For these reasons and the inherent uncertainty of traditional resistivity-based methods for computing water saturation, a cementation factor of 1.85 and saturation exponent of 2.2 were selected to be applied to well-logging interpretation. These remained constant in the entire interpreted profile, regardless of porosity.

5.2.5 Relative Permeability

Gas-oil relative permeability data was provided by PEMEX for two samples of well HUM-4036 in the study area. The unsteady-state dynamic displacement method (Johnson *et al.*, 1959) at reservoir temperature and *in situ* stress conditions was used. The sample is completely saturated with synthetic brine. Then, the brine is displaced by refined oil (*i.e.* drainage) until no further water is produced, achieving irreducible water condition. Permeability to oil at connate water saturation ($k_o@Sw_i$) is determined. At irreducible condition, gas is pumped into the sample to displace oil (*i.e.* imbibition) at permanent flow rate until it breaks through at the outlet end of the core. By measuring the produced fractions of gas and oil, together with the pressure drop across the core, the relative permeability curves are calculated. Oil is displaced by gas until no oil is produced, achieving residual oil saturation (So_r). Permeability to gas is obtained at this point ($k_g@So_r$). The relative permeability to gas and oil are scaled in terms of the percent of $k_o@Sw_i$ (Fig. 5.38).

Although this method has uncertainties due to an assumption of an efficient immiscible displacement (*i.e.* no gas is dissolved in oil), and that irreducible water saturation in the sample should remain constant during the entire experiment, these tests are useful to reproduce the process of reservoir depletion when crude-oil reaches bubble-point. At initial conditions, only two phases exist within pores: the undersaturated crude-oil (*i.e.* no gas evolves from the oil) and connate water saturation. This point is shown in position 1 in Figure 5.38. As production of oil commences and the reservoir pressure is reduced from the initial reservoir pressure (P_i) to the bubble-point pressure (P_b), gas is formed initially as scattered, immobile bubbles, until it reaches a critical saturation value where it becomes mobile (position 2, Fig. 5.38). Relative permeability to oil (k_{ro}) reduces as more gas evolves from crude-oil. k_{rg} increases until saturation of oil becomes discontinuous and only gas is produced (position 3, Fig. 5.38).

As observed in Figure 5.38, the critical gas saturation is achieved at relatively low saturations. Lower critical gas saturation is observed in Figure 5.38b, which has lower k/Ø ratio and higher irreducible water saturation than the sample in the opposite. End-point k_{rg}/k_{ro} ratios resulted of 1486 and 508, respectively. Total flow capacity of oil is function of the petrophysical rock properties, the wetting characteristics of the formation and the gas saturation (which in solution gas reservoirs depends upon the crude-oil properties).

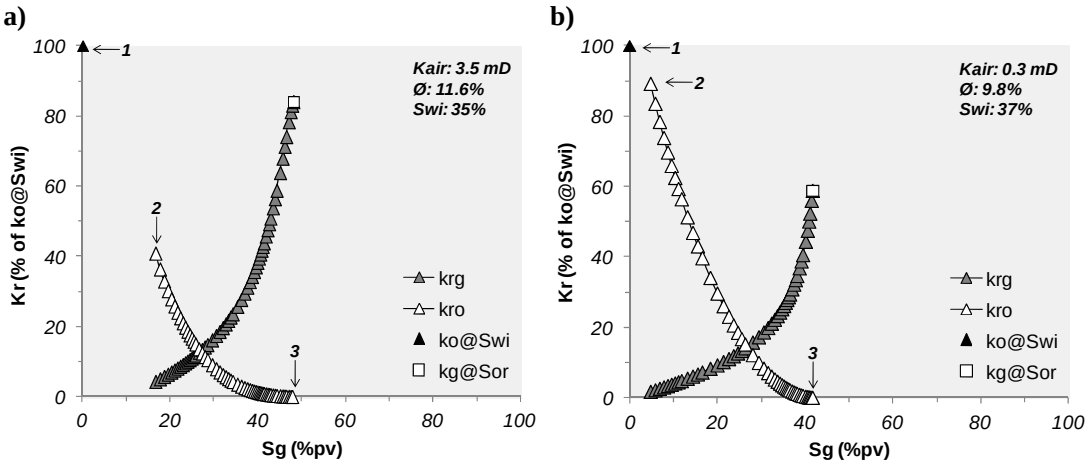

Figure 5.38 Gas-oil relative permeability curves obtained from HUM-4036 well. The relative permeability data is expressed as the percent of permeability to oil at irreducible water saturation (crossplots constructed using studies provided by PEMEX)

Substantial end-point effective permeability data in gas-oil and water-oil systems exist in other Chicontepec oilfields. This information was obtained at reservoir temperature and *in situ* stress conditions, using the unsteady-state dynamic displacement method. The data were compared to their k/Ø ratios (air permeability and gas-porosity) and the resulted correlations are illustrated in Figure 5.39 and 5.40.

These correlations may be useful due to relate variables that can be obtained easily in the laboratory (*e.g.* porosity and permeability) with dynamic rock properties (*i.e.* k_o, k_w, and k_g at their end-point saturations). For a particular Chicontepec reservoir rock with a determined k/Ø ratio, the average effective permeability to oil, water and gas can be estimated. If these are also combined with relative permeability correlations (*e.g.* Corey, Wyllie and Gardner or Pirso), together with irreducible and residual saturations; a very detailed description of the rock's capacity to transmit fluids can be evaluated. Since to these correlations were constructed using rock samples from other Chicontepec oilfields, it is unclear whether these may be applicable to the reservoirs of this study. k/Ø ratios in these graphs (Figs. 5.39 and 5.40) seem to be comparable to the reservoirs in this study. No further analysis was conducted on this matter; however, the interpreted correlations contribute to knowledge on the understanding of Chicontepec reservoirs.

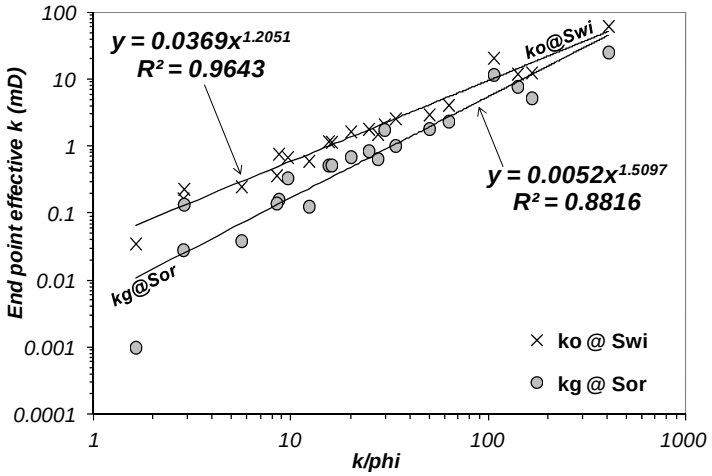

Figure 5.39 End-point effective permeability data-points of gas-oil systems compared to their k/Ø ratios. Observe that although the evident dispersion due to different pore geometries, there is an acceptable correlation
(crossplot constructed using studies provided by PEMEX)

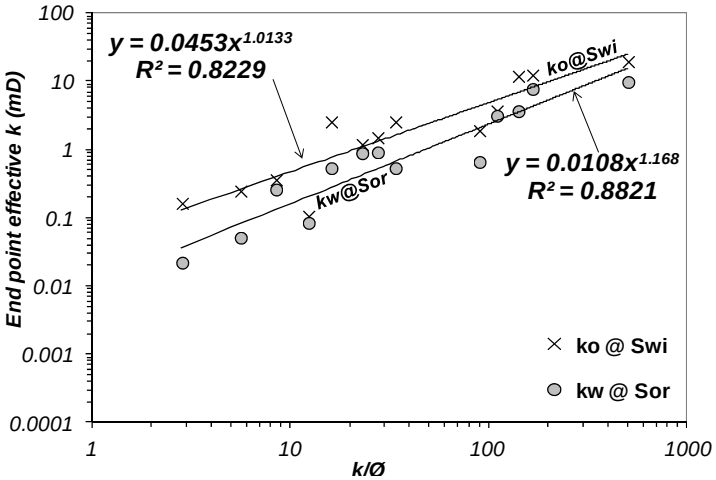

Figure 5.40 End-point effective permeability data-points of water-oil systems compared to their k/Ø ratios
(crossplot constructed using studies provided by PEMEX)

5.2.6 Rock Typing

The reservoirs in this study consist of sandstone bodies with variable petrophysical characteristics that are normally interbedded with shale beds. Each sand unit describe different flow capacity trend depending on their k/Ø relationship and pore size distribution. Rock typing, especially in this study, permits to recognize the contribution to fluid-flow of the different sand units that integrate the reservoir.

Based on the correlations previously described and integrating the textural and mineral information of the reservoirs of this study, guide to the definition of petrophysical rock types, which was conducted using terminology of Gunter *et al*. (1997). A petrophysical rock type is defined as a part of the reservoir that has unique k/Ø relationship, capillary pressure profile and water saturation for a given height above free-water level (Gunter, 1999). Rock types of the reservoirs in this study are shown in Figure 5.41.

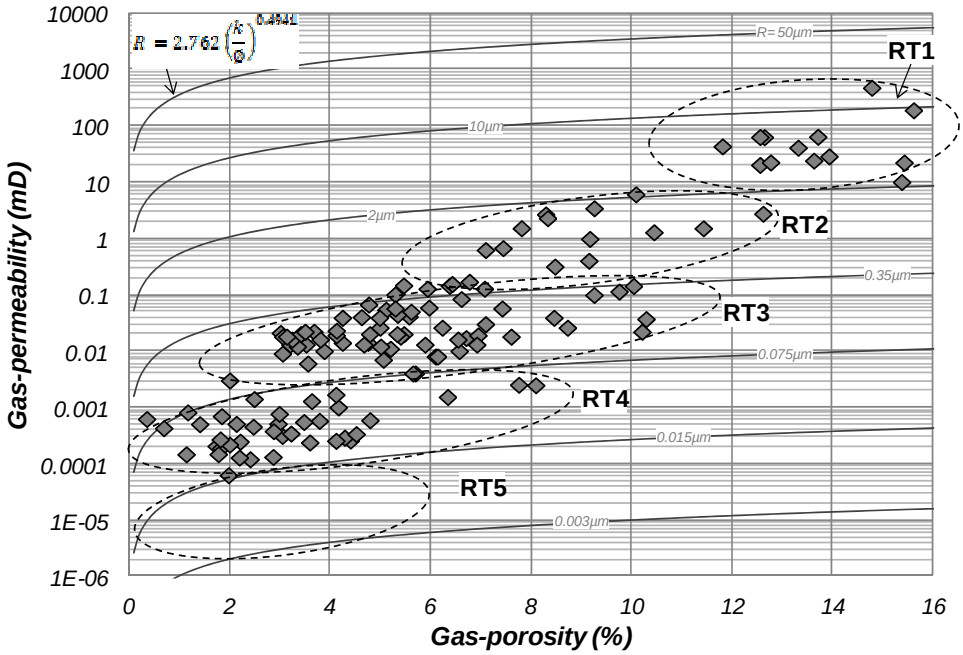

Figure 5.41 Rock type definition of the reservoirs in this study. Pore radius plotted in this chart is estimated based on the obtained correlation using √k/Ø ratios illustrated in Figure 5.25. Rock type 5 was defined using mercury injection data. No k/Ø ratios were available from this rock type

Average properties of each rock type are listed on Table 5.3. The first two rock types offer the most attractive characteristics as these are associated to permeabilities greater than 0.1 mD and pore sizes greater than 0.35 µm. Most of the flow capacity of the reservoirs will be controlled by the relative proportion of rock types 1 and 2. Although rock types 3 to 5 will not contribute significantly to the flow, they do participate in the storage capacity of the reservoir.

Table 5.3 Petrophysical Properties of Rock Types

ROCK TYPE	Porosity (%)	Permeability (mD)	Pore radius (μm)	Mean Grain Size (mm)	Swi* (%pv)
1	*>11*	*>10*	*>2*	*>0.25*	*<25*
2	*6 - 11*	*0.1 - 10*	*0.35 - 2*	*0.15 - 0.25*	*25 - 30*
3	*3 - 11*	*0.003 - 0.1*	*0.075 - 0.35*	*0.1 - 0.15*	*30 - 50*
4	*2 - 8*	*0.0001 - 0.003*	*0.015 - 0.075*	*0.1 - 0.15*	*60 - 90*
5	*1 - 4*	*<0.0001*	*<0.015*	*<0.1*	*>90*

**Determined from MICP data @ 200 psi*

A correlation is found between mineral type and content with petrophysical properties and textural character of the reservoirs in this study, as it is shown in Table 5.4. The mineral classes quantified by XRD were classified according to their primary chemical component (*i.e.* silicates and carbonates). In this way, quartz, feldspar, and plagioclase were added into *silicates*; whereas calcite, ankerite and dolomite as *carbonates*. The clays, which correspond to the third most abundant mineral in these rocks, were listed separately.

Table 5.4 XRD Mineral Composition (% Bulk volume)

ROCK TYPE	Bulk Fraction*					Clay Fraction*		
	Quartz	Calcite	Clay	Plagioclase	Dolomite	Illite/ smectite	Kaolinite	Chlorite
1	*48.5*	*33.2*	*8.8*	*5.7*	*1.5*	*5.3*	*1.9*	*1.6*
2	*44.3*	*34.3*	*9.9*	*8.2*	*1.8*	*6.3*	*1.9*	*1.7*
3	*41.3*	*39.6*	*9.1*	*6.0*	*1.8*	*6.1*	*1.6*	*1.4*
4	*34.1*	*43.5*	*10.1*	*8.5*	*2.3*	*6.0*	*2.8*	*1.3*
5	*33.2*	*44.7*	*9.7*	*7.9*	*2.3*	*6.5*	*1.6*	*1.6*

**Figures may not add-up as only most abundant minerals are shown*

It is found that silicate-to-carbonate ratios (or quartz-to-calcite ratios) greater than 1, combined with well-sorted, fine to medium sand grain sizes, generally are associated to greater k/Ø values. Minor variations in such ratio have a significant effect on petrophysical properties. The authigenic clay fraction, which is similar in most rock types as illustrated in Figure 5.42, seems to not being exerting great influence in controlling rock quality. A crossplot comparing k/Ø and silicate/carbonate ratios is shown in Figure 5.43. A summary of each rock type is displayed in Figure 5.44.

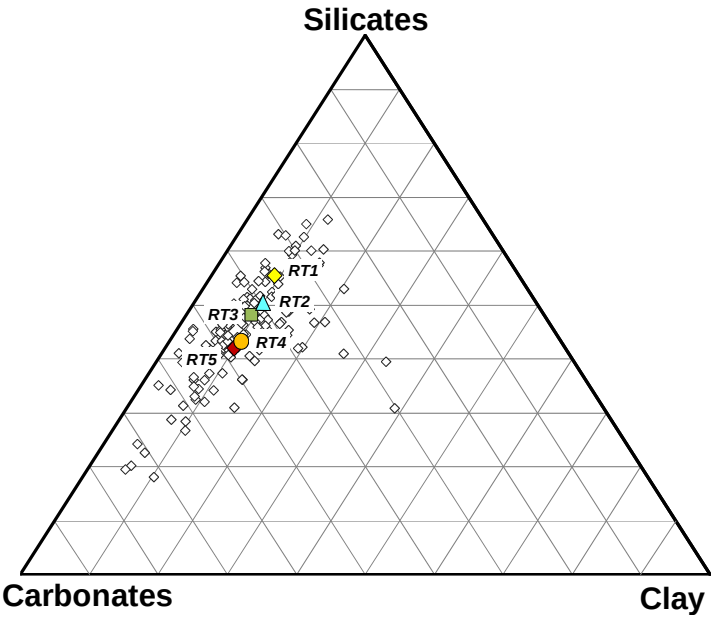

Figure 5.42 Mineralogical characteristics of the rock types identified. Average mineral content is shown for each rock type

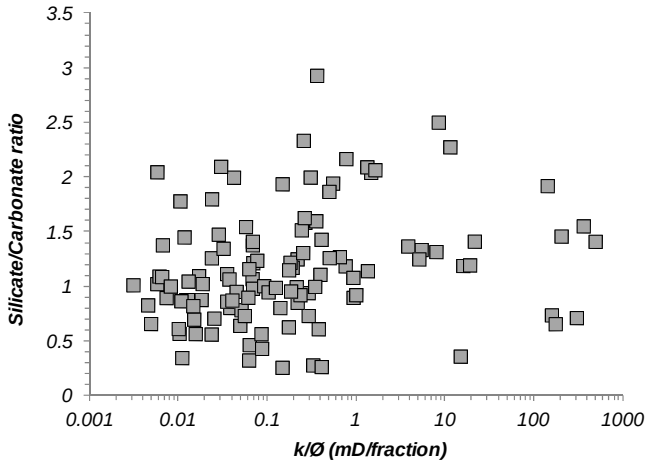

Figure 5.43 Correlation of the Silicate to Carbonate content and k/Ø ratios of rock samples used in this study. Observe that a number of trends are developed with a general tendency of greater k/Ø ratios in silicate-rich lithologies. Note that minor changes on mineral content generally reflect profound effect in k/Ø ratios

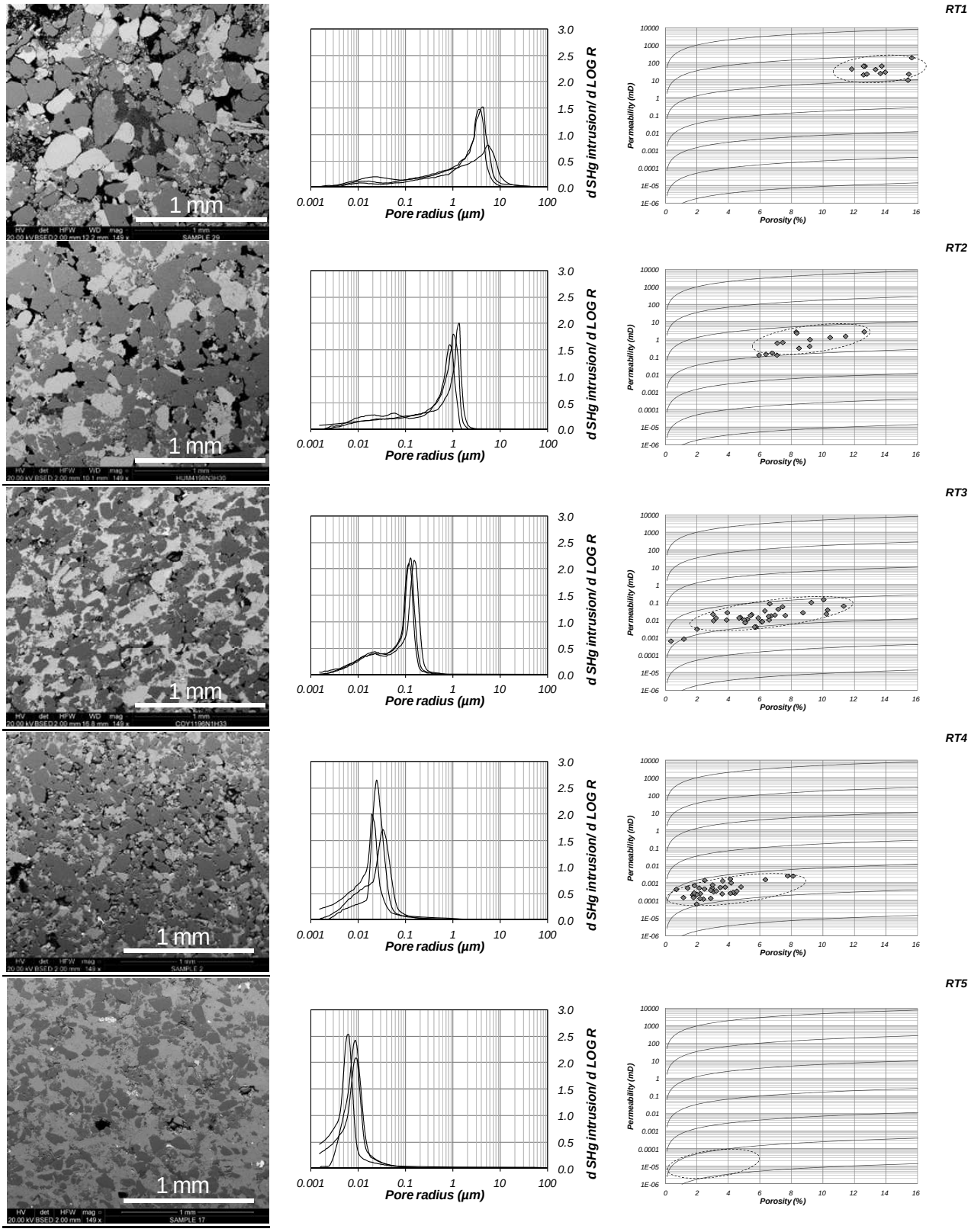

Figure 5.44 Textural, pore size and k/Ø relationship of the identified rock types

5.3 Discussion

Two datasets were used to make comparisons and construct petrophysical correlations. Overall, these datasets were comparable as the instrumentation, methodology and analytical procedures were equivalent. Minor deviations were observed in electrical properties determination (*i.e.* saturation and cementation exponents), possibly due to different sample conditioning or resulted from dissimilar instrumentation characteristics. Despite this, both datasets were integrated and used to build a number of correlations that would be useful not only to calibrate well-logs, but also to improve the general understanding of the reservoirs in this study. The correlations are thought to be predictable in most cases; however, it is expected that deviations may occur, especially in properties that due to their inherent uncertainty in their determination, as it was explained earlier in Chapter 3, show high dispersion (*e.g.* permeability).

In general, the reservoirs of this study describe petrophysical characteristics rather comparable to tight-gas or tight-oil reservoirs. When their petrophysical properties are contrasted with published data from other siliciclastic reservoirs (*e.g.* Ehrenberg and Nadeau, 2005; Nelson, 2009), these sands have rock qualities normally ascribed between moderate to low.

The reservoirs in this study are characterised by having low storage capacity as their porosity normally ranges between 1 to 15%. This low porosity mainly results from the poorly-sorted fabric of the detrital components and the intense calcite cementation experienced during diagenesis. The low-transmissivity capacity of these reservoirs is primarily a consequence of the authigenic cement and their fine-grained texture which normally produces small-size pores. Although rarely observed in thin sections, secondary pores by grain dissolution appear to not being increasing the pore connectivity significantly. Overall, these rocks describe low-storage capacities and poor-flow efficiencies as the pores are few, small and poorly connected.

At the beginning of the project, efforts were made in trying to produce a predictive tool to forecast the reservoirs of this study. In this way, the author classified the studied reservoirs in a number of rock types. A distinctive k/Ø relationship, capillary pressure profile and irreducible water saturation were assigned for each rock type and it was intended to construct a simulation model to predict the flow behaviour, a powerful tool aimed to support the exploitation labours of this project. However, in the majority of occasions, no correlation was found between the predicted rock types and the sedimentary facies. In most cases, channel facies were interpreted to be composed of rock types 1 and 2, whereas lobes of mostly rock types 3, 4 and 5. In this way, channels were predicted to produce better flow performances than lobes, which is not a general production behaviour observed in these reservoirs.

Additionally, it was intended to assign electrical properties (*m* and *n*) for each rock type in an attempt to produce more predictive water saturations. Cementation factor (*m*) is closely related to the degree of consolidation of the sample, whereas the saturation exponent (*n*) is generally associated to the wetting rock behaviour. Rock types 1 and 2 normally describe low cement content but since they describe low entry capillary pressure, they were thought to behave as strongly oil-wet (*i.e.* during the secondary migration, these rock types were thought to be first invaded by oil and then subjected to change their wetting characteristics to more oil-wettness). In contrast, rock type 3 depicts lower porosities than previous rock types, mainly because an increase of the authigenic calcite cement, and greater capillary entry pressures. Rock type 3 was thought to behave as intermediate-wet since oil was only able to invade the large pores. Finally, rock types 4 and 5 describe low porosities produced by the widespread calcite cement and great capillary entry pressures. In this context, a cementation factor (*m*) of 1.7 was used for rock types 1 and 2, whereas 1.8 was assigned to rock type 3 and 1.9 for rock types 4 and 5. A saturation exponent (*n*) of 2.3 was selected for rock types 1 and 2, whereas 2.2 was assigned to rock type 3 and 2.1 for the rest of rock types. No significant variations in water saturations were observed by using variable electrical properties for each rock type in comparison with the obtained using constant values. It was not clear whether the selected electrical properties were actually representative of the reservoirs in this study. It seemed necessary to characterise in more detail these properties, especially in terms of their wetting behaviour. Characterisation of the saturation exponent (*n*) for each rock type using aged rock plugs was not performed in this study.

Rock typing exercise performed in these reservoirs was only useful to distinguish attractive intervals and its use for simulation purposes seems limited to the capacity to associate each rock type to a specific sedimentary facies. Additionally, a more detailed characterisation of the electrical properties using aged-plugs appears an area of opportunity worth to be evaluated in these reservoirs.

5.4 Conclusions

The aim of this chapter was to evaluate the petrophysical properties of the reservoirs of this study. This was conducted through the examination of measured rock properties that described porosity, permeability, pore size, and irreducible water saturation; plus electrical properties and relative permeabilities.

A number of petrophysical correlations were found which are summarised in Table 5.5. These will be useful for calibrating some of the parameters in the well-log analysis presented in chapter six. An agreement was found between the textural and mineral content with the petrophysical rock properties in these reservoirs.

Table 5.5 Summary of Petrophysical Correlations

Permeability (k):		
Porosity based:	$k = 0.0001e^{0.8958\emptyset}$	*Ø= gas porosity (%)* *e= Euler's number (2.7182)*
MICP based:	$k = 14.583\left(\frac{Sb}{Pc_{air-Hg}}\right)^{2.231}$	*Sb= mercury saturation at apex (%pv)* *Pc= air-mercury capillary pressure (psi)*
NMR T2 based:	$k = \left[11.41 \cdot \emptyset_{NMR}^2 \left(\frac{FFI}{BVI}\right)\right]^2$	*$Ø_{NMR}$= porosity from NMR (fraction)* *FFI= effective porosity from NMR (fraction)* *BVI= capillary-bound porosity from NMR (fraction)*
Pore throat size (r):		
k/Ø based:	$r = 2.762\left(\frac{k}{\emptyset}\right)^{0.4941}$	*k= permeability (mD)* *Ø= porosity (%)*
NMR based:	$r = 0.0081 \cdot NMR\ T2_{LM}{}^{1.589}$	*NMR $T2_{LM}$= logarithmic mean of fully saturated samples (ms)*
MICP based:	$r = 189078 \cdot Sw_i{}^{-3.26}$	*Sw_i= irreducible water saturation obtained at 200 psi air-mercury pressure(% of pv)*
	$r = 1849 \cdot Sw_i{}^{-2.376}$	*Sw_i= irreducible water saturation obtained at 1000 psi air-mercury pressure(% of pv)*
Irreducible Water Saturation (Swi)		
MICP based:	$Sw_i = 36.75\left(\frac{k}{\emptyset}\right)^{-0.1215}$	*Swi @ 200 psi air-mercury threshold* *k= permeability (mD)* *Ø= porosity (%)*
	$Sw_i = 16.59\left(\frac{k}{\emptyset}\right)^{-0.196}$	*Swi @ 1000 psi air-mercury threshold* *k= permeability (mD)* *Ø= porosity (%)*

CHAPTER VI.
WELL-LOG EVALUATION

The aim of this chapter is to evaluate the petrophysical properties of the reservoirs in this study through the analysis of well-logs. In the preceding chapter, the petrophysical properties were described based on measured rock data. Now, the analysis is extended through the interpretation of wireline data from the study area. The well-log interpretation described in this chapter was conducted to accomplish two objectives: 1) to complement the evaluation of petrophysical characteristics of these reservoirs; and 2) to provide input parameters for reservoir modelling analysis and simulation case scenarios latter described in this work.

6.1 Introduction

The study area is in its development stage. As of May 2014, there were 284 wells drilled with complete set of basic logging data that included for each well: gamma ray (*GR*), induction resistivities (*AO90, AO60, AO30, AO20*), neutron-density (*NPHI/RHOB*), and compressional slowness (*DT*) logs. Resistivity curves consisted of one-foot (30 cm) vertical resolution at four depths of horizontal investigation. Special logs (*e.g.* NMR, electrical images) were available in selected wells. Four logging companies acquired the wireline data, and each company has its own mnemonics criteria. To avoid confusion, all the curves were re-named as shown in Table 6.1, which also summarises the well-logging information existent in this study.

Table 6.1 Well-log data database

Number of curves	Log
284	*Gamma Ray (GR)*
284	*One-foot Resistivity at four horizontal depths*
284	*Neutron (NPHI)*
284	*Density (RHOB)*
284	*Compressional Slowness (DT)*
268	*Borehole temperature (Temp)*
18	*Dipolar Sonic (DTC, DTS)*
4	*Nuclear Magnetic Resonance (NMR)*
3	*Electric images*

The complete data was uploaded into the *Interactive Petrophysics*® software in which the interpretation was conducted. Borehole trajectory survey and elevation information (*i.e.* ground surface, derrick floor, kelly-bushing) were accessible in all wells. Both vertically-corrected measured and sub-sea depths (TVD, TVDSS, respectively) were calculated.

The generalised workflow of well-log interpretation is illustrated in Figure 6.1.

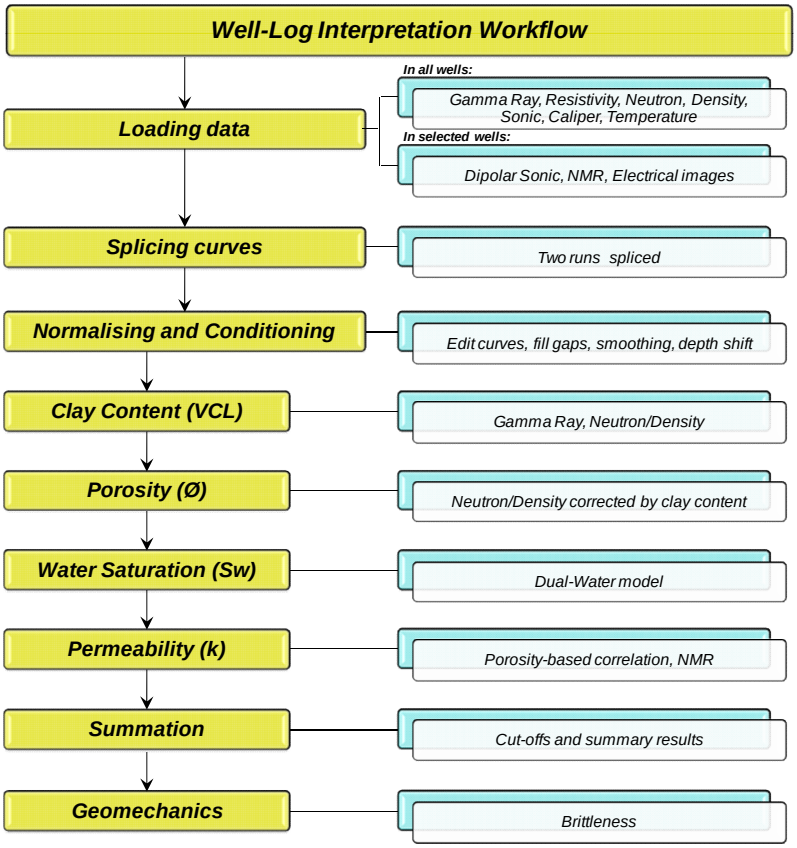

Figure 6.1 Workflow of the well-log interpretation

All the wells in the study area were drilled in two stages. The curves acquired in each run were merged to obtain continuous logging information in the entire drilled section. Prior to interpreting the data, well conditioning procedure was conducted using the *Interactive Petrophysics*® software. This procedure consisted of editing curves to fill information gaps, placing the logs into their correct depth position (*i.e.* depth shifting), and converting the neutron curve from sandstone to limestone matrix. For convention, the deep resistivity (*AO90*, *Rt*) was employed as a reference curve for depth shifting, since it is less affected by the geometry of the borehole and the temperature. Normalisation process was performed in a number of wells with anomalous curve readings caused by borehole rugosity (*e.g.* HUM-1662, COY-295A, HUM-4011). Caliper (CALI) and compensated density values (DRHO) were also analysed to evaluate the quality of the data. The caliper measures the borehole diameter, so that is an indicator of the borehole rugosity. DRHO curve shows the magnitude of the correction applied to the density log and normally is used as quality control of the density curve.

Once conditioned, the curves were ready to be used for interpretation. The *GR* and *Rt* curves of each well were exported to *Petrel*® software to conduct the stratigraphic interpretation of the study area. The following sections describe the interpretation procedure according to the workflow depicted in Figure 6.1.

6.2 Well-log Analysis

6.2.1 Clay Content (*Vcl*)

Clay volume was calculated employing *GR* (VCL_{GR}) and Neutron-Density (VCL_{ND}) logs as clay indicators. From these, the minimum clay volume was selected for calculation since this matched better with the observed clay distributions from core data. The *GR* log records the formation radioactivity that naturally emanates from uranium, thorium and potassium. In sedimentary rocks, shales generally have by far the strongest radiation (Rider, 2002), so *GR* is widely used as shale indicator. The procedure to estimate the clay content in these reservoirs should properly be referred to as shale content since no shale is entirely composed by clay. Linear method was used in combination with variable "clean" and "clay" cut-offs for selected zones, using the following expression:

$$VCL_{GR} = \frac{GR - GR_{clean}}{GR_{clay} - GR_{clean}}$$

where: *GR* is the wireline log readings (API), GR_{clean} is the selected minimum *GR* cut-off (API), GR_{clay} (API) is the selected maximum *GR* cut-off. Figure 6.2 illustrates the procedure. When available, the resulted clay content was calibrated employing quantitative X-ray diffraction (XRD) data obtained from core analyses. Core data was depth adjusted employing core Gamma Ray logs.

The clay volume using *NPHI/RHOB* curves was calculated graphically, as it is shown in Fig. 6.3. The neutron log is related to the formation's hydrogen index (*i.e.* water), as it measures the attenuation of fast neutron signals that bombards formation. The maximum energy loss of the neutrons emitted into the formation generally occurs in front of particles of similar atomic mass (*e.g.* hydrogen nuclei). Neutron log is normally recorded in limestone units, which means that their porosity values are reported empirically assuming that the formation is pure limestone. Correction from limestone porosity to equivalent sandstone porosity is necessary and generally 1 limestone p.u. (porosity unit) is approximately equivalent to 4 sandstone p.u. (Smithson, 2012).

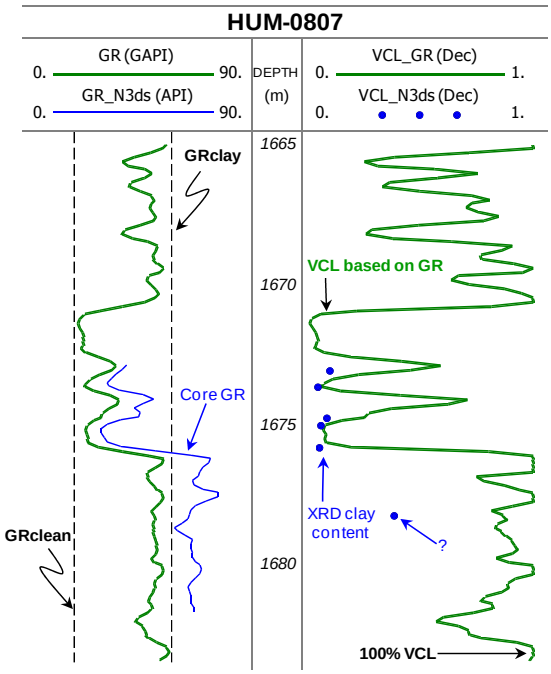

Figure 6.2 Clay content estimation using the linear normalisation of the GR log. The first track in the image shows the GR log and their selected cut-offs, whereas the resulted clay volume is shown in track three together with the clay-content observed from core data and used for calibration. The dot marked as "?" corresponds to a thin sandstone bed with 40% clay content. The blue curve in track one is the GR log obtained from a conventional core sample

The log density, by contrast, measures the formation's bulk density, as it records the energy attenuation of gamma rays that collide with formation. The attenuation is a function of the electron density of the formation, which is closely related to its bulk density.

Combined neutron/density logs provide an indication of the clay content. The neutron log responds to hydrogen and therefore the increase of bound-water associated to clay is expressed as an increase in neutron porosity. However, the clay fraction is generally less dense than the rock matrix, so the effect of clay is to lower the bulk density response. Clay content is determined by selecting "clay" and "clean" points in a *NPHI/RHOB* crossplot (Fig. 6.3), and the clay volume is estimated using the following expression:

$$VCL_{ND} = \frac{(\rho_{clean2} - \rho_{clean1}) \cdot (NPHI - NPHI_{clean1}) - (\rho - \rho_{clean1}) \cdot (NPHI_{clean2} - NPHI_{clean1})}{(\rho_{clean2} - \rho_{clean1}) \cdot (NPHI_{clay} - NPHI_{clean1}) - (\rho_{clay} - \rho_{clean1}) \cdot (NPHI_{clean2} - NPHI_{clean1})}$$

where: $\rho_{clean1\ and\ 2}$ and $NPHI_{clean1\ and\ 2}$ are the "clean" density/neutron values obtained from NPHI/RHOB crossplot illustrated in Figure 6.3; ρ_{clay} and $NPHI_{clay}$ are the neutron/density coordinates that describe the 100% clay point and determined from the same crossplot. ρ_{clean1} corresponds to the matrix density which is normally 2.68 g/cm^3 in the reservoirs of this study.

The minimum clay volume (*Vcl*) estimated by both methods generally was in agreement with observed core data (*e.g.* XRD), thus this was selected as clay indicator and used in further calculations. The interpreted clay volume (*Vcl*) generally resulted in less than 10% in most cases, which is normally the observed clay content in the reservoirs of this study. Figure 6.4 is a frequency histogram of the clay content of 143 rock samples of this study. Observe that in the majority of cases, relatively low-clay content exist in the reservoirs of this study.

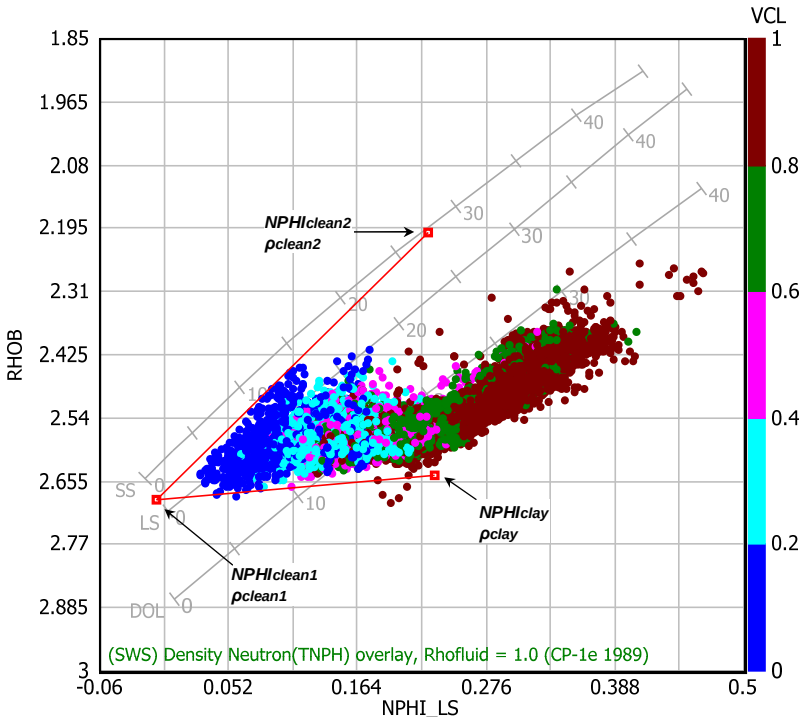

Figure 6.3 Neutron/Density crossplot which is used to estimate the formation's clay content. The "clean" and "clay" points are graphically determined. The colours show the interpreted clay volume

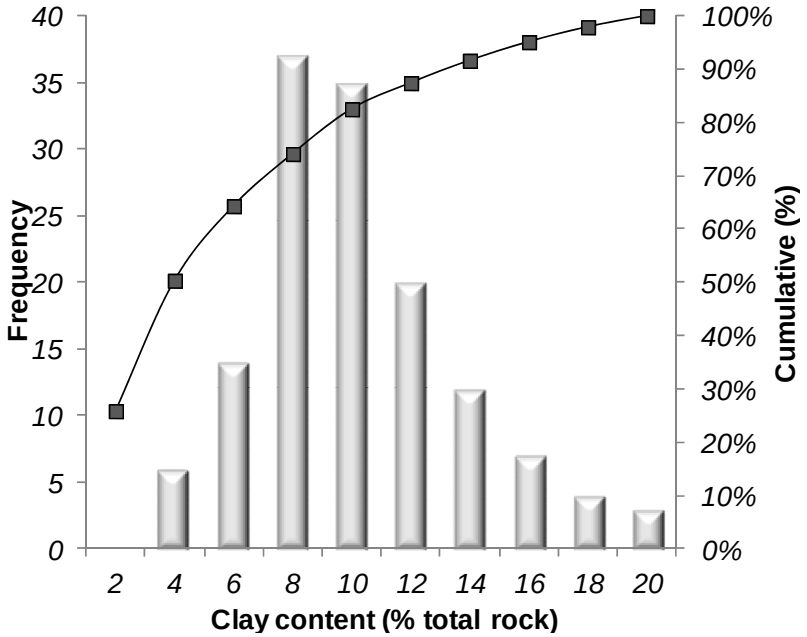

Figure 6.4 Clay content frequency histogram constructed from 143 XRD analyses from sandstone core samples obtained from reservoirs of this study

6.2.2 Porosity (Ø)

Porosity was estimated employing the combination of neutron ($Ø_N$) and density ($Ø_\rho$) logs and calibrated with core data when possible. Porosity (Ø) was estimated using the following expression:

$$\emptyset = \frac{\emptyset_{\boldsymbol{\rho}} + \emptyset_{\boldsymbol{N}}}{\mathbf{2}}$$

$Ø_N$ and $Ø_\rho$ are defined as:

$$\emptyset_\rho = \frac{\left(\rho_{ma} - \rho - Vcl(\rho_{ma} - \rho_{cl})\right)}{\left(\rho_{ma} - \rho_{fl} \cdot Sx_o - \rho_{HyAp} \cdot (1 - Sx_o)\right)}$$

$$\emptyset_N = \frac{(\emptyset_{neu} - Vcl \cdot NeuCl)}{(Sx_o + (1 - Sx_o) \cdot NeuHyHI)}$$

where: Ø is the interpreted effective or interconnected porosity, $Ø_\rho$ is the density-based porosity, $Ø_N$ is the neutron-based porosity, ρ_{ma} is the average matrix density (2.68 g/cm^3 for the reservoirs in this study), ρ is the bulk density log, ρ_{HyAp} is the apparent hydrocarbon density (0.8 g/cm^3 for the reservoirs in this study), ρ_{fl} is the assumed filtrate density (2.00 g/cm^3), *Vcl* is the clay volume, $Ø_{neu}$ is the neutron-log porosity, *NeuHyHI* is the apparent hydrogen index (selected as 1.0, *i.e.* no corrections for hydrocarbon). S_{xo} is the flushed zone water saturation and it was estimated assuming an invasion factor (*InvFact*) of 0.5 and using the following empirical formula:

$$S_{xo} = \frac{Sw + InvFact}{1 + InvFact}$$

ρ_{cl} and *NeuCl* are the coordinates of the interpreted 100% clay point determined from neutron/density crossplot for a selected zone as shown in Figure 6.5. Imaginary lines are extrapolated from this point to the zero porosity point (*i.e.* the formation's matrix density which in this case is of 2.68 g/cm^3) and to the 100% porous point (*i.e.* free fluid). Porosity is then estimated by drawing equidistant lines of porosity within the area formed by these points (Fig. 6.5). The porosity is corrected by clay content according to the previous equations. Observe that if no clay exists in the rock, porosity estimation relies directly on the neutron/density readings and no corrections should be necessary.

ρ_{cl} and *NeuCl* are normally referred to as the wet-clay values and are important input parameters for porosity calculation due to they vary according to the type of formation and their fluid

content. These were determined individually on each well. Figure 6.6 illustrates the frequency histograms of such parameters.

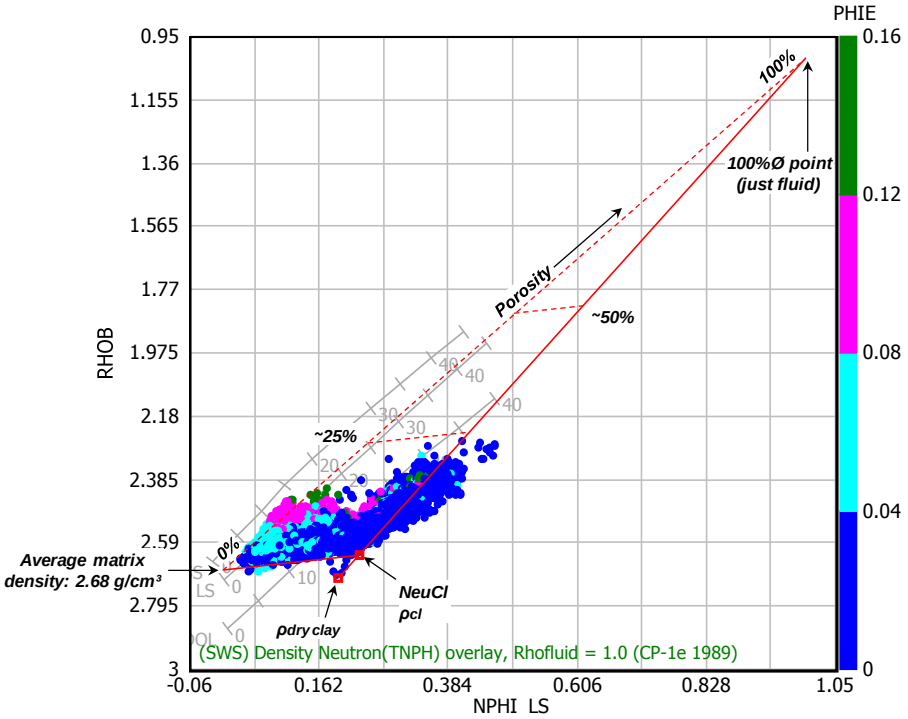

Figure 6.5 Neutron/density crossplot from which the interpreted wet-clay points are determined. The colours show the clay-corrected porosity

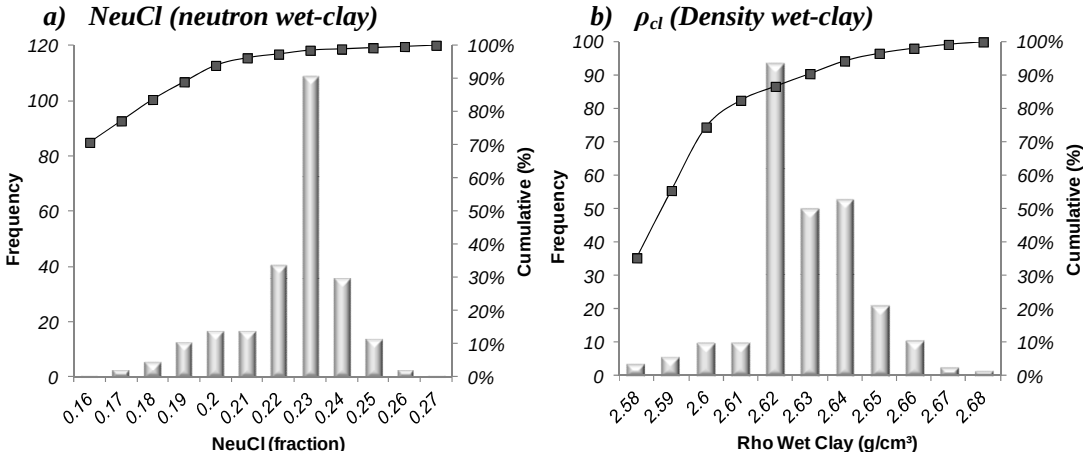

Figure 6.6 Frequency histograms of the selected wet-clay parameters of 284 wells. Observe that in most cases, the selected neutron wet-clay was of 0.23, and the density wet-clay of 2.62 g/cm^3

Interpreted well-log porosity was calibrated against any core data that was available; this is shown in Figure 6.7. Calibration was conducted by varying the clay content or changing ρ_{cl} and *NeuCl* parameters. Normally, minor variations of clay content resulted in significant changes in porosity.

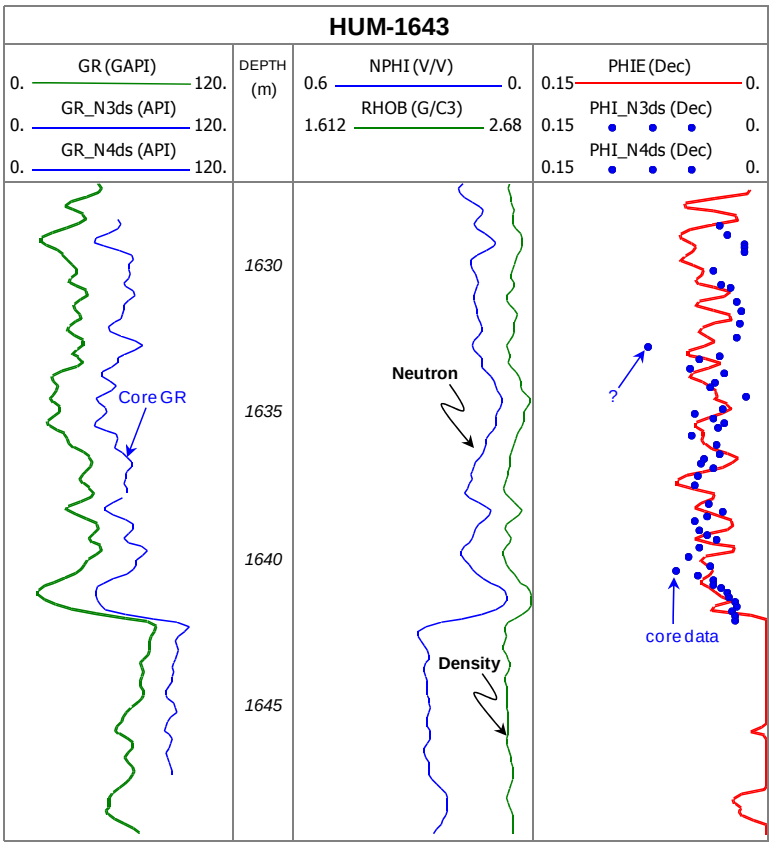

Figure 6.7 Porosity estimation using neutron/density logs calibrated with core data. Note the dense sampling of core data obtained for this particular well and their comparison to well-log porosity. The core data was depth-shifted using the core gamma-ray. Log resolution is sometimes unable to resolve thin beds as expressed by core data

The interpreted porosity of the reservoirs in this study generally varied from 0 to 16%, which corresponds to the general trend observed from core data (discussed in chapter five). Figure 6.8 is a frequency histogram of the porosity interpreted from well-logs constructed from selected wells in the study area. Observe that most of the porosity ranges between similar porosity values observed in core data.

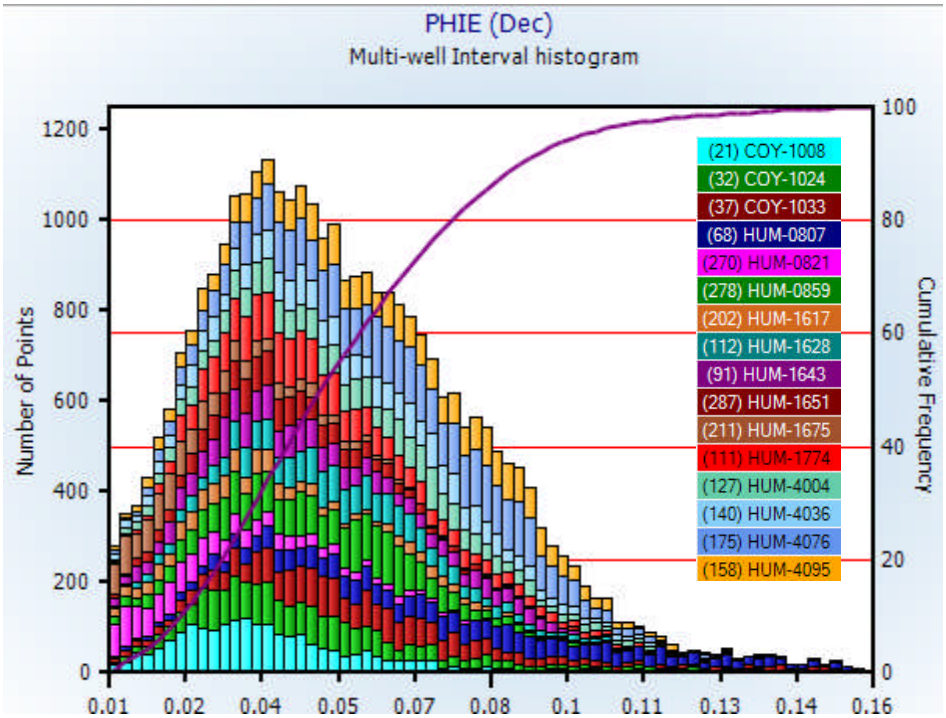

Figure 6.8 Frequency histogram of porosity from selected wells of the study area. The values correspond to sandstone units

6.2.3 Water Saturation (*Sw*)

The Archie equation (Archie, 1942), used to estimate water saturation (*Sw*) was developed specifically for clay-free, isotropic reservoirs, in which the electric current describes uni-directional flow through pores and pore-throats. The generalised Archie's equation to estimate *Sw* is normally expressed as:

$$\frac{1}{R_t} = \frac{\emptyset^m}{a}\frac{Sw^n}{R_w}$$

where: *Ø* is the porosity, *Rw* is the formation water resistivity, *Rt* is the total resistivity of the rock and contained fluids, *m* and *n* are the cementation and saturation exponents, respectively (both normally expressed as 2), and *a* is the tortuosity factor (usually 1).

When clay or other conductive component (*e.g.* clay, pyrite) exists in the rock matrix, the bulk electrical behaviour of the rock is modified. Clay minerals usually display negative electrical surface charge when immersed in aqueous solutions, which is compensated with the dissolved ions. The ions tend to diffuse away from the clay surface towards the bulk of solution. The action of the two attractive tendencies results in a high concentration of ions near the clay surface, acting as if this were electrically-charged media. The excess of electric conductivity tends to lower resistivity which generally results in high water saturation computations. When conductive clay is present, the Archie equation does not accurately estimate water saturation and a correction must be made to account for this.

Diverse attempts have been made to produce water saturation equations to take into consideration the electric contribution of the clay. Some of these models rely on shale volume approaches (*e.g.* Simandoux, 1963; Poupon and Leveaux, 1971) or the clay's cation exchange capacity (*e.g.* Waxman and Smits, 1968; Juhasz, 1981). A comprehensive analysis of these models is presented by Worthington (1985).

The Dual-Water model developed by Clavier *et al.* (1984) takes into account the effects of the clay by dividing the total pore water of the reservoir in two portions: the volume of water that is bound to the clay surface and in which conduction take place (generally referred as the double-layer effect), and the remaining water volume that is in the pores and free of any clay-surface effects. The Dual-Water model is generally expressed as:

$$\frac{1}{Rt} = \frac{\emptyset_t^m \cdot Sw_t^n}{a} \times \left[\frac{1}{Rw} + \frac{Sw_b}{Sw_t}\left(\frac{1}{Rw_b} - \frac{1}{Rw}\right)\right]$$

from which:

$$Sw_t = Sw(1 - Sw_b) + Sw_b$$

$$Sw_b = 1 - \frac{\emptyset}{\emptyset_t}$$

where: $\emptyset_t$ is the total porosity (connected and isolated pores. Total porosity is obtained directly from neutron/density logs, no clay-corrected), $\emptyset$ is the clay-corrected porosity (or the interpreted interconnected porosity), Sw_t is the total water saturation that includes free and bound-water, Sw_b is the bound-water saturation (*i.e.* the portion of water in the pores that is bound to clay), Sw is the effective water saturation (*i.e.* the portion of water in the pores that is free to move), Rw_b is the bound-water resistivity (input parameter of 0.10 Ω·m).

In the case of the reservoirs of this study: m= 1.85 and n= 2.2. These parameters were selected as these seemed to honour the overall electrical behaviour of Chicontepec samples. The tortuosity factor (a) was determined based on Rt vs $\emptyset$ plots (*i.e.* Pickett plot) and generally adjusted to a value of 0.9 (Fig. 6.9). Formation water resistivity (Rw) was calculated employing Pickett plots (Fig. 6.9) and calibrated with water samples directly obtained from producing intervals. The resulted Rw was of 0.0817 Ω·m, equivalent to a formation water salinity of 35,000 ppm of NaCl at reservoir average temperature of 80°C.

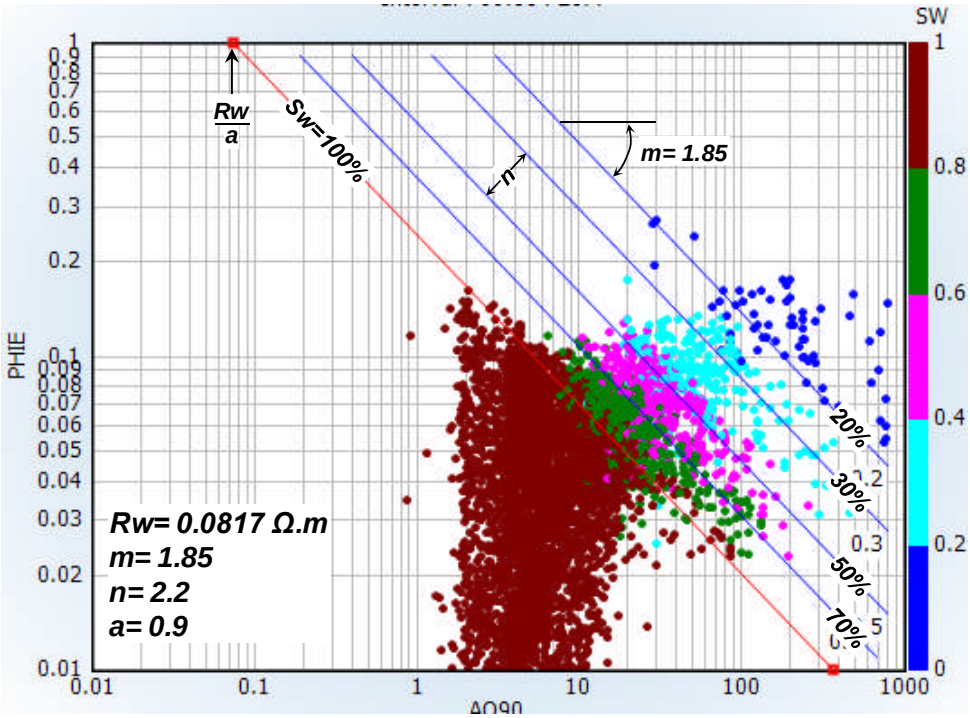

Figure 6.9 Graphic solution of the water saturation equation (Pickett plot) for a selected well of this study. A 100% *Sw* line of slope *m* is positioned above a porous invaded zone which is believed to be completely water saturated. Projection of this line to a 100% porosity (free fluid) results into the equivalent formation's water resistivity (*Rw/a*). Iso-saturation lines are drawn equidistantly according to the selected *n* exponent

Temperature was continuously recorded from well-logging devices in most wells. A temperature gradient of 2.85°C/100m was estimated from these logs (Fig. 6.10) and applied to those wells with no temperature information (surface temperature was assumed to be of 30°C). Temperature gradient was corrected by borehole deviation.

The Dual-Water equation reduces to the Archie's basic expression (*i.e.* Sw_b =0) when no clay was interpreted to exist in the reservoir. It is recognised that the reservoirs of this study usually have low-clay content, which in turn may be interpreted as a poor influence in the electric behaviour. However, this has not been demonstrated by experimental studies in these reservoirs. The presence of conductive minerals (*e.g.* pyrite), together with thin laminations observed regularly in core data, may exert additional electrical pathways which would control the bulk electric flow behaviour in these reservoirs.

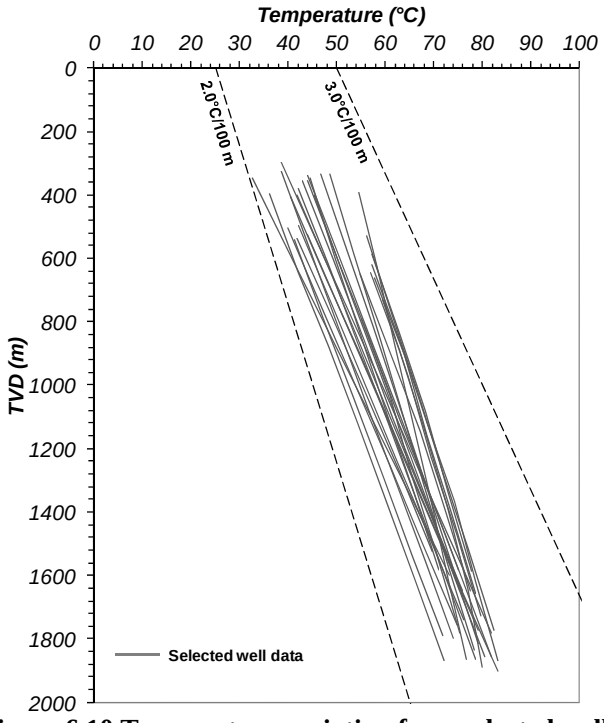

Figure 6.10 Temperature variation from selected wells

Although no core data was available to validate the water saturation estimations (*e.g.* retort distillation or Dean-Stark tests), an alternative water saturation computation was conducted using mercury injection data. The technique is a modification of Leverett J function and is described in Gunter *et al.* (1999). Irreducible water saturation correlation obtained at 1000 psi air-mercury threshold (discussed in previous chapter), was:

$$Sw = 16.59 \cdot \left(\frac{k}{\emptyset}\right)^{-0.196}$$

where: *k* is the permeability (mD) and *Ø* is the porosity (%). The neutron/density porosity (corrected by clay-content) was used, whereas the permeability model was estimated by a porosity-based correlation, which is discussed in the next section of this chapter.

The MICP correlation was applied in wells where according to their structural position were believed they were at their irreducible water saturation conditions. Normally, zones at irreducible water saturation in a moderately homogeneous reservoir rock should lie in a common bulk volume water (*BVW)* value (Asquith and Krygowski, 2004). The BVW is the product of porosity and water saturation and expresses the volume of water per unit rock volume.

A comparison of water saturations is presented in Figure 6.11 which corresponds to the reservoir S4 of HUM-3277 well in the study area. The well is located in one of the highest structural positions and is composed of a thick porous sand interval. The water saturation estimated by the Dual-Water model and with the mercury injection correlation are displayed (Fig. 6.11). The MICP correlation was only computed in clean and porous sand intervals (*i.e.* porosities greater than 5%) in which the irreducible condition is best observed.

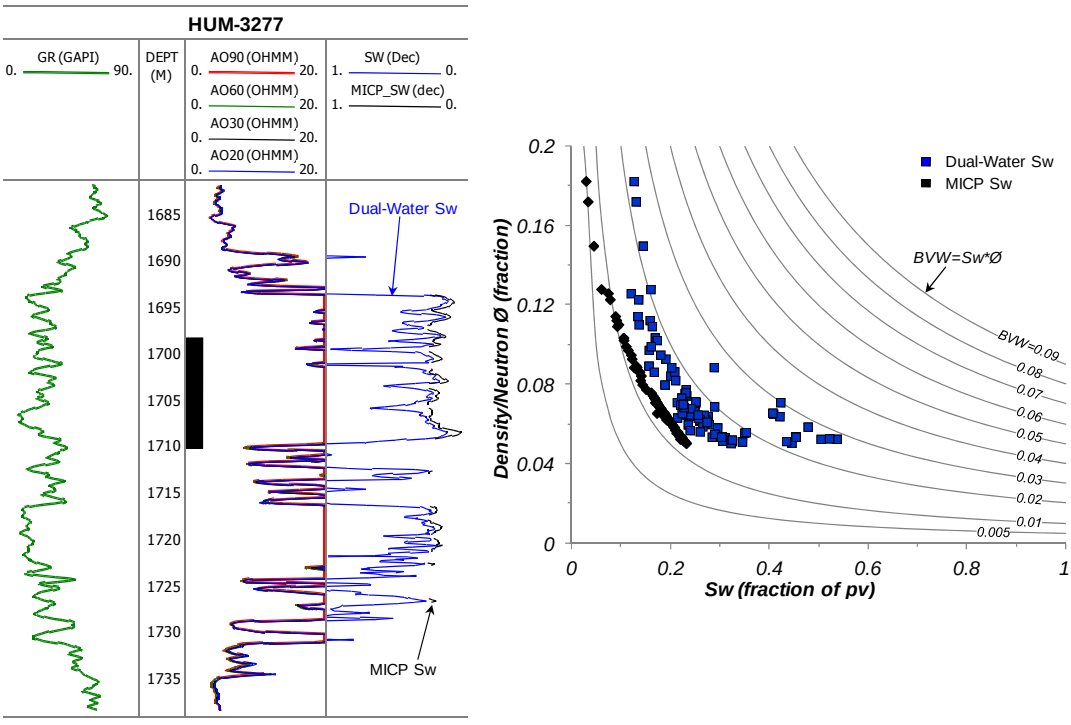

Figure 6.11 Comparison of water saturation estimations using the Dual-Water model (blue) and the MICP correlation (black). The *Sw* by MICP is displayed discontinuously since it has been calculated only to intervals with porosities greater than 5%. Note the minor differences between the two models. Observe that BVW values are fairly constant, which suggest that the reservoir is at irreducible conditions. The well was completed at the top of the sequence (black bar) with an initial production of 168 BOPD and no water-cut after fracturing

Minor differences, between 2 to 5% error, were observed between the two *Sw* models, suggesting that the saturation estimation based on the Dual-Water model in the reservoirs of this study (at least in the irreducible water volume) seems to be acceptable.

6.2.4 Permeability (*k*)

The free-fluid permeability model (Coates and Denoo, 1981) that was calibrated with core data (and discussed in previous chapter) resulted in the following expression:

$$k = \left[(11.41 \cdot \emptyset_{NMR})^2 \left(\frac{FFI}{BVI}\right)\right]^2$$

where: *k* is the permeability (mD), *FFI* is the free-fluid index , *BVI* is the irreducible water volume, and $\emptyset_{NMR}$ is the total porosity determined by NMR. This model was applied to wells with NMR log data. The interpretation of the free and bound volumes was conducted by applying a cut-off of 20 ms (instead of the industry standard of 33 ms) to the NMR T2 relaxation curve as this value was determined from core tests. Figure 6.12 illustrates the obtained permeability which is compared to core data.

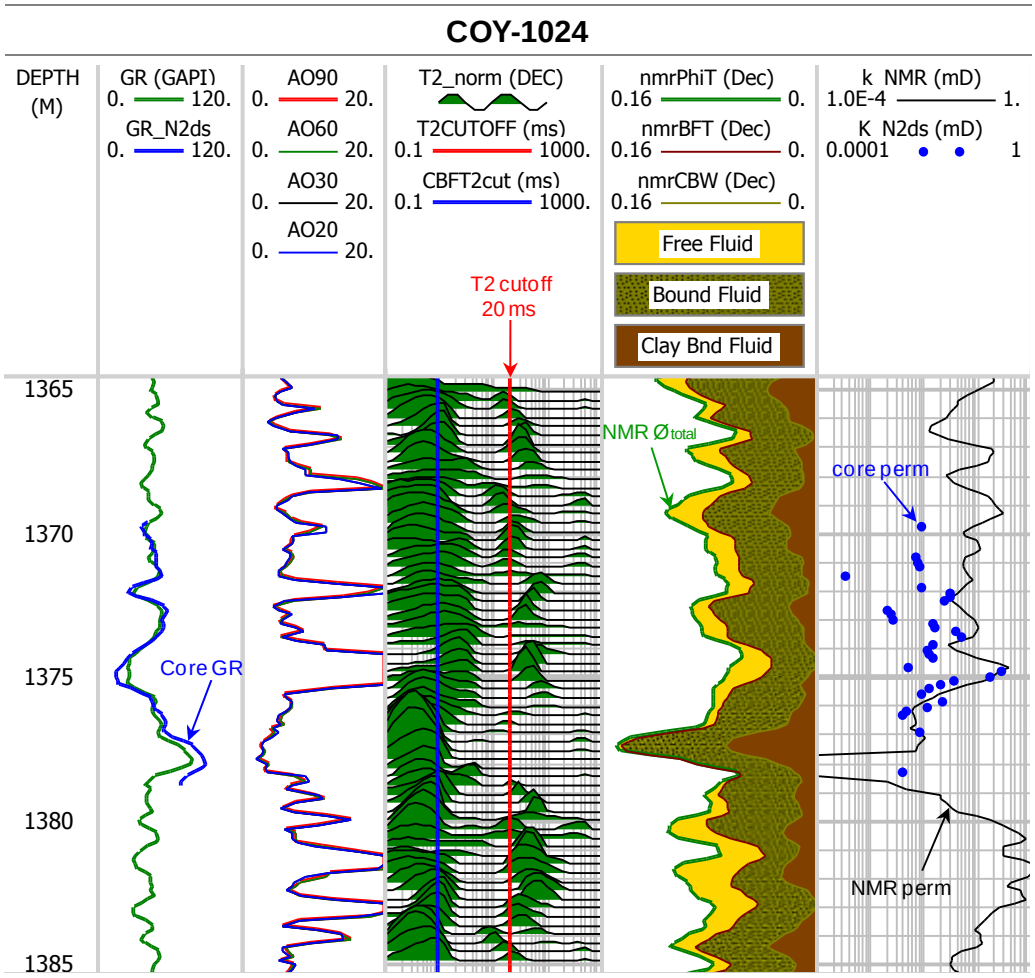

Figure 6.12 Permeability estimation using the calibrated free-fluid model. Observe the acceptable correlation with core data, although the vertical resolution of the NMR log seems to be insufficient to resolve the laminated character of these reservoirs. Note that resistivity logs are able to better resolve thin-beds as compared to NMR (see interval between 1380-1385 m)

Overall, a poor match was achieved in most of the wells analysed; however, the NMR log seems to give a low resolution response that is sometimes unable to resolve thin beds (Fig. 6.12).

Since the free-fluid model is only applicable to wells with NMR log, other attempts to estimate permeability from well-logs were conducted. Diverse models to calculate permeability from well-log data are available in the literature (*e.g.* Balan *et al.*, 1995; Mohaghegh, *et al.*, 1995). The tendency of most of them is to use the following general expression:

$$k = a\frac{\emptyset^b}{Swi^c}$$

where: *Ø* is the porosity (fraction), *Swi* is the irreducible water saturation (fraction), and *a*, *b*, *c* are statistically calibrated parameters. Three permeability models were applied in a number of wells of this study and the results were compared with core permeability. The models have the same appearance of previous equation and the parameters used on each one are displayed in Table 6.2.

Table 6.2 Well-log permeability models

Model	Parameters		
	a	**b**	**c**
Timur	*8581*	*4.4*	*2.0*
Biggs	*62500*	*6.0*	*2.0*
Schlumberger (Chart K3)	*10000*	*4.5*	*2.0*

The porosity employed in the equations was the combination of neutron/density corrected by clay content (*Ø*). The bound water saturation (Sw_b), which was estimated during the water saturation calculations in previous section, was also used. The results are displayed in Figure 6.13.

Since Timur and Schlumberger equations are practically the same, only the Timur and Biggs models are displayed and compared to core data (Fig. 6.13). In most of the wells analysed, the three models generally overestimate permeability over one order of magnitude and in some cases over two orders. No correlation was observed with core data, even when porosity seems to be well calibrated.

Finally, the porosity-based correlation was used to estimate permeability in well-log data. The correlation obtained was:

$$k = 0.0001e^{0.8958\emptyset}$$

where: Ø is the porosity (%) and *e* is the Euler's number (2.718). The equation was used in wells with core data and an example of this comparison is shown in Figure 6.14. Observe that in contrast with other models, this simple correlation seems to be more predictive.

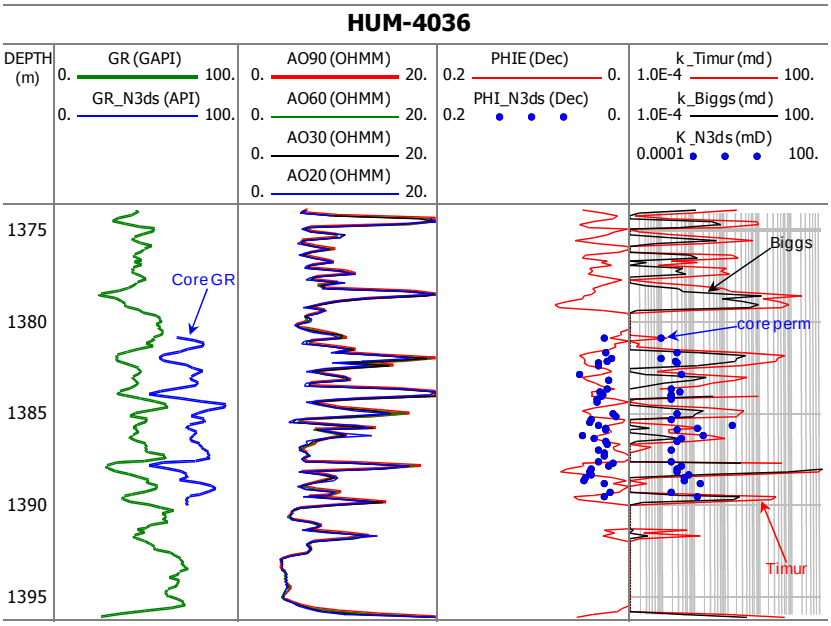

Figure 6.13 Comparison of permeability estimation using Timur and Biggs models. Observe the excess of permeability compared to core data even when porosity seems to be well calibrated

Although is recognised that the porosity-based correlation is prone to error due to the relatively wide variations in permeability, it generally shows a good agreement with core data in most cases. This model predicts permeability consistently when porosity is well calibrated with cores. The porosity-based correlation was used to estimate permeability in the entire wells of this study.

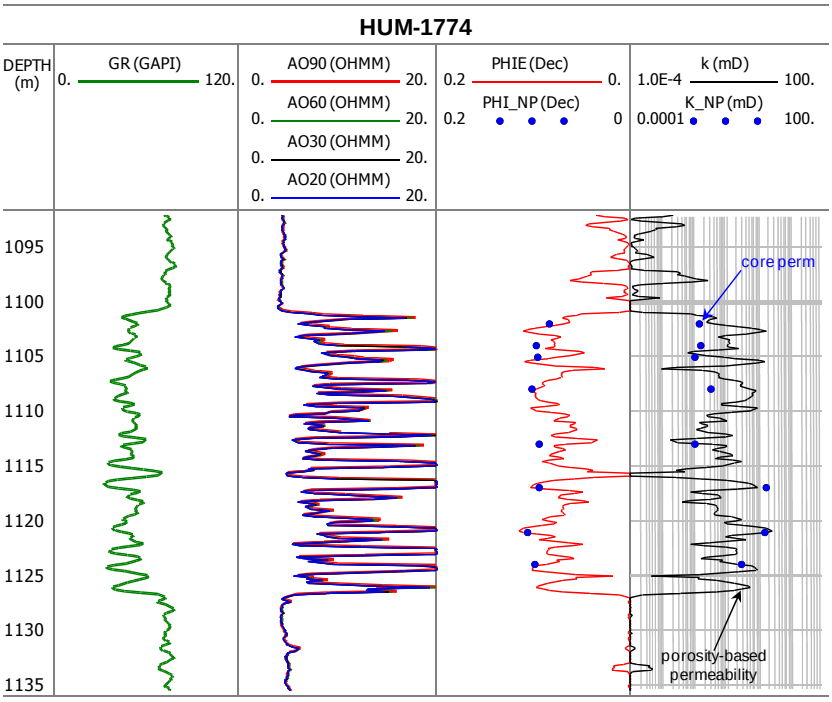

Figure 6.14 Permeability estimation using the porosity-based correlation. Observe the acceptable match with core data, which in this case are sidewall cores

6.2.5 Net-Pay Estimation

Net-pay thickness (*i.e.* equivalent oil-impregnated interval that represents the economic rock volume) was estimated employing *Vcl*, *Ø* and *Sw* cut-offs. The values selected for this approach provide a reasonable estimation of the sand (*NetSand*), the porous-sand (*NetReservoir*) and the porous-impregnated-sand (*NetPay*) intervals observed in both conventional core and outcrop data (PEMEX, 2009). Oil-stained intervals observed in conventional core data of the study area vary from 0 to 60% of the total length of the core, although this diverges widely depending upon the sedimentary and petrophysical characteristics of the sand units. Table 6.3 shows the criteria for thickness calculation:

Table 6.3 Cut-off criteria for thickness estimation

Thickness	Petrophysical variables		
	VCL<	*Ø>*	*SW<*
Gross	-	-	-
NetSand	*50%*	-	-
NetReservoir	*50%*	*6%*	-
NetPay	*50%*	*6%*	*70%*

Figure 6.15 exemplifies the methodology of calculation. The cut-offs are applied to each input curve and thickness reports are estimated. The results are reported as total rock thickness.

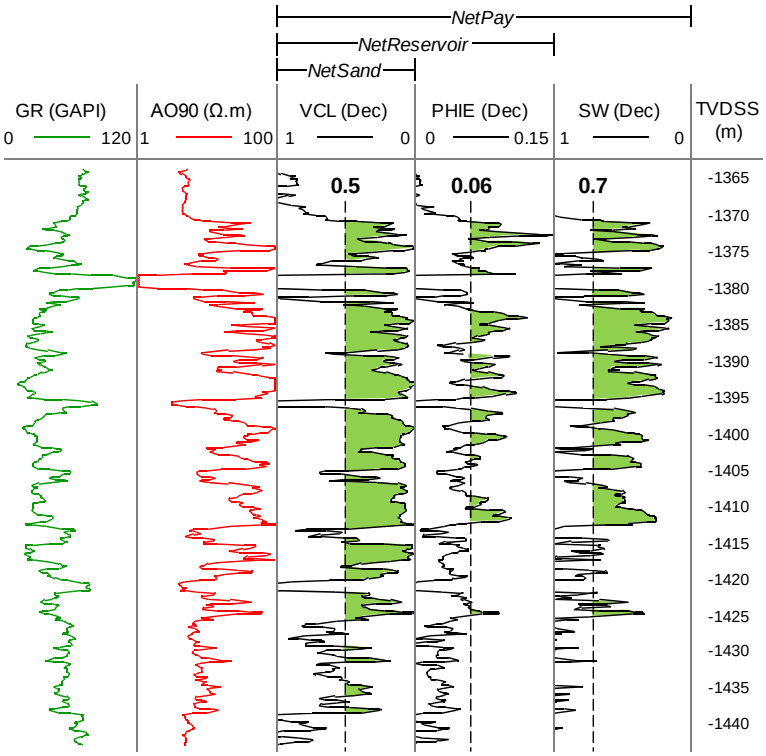

Figure 6.15 Example of NetPay estimation. Thickness reports account for the borehole deviations

The analysis was applied to the S4 reservoir, which is intersected by 263 wells in the study area. Most of these wells are drilled vertically in this section, thus minimum corrections by borehole deviation were applied. Figure 6.16 displays the average thickness results from this approach. The data is expressed as frequency histograms. Observe, for example, that average *NetSand* thickness of most wells intersecting the S4 reservoir is of 35 metres.

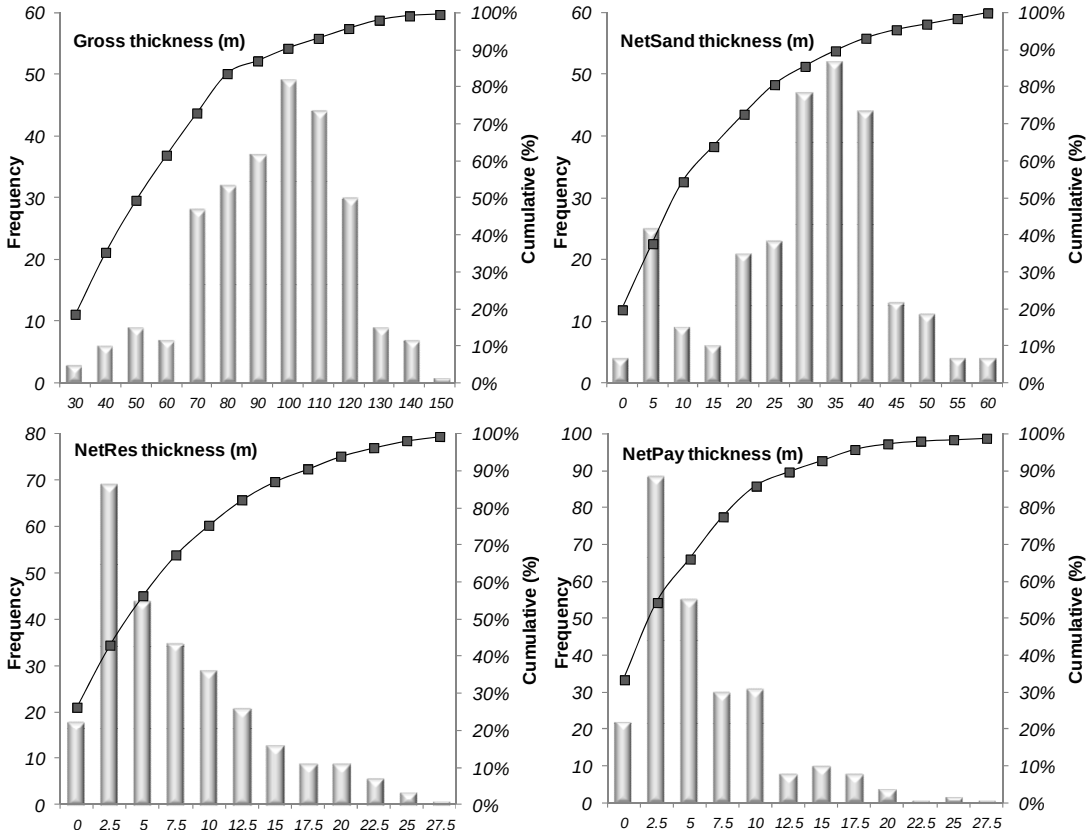

Figure 6.16 Frequency histograms of the different thickness reports estimated. These correspond to 263 wells at S4 level

The large reserve volumes in Chicontepec reservoirs have been recently questioned, in part, as result of the inherent problems related to the volumetric method for reserves estimation (CNH, 2010). *NetPay* thickness is probably one of the properties with major uncertainties because the non-uniqueness solution of their input variables (*Vcl*, *Ø*, *Sw*) and selected cut-offs. A simple cut-off sensitivity analysis was performed in 263 wells at S4 reservoir. This was conducted through a multi-well cut-off sensitivity option available at *Interactive Petrophysics*®. The software estimates the *NetPay* by varying the cut-off parameters (*i.e. Vcl, Ø, Sw*). The procedure is calculated in each well and the results are averaged and displayed as the variation of *NetPay* versus the cut-off parameter (Fig. 6.17).

Porosity cut-off proved to be the most sensitive as minor variations generally results in significant *NetPay* estimations. For example, changing the porosity cut-off from 6 to 7% may

result in up to 60% change of reserves. As Figure 6.17 suggests, the cut-offs selected for *NetPay* estimation in the studied reservoir are rather conservative.

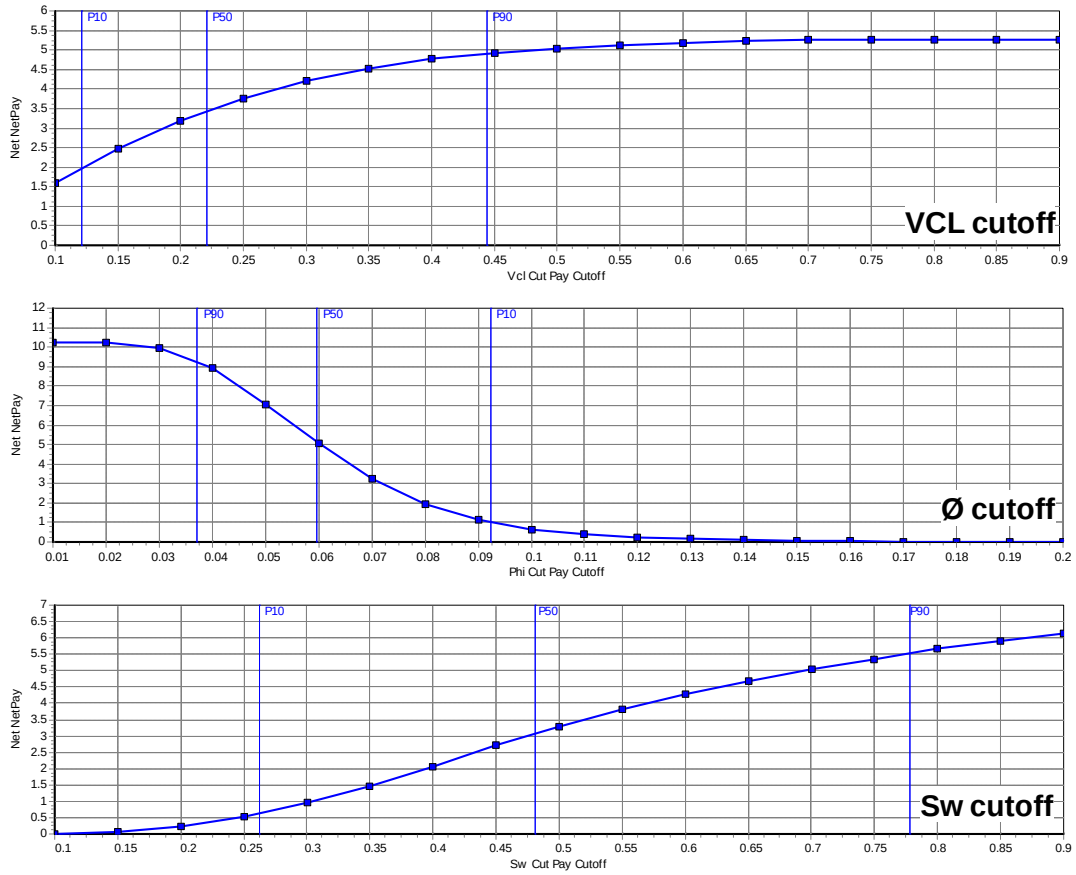

Figure 6.17 Average NetPay estimation of 263 wells at S4 level as cut-off varies

6.2.6 Brittleness

The petrophysical understanding of the reservoirs in this study also integrated their mechanical behaviour. Hydraulic fracturing design is a determinant for developing Chicontepec reservoirs and fracture creation and propagation are governed by both mechanical rock properties and the state of stresses (Hubbert and Willis, 1957). Detecting the most "frackable" zones to stimulate is fundamental not only for enhancing hydro-fracturing performance but also for optimizing costs. Elastic Modulus (*i.e.* Poisson's Ratio, Young's Modulus) reflect the rock's behaviour when stressed, providing important data for hydrofrac creation and propagation. These were estimated based on dipole sonic logs available in eighteen wells in the study area, which were qualitatively calibrated employing mechanical rock properties of seven rock plugs from HUM-4036 and HUM-4198 wells.

A basic petrophysical relationship between compressional slowness (*DTC*), deep resistivity (*AO90*), neutron porosity (*NPHI*) and bulk density (*RHOB*) was employed for creating a regional model to predict the shear slowness (*DTS*) in those wells with no dipole sonic logs available. This was done to produce a local geomechanical model for the study area. Shear slowness was available in eighteen wells in the study area. Correlations of DTS with other curves in these wells are shown in Figure 6.18.

Multiple regression analysis by least squares routine performed in the eighteen wells resulted into the following correlation:

DTS= -30.51+2.62*DTC+5.28*Log(AO90)+78.68*NPHI-16.24*RHOB.....R^2= 0.95

The model was validated by comparing measured and calculated DTS curves in those wells with dipole sonic logs, finding an acceptable correlation (Fig. 6.19). Shear sonic log was then estimated in the rest of the wells employing this correlation.

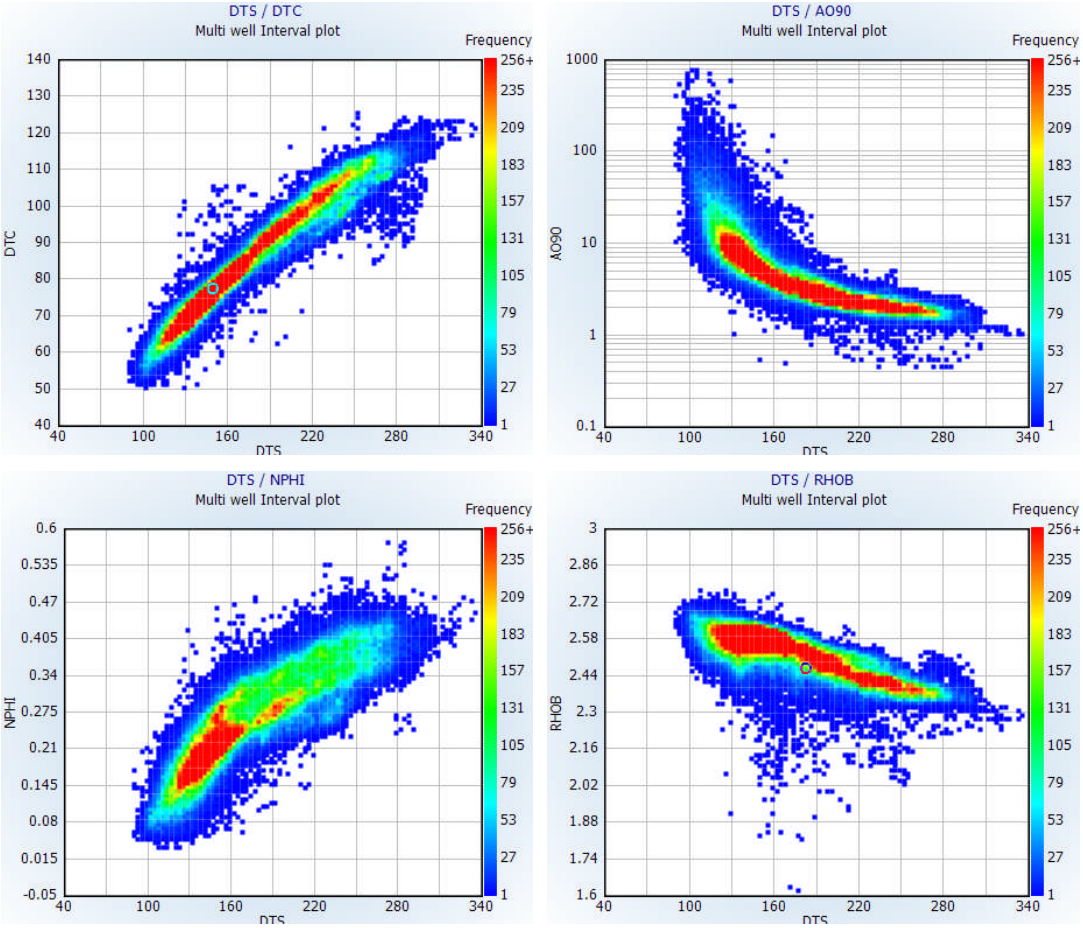

Figure 6.18 DTS relationship with DTC, AO90, NPHI and RHOB logs. The average trend of the eighteen wells is displayed

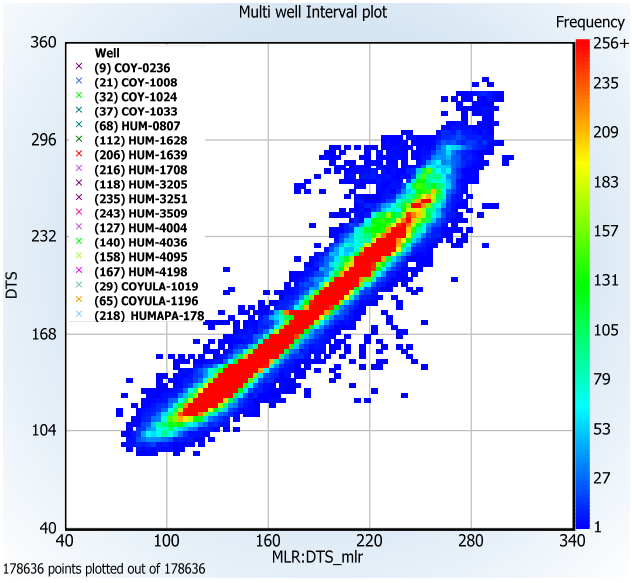

Figure 6.19 Comparison of measured (DTS) and calculated (DTS_mlr) shear slowness in the eighteen wells employed

A brittleness index (*i.e.* the rock's susceptibility to break and propagate when is subjected to stress) was built in the study area employing the measured and synthetic dipole sonic logs from 263 wells intersecting the S4 reservoir. This was done following the process described by Grieser and Bray (2007), Rickman *et al.* (2008) and Mullen *et al.* (2007) for shale-gas reservoirs and adapted to this study with minor modifications.

Poisson's ratio (*PR*) was estimated by:

$$PR = \frac{2 - (DTS^2/DTC^2)}{2 \cdot [1 - (DTS^2/DTC^2)]}$$

Young's Modulus (*YM*):

$$YM = \left[\frac{\rho/_{DTS^2} \cdot (3 \cdot DTS^2 - 4 \cdot DTC^2)}{(DTS^2 - DTC^2)}\right] \cdot 13483.74$$

where: *DTS* is the shear slowness (μsec/ft), *DTC* is the compressional slowness (μsec/ft), ρ is the bulk density (g/cm^3), *PR* is the Poisson's ratio (dimensionless), and *YM* is the Young's modulus ($\times 10^6$ psi).

Young's Modulus Brittleness index (YM_{BRIT}) was defined as:

$$YM_{BRIT} = \left(\frac{YM - YM_{min}}{YM_{max} - YM_{min}}\right) \cdot 100$$

Poisson's Ratio Brittleness index (PR_{BRIT}):

$$PR_{BRIT} = \left(\frac{PR - PR_{max}}{PR_{min} - PR_{max}}\right) \cdot 100$$

The average brittleness index ($BRIT_{av}$) was then estimated by:

$$BRIT_{av} = \frac{YM_{BRIT} - PR_{BRIT}}{2}$$

where: YM_{min}= 0.5×10^6psi, YM_{max}= 13×10^6psi, PR_{min}= 0.13, PR_{max}= 0.4. Boundary limits to distinguish ductile/brittle areas were arbitrarily selected from Figure 6.20, following those areas where the data points were more frequent.

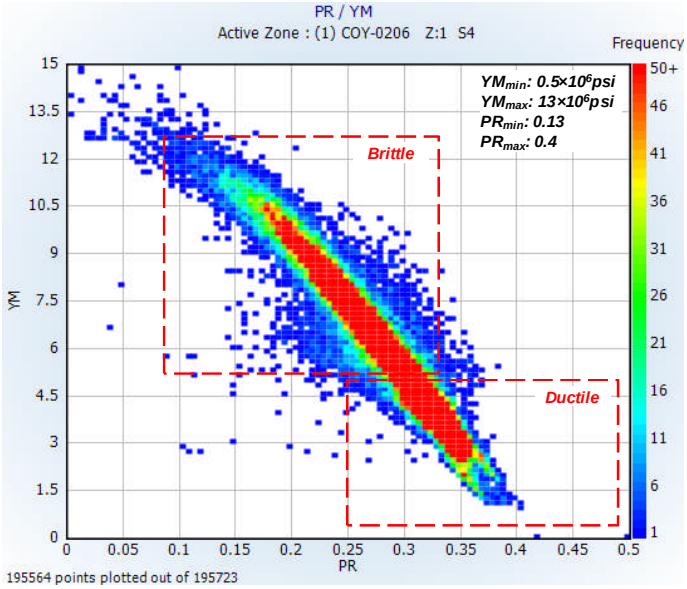

Figure 6.20 Poisson's Ratio and Young's Modulus crossplot of 263 wells intersecting S4 reservoir. Approximated areas of ductile and brittle rock's behaviour are shown

The calculated brittleness index (expressed as the % of rock likely to break and propagate) was compared to cumulative oil production data in wells producing at S4 reservoir. In some wells, greater oil recoveries were observed as the brittleness index increases within the perforated interval. Additionally, the occurrence and distribution of more "brittle zones" in conjunction with the location of the perforated interval, seems to influence production performance. Fluid flow efficiency and recovery may not only be associated to depositional and diagenetic characteristics in these reservoirs, but also to the reservoir's mechanical properties (Figs. 6.21 and 6.22). Similar results have been obtained in equivalent reservoirs (*e.g.* Zongqiang *et al.*, 2012).

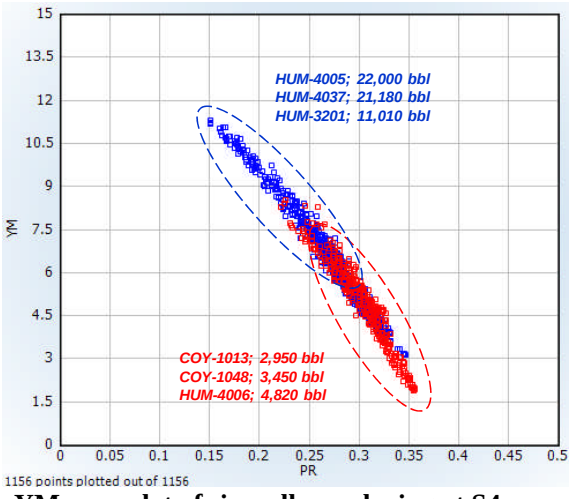

Figure 6.21 PRvsYM crossplot of six wells producing at S4 reservoir. The values correspond to the perforated interval. 180-day cumulative oil production is shown on each well for comparative purposes. Greater productions tend to be associated to more brittle intervals

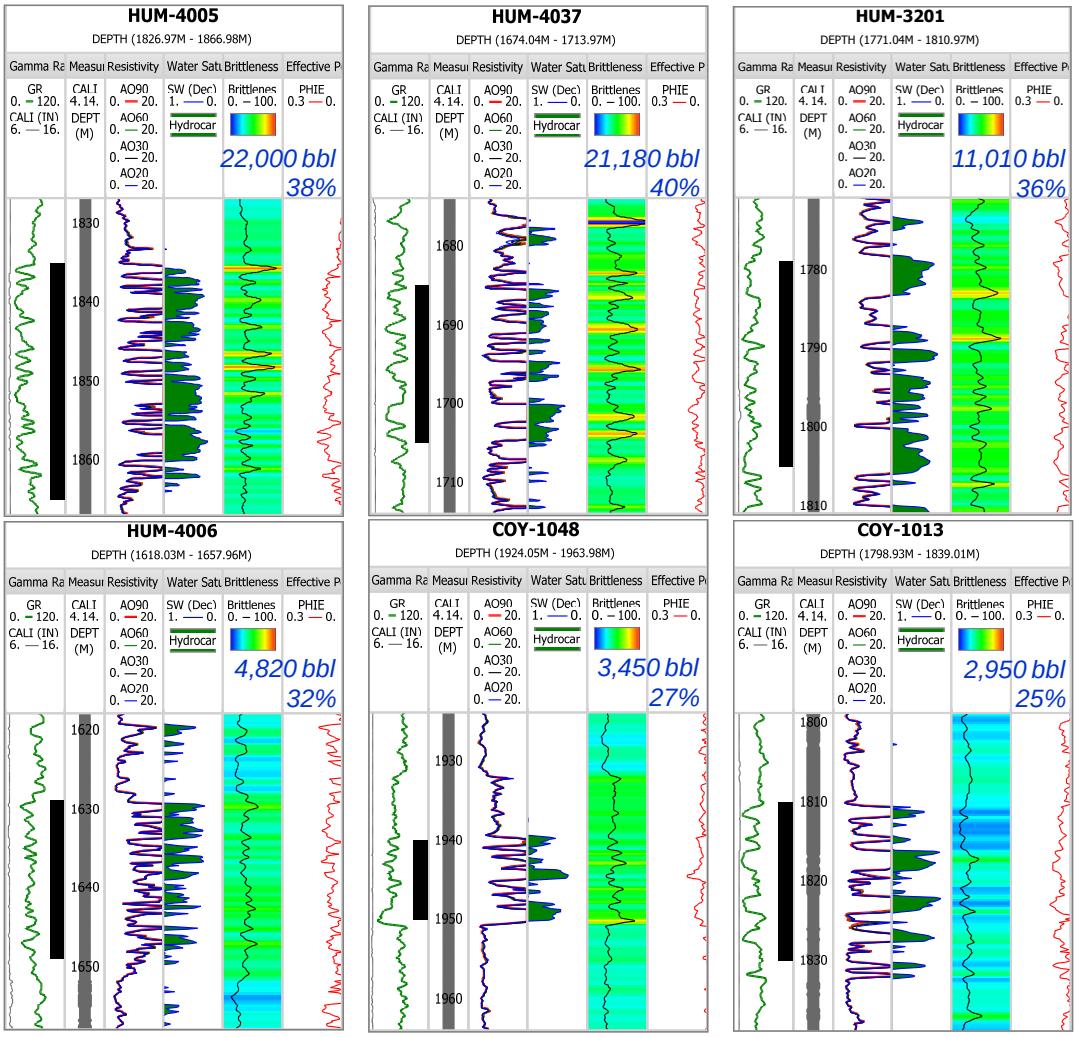

Figure 6.22 The six wells shown in previous figure. Note that the location of the perforated intervals (black bar) together with the cumulative oil volume and the average brittleness index shown in the header of each well. Observe the apparent correspondence of brittleness, location of the perforated interval and reservoir performance

6.3 DISCUSSION

Well-logs do not measure petrophysical properties *per se*, but indirectly records a number of physical phenomena that are transformed to estimate petrophysical properties. In this way, the naturally occurring formation's radiation is interpreted as clay-content indicator, in the same means that attenuation of fast neutron signals are traduced in formation's porosity. Deviations in petrophysical estimations may occur if well-logs are not calibrated with core data. An example of this is shown in Figure 6.23 where a number of wells in the study area show an anomalous response in their gamma-ray logs. The estimation of clay content using conventional cut-offs as explained in this chapter results into high clay computations. However, a close examination of the neutron/density logs reveals porosity values greater than 20%. Although it is not clear the source of this irregular behaviour, the formation seems to actually contain very low clay, mainly due to their neutron/density behaviour. Unfortunately, none of these intervals were completed and no core data was available to analyse their mineral content (*e.g.* glauconite, mica, potassium-rich feldspar). The examples illustrate the necessity to calibrate well-logs with core data, and the uncertainty associated of existing methods.

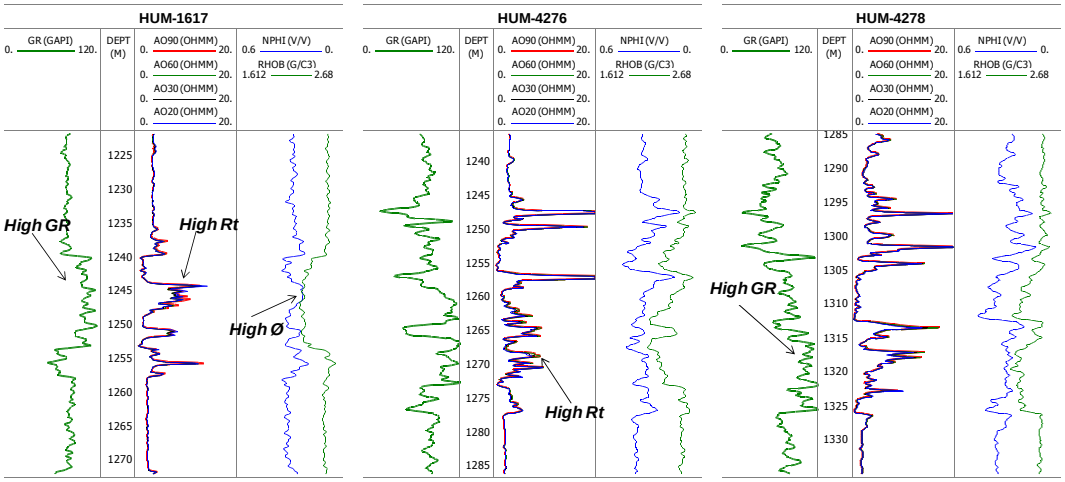

Figure 6.23 Anomalous high Gamma-ray readings in three wells of the study area. It is not clear the origin of this phenomenon which is associated to very attractive porosities. The response has only been seen in the northeast portion of the study area. Similar behaviour has been reported in different portions of the Chicontepec basin and ascribed to igneous rock intrusions that partially metamorphized the surrounding rock

Similarly, well-logs provide a continuous record of a particular formation's feature which is normally used in multiple interpretation processes (*e.g.* reserves estimation, numerical modelling). Well-logs reflect the average response of a narrow rock volume around the borehole, which is generally affected by subsurface conditions (*e.g.* temperature, pressure, mud weight). Despite that corrections are normally applied to well-logs and a number of precautions

are taken, this information should be treated with care due to their inherent area of investigation, resolution and sensitivity to borehole conditions.

When possible, the interpreted petrophysical properties were calibrated using core data and in this way it was intended to reduce the uncertainty in their estimation. As the core data sampling is significantly minor than well-logs, the results were compared by means of frequency histograms to verify ranges and tendencies. Overall, the results obtained showed an acceptable match.

Well-log analysis was mainly conducted to estimate porosity, permeability and water saturation, which in turn were used for volumetric assessment (*i.e.* hydrocarbon pore volume estimations), *NetPay* sensitivity analysis and for conducting reservoir modelling and simulation case studies which are discussed in further chapters. Overall, the interpreted petrophysical properties from well-logs show an acceptable agreement with the properties observed in core analyses. Porosity and water saturation are probably the properties with the largest uncertainty, mainly due to their dependence to other parameters. Porosity is function of the clay indicator model (*i.e.* gamma-ray or density/neutron), the selected cut-offs, the porosity curve indicator, etc. Similarly, water saturation depends on the formation's water resistivity (*Rw*), the temperature, the Archie-based parameters (*m*, *n*), etc. Minor variations in these parameters usually reflect significant variations in property estimation. Porosity ranges observed from core data varies from 1 to 16%, which is approximately the same range estimated in wireline data. Water saturation observed the widest variation as the property practically varied from 0 to 1 with no apparent preferred value.

As water saturation estimated by well-logs depends on a number of variables, its estimation is not unique (*i.e.* water saturation is the parameter with the greatest uncertainty). An error analysis was applied to a number of wells in the study area using a Monte Carlo simulation procedure in the *Interactive Petrophysics*® software. This was conducted to evaluate the sensitivity of these variables to the water saturation solution. The results are shown as error bars (tornado plot), displayed from the greatest to the lowest sensitive parameter (Fig. 6.24). From the variables used for *Sw* estimation, the Archie's cementation factor (*m*) has the greatest impact. Water saturation ranges between 47 to 85% by just varying cementation factor from 1.65 to 2.05, respectively. To try to reduce the uncertainty associated to its calculation, it is highly recommended to incorporate additional core studies. For example, it is uncertain the grade of electrical contribution of clays in these formations. The integration of cation exchange capacity (CEC) or Co/Cw experiments would provide with a better scope of water saturation. No data of this kind was available to consult and is uncertain the electrical behaviour of clays. Similarly, as oil-based muds are used for drilling Chicontepec wells, the Dean Stark method would be used to improve the accuracy of water saturation distributions. The technique does not

require additional effort greater than just making some instrumentation arrangements in the cleaning procedure of cores.

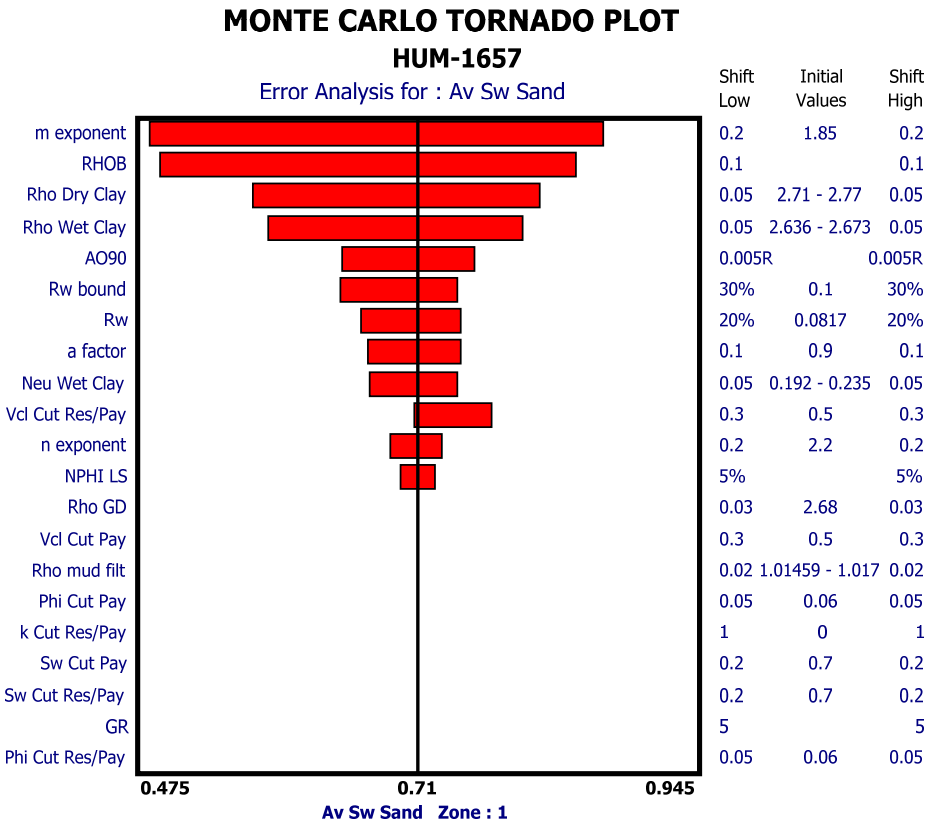

Figure 6.24 Error analysis plot of the water saturation estimation in HUM-1657 well. Observe that cementation exponent (*m*) and density/neutron based parameters are the variables exerting the greatest influence to water saturation computation

In terms of permeability estimation, the porosity-based model showed a better reproducibility in comparison to other models. Their use in well-logs is practical and does not require any other variable than just porosity for their computation, which can be easily obtained. The model was calculated from gas measurements which generally compute greater values than liquid perms. In this way the model should be properly referred as a permeability index, since no fluid-saturation variations (*e.g.* gas or water) were accounted for. Consequently, the model estimates permeability in front of any interval with porosity readings, regardless their pore connectivity and fluid type.

The average saturation exponent (*n*) obtained from core data and used for well-log analysis was 2.2. This value seems to honour the overall electrical behaviour of Chicontepec rock samples, which appears to follow a non-Archie rock trend. The wetting characteristics of the rock also exert an effect on the saturation exponent, as this partially controls the distribution of fluids (water or oil) in the pore space.

For strongly water-wet core samples, Donaldson and Siddiqui (1987) obtained saturation exponents around 2, whereas for strongly oil-wet samples they reported values above 8. This is generally ascribed as variations in fluid distributions resulted from different wetting scenarios. At reducing water saturations, water remains as continuous phase through the sample for water-wet states and no significant electrical conductivity variations are obtained. For strongly oil-wetted samples at reducing water saturations by the contrary, water behaves discontinuously and electrical conductivity is significantly reduced which results into greater *Rt/Ro* ratios (*i.e.* greater *n* values) compared to strongly water-wet states.

For mixed-wet conditions, the overall electrical behaviour of the sample appears to be governed by the relative contribution of the large oil-wetted pores (insulator) and the small water-wetted pores (conductive). In this way, defining a characteristic *n* value for these reservoirs implies to discriminate large and small pores, which seems to be challenging. In the case of the reservoirs in this study, which are believed to describe a mixed-wet behaviour (this is discussed in chapter seven), the selected saturation exponent appears to describe its overall electrical behaviour that seems to be a complex combination of electrically well-connected microcracks, isolated macropores, and relative contribution of large/small pores. A saturation exponent of 2.2 was selected since it seems to properly average the conductive/insulator pathways of the samples analysed. Abdassah *et al.* (1996) proposed an *n* value varying from 2.1 to 2.53 for mixed-wet reservoirs.

6.4 CONCLUSIONS

The aim of this chapter was to evaluate the petrophysical properties of the reservoirs in this study. Their petrophysical characteristics were estimated using well-logs. When it was possible, the interpreted petrophysical properties were calibrated using core data and in this way it was intended to reduce the uncertainty in predicting petrophysical properties. Overall, an acceptable match between the estimated petrophysical properties with core data was observed.

Combining the measured rock properties reported in previous chapter with the petrophysical estimations using well-logs, the results show that the reservoirs of this study have rock qualities comparable to tight-gas or tight-oil reservoirs. While porosity ranges from 13 to 28% in most conventional reservoirs at similar burial conditions (Ehrenberg and Nadeau, 2005), a range from 1 to 15% is observed in the reservoirs of this study. Permeability ranges are also low, typically displaying values below 10 mD.

The low storage capacity and the limited fluid-flow efficiency of these reservoirs, have an effect on the hydrocarbon recovery, which is analysed in further chapters of this work. From the estimated petrophysical properties, water saturation seems to be the most uncertain due to its dependence to a number of parameters. Overall, the petrophysical properties of these reservoirs are observed to behave erratically, which can also increase their grade of complexity. The interpreted well-log information is employed as input parameter for modelling the S4 reservoir and for conducting a number of simulation scenarios. This is reported in the following chapters.

CHAPTER VII. FORMATION DAMAGE EXPERIMENTS AND WETTABILITY

This chapter presents the results of a number of experiments conducted to evaluate rock-fluid interactions and formation damage in the reservoirs of this study. The aim of conducting these experiments was to improve the current stimulation practices in the reservoirs of this study, to assess secondary/tertiary applications to oil recovery planned to be implemented in the basin, and to enhance the overall understanding of these reservoirs. The rock samples used in the fluid-displacement experiments shown in this Chapter have permeabilities greater than 1 mD. The sample selection criteria had two objectives: 1) to observe the permeability impairment in samples where the effects of formation damage may significantly impact on production, and 2) to favour short time periods during fluid-displacement experiments.

Three experiments were performed to evaluate formation damage by: 1) clay-swelling, 2) particle plugging, and 3) polymer adsorption. The wetting characteristics of the reservoirs in this study were then evaluated by different approaches. First, the crude-oil affinity to surface flat minerals was assessed by a series of adhesion tests in a way to replicate the wetting preference of calcite and quartz minerals using a crude-oil sample directly obtained from a producing interval in the study area. The wetting analysis was extended by applying three methods. These were conducted using restored-state plugs to mimic oil/brine/rock interactions. The impact of wettability on fluid-flow efficiency was evaluated by continuous end-point relative permeability measurements in which the low fluid-flow efficiency and large residual oil saturations in these reservoirs were analysed.

A number of surface active materials were then employed to try to increase oil recovery in Chicontepec samples as a way to evaluate chemical EOR. This was conducted by spontaneous imbibition tests and using commercial surfactant solutions. Finally, the onset of asphaltene precipitation from a crude-oil sample was assessed by NMR T2 observations. A solvent-to-oil ratio was determined to prevent asphaltene precipitation in a crude-oil sample obtained from a producing interval in the study area.

7.1 Introduction

A poor performance in oil production has been observed in a number of wells in the study area, an anomalous trend compared to most production profiles. This behaviour is illustrated in Figure 7.1, in which a pronounced decline in the oil rate and a sudden drop of the flowing pressure after fracturing is observed.

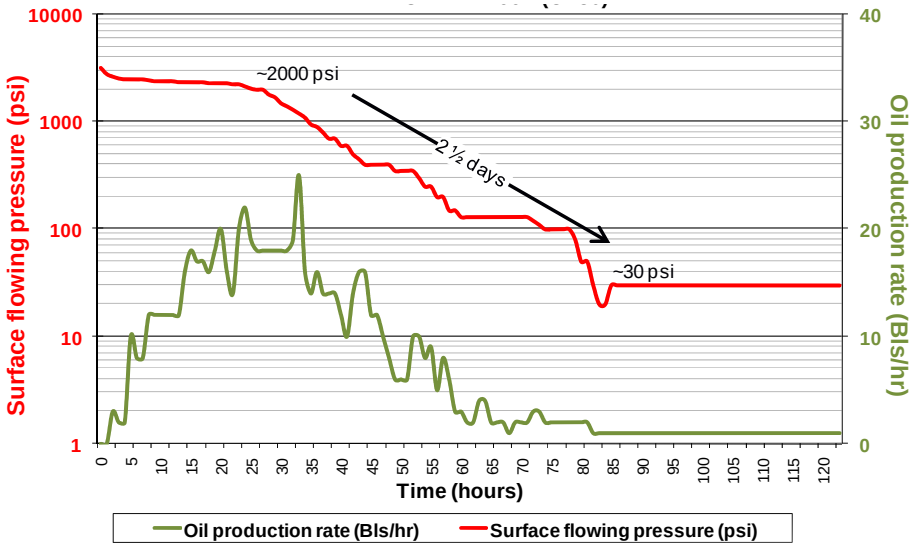

Figure 7.1 Abrupt oil production performance after fracturing in a reservoir of the study area. Observe the sudden drop of pressure and consequent reduction in the oil rate

It is unclear whether this performance indicates an incompatible interaction of stimulation fluids and formation (*i.e.* formation damage) or it is simply the nature of these reservoirs. To clarify this, a number of experiments were conducted to evaluate formation damage in the reservoirs of this study. These were designed not only using similar fluid mixtures normally used in the study area, but also applying a number of mixtures at different concentrations to try to identify the least-damaging combination.

Normally, the fluids used for stimulation in the reservoirs of this study have a low-ionic concentration (*i.e.* lower than 2% of total dissolved salts). Since the reservoirs of this study have expandable and/or migratory clay minerals (*i.e.* illite/smectite and kaolinite), it is then expected that a negative reaction may occur. However, no experimental data exist to assess whether formation damage may be the cause of poor reservoir performance.

Similarly, the wettability state of Chicontepec reservoirs has not been clearly established; it is often referred to as fractional (Gachuz-Muro, 2009) or oil-wet (Rivera, 2003; Estrada *et al.*, 2010), but no experimental data has been provided to support these claims. Determining the wetting characteristics of the reservoirs in this study is important, especially for evaluating the implementation of secondary/tertiary processes to oil recovery. In this way, the experiments

conducted during this research project were mainly aimed to evaluate formation damage and rock/fluid interactions. The results of these and a number of additional experiments are discussed in this chapter.

7.2 Critical Salt Concentration (CSC)

Most stimulation fluids that have been used in the study area consist of water-based mixtures. These generally have variable low-ionic concentrations as recorded in a number of field reports. The reservoir rock at Chicontepec is normally composed by 6% illite/smectite mixed-clay (Granados-Hernandez and Fisher, 2014), prone to formation damage by volumetric expansion. The aim of the CSC test is to identify the brine concentration at which a reduction of permeability occurs.

Khilar and Fogler (1984) noticed a drastic permeability reduction in Berea core samples while the ionic strength of the fluid was progressively reduced. They determined a critical value of the salt content below which a permeability reduction occurred. Permeability reduction caused by 'water shock' process is normally ascribed to the hydratation of the mixed-clay groups. The negative charge of smectite platelets is balanced by means of the positive charge of K^+, Na^+, Ca^{2+} and Mg^{2+}. When exposed to low-ionic strength aqueous solutions (*i.e.* low-salinity or fresh fluids), the interlayer cations adsorb water molecules resulting in swelling. Hydratated smectites can expand as much as 1000% of their volume (Davies, 1980). Hydratation of clays can also trigger secondary effects of permeability reduction such as particle mobilisation and pore plugging. The CSC experiment (Mungan, 1965; Khilar and Fogler, 1984) was conducted to evaluate the effects of the low-ionic concentration on permeability.

7.2.1 Materials

Three core samples obtained from producing sand units in the study area were employed. These have similar mineral and petrophysical characteristics as shown in Tables 7.1 and 7.2. The samples were selected to try to have a comprehensive representation of the observed permeability. Ambient gas porosity and *in situ* stress Klinkenberg-corrected permeability were obtained. The cores were saturated with synthetic brines employing sodium, potassium and calcium-chloride ions at 3.5% concentration (see Table 7.1). The samples remained immersed in their brine for a week to achieve ionic equilibrium. Figure 7.2 shows a microscopic detail of one of these rock samples. Observe the apparent lack of authigenic calcite in the sample, which is generally the case for most of high permeability rocks (*i.e.*>1mD) in the study area.

Table 7.1 CSC core samples

Sample	*Gas Porosity (%)*	*Klinkenberg Permeability (mD)*	*k brine @ 3.5% (mD)*	*Saturating Brine*
N1H34a	*13.32*	*3.08*	*0.69*	*NaCl*
N1H8	*13.27*	*50.73*	*22.32*	*$CaCl_2$*
N1H21	*12.53*	*22.60*	*7.67*	*KCl*

Table 7.2 XRD Mineral Composition (%Bulk volume)								
Sample	Bulk Fraction					Clay Fraction		
	Calcite	Quartz	Clay	Feldspar	Dolomite	Illite & smectite	Kaolinite	Chlorite
N1H34a	*34.7*	*41.8*	*11*	*10*	*2.1*	*7.5*	*1.9*	*1.6*
N1H8	*35.6*	*46.1*	*9.9*	*5.5*	*1.1*	*6.7*	*1.8*	*1.4*
N1H21	*39.5*	*42.3*	*8.6*	*7.2*	*2.1*	*5.4*	*2.2*	*1*

**Figures may not add-up due to minerals of less than 1% bulk volume are not shown*

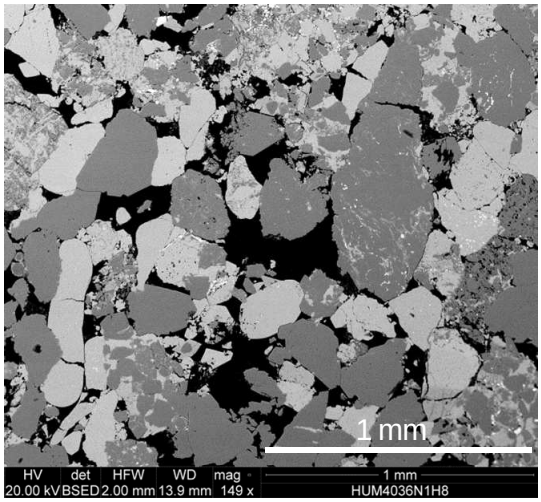

Figure 7.2 BSEM section of N1H8 sample. Similar characteristics are found in N1H34a and N1H21 samples. Observe that the rock is mainly composed by quartz grains and limestone rock fragments

To investigate in more detail, an extra core sample was used to conduct an extended CSC test. This test included continuous pH monitoring during displacing brine at different concentrations, and chemical analyses of the effluent fluids.

A new core sample was prepared in similar way as described above and saturated with 3.5% NaCl brine. Mineral composition and petrophysical characteristics of the studied sample are shown in Tables 7.3 and 7.4.

Table 7.3 Extended CSC core sample				
Sample	***Gas Porosity (%)***	***Klinkenberg Permeability (mD)***	***k brine @ 3.5% (mD)***	***Saturating Brine***
M4F22a	*13.6*	*24.1*	*10.6*	*NaCl*

Table 7.4 XRD Mineral Composition (%Bulk volume)								
Sample	Bulk Fraction					Clay Fraction		
	Calcite	Quartz	Clay	Feldspar	Dolomite	Illite & smectite	Kaolinite	Chlorite
M4F22a	*49.5*	*29.2*	*15.4*	*3.8*	*1.1*	*12.5*	*1.8*	*1.1*

**Figures may not add-up due to minerals of less than 1% bulk volume are not shown*

Figure 7.3 shows the microscopic image of the sample used in this extended CSC test. Observe that, although differ in grain-size to some extent, this sample is comparable to the rock samples described in the first set of CSC tests.

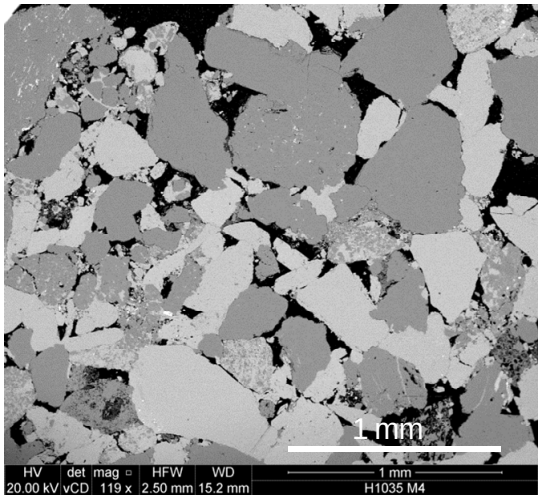

Figure 7.3 BSEM section of M4F22a sample

7.2.2 Methodology

The samples were placed into a Hassler-type core holder within a flexible sleeve to maintain a constant radial confining stress during the test. Single-phase permeability was determined by continuously displacing brine through the sample at constant flow-rates until steady-state conditions were achieved and at least 10 pore volumes (pv) of synthetic brine at 3.5% concentration were displaced through the sample. Pressure disturbance through the core was monitored by a high resolution transducer connected to the upstream end of the core holder. The downstream side was assumed to be at ambient pressure. Initial permeability was obtained at 3.5% fluid concentration in each sample, which is considered the base permeability. The brine concentration was progressively reduced by step decrements of 1.0% (absolute concentration), from 3.5% to 0.5%. Deionised water (DW) was also used to verify the permeability change when no ions were present in the solution. Then the brine concentration was progressively increased until reaching initial conditions. The latter was conducted to verify hysteresis in permeability behaviour.

Permeability changes were determined at each brine change and compared to the initial permeability. The dynamic viscosity of the brine in each concentration was estimated using the correlation of El-Dessouky and Ettouney (2002) and used for calculating permeability. Viscosity varied from 1.049 cP for 3.5% brine concentration to 0.978 cP for DW solution at constant room temperature of 21°C.

The results are plotted as the variation of initial permeability (% of permeability change) *versus* the brine concentration and the pore volumes injected. The aim of the test is to identify the brine concentration at which a reduction of permeability occurs. Figure 7.3 shows the permeability variations (expressed as % of initial permeability) by brine concentration on the first set of core samples.

The pH of the injected and produced solutions was monitored using a manual pH meter during the extended CSC test. The pH device was previously calibrated using acidic and alkaline solutions with known ph to verify consistency in their readings. It was assumed that the injected fluid remained at a pH value of 7.0 ± 0.8 for comparative purposes. Effluent fluids were collected and analysed by inductively coupled plasma by atomic emission spectroscopy (ICP-AES) technique for chemical determination. ICP-AES permits the identification of trace elements in concentrations as low as one part in trillion (1×10^{12} ppt). Five elements were analysed: Al, Ca, Fe, K, and Mg. Both effluent and injected (blank samples) fluids were also analysed with this technique to corroborate results.

Prior analysis with ICP-AES, the collected fluids were diluted with de-ionised water (DW) to produce approximately 20 ml of solution at uniform 1.5% NaCl concentration. This permitted a better quantification of trace elements.

Brine concentration changes in the extended CSC test was of 0.5% increments to provide a better resolution in permeability variations. The outcome of the extended CSC experiment is shown in Figure 7.5. Permeability variation is expressed as % of the base permeability. The trace-element concentrations on each solution change are also displayed.

7.2.3 Results

Permeability reduction was observed in all the samples as the ionic concentration of the brine was reduced. The first three samples (*i.e.* N1H34a, N1H8, N1H21) observed the maximum permeability reduction when deionised water was employed (Fig. 7.4). Permeability recovery in these samples was partially achieved by $CaCl_2$ and KCl brines; however, it was significantly increased by NaCl brine. KCl and $CaCl_2$ brines show less severe damaging effects as less permeability variations and better permeability recoveries were obtained (Fig. 7.4).

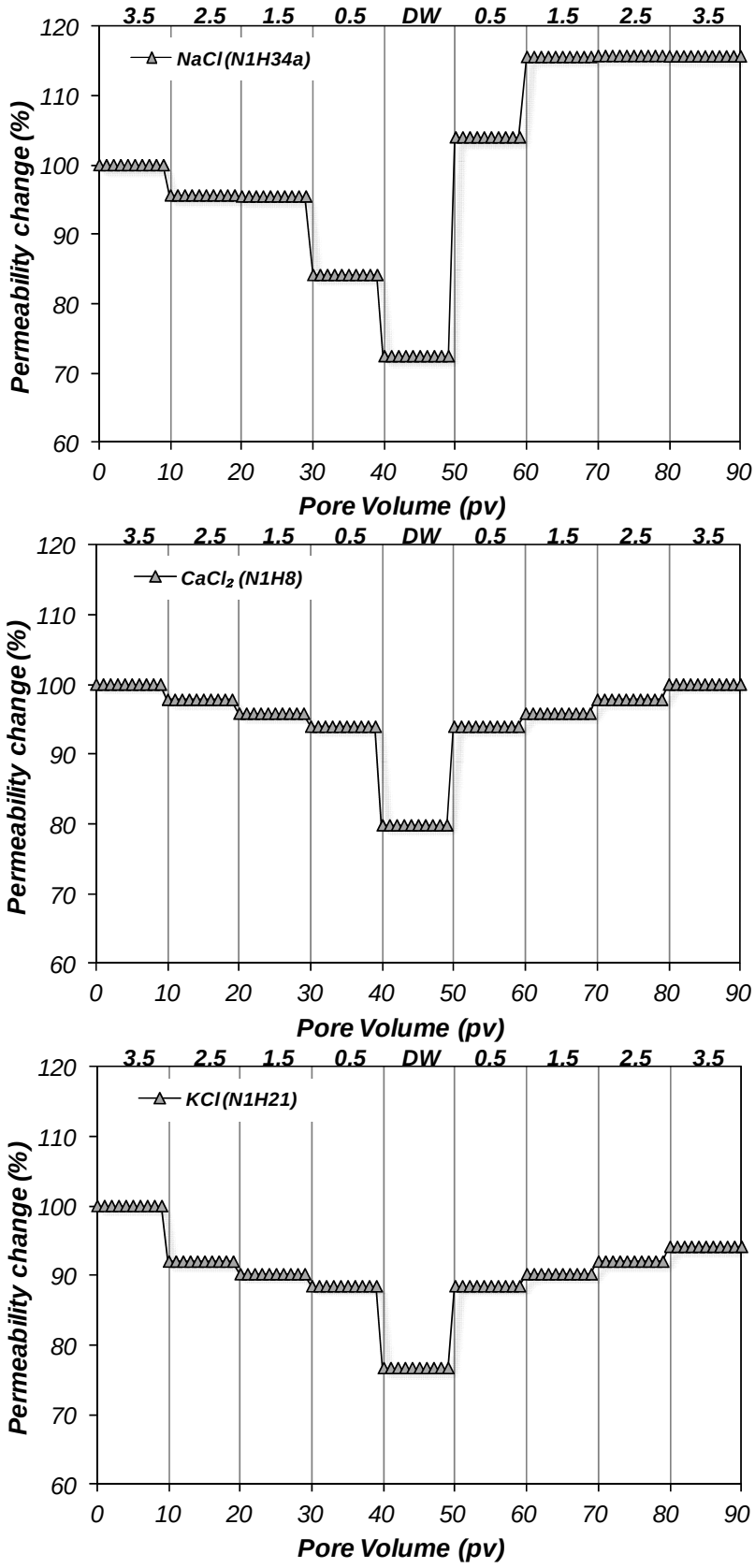

Figure 7.4 CSC tests results. Permeability reduction was observed in all the samples as the ionic strength was reduced

Similar results were observed in the extended CSC test (Fig. 7.5). A reduction of the base permeability was registered as the ionic concentration of the brine was progressively reduced, in the same way as previous tests. An increment in the concentration of trace elements as well as in pH values was also observed. Greater pH readings were obtained at lower brine concentrations. Stepwise increasing concentration of NaCl brine generally re-established the pH values and trace-element concentrations, although the damage seemed to be irreversible. pH and trace-element concentrations in the effluent fluids describe a symmetrical behaviour with the brine concentration used. Permeability reduction after flowing 150 pore volumes of NaCl brine at different concentrations was of 65% (Fig. 7.5).

From the trace-elements identified in the effluent fluids, calcium described the greatest concentration, obtaining a maximum value of 43 mg/l. This was followed by descending concentrations of K, Mg, Al and Fe (Fig. 7.5). No permeability recovery was obtained to its original value after flowing DW through the M4F22a sample, even after increasing brine concentrations and obtaining similar pH readings comparable to those obtained at the start of the experiment.

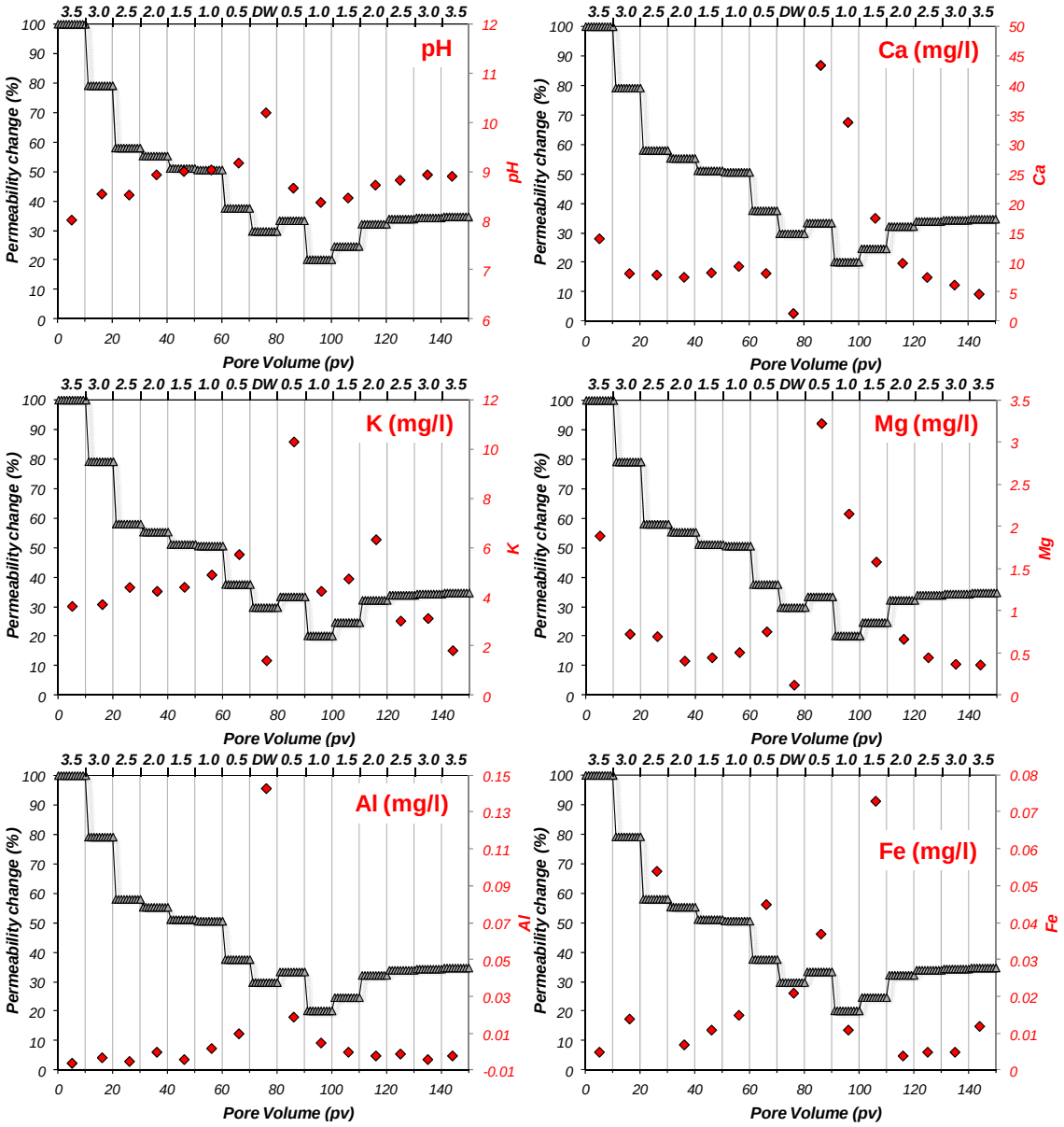

Figure 7.5 Extended CSC tests results (M4F22a sample). Permeability variations and concentration of trace-elements are plotted against equivalent pore volumes injected. Note the relative increment of the effluent pH and analysed elements as the brine concentration is progressively reduced. Initial permeability is not recovered, even after increasing the ionic concentration of the brine

7.2.4 Discussion

What it seems to be clear from CSC tests applied in Chicontepec rock samples is the incompatibility between rock minerals and the displaced fluids, which may be the origin of permeability variations. Two main observations were resulted from the CSC tests. First, permeability is reduced as the ion concentration of the brine is progressively reduced. This does not seem to be reversible. Second, an increment of trace-element concentration identified in the effluent fluids may indicate mineral dissolution processes or perhaps a change in the clay composition.

Permeability reduction was attributed to two possible causes: 1) swelling of the mixed-layer illite-smectite clay; or 2) particle mobilisation and plugging. Since an increase of trace-element concentration was observed and these show more affinity to mixed-layer clays (*e.g.* Ca and K show more affinity to illite/smectite than kaolinite), the volumetric expansion of the clay appears to be more plausible. However, it is not clear what the increase in permeability in the N1H34a sample was resulted from. Possibly, this was due to clay expansion as first process and then particle mobilisation and production thereafter. It has been reported by Reed (1977) that mineral dissolution is able to promote particle liberation.

The pH variations recorded during the experiment may indicate extensive chemical reactions occurring at the pore level. It has been shown that the rate of brine concentration change plays an important role in determining the extent of damage in Berea core samples (Mohan, *et al.*, 1993; Mungan, 1965). They observed that an abrupt change in salinity causes a sharp pH transient in the core, attaining high values of pH up to 10.5. This pH increase gives kaolinite clays to develop sufficiently high potentials to cause them to dislodge from the pore walls. In contrast, if the brine concentration is gradually reduced, the pH transient becomes broad and pH is not increased. Probably, the pH variations in conjunction to trace-element concentrations, suggest that a combination of clay-swelling and particle plugging, together with rapid transitions in brine concentrations may be occurring in the samples analysed.

Hydration of smectitic clay, which is thought to be the main process of permeability reduction in the samples of this study, occurs when the negative surface charge of the clay is not sufficiently balanced by positive K^+, Na^+ and Ca^{2+} cations. As brine concentration is reduced, fewer cations are available for maintaining the clay platelets together allowing water adsorption (*i.e.* clay expansion).

7.3 Critical Velocity Test (CVT)

Apart from being composed of expandable clays, the reservoirs of this study normally contain 3% of pore-filling kaolinite. This clay is generally referred in the literature as migratory and prone to reduce permeability by plugging the pore throats (Mohan and Fogler, 1997). Although it is irregularly distributed in pore space, an experiment for validating the existence of fines mobilisation was conducted. The CVT is performed to detect the interstitial velocity necessary to detach fine particles from pore surface (Amaefule *et al.*, 1987). Generally, the released particles are jammed in narrow pore throats and cause permeability reduction.

The core samples previously prepared and shown in Tables 7.1 and 7.3 were used for conducting the critical velocity tests, as these were exposed to de-ionised water and clays may have been disturbed by the low-ionic concentration of brine.

7.3.1 Methodology

The samples were mounted into a Hassler-type core holder within a flexible sleeve to maintain constant radial stress. Brine was continuously displaced through the sample at step-increasing flow rates until steady-state condition was achieved on each flow rate. Approximately 5 pv of brine were displaced in each flow-rate stage. Pressure disturbance through the core was monitored by a high-precision pressure transducer connected at the inlet end of the core holder. A constant brine concentration of 3.5% was employed during the entire tests and different compositions were employed, according to the saturating brine in each core reported in Tables 7.1 and 7.3. The initial permeability was obtained at a low flow-rate and then gradually increased.

Permeability variation during the change of flow rates was plotted against the interstitial velocity (U), which was determined by:

$$U = \frac{q}{A \cdot \emptyset}$$

where: q is the flow rate (ml/min), A is the plug's sectional area (cm^2), and $\emptyset$ is the porosity (fraction). Flow rate was varied in two directions from 0.1 to 3.5 ml/min in 0.2 ml/min increments. Brine was continuously displaced throughout the sample at constant flow-rates until steady-state condition was achieved and at least 3 pv of solution were pumped. It was assured that the flow rates employed met the Darcy's Law requirements to avoid turbulent regime. A total of approximately 100 pv were displaced on each sample. The results are displayed in Figure 7.6 which corresponds to samples N1H34a, N1H8 and N1H21 samples.

An additional CVT was conducted using the sample M4F22a previously prepared (Table 7.3). The technique was similar as described above and the pH of the effluent fluids was monitored on each flow-rate stage. Flow rate in this experiment was in a single direction and varied from 1 to 5 ml/min in 0.5 ml/min increments. It was assured that the injected fluid remain at a pH value of 7.0 ± 0.8 to verify differences with produced fluids. The results of this second CVT are shown in Figure 7.7.

7.3.2 Results

Figure 7.6 depicts the CVT results conducted in the first three samples. The results are expressed as % of permeability change versus interstitial velocity in ascending/descending flow directions. Note that the flow-rate is also plotted for comparative purposes. Contrary to what was expected, no significant permeability reduction was observed. Conversely, an increase of permeability occurred in the three samples, obtaining an increment of up to 160% of the initial permeability. The resolution of the pressure transducer was sufficient enough to observe these changes.

Sodium, calcium and potassium brines observed an increment of permeability as the injection flow was increased. The largest permeability reading was obtained from $CaCl_2$ brine. At decreasing flow-rates, the NaCl brine observed a significant permeability reduction below its initial value, which did not occur in the other two samples. Calcium and potassium brines attained their initial permeability lecture at the end of the experiment. In contrast, the sample flooded with KCl brine has almost identical permeability readings in both flowing directions (Fig. 7.6).

Similar results were obtained in the M4F22a sample (Fig. 7.7). An increase in permeability was obtained in direction to greater interstitial velocities. The pH of produced fluids converged almost symmetrically to permeability variations.

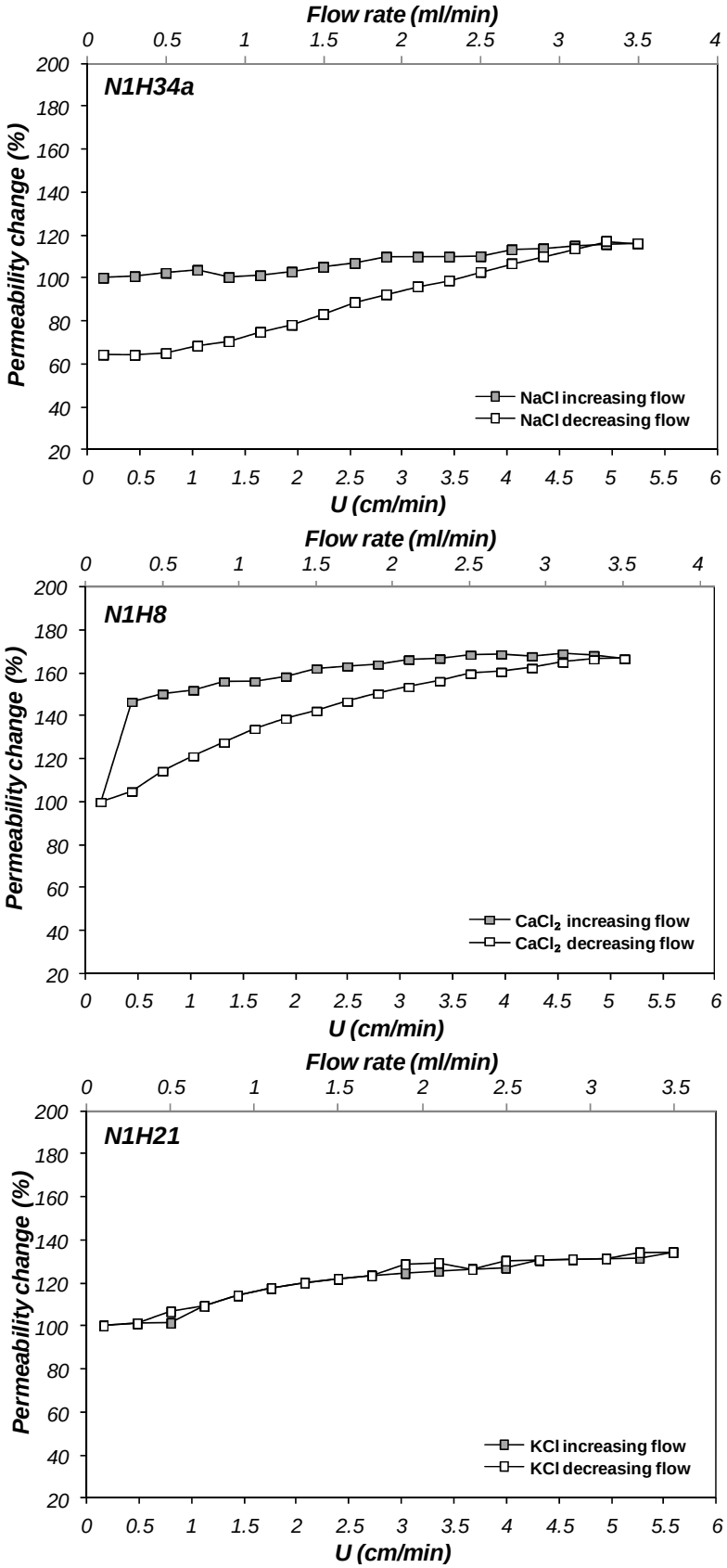

Figure 7.6 CVT results. No evident critical velocity threshold was observed

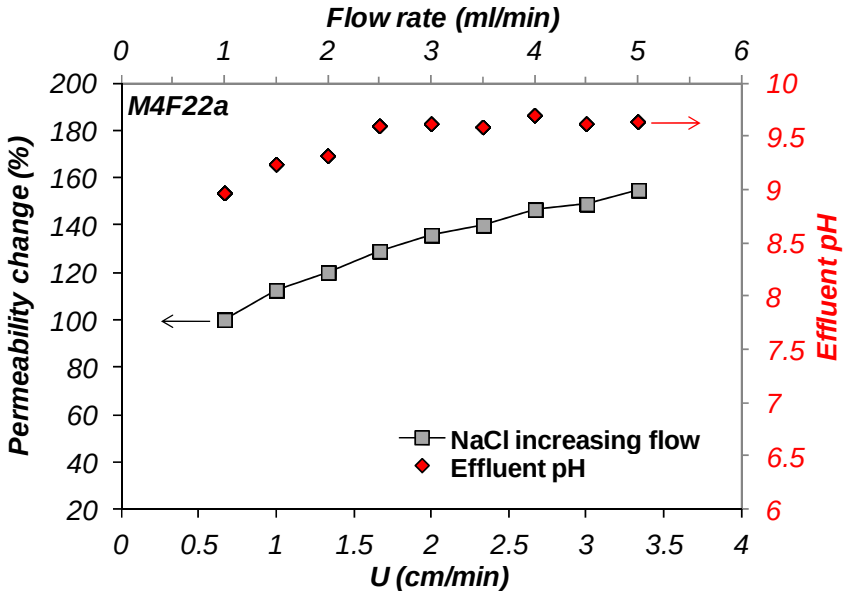

Figure 7.7 CVT with pH monitoring (M4F22a sample). Observe the relative correspondence of permeability change and pH

7.3.3 Discussion

It is unclear the permeability increase observed in the CVT experiments, especially because no change in the brine concentration was made. The pH variations during injection may be indicating rock-fluid reactions possibly caused by abrupt changes in the flow regime, although it is uncertain in how this affects permeability. No significant changes in pH were observed during the experiment.

Two alternatives are proposed to elucidate the increase of permeability in these samples: 1) dislodging and mobilisation of fine particles took place. The particles were too small and produced away so an increase in pore's surface area lead to permeability increase; or 2) viscosity variations of the brine at increasing flow-rates occurred.

If the first option is true, that would means that large amount of particles were removed from pore walls so that the pore was sufficiently increased to have an effect in permeability. This can be verified using the Kozeny correlation (Kozeny, 1927) which relates porosity and pore size to estimate permeability. For a rock composed of uniform capillary tubes in parallel with same radius (r) and length, the Kozeny equation can be expressed in terms of porosity (Ø) as:

$$k = \frac{\emptyset r^2}{8}$$

Using this equation for reproducing the increase in permeability from 3.52 mD to 5.44 mD (observed in M4F22a sample), a magnification of the pore throat radius from 0.045 to 0.056 cm was necessary (assuming that no significant changes in porosity were produced and using the

following correspondence: 1 cm^2= $1.013x10^8$ Darcy). Figure 7.8 illustrates the increase of permeability by the pore radius enlargement.

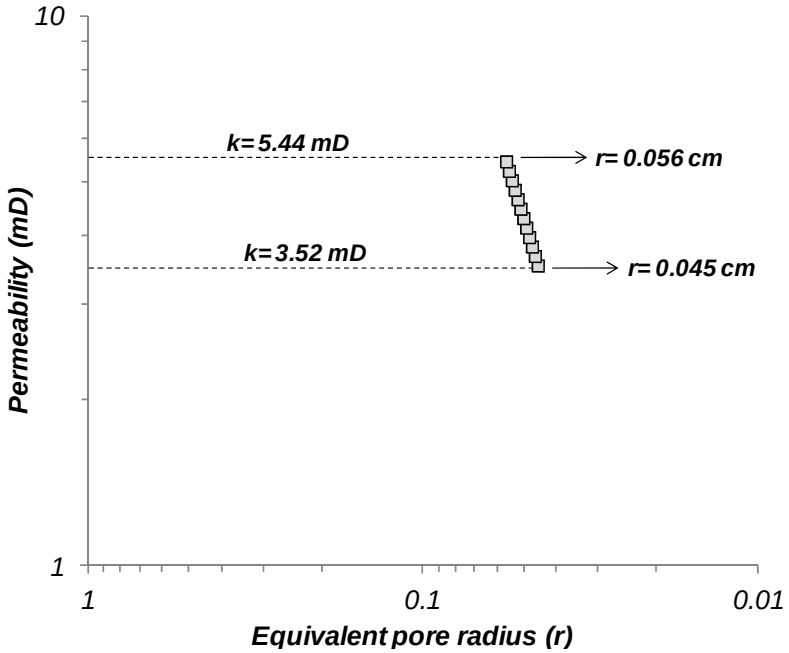

Figure 7.8 Pore-size based permeability using the Kozeny equation. The model assumes uniform dimensions of the capillary tubes which may not correspond to the pore-sizes observed in thin sections and mercury injection samples of this study; however, the model was used just to exemplify the rate of pore size variations to exert a control on permeability

The Kozeny correlation gives anomalous equivalent pore throat sizes that are beyond the sizes observed in MICP data of samples in this study. This is because it assumes the ideal case of uniform capillary tubes connected in parallel (*i.e.* no tortuosity). However, the model can be used to observe the rate of pore size variations necessary to produce an effect on permeability.

Note that an excess of approximately 125% of the pore size was necessary to reproduce permeability variations, which does not seem realistic. No significant weight differences were observed in the core samples once these were cleaned and dried, indicating that volumetric changes in the samples may be improbable.

In contrast, if it is taken the second option as granted, that would means that brine viscosity should have increased in direction to flow-rate to produce an effect on permeability, which also does not seem convincing. The pH readings observed during the test suggest that chemical reactions occurred at the pore scale level and that possibly are beyond the understanding of this work. Further investigation should be conducted on mineral dissolution/dislodging by aqueous solutions in these reservoirs, especially due to the potential of scale deposition and consequent permeability reduction. In particular, it seems likely that the injectivity efficiency of these

reservoirs may not be fully controlled by rock connectivity, but also may be influenced by the composition of the injected brine.

Overall, both CSC and CVT experiments illustrate the high sensitivity of the formation to the brine's type, concentration and interstitial velocity. The fluids planned to be injected into the reservoirs of this study should be properly conditioned to avoid formation damage. Clay swelling may potentially be avoided employing at least 3.5% concentration in treatment brines. $CaCl_2$ and KCl brines seem to prevent better formation damage than NaCl.

Amongst the brines used, K^+ seems to stabilize the formation better in comparison to Na^+ and Ca^{2+} cations, as permeability variations were almost identical in both flowing conditions (Fig. 7.6). This may be due to its relative size which fits better into platelets, keeping clays stabilised (Reed, 1977).

7.4 Fracturing Fluid Test

Most of the fracturing fluids used in the study area are crosslinked water-based mixtures, thickened with polymer-based gelling agents. The polymers used in hydraulic fracture stimulations are dry powders that swell when are mixed in aqueous solutions, forming a viscous gel. These are mainly employed as viscosifiers, fluid-loss controllers and proppant transporters. An experiment for analysing the permeability change due to the forced invasion of fracturing fluid into formation was conducted. Adsorption of polymer-based substances into rock surface has been documented to result in formation damage (Bennion *et al.,* 1995 and 1998; Williams *et al.,* 2012).

Fracturing treatments are generally conducted in four pumping stages in the reservoirs of this study. The initial, known as minifrac, consists of pumping fluid into a perforated formation. The fluid is normally formulated by 2.0% KCl brine which is injected at high rates to drive formation to its fracture point. During the second and third stages, known as pad and slurry stages, respectively; synthetic sand is injected into formation. The sand is transported by a polymer-based fluid, which is prepared by a natural gelling agent (*e.g.* guar gum); normally in 2-4 g/l concentrations. Finally, the fracture is cleaned employing polymer-free solutions combined with injection of N_2 or CO_2 for maximise fluids flowback; this last stage is referred as flush.

A hydraulic fracturing pumping sequence was recreated using a core plug from the reservoirs of this study. It was not the intention to fracture the sample as the experiment was mainly focused on analysing the potential of polymer invasion into pore walls and consequent permeability variations.

7.4.1 Materials

Petrophysical properties and mineral composition of the sample used in this experiment are shown in Table 7.5 and 7.6. Their microscopic characteristics are illustrated in Figure 7.9.

Table 7.5 Fracturing fluid core sample

Sample	*Gas Porosity (%)*	*Klinkenberg Permeability (mD)*	*k brine @ 3.5% (mD)*	*Saturating Brine*
M3F26b	*12.8*	*22.4*	*8.3*	*NaCl*

Table 7.6 XRD Mineral Composition (%Bulk volume)								
Sample	Bulk Fraction					Clay Fraction		
	Calcite	Quartz	Clay	Feldspar	Dolomite	Illite & smectite	Kaolinite	Chlorite
M3F26b	*48.2*	*32.2*	*12.4*	*4.4*	*1.8*	*9.0*	*2.7*	*0.7*

**Figures may not add-up due to minerals of less than 1% bulk volume are not shown*

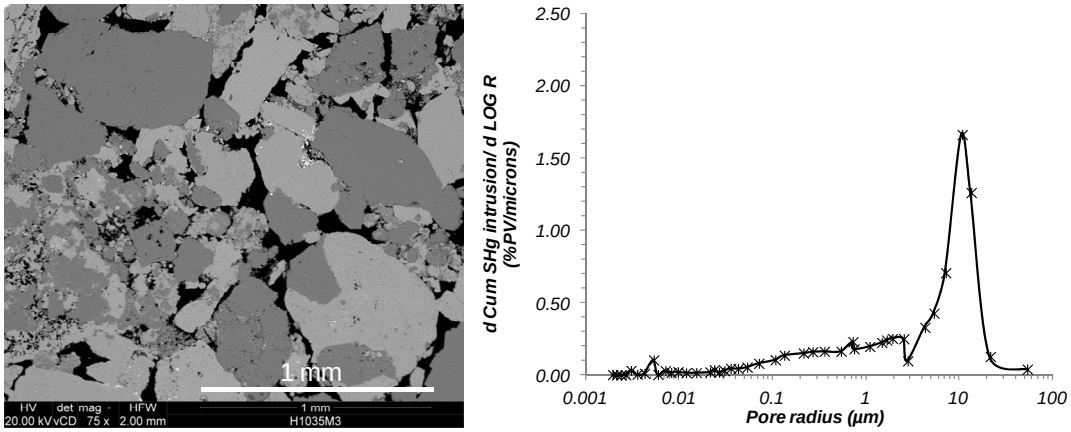

Figure 7.9 Microscopic characteristics of M3F26b sample. Intrusion plot of mercury injection data of the same sample is also shown. Observe its exceptional pore-size distribution

The sample used in this experiment illustrates one of the best petrophysical properties observed in the core plugs of this study. It was chosen to observe changes in permeability more easily. Observe in Figure 7.9 the large intergranular pores that according to mercury injection data corresponds to a pore throat radius of 10 µm. The sample was saturated with 3.5% of NaCl brine and left immersed in this brine for a week to achieve ionic-equilibrium.

Xanthan gum was bought from Sigma-Aldrich®. Xanthan gum is a refined natural gelling agent that is comparable to most thickeners used in field practices. This is a biodegradable substance that readily mixes in aqueous solutions.

7.4.2 Methodology

A single-phase permeability setup was used to perform the experiment. The sample was placed into a Hassler-type core holder within a sleeve to simulate the reservoir stress conditions of 1700 psi. A high-resolution pressure transducer was connected to the inlet end of the core whereas the downstream was at ambient pressure. A constant pumping rate of 0.5 ml/min was used during the entire experiment. The test tried to reproduce the pumping sequences normally conducted in hydraulic fracturing treatments in the reservoirs of this study.

Initial absolute permeability was obtained after flowing 20 pv of 3.5% NaCl brine through the plug, followed by 10 pv of 2.0% KCl brine to mimic the minifrac stage. Fifteen pore volumes of a mixture composed of 2.0% KCl+3.5 g/l of Xanthan gum were then injected in the same injection direction. The concentration of Xanthan gum of 3.5 g/l was similar as generally used in fracturing treatments. Injection direction was reversed and a 3.5% NaCl brine was immediately pumped. Viscosity of the gelling agent was of approximately 20 cP.

The complete pumping sequence and the resulted pressure difference (*i.e.* permeability determination) are shown in Figure 7.10.

7.4.3 Results

Figure 7.10 illustrates the complete pumping sequence performed during this experiment. Pressure disturbance through the core (DP) and the corresponding permeability change are plotted against equivalent pore volumes of fluid injected.

Initial absolute permeability of 8.3 mD was estimated by displacing 20 pv of 3.5% NaCl brine through the plug. Then, approximately 10 pv of 2.0%KCl brine were injected to simulate the minifrac stage. No significant change in permeability was observed.

A reduction of 97% of the original permeability was observed after injecting only 15 pv of gelling agent. Initial permeability was not recovered, even after *flushing* with 220 pv of reservoir brine in the flowback direction. Pressure disturbance in Figure 7.10 after injecting the gelling agent shows discontinuity due to pump re-filling.

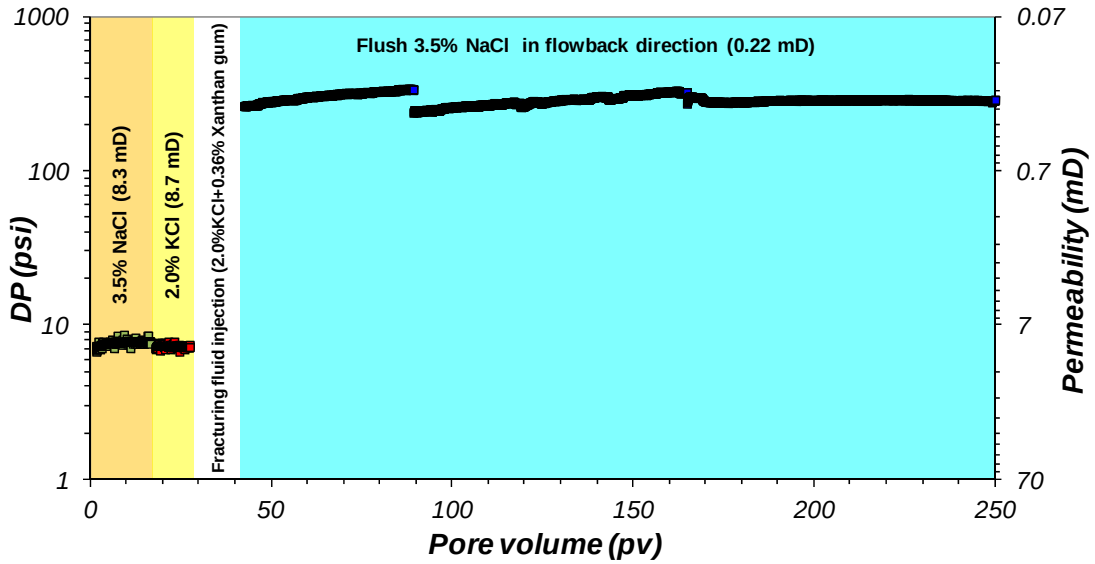

Figure 7.10 Fracturing fluid test. Note the increase in pressure difference (DP) after pumping the polymer-based fluid. No permeability recovery was observed even after of pumping more than 200 pore volumes of reservoir brine

7.4.4 Discussion

Although the results obtained may also be resulted from the viscous gelling agent blocking the pore throats, the permeability reduction was attributed to polymer adsorption into rock surface and pore walls. Two-hundred pore volumes (approximately 1.3 litres) of reservoir brine were immediately pumped through the sample in the flowback direction and a portion of the fracturing fluid was produced away even after water breakthrough. No significant permeability variations were observed, indicating that damage is not reversible. It is uncertain whether by reducing the polymeric load it may exert less negative effects to permeability, though the fluid may reduce its carrying capabilities. Holditch (2009) came to the conclusion that the primary problem of permeability impairment using guar-based fluids in tight-gas reservoirs is that the gel has a static yield stress that cannot be overcome by gas flow gradients anywhere in the fracture except near the wellbore.

Although the experiment did not recreate the extra flowback energy provided by N_2 or CO_2, the results show how critical is the flush stage and flowback recovery in the reservoirs of this study. The latter is significant, especially because the flowback fluid efficiency of hydrofrac treatments in Chicontepec reservoirs has been estimated of only 11% (Hurtado *et al.*, 2005). Water-based polymeric mixtures are preferred in Chicontepec reservoirs because their excellent rheological properties and costs. However, significant changes in oil productivity would be obtained by using non-aqueous, non-polymer fluids.

Polymer adsorption has also been associated to wetting alterations, generally to a more oil-wet condition (Bennion *et al.*, 1998). Adsorption of fracturing fluid not only reduces permeability, but also it may change the wetting state of the reservoir, which ultimately may result in lowering oil recoveries. This has reported extensively in published examples (Leontaritis *et al.*, 1994; Piro *et al.*, 1996; Sim *et al.*, 2005; Gholami *et al.*, 2008; Rezaian *et al.*, 2010).

Water-based fluids may also promote phase-trapping effects. Phase-trapping results from forced imbibition of water-based fluids into the pore space during fracturing treatments. The temporary increase of water saturation around the wellbore reduces the effective permeability to oil. Since these reservoirs have low-permeability, the cleaning-up process once the water has invaded the pore space may be difficult. Non-aqueous systems have also proved to be efficient in other tight-reservoirs (Smith, 1973), not only as proppant carriers but also as formation damage preventers; these include oil- and methanol-based systems.

Polymer-free systems include viscous-elastic gels, liquid CO_2-based, hydrocarbons, or gelled-methanol systems (Rae and Di Lullo, 1996; Gupta and Bobier, 1998; Gupta *et al.*, 1997). Viscous-elastic fracturing fluids have even proved to be efficient in Chicontepec reservoirs

(Centurion *et al.*, 2006). The results of this experiment suggest that alternate stimulation fluids may prevent formation damage more efficiently than polymer-based fluids.

Oil performance in the reservoirs of this study would be improved with the use of non-damaging stimulation systems. Further investigation on this matter should be necessary to evaluate alternative methods. As observed in this and previous experiments, the reservoirs of this study are water-sensitive and highly affected by polymer-based fluids.

7.5 Wettability

The following set of experiments was conducted to evaluate the wetting characteristics of the reservoirs of this study which has not been clearly established. Since secondary/tertiary oil recovery applications are planned to be implemented in Chicontepec reservoirs in the future, the analysis of the wettability is a key element to be evaluated.

Wettability is normally defined as the rock's preference to allow a fluid (*e.g.* water or oil) to spread over into its mineral surfaces. The literature shows that wettability may have a significant impact in the fluid distribution within pore space, which affects the capillary phenomena as well as the relative permeability that ultimately governs hydrocarbon productivity and recovery.

7.5.1 Adhesion Tests

Adhesion tests were conducted in this project to evaluate the wetting characteristics of quartz and calcite flat surfaces, as these are the main mineral fractions of Chicontepec reservoirs. The wetting behaviour was evaluated by direct measurement of oil-brine-mineral contact angles employing a crude-oil sample from the reservoirs of this study.

The adhesion test was developed by Buckley and Morrow (1990) and provides with significant information that can be obtained at controlled scenarios and employing a number of variables that are used to resemble wetting conditions. This technique is routinely applied to assess the wetting variations of flat mineral surfaces by changing the oil/brine/mineral conditions, such as salinity, pH, aging, aging time, and temperature. The aim of the adhesion test is to identify the conditions in which oil adhesion occurs into a mineral surface through the brine phase.

7.5.1.1 Materials

Pure quartz and calcite crystals were impregnated with a low viscosity resin to create blocks of 1.5x1.5x1.0 cm. Flat mineral surfaces were produced by polishing these blocks with successively finer grades of diamond paste.

A dead-oil sample was obtained at separator conditions from a producing interval of HUM-1689 well at S5 sequence in the study area. Saturate, Aromatic, Resin and Asphaltene analysis (SARA) was acquired by Intertek Testing Services UK, employing the adsorption chromatography method (IP469) and shown in Table 7.7. Physical properties of fluids were also measured (Table 7.8). Interfacial tension (IFT) between crude-oil and brine interface was measured by the axisymmetric drop shape analysis (ADSA) described in chapter three.

Table 7.7 Crude-oil composition

Sample	SARA Analysis			
	Saturates (%)	Aromatics (%)	Resins (%)	n-C7 Asphaltenes* (%)
HUM-1689	50.9	37	7.1	5

*As obtained by IP469 method

Table 7.8 Physical Fluid Properties (at 21°C)

Sample	Acid Number (mgKOH/gr)	Base Number (mgKOH/gr)	Asphaltene content* (%mass)	Density (g/cm^3)	Viscosity (mPa·s)	IFT (mN/m)
3.5%Brine	-	-	-	1.024	1.049	31
HUM-1689	0.05	0.7	0.2	0.83	9.21	

*As obtained by IP143 method

Synthetic NaCl brines at different concentrations varying from 3.5% to 0.5% and de-ionised water (DW) were employed. These were prepared with pure salts, filtered through 0.45 μm sieve and degassed. Brines with specific pH value were produced by adding alkaline/acidic buffer solutions into brines until reaching the desired value. Continuous pH monitoring was determined by a manual pH-meter device at room temperature of 21°C.

The aim of the adhesion test is to identify the conditions in which oil adhesion occurs into a mineral surface through the brine phase.

7.5.1.2 Methodology

The flat mineral blocks were cleaned with acetone and DCM, and then immersed in a 3.5% NaCl brine for a week in closed flasks to establish ionic equilibrium. Pairs of these samples were then immersed directly into a crude-oil sample in closed glass containers. Aging process was carried out employing a water bath device at 65°C for 72 hrs. After aging, the blocks were rinsed with Decalin which is an intermediate solvent that has been reported to preserve the wetting state of previously-aged surfaces (Tong *et al.*, 2002). The blocks were dried at ambient temperature in closed containers. The samples were identified as aged and non-aged.

The mineral blocks were placed into a transparent cell filled with brine at adaptable constant temperature (Fig. 7.11). A drop of oil is formed by an adjustable drop dispenser and it is forced to contact the mineral surface. Contact time was of 5 minutes in which adhesion or repulsion of oil into the surface is established. A high-resolution video camera records the oil-brine-mineral interaction. Contact angle of the crude-oil phase was determined using the sessile-drop technique in a Krüss Easy Drop goniometer apparatus (Figs. 7.11 and 7.12). The device is

equipped with Drop Shape Analysis (DSA) software which captures the drop dimensions. The DSA determines the drop edge coordinates, height and diameter, and the profile of the drop is extracted to estimate the contact angle (Fig. 7.12) by fitting the Young-Laplace equation.

In cases where no adhesion was produced, the advancing contact angle was recorded by enlarging the oil drop at continuous rate of 1 µl/s against the mineral surface. When adhesion occurred, the static contact angle was recorded by placing 20 µl of oil in the solid phase. Contact angles through the oil-phase of 0°-62°, 62°-133° and 133°-180° are normally used to define water-, intermediate- and oil-wet states, respectively. Examples of adhesion and non-adhesion are shown in Fig. 7.12.

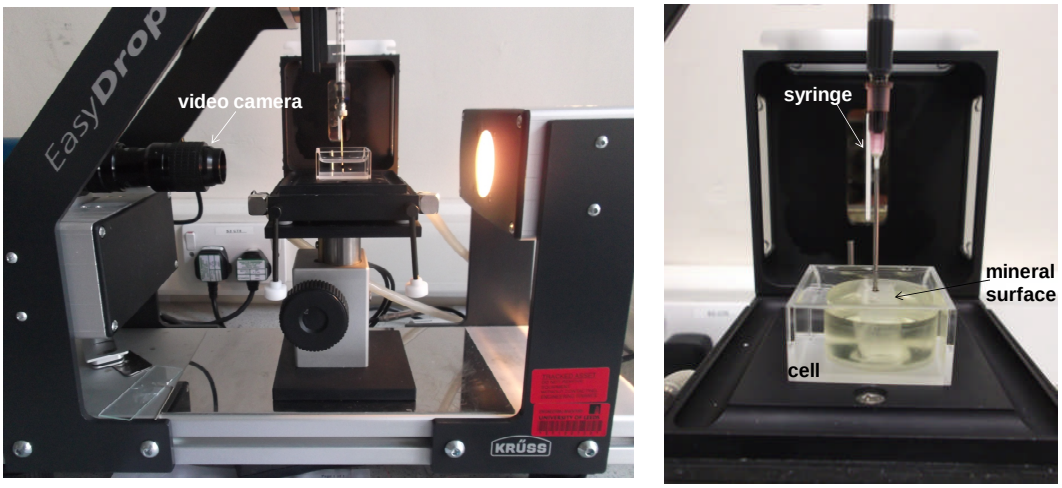

Figure 7.11 Contact angle setup and mineral surface blocks. A drop of oil is forced to contact the mineral surface and adhesion/repulsion is observed by the high resolution video camera. The device captures the shape of the crude-oil drop against the solid phase and estimates the contact angle

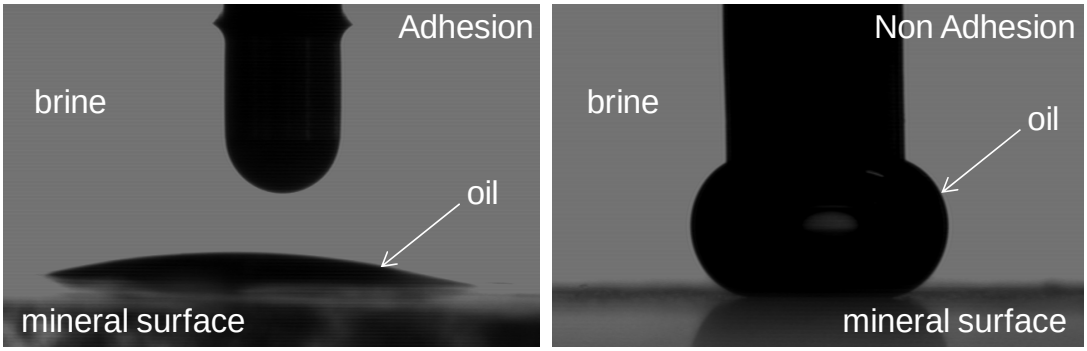

Figure 7.12 Examples of adhesion and non-adhesion. Crude-oil/brine/mineral interaction is visually evaluated by the adhesion test

Aged and non-aged mineral surfaces were forced to contact crude-oil by a variety of temperature, pH and brine concentration conditions. Quartz surfaces were evaluated examining four variables: aging, brine concentration, pH and temperature. Calcite surfaces were assessed

by analysing aging, brine concentration and temperature. The results are reported in the following paragraphs.

7.5.1.3 Results

Non-aged quartz and calcite surface minerals showed no adhesion of crude-oil independently of the brine concentration and temperature (Fig. 7.13a and 7.13c). No adhesion was also observed in quartz surfaces by pH variations at ambient temperature (Fig. 7.13b). Maximum contact angle registered in non-aged samples occurred in the acidic low-salinity quartz conditions. Quartz and calcite minerals remained water-wet as illustrated in diagrams of Figure 7.13.

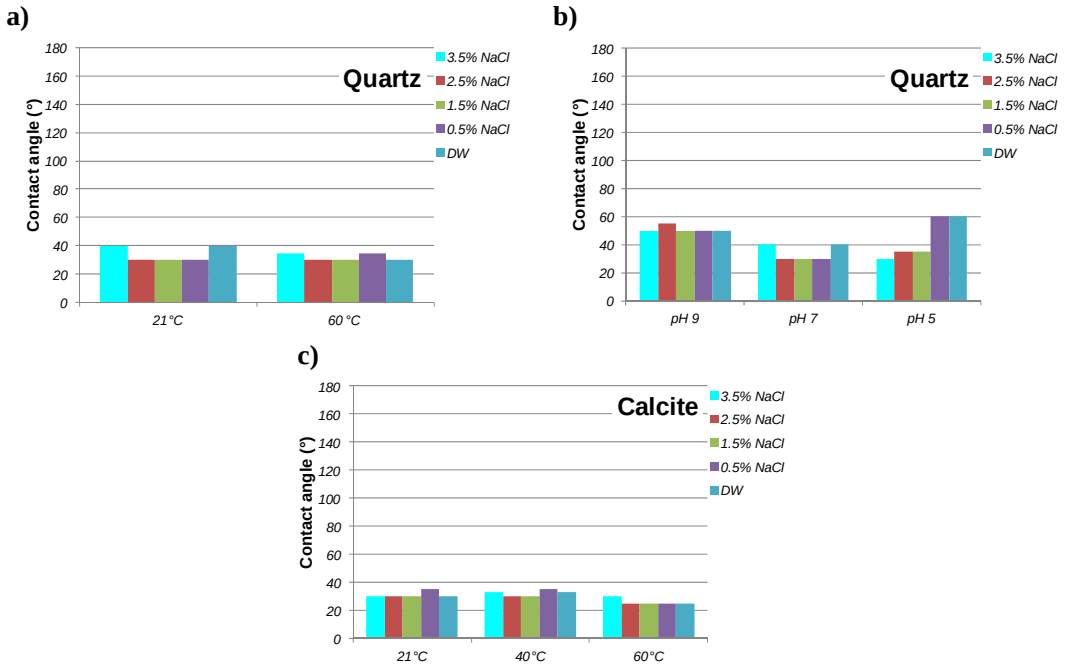

Figure 7.13 Contact angles of non-aged quartz and calcite surface minerals. The graphs show the oil's contact angle in quartz and calcite surface minerals by varying temperature, brine concentration and pH

Significant differences were observed in **aged** samples (Fig. 7.14). Crude-oil adhesion into calcite occurs readily, normally producing contact angles greater than 140° (Fig. 7.14c). Calcite surfaces behave as strongly oil-wet regardless temperature and brine concentration. A minor reduction in contact angles was produced at increasing temperatures, although calcite surfaces remained oil-wet. Similarly, decreasing brine concentrations, independently to temperature, generally produced a more oil-wet tendency in aged calcite surfaces.

Aged quartz surfaces (Fig. 7.14a and 7.14b), exhibit lower contact angles compared to calcite and describe a stronger dependence to temperature. Quartz surfaces changed from oil-wet to intermediate-wet as temperature increased from 21°C to 60°C, respectively. Similarly to calcite, greater contact angles were obtained at decreasing brine concentrations, although no significant

variations were observed. Acidic, low-salinity conditions produced the greatest contact angles with the quartz surface, equivalent to the results obtained in non-aged quartz. Aged-quartz surface changes from intermediate to oil-wet, from alkaline to acidic conditions, correspondingly (Fig. 7.14b).

Overall, adhesion tests indicate that aging produced a significant change in both minerals, as non-aged surfaces described a strong water-wet tendency. Aged minerals showed a strong oil-wet affinity in calcite surfaces and intermediate to oil-wet behaviour in quartz, depending to brine concentration and pH. Major changes in contact angles were observed at high temperature, as well as from alkaline to acidic conditions in aged-quartz surfaces. Similar behaviour was observed by Bondino *et al.* (2013).

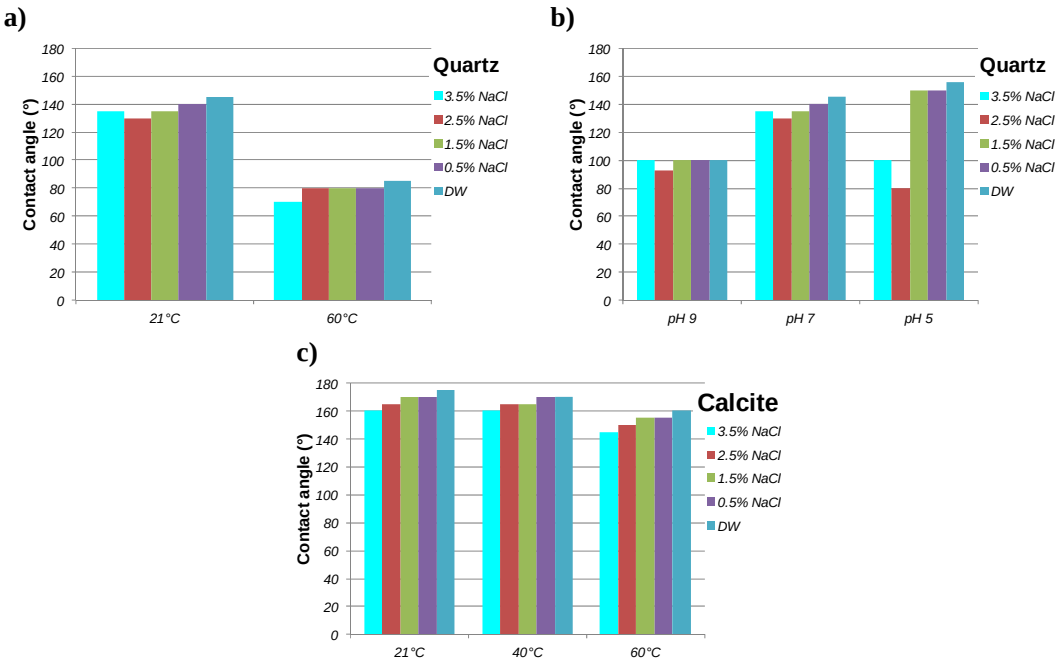

Figure 7.14 Contact angles of aged quartz and calcite surface minerals

7.5.1.4 Discussion

Several studies have shown that quartz and calcite have affinity to water and oil, respectively (Donaldson and Alam, 2008). This reflects silicate minerals having weakly acidic surfaces and negative surface charge. In contrast, most carbonate-based minerals have net positive surface charges and behave as alkaline material. Thus, silicate surfaces tend to repel acidic polar compounds normally found in crude-oils that calcite tends to attract (Donaldson and Alam, 2008). As result of this mineral interaction, siliciclastic reservoirs are mainly regarded to as water-wet whereas carbonate reservoirs to as preferentially oil-wet. However, research over the last four decades indicates that reservoirs have a range of wettabilities from strongly water-wet to strongly oil-wet, with mixed and fractional wettability being common (Brown and Fatt, 1956;

Trieber *et al.,* 1972; Salathiel, 1973; Lorenz *et al.,* 1974; Morrow, 1976; Chilingar and Yen, 1983; Buckley *et al.,* 1989; Radke *et al.,* 1992; Dixit *et al.,* 1998; Skauge *et al.,* 2003).

The wetting characteristics of a rock is mainly dominated by the stability of the oil/brine/mineral film, which is function of pH, brine composition, temperature, brine strength, pore roughness, aging-time and crude-oil properties (Buckley and Liu, 1998; Chow and Takamura, 1988; Oshima *et al.,* 1983; Buckley *et al.,* 1989; Morrow, 1990; Zhou *et al.,* 1996; Ma *et al.,* 1999; Al-Aulaqi *et al.,* 2011). In this way, the wettability condition of a rock is more complex and resulted from the interaction of minerals and fluids.

Although further investigation should be continued, especially by examining the effects of crude-oil properties on contact angles, as well as aging times and aging temperatures, mineral surface preparation, contacting time, etc.; the results indicate that HUM-1689 crude-oil is able to adhere mainly into aged-calcite surfaces. At reservoir conditions, where is expected that a neutral condition prevails, quartz behaves as intermediate-wet whereas calcite as strongly oil-wet. The latter is particularly important as the reservoirs of this study are generally composed by approximately 40% of calcium carbonate minerals.

The crude-oil used in these experiments consisted of 5% asphalthenes. Asphaltenes have been identified as key parameter that controls the water film stability (*e.g.* Yang, *et al.,* 2003; Buckley and Fan, 2005). Possibly, the relative high proportion of asphaltenes in the crude-oil sample used in adhesion tests is the controlling variable that makes calcite to behave as strongly oil-wet and quartz as intermediate-wet.

The clays have been known to exert a significant control on wettability (Lebedeva *et al.,* 2010; Watson and Boukadl, 1991). Clays are the third most abundant minerals within the Chicontepec reservoir sandstones, usually in proportions lower than 10%. Adhesion tests do not include clay surface minerals since it was difficult to represent illite/smectite mixed-clay in a surface. The effect of clays on wettability is analysed through a number of wettability experiments in the next section of this chapter. The tests were conducted in restored-state core samples where the whole wetting behaviour of the rock is evaluated.

7.5.2 Restored-state rock samples

The wetting characteristics of a number of Chicontepec reservoir samples was evaluated employing three methods: Amott-Harvey index (Amott, 1959), spontaneous imbibition rate (Mattax and Kyte, 1962; Ma *et al.,* 1999) and NMR wettability index (Al-Mahrooqi *et al.,* 2006). The experiments were carried out with restored-state subsurface sandstones and a crude-oil fluid directly obtained from producing intervals. The effect of mineralogy (silicate/carbonate ratio) and crude-oil composition on wettability was analysed. For comparison purposes two Berea sandstone samples were also evaluated.

7.5.2.1 Materials

Four rock plugs of 1.5" diameter were obtained from conventional full-diameter cores drilled in reservoir-pay zones of this study (named M1F30a, M1F30b, S29a1 and S29a). The samples were acquired from the inner portion of the cores to try to obtain virgin rock pieces. Two Berea Sandstone core samples were also obtained (named Berea 1 and Berea 2). Gas porosity at ambient conditions and steady-state Klinkenberg-corrected permeability were measured at *in situ* stress conditions. The relation of samples together with petrophysical properties are shown in Table 7.9.

Table 7.9 Core Samples and Petrophysical Properties

Sample	*Gas Porosity (%)*	*Gas Permeability (mD)*	*Sw* (%pv)*	*Sw** (%pv)*	*Saturating Oil*
M1F30a	*13.3*	*40.8*	*14.0*	*5.9*	*H1689*
M1F30b	*12.6*	*63.2*	*22.6*	*19.1*	*PO*
S29a1	*15.4*	*10.0*	*8.8*	*5.0*	*H1689*
S29a	*10.5*	*1.3*	*7.5*	*7.5*	*PO*
Berea 1	*21.7*	*196.5*	*27.3*	*27.3*	*H1689*
Berea 2	*21.4*	*184.3*	*18.3*	*18.3*	*PO*

**After primary drainage*
***After aging*

Quantitative X-ray diffraction (QXRD) and backscattered electron microscopy (BSEM) analysis were conducted to assess the bulk mineralogy and microstructure characteristics (Table 7.10). Observe the microscopic details of the samples used in Figures 7.15 and 7.16.

Table 7.10 XRD Mineral Composition (%Bulk volume)

Sample	Bulk Fraction					Clay Fraction		
	Calcite	Quartz	Clay	Feldspar	Dolomite	Illite & smectite	Kaolinite	Chlorite
M1F30a *M1F30b*	*47.4*	*31.3*	*16.0*	*3.5*	*1.8*	*13.6*	*1.4*	*1.0*
S29a1 *S29a*	*29.9*	*49.4*	*9.5*	*10.0*	*1.2*	*4.3*	*1.8*	*3.4*
	Quartz	Mica	Feldspar	Dolomite	Plagioclase	Kaolinite		
Berea 1 *Berea 2*	*80*	*8.0*	*5*	*1.8*	*1.7*	*3.5*		

a) M1F30a

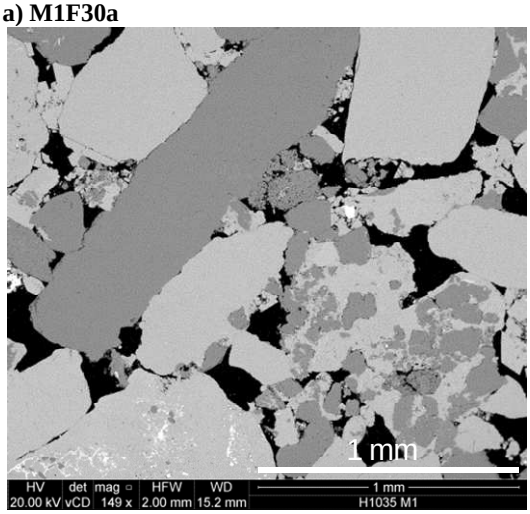

b) M1F30b

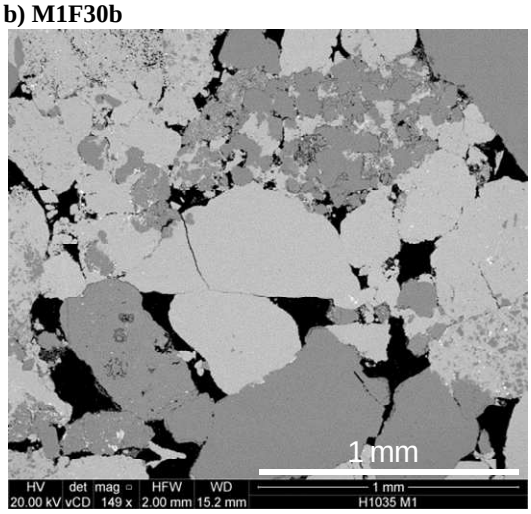

c) S29a1

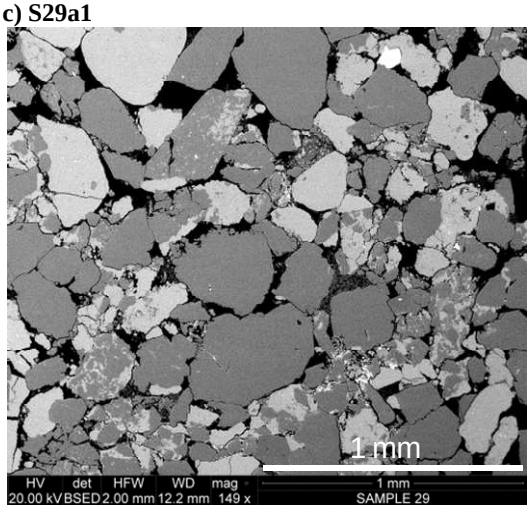

d) S29a

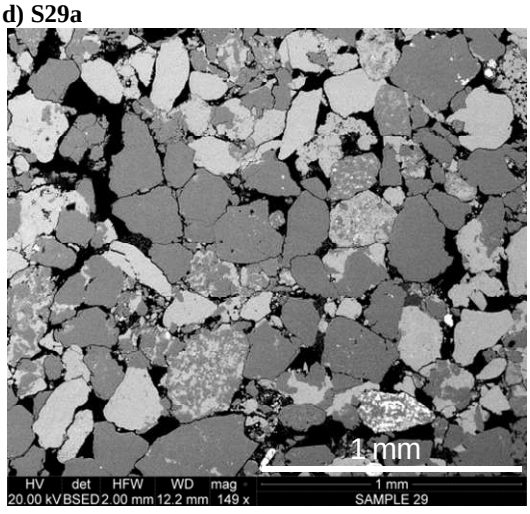

Figure 7.15 Microestructure detail of Chicontepec samples

a) Berea 1 **b) Berea 2**

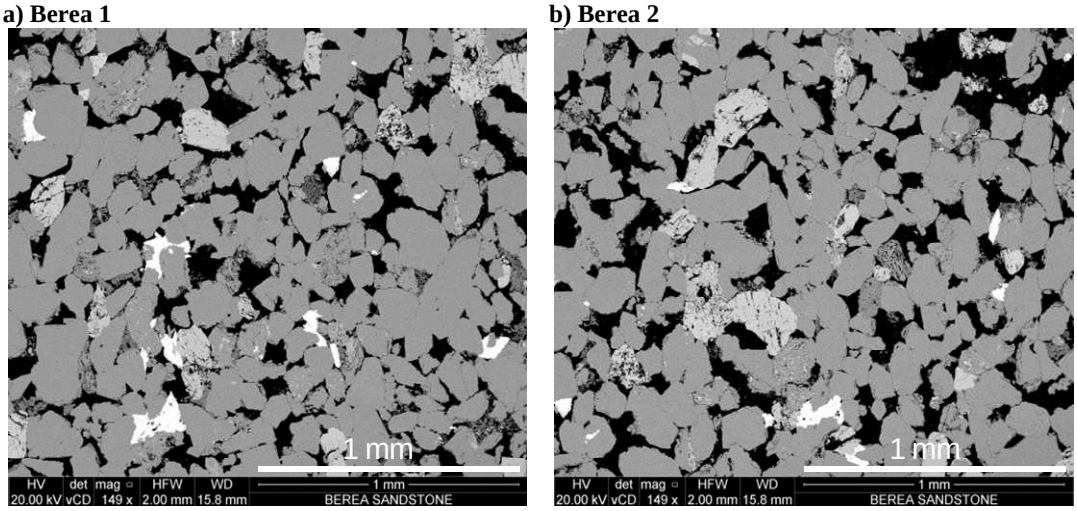

Figure 7.16 Microestructure detail of Berea samples. Observe their greater proportion of quartz compared to Chicontepec samples

A 3.5% sodium chloride brine, which corresponds to reservoir brine salinity, was prepared with DW and pure salts, filtered throughout 0.45 µm sieve and degassed. Dead-oil sample employed in these experiments was the same employed in the adhesion tests (HUM-1689). Crude-oil was centrifuged and filtered through 0.45 µm sieve to remove brine and any suspended particles.

Isopar-V oil (referred here as PO) was bought from ExxonMobil Chemical laboratory and employed here for comparative purposes. PO consists of paraffinic oil (linear saturated hydrocarbon) with similar physical properties as HUM-1689 (Table 7.11). No polar-organic compounds are found in PO, which have been associated to alter wettability to more oil-wet state (Table 7.12). Physical properties of HUM-1689 and synthetic brine were presented previously (Tables 7.7 and 7.8).

Table 7.11 Oil Composition

Sample	SARA Analysis			
	Saturates (%)	Aromatics (%)	Resins (%)	n-C7 Asphaltenes (%)
PO	99	<1	0	0

Table 7.12 Physical Fluid Properties (at 21°C)

Sample	Acid Number (mgKOH/gr)	Base Number (mgKOH/gr)	Asphaltene content (%mass)	Density (g/cm^3)	Viscosity (mPa·s)	IFT (mN/m)
PO	-	-	0	0.815	13.3	30.5

7.5.2.2 Methodology

The main purpose of these experiments was to evaluate the wettability of a number of Chicontepec samples, taking into account its mineralogy as well as the composition of the oil. Adhesion tests performed previously in mineral surfaces showed HUM-1689 crude-oil to have strong preference to calcite and in minor proportion to quartz. These experiments were designed to examine a more realistic approach of wettability in reservoir samples.

For evaluating the effect of mineral content on wettability, the Chicontepec samples were divided in two pairs: a pair of silicate/carbonate ratio greater than 1 (S/C>1; *i.e.* S29a1 and S29a), and a pair with S/C<1 (*i.e.* M1F30a, M1F30b). For evaluating the impact of oil composition on wettability, the quartz-rich Berea sandstone samples were saturated with HUM-1689 and PO oils, respectively. Two Chicontepec samples were also saturated with PO oil and compared to those saturated with HUM-1689. To see the saturating oils on each sample refer to Table 7.9.

All core samples were cleaned with DCM solvent and dried to constant weight in a convection oven at 60°C. These were evacuated and saturated with 3.5% NaCl brine overnight in a pressure vessel at 1000 psi. Once saturated, the samples remained at room temperature for a week to establish ionic equilibrium.

NMR T2 relaxation distribution and permeability to brine were acquired in all samples. NMR measurements were performed using an Oxford Instruments™ MARAN Ultra™ spectrometer (described in chapter 3) at 2MHz frequency, at ambient pressure and operating temperature of 35°C. Liquid permeability was determined using a steady-state permeability setup described in chapter 3.

Once equilibrated, the samples were mounted into a Hassler-type core holder and brine was displaced with its respective oil. At confining stress conditions (1700 psi for M1F30 samples and 1400 psi for S29 and Berea samples), oil was injected into the sample until no brine was produced (primary drainage cycle). The samples were then removed from the core holder and placed into glass-sealed containers filled with oil. Aging was carried out employing a water bath device at 65°C for 72 hours, following aging preparation from Rühl *et al*. (1963), Salathiel (1973) and Cuiec *et al*. (1979); although different authors advise longer restoration times (Mungan, 1972; Anderson, 1986a).

Once aged (at irreducible water saturation conditions), NMR T2 was acquired again and the samples were immersed into brine in Amott imbibition cells. The procedure for the three wettability methods is described in more detail below.

7.5.2.2.1 Amott-Harvey Index

Amott-Harvey Index (I_{AH}) involves spontaneous imbibition and forced displacement of brine and oil (Anderson, 1986b). The ratio of the oil and brine produced are measured to calculate the Water and Oil Wettability Indexes. Water wettability index (I_W) is estimated by:

$$I_W = \frac{V_{o,si}}{V_{o,si} + V_{o,fd}}$$

where: $V_{o,si}$ is the volume of oil produced by spontaneous imbibition of brine (cm^3), $V_{o,fd}$ is the volume of oil produced by forced displacement (cm^3). Similarly, oil wettability index (I_O) is estimated by:

$$I_O = \frac{V_{b,si}}{V_{b,si} + V_{b,fd}}$$

where: $V_{b,si}$ is the volume of brine produced by spontaneous imbibition of oil (cm^3), $V_{b,fd}$ is the volume of brine produced by forced displacement (cm^3). The average wettability affinity to the sample is obtained by: $I_{AH}= I_W-I_O$. The fluid that spontaneously imbibes most into the sample is normally ascribed as the wetting fluid.

Spontaneous imbibition was measured on Amott imbibition cells at constant room temperature of 21°C. Forced displacement was carried out by flooding at constant rate in a Hassler-type core holder. Water saturation was monitored by collecting and separating the effluent fluids (*i.e.* material balance), and by sample's weight differences (described in Experimental procedures).

7.5.2.2.2 Spontaneous Imbibition Rate

The rate at which brine imbibes spontaneously into core sample displacing oil is a qualitative measurement of the rock's wettability, when compared to an ideally water-wet response (Tang and Morrow, 1999 and 2005; Nasiri and Skauge, 2009; Ma *et al.*, 1999). The samples were immersed into brine in imbibition cells which consists of a graduated burette where oil naturally expelled (*i.e.* displaced) from the sample is recorded.

The volume of oil naturally produced from the samples, expressed as the percent of oil in place recovered (%OOIP), was registered through time until no expulsion was observed, which normally occurred after 40 days in most of the studied samples. The produced oil from each sample was plotted against dimensionless time (t_d), which permits comparisons to be made between different sample geometries and diverse fluid systems (Ma *et al.*, 1999):

$$t_d = C\sqrt{\frac{k}{\emptyset}} \cdot \frac{\sigma}{\sqrt{\mu_o \mu_w}} \cdot \frac{t}{L_c^2}$$

where: t_d is the dimensionless time; C is a constant unit conversion (0.018849); k is the permeability (mD); $\emptyset$ is the porosity (fraction); σ is the interfacial tension (dyne/cm); μ_o is the viscosity of oil (cP); μ_w is the viscosity of brine (cP); t is the imbibition time (min); and L_c is the plug's length (cm).

After spontaneous imbibition of brine, the samples were placed into a Hassler-type core holder at *in situ* stress conditions. Brine was then injected into the sample at constant rate until no further oil was produced. Injection rate was adjusted by a metering pump, thus resembling an ideal, linear displacement (waterflooding).

Effluent fluids, oil and brine, were continuously collected and later separated mechanically (*i.e.* centrifuging). Average water saturation of the samples was estimated by:

$$Sw = \frac{V_{oil\ (expelled)}}{V_p} + Sw_i$$

Final core water saturation was corroborated by:

$$S_w = \frac{\left[M - D_m - \left(V_p \cdot \rho_o\right)\right]}{\left[V_p \cdot (\rho_w - \rho_o)\right]}$$

where: V_{oil} is the volume of produced oil; V_p is the pore volume; M is the total mass of the core and fluids; D_m is the dry mass of the core; ρ is the fluid density (brine, oil).

a) Spontaneous imbibition of brine **b) Spontaneous imbibition of oil**

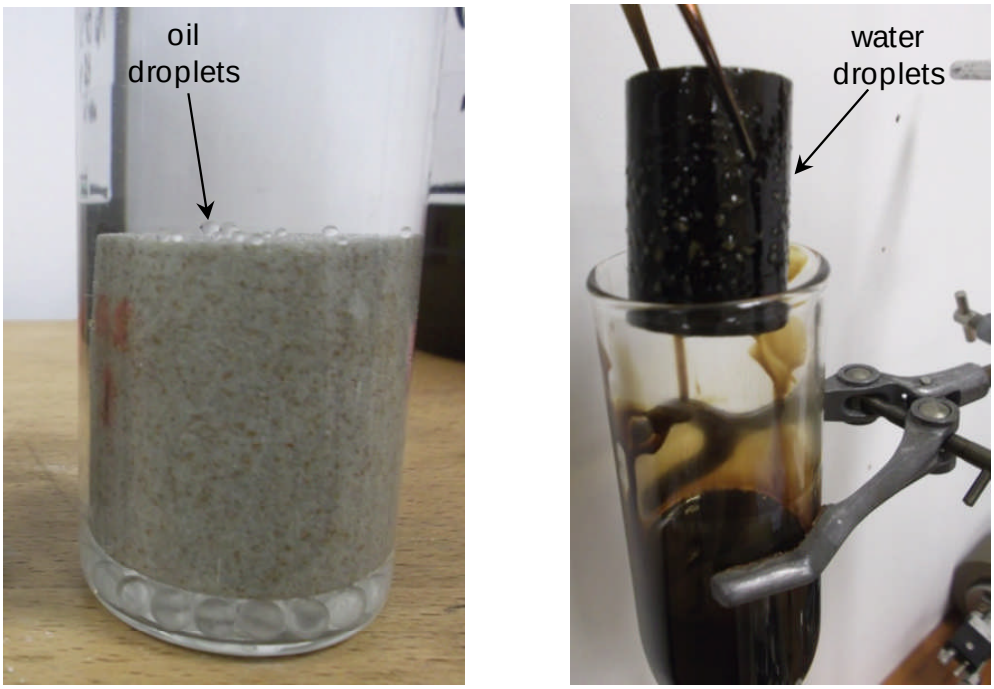

Figure 7.17 Spontaneous imbibition experiments. Observe the oil and water droplets naturally expelled from core samples, indicating imbibition of water and oil, respectively

7.5.2.2.3 NMR Index

NMR T2 relaxation distribution allows establishing a wettability index through the comparison of the logarithmic mean of T2 relaxation values ($T2_{LM}$). The method is described by Al-Mahrooqi *et al.* (2006) and was preferred to other techniques (*e.g.* Fleury and Deflandre, 2003; Guan *et al.*, 2002) since it only requires NMR measurements at two saturation stages (*i.e.* irreducible water saturation, Sw_i, and residual oil saturation, So_r) using the following expression:

$$NMR_{Wettability\ Index} = \left(\frac{T2_{LM}@Sw_i}{T2_{LM}@S_{or}}\right) - 1$$

After forced displacement and at So_r conditions, NMR T2 relaxation distribution was acquired and then compared to the relaxation times obtained at irreducible water state.

Later, the samples were immersed into oil. The amount of water produced by spontaneous imbibition and forced displacement was used to obtain Amott's Oil Wettability.

7.5.2.3 Results

During aging, three of the four Chicontepec samples observed a reduction in water saturation as reported in Table 7.9, suggesting that oil had imbibed during the process. No variation in water saturation was observed in Berea samples after aging.

Oil recovery by spontaneous imbibition of brine resulted in less than 7% of the OOIP in Chicontepec samples (Fig. 7.18, Table 7.13), independent of the oil type and their silicate to carbonate ratio (S/C). The highest oil recovery was from Berea 2 sample, saturated with PO oil, which illustrates the behaviour of a strongly water-wet rock. Forced displacement (*i.e.* waterflooding) averaged 37% of the OOIP in Chicontepec samples and practically did not make significant difference in Berea samples.

a) Samples saturated with HUM-1689 oil

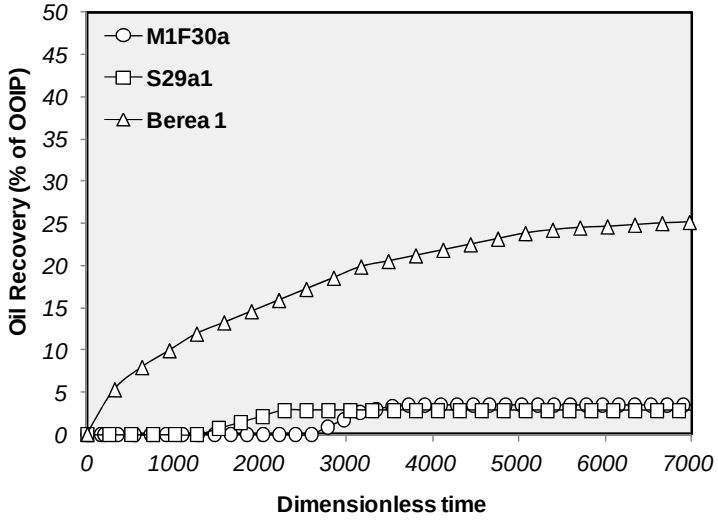

b) Samples saturated with PO oil

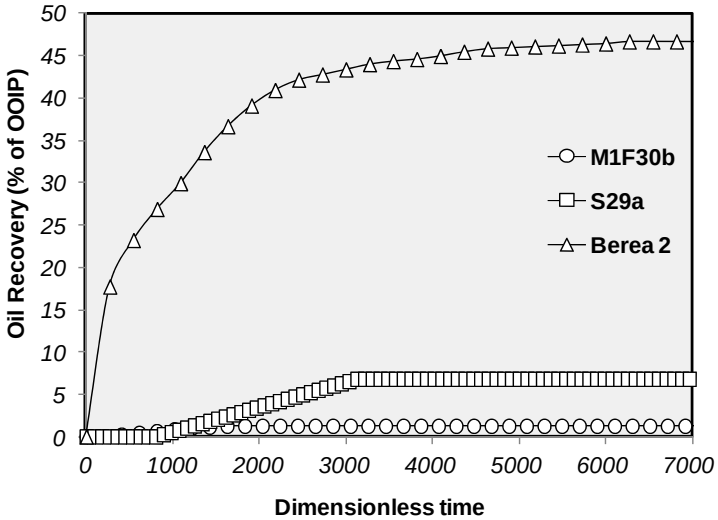

Figure 7.18 Oil recovery by spontaneous imbibition of brine: a) samples saturated with HUM-1689 crude-oil; b) samples saturated with paraffinic oil. Observe the low oil recovery of Chicontepec samples

Table 7.13 Spontaneous Imbibition and Forced Displacement Results

Sample	After Spontaneous imbibition		After Forced Displacement	
	Sw (%pv)	Oil Recovered (%OOIP)	Sor (%pv)	Oil Recovered (%OOIP)
M1F30a	9.14	3.5	56.2	40.3
M1F30b	20.1	1.3	54.5	32.7
S29a1	7.7	2.8	66.5	30.0
S29a	13.7	6.8	49.2	46.8
Berea 1	46.1	25.8	44.6	38.8
Berea 2	56.7	47	43.3	47

Both Amott-Harvey and NMR wettability indexes reveal a strong hydrophobic condition of Chicontepec samples and hydrophilic affinity in Berea samples, assuming a -1 to 1 scale as magnitude indicator (Tables 7.14 and 7.15). There is no agreement in the magnitude of both indexes, as the procedure and method for their calculation are intrinsically different. There is no relationship between I_{AH} and S/C ratio or oil type in Chicontepec samples, either.

Table 7.14 Amott-Harvey Wettability results

Sample	Brine		Oil		Amott-Harvey Index
	Spontaneous imbibition (cm^3)	Forced displacement (cm^3)	Spontaneous imbibition (cm^3)	Forced displacement (cm^3)	
M1F30a	0.2	2.6	1.04	1.28	-0.4
M1F30b	0.06	1.5	1.23	0.7	-0.6
S29a1	0.1	0.96	0.4	0.57	-0.3
S29a	0.15	0.91	0.66	0.25	-0.6
Berea 1	1.95	0.95	0.02	2.11	0.7
Berea 2	3.85	0	0.05	3.4	1.0

Table 7.15 NMR-Index Wettability results

Sample	Irreducible Water Saturation		Residual Oil Saturation		NMR Wettability Index
	Swi (%pv)	NMR $T2_{LM}$ (msec)	Sor (%pv)	NMR $T2_{LM}$ (msec)	
M1F30a	5.9	89.6	56.2	185.8	-0.51
M1F30b	19.1	86.1	54.5	171	-0.49
S29a1	5.0	29.7	66.5	60.83	-0.51
S29a	7.5	27.8	49.2	45.3	-0.38
Berea 1	27.3	114.8	44.6	101.7	0.12
Berea 2	18.3	109.7	43.2	98.1	0.11

Significant variations of T2 distributions were obtained at different saturating states in Chicontepec samples (Fig. 7.19, Table 7.15). Greater T2 distributions were observed at So_r conditions in comparison to those obtained at Sw_i in Chicontepec samples. In contrast, no

significant variations in T2 distributions were observed in Berea samples at different saturating conditions.

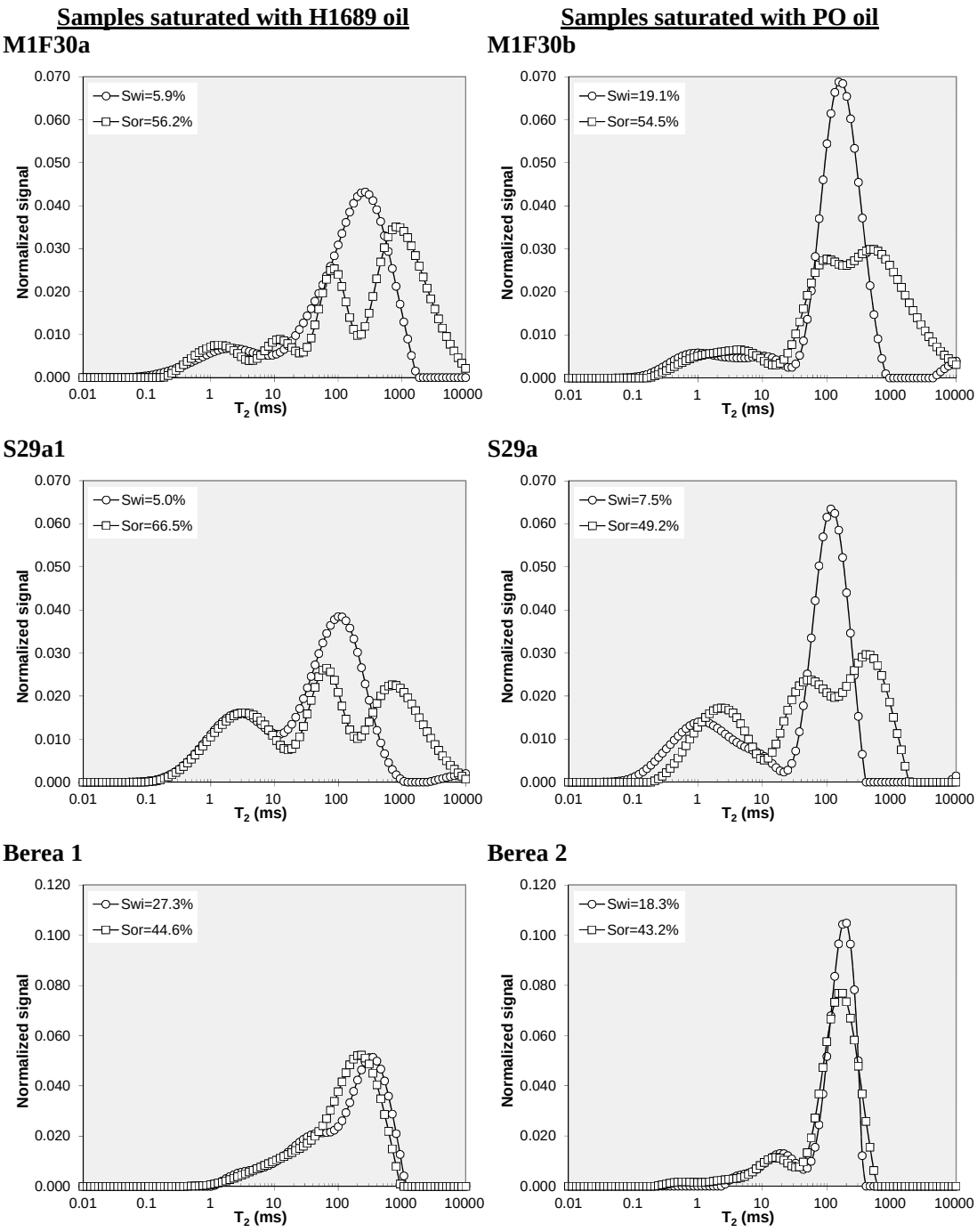

Figure 7.19 Individual NMR T2 relaxation distributions for the samples analysed. Observe the significant variation of the T2 at larger relaxation times developed in Chicontepec samples at *Sor* conditions

An acceptable agreement was observed when *Sw* (obtained after spontaneous imbibition of brine) was compared to the wettability indexes (Fig. 7.20 a, b). A better match was observed

using I_{NMR} (Fig. 7.20b). Greater oil recoveries were attained as the sample show more water-wetness affinity (Fig 7.20 c, d). Similarly, I_{NMR} better describes oil recovery efficiencies than I_{AH}.

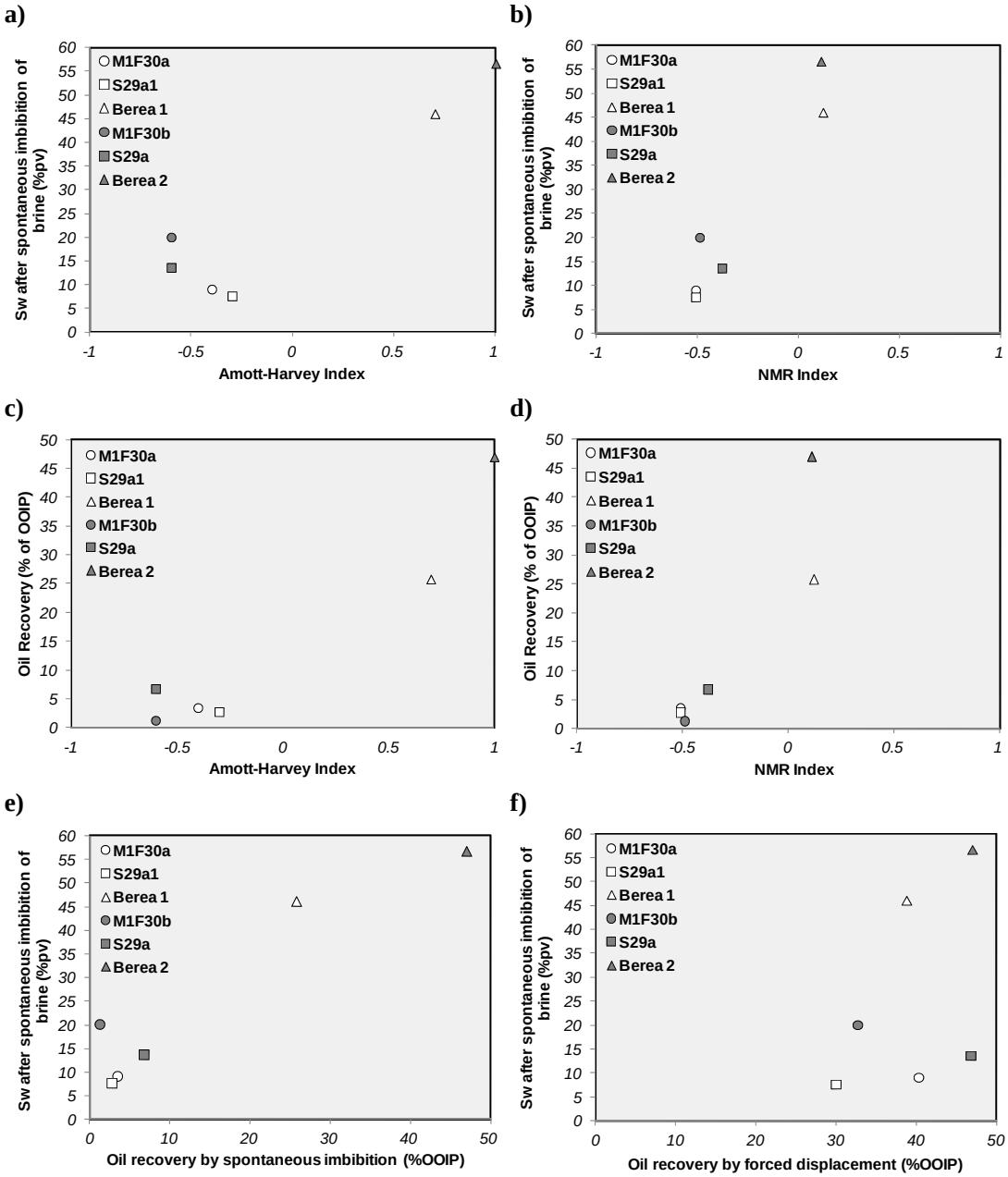

Figure 7.20 Wettability indexes correlations

Overall, the Chicontepec samples exhibit a strong hydrophobic affinity, independently of their S/C ratio or the saturating-oil type. This preference is thought to be produced by the combination of the reservoir rock mineralogy and the crude-oil properties, which may be interacting simultaneously. Both Berea samples display strong water-wet affinity.

7.5.2.4 Discussion

Chicontepec samples imbibe both brine and oil, which is an indication of non-uniform wettability (*i.e.* both oil- and water-wet surfaces are present in these cores). Oil is the fluid that most imbibes into Chicontepec samples, which makes I_{AH} negative. For this reason, oil recovery by spontaneous imbibition of brine is significantly lower than the Berea samples. Berea 1 sample observed a reduction of oil production efficiency by spontaneous imbibition compared to Berea 2 sample (Fig. 7.18, Table 7.13). However, their I_{AH} and I_{NMR} values suggest rather a strongly water-wet condition. This may indicate that Chicontepec crude-oil may be able to adhere on surface minerals (silica and carbonate) by means of either asphaltene precipitation or electrostatic reactions, but its effect, although sufficient for reducing oil recovery by spontaneous imbibition, is more significant in the carbonate-rich Chicontepec samples. The results are in agreement with adhesion tests.

Results from crude-oil/brine/rock (COBR) interaction studies (Buckley and Liu, 1998; Chow and Takamura, 1988; Oshima *et al.,* 1983; Buckley *et al.,* 1989; Morrow, 1990; Zhou *et al.*, 1996; Ma *et al.,* 1999; Al-Aulaqi *et al.,* 2011; AlShaikh and Mahadevan, 2014) have demonstrated that adhesion of crude-oil into mineral surface is dominated by the stability of the oil/brine/mineral film, which is mainly function of variations in pH, brine type and composition, temperature, aging-time and crude-oil.

The hydrophobic state observed in Chicontepec samples, as it is shown in the literature, may be originated by either: (a) the wide calcite content that is likely to adsorb acidic compounds in crude-oils (Block and Simms, 1967; Tiab and Donaldson, 2012); (b) the precipitation of asphaltenes that can be adhered to rock surface (Donaldson and Alam, 2008); and/or (c) electrostatic reactions of polar compounds and rock surface (Bennet *et al.,* 2004). Further investigation needs to be completed to discriminate which element impacts most on these samples, particularly because the HUM-1689 oil was observe to precipitate asphaltenes continuously.

I_{AH} values indicate a strongly oil-wet condition of Chicontepec samples. However, this may not be considered as definitive since I_{AH} has shown numerical discrepancies on intermediate-wetted states and interpretations of wettability state using this approach should be treated with caution, as pointed-out by Skauge *et al.* (2003). Additionally, experimental techniques for assessing wettability (*i.e.* USBM, Amott-Harvey Index) are partially accurate in reproducing non-uniform wetting states (McDougall and Sorbie, 1995; Ma *et al.,* 1999). Based on pore-network simulations, Dixit *et al.* (1998, 2000), demonstrated that I_{AH} beyond the range $-0.5<I_{AH}<0.5$ rather indicate a fractional or mixed-wet condition.

Although the Chicontepec crude-oil sample seems to be able to adhere into quartz and calcite minerals, which in turn may indicate a fractional-wet behaviour, the results indicate that Chicontepec samples are mostly consistent with a mixed-wet of large pore condition. Brown and Fatt (1956) introduced the concept of fractional wettability, in which the wetting fluid is randomly distributed throughout the pore surfaces as function of the heterogeneous distribution of minerals. Salathiel (1973) proposed the term 'mixed-wettability' to describe a wetting condition in which larger pores are strongly oil-wet and filled with oil, and smaller pores remain strongly water-wet and filled with water. Salathiel reasoned that this is the result of the oil migration and entrapment process, in which oil preferentially migrated into the larger pores due to their lower capillary entry pressure and that these became oil-wet due to crude oil-brine-rock (COBR) interactions. Smaller pores remained water-wet as greater pressure threshold was required for the oil to invade.

The mixed-wet condition of Chicontepec samples seems to be best described by the NMR T2 method. The significant increase in the T2 signal (at So_r conditions) of Chicontepec samples compared to Berea samples, indicate the oil-wetting preference of larger pores (Fig. 7.19). As brine does not exist as continuous phase throughout the pore surface at residual oil condition (*i.e.* brine is not in contact with all mineral surfaces but only in small water-wet pores and at the centre of the large oil-wetted pores), T2 relaxation is dominated by its bulk rate. Conversely, in the Berea samples at So_r conditions, NMR T2 is dominated by its surface relaxation as brine coats the complete mineral surface and oil remains in small crevices. I_{NMR} show better correlation coefficients with *Sw* and OOIP than I_{AH} (Fig. 7.20d and 7.20b). This may be partially due to its ability to observe the fluid and pore surface interactions. It is also noted that lower water saturation values increase the oil-wetness state of the samples and reduce the amount of oil recovered (Fig. 7.20e and 7.20f). These results are consistent with previous work (*e.g.* Salathiel, 1973; Tong *et al.*, 2002; Zhou *et al.*, 1996).

The results of these set of experiments, demonstrate the importance of incorporating different approaches for wettability characterisation. Traditional techniques are partially accurate in reflecting the wetting conditions of non-homogeneous systems, and the necessity to incorporate supporting experimental techniques such as adhesion tests and NMR measurements, is recommendable. Additionally, more representative results are obtained by using pre-conditioned rock samples (*i.e.* aged), so the geological conditions (*i.e.* secondary migration of oil) are replicated.

7.6 Continuous End-point Relative Permeability

Continuous end-point relative permeability experiments were conducted for evaluating oil/brine production efficiencies in two wetting scenarios. Two core plugs were employed: the strongly water-wet Berea 1 sample and the mixed-wet M1F30a sample. These were previously prepared and used for wettability experiments. Mineralogy and petrophysical properties of these are shown in Tables 7.9 and 7.10.

7.6.1 Methodology

The samples were mounted into a Hassler-type core holder at *in situ* stress conditions. Two pore volumes of Decalin were pumped through each sample to displace HUM-1689 crude-oil, thus avoiding asphaltene precipitation during the experiments. Decalin is an intermediate solvent which proved to retain wettability state in previously-aged surface minerals during adhesion tests. Decalin was later removed by flowing 3.5% NaCl synthetic brine until reaching So_r condition in both samples.

A pressure transducer was connected to the upstream side of the core holder whereas the downstream end was at ambient conditions. A metering pump was used for injecting fluids (brine or oil) at steady flow-rates. Measurements were obtained at constant room temperature of 21°C.

At So_r conditions, the paraffinic oil was injected into the sample at increasing flow-rate stages until pressure equilibrium was achieved through the core on each rate-point and brine was no longer produced (*i.e.* stepped end-point saturation). Injection rates varied from 0.1 to 2 ml/min. On each stage, effluent fluids were collected and later separated (*i.e.* centrifuged) to estimate the average water saturation of the sample. To corroborate water saturation, the core holder was disassembled and the sample weighted in each end-point stage. Irreducible water saturation was achieved (Sw_i) until no more water was produced and no significant weight differences of the sample were obtained. Effective permeability to oil at Sw_i was registered ($k_o@Sw_i$).

Similarly, at Sw_i conditions, brine was injected at stepped rates to displace oil. Residual oil saturation (So_r) was achieved until no more oil was produced and no significant weight differences of the sample were observed. The obtained effective permeabilities to oil and water (k_{eo}, k_{ew}) at a range of Sw variations, were normalised at $k_o@Sw_i$, thus continuous end-point relative permeability curves to oil and water were estimated.

7.6.2 Results

The results of continuous end-point relative permeability tests are shown in Fig. 7.21 and Table 7.16. The shape of the calculated end-point relative permeability curves describes a smooth and continuous pattern. Significant variations in Sw_i, $k_{rw}@So_r$, and relative permeability crossover are observed in both samples, which illustrate the differences in fluid distributions within pore space (Fig. 7.21).

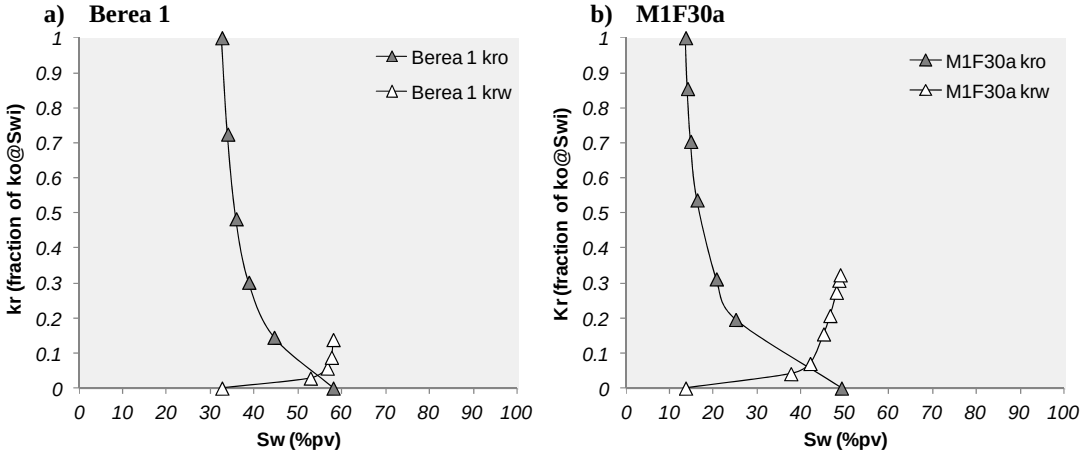

Figure 7.21 Continuous end-point relative permeabilities

The Sw_i and the saturation at which oil and water relative permeabilities are equal resulted to be of 14% and 41% in the M1F30a sample, respectively; whereas Berea 1 sample obtained 33% and 53% values, correspondingly. The ratio of relative permeabilities (k_{ew}/k_{eo}) of Berea sample resulted of 0.14, whereas for M1F30a of 0.31.

Table 7.16 Continuous End-point Relative Permeability

Berea 1			***M1F30a***		
Sw (%pv)	*fraction of kro@Swi*		***Sw (%pv)***	*fraction of kro@Swi*	
	kro	***krw***		***kro***	***krw***
32.5	*1.000*	*0*	*13.6*	*1.000*	*0*
35.1	*0.550*	*0.003*	*17.2*	*0.480*	*0.006*
37.6	*0.370*	*0.007*	*20.7*	*0.300*	*0.012*
40.2	*0.250*	*0.010*	*24.3*	*0.210*	*0.017*
42.7	*0.180*	*0.013*	*27.8*	*0.170*	*0.023*
45.3	*0.140*	*0.016*	*31.4*	*0.140*	*0.029*
47.8	*0.100*	*0.019*	*35.0*	*0.110*	*0.037*
50.35	*0.080*	*0.023*	*38.5*	*0.080*	*0.043*
52.9	*0.050*	*0.030*	*42.1*	*0.060*	*0.080*
55.45	*0.025*	*0.040*	*45.6*	*0.030*	*0.180*
58	*0*	*0.140*	*49.2*	*0*	*0.310*

7.6.3 Discussion

In general, the relative permeability to oil increases and the relative permeability to water decreases as wettability becomes more water-wet (Donaldson and Alam, 2008). Conversely, the relative permeability to water increases (in detriment to relative permeability to oil) while wettability turns more oil-wet. In mixed-wet states, which are thought to be the case of the Chicontepec sample, the relative permeability is function of the relative proportion of oil-wetted and water-wetted pores.

The shape of the relative permeability curves in both samples results from the integranular porosity and uniform distribution of pore sizes as observed in their microscopic images (Figs. 7.15 and 7.16). The results obtained coincide with the rules of thumb of Craig (1971) for differentiate strongly-wetted scenarios: for strongly oil-wet case, the samples describe Sw_i less than 25% and water saturations at cross-over point of less than 50%. Relative permeability to water at end-point conditions ($k_{rw}@So_r$) is normally less than 50%. In contrast, for strongly water-wet scenarios, Sw_i is usually more than 25%, the water saturation at cross-over point is more than 50% and the $k_{rw}@So_r$ is less than 30%.

In the water-wetted case (Berea 1) brine occurs as continuous phase through the entire rock surface, filling the small pores and crevices, and coating the entire grain surfaces. An even distribution of oil at increasing displacing pressures is developed when oil is displaced by water. On the contrary, in the mix-wetted case (M1F30a), water is located in the small water-wet pores, whereas oil in the large, oil-wetted ones. No uniform displacement occurs when oil is displaced by water, since oil remains as a film coating the larger pore walls. Thus, the oil displacement efficiency compared to the water will be different between the two wetting scenarios. Similarly, as oil remains adhered into larger pores, greater residual oil saturation is observed in the mixed-wet Chicontepec sample compared to the strongly water-wet Berea 1 sample.

The relative proportion of the oil-wet and water-wet pores (or large and small pores, respectively) may contribute to the relative permeability behaviour in mixed-wet samples. It should be expected that as the amount of the large oil-wet pores increases in comparison to the small water-wet pores; the water-to-oil permeability (k_{rw}/k_{ro}) should also increase. In contrast, as the amount of the small water-wet pores is more dominant than the large oil-wet ones, lower k_{rw}/k_{ro} ratios would be expected.

7.7 Surfactant Evaluation

Results of previous experiments evaluating the wetting characteristics of Chicontepec samples indicate a mixed-wet condition. Greater residual oil saturations (So_r) are expected to be produced in this condition since oil remains adhered into the large oil-wetted pores.

A number of surfactants were used in reservoir samples of this study to evaluate their effectiveness to increase oil recovery. Previous spontaneous imbibition experiments in Chicontepec samples resulted in less than 7% of the OOIP (Fig. 7.18). These were obtained using just synthetic brine. In the experiments described below, the samples were immersed in a mixture of surfactant plus synthetic brine. Thus, the compatibility of surfactants with brine and the efficiency of this mixture to improve oil recovery by spontaneous imbibition were evaluated.

The aim of these experiments was to assess the ability of the surfactant to improve the amount of oil recovered. It has been demonstrated that certain surfactant solutions mixed in brine are able to improve oil recovery by lowering the oil-brine interfacial tension (IFT) or modifying the wetting conditions. Surfactant efficiency is routinely evaluated through spontaneous imbibition tests (Xie *et al.*, 2004; Austad and Milter, 1997).

7.7.1 Materials

Table 7.17 lists the core samples used in these experiments. Gas porosity at ambient conditions and steady-state Klinkenberg-corrected permeability at *in situ* stress were measured. Note that M1F30b and S29a1 samples, saturated with PO and H1689 oils, respectively; were previously used for wettability experiments (see Table 7.9).

Table 7.17 Core Samples and Petrophysical Properties

Sample	*Gas Porosity (%)*	*Gas Permeability (mD)*	*Sw* (%pv)*	*Sw** (%pv)*	*Surfactant*
M3F26a	*12.5*	*20.2*	*22.4*	*13.0*	*CO-520*
M4F22b	*13.8*	*63.9*	*21.2*	*16.0*	*Rhamnolipid*
M1F30b	*12.6*	*63.2*	*19.1*	*19.1*	*SDBS*
S29a1	*15.4*	*10.0*	*5.0*	*5.0*	*C12TAB*

**After drainage*
***After aging*

QXRD and BSEM images were obtained to assess mineral composition and microstructure characteristics (Table 7.18). Observe that quartz and calcite proportions, together with the fabric of the rock (Fig. 7.22), resemble most of the characteristics observed in the reservoirs of this study.

Table 7.18 XRD Mineral Composition (%Bulk volume)

Sample	*Bulk Fraction*					*Clay Fraction*		
	Calcite	Quartz	Clay	Feldspar	Dolomite	Illite & smectite	Kaolinite	Chlorite
M3F26a	*48.2*	*32.2*	*12.4*	*4.5*	*1.8*	*9.0*	*2.7*	*0.7*
M4F22b	*49.6*	*29.2*	*15.4*	*3.8*	*1.1*	*12.4*	*1.8*	*1.2*
M1F30b	*47.4*	*31.3*	*16.0*	*3.5*	*1.8*	*13.6*	*1.4*	*1.0*
S29a1	*29.9*	*49.4*	*9.5*	*10.0*	*1.2*	*4.3*	*1.8*	*3.4*

a) *M3F26a* **b) *M4F22b***

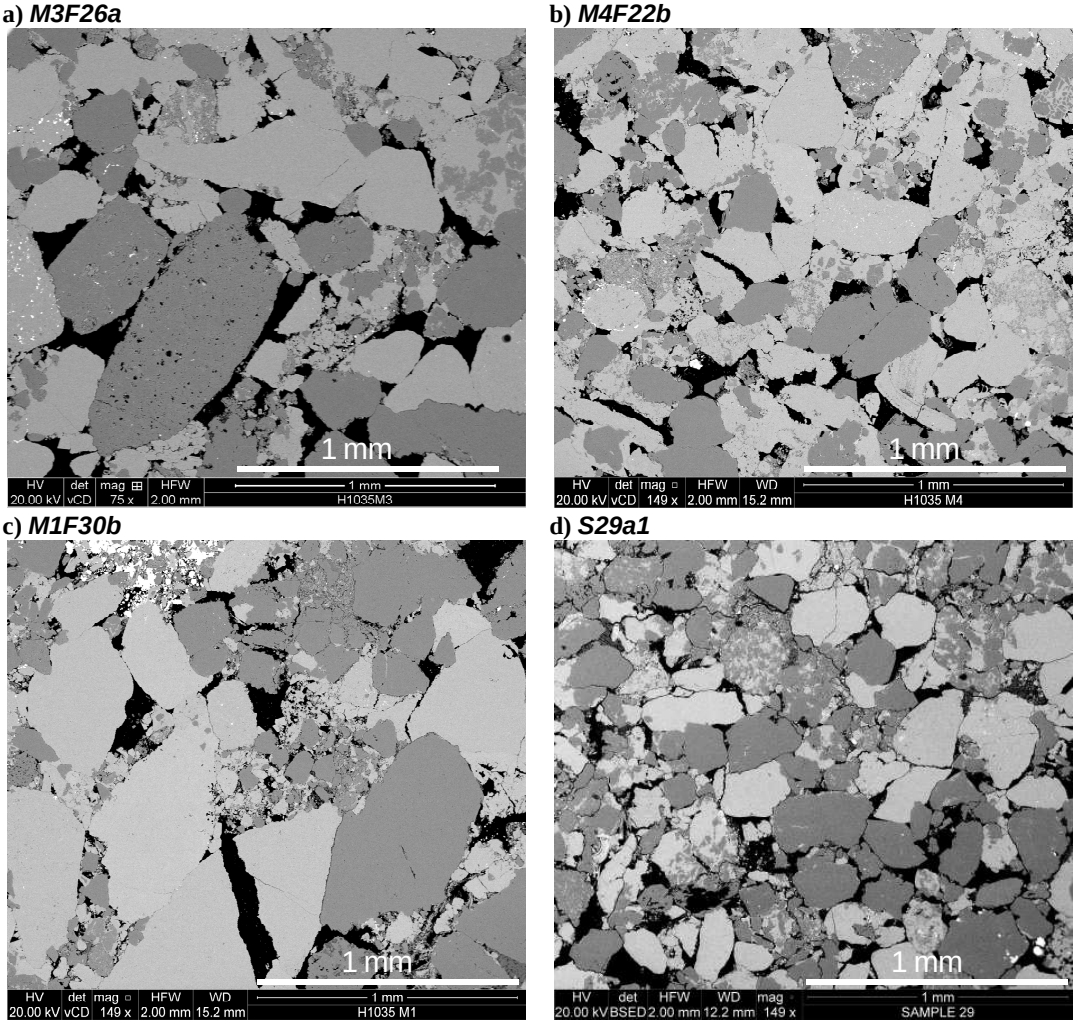

c) *M1F30b* **d) *S29a1***

Figure 7.22 BSEM microstructure detail of the samples used. Observe that these correspond from medium to coarse-grained sandstones

Synthetic brine at 3.5% NaCl was prepared with DW and pure salts. Once prepared it was filtered throughout 0.45 µm sieve and degassed. The HUM-1689 crude sample, previously employed in adhesion and wettability tests, was also used. This was centrifuged and filtered through 0.45 µm sieve to remove precipitated particles.

A number of commercial surfactants were selected since these have been mentioned in the literature as efficient IFT reducers for maximising oil recovery (*e.g.* Fang *et al.*, 2007; Goddard *et al.*, 2007; Standnes and Austad, 2000; Golabi *et al.*, 2012; Torres *et al.*, 2011; Wu *et al.*, 2006). These have also shown acceptable capabilities in conditions similar to the reservoirs of this study (*e.g.* temperature and formation water salinity).

The relation of surfactant solutions and their physical properties is listed in Table 7.19. Anionic and non-ionic surfactants were bought from Sigma Aldrich® and named here as SDBS and CO-520, respectively. Cationic surfactant is referred here as C12TAB and acquired from ACROS Organics®. The *Rhamnolipid* biosurfactant was purchased from AGAE Technologies®. *Rhamnolipid* is a natural biosurfactant mainly produced by *Pseudomonas sp.* bacteria (Torres *et al.*, 2011).

Table 7.19 Physical properties of surfactants

Surfactant	*Commercial Name*	*Grade (%)*	*Linear Formula*	*Molecular weight (g/mol)*	*C* (%)*
Non-ionic	*CO-520*	*99*	$(C_2H_4O)_n \cdot C_{15}H_{24}O$, n~5	-	*0.5*
Biosurfactant	*Rhamnolipid*	*90*	-	-	*0.03*
Anionic	*SDBS*	*99*	$CH_3(CH_2)_{11}C_6H_4SO_3Na)$	*348.5*	*0.5*
Cationic	*C12TAB*	*99*	$C_{15}H_{34}BrN$ $CH_3(CH_2)_{11}N(Br)(CH_3)_3$	*308*	*2*

**C: concentration of surfactant solution in 3.5% NaCl brine*

The surfactant concentration used in synthetic brine is reported in Table 7.19. These concentrations were used since they have been referred as their optimal value, according to their critical micelle concentration (CMC) and reported compatibility with water solutions. For example, Stadnes and Austad (2000) report that up to 70% of OOIP was recovered from chalk samples using 1% of C12TAB surfactant in a 4.5% NaCl brine.

Surfactant and brine were mixed and hand-shacked vigorously. The mixtures remained at room temperature in closed flasks overnight.

7.7.2 Methodology

The core samples were evacuated and saturated with a 3.5% NaCl brine overnight in a pressure vessel at 1000 psi. Once equilibrated, the samples were mounted into a Hassler-type core holder and brine was displaced with HUM-1689 crude-oil until no brine was produced, achieving irreducible water saturation. The samples were then removed from the core holder and placed into glass-sealed containers filled with crude-oil. Aging process was carried out employing a water bath device at 65°C during a week. Water saturation variations after aging are listed in Table 7.17.

Once aged, two pore volumes of Decalin were pumped through each sample to displace crude-oil. Decalin is an intermediate solvent which proved to retain wettability state in previously-aged surface minerals during adhesion tests. Decalin was later removed by flowing PO oil (used for wettability tests) until reaching irreducible conditions. Note that samples M1F30b and S29a1, previously used in wettability experiments and aged with PO and HUM-1689 oils, respectively (Table 7.9), were also used in these tests. M1F30b sample remained with its PO oil.

At irreducible water conditions, the samples were immersed in their respective surfactant + brine mixture in Amott imbibition cells. The cell consists of a graduated burette where oil naturally expelled (*i.e.* displaced) from the sample is recorded. Measurements were conducted at room temperature.

7.7.3 Results

C12TAB and Rhamnolipid surfactants observed good compatibility with brine (Fig. 7.23). The appearance of their solutions was clear and surfactants show acceptable miscibility in water. In contrast, the mixtures of CO-520 and SDBS produced viscous substances. SDBS show no solubility in brine and produced a sort of snowflakes floating in water. CO-520 surfactant precipitated a milky-like viscous solution. Figure 7.23 illustrates the brine/surfactant compatibility.

a) CO-520 **b) Rhamnolipid**

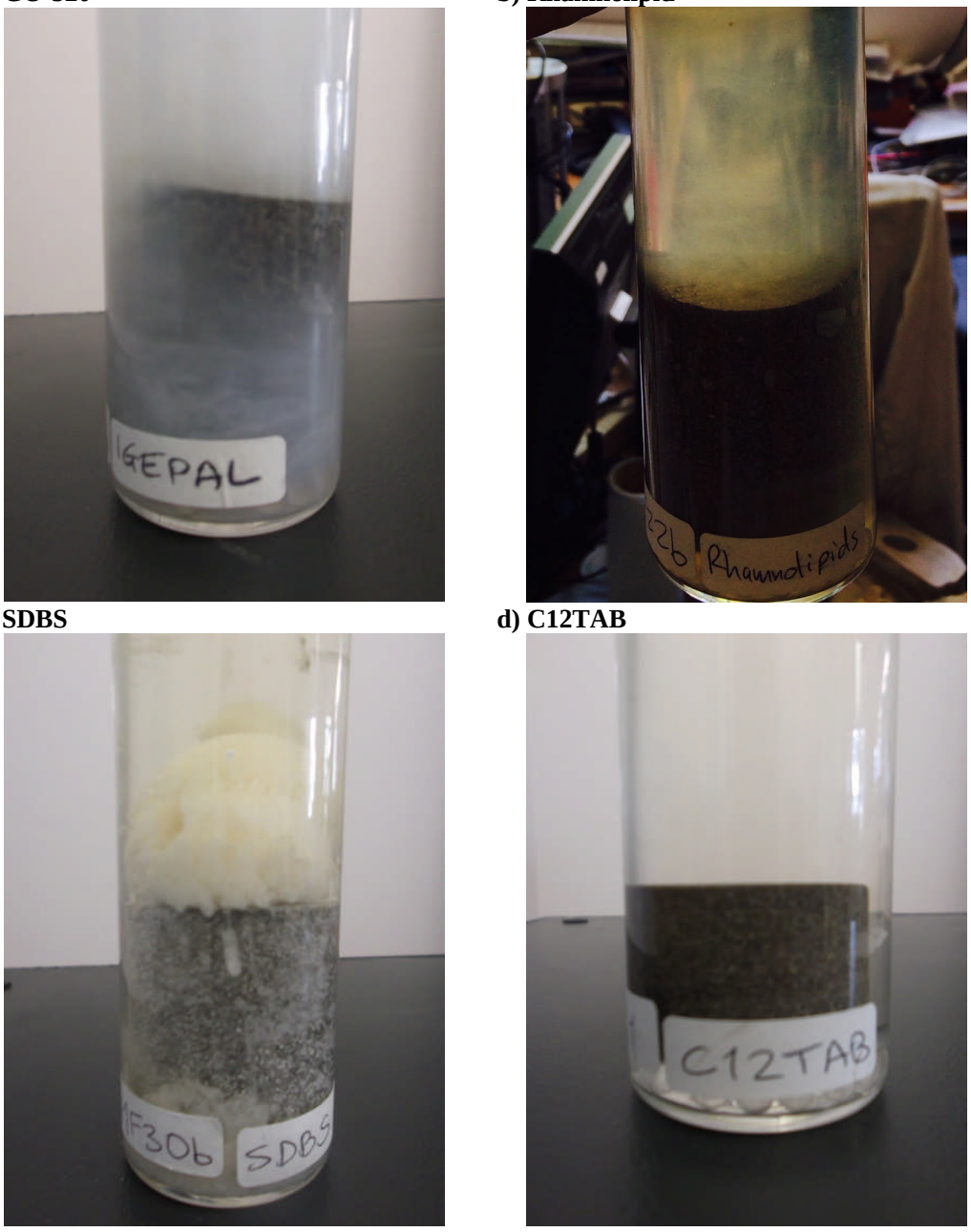

c) SDBS **d) C12TAB**

Figure 7.23 Surfactant/brine appearance. Observe the incompatible results of CO-520 and SDBS surfactants

Figure 7.24 shows the results obtained by using surfactants in spontaneous imbibition tests. No oil was recovered from M3F26a, M1F30b and S29a1 samples, even after 40 days of continuous testing. In previous spontaneous imbibition experiments (using just synthetic brine), M1F30b and S29a1 samples recovered 1.3 and 2.8% of their OOIP, respectively (Table 7.13).

Significant results were obtained in M4F22b sample which was immersed in *Rhamnolipid* biosurfactant mixture (Fig. 7.24). The oil recovered was of 11%, *i.e.* more than three times the average oil recovered in previous experiments using rock samples with equivalent characteristics (see Figure 7.18 and Table 7.13). The added oil recovered was ascribed as resulted from the surface active material.

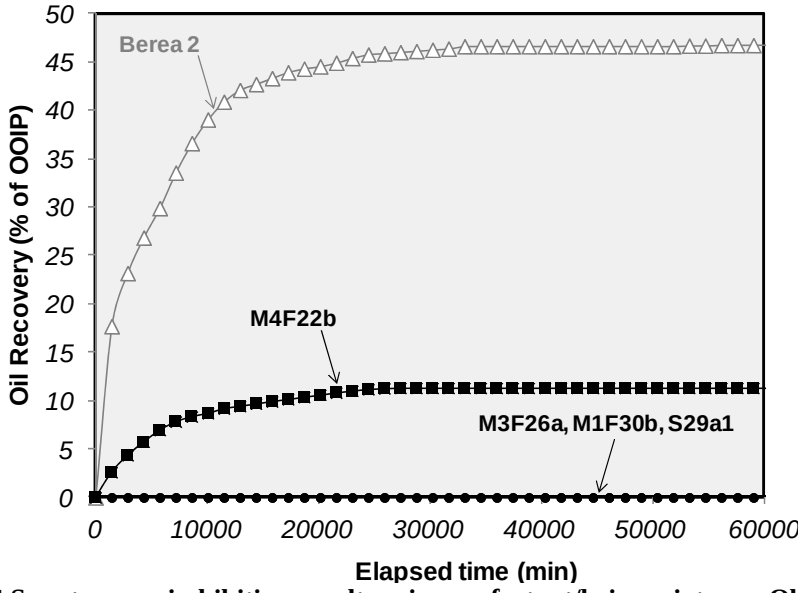

Figure 7.24 Spontaneous imbibition results using surfactant/brine mixtures. Observe that a recovery of up to 11% of the OOIP resulted from the *Rhamnolipid* solution. The strongly water-wet response of Berea 2 sample is also displayed for reference

7.7.4 Discussion

Although pragmatic, the results of these tests provide with additional information to be used for improving the oil recovery in Chicontepec reservoirs. Amongst the substances used, the biosurfactant show promising results, especially for improving the oil recovery efficiency in these reservoirs. *Rhamnolipid* has been referred in the literature as a substance with encouraging characteristics, due to it can yield a very low IFT at low concentrations (Fang *et al.,* 2007; Gray *et al.,* 2008), which in turn can lead to oil mobilisation.

The mechanism by which oil is recovered in M4F22b sample (*i.e.* whether is produced by lowering the oil/brine IFT or wettability modification) is uncertain, but the results are clearly encouraging. Further investigation should be conducted, especially to examine variations of oil recovery in a number of operating scenarios (*e.g.* surfactant concentration, temperature, brine

type). *Rhamnolipid* is currently available for laboratory applications only; however, commercial manufacturing would be feasible (Fang *et al.*, 2007).

It is unclear why in M1F30b and S29a1 samples (previously used for wettability experiments), no oil was recovered. The oil-wetness in both samples possibly increased since the samples remained immersed in oil for a period of six months before they were used for surfactant evaluation tests. No oil was produced in M3F26a sample either. This was interpreted as the result of the lack of compatibility between the surfactant and brine.

Stimulation fluids planned to be used for secondary and enhanced recovery mechanisms in Chicontepec reservoirs, should be specially designed not only for reduce capillary pressure by lowering the IFT, but also for reverse the wetting state of large pores from oil-wet to water-wet. The results obtained using *Rhamnolipid* biosurfactant may be promissory, although further analysis should be conducted.

7.8 Asphaltene Onset

During the development of this study, it was noticed a continuous production of bituminous particles in the HUM-1689 crude-oil sample (Fig. 7.25). These were ascribed as asphaltenes. Asphaltenes are normally referred as the most polar crude-oil fraction and are regarded to alter the formation wettability (to a more oil-wet state) by molecular adhesion in surface grains (Buckley, 1995; Anderson, 1986a).

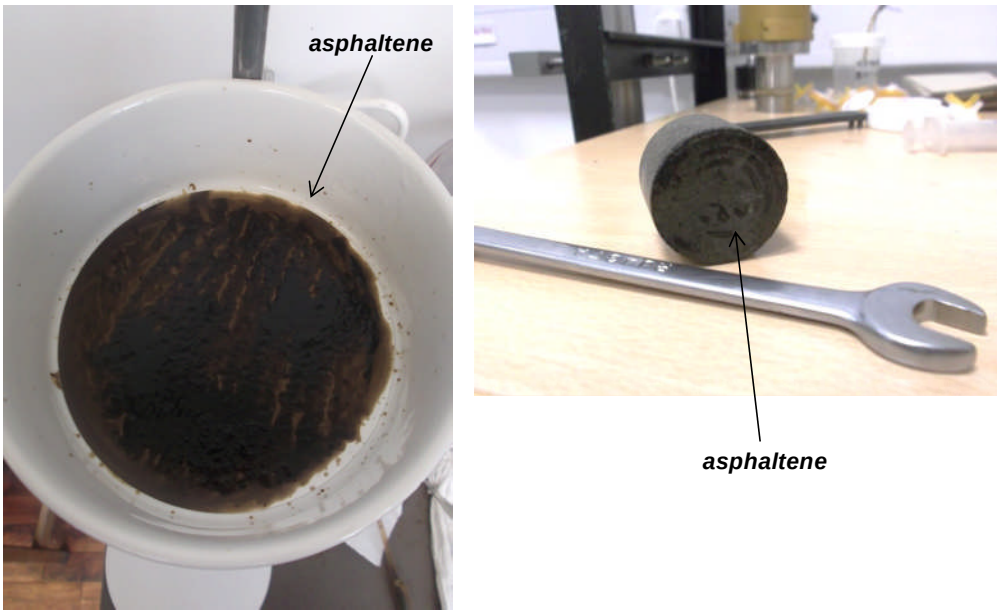

Figure 7.25 Residue remaining after crude-oil is filtrated and that is ascribed as asphaltene. In the opposite image, the plugging effect caused by asphaltene precipitation in one of the core's face during a fluid-displacement test

Predicting the onset of asphaltene precipitation is important in the petroleum industry for the following reasons: 1) to avoid production declination by scaling in ducts and pipes; and 2) to avoid permeability impairment due to precipitation around the wellbore. For laboratory applications, predicting the onset of asphaltene would be especially important to improve the core analysis procedures to ensure that formation conditions are effectively represented. The latter point is of special interest for conducting wettability experiments and relative permeability measurements.

A test was conducted to analyse the onset of asphaltene in the HUM-1689 crude-oil. The methodology was based on Al-Mahrooqi *et al.* (2006). The test consisted on examining the point at which asphaltene dissolves in toluene and the point at which asphaltene precipitates using n-heptane. The analysis of the asphaltene dissolution/precipitation was conducted through NMR T2 monitoring, and corroborated by Refractive Index (RI) measurements and weight differences of filtrate residues.

7.8.1 Materials

A dead-oil sample was obtained at separator conditions from a producing interval of HUM-1689 well in the study area. Compositional and physical properties were acquired and listed in Tables 7.7 and 7.8 in this chapter. Prior commencing the experiment, the heaviest fraction (*i.e.* asphaltene, resins, waxes, etc.) was removed from the crude-oil by centrifugation and by filtering through a 0.22 μm sieve. Two fractions were produced: the clean crude-oil and the asphaltene residue (*i.e.* sludge). The asphaltene sludge was re-dissolved by gradually adding toluene. The mixture obtained from asphaltene plus toluene (referred here as AT) was continuously filtered until no precipitate remained. Toluene is known to be a good asphaltene solvent.

7.8.2 Methodology

Samples of 4 ml volume were prepared in glass flasks by mixing clean-oil with the AT solution. The fluid proportions varied from 0 to 100% in 10% increments as described in Table 7.20. NMR relaxation distributions were acquired on each sample and their $T2_{LM}$ was recorded. NMR measurements were performed using an Oxford Instruments™ MARAN Ultra™ spectrometer at 2MHz frequency (described in chapter 3), at ambient pressure and operating temperature of 35°C.

Table 7.20 Asphaltene onset samples

Flask number	Clean-oil		AT	
	(%)	ml	(%)	ml
1	*100*	*4.0*	*0*	*0*
2	*90*	*3.6*	*10*	*0.4*
3	*80*	*3.2*	*20*	*0.8*
4	*70*	*2.8*	*30*	*1.2*
5	*60*	*2.4*	*40*	*1.6*
6	*50*	*2.0*	*50*	*2.0*
7	*40*	*1.6*	*60*	*2.4*
8	*30*	*1.2*	*70*	*2.8*
9	*20*	*0.8*	*80*	*3.2*
10	*10*	*0.4*	*90*	*3.6*
11	*0*	*0*	*100*	*4.0*

After NMR measurements, 2 ml of each sample was filtered through a 0.22 μm sieve to determine the presence of precipitate. The filters were then dried in a convection oven at 50°C until no change in weight was observed. The mass of the precipitate (attributed as the asphaltene) was determined by the change in filter's weight. The proportion of clean-oil/AT was plotted against $1/(T2_{LM})^2$ and a transition point is determined by the change in the linear trend

which was ascribed as the asphaltene dissolution threshold. The mass of the asphaltene was also used to validate NMR observations.

Having determined the transition point at which asphaltene fully dissolves in the crude-oil, six samples of mixtures of n-heptane and AT solution were prepared (n-heptane induces asphaltene precipitation, Table 7.21). Similarly, NMR relaxation distributions were acquired on each sample together with Refractive Index (RI) to validate observations. RI is normally used to determine the onset of asphaltene precipitation (*e.g.* Buckley and Wang, 2002; Wang and Buckley, 2001; Wang *et al.*, 1999).

Two millilitres of each solution were filtered through 0.22 μm sieve and the mass of the precipitated fraction was determined by weight differences. A plot of AT/n-heptane *versus* $1/(T2_{LM})^2$ was made to determine the transition point at which asphaltene in crude-oil is precipitated.

Table 7.21 Asphaltene onset samples

Flask number	n-heptane		AT	
	(%)	ml	(%)	ml
13	*90*	*3.6*	*10*	*0.4*
14	*80*	*3.2*	*20*	*0.8*
15	*70*	*2.8*	*30*	*1.2*
16	*60*	*2.4*	*40*	*1.6*
17	*50*	*2.0*	*50*	*2.0*
18	*40*	*1.6*	*60*	*2.4*

By observing the fluid proportions at which asphaltene fully dissolves in crude-oil and by inducing asphaltene precipitation with n-heptane; the transition points are compared and validated with RI and differences in weight of the precipitated residues.

7.8.3 Results

A transition point between 30 to 40% of oil/solvent ratio was determined (Fig. 7.26b). Asphaltene is dissolved in the crude-oil below 30% of oil/solvent ratio. This means that between 60-70% of solvent is necessary to maintain asphaltene flocculated.

Shorter relaxation distributions (or greater $1/(T2_{LM})^2$ values) were observed as the amount of oil increases. The most significant change in T2 distribution occurs at a threshold of 30-40%. This change was attributed to precipitation of asphaltene particles causing faster T2 responses. Figure 7.26 illustrates the results obtained.

Similar results were obtained when asphaltene was induced to precipitate in selected samples. The results are shown in Figure 7.27. A transition point between 30 to 40% of AT/n-heptane ratio was determined, indicating that between 60-70% of n-heptane is necessary to induce asphaltene precipitation in the HUM-1689 crude-oil. A change in the mass of the precipitated residue corroborates the results (Fig. 7.27b).

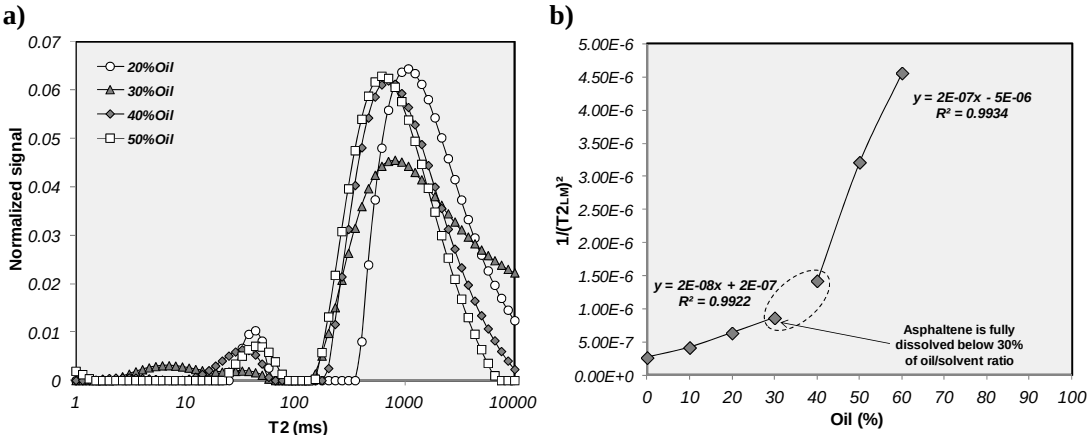

Figure 7.26 a) NMR relaxation distributions at different oil/solvent ratios; b) transition point at which the onset of asphaltene precipitation is determined

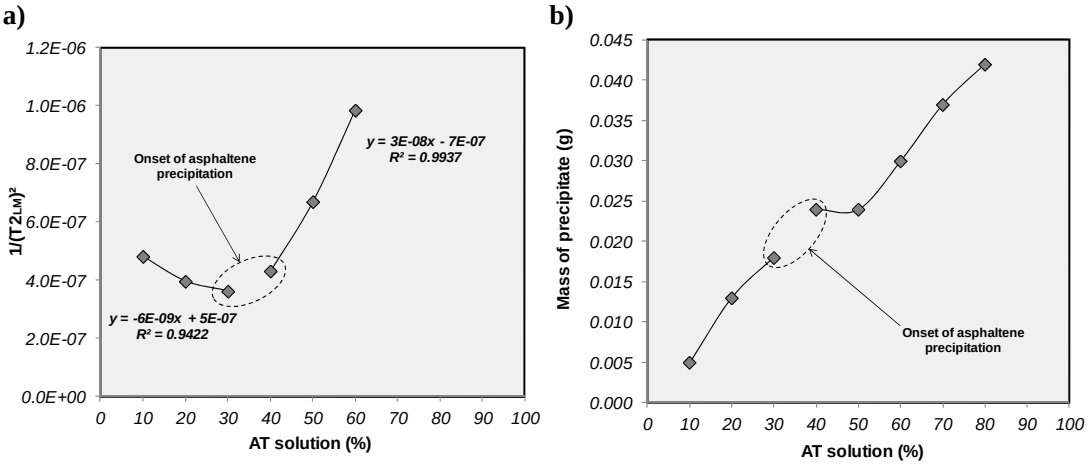

Figure 7.27 a) NMR observations at different AT/n-heptane ratios; b) change in the mass of the precipitated residue that is interpreted as asphaltene

Refractive Index also confirms the results (Figure 7.28). The RI was plotted against the AT/n-heptane ratio and a similar transition point was observed. Table 7.22 summarises the results obtained.

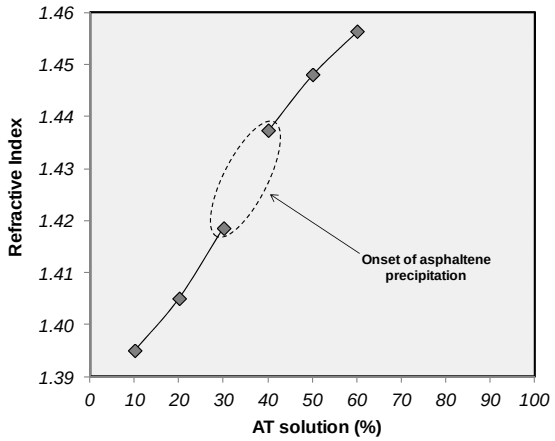

Figure 7.28 Refractive Index versus AT/n-heptane ratios. A transition point is determined between 30-40% oil volume fractions

Table 7.22 Asphaltene onset results

Flask number	n-heptane (%)	AT (%)	$1/(T2_{LM})^2$	Mass of precipitate (g)	RI
13	*90*	*10*	*4.82E-07*	*0.005*	*1.395*
14	*80*	*20*	*3.97E-07*	*0.013*	*1.405*
15	*70*	*30*	*3.63E-07*	*0.018*	*1.419*
16	*60*	*40*	*4.32E-07*	*0.024*	*1.437*
17	*50*	*50*	*6.70E-07*	*0.024*	*1.448*
18	*40*	*60*	*9.85E-07*	*0.03*	*1.456*

7.8.4 Discussion

The results obtained validate a novel procedure to evaluate the onset of asphaltene precipitation using NMR T2 relaxation distributions. Since asphaltenes are normally referred to influence the wetting characteristics of formations (Buckley, 1995; Anderson, 1986a), it would be expected changes in the wettability behaviour of rock samples when a stabilised crude-oil is used. Similarly, changes in relative permeability measurements are also expected since wettability partially controls the fluid distribution within pore space.

The results indicate that at least 70% in volume of toluene is necessary to be added to HUM-1689 crude-oil to keep asphaltene fully dissolved. The latter is significant to prevent particle precipitation or plugging effects during laboratory analyses and possibly to prevent formation damage around the wellbore during drawdown.

There is no prior information evaluating the precipitation of asphaltene in Chicontepec reservoirs. The results of this technique would be important for characterising the different crude-oils producing from Chicontepec basin. More importantly, the test can be used as a routine protocol to characterise crude-oils in these reservoirs.

7.9 DISCUSSION

The aim of the preceding experiments was to improve the general understanding of the rock/fluid interactions and formation damage mechanisms of reservoirs in this study, with the ultimate intention of enhancing stimulation practices in these.

Rock samples of this study reunite a series of characteristics important to be acknowledged, especially for trying to maximise oil recovery efficiency in the reservoirs of this study. The results describe a sensitive reservoir rock that is especially reactive to foreign fluids and with wetting properties rather comparable to a mixed-wet condition. Although more experiments are needed to be performed, the results show that special care should be taken when using fluids for completing/stimulating these reservoirs.

During the CSC tests, a number of trace elements were analysed using the ICP-AES technique since these were thought to be lixiviated from core samples. Although chemical analyses conducted to blank samples showed consistency with the obtained concentrations, a source of contamination should be produced from the device used. For example, the permeability setup used to conduct these experiments (*i.e.* pump, core-holder, pipes) is almost entirely made of a steel and aluminium. Since large amount of fluid was pumped in these experiments, it is expected that a portion of Al or Fe would be derived from the equipment. Similarly, the ICP-AES technique is highly sensitive to observe minor changes in element concentration, although in general it tends to be accurate. Unexpected readings were observed in element concentration and these were ascribed as the result of the device sensitivity (Fig. 7.5).

The flowback fluid efficiency of hydrofrac treatments in Chicontepec reservoirs is low and approximately accounts for 11% of the total fluids injected (Hurtado *et al.,* 2005). As it was demonstrated experimentally, the adhesion of polymer-based fluids into pore walls significantly reduces permeability for about 97%. Mitigation of damage in such low-permeability formations may be almost impossible because of the large capillary pressures needed. Alternative stimulation methods should be tested, especially for preventing from formation damage. Polymer-free, non-aqueous systems seem to be an alternate option to stimulate Chicontepec reservoirs.

One of the most significant achievements during the analysis of crude-oil/brine/rock interactions was the wettability assessment. The tests seem to provide a clearer picture of the wetting state of Chicontepec reservoirs and the series of experiments conducted for such purpose can be used as laboratory protocol for further analyses. At present, only the Amott-Harvey and the USBM (Donaldson *et al.,* 1969) methods are normally used as wettability assessment techniques not only in Chicontepec reservoirs but in the majority of the Mexican oilfields (onshore and

offshore projects). The wettability experiments conducted in this work demonstrate the importance of using diversified and complementary techniques to evaluate the wetting characteristics of such formations since no single method should be used as diagnostic.

The mixed-wet condition seems to be a proper term to refer the wetting state of the reservoirs in this study. Since Chicontepec reservoirs produce crude-oils with variable compositions, it should be expected that these may exert different wetting tendencies. Further analysis should be conducted to evaluate this variability. Wettability assessment by crude-oil adhesion tests and using restored-state core samples show an agreement in their results.

The surfactant concentration used in spontaneous imbibition experiments was selected since these have been referred as their optimal value in similar conditions of the reservoirs in this study (Fang *et al.,* 2007; Goddard *et al.,* 2007; Standnes and Austad, 2000; Golabi *et al.,* 2012; Torres *et al.,* 2011; Wu *et al.,* 2006). Two surfactants show incompatibility with reservoir brine and this was possibly due to either the type of brine (*i.e.* dissolved ions) or surfactant concentration. A prior screening of brine type and surfactant concentration is recommended for further experiments. Diverse authors suggest conducting a pre-analysis process to determine the optimum surfactant concentration in brine. For example, Goddard *et al.* (2007) suggest using aged calcite chips immersed in different surfactant concentrations. The optimum surfactant concentration is determined by means of their efficiency to remove crude-oil from the aged calcite surfaces.

7.10 CONCLUSIONS

A number of experiments to evaluate formation damage and crude-oil/brine/rock interactions in rock samples of this study were conducted. The results increase the level of understanding of Chicontepec reservoirs, and they may be used not only to improve the stimulation practices but also to support the exploitation labour of these reservoirs.

The CSC tests demonstrate that reservoirs of this study are water-sensitive at a critical brine concentration of 3.5%. Permeability reduction is possibly due to clay swelling. Lixiviation of the rock minerals is indicated by the increase of trace-element concentration (mainly Ca, K and Mg). The relative concentration of trace-elements in produced fluids behaves symmetrically with the ionic-strength of the brine, indicating the strong influence of ion-concentration and clay's stabilisation. Stimulation fluids employed in these reservoirs (to completion or secondary/tertiary applications to oil recovery) should avoid employing brine concentrations below this critical value.

Significant formation damage is produced by polymer-based gelling agent normally used for fracturing treatments. This indicates that either: 1) the flowback recovery efficiency should be improved in these reservoirs to prevent polymer adsorption, or 2) alternate fracturing fluids (*e.g.* CO_2-based, gelled-methanol or viscous-elastic fluids) should be employed to prevent formation damage. The poor performance in oil production observed in a number of reservoirs in this study may be resulted from this mechanism.

A mixed-wet affinity is observed in rock samples of this study. The latter is thought to be produced by the combination of the reservoir rock mineralogy and the crude-oil properties. Observations made from adhesion tests show that crude-oil has more affinity to calcite than quartz which may indicate a fractionally-wet condition of the reservoirs in study. However, the term that describes best the wetting conditions of these samples, as observed from experimental data, is mixed-wet and refers that oil is preferentially located as continuous phase in the larger pores whereas smaller ones behave as strongly water-wet. This condition results in greater residual oil saturations and greater k_{ew}/k_{eo} ratios during fluid-displacement tests, compared to strongly water-wetted scenarios. The relative permeability behaviour of these reservoirs is complex and may be controlled by the relative contribution of large oil-wet and small water-wet pores.

After primary depletion, the remaining oil in the reservoirs of this study would preferentially be located coating the surface of the larger pores. This is an important input parameter to be considered for IOR/EOR applications. The selected method for oil recovery should not only address the problem of recovering oil by reducing IFT, but also to try to modify the wettability

condition of the oil-wetted larger pores. This was intended by using four commercial surfactants during a series of spontaneous imbibition tests. Amongst the surfactants evaluated, the biosurfactant (*Rhamnolipid*) showed interesting characteristics that should be analysed in more detail in further work. The oil recovered using this surface active material was almost three times the amount recovered by using synthetic brine in similar rock samples.

Finally, a novel laboratory procedure to evaluate the onset of asphaltene precipitation was conducted. The technique used NMR T2 relaxation distributions to determine the amount of solvent necessary to prevent precipitation of asphaltene. The test was validated with refractive index measurements and additional data. The procedure may be incorporated as a routine test to characterise crude-oils in the Chicontepec basin.

CHAPTER VIII. RESERVOIR MODELLING AND SIMULATION

The aim of this chapter is to analyse the spatial distribution of rock properties of a selected reservoir unit in the study area and assess their impact on oil productivity and recovery. The analysis is conducted through the modelling of the S4 reservoir, which is the most prolific sand unit in the study area. Rock properties interpreted from wireline data were modelled using a series of analytical techniques to evaluate their vertical and horizontal variability. These were then upscaled and combined with the interpreted sedimentary facies to predict their likely spatial distribution. The modelled rock properties resulted from this approach were used as input for conducting a number of simulation scenarios to try to explain the low productivity of these reservoirs. The effect of rock property distribution together with the extension of the induced fracture on oil productivity was analysed.

8.1 Introduction

It has been previously discussed that the reservoirs of the study area are compartmentalized as is evidenced by the segregated pattern of their produced fluids and production performances. This is illustrated in Figure 8.1 in which a high variation in productivity is observed in a stratigraphically-equivalent unit. In the image, three wells were completed almost simultaneously at the S4 reservoir. The stimulation treatment and their petrophysical properties were similar but the production performance and their cumulative oil resulted significantly different. This behaviour describes a characteristic that is consistent not only in the reservoirs of this study but also in almost the entire sand units of Chicontepec basin.

The wide variation in production performances may be attributed to the heterogeneous character of the reservoir. An additional example to illustrate the high heterogeneity in these reservoirs is shown in Figure 8.2, in which the equivalent drainage area of wells producing at the S4 reservoir is estimated. The example depicts the net-to-gross (NTG) ratio which was produced by interpolating (*i.e.* convergent interpolation) the NTG values of each well, resulted from the well-log analysis. The estimated drainage areas are displayed only in those wells completed in a single interval at the S4 sand unit (*i.e.* commingled production is not considered).

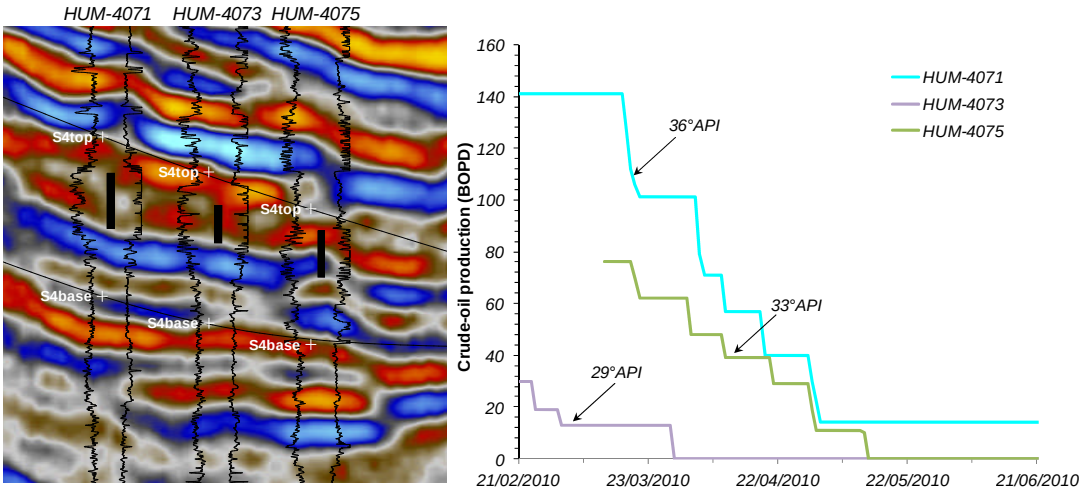

Figure 8.1 Example of the compartmentalization typically observed in the reservoirs of this study. The three wells were completed in similar conditions (the perforated interval is shown by the black rectangle) but the production performance differs widely. The graph shows the four-month production behaviour and the gravity of the produced oil. Note the apparent sandbody discontinuity between wells, which may explain the different well performance. The wells are 400 m spaced

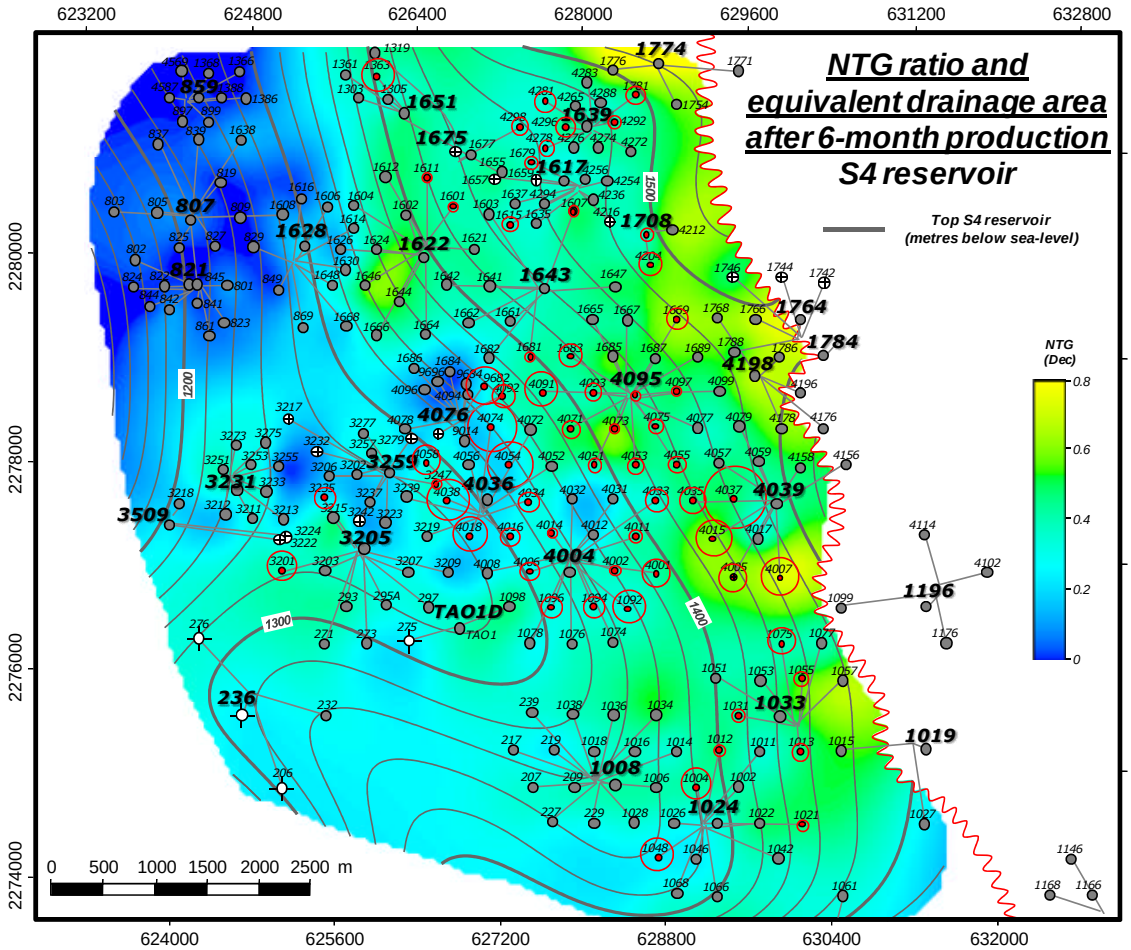

Figure 8.2 Equivalent drainage area per well after six-month production at the S4 reservoir. Observe the apparent low-drainage influence per well even in sand-rich areas

The volume of oil produced after six months (time during which most wells deplete by their primary drive mechanism and more than 60% of the total accumulated oil is produced in most wells) was converted into equivalent drainage areas. This was calculated assuming an oil formation volume factor (B_o) of 1.2 rb/STB and individual rock properties of each well in the S4 sand unit. In most cases (Fig. 8.2), the well's drainage area covers only half of the well spacing, demonstrating the low-drainage areas of each well, which may be caused by the reservoir's heterogeneity and/or low effective permeability. This means that a significant portion of the reservoir seems to not be drained, suggesting that infill drilling should be evaluated. Occasionally, the drainage area of a number of wells surpasses the 200 m drainage radius; however, this is not a consistent behaviour.

The apparently small-drainage area of wells and consequent low-oil recoveries may be attributed to the heterogeneous character of the rock properties. Tyler and Finley (1992) demonstrated that highly-heterogeneous reservoirs typically describe poor recovery efficiencies. To evaluate the role of rock property distribution in productivity (and in this way to evaluate the well-to-well communication), the S4 reservoir was analysed through a series of modelling techniques. Property distribution was also evaluated considering the sedimentary facies previously described. The outcome of this analysis served as an input parameter for reservoir simulation.

Figure 8.3 illustrates the workflow of the analysis conducted to the S4 reservoir. Each stage shown in Figure 8.3 is described in detail in the following paragraphs.

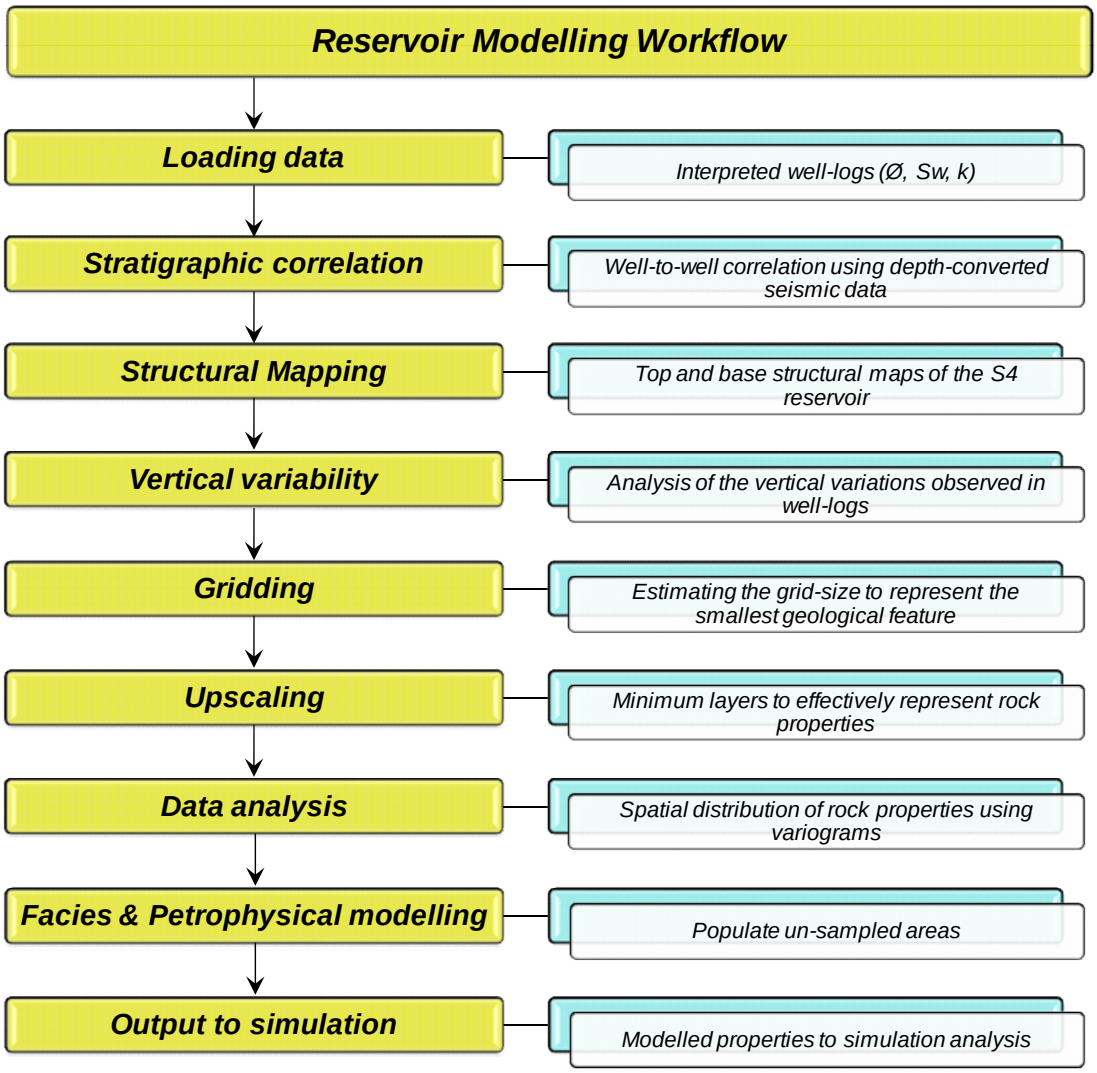

Figure 8.3 Reservoir modelling workflow

8.2 Reservoir Modelling of S4 Unit

Once the well-logs were processed in the *Interactive Petrophysics*® software, they were uploaded into *Petrel*®. In this platform, a well-to-well correlation was conducted using depth-converted seismic data thus the regional stratigraphic framework of the study area was produced. The S4 reservoir was selected to conduct a more detailed analysis as this is the most prolific unit in the study area and subjected to future development strategy.

Since an acceptable number of data-points were available in the S4 reservoir (*i.e.* 263 wells) and these were uniformly distributed from each other (*i.e.* regularly spaced every 400 m); a simple interpolation was applied to construct structural maps (Fig. 8.4). Most of the wells intersect this unit vertically; however, a number of wells were observed to have a slight deviation from the vertical. Spatial position of data-points was conducted using the deviation surveys of each well.

Kriging was selected as the preferred interpolation method since this provided a fairly good estimate of the structure as it was observed by the interpreted data-points. Kriging is an interpolation method that estimates the value at an unsampled location in a statistically rigorous manner so the error involved in the prediction is minimised (Shepherd, 2009). The algorithm produces a rather smooth surface map compared to other methods (*e.g.* convergent, minimum curvature, Gaussian) and more suitable for simulation purposes. Both top and base structural maps of S4 reservoir were produced (Fig. 8.4).

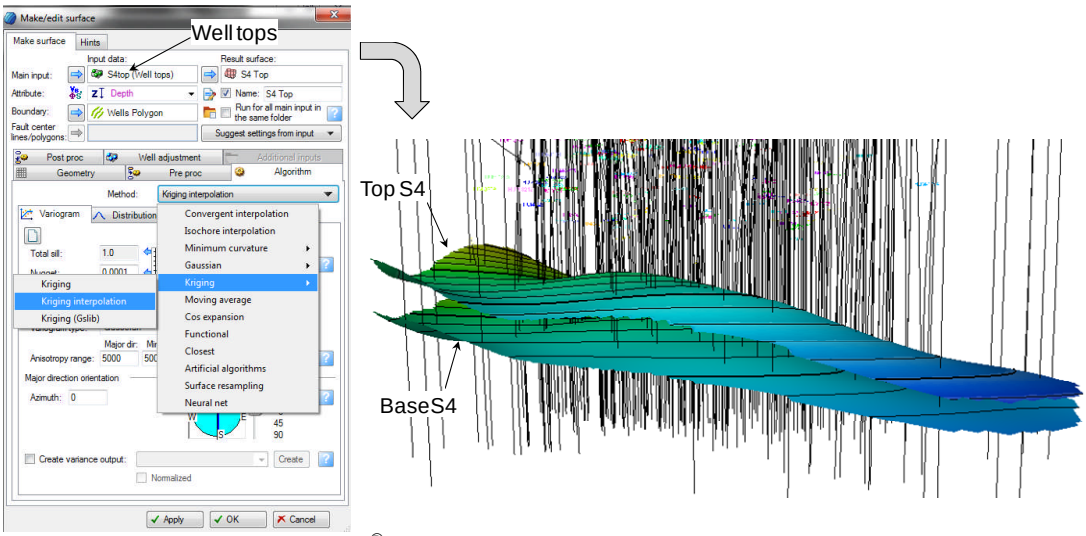

Figure 8.4 Dialog box in *Petrel*® for estimation of structural maps of the S4 reservoir. No faults were recognised in the entire study area

8.2.1 Vertical Variability

Lorenz and Dykstra-Parsons coefficients were used to evaluate the grade of vertical heterogeneity in two pairs of wells in the study area. This was conducted as an aid in the upscaling process to estimate the number of layers necessary to represent the vertical variations of rock properties.

Lorenz coefficient (L_k) was developed by Law (1944) to describe the grade of dissimilarity between porosity and permeability. The technique consists of computing the cumulative capacities of porosity (*i.e.* *Storativity*=$\sum(\emptyset h)_i/\sum(\emptyset h)_i$) and permeability (*i.e.* *Transmissivity*=$\sum(kh)_i/\sum(kh)_i$), plotted in a Cartesian graph. The coefficient is estimated by comparing the resulting curve with the behaviour described by a completely homogeneous reservoir.

Dykstra-Parsons coefficient (V_k) measures the grade of permeability dispersion by comparing the fluctuations of the arithmetic and harmonic averages of permeability (Jensen *et al.*, 1997). For log-normal permeability distributions, V_k is estimated by:

$$V_k = 1 - EXP\left[-\sqrt{\ln\left(\frac{k_a}{k_h}\right)}\right]$$

where k_a and k_h are the arithmetic and harmonic permeability averages, respectively.

Both coefficients were used to describe the grade of heterogeneity between rock properties. The reservoir is considered to have a uniform property distribution if coefficients approach zero. In contrast, the reservoir is considered to be completely heterogeneous if both indexes move towards the unity.

Two pairs of wells were used to evaluate the grade of vertical variability of petrophysical properties. The first pair was selected from a uniform alignment of high-NTG ratios in the study area (*e.g.* HUM-4005 and HUM-4007), where it is expected that vertical variation between sands may be low and the communication between wells is likely to be high. The other pair of wells (*e.g.* HUM-4093 and HUM-4073) was located in an area with lower NTG ratios. Figure 8.2 shows the location of wells. The coefficients were computed using the same sample increment of 0.1524 m in each well.

Figures 8.5 and 8.6 illustrate the comparison between low- and high-NTG wells and their vertical variation of rock properties. The wells are displayed in the same scale and spaced 400 m each other. The estimated petrophysical properties of each well are plotted together with their vertical heterogeneity coefficients. Lorenz coefficients are low (*i.e.* less heterogeneous) in the

pair of wells with uniform high-NTG ratios (Fig. 8.5). Dykstra-Parsons indexes, in contrast, are fairly similar in the four wells. Even by visual comparison, it can be observed that vertical property distributions vary significantly. The GR log even expresses what seems to be a completely different sand unit, despite their relative proximity. A more scattered behaviour in the vertical direction of water saturation can be observed in comparison to porosity and permeability in the four wells.

Lorenz and Dykstra-Parsons coefficients were also estimated in the remaining wells of the study area at the S4 reservoir. Overall, high vertical heterogeneity is observed in most wells. Lorenz coefficients varied from 0.3 to 0.97, whereas the Dykstra-Parsons index averages 0.87. The grade of vertical heterogeneity is high and mainly controlled by the sand/shale proportions (*i.e.* NTG ratios).

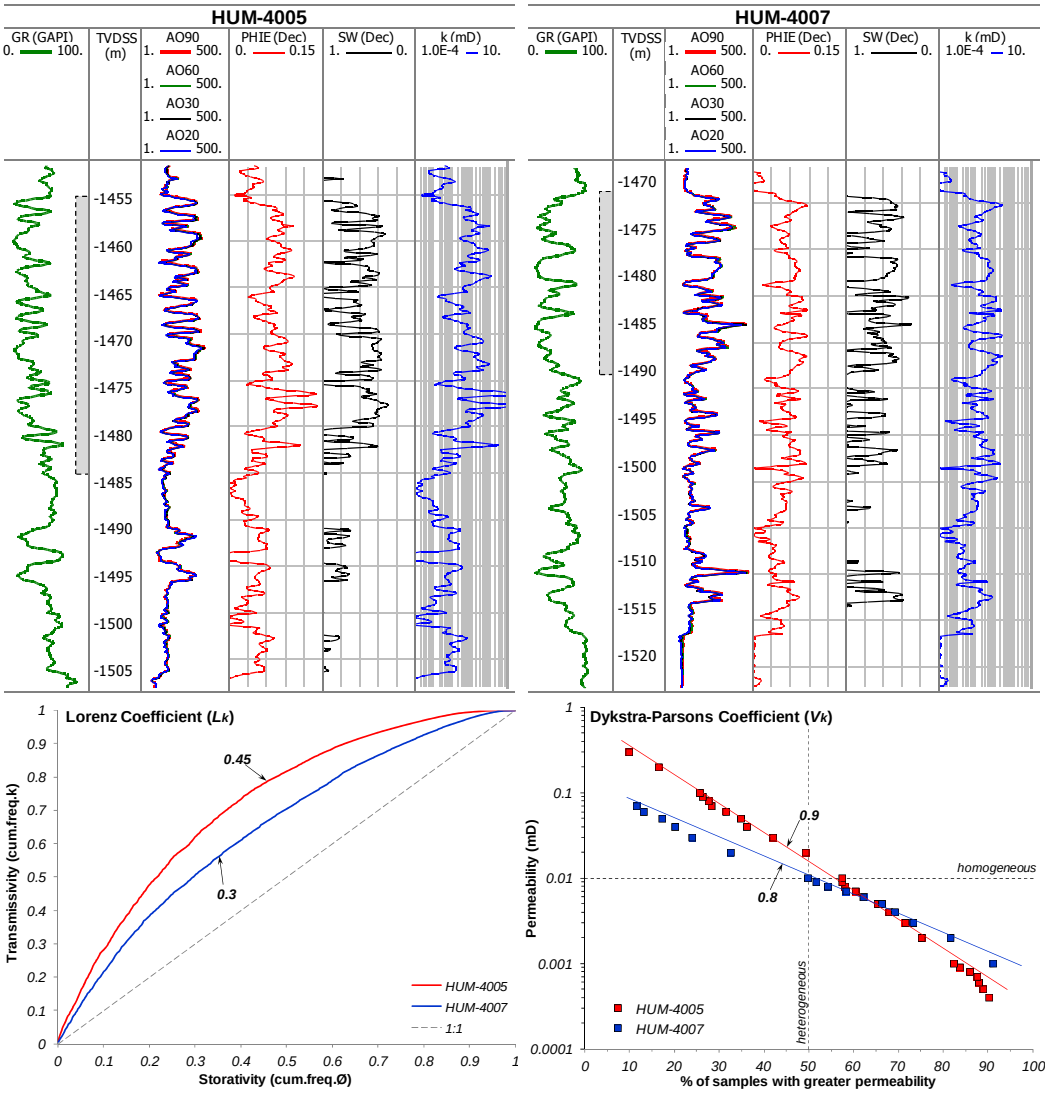

Figure 8.5 Comparison of vertical heterogeneity in two wells with similar NTG ratios (~75%). High variability in their petrophysical properties is observed

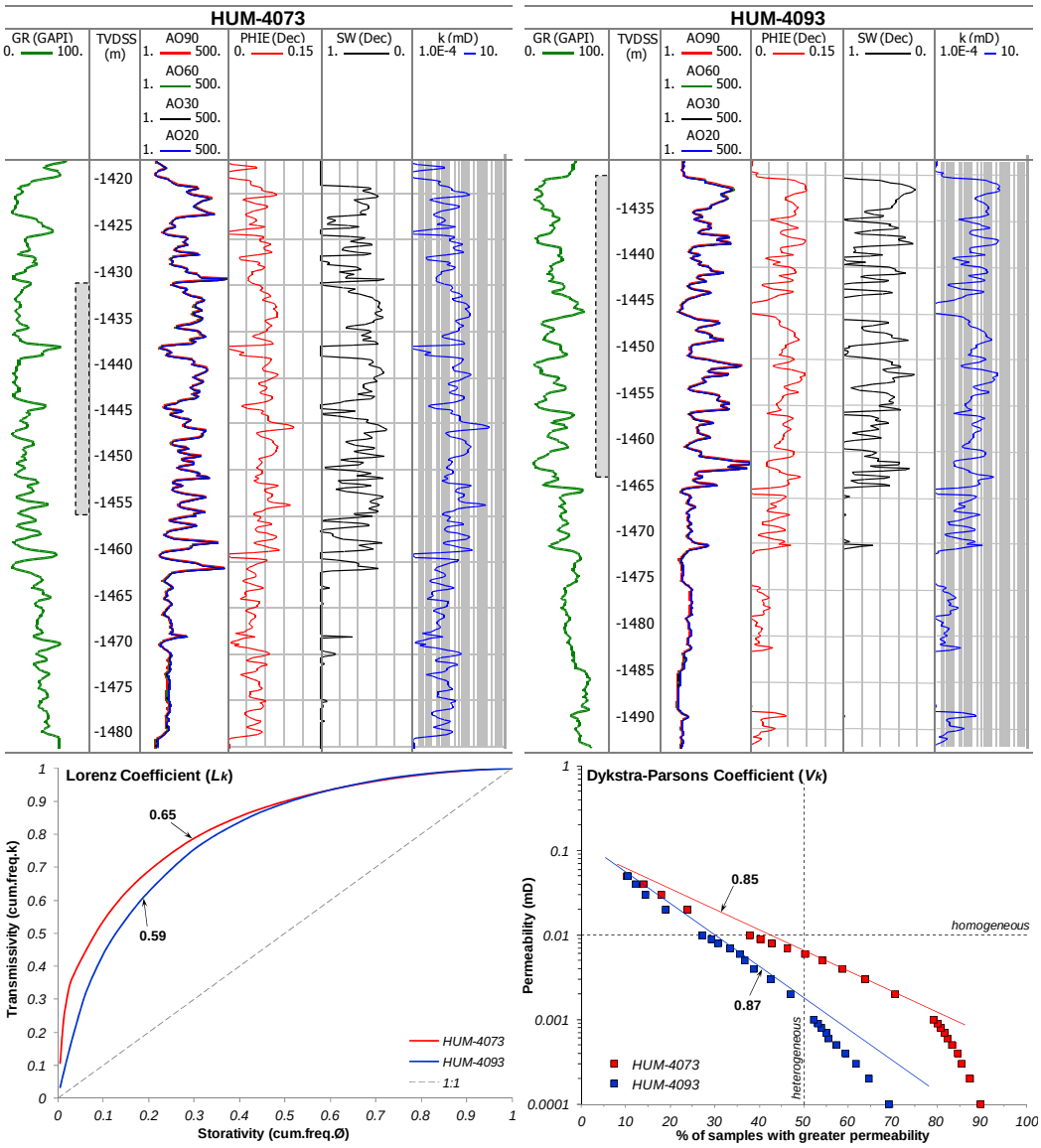

Figure 8.6 Comparison of vertical heterogeneity in two wells with different NTG ratios (75% and 55%, respectively). As occurred in previous example, wide fluctuations in their petrophysical properties are observed

To analyse the grade of spatial heterogeneity of rock properties in the S4 reservoir, a number of approaches were conducted. The study area was gridded and well-logs upscaled to make further analyses.

8.2.2 Grid-size and Upscaling

Grid size was selected to reproduce the narrowest geological feature desired to be evaluated. This feature was a channel-like geometry associated to a high-amplitude reflector that was partially intersected by HUM-1624 and HUM-1644 wells (Fig. 8.7). Its minimum width is approximately 100 m and is 700 m long. The grid size selected was of 50×50 m, *i.e.* at least two cells were used to resolve this feature. Similarly, between 6 and 8 cells were used to fill-in between wells, as these are spaced between 300 to 400 metres. A simple grid was constructed between the top and base of the S4 structural maps. No faults were recognised in the entire study area.

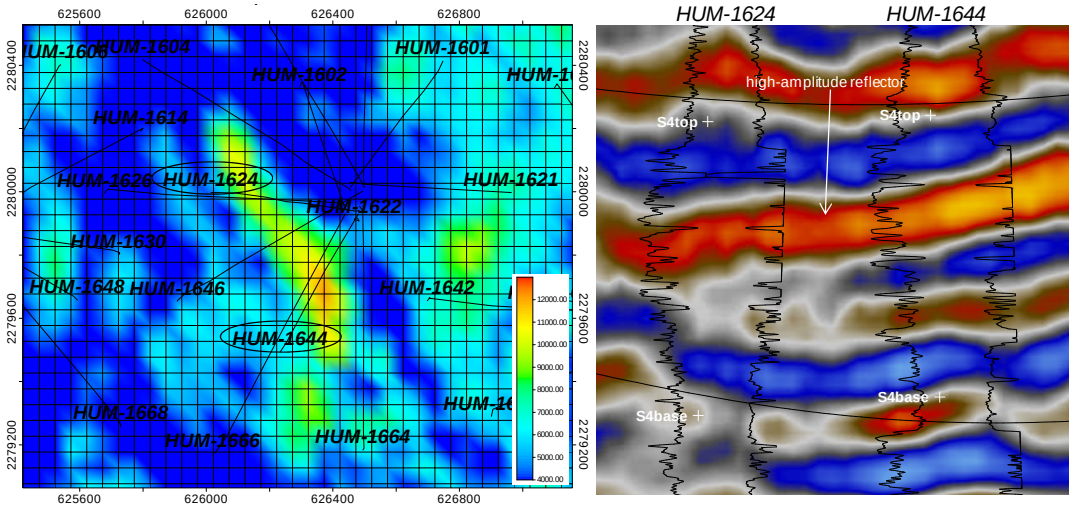

Figure 8.7 Maximum amplitude map at S4 reservoir level. Observe the channel-like geometry corresponding to high-amplitude values. Grid-size (50x50m) is also displayed to validate cell dimensions. Seismic line in the opposite follows the orientation of the channel. Observe the apparent sandbody discontinuity between wells

Gross sand thickness of S4 reservoir varies from 30 to 150 m, averaging approximately 100 m in most wells. Different scenarios were analysed to upscale well-logs to ensure that properties was properly replicated without employing an excessive number of layers (*i.e.* avoiding long computer run times). These methods included arithmetic, median and random pick techniques. Seventy layers were selected to upscale well-logs which seem to be sufficient to reproduce their vertical variability. Considering that S4 gross thickness is approximately 100 m thick and that this was subdivided into 70 layers, then log values were averaged (scaled) every 1.4 m.

Different averaging methods were analysed to upscale well-logs (*e.g.* arithmetic, harmonic, geometric, etc.). Among these, the Median technique was selected to upscale porosity and water saturation. Permeability shows an acceptable fit with the Random Pick method. The Median interpolation method selects the median value between cells and generally provides an acceptable prediction of continuous parameters (*i.e.* with normal distributions), such as porosity

and water saturation. The Random Pick technique selects a value at random within the cell. This technique avoids the smoothing tendency of other methods and is more likely to give a property with similar distribution of values as the original well log data. The porosity property was resulted from the wireline interpretation and it was estimated by a combination of neutron/density logs corrected by clay content. The water saturation was estimated using the Dual-Water equation whereas permeability was resulted from the porosity-based model.

The selected averaging method for each category reproduced the property consistently, according to their histogram comparison (Fig. 8.9). The log values were averaged for all cells that the well trajectory penetrates. Figures 8.8 and 8.9 illustrate the results obtained.

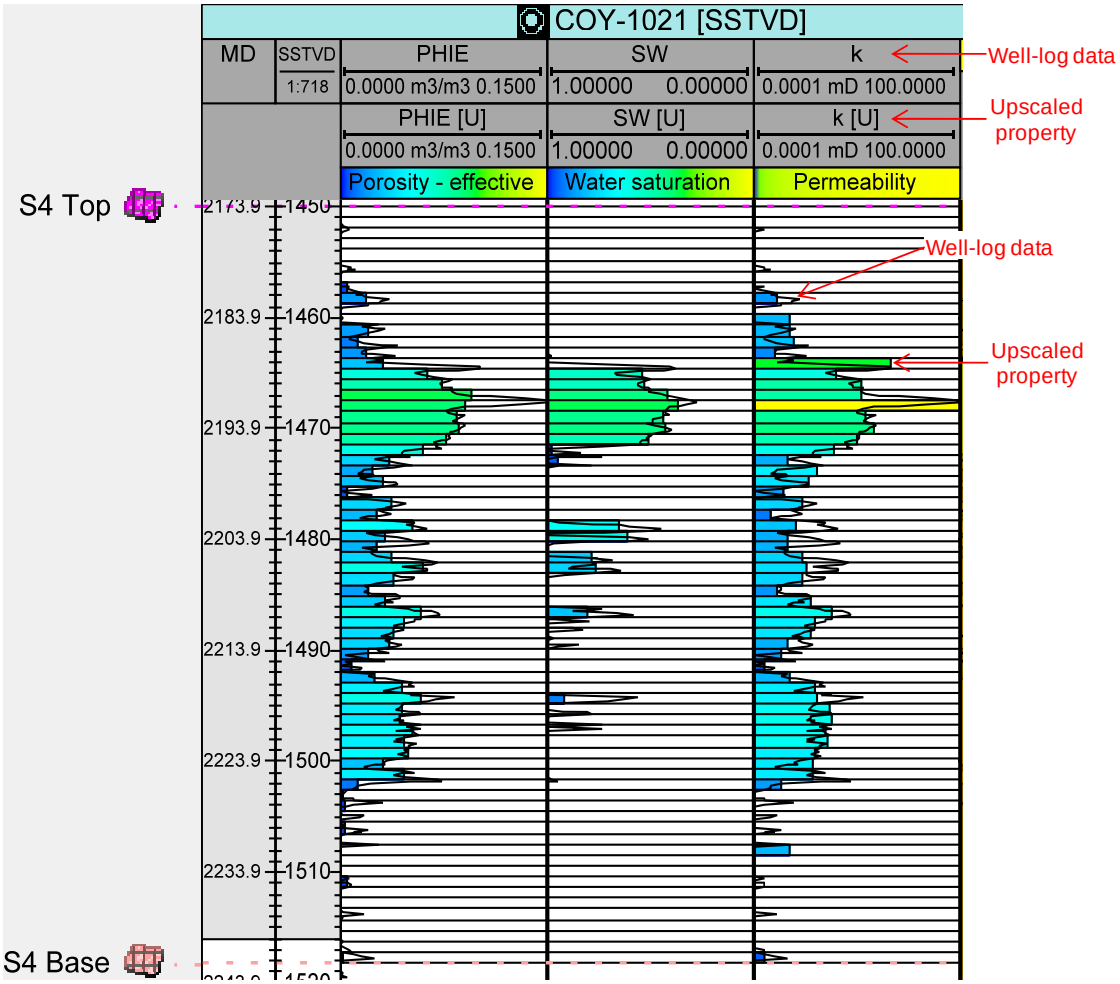

Figure 8.8 Comparison of well-log values and upscaled property in a well of the study area. Upscaled property is shown as block bars. Overall, an acceptable agreement was obtained

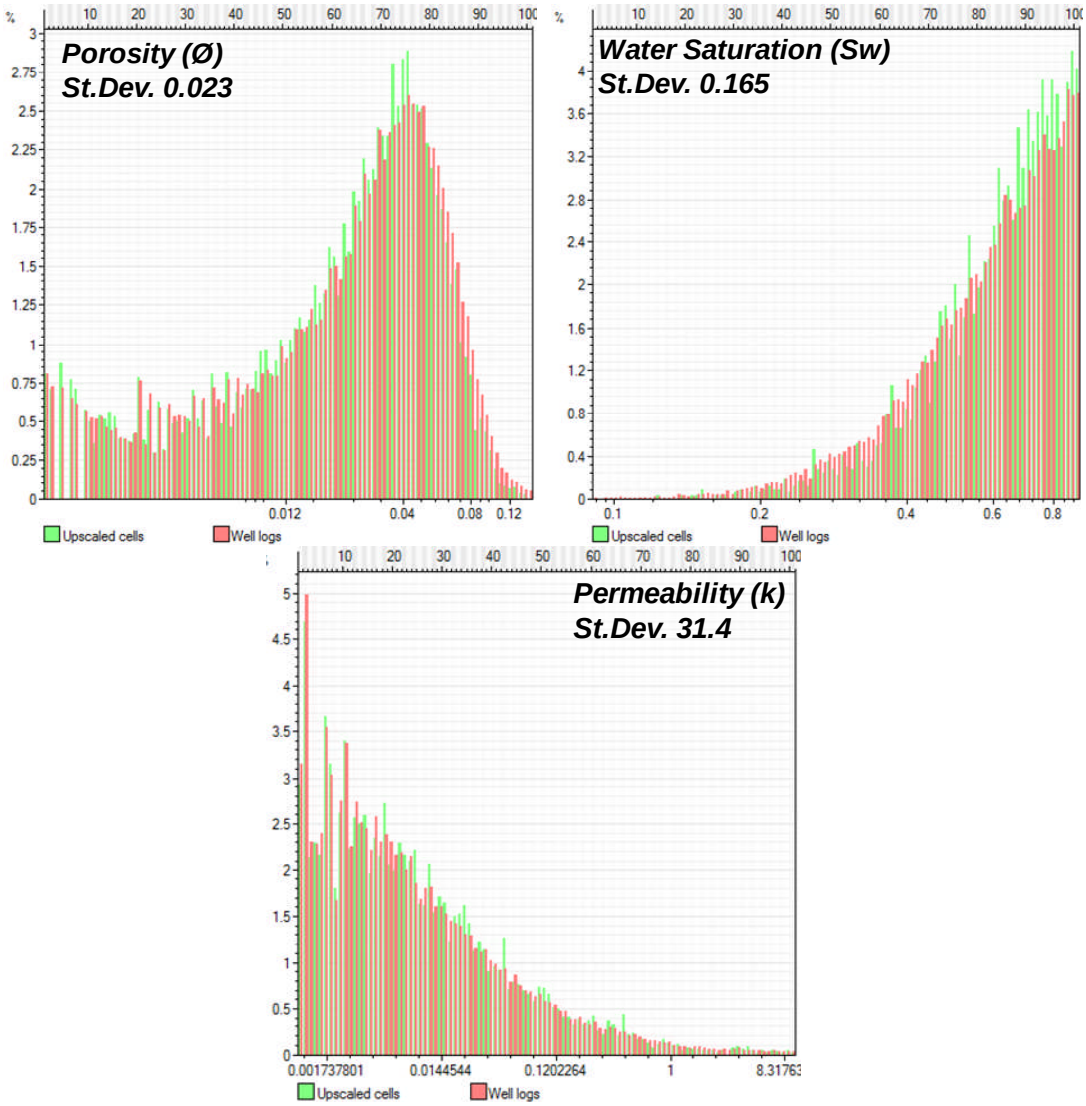

Figure 8.9 Frequency histograms of the upscaled rock properties and their comparison to well-logs. Overall, an acceptable match was observed. Minor differences were observed (especially in the high-end values of Sw) which are the intrinsic effect of the selected interpolation model

8.2.3 Spatial Continuity

A number of techniques were used to evaluate the grade of heterogeneity of petrophysical properties. Diverse variograms were constructed to describe and quantify the spatial order of rock properties in the S4 reservoir. These were later employed as input parameter data for predicting rock properties in un-sampled locations of the study area (*i.e.* stochastic modelling). A variogram is the representation of the variability of a given rock attribute through distance. It is based on the concept that two data-points tend to be more similar when they are close together. As the distance of comparison increases, the data-points tend to be more different until they reach a point in which there is no correlation between them. The variogram is the sum of the squared differences of data-points falling within a specific range of distances, divided by twice the number of the pairs compared (Chambers *et al.*, 2000). For example, the variability of porosity through distance may be expressed as:

$$\gamma(h) = \frac{1}{2N(h)} \sum_{i} (\emptyset_i - \emptyset_{i+h})^2$$

where: $\gamma(h)$ is the variogram or the semivariance, $N(h)$ is the number of data pairs, and $(\emptyset_i - \emptyset_{i+h})$ is the difference between porosity values. The main elements that describe the variogram are shown in Figure 8.10. The variability should increase with increasing distance. This means that the rock property values are becoming more different until they reach a plateau point. The variogram value where the plateau is reached is known as the *sill*, and the corresponding distance to the *sill* is the *range*. The rock property values are considered to be completely uncorrelated (*i.e.* unpredictable) beyond the *range*. The variogram will develop a positive value known as the *nugget* when a significant variation in rock properties exists at distances shorter than the sample spacing.

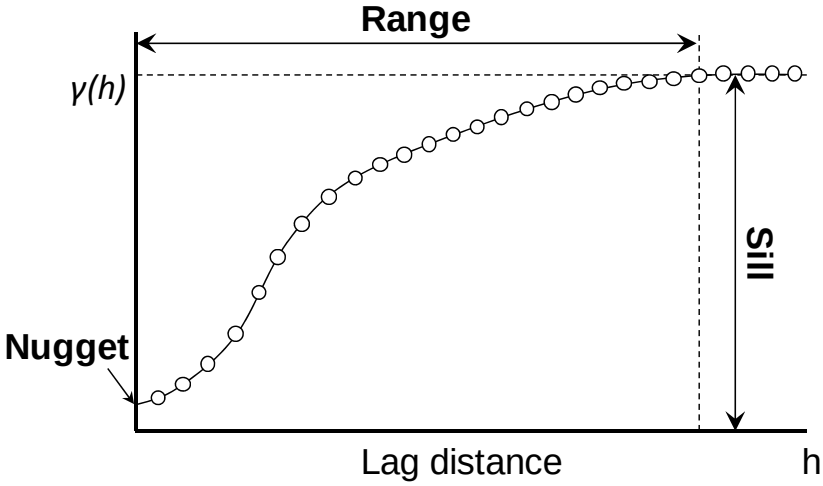

Figure 8.10 A variogram is the graphic representation of how a rock attribute varies over distance (modified from Shepherd, 2009)

In general, large *range* values are representative for rock property distributions with homogeneous behaviour. This signifies that the rock attribute can be correlated over large distances. In contrast, small *range* values mean less continuity between widely spaced points.

Rock properties can also vary according to orientation. Shepherd (2009) states that the rock attributes tend to be more predictable for longer distances along depositional strike than they are along depositional dip. To improve the degree of comparison between rock attributes, the data pairs can be grouped into lag distances and use different orientations. Figure 8.11 illustrates an example of how the data is grouped into different lag distances. The variogram is constructed comparing pairs of data from wells falling in the same searching cone.

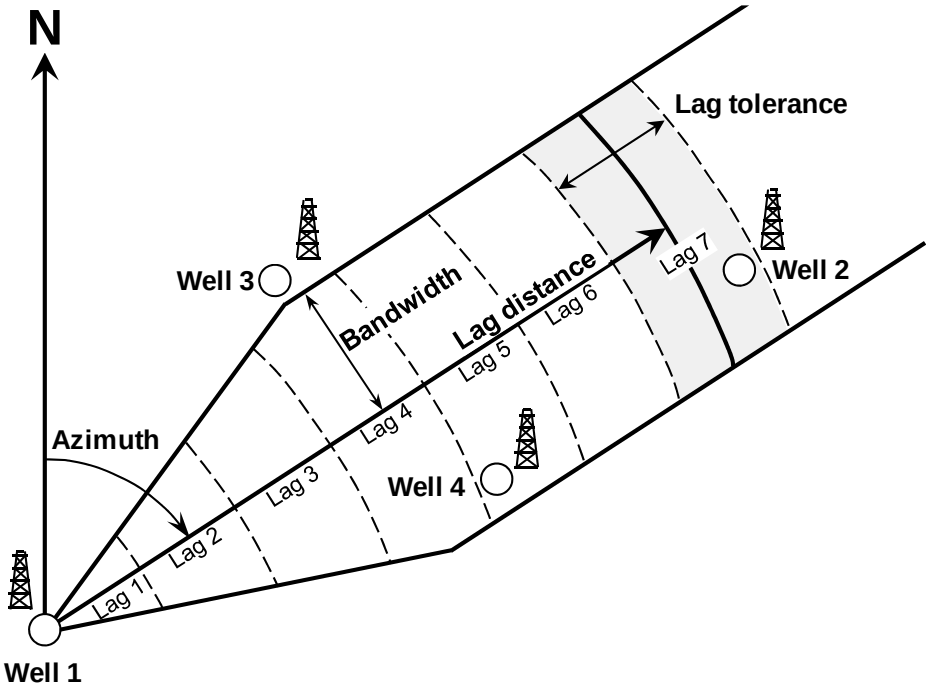

Figure 8.11 Example of how the data is binned into different lag distances. In the image, well 3 is discarded for comparison (modified from Shepherd, 2009)

A number of horizontal variograms were constructed to analyse the grade of heterogeneity of porosity, water saturation and permeability between wells in the study area. These were built covering the entire radial orientation of the project and at different searching distances. A significant variation in rock properties is observed in most directions even at short well spacing. The variograms were characterised by having *nuggets* above 0.5 and normally the *sill* was reached in the first hundred meters. Figure 8.12 shows an example of the search cone parameters used for comparing rock properties in the reservoir S4 of this study. In the image, the parameter to be evaluated is the upscaled porosity. The search cone has 80° orientation (*i.e.* almost East-West direction), covers a maximum distance of 2000 m (*i.e.* five well spacing) and has a bandwidth of 400 m. The cone is divided into 10 lags (*i.e.* 200 m each, half of the well

spacing). The resulting variogram is shown at the bottom of the image. In the example, the *nugget* value is 0.47 and major/minor *ranges* are automatically computed by the software, although in this case the *range* is approximately 1800 m. The model used to fit the variogram and that showed the best correlation was the Exponential. The Gaussian and Spherical methods did not replicate the characteristic high *nugget* values and the steeped slopes observed in the variogram.

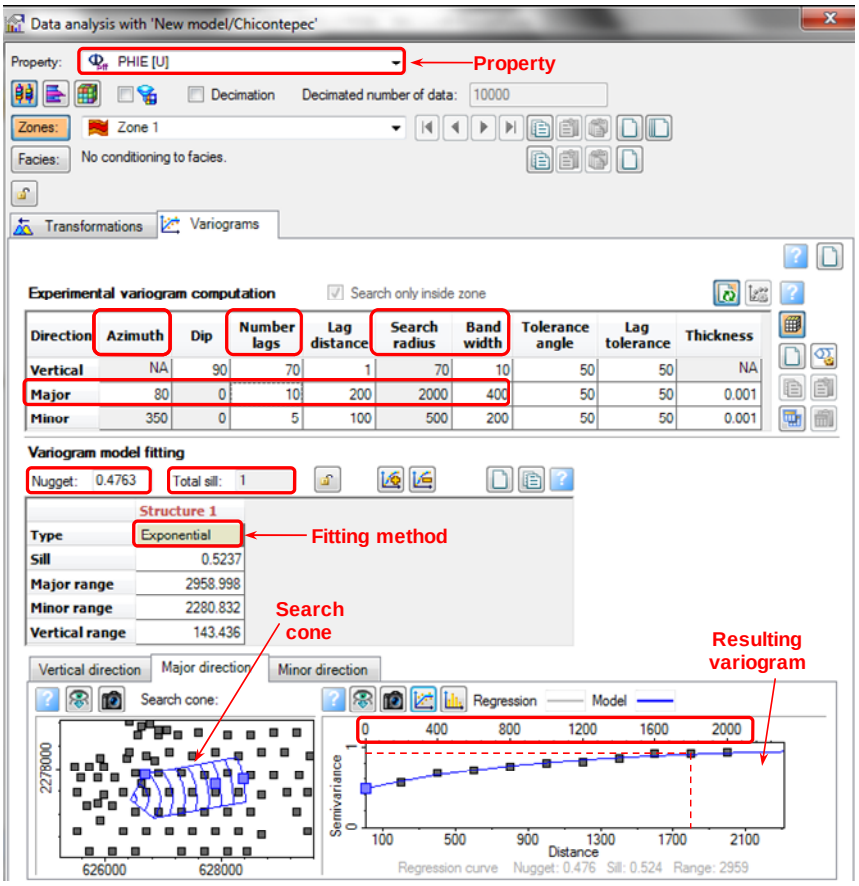

Figure 8.12 Dialog box for comparing porosity in a 2000 m search radius in the study area. Observe that well-to-well vertical comparison is made using the 70 layers in which the model was upscaled

Variograms were built from 0 to 170° of radial coverage and the results are shown in Figures 8.13 and 8.14. Note that the variogram values are normalised to the unity, thus *nugget* and *sill* values are correspondent. Overall, rock properties were observed to have a high spatial heterogeneity. Porosity was found to have more continuity over distance than permeability and water saturation. A maximum *range* distance of 1800 m was observed for porosity at 80° azimuth (Figs. 8.12, 8.13). This means that the property can be correlated in almost five well spacing in that particular orientation. The *range* values for permeability and water saturation varied between 400-600 m and 200-400 m respectively, revealing that these can be correlated in no more than just one and a half well spacing. From the three variables, water saturation

observed the least continuity over distance, possibly because its dependence to other parameters (*e.g.* pore geometry, fluid distributions, wettability).

The highest degree of correlation between rock properties was found at 80° azimuth in the three attributes (Fig. 8.13). This orientation is approximately orthogonal to the channelized area described in previous chapters, confirming that rock attributes seem to be more predictable along their depositional strike (Shepherd, 2009).

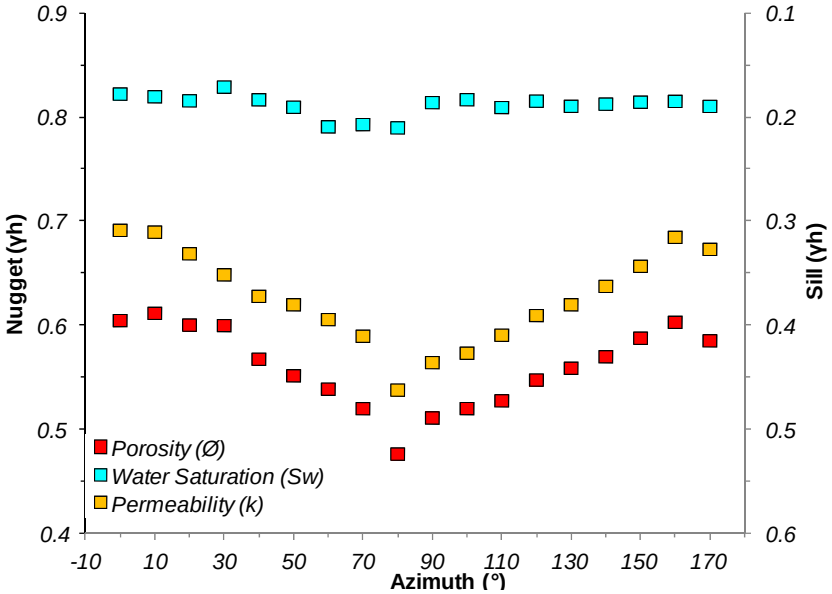

Figure 8.13 *Nugget* and *sill* values for each rock property at different search cone orientations. Note that the highest degree of continuity was found at 80° azimuth in the three attributes

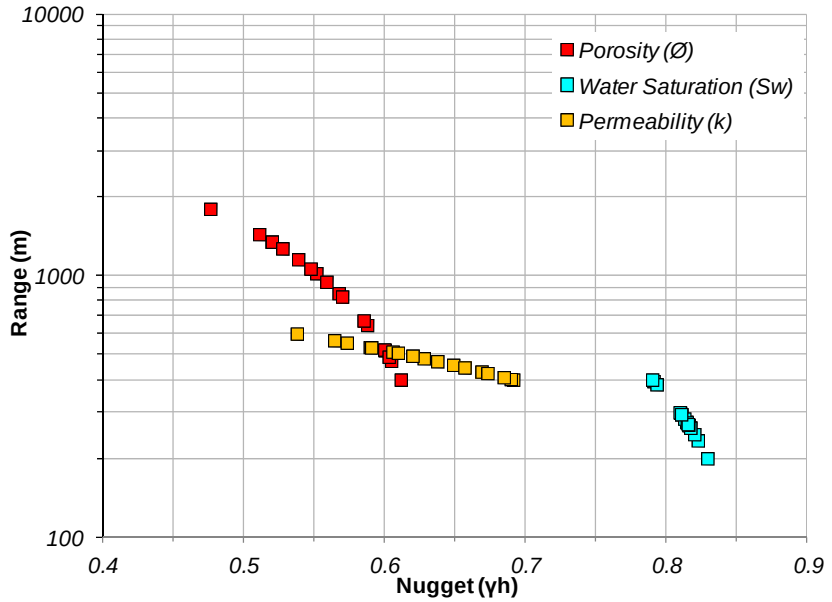

Figure 8.14 *Range* and *nugget* estimates at diverse variogram orientations. Porosity can be best correlated over distance than permeability and water saturation, although the overall behaviour of the rock attributes describes a low spatial continuity

Rock property variation was also analysed by facies conditioning. Overall, as the facies were invoked, the properties resulted even more heterogeneous. For example, a *range* of 990 m and a *nugget* of 0.76 were estimated for porosity at 80° azimuth in lobe facies.

Vertical variograms were also constructed to complement the evaluation of vertical heterogeneity of the rock properties. The resulting vertical variograms together with their descriptive parameters are shown in Figure 8.15. The results obtained from vertical and horizontal variograms were used as input parameter for stochastic modelling.

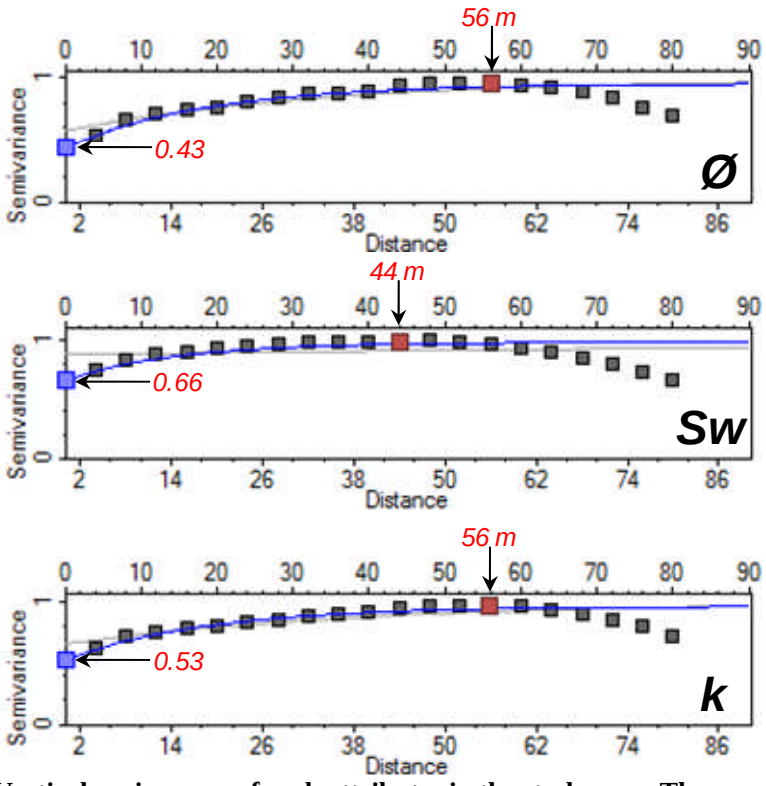

Figure 8.15 Vertical variograms of rock attributes in the study area. These were estimated using the average values of 263 wells through the 70 vertical layers at the S4 reservoir. Observe the characteristic high *nugget* values and *ranges* normally varying from 40 to 60 meters. The curve that best fitted variability was exponential

8.2.4 Facies Modelling

It has been previously discussed that despite of the intense diagenetic alteration, the sedimentary facies still exert a significant control on rock quality in the reservoirs of this study area. Sedimentary facies were also used as a guide to model petrophysical properties. These were defined in the well-logs, upscaled to the project's grid, and modelled according their interpreted spatial distributions. The sedimentary facies were later employed for conditioning petrophysical modelling.

The S4 reservoir describes a coarsening-upward sequence that is mainly composed of three sedimentary facies: stacked lobes (*i.e.* overbank and levee deposits), channel complexes, and shale intervals (*i.e.* interlobe or non-reservoir rocks).

Channels were manually defined as they are easily recognised from their characteristic well-log response (*i.e.* blocky-shaped signatures). Lobe and mud facies were then calculated as it is shown in Figure 8.16. Mud facies were defined as anything different from channel with porosities lower than 3%, which in most wells corresponds to intervals with water saturations between 70 and 100%. The remaining rock volume (*i.e.* anything different from channel and mud) was interpreted as lobe facies.

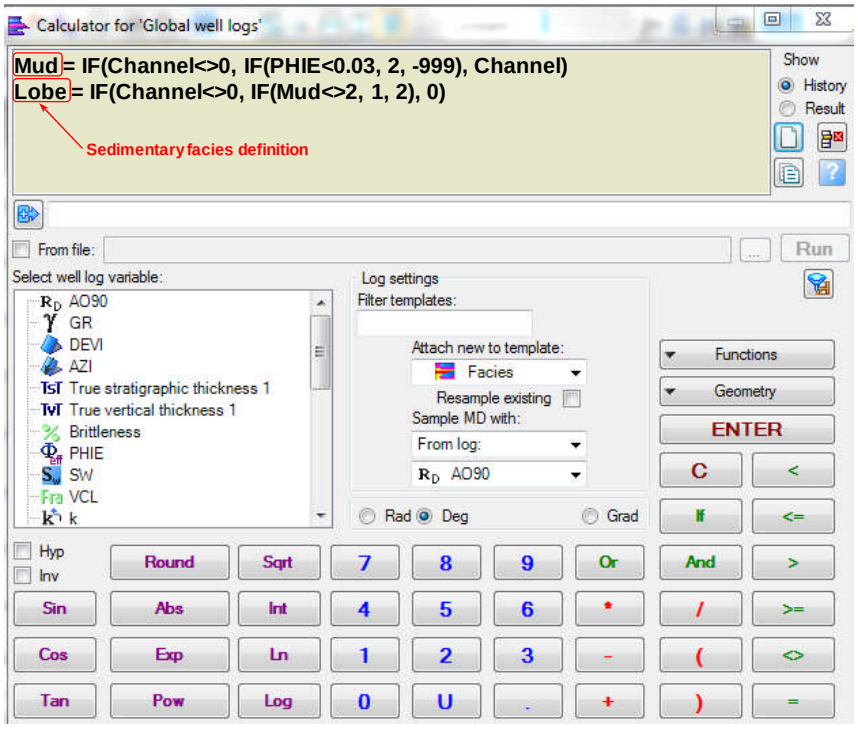

Figure 8.16 Calculator box dialog where the facies were defined as discrete data. This was conducted as a guide to evaluate rock property distributions. Note that channel, lobe and mud were internally codified as 0, 1 and 2, respectively

The facies were upscaled using the arithmetic technique which gave an acceptable reproducibility as observed in Figure 8.17. Sedimentary facies definition using this approach permitted correlation of petrophysical properties and facies. Figure 8.17 shows the comparison of rock attributes with the upscaled sedimentary facies. The S4 reservoir describes a coarsening-upward sequence and the best rock qualities are normally observed at the mid- to top-portion of the sequence that is mainly composed by lobe and channel facies (Fig. 8.17). Mud facies were mostly distributed at the bottom of the sequence and occasionally interbedded between channels and lobes.

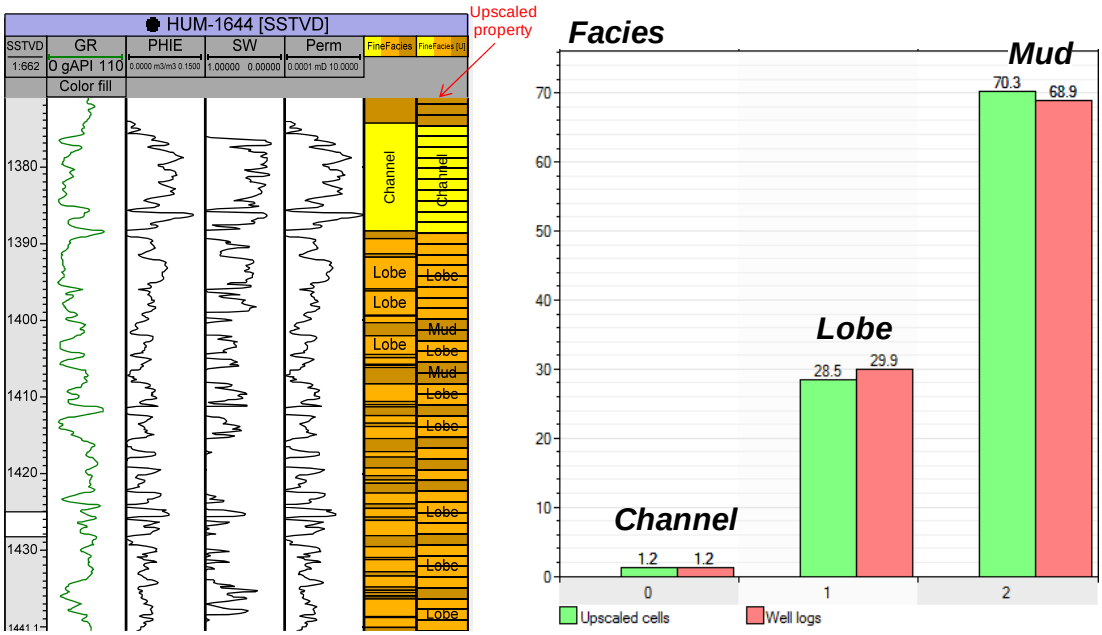

Figure 8.17 Interpreted sedimentary facies and their corresponding petrophysical properties. Observe that rock quality distribution is generally in agreement with the coarsening-upward nature of the sequence. Best rock qualities are normally developed in the mid to upward portions of the sequence mainly composed by channel and lobe facies. The image at the right shows the comparison of facies observed in well-logs (red) and upscaled (green)

From the total rock volume evaluated (*i.e.* 263 wells intersecting S4 reservoir), channel and lobe facies represent together a proportion of 29.7%, corresponding only 1.2% to channel. The rest (70.3%) corresponds to mud facies. From the interpreted wells, only 16 were observed to contain channelised facies, indicating their apparent low-frequency or possibly their moderate to high sinuosity.

Once the sedimentary facies were upscaled, these were modelled according to their interpreted spatial distribution that was previously discussed in chapter four. Channels were interpreted to follow a -20° orientation (*i.e.* sedimentary supply was interpreted to origin from northern portions of the study area), have moderate sinuosity and apparent poor amalgamation. A width-

to-thickness ratio of 5:1 was estimated from well-log and seismic attribute observations. This information was used to model channels in the study area, which is shown in Figure 8.18.

Channels were interpreted in *Petrel*® using the Object Modelling option shown in Figure 8.18. Four channels were selected as this was the optimum number that approximately reproduced the percentage of channels observed in well-logs. No levee was selected since this was interpreted to be part of the lobe facies which in turn were analysed separately.

High deviation in NTG ratios were observed in channel facies at inter-well distances. This seems to be the result of moderate to high sinuosity of channels. The spatial distribution of the channels in the study area was defined based on their amplitude and wavelength. Their amplitude was interpreted to vary from 300 to 800 m. Their wavelength was interpreted to be approximately twice the amplitude length to give the channels a rough geometrical shape (Fig. 8.18).

The channel section was defined by integrating the maximum amplitude map (Fig. 8.7) with their interpreted aspect ratio. The width of the channel varied from 50 (*i.e.* the grid size) to 200 m, whereas the channel thickness was then estimated using a width-to-thickness ratio of 5:1. Finally, the channels were interpreted to follow a -20° orientation, as this was delineated by observing the position of channels intersected by wells. Flow lines oriented in this direction were used to give the channels that determined trend.

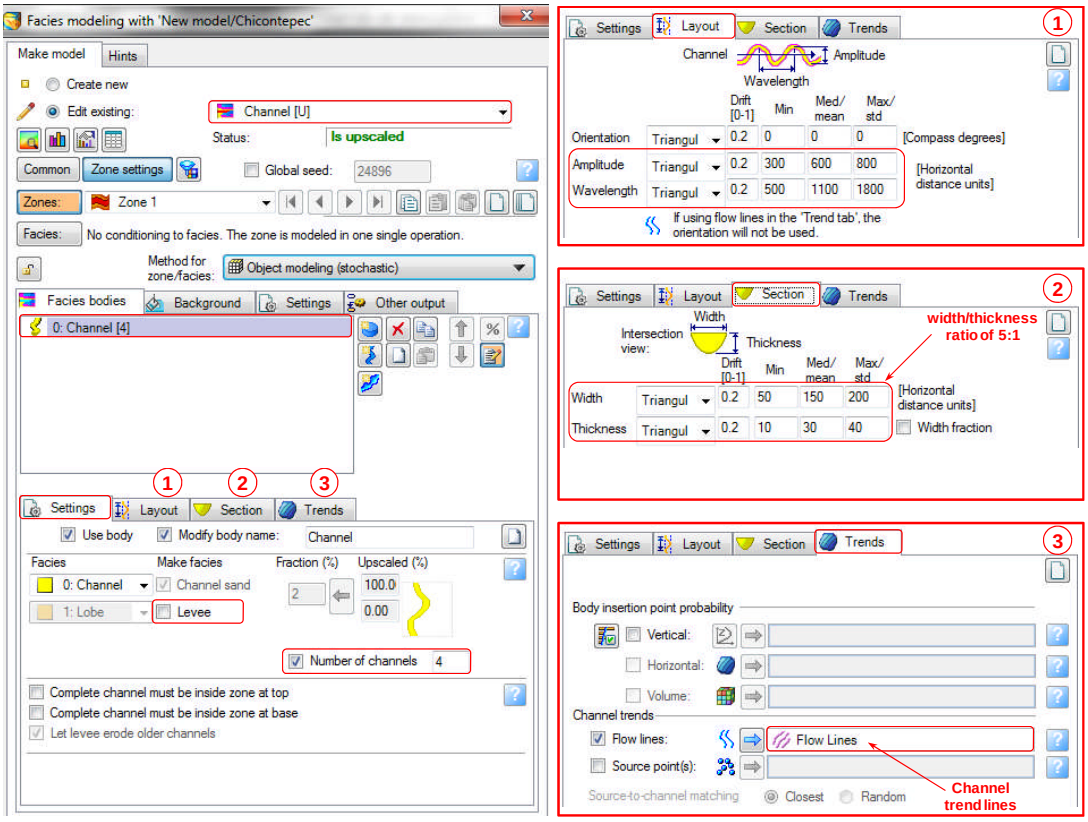

Figure 8.18 Dialog box showing the input data to model channels in the study area. The input parameters used to define their spatial geometry and internal characteristics were resulted from sedimentary and well-log observations

Figure 8.19 shows the modelled channels. These follow a -20° orientation, show poor amalgamation and moderate sinuosity, as they were interpreted from sedimentary and well-log observations.

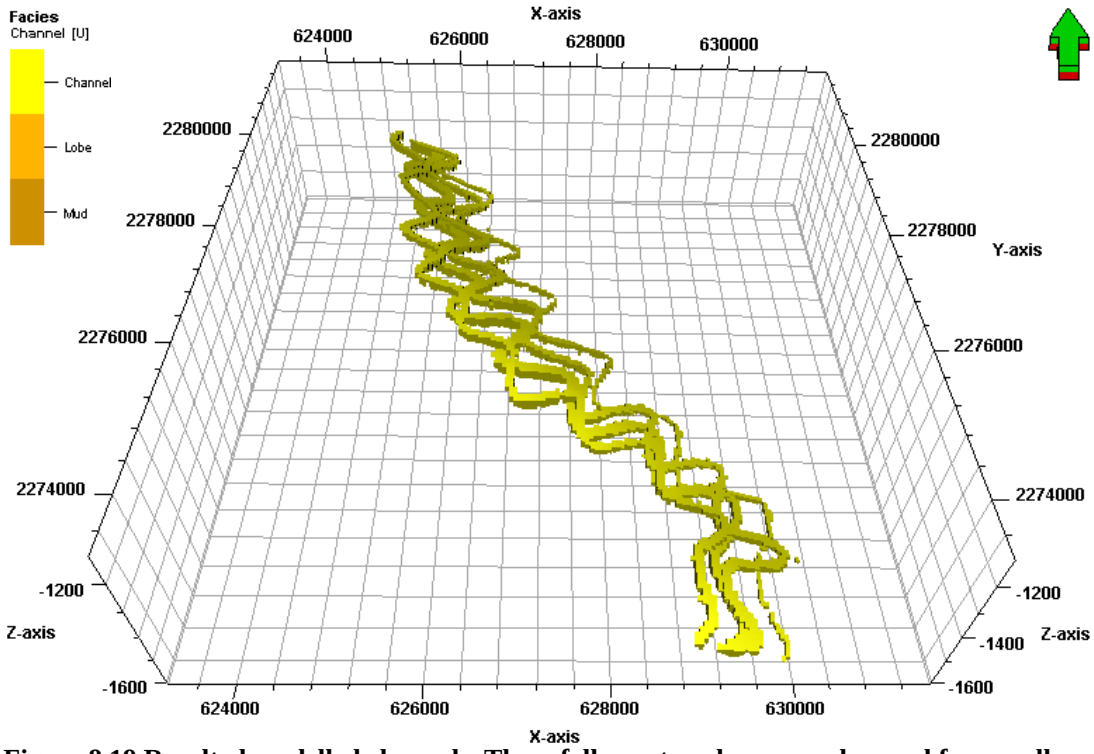

Figure 8.19 Resulted modelled channels. These follow a trend as were observed from well-log data, following a general -20° orientation (maximum longitudinal extension of channels is approximately 9.5 km)

Despite channels, lobes were interpreted to develop more continuous behaviour as these are mainly composed of multiple stacked sand units. Their spatial distribution is thought to result from their sand-to-shale proportions (*i.e.* NTG ratios). Overall, the NTG ratios were observed to be greater in the structurally downdip direction as S4 sequence shortens (Fig. 8.2). At this downdip portion, it was interpreted to the sands to be likely more interconnected than other areas. Integrating this descriptive information, lobe facies were modelled using the Sequential Indicator Simulation (SIS) method and the parameters shown in Figure 8.20. Mud and lobe facies were modelled using the same criteria.

The SIS technique is suitable for modelling discrete data (*e.g.* lithology, facies). It is based on a variogram model that is used to populate the grid (Journel and Gomez-Hernandez, 1989). The model randomly selects an un-sampled cell (*i.e.* seed value), then estimates a probability distribution function of the categories likely to be in that cell and chooses the value with more probability to occur. In this case, only lobe and mud facies were the available categories. The procedure is repeated until the entire un-sampled cells are populated.

Figure 8.20 shows the parameters used to model lobe and mud facies. The model variogram selected has very low *nugget* (*i.e.* low variability at data sampling) and an anisotropy range that covers the equivalent area of inter-well spacing. These parameters permitted reproduction of

continuous trends in areas where the sand units seem to be more homogeneous and likely to be more interconnected; and scattered styles in zones where the sands were interpreted to be more heterogeneous.

Since the sediment was mainly supplied by channels and these were estimated to follow a -20° orientation, the preferential areal distribution of lobe and mud facies was interpreted to be developed orthogonally to this direction (*i.e.* 70°).

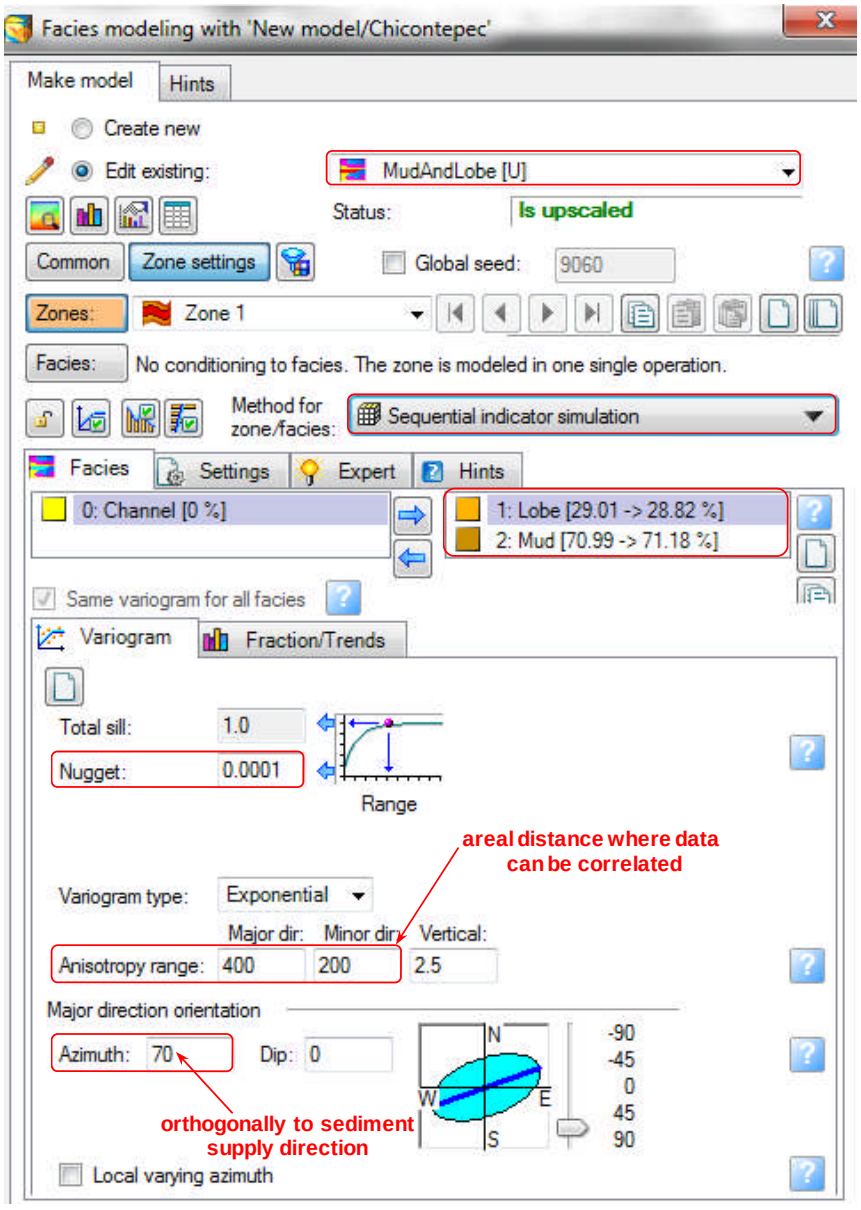

Figure 8.20 Parameters used to model lobe and mud facies. The Sequential indicator simulation method was selected. The areal distribution of these facies was oriented orthogonally to the sediment supply direction (*i.e.* 70°) where lobes were thought to be preferentially distributed

Figure 8.21 shows the comparison of the modelled facies using the SIS technique with the facies distribution interpreted by well to well analysis described in chapter four. Although the model shown in Figure 8.21 represents one of many versions possible, this seems to be an acceptable spatial representation of the interpreted sedimentary facies of the S4 reservoir.

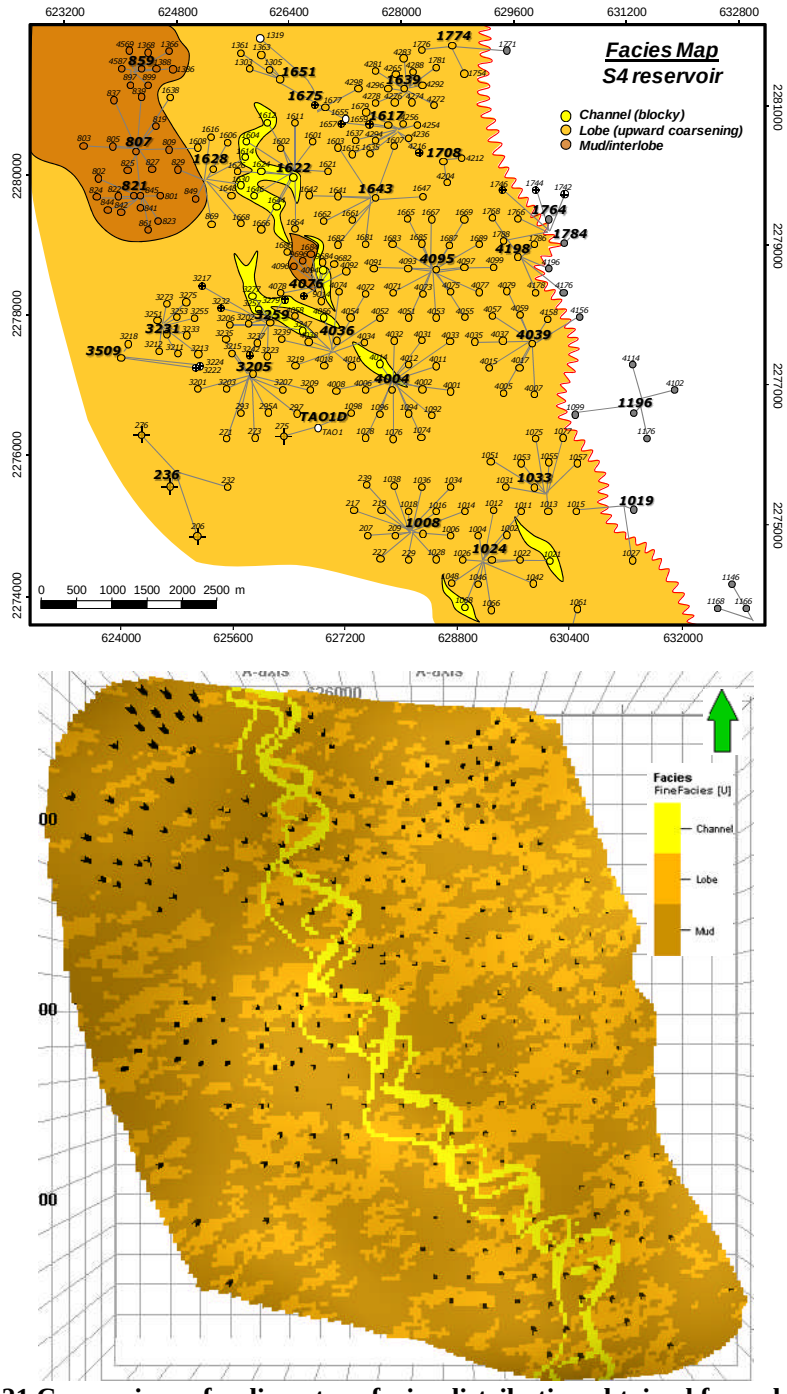

Figure 8.21 Comparison of sedimentary facies distribution obtained from descriptive analyses and sequence indicator simulation. The simulation image at the bottom corresponds to the layer number 30. SIS method honours input data and permits to reproduce heterogeneities

8.2.5 Rock Property Modelling

Rock attributes were modelled using the upscaled rock properties and the interpreted sedimentary facies distributions described in previous section. Sequential Gaussian Simulation (SGS) method was used to model petrophysical properties. The SGS algorithm is recommended for continuous variables such as rock properties (Deutsch and Journel, 1992). The technique is similar to the SIS method, in terms of using a variogram for populating cells. The model randomly selects an un-sampled cell from which estimates a probability distribution function. This distribution has a mean and standard deviation calculated by the Kriging interpolation method. The value is assigned based on this distribution and honouring the input data for each facies category.

A probability distribution function for porosity, permeability and water saturation was built for each sedimentary category (Fig. 8.22). Before the simulation algorithm is run, a final transformation is used by the software. This transformation has a standard normal distribution (*i.e.* mean= 0, standard deviation= 1). The rock property distributions that were used as an input for modelling are shown in Figure 8.22. Porosity and water saturation were modelled using normal distributions. Log normal distribution was used for permeability instead because of the high variation in their numerical values.

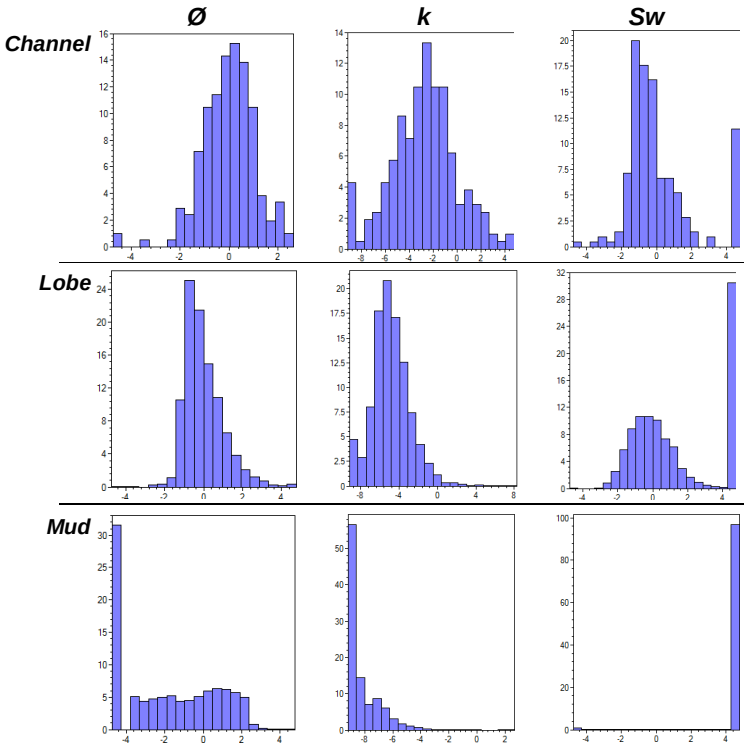

Figure 8.22 Transformations used for each sedimentary facies to model petrophysical properties. Approximate data ranges of attributes are 0.1<Ø<16%; 0.0001<k<10 mD; 0<Sw<1%

Figures 8.23 and 8.24 show the input data used for modelling rock attributes. In all cases, the property was conditioned to the facies distribution that had previously been interpreted. In this way the property was populated into a more geological context. The degree of continuity for each property was controlled by the variogram previously analysed for each rock attribute (Figs. 8.13 and 8.14). Average *nugget* and *range* values were used for each attribute according to the values observed at different directions. For example, an anisotropy *range* of 1800x400 m (Fig. 8.23) was used for porosity as these were the maximum and minimum values analysed in their variograms. Similarly, an average *nugget* value of 0.56 was selected.

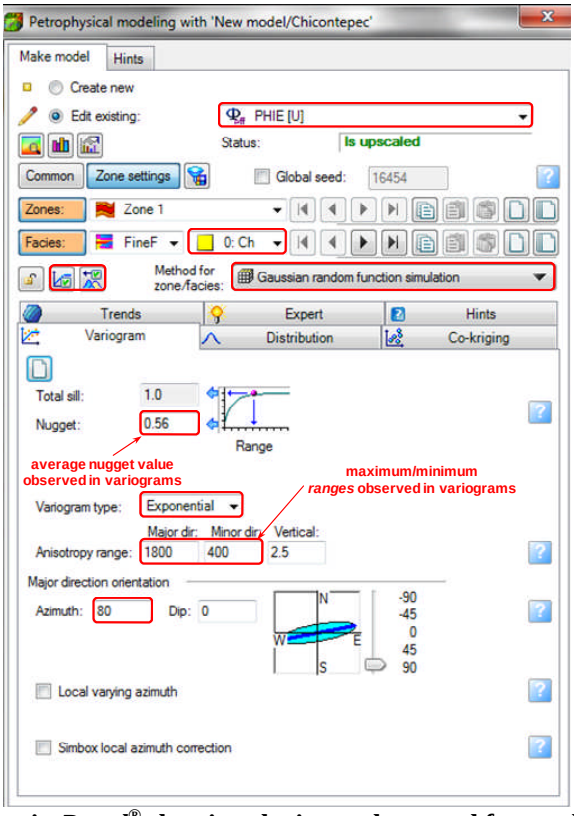

Figure 8.23 Dialog box in *Petrel*® showing the input data used for modelling porosity. This property resulted to have more continuity over distance than permeability and water saturation. Property population in un-sampled cells was controlled by means of the variogram and the sedimentary facies distribution

Correspondingly, Figure 8.24 illustrates the input parameters for modelling permeability and water saturation. As observed from their variograms (Fig. 8.13 and 8.14), water saturation showed the least continuity over distance. This is represented by a *nugget* of 0.81 and an anisotropy *range* of 400x200 m.

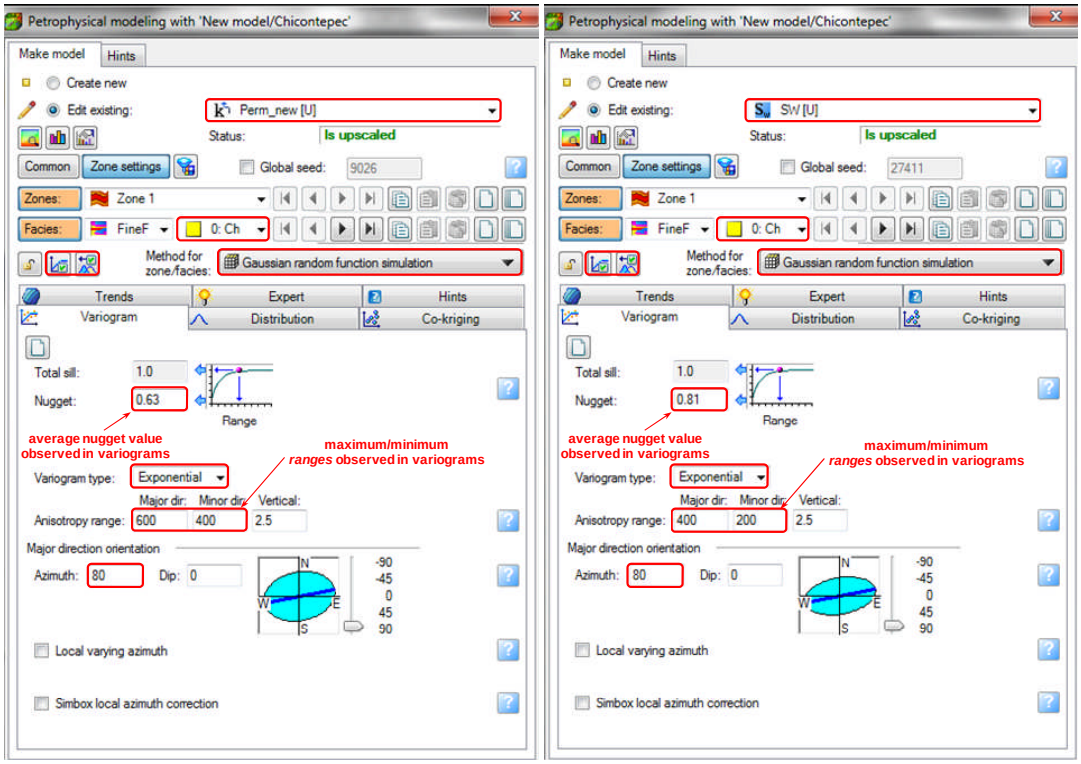

Figure 8.24 Dialog box showing the parameters used for modelling permeability and water saturation. Amongst the rock properties analysed, water saturation observed the least continuity over distance. Observe that nugget and anisotropy range used in each model were selected from the average values obtained from their variograms. The interpreted facies distributions were also used for property population

The modelled rock properties were compared with the upscaled cells to confirm their reproducibility (Fig. 8.25). Overall, an acceptable agreement was observed. Standard deviations were also estimated to evaluate their grade of dispersion.

Figures 8.26 through 8.28 display the modelled rock properties of the S4 reservoir. Overall, a discontinuous character in rock property distribution is observed, which describes in a comprehensive way the characteristic feature of the reservoirs in this study. Note the irregular style of water saturation and the more continuous trend of porosity over permeability. As sedimentary facies were also used for property population, the rock distributions follow a sedimentary trend. Best rock property values (*i.e.* high *k/Ø* and low *Sw*) are generally distributed in channelized and lobe facies.

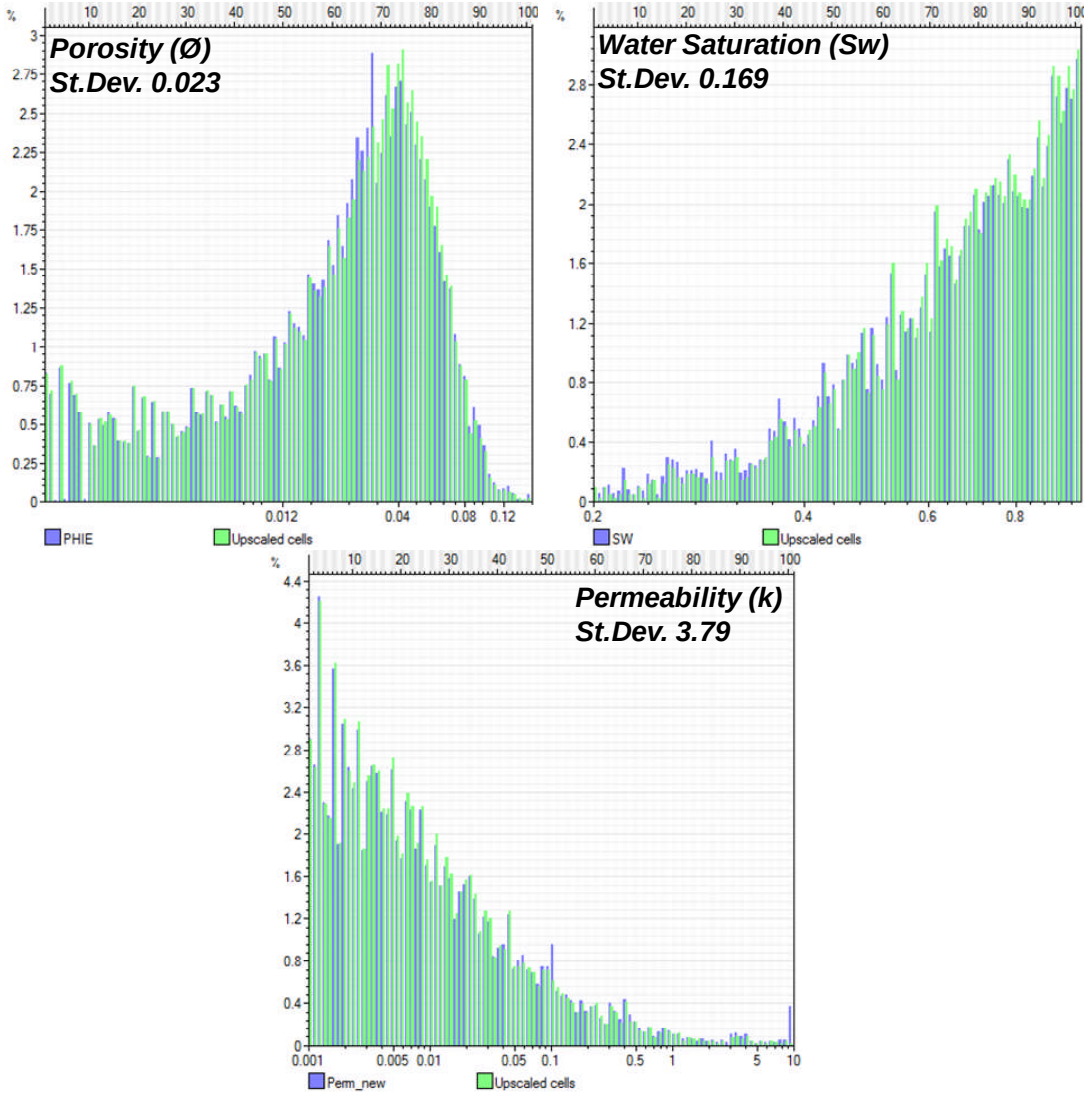

Figure 8.25 Frequency histograms comparing upscaled with modelled property using SGS algorithm. Overall, an acceptable agreement is observed

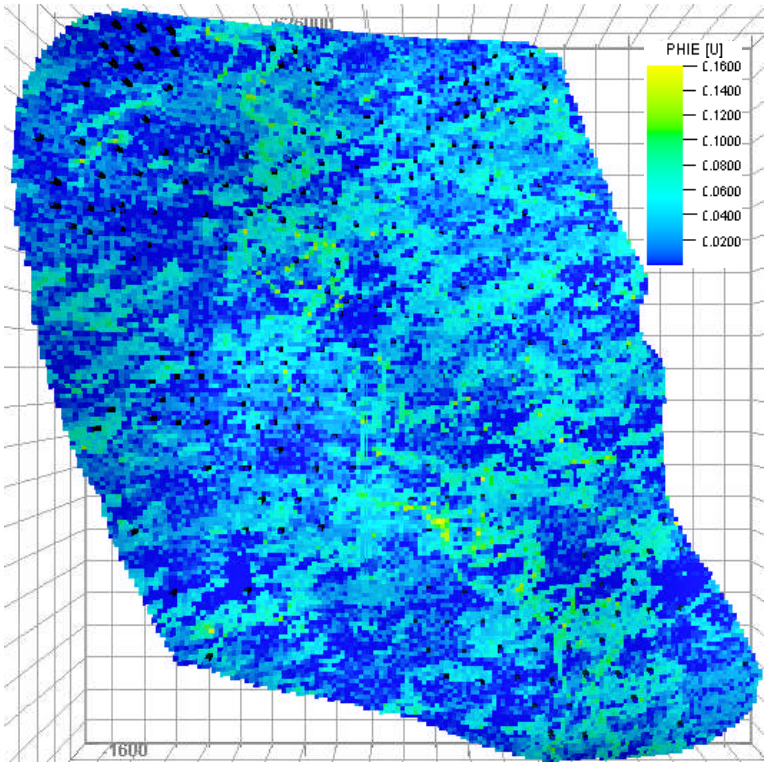

Figure 8.26 Modelled porosity corresponding to the layer number 30. Note that the interpreted rock property follows a sedimentary trend

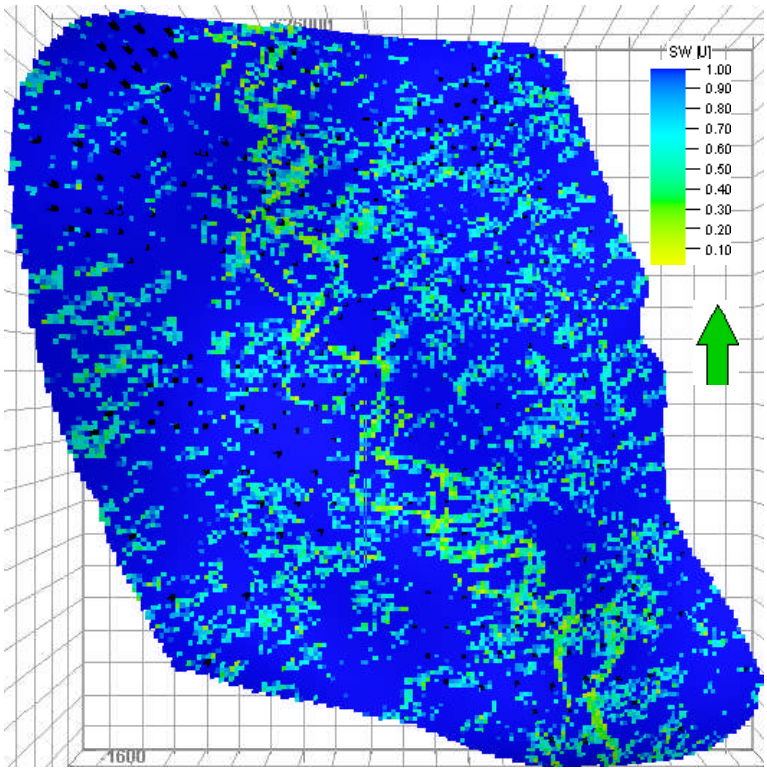

Figure 8.27 Modelled water saturation corresponding to the layer number 30. Observe the scattered pattern of the rock property compared to porosity and permeability. Water saturation observed the least continuity over distance

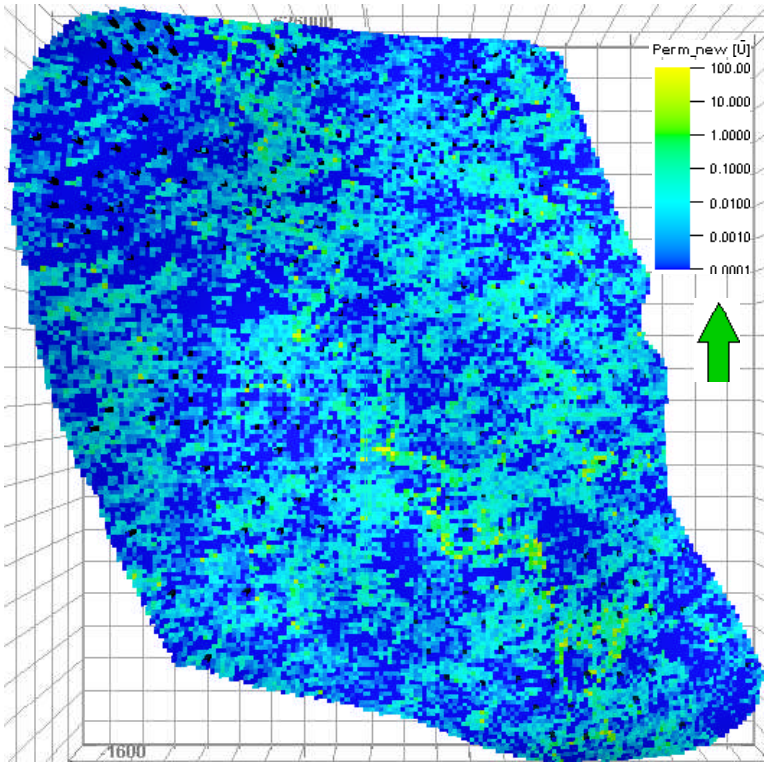

Figure 8.28 Modelled permeability corresponding to the layer number 30. Permeability distribution shows a more continuous behaviour than water saturation. Note that values are expressed in logarithmic scale and the sedimentary imprint on rock attribute distribution

8.2.6 Output to Simulation

The modelled properties were used as input parameter data for conducting a series of simulation exercises. Porosity and permeability obtained from rock property modelling were extracted from the entire model. The volume of information taken out was equivalent to the well's drainage influence which corresponds to a drainage radius of 200 m (*i.e.* 400 m well spacing). In this way, a grid composed of 9x9 cells was extracted. As dimension of each cell is 50x50 m, a model of 450x450 m was produced. The well remained at the centre of the volume extracted, intersecting 70 modelled layers (Fig. 8.29).

Figure 8.29 illustrates the volume of information extracted from HUM-4005 well. The extraction was conducted using the 'simulation case' option in *Petrel*®. A data file is generated in a format normally used in *Eclipse100*® simulation software. The file contains the basic geometry of the simulation grid together with the rock properties modelled in each grid cell (*e.g.* porosity and permeability). The structural component is also incorporated to the model and is represented by placing the cells into a Cartesian grid (*i.e.* X, Y, Z).

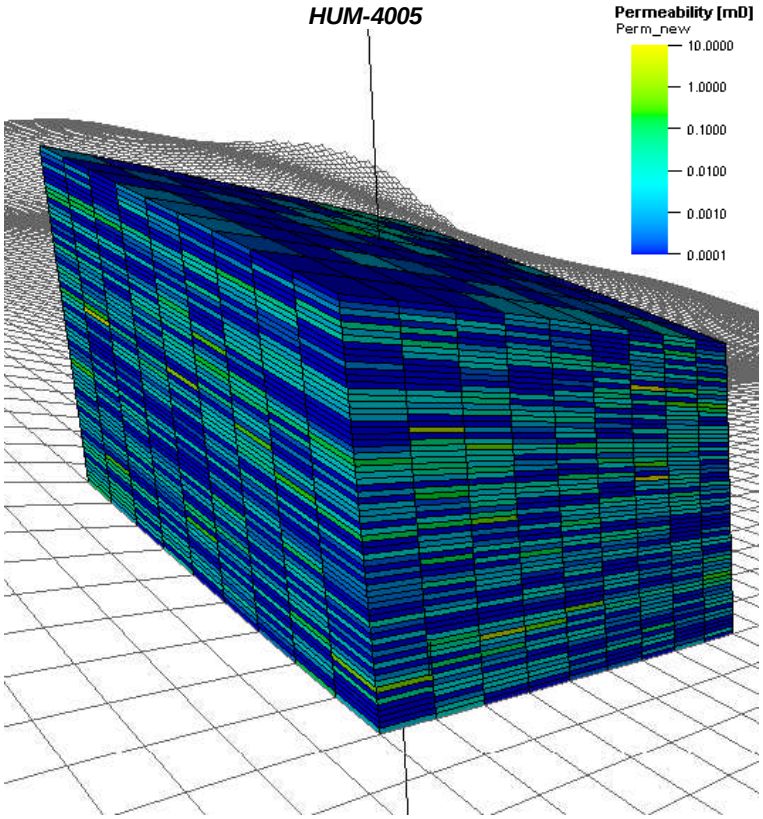

Figure 8.29 Rock property extraction to simulation. The example shows the distribution of permeability of HUM-4005 well. The volume consists of 5670 cells (9x9x70) approximately covering the estimated well's drainage influence

8.3 Simulation

According to previous interpretations, the wells of this study appear to describe a very high diffusivity in production (as observed in Figure 8.2). Hydraulic communication between wells was interpreted to be null and the drainage influence of the wells seems to remain under their spacing area. The simulation exercises described in the following section were developed to evaluate the well's drainage influence (*i.e.* whether communication between wells exists) and to analyse the reservoir heterogeneity on oil production and recovery.

The modelled rock properties obtained from previous section were extracted from the main static model constructed in *Petrel*® to conduct a number of simulation exercises to analyse the impact of rock property variability and fracture propagation on oil production in the reservoirs of this study. The model was applied to HUM-4005 well, which is the most prolific well producing at the S4 reservoir.

A simulation model was constructed in *Eclipse100*® software, which is a fully-implicit, three-phase, three-dimensional, general purpose Black-oil simulator. Reservoir fluid properties were obtained from PVT analysis and fluid-flow efficiency was represented in the model by three-phase relative permeability curves and saturation profiles using capillary pressure correlations.

8.3.1 Flow equations

The black-oil model considers the reservoir being made of three fluid components: oil, water, and gas (free and dissolved in oil). Oil and gas are assumed to be immiscible; therefore no mass transfer occurs between these phases. As gas is assumed to be soluble in oil, mass transfer occurs only between oil and gas components.

Multiphase flow equations are defined based on: 1) Darcy's law, 2) conservation of mass, 3) three-phase flow, and 4) pressure and saturation equations. Continuity equation for each fluid phase is described as:

$$-\frac{\partial}{\partial x}\left(\rho_f u_f\right) = \frac{\partial}{\partial t}\left(\emptyset \rho_f S_f\right)$$

Darcy equation for each phase:

$$u_f = -\frac{k k_{rf}}{\mu_f}\frac{\partial P_f}{\partial x}$$

where: ρ_f is the fluid phase density, u_f is the superficial velocity of each fluid phase, t is time, $\emptyset$ is the porosity of the porous medium, S_f is the fluid phase saturation, P_f is the fluid phase

pressure, k is the absolute permeability, kr_f is the relative permeability of each fluid phase, μ_f is the fluid phase viscosity, and f represents the fluid phase (oil, water, or gas).

Mathematical formulation of multiphase flow in petroleum reservoirs results from combining the continuity equation with Darcy's law, Black-oil fluid properties and including well rate terms. Standard Black-oil initial condition assumes the oil to be undersaturated, *i.e.* the pressure in the reservoir can be reduced to the bubble point pressure (P_b) before gas is released into the formation. As the pressure is dropped as a result of production of fluids (*i.e.* drawdown), the oil/gas/water producing phases are defined according to their properties (*e.g.* density, viscosity, gas solubility, compressibility, etc.) and prevailing pressure and temperature conditions.

Gas solubility (R_s) is defined as the amount of gas which will come out of solution as the reservoir's pressure decreases. R_s is expressed as the number of cubic feet of gas measured at standard conditions which will dissolve in one barrel of stock tank oil (scf/STB). Formation volume factor (B_o, B_g and B_w for oil, gas and water, respectively) relates the volume of the fluid phase at reservoir conditions, to its volume measured at standard conditions. In this way, the oil formation volume factor (B_o) is defined as the ratio of volume of oil (plus its gas in solution) at the prevailing reservoir temperature and pressure to the volume of oil at standard conditions (rb/STB).

Combining continuity equation with Darcy's law and Black-oil properties, the flow equations for oil, gas, and water phases can be defined as:

$$\frac{\partial}{\partial x}\left(\frac{kk_{ro}}{\mu_o B_o}\frac{\partial P_o}{\partial x}\right) - q'_o = \frac{\partial}{\partial t}\left(\frac{\emptyset S_o}{B_o}\right)$$

$$\frac{\partial}{\partial x}\left(\frac{kk_{rg}}{\mu_g B_g}\frac{\partial P_g}{\partial x} + R_s\frac{kk_{ro}}{\mu_o B_o}\frac{\partial P_o}{\partial x}\right) - q'_g - R_s q'_o = \frac{\partial}{\partial t}\left(\frac{\emptyset S_g}{B_g} + R_s\frac{\emptyset S_o}{B_o}\right)$$

$$\frac{\partial}{\partial x}\left(\frac{kk_{rw}}{\mu_w B_w}\frac{\partial P_w}{\partial x}\right) - q'_w = \frac{\partial}{\partial t}\left(\frac{\emptyset S_w}{B_w}\right)$$

where: B_o is the oil formation volume factor (rb/STB), B_w is the water formation volume factor (rb/STB), B_g is the gas formation volume factor (cf/scf), R_s is the solution gas in the oil phase (scf/STB).

Implicit-pressure, implicit-saturation method is used for *Eclipse100*® to solve simultaneously the partial differential equations for flow of oil, water and gas to obtain the pressure in each phase. The saturation of each phase is calculated implicitly using capillary pressure relations. The three phases are assumed to fill entirely the porous media satisfying the following expression:

$$S_w + S_o + S_g = 1$$

Immiscible fluid pressure differences are defined by:

$$Pc_{go}(S_g) = P_g - P_o$$

$$Pc_{ow}(S_w) = P_o - P_w$$

where: *S* is the saturation and sub-indexes *w*, *o*, *g* stand for water, oil and gas, respectively; *Pc* is the capillary pressure (in gas-oil and oil-water systems), *Pg* is the pressure of the gas phase, *Po* is the pressure of the oil phase and *Pw* is the pressure of the water phase.

According to the technical description of the software (Schlumberger, 2009a), the non-linear residual R_{fl}, for each fluid phase in each grid block at each time step is defined in *Eclipse100*® as:

$$R_{fl} = \frac{dM}{dt} + F + Q$$

where: *dM* is the mass per unit surface density accumulated during each time step *dt*, *F* is the net flow rate into neighboring grid blocks, and *Q* is the net flow rate into wells during each time step.

Residual equations are solved using a set of solution variables and employing the Newton's method. The primary solution variables *X* are pressure (*P*) and two saturations for a three-phase Black-oil system. The water saturation *Sw* and either *Sg*, *Rs* or *Rv* are chosen to complete the set. For example, for a three component black-oil study, the residual *R* and the solution *X* are three component vectors in each grid cell defined implicitly as:

$$R = \begin{bmatrix} R_o \\ R_w \\ R_g \end{bmatrix} \quad X = \begin{bmatrix} P_o \\ S_w \\ S_g or\ R_s\ or\ R_v \end{bmatrix}$$

and the Jacobian matrix, $J = \frac{dR}{dX}$, takes the form:

$$\frac{dR_i}{dX_j} = \begin{bmatrix} \frac{dR_o}{dP_o} & \frac{dR_o}{dS_w} & \frac{dR_o}{dS_g} \\ \frac{dR_w}{dP_o} & \frac{dR_w}{dS_w} & \frac{dR_w}{dS_g} \\ \frac{dR_g}{dP_o} & \frac{dR_g}{dS_w} & \frac{dR_g}{dS_g} \end{bmatrix}$$

The mass change during each time step, *dt*, is then proportional to:

$$dM = M_{t+dt} - M_t$$

with:

$$M = PV\begin{bmatrix} \frac{S_o}{B_o} + \frac{R_v S_g}{B_g} \\ \frac{S_w}{B_w} \\ \frac{S_g}{B_g} + \frac{R_s S_o}{B_o} \end{bmatrix}$$

where: PV is the pore volume, B_o is the oil formation volume factor (rb/STB), B_w is the water formation volume factor (rb/STB), B_g is the gas formation volume factor (rcf/scf), R_s is the solution gas in the oil phase (scf/STB).

Hydrocarbon states and the variables to be solved in *Eclipse100*® are shown in Table 8.1:

Table 8.1 Hydrocarbon states in *Eclipse100*®

States	*Phase*	*Variables*
1	*Gas only (i.e. Rs= 0 and Sg= 1-Sw)*	*Po, Sw, Rv*
2	*Gas and Oil (i.e. Rv=Rv sat, Rs= Rs sat)*	*Po, Sw, Sg*
3	*Oil only (i.e. Rv= 0, Sg= 0)*	*Po, Sw, Rs*

8.3.2 Description of the model

The model was built to represent a vertical well completed in a single interval and stimulated through hydraulic fracturing. The model was applied to the HUM-4005 well. The extension and approximated geometry of the induced fracture was represented in the model according to the post-frac analysis report conducted by the contractor. These estimations were used to characterize a high-conductive path (*i.e.* the induced fracture) of finite dimensions. The grid obtained from *Petrel*® was edited considering this feature.

Fluid-flow efficiency was represented in the model by three-phase relative permeability curves and initial saturation profiles using capillary pressure correlations. Characterisation of hydrocarbon fluids was conducted using a PVT report of a crude-oil sample obtained from a producing interval in one of the wells in the study area. History matching of the oil phase was conducted by varying the three-phase relative permeability curves using Corey-type correlations.

8.3.2.1 Hydraulic fracture definition

Analysis of the post-fracture conducted by the PEMEX's contractor in the HUM-4005 treatment indicates the development of an induced fracture with maximum propped half-length of 100 m (328 ft) and average fracture width of 1.54 cm (0.0505 ft). Completion consisted of a perforated interval of 30 m (98.4 ft) through a tubing inner diameter of 13.75 cm (0.45 ft). Post-fracture analysis is normally conducted in the reservoirs of this study by comparing the pre/post flow-rates to evaluate the treatment efficiency.

The induced hydraulic fracture was defined by a high-conductive path of tabular shape, deployed longitudinally along the completion interval of the well (Fig. 8.30). Fracture orientation defined in the model follows a north-south direction as a way to mimic the direction in which most fractures are normally propagated in Chicontepec reservoirs. Hydrofracture propagation in these reservoirs follows a regional direction between N14°E to N44°E, according to a number of microseismic surveys obtained in the basin (Berumen *et al.*, 2004a, 2004b; Gachuz-Muro, 2009; Gutierrez *et al.*, 2010; Gutierrez *et al.*, 2014a, 2014b, 2014c; Rabe and Ortiz-Ramirez, 2010).

Local grid refinement option was used to represent the hydraulic fracture. This permits dividing of a portion of the main grid in a number of smaller cells. Twenty refined cells of varying size in the X-axis direction were created (Fig. 8.30). The cell at the centre of the local grid was adjusted to an equivalent fracture width of 1.54 cm (0.0505 ft) according to the post-fracture report. A permeability value of 10 Darcy in its three directions (PERMX, PERMY, PERMZ) was given to this minute local cell to replicate the high-conductive path of the hydraulic fracture. Figure 8.30 shows the top view of the model defined in *Eclipse100*® software.

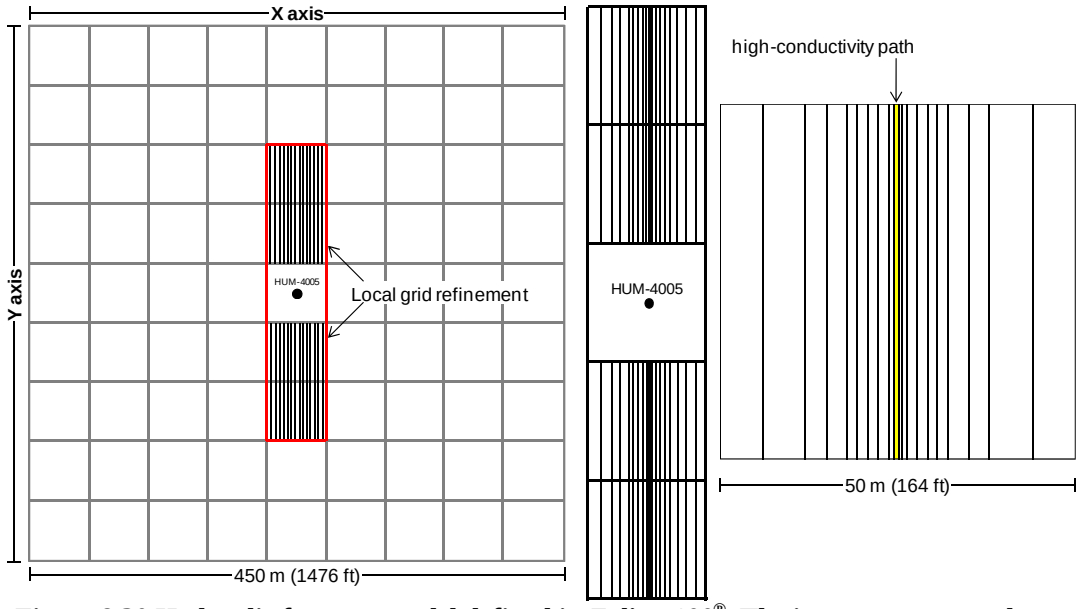

Figure 8.30 Hydraulic fracture model defined in *Eclipse100*®. The images correspond to the top view of the model. A high-conductivity path of tabular shape corresponding to the estimated fracture width was deployed longitudinally along the completion interval. The induced fracture propagates along the vertical well at a distance equivalent to the interpreted half-length

8.3.2.2 Fluid property data

A PVT analysis was available from a producing crude-oil sample in the study area. The crude-oil sample was obtained from HUM-1642 well at the S3 sequence, just below the S4 sand unit. No other report of this kind was available in the entire study area. Constant-composition expansion and differential liberation (vaporisation) tests were conducted. Formation volume factor of oil and gas phases (B_o and B_g, respectively), together with gas solubility (R_s) and fluid viscosities are reported as function of pressure (Tables 8.2 and 8.3). As normally occur in Chicontepec crude-oil samples, the bubble pressure (P_b) was determined to be just 780 psi below the estimated reservoir's pressure in the producing interval where the crude-oil sample was collected.

Table 8.2 PVT properties of live-oil with dissolved gas

Gas solubility Rs (scf/STB)	*Pressure (psia)*	*Oil Formation Volume Factor Bo (rb/STB)*	*Oil Viscosity μ (cP)*
0.006	*14.7*	*1.048*	*3.014*
5.150	*100*	*1.057*	*2.915*
43.454	*300*	*1.078*	*2.267*
84.084	*600*	*1.102*	*2.038*
192.255	*1200*	*1.150*	*1.398*
313.069	*2000*	*1.201*	*1.041*
417.034	*2875**	*1.225*	*0.898*
417.034	*3000*	*1.224*	*0.954*
417.034	*4000*	*1.215*	*1.164*
417.034	*5000*	*1.207*	*1.362*
417.034	*6000*	*1.199*	*1.620*
417.034	*7000*	*1.193*	*1.900*
417.034	*8000*	*1.186*	*2.133*

**Bubble-point pressure*

Table 8.3 PVT properties of dry gas

Pressure (psia)	*Gas Formation Volume Factor Bg (rb/Mscf)*	*Gas Viscosity μ (cP)*
14.7	*216.704*	*0.0106*
100	*31.472*	*0.0119*
300	*10.330*	*0.0128*
600	*5.058*	*0.0135*
1200	*2.458*	*0.0146*
2000	*1.443*	*0.0167*

8.3.2.2.1 Relative permeability and Capillary pressure

Relative permeability has great influence in fluid-flow productivity and recovery. The curve contains important components that describe rock attributes and fluid sweep efficiencies, together with the reservoir's wetting characteristics. A series of relative permeability curves in oil-water and gas-oil systems were built using Corey-type correlations. This was conducted to select a characteristic set of curves that describe the observed oil-phase production and recovery (*i.e.* history matching). A code was written to simulate the relative permeability curves by varying their end-point permeability, the end-point saturation, and curvature. History matching was conducted using *Tempest-ENABLE*® software.

For a three-phase system (oil/gas/water), the Corey-type model correlation was used to determine the relative permeability of each phase (k_{ro}, k_{rg} and k_{rw}).

Relative permeability for oil-water system was defined as:

$$k_{rw} = \left(\frac{S_w}{1 - S_{wi}}\right)^n$$

$$k_{row} = \left(\frac{1 - S_w}{1 - S_{wi}}\right)^n$$

For gas-oil system:

$$k_{rg} = S_g^n$$

$$k_{rgo} = \left(1 - S_g\right)^n$$

Capillary pressure curves were used to build implicit initial saturation distributions in the simulation model. The shape of the capillary pressure curve is mainly defined by the pore-size distribution and fluid interfacial tensions. Capillary pressure curves were modelled by varying curvature and saturation end-points in the same way as relative permeability curves. This was done using *Tempest-ENABLE*® software to reproduce representative set of curves.

For oil-water system:

$$Pc_{ow} = (1 - S_w)^n$$

For gas-oil system:

$$Pc_{og} = \left(1 - S_g\right)^n$$

where: k_{rw} is the relative permeability to water, k_{row} is the relative permeability to oil in presence to water, k_{rg} is the relative permeability to gas, k_{rgo} is the relative permeability to gas in presence to oil, *Sw* is the water saturation, *Sg* is the gas saturation, Sw_i is the irreducible water saturation, and *n* is an arbitrary value used to change the curve shape (it varied from 1 to 5).

The set of curves used in the model which were able to replicate oil production observed in the HUM-4005 well are shown in Figure 8.31. Observe that the relative permeability to water at end-point conditions ($k_{rw}@So_r$) is about 40% and the crossover saturation at which k_{rw} and k_{ro} are equal is below 50%. The curves describe a reservoir with irreducible water conditions of 16% and gas saturation exerting an important control in the relative permeability to oil as normally observed in Chicontepec reservoirs. Residual oil saturation after complete depletion (*i.e.* k_{ro} equals to zero) is approximately 34% which is a recurrent value observed from gas-oil displacement experiments.

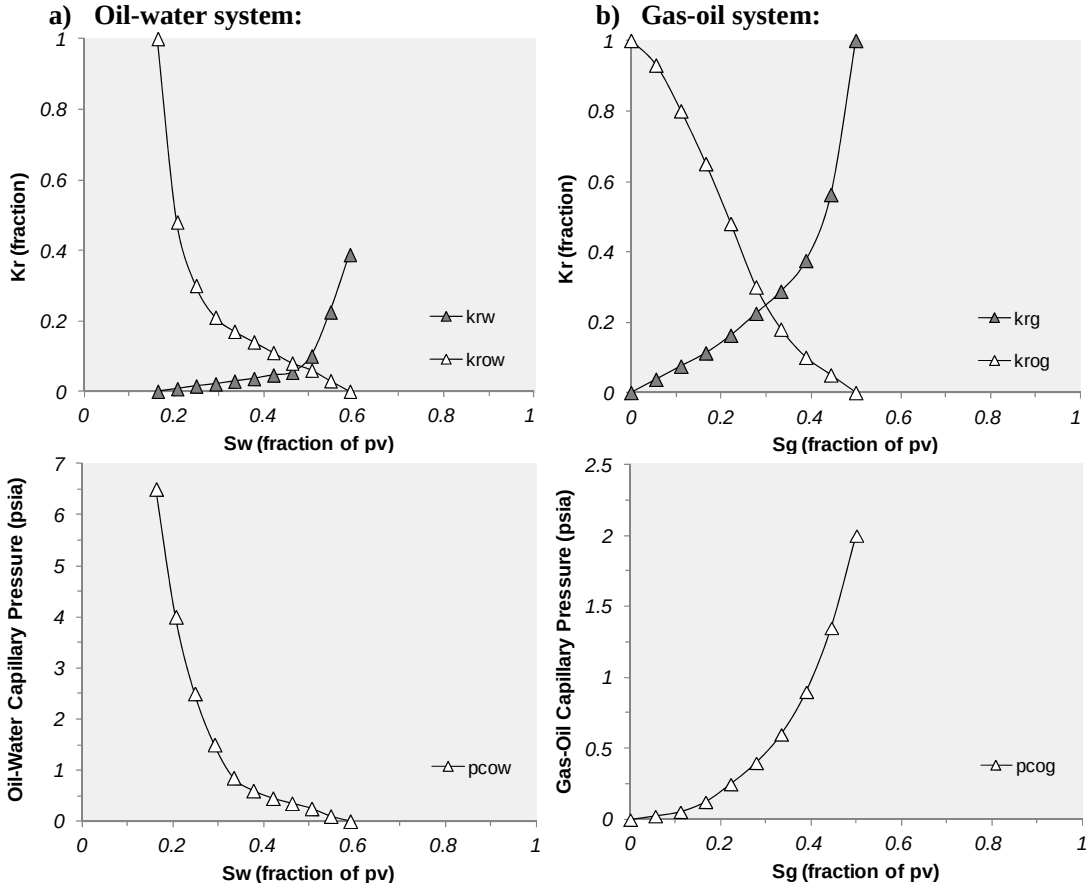

Figure 8.31 Relative permeability and capillary pressure curves used in simulation model. End-point permeability and end-point saturations at a variety of curve shapes were modelled to obtain representative set of curves

8.3.2.2.2 End-point saturations

End point saturations define the range of the movable fluid fractions and are directly associated to the amount of recoverable oil. End points determine the sweep efficiency during production of fluids and are an important component in simulation.

Irreducible water saturations (Sw_i) from oil-water relative permeability curves observed from PEMEX databases and from experiments developed from this study show a range from 18 to 50%. However, when the experiments were conducted using aged rock samples, the range is reduced from 5 to 33%. Similarly, residual oil saturations (So_r) were observed to vary from 13 to 26% for non-aged and from 15 to 65% for aged samples. The oil-water saturations selected for simulation (Fig. 8.31a) define a reservoir with a Sw_i of 16% which seems to represent the end-point saturations observed from experimental data.

Critical gas saturation (Sg_c) seen in gas-oil relative permeability systems in Chicontepec rock samples is typically low. Sg_c describes the gas saturation at which gas becomes mobile and consequently reduces the relative permeability to oil. Normally, Sg_c is observed to range from 3 to 20% whereas residual oil saturation in gas-oil systems and at irreducible water conditions varies from 13 to 40% in Chicontepec samples. Gas-oil saturations resulted from Corey-type correlations (Fig. 8.31b) and used for simulation describe typical values of the reservoirs in this study.

8.3.2.3 Initial and boundary conditions

The simulation scenario was applied to a rock volume equivalent to the well's drainage area at the S4 sand unit. In this way it was possible to analyse the effective surface influence of the well and corroborate whether interference beyond its spacing exists. A grid of 9x9x70 cells was extracted corresponding to a rock volume of 450x450x100 m^3 (1476x1476x328 ft^3).

The S4 reservoir extends vertically between 1420 to 1520 m (4655-4986 ft). Initial conditions assume an oil-phase pressure of 3000 psi at 1460 m (4790 ft) depth, which corresponds to the mid-point of the perforated interval. Gas-oil and oil-water contacts were defined at 1445 m (4740 ft) and 1509 m (4950 ft), respectively. The fluid contacts were positioned just a short distance away from the completed interval, assuming that no free gas and no mobile water exist in the reservoir initially. Water, gas and oil initial saturations above and below the transition region were set at the end-point saturations in their oil-water and gas-oil capillary pressure curves.

Table 8.4 summarises the basic data used for simulation.

Table 8.4 Basic data used for simulation (in field units)

Main grid geometry	
Number of cells:	*Nx=9; Ny=9; Nx=70 (5670 cells)*
Cell dimensions (DxDyDz):	*164 x 164 x ~3.28 ft*
Depth of top layer:	*4655 ft*
Depth of bottom layer:	*4986 ft*
Local grid geometry	
Number of cells:	*Nx=20; Ny=2; Nx=31 (1240 cells)*
Cell dimensions (DxDyDz):	*Dx= variable, Dy= 1, Dz= 1 ft*
Depth of top layer:	*4741 ft*
Depth of bottom layer:	*4835 ft*
Rock and Fluid data	
Model:	*Black oil*
Phases:	*Oil, Gas, Water*
Units:	*Field*
Rock compressibility:	*7.0E-6 psi^{-1}*
Water compressibility:	*3.0E-6 psi^{-1}*
Stock-tank oil density:	*50.8 lb/ft^3*
Stock-tank water density:	*62.4 lb/ft^3*
Standard-conditions gas density:	*0.075 lb/ft^3*
Initial Conditions	
Initial reservoir pressure:	*3000 psi*
Depth of pressure datum:	*4790 ft*
Depth of Gas/Oil contact:	*4740 ft*
Capillary pressure at Gas/Oil contact:	*0 psi*
Depth of Water/Oil contact:	*4950 ft*
Capillary pressure at Water/Oil contact:	*0 psi*
Well data	
Completion interval:	*4741-4835 ft*
Completed grid layers (Nz):	*7 through 37*
Completion tubing inner diameter:	*0.45 ft*
Propped fracture half-length:	*328 ft*
Fracture width:	*0.0505 ft*
Simulation time period	
Start simulation:	*24 September 2011*
End simulation:	*21 June 2012*
Total time:	*270 days*

8.3.3 Sensitivity Analysis

Apart from the simulation exercise described above (referred here as the 'real case' as it describes the actual reservoir characteristics of HUM-4005 well), three extra simulation exercises were conducted to evaluate the rock property distribution and the fracture extension on oil productivity and recovery. These were also designed to analyse their effect on the well's drainage coverage.

Half-length fracture extensions in the S4 reservoir vary from 40 to 180 m as reported from field data. To evaluate the effect of fracture propagation, two cases were considered. The first was designed assuming a short extension of the induced fracture. This case was referred as the ‘constrained frac’ and consisted of a fracture half-length of only 50 m. The second case was the opposite. An extended frac half-length of 150 m was assumed and this exercise was referred to as ‘extended frac case’. No other assumption but the change in fracture extension was made in both cases. The remaining characteristics (*e.g.* rock property distribution, fluid contacts, fluid property, etc.) were left with no change as in the ‘real case’ in both exercises.

The third case analysed the effect of rock property distribution. This scenario was basically the ‘real case’ study but rock properties were modified as if these were homogeneous. Distribution of rock properties were defined assuming a uniform reservoir. Porosity and permeability were set as 6% and 0.1 mD in the entire cell grids, respectively. This scenario was referred as ‘homogeneous rock property case’.

8.3.4 Results

Simulated oil-rates and cumulative oil volumes in the **real case** scenario are compared to the observed data and shown in Figure 8.32. The first 270 day-production were simulated as HUM-4005 well was optimized by artificial lift pumping after this period (*i.e.* only primary production by indigenous energy of the reservoir is recreated). HUM-4005 well observed the greatest cumulative oil by primary depletion at the S4 reservoir in the study area, although the majority of the wells in the study deplete within the first six-month production. During this time, the well produced 73% of its total cumulative oil.

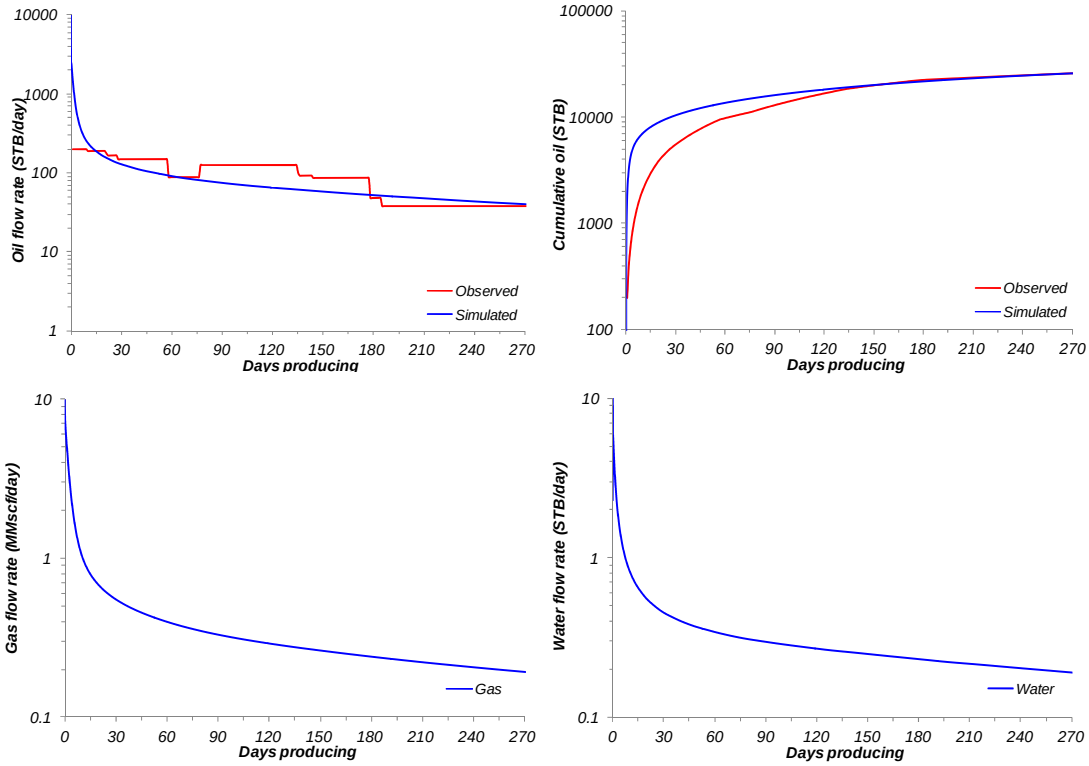

Figure 8.32 Comparison of simulated oil-rates and cumulative oil volumes with observed production data (real case). Observe that although differences in oil flow-rates are clear, the accumulated oil after six months seems to be accurate. Gas and water flows are also displayed although no production reports were available for calibration

Total cumulative oil produced from HUM-4005 well after 270-day production was 25,740 STB, whereas the simulated value obtained was 25,766 STB, *i.e.* despite showing differences in the daily oil production, the simulated oil recovered seems to be close to the measured values. Gas and water production are also displayed in Figure 8.32, although no production reports for comparison were available. Nevertheless, the flow rates describe typical values observed in most reservoirs in the study area (*e.g.* normally less than 1 MMscf/day of gas and less than 10 STB/day of water).

Pressure disturbance after six-month drawdown in the **real case** shows that the drainage influence seems to be inhibited at short distance around the well (Fig. 8.33). Pressure disturbance is interpreted here as the well's equivalent area of influence (*i.e.* drainage area). The average pressure disturbance cloud extends an equivalent surface area of 0.095 km^2 in most of the simulated layers in the model, indicating that the well is draining between 43 to 47% of the total surface grid. The equivalent well's drainage radius considering the apparent low surface influence resulted of approximately 173 m.

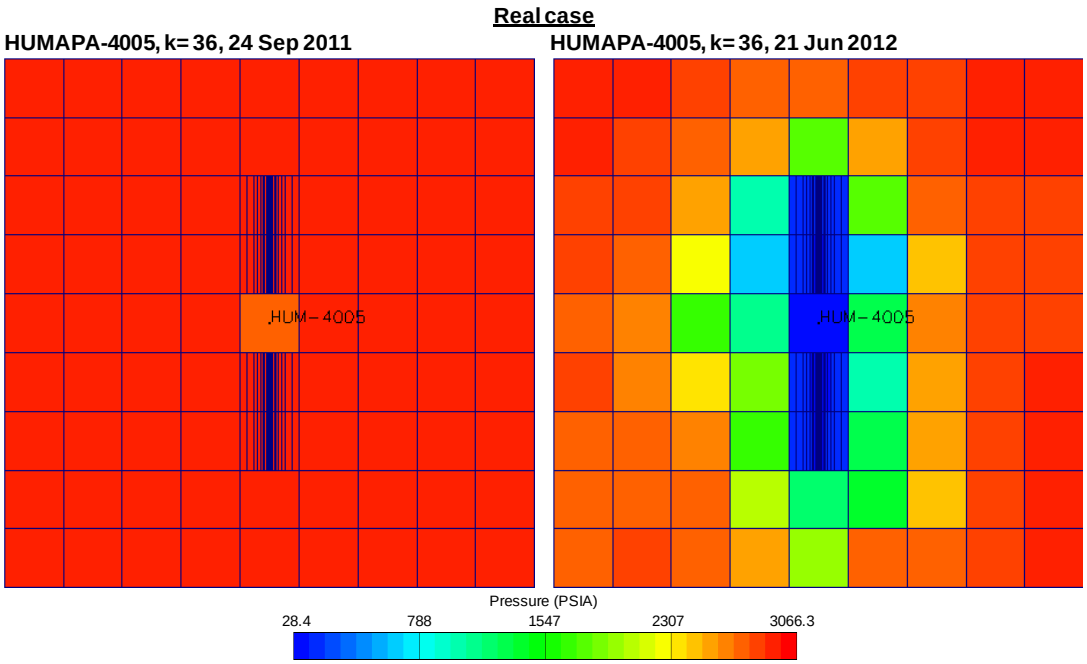

Figure 8.33 Pressure disturbance after 6-month production of layer 36 (real case). Observe the elliptical shape of the pressure disturbance following the conductive path of the induced fracture. The well drains between 43 to 47% of the total surface grid

Residual oil saturation after six-month production is shown in Figure 8.34 together with gas saturation. As similar to pressure disturbance, a very restricted surface area around the well seems to be swept. Similar behaviour was consistently observed in the entire layers of the model. Average residual oil saturation after 270-day production is approximately 75% whereas gas saturation is only around 8%.

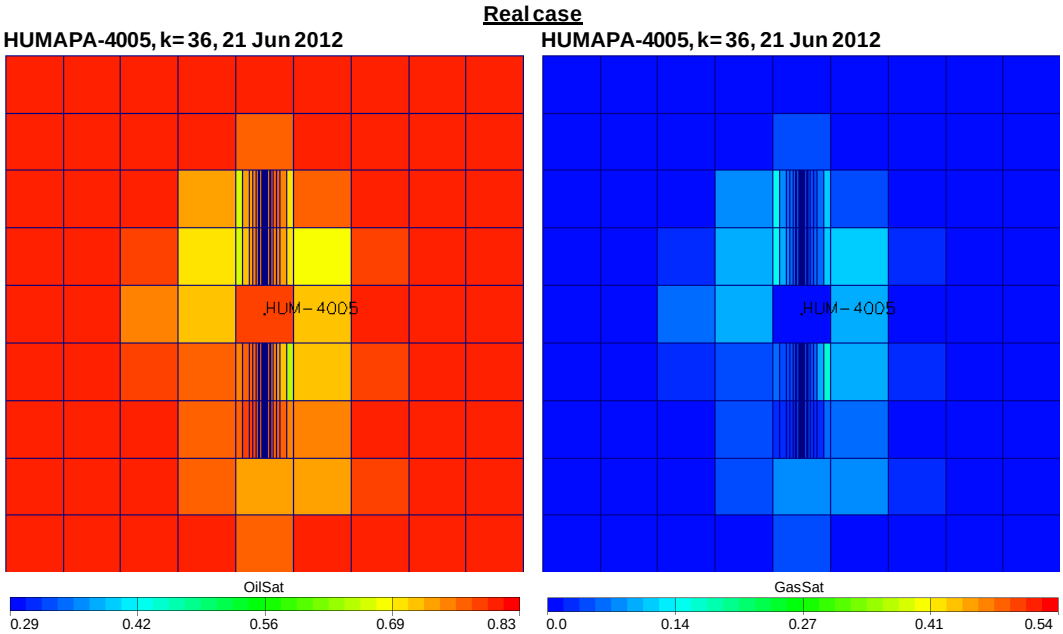

Figure 8.34 Oil and gas saturations of layer 36 after six-month production (real case). Note the apparent poor fluid-sweep efficiency

Variations in the extension of the induced fracture obviously impacts on the equivalent well's drainage area (Fig. 8.35). Only 35% of the total surface grid appears to be drained when the fracture half-length is fixed to 50 m (*i.e.* the **constrained case**). When this is extended to 150 m, the equivalent well's drainage area covers approximately 65% of the total grid (*i.e.* the **extended case**). The latter also exerts an effect on cumulative oil volumes, although no significant differences in oil recoveries were noticed (Fig. 8.35). Only 4,300 STB of extra oil are recovered when the induced half-length fracture increases from 100 to 150 m. On the contrary, when the fracture is reduced from 100 to only 50 m, about 6,600 STB are left to recover. Approximately 100 STB of extra oil is recovered per added metre of induced half-length fracture.

Figure 8.35 shows the comparison results between the constrained and the extended fracture geometries. The top view of the pressure disturbance around the well is displayed together with the simulated oil volumes recovered for each case.

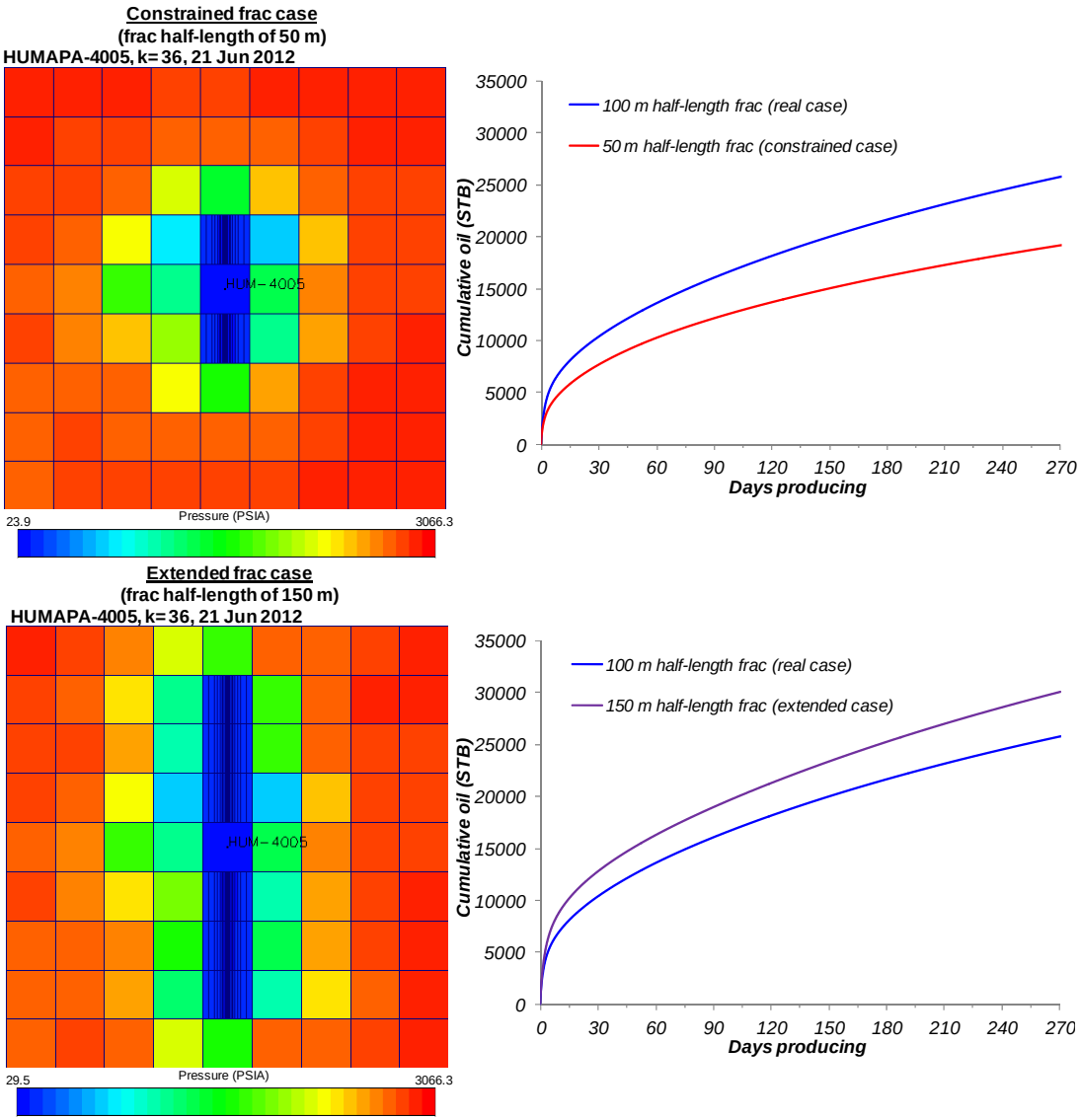

Figure 8.35 Comparison of the pressure disturbance after nine-month production assuming two scenarios of fracture propagation. The images correspond to the top view of layer 36

Significant differences in oil production and drainage area were obtained when the reservoir was assumed to have a uniform rock property distribution (*i.e.* the **homogeneous rock case**). When rock properties were uniformly modified, the cumulative oil increased by 3 times in comparison to the real case (Fig. 8.36). Moreover, the pressure disturbance cloud extends almost entirely in all grid cells, resulting in equivalent well's drainage efficiency of 96%.

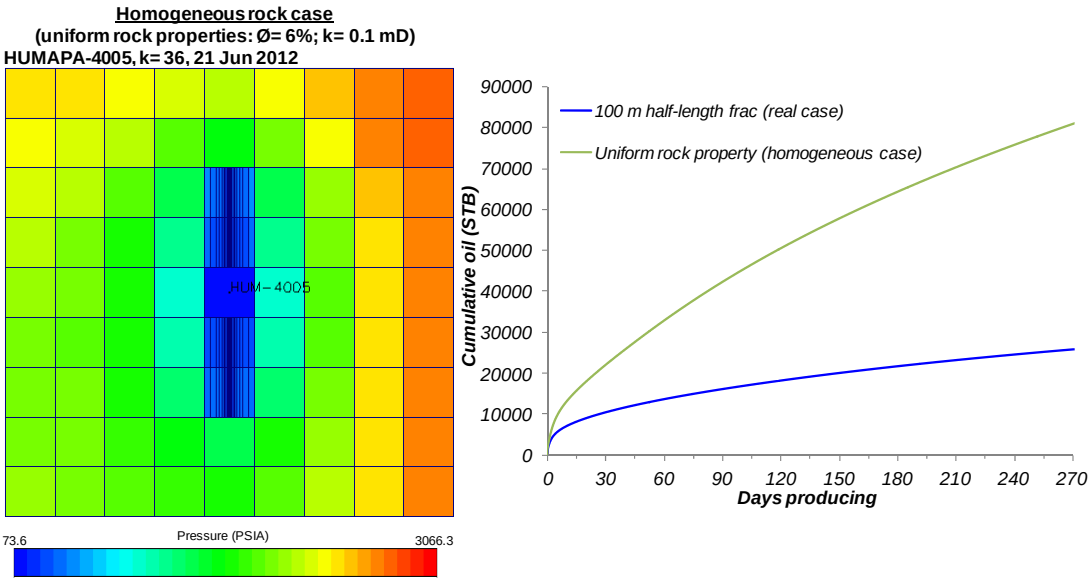

Figure 8.36 Simulation results considering the reservoir to have uniform rock property distribution. The drainage coverage by observing the pressure disturbance results of approximately 96%. Cumulative oil increased by 3 times as compared to the real case scenario

8.4 Discussion

The effect of rock property distribution and induced fracture propagation on oil productivity was analysed. Sedimentary facies exert an important control in rock quality in the reservoirs of this study, thus they were used as a guide to model rock properties. The resultant rock property models are thought to be a comprehensive representation of the petrophysical complexity of such reservoirs, although these should be considered as one of innumerable versions (*i.e.* realisations) possible. In this way, significant variations in rock property population may result by varying for example, the number of channels, the channel's sinuosity, the lobe orientation, the variogram input data, etc. Continuous calibration of the model should be conducted, trying to incorporate new data during the field development. Similarly, the sedimentary facies definition conducted in this work was not exhaustive and included only three general classes since these were observed to display characteristic rock properties. However, a more detailed categorization would provide with a clearer idea of the rock property distribution. For example, distinguish levee and overbank from lobe deposits would enrich the understanding of the channel geometry and distribution.

The overall behaviour of rock properties in the S4 reservoir was observed to have a high spatial heterogeneity. Amongst the rock attributes modelled, porosity was found to have more continuity over distance than permeability and water saturation. Surprisingly, permeability showed more continuity over distance than water saturation, possibly because permeability was estimated using a linear porosity correlation and this may have given it with added spatial continuity. Water saturation observed the least continuity over distance, mainly because its dependence to other parameters (*e.g.* pore geometry, capillary fluid contacts, wettability).

A simulation exercise was applied to HUM-4005 well, which is the most prolific well producing at the S4 reservoir. According to the modelled rock properties, this well intersects a portion of the study area with high NTG values. Its high productivity was ascribed to greater sand connectivity likely produced in high NTG zones. The average well's drainage radius after primary depletion was simulated to be of only 173 m, *i.e.* the well is actually draining an area equivalent of 0.095 km^2 instead of 0.125 km^2 estimated in the current field's development plan. A significant segment of the reservoir may not be drained. These results suggest that infill drilling or re-stimulation operations should be evaluated. The poor drainage efficiency obtained from simulation may even be smaller considering that drainage area may describe elliptical shapes in direction to the induced fracture deployment. According to a number of hydraulic fracture reports conducted by PEMEX contractors, the propped half-length fractures in the S4 reservoir average 140 m.

Even when HUM-4005 well was interpreted to produce from a high NTG zone in the study area, its drainage area after 270-day production resulted to be lower than estimated. It is then expected that lower drainage areas may likely be developed by wells in zones with lower NTG ratios.

Although increasing the extension of the fracture half-length impacts in the well's drainage efficiency and also in the resultant oil recovery, no significant difference seems to be resulting as only 100 STB of extra oil is recovered per added metre of induced fracture. This is probably due to the well's completion characteristics. In the particular case, the HUM-4005 well was completed through a perforated interval of 30 m. No significant oil is recovered per stimulated metre as the induced fracture is confined within the perforated interval. The S4 reservoir in the study area is generally stimulated through an average perforated interval of 25 m in wells producing from a single interval. The reservoir contact effectiveness may also be limited as almost the entire wells of the study area intersect the S4 sand unit vertically. This practice is common not only in the study area but in almost the entire Chicontepec reservoirs.

Sensitivity analysis suggests that rock property heterogeneity plays a significant role in drainage efficiency and oil recovery. If the reservoir is assumed to be homogeneous without being too optimistic in their assigned rock attributes, better fluid-sweep efficiency and greater oil recoveries are observed. This result agrees with the work of Tyler and Finley (1992) in demonstrating the importance of rock heterogeneity on oil recovery efficiencies. As the S4 reservoir, and perhaps the entire reservoirs of Chicontepec basin, are composed of rock types of highly-dispersed quality, fluid-flow will be via tortuous pathways that make oil recovery difficult. This demonstrates that the architectural controls together with rock property distribution in the reservoirs of this study, exerts a fundamental control on oil recovery efficiency.

No attempt was made to presume different fluid properties than normally observed in Chicontepec crude-oils (*e.g.* varying bubble pressure or solution gas) as low-oil recovery by solution gas is assumed to apply entirely to these reservoirs. Simulation exercises were mainly focused on evaluation of sub-bubble production by rock property variation and fracture propagation. Solution gas drive is known to be the least efficient drive mechanism (Ahmed, 2006) and in these reservoirs accounts for a minor proportion of their estimated OOIP. After 270-day production, the HUM-4005 well reached a cumulative oil production equivalent to 5% recovery factor. This agrees with oil recovery efficiencies observed in most Chicontepec reservoirs. Recovery factors of 4, 6 and 17% were obtained for constrained, extended and homogeneous simulation case scenarios.

Modelled relative permeability curves for HUM-4005 well describe a reservoir with limited flow capacity. These indicate that permeability to oil should be zero (*i.e.* no oil production) when solution gas reaches 50% saturation at irreducible water conditions (Fig. 8.31). Unfortunately, no gas production reports were available to simulate gas rates and in this way calibrate the end-point gas saturation. Calibration of gas production was only conducted by comparison of gas rates normally observed in these reservoirs. Generally, gas rates are under 1 MMscf/day in the first months of production.

By contrast, water production in these reservoirs is highly variable and normally does not follow a continuous trend in their production profiles. Water rates in most Chicontepec reservoirs range from 1 to 30 STB/day, although some wells produce no water. The oil-water relative permeability curves rather describe a reservoir with mixed wettability. As large pores are oil-wet and are assumed to be filled with oil, and small pores are water-wet and filled with water (Salathiel, 1973), the pore size distribution (*i.e.* the proportion of oil- and water-wet pores) determines the oil-water relative permeability behaviour.

Overall, the S4 reservoir behaves as a very compartmentalized unit, mainly because the low-connectivity of the reservoir rock, which is product of the combination of the low-permeability fabric and the high-variability of rock attributes. Unique production profiles, recovery efficiencies and drainage area are developed by wells in the study area.

8.5 Conclusions

Rock properties of the S4 reservoir were modelled using a series of analytical techniques to evaluate their heterogeneity. The spatial analysis of rock attributes together with the interpreted sedimentary facies, were integrated as a medium to populate un-sampled zones in the study area.

The modelled rock properties resulted from this approach were used as input parameter data for conducting a number of simulation scenarios to try to explain the low productivity of the reservoirs in this study. The spatial distribution of rock properties and their impact to oil production was analysed, together with the fracture propagation.

Overall, rock properties of the reservoirs in this study, and perhaps in the majority of Chicontepec's, are spatially heterogeneous. This exerts an important control in fluid-flow efficiency and consequently on oil productivity and recovery. Stimulation efficiency also impacts on oil productivity, although no significant difference on oil recovery is observed. The current field's development design together with the limited extension of the completion intervals seem to also contribute to the low recovery efficiencies. Infill drilling or re-stimulation activities should be evaluated.

Each well behaves as a completely separated reservoir unit with its own production performance, cumulative oil volumes and drainage coverage efficiencies. This is mainly the result of the low-permeability trend, the variability in the rock property distribution and to the induced-fracture extension.

CHAPTER IX. DISCUSSION

The aim of the present research project is to provide experimental evidence and tools to increase the level of understanding of the Chicontepec reservoirs. The ultimate objective is to support the overall exploitation of these by providing results that will lead to increases in oil productivity and recovery. In the following paragraphs there will be discussed the key points resulted from this study, as well as their applicability and uncertainties.

9.1 Representativeness of data used in this study and implications for other Chicontepec oilfields

This study used rock samples, fluid mixtures and general subsurface data from a study area that was assumed to represent most of the characteristics observed in the Chicontepec reservoirs. Comparison of petrophysical and mineral properties of these with those observed in the rest of Chicontepec oilfields is shown in Figures 9.1 and 9.2. Overall, the rock data employed in this study, as observed from their porosity/permeability trend and their bulk mineral fractions, seems to be a comprehensive representation of most reservoirs in the Chicontepec basin.

Similarly, the crude-oil sample used for conducting the wettability experiments in this study observed comparable compound classes of most crude-oils in Chicontepec reservoirs (Fig. 9.3), although it is generally accepted that composition of Chicontepec crude-oils is highly variable. Chicontepec crude-oils show significant variation mainly in their polar compounds (NSO), which has been referred to in the literature as one of the key parameters that controls the wetting characteristics of a rock (*e.g.* Buckley and Liu, 1998; Yang *et al.*, 2003; Buckley and Fan, 2005). It is expected that different adhesive characteristics of oil can be produced, thus different wetting tendencies (*e.g.* strongly-wetted, fractional, mixed) may potentially result.

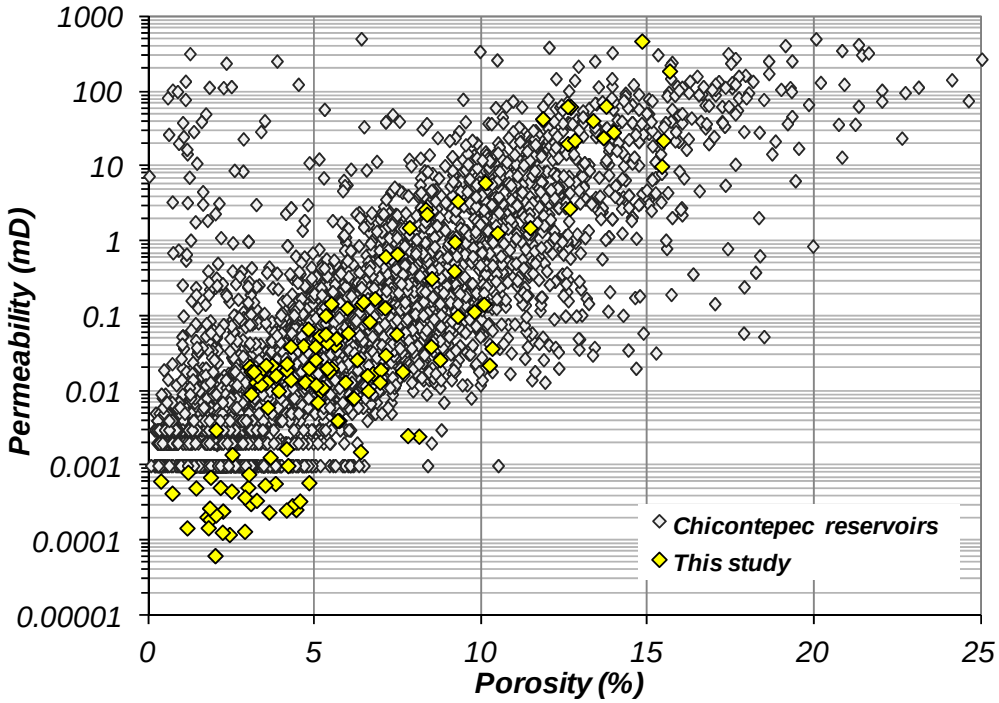

Figure 9.1 Comparison of porosity *vs* permeability trend between rock samples used in this study and Chicontepec rock samples from diverse oilfields (crossplot constructed using PEMEX databases and results obtained from this study)

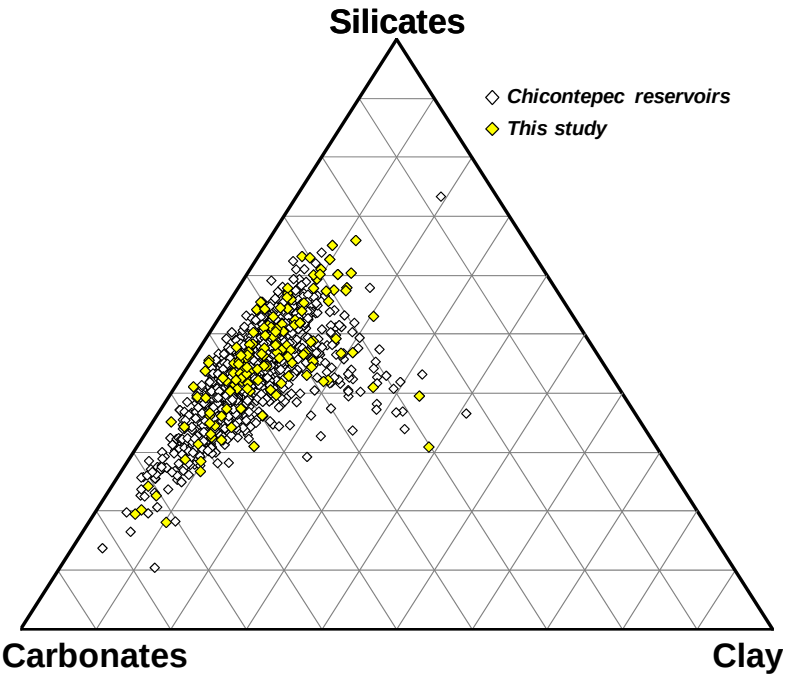

Figure 9.2 Comparison of bulk mineral constituents of samples used in this project with the rest of Chicontepec oilfields, where *Silicates*=Quartz+Feldspar+Plagioclase; *Carbonates*=Calcite+Ankerite+Dolomite. (Ternary diagram constructed using PEMEX databases and results obtained from this study)

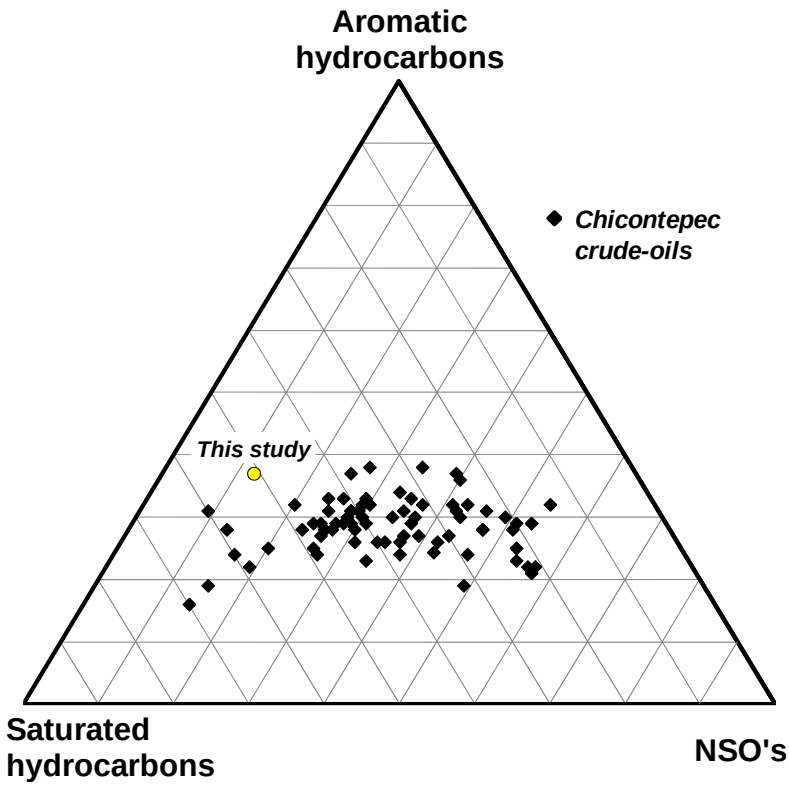

Figure 9.3 Comparison of Chicontepec crude-oils and the sample used in this study (data courtesy of Mayol-Castillo, 2005; ternary diagram modified from Tissot and Welte, 1985)

Figure 9.1 display the porosity/permeability trend of Chicontepec oilfields, including the samples used in this study. As it is observed, there are tendencies that were not captured in this study and that may reflect interesting characteristics worth to be analysed in further studies. For example, an anomalous high permeability tendency (*i.e.* greater than 1 mD) is developed at porosities lower than 5%. It is unclear whether this area is produced by the use of damaged cores, highly-laminated samples or naturally fractured plugs. However, those samples falling in this area were removed from this study as these were considered not representative of the general trend. Natural fractures in Chicontepec reservoirs deserve a special analysis that was not covered in this study. These are relatively frequent as reported by PEMEX (2009), Tyler *et al*. (2004) and Luces *et al*. (2012), and are seen from outcrops and well-logs to subsurface core samples. Tyler *et al*. (2004) observed that the fractures in cores are partially cemented with calcite and frequently oil-stained, which suggest that they are natural. Still is debatable the role of natural fractures on production in the Chicontepec reservoirs. They seem to not being exerting a significant influence on oil production; however, this should be analysed in more detail in further studies. In some areas, the presence of what it seems natural fractures is rather obvious as displayed in Figure 9.4. These observations were made during the interpretation of well-logs. Since this behaviour does not seem to be related to borehole rugosity effects nor logging-tool failures, this has been interpreted as being due to the presence of fractures. For

example, Figure 9.4 shows that neutron, density and sonic deflections appear to highlight a high porosity interval. The bulk density readings correspond to values close to the drilling-mud density, suggesting that the interval may be filled with mud. Similarly, the sonic signal observes significant velocity attenuation, which normally is produced by fluids. Although it is uncertain whether fractures are natural or drilling-induced by just observing conventional well-logs, this same expression has been consistently associated to natural fractures in a number of wells with image log information in the Chicontepec basin.

Despite their apparent influence on flow, no significant improvement in oil performance is observed when apparent naturally fractured intervals are completed (such as illustrated in Figure 9.4). This may indicate that the natural fractures, or fissures, are not well connected and do not form a continuous path for fluid flow. The rock samples suspected to be naturally fractured were removed from this study since fractures do not seem to significantly control fluid flow in the Chicontepec reservoirs.

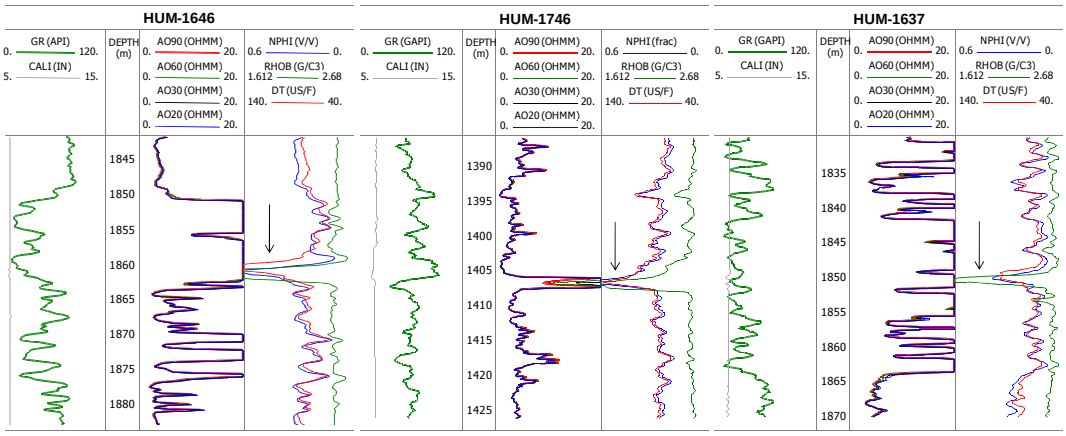

Figure 9.4 Apparent naturally fractured zones in wells of the study area. Observe the high-porosity deflection in the three porosity curves (black arrow). No significant improvement in oil production (other than ordinarily observed in most Chicontepec production profiles) is observed when this type of response is completed

Other porosity/permeability trends are also observed in Figure 9.1 and that were not represented with the rock samples provided in this study. A high porosity trend (*i.e.* greater than 15%) with no significant improvement in permeability values (as compared to the general tendency) is also developed. No rock samples were available to capture this trend. An additional tendency is seen at porosities ranging between 10-20% and permeabilities between 0.01-1 mD. Again, the rock samples used in this study were unable to represent this tendency. The different porosity/permeability tendencies developed in Figure 9.1 reflects different trends of storage/flow capacities that perhaps were produced by a diversity of sedimentological and diagenetic histories. It would be interesting to compare each trend by their sedimentary facies that may explain the differences in porosity/permeability tendencies. Overall, the rock samples

used in this study were able to represent a range of porosity/permeability trend that is consistently observed in most Chicontepec reservoirs. Some other trends that seem to be least frequent in the general behaviour were unable to be captured. Precautions should therefore be taken in applying results of this study to the entire Chicontepec sand units.

9.2 Causes of low productivity in the Chicontepec reservoirs

Chicontepec reservoirs produce at low-oil rates and have low recovery efficiencies because they combine three main characteristics: low-transmissivity capacity of the reservoir rock, severe heterogeneity and solution-gas drive as the main source of energy for oil production. The radial flow equation, defined earlier in this work (Chapter 2), can be used to understand the low-oil productivity in the Chicontepec reservoirs.

The oil rate (Q_o) for a radial flow of incompressible fluid is defined as:

$$Q_o = \frac{0.00708kh(p_e - p_{wf})}{\mu_o B_o ln(r_e/r_w)} \ldots\ldots\ldots\ldots\ldots\ldots (9.1)$$

where: Q_o is the oil flow rate (STB/day), p_e is the external pressure (psi), p_{wf} is the bottom-hole flowing pressure (psi), k is permeability (mD), μ_o is the oil viscosity (cP), B_o is the oil formation volume factor (rb/STB), h is the reservoir thickness (ft), r_e is the external or drainage radius (ft), r_w is the wellbore radius (ft).

Amongst the variables that control the oil production (equation 9.1), permeability is probably the factor that exerts the most significant influence. The reservoirs of this study, and perhaps most of the Chicontepec basin, have low permeability values (*i.e.* generally lower than 1 mD). Their reduced permeability is mainly the result of its textural nature and extensive diagenesis. Texturally, these reservoirs are composed by fine- to very-fine sand grains and their distribution (as well as their shape) is normally variable, resulting in poorly-sorted textures. The combination of fine-grained and poorly-sorted textures usually produces small pore-size distributions. Additionally, the pore space has been reduced significantly by the extensive calcite precipitation, which has diminished by up to 50% the intergranular volume in some cases. The reduced pore space resulting from fine-grained and poorly-sorted textures, together with the widespread cementation, develops low-permeability trends, which results into the development of tortuous pathways to fluid-flow. The small pore-size distribution also means that these reservoirs have high capillary pressures and irreducible water saturations. Secondary pores do not seem to improve permeability as they are not well connected.

Apart from the low-permeability, these reservoirs are highly heterogeneous. This means that permeable beds are erratically distributed according to their architectural elements (*i.e.*

sedimentary facies) and the extent of diagenetic alteration. These beds of variable thickness are separated by ultralow permeability bodies (*e.g.* shales, silts or highly-cemented sandstones), resulting in uneven NTG ratios. As result, the movement of fluids during drawdown occurs within small drainage areas. Low-recovery efficiencies are generally developed as consequence of the small drainage area described by the wells and the poor-recovery that is generally associated with solution-gas drive.

It is generally accepted that Chicontepec reservoirs were initially undersaturated; however, less than 800 psi drawdown is generally required to reach bubble-point. During sub-bubble production, gas evolves continuously from the oil phase and the critical gas is reached at relatively low saturations. After primary production, the reservoirs in this study area usually have large residual oil saturations which have been observed in displacement experiments and during production simulation. The Chicontepec reservoirs are subjected to secondary/tertiary applications of oil recovery.

Overall, the descriptive, analytical and numerical results of this research project, demonstrates that the Chicontepec reservoirs produce at low oil rates because they combine a low-transmissivity capacity of its reservoir rock, a high spatial variation of their petrophysical properties and a drive mechanism that is well known to be the least efficient.

9.3 Impact of formation damage on production from the Chicontepec reservoirs

At the very beginning of this research project it was suspected, as first hypothesis, that formation damage was playing a significant role on the low oil production in these reservoirs. The latter was based on the presumption of the incompatibility of stimulation fluids and formation minerals. In this way, one of the first series of experiments conducted in this project was designed to analyse formation damage mechanisms. As result, the experiments demonstrated that the Chicontepec reservoir rock may show high sensitivity to the forced injection of low-ionic strength brines and polymer-based fluids, and is prone to formation damage. Clay swelling and polymer adhesion seem to be the main mechanisms of permeability impairment, together with gas-trapping and asphaltene precipitation.

Although experimental data suggest that current stimulation practices may potentially produce significant permeability reductions in core plugs and that phase-trapping and asphaltene precipitation may also exert certain influence on oil productivity, it remains uncertain exactly how much formation damage contributes to the overall crude-oil output in the reservoirs of this study. This is mainly due to the extreme heterogeneity of these reservoirs that makes difficult to identify a particular mechanism of formation damage. For example, the invaded fluids can

extend into the reservoir at variable distances depending upon the injection rates and pumping periods, the reservoir characteristics and the fracture length, amongst other variables that can be specific for every sand unit. Formation damage may be difficult to evaluate mainly due to the complexity of determining the extent of the damaged region and its permeability, and in this way analyse its total contribution to oil productivity.

Despite its potential to influence oil production, formation damage does not seem to be required to explain the low-oil production of these reservoirs. Production modelling conducted in this work suggests that the overall oil production is mainly governed by the combination of the poor-connectivity, low-permeability and the poor driving force. The simulation exercise conducted in the HUM-4005 well assumed a fracture as a high-conductive path of uniform permeability. No permeability impairment mechanisms around the fracture-face were necessary to explain the low-oil recoveries and poor drainage efficiencies. Formation damage does not seem governing oil production in the reservoirs of this study. This may possibly due to their short-term pumping periods invading a limited region of the reservoir or effective cleanup process of the fracturing fluids. It may be expected that more drastic effects of permeability impairment by fluid incompatibility in the reservoirs in this area may be developed in long-term water injection applications such as waterflooding.

Formation damage by phase-trapping in the reservoirs of this study seems to exert different outcomes, mainly because the variability of oil composition. According to the simulation analyses conducted, the gas liberation during sub-bubble pressure production creates temporary trapping of gas in the near-fracture face where the greatest drop of pressure is developed during drawdown. The oil relative permeability will be lower than that of gas in this region because gas will occupy the largest pores. The near-fracture region of high-gas saturation impeding oil to flow may cover variable distances and their effect on oil productivity may take place at variable time-periods during oil production depending upon the crude-oil properties, the pressure variations during production and the reservoir characteristics. The Chicontepec crude-oils show wide variation not only in composition but also in bubble-point (P_b) and solution gas content (R_s), even in genetically-related producing units. In this way, gas-trapping together with the extreme heterogeneity and low matrix-permeability may result in large variations in the production characteristics of the reservoirs in this study area. The erratic behaviour of wells appearing to deplete at variable time-periods or producing at uneven gas-to-oil ratios, can be considered a result of this complex combination.

Another formation damage mechanism that is difficult to evaluate and may potentially occur in these reservoirs is asphaltene precipitation. It is generally accepted that asphaltenes precipitate when crude-oil loses its ability to disperse the particles, which normally occurs due to pressure

and temperature changes. During oil production, asphaltene deposition may take place in the near-fracture face region where the pressure differential is greatest. Similarly to the gas-trapping phenomena, asphaltene deposition may create a damaged region around the fracture face at variable geometries depending on the crude-oil properties and the pressure drop (*i.e.* drawdown). Chicontepec crude-oils are generally rich in high molecular weight compounds (or NSO) and prone to precipitate asphaltenes, as was observed from crude-oil sample used in this study (Chapter seven explains a method to determine the onset of asphaltene in the HUM-1689 crude-oil). Their true effect in the overall oil productivity in the reservoirs of this study depends on the size of the damaged zone and the formation's permeability reduction.

Overall, formation damage mechanisms recognized during the experimental work of this study, do not seem to exert significant controls on oil production, at least during primary depletion. The simulation case scenarios developed during this project, suggest that the oil production is mainly controlled by the low-transmissivity capacity of the reservoir rock, the high spatial variation of petrophysical properties and the primary drive energy. The impact of formation damage on oil productivity should properly be analysed through pressure transient tests (*i.e.* pressure disturbance monitoring in the reservoir) that permit the comparison of the flow efficiency index of an undamaged wells (ideal case) with those that are believed to be damaged. No pressure transient data was available in wells of this study.

9.4 Impact of the contemporary tectonic stress regime on stimulation

Microseismic analysis undertaken during a number of hydraulic fracture treatments in the Chicontepec basin (Berumen *et al.*, 2004a, 2004b; Gachuz-Muro, 2009; Gutierrez *et al.*, 2010; Gutierrez *et al.*, 2014a, 2014b, 2014c; Rabe and Ortiz-Ramirez, 2010), indicate that hydraulic fractures have an orientation that is consistently in North-Eastern directions, varying from N14°E to N44°E. This same orientation is also observed in well-log data and for natural fractures in outcrop (PEMEX, 2009). Figure 9.6a is a stereogram displaying stress-induced failures (*i.e.* breakouts) in the HUM-4004 well. This was interpreted using the micro-electrical image log. Breakouts are cross-sectional elongations caused by localized failures around the borehole. These are normally developed in a direction parallel to the minimum horizontal stress (Nordgård Bolås and Hermanrud, 2002) as it is illustrated in Figure 9.5. The orientation of breakouts together with the wellbore obliquity reflects an indication of the contemporary horizontal stress field.

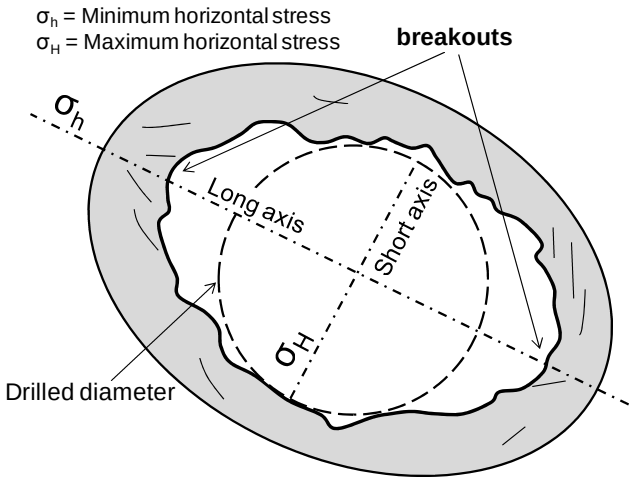

Figure 9.5 Schematic illustration of breakout detection; the wellbore tends to elongate parallel to the minimum horizontal stress (modified from McLellan, 1994)

Understanding the current tectonic stress regime in Chicontepec basin is important when trying to maximise fracture propagation. Hydraulic fractures propagate parallel to the maximum horizontal stress (Hubbert and Willis, 1957) and in the case of most Chicontepec reservoirs this tends to be developed consistently between N14°E to N44°E direction. The horizontal stress appears to be the largest (S_1) in these reservoirs, mainly because the sand units are relatively shallow and strongly influenced by tectonism. The main tectonic event that appears governing horizontal stress distributions in Chicontepec basin is the Cocos Plate subduction zone (Fig. 9.6b). The compressive direction of the Cocos Plate against the North American Plate coincides to the orientation of hydraulic fracture propagation in Chicontepec reservoirs.

a) **b)**

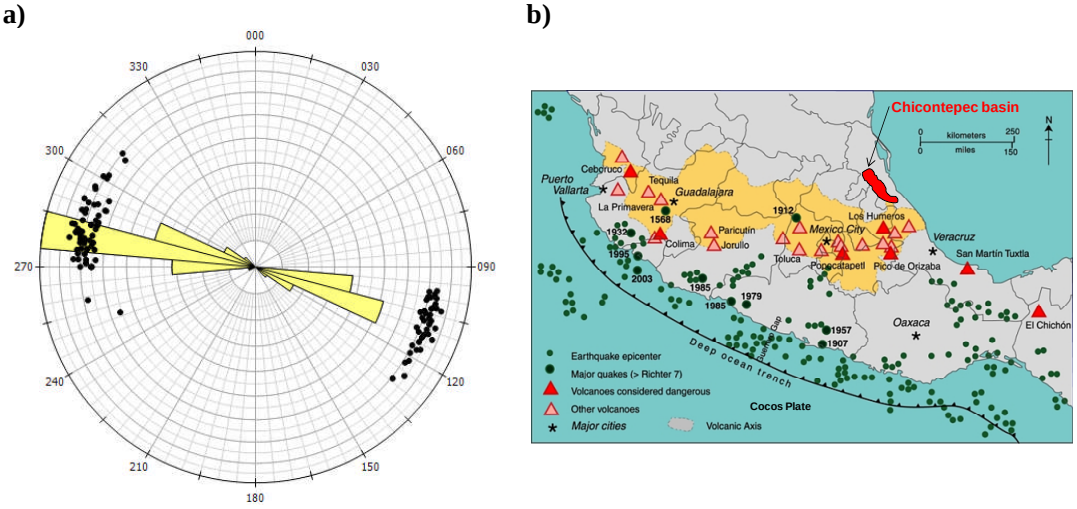

Figure 9.6 a) interpreted breakouts in HUM-4004 well. Breakouts are developed orthogonally to the direction of maximum horizontal stress. Black data-points in the image on the left show the direction of multiple breakouts observed in the wellbore, and yellow bars are the most frequent direction of these (interpretation of Estopier, 2009); b) the Cocos plate subduction zone that appears governing horizontal stress distribution in Chicontepec basin (modified from http://geo-mexico.com/?tag=geology)

As hydrofractures propagate in a known direction, the use of oriented guns or oriented completions to maximise hydrofracture creation and proppant placement would be an option to increase the stimulated reservoir volume in the reservoirs of this study. Moreover, oriented perforations would not only maximise the hydraulic fracture length, but also these may be used to take advantage of the stress regime to reactivate the partially cemented natural fractures observed in these reservoirs and create preferential flow-patterns to try to increase oil recovery efficiency. Although the combination of oriented completions and the apparent high horizontal stress-anisotropy may potentially produce simple fracture geometries and a large rock volume would be left undrained; it is expected that more efficient sweep-patterns, as compared to those developed by conventional completions, may be produced. Oriented fracturing completions have been applied in diverse oilfields with positive results on production (*e.g.* Pospisil *et al.*, 1995; Gama *et al.*, 2009).

9.5 Evaluating reservoir connectivity in Chicontepec reservoirs

The rock properties of the reservoirs in this study, and perhaps in the majority of Chicontepec's, are spatially heterogeneous. Reservoir modelling and simulation case studies conducted in this project demonstrate that heterogeneity plays a significant role in controlling the drainage efficiency and oil recovery; this is in agreement with data reported by Tyler and Finley (1992). They demonstrated that heterogeneity tends to significantly influence the ultimate recovery efficiency of the reservoirs. In general, lower recovery efficiencies are produced as the degree of heterogeneity of the reservoir increases.

The way in which the heterogeneity has been addressed in the Chicontepec reservoirs normally relies on descriptive approaches, which have generally been produced by integration of sedimentary characteristics and seismic imaging techniques (*e.g.* Tyler *et al.*, 2004; PEMEX, 1998; PEMEX, 2004; PEMEX, 2008). Other methods have included purely geostatistical applications (*e.g.* Abbaszadeh *et al.*, 2008; Takahashi *et al.*, 2006; Ataei, 2012) without incorporating detailed sedimentary analyses; whereas few examples have integrated dynamic data (*e.g.* Tyler *et al.*, 2004).

Overall, the heterogeneity of the Chicontepec reservoirs has been partially assessed since it has mainly been studied only from a descriptive point of view. Detailed sedimentary descriptions combined with geostatistical tools allow estimates to be made of the likely distribution of rock properties, which are frequently used to infer sand connectivity. An example is presented in Figures 9.7 and 9.8, which are part of the reservoir modelling analysis of this study. The modelled permeability distribution across a number of wells in the study area is shown (Fig. 9.7). The interpretation corresponds to layer 12 of the S4 reservoir. The area was selected since

it shows relatively low-permeability contrasts compared to other regions, *i.e.* the sands are believed to potentially be connected according to their sedimentary facies distribution and modelled permeability. Figure 9.8 shows the permeability variations across a number of these wells, where the sand connectivity may be inferred. Wells are equidistantly spaced every 400 m.

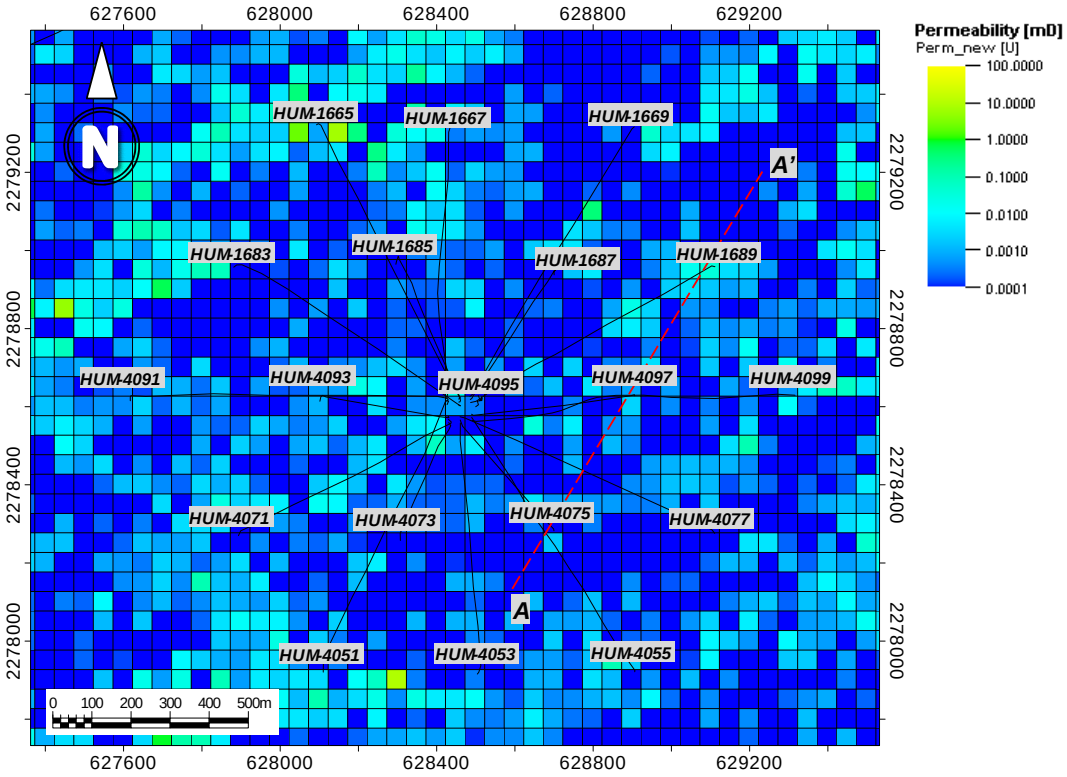

Figure 9.7 Permeability distributions of layer 12 in the modelled S4 reservoir

Although the type of information shown in Figures 9.7 and 9.8 is valuable in terms of imaging rock property distributions in the subsurface, this should only be considered as the best estimate of the reservoir heterogeneity. Innumerable versions (*i.e.* realisations) of the rock property distribution may be possible by varying the input sedimentary controls (*e.g.* supply direction, number of channels, etc.) and their degree of continuity (*i.e.* variogram). Therefore, the rock property distribution resulting from descriptive/analytical methods is not unique.

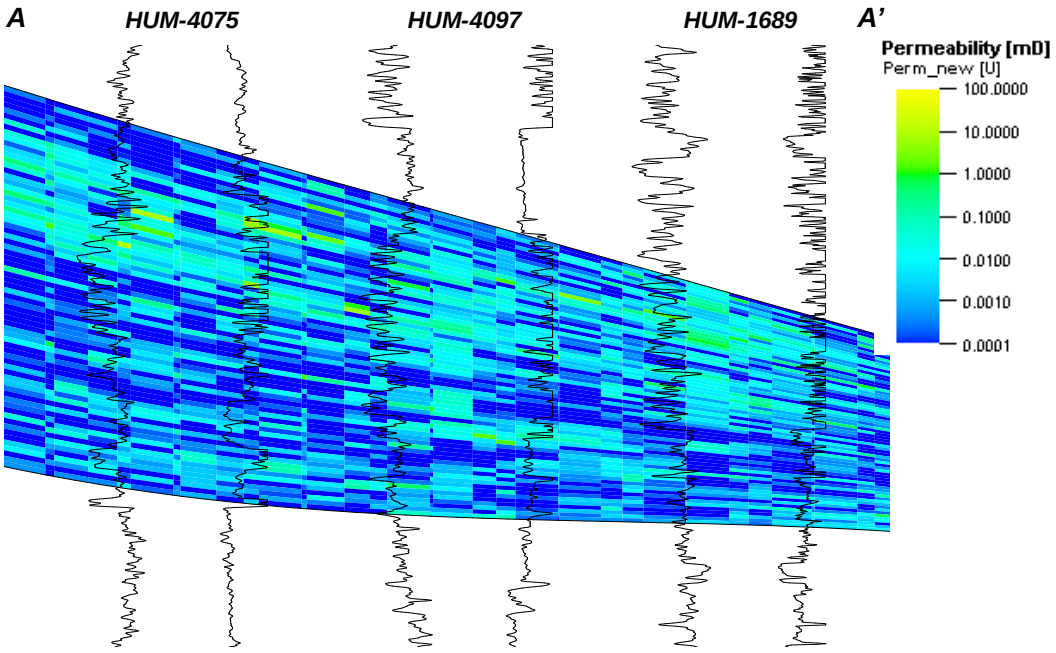

Figure 9.8 Cross-section of a number of wells shown in Figure 9.7 illustrating permeability distributions across the S4 reservoir. One may think that these sand units may be hydraulically connected to some degree; however, sand connectivity should be evaluated by integrating with dynamic approaches. Well spacing is 400 m

The sand connectivity analysis should be complemented with more realistic evaluations. Pressure interference tests (*i.e.* pressure disturbance monitoring across injecting/producer wells) or chemical/radioactive tracers can be used in complement the descriptive approaches to effectively assess the sand connectivity in these reservoirs. The interference test consists of measuring the change in pressure that occurs in an offsetting, shut-in observation well, when changes in flow-rate at one or more active wells in the area occur. Changes in pressure of the offset well are attributed to hydraulic communication (*i.e.* connectivity). The chemical/radioactive tracer tests are used to monitor fluid movement between injection and observation wells. A chemical substance or radioactive material is injected downhole into an injection well during, for example, a waterflooding pilot test. The substance is monitored in one or more active wells in the area to establish whether communication between wells exists.

Although the mentioned methods cannot determine quantitatively the degree of connectivity, they may be used in combination with descriptive/analytical approaches to improve the sand connectivity evaluation of the Chicontepec reservoirs. Success on the exploitation of these reservoirs, as well as the implementation of EOR applications; may strongly depend on the way the reservoir heterogeneity is evaluated.

Imaging the degree of heterogeneity in the Chicontepec reservoirs is important since it may produce different outcomes during the oilfield cycle. For example, during the exploitation stage,

the understanding of the heterogeneity may guide the position of wells and their optimal spacing. In contrast, during secondary and enhanced recovery mechanisms, the appreciation of the heterogeneity will be a fundamental parameter for optimum oil-sweep efficiency. Improving the subsurface image (*i.e.* seismic data) would also improve the way the heterogeneity is evaluated.

Conceptualising the reservoir heterogeneity of the Chicontepec sands in their different oilfield stages, is still an area of opportunity to be explored not only in this project but perhaps in the majority of the Mexican oilfields.

9.6 Increasing reservoir contact effectiveness

At the very beginning of the exploitation of the Chicontepec reservoirs, it was thought that by drilling a large number of vertical wells would be enough to compensate their low-permeability, and in this way achieve a steady oil output. Initial production projections even estimated that the project would able to produce nearly a million of barrels per day (Morales-Gil, 2009). After drilling more than three thousand wells and observing the high-declination profiles in most wells, it is clear that this conception was not only naive but reflected of profound lack of understanding of the nature of these reservoirs.

The majority of wells in Chicontepec basin have been drilled vertically and hydraulic fractures in these normally reach propped half-lengths of 140 m. Simulation results reported in Chapter 8 indicate a poor drainage efficiency developed by wells, mainly due to the low-transmissivity capacity of the formation, the severe heterogeneity and drive mechanism. As these reservoirs are exploited from vertical wells and single completion designs, no significant oil volume is recovered for each added metre of induced fracture in vertical wells. This is mainly because the well and fracture system contacts a very small portion of the reservoir. In light of the results obtained in this project, it becomes clear that the current exploitation technique deployed in the Chicontepec reservoirs (*i.e.* combination of vertical drilling and conventional fracturing completions) is inefficient.

Unconventional well completions, such as the combination of horizontal drilling and multi-stage hydraulic fracturing technologies (HD+MSHF), have allowed significant oil to be produced in tight-oil reservoirs (*e.g.* Li *et al.*, 2008; Nemirovich and Islamgaliev, 2014). The technique aims to increase the reservoir contact effectiveness by placing greater wellbore lengths in the pay zone. Multiple conductive paths are produced by fracturing a number of pay intervals along the horizontal section, which are completed separately and set on production at the same time. Compared to vertical wells, a greater well drainage area is developed and thus superior oil volumes are normally recovered. An evaluation of such completion technique in

reservoirs of this study is shown in Figure 9.9. This illustrates the simulated oil production by the combination of HD+MSHF. The model constructed is basically the 'real case' study described in Chapter 8 but the HUM-4005 vertical well was assumed to be horizontal.

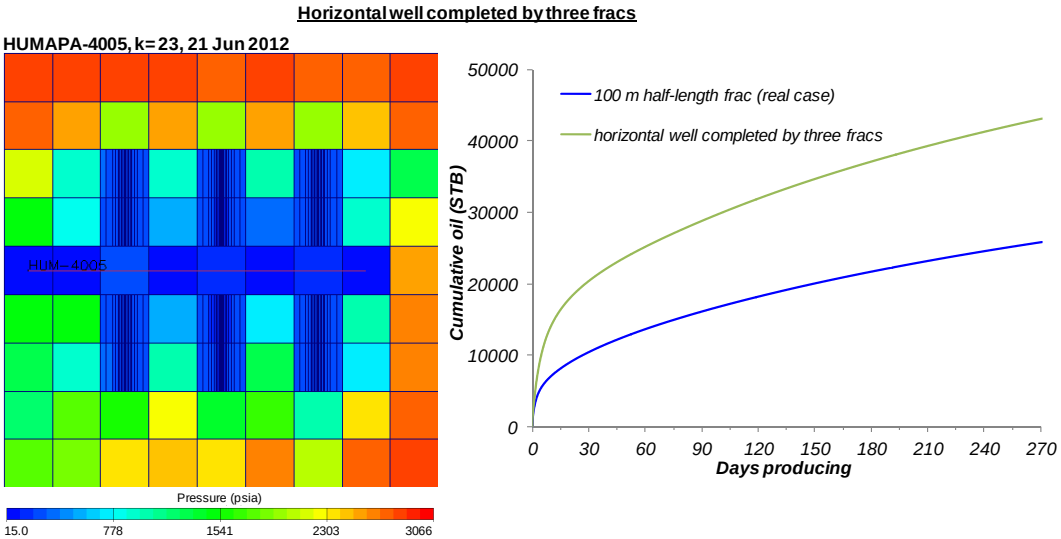

Figure 9.9 Enhanced oil production by the combination of horizontal drilling and multi-stage hydraulic fracturing. The blue curve at the right image describes the cumulative oil produced by a vertical well completed in a single interval, whereas the green curve the extra oil produced by the horizontal well

Three hydraulic fractures in Figure 9.9 were placed along the wellbore's horizontal trajectory and oil-production was assumed to be commingled. Uniform half-propped lengths of 100 m were supposed in each case. No other change but the number of induced fractures and the change in wellbore geometry and extension were made, *i.e.* rock property distribution, fluid contacts, fluid property, etc. were left with no change as it was described in the 'real case' study.

As one would expect, better drainage coverage is developed by the horizontal well with three hydraulic fractures. The pressure transient cloud after nine-month production extends to almost all grid cells, indicating better drainage efficiency. The extra oil produced was around double that obtained from the 'real case' at the same producing periods (Fig. 9.9). The additional oil recovered does not seem as large as that produced from the conventional completion, probably because only three fractures were set on production. The oil productivity in horizontal wells seems largely dependent on the length of the horizontal section, the sand quality intersected by the wellbore, and the number of intervals completed and opened for production. There is an economic limit to be considered in which the cost of added metre of horizontal drilling together with the fractures must be feasible. A comprehensive analysis to evaluate the point of diminishing return of fracture stimulations is presented by Mace *et al*. (2011).

With a current oil price of USD $70/barrel, a conventional well (*i.e.* vertically drilled with single fracture completion) in Chicontepec basin must produce at least 20,000 STB to surpass the economic limit (the average cost of conventional wells in Chicontepec is USD $1.4 million). A horizontal well can exceed between four to eight times the average cost of a vertical well in the Chicontepec project (Narvaez, 2012). The expenditure can even be more considering the number of hydraulic fractures planned to be conducted or the complications experienced during the drilling stage, which in horizontal wells is a recurring problem. That would mean that unconventional wells in these reservoirs (*i.e.* HD+MSHF) should produce at least between 80,000 to 160,000 STB to achieve profitability.

Despite their cost, the combination of horizontal drilling and multi-stage fracturing has recently given encouraging results in these reservoirs. An example is reported by Gutierrez *et al*. (2014a) in which two horizontal wells were drilled parallel to each other in a sand unit of the Escobal oilfield, located 15 km south to the study area. Both wells were drilled parallel to the minimum horizontal stress and simultaneously fractured in multiple stages to try to communicate fractures along each horizontal lag. Both wells were fractured in alternate sequence from toe to heel, with one well holding the fracture pressure while the adjacent well was fractured. Microseismic monitoring indicated that large and complex fracture geometries were produced, which normally is regarded to favour oil productivity (Mayerhofer *et al.*, 2010). Cumulative oil produced from both wells after three-month production was 240,000 STB, which is fourteen times the average cumulative oil in the entire field at equivalent production periods. By the time this thesis was written, oil production in both wells was nearly one million barrels. The extra oil produced was ascribed as the result of greater stimulated reservoir volume (SRV) produced by large and more complex fracture geometries. The latter is significant in terms of demonstrating that unconventional completions can be a key parameter to change the economic equation of the tight-oil reservoirs such as Chicontepec.

9.7 Scope for secondary/tertiary oil recovery in the Chicontepec reservoirs

Unconventional exploitation techniques (*e.g.* HD+MSHF) may significantly increase the initial oil productivities and cumulative volumes in these reservoirs, compared to those obtained in vertical wells with single fracturing systems. However, despite their apparent positive results, this technology is designed to improve the primary recovery efficiency by increasing the equivalent wellbore drainage area and enhancing reservoir contact area. Nevertheless, large amounts of oil remain unproduced after primary depletion. This is mainly due to the combination of their low-permeability, extreme heterogeneity and their low-efficient drive mechanism. The Chicontepec reservoirs are therefore candidates for secondary/tertiary applications of oil recovery. Oil recovery mechanisms are synthesized in Figure 9.10.

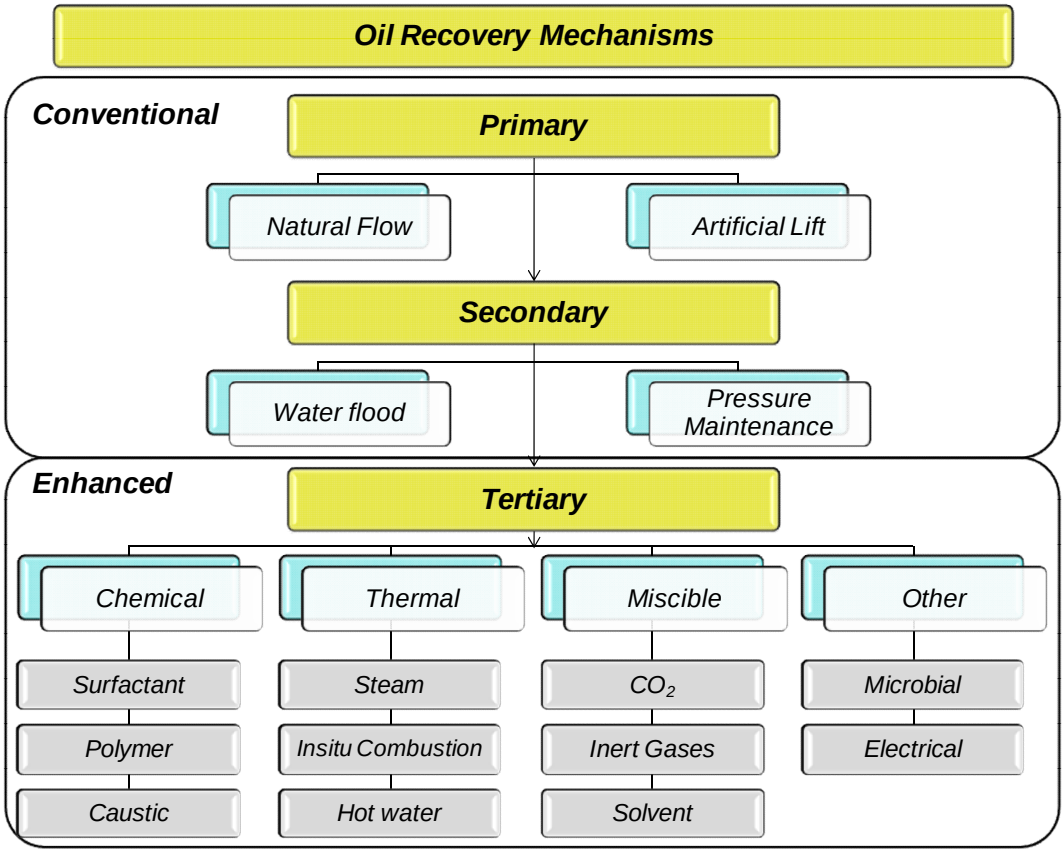

Figure 9.10 Oil recovery mechanisms (modified from Green and Willhite, 1998)

It has been discussed in preceding chapters that the reservoirs of this study (and potentially the entire Chicontepec reservoirs) have non-uniform wettability. The tests applied to restored-state rock samples, indicate that the mixed-wet condition best describes their wettability. Mixed-wettability is a term defined by Salathiel (1973) to describe the condition in which smaller pores in the rock are water-wet and saturated with water; and the larger pores are strongly oil-wet.

Mixed-wet state results from the oil migration and entrapment process, in which oil preferentially migrated into the larger pores due to their lower capillary entry pressure and thus became oil-wet due to surface active compounds found in crude-oil. Smaller pores remained water-wet as greater pressure threshold was required for them to be invaded by oil.

Figure 9.11 illustrates the capillary hysteresis loop of strongly-wetted systems, whereas Figure 9.12 shows the capillary trend described in mixed-wet scenarios. Observe in Figure 9.11 that a threshold capillary pressure must be exceeded to displace brine with oil in water-wet systems (Fig. 9.11a, position 1 and 5). At irreducible water saturation, brine will imbibe spontaneously into the core (Fig. 9.11a, position 2). In comparison, in oil-wet systems, oil will displace brine spontaneously (Fig. 9.11b, position 4) and no threshold capillary pressure is developed during the secondary drainage cycle (Fig. 9.11b, position 5). Better oil recoveries by spontaneous imbibition of water are normally produced in strongly water-wet reservoirs (Donaldson and Alam, 2008).

By contrast, in mixed-wet scenarios (Fig. 9.12), no threshold pressure is developed in both the secondary drainage and spontaneous imbibition cycles (*i.e.* the rock has both oil-wetted and water-wetted pores). As larger pores are oil-wet in this wetting condition, greater amounts of oil compared to that of water are generally imbibed into the sample. This is why the Amott-Harvey wettability index (I_{AH}) is partially accurate in describing non-homogeneous wetting systems.

During simulated waterflooding (*i.e.* forced displacement of oil by water, indicated by position 3 in Figures 9.11 and 9.12) a large portion of the oil is recovered before water breakthrough in strongly water-wetted reservoirs; whereas in both strongly oil-wetted and mix-wetted reservoirs, most of the oil is recovered after water breakthrough, permitting them to reach even lower residual oil than in water-wet reservoirs (Morrow, 1990; Anderson, 1987b; Donaldson and Alam, 2008; Skauge *et al*., 2003). Oil forms a continuous path through larger pores in mixed-wetted systems, thus waterflooding displaces oil more efficiently (*i.e.* lower injection pressures are needed) allowing the rock to reach lower *Sor* values after injection of large amount of water (Anderson, 1987a; 1987b). This is explained by Mattax and Kyte (1961) to be the result of thin oil filaments that permits oil to be drained behind the waterfront (*i.e.* film drainage).

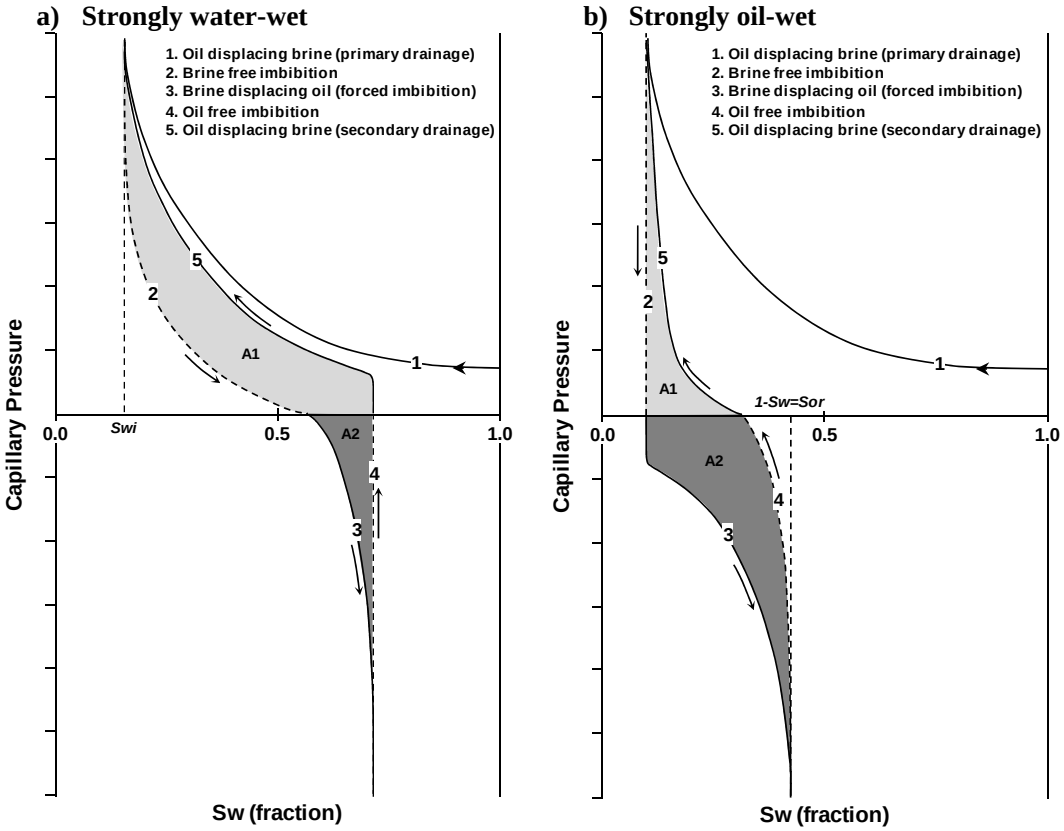

Figure 9.11 Drainage and imbibition capillary pressure curves for strongly wetted reservoirs (modified from Donaldson *et al.*, 1969)

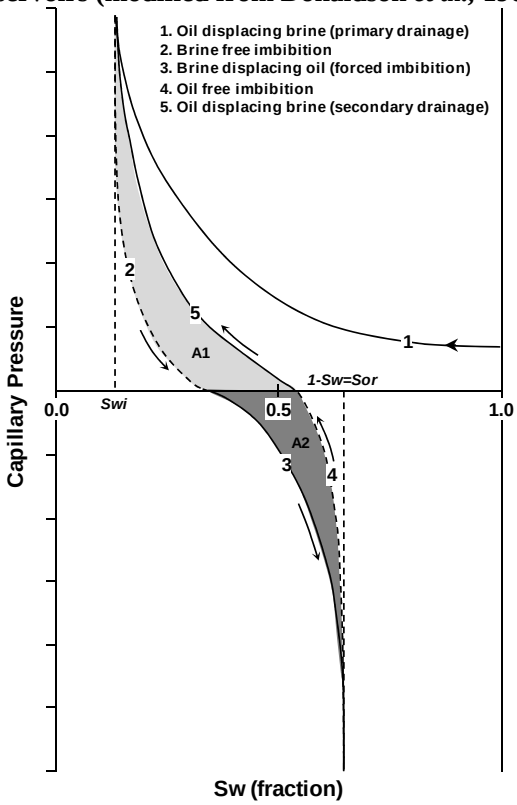

Figure 9.12 Schematic drainage/imbibition trends for a mixed-wet system (modified from Morrow, 1990)

Nevertheless, waterflooding seems to be suitable for the Chicontepec reservoirs, particularly because their mixed-wet condition and that water injection generally involves low capital investment (*i.e.* water is inexpensive); the reservoir heterogeneity appears to be the decisive variable. As was previously discussed, a careful sedimentary analysis together with geostatistical tools may not be sufficient to evaluate sand connectivity in these reservoirs, and additional data such as pressure interference tests or chemical/radioactive tracers should also be integrated. Considering the complexity of the Chicontepec reservoirs, which generally have multiple sand distributions; waterflooding projects may only be beneficial in exceptional cases in the basin. Planning a waterflooding program should also take into consideration that Chicontepec reservoir is easily damaged by low-ionic strength solutions, as reported in this work. A pre-conditioning process for the water planned to be used for injection is therefore needed.

Tertiary mechanisms (*i.e.* EOR) attempt to recover oil beyond secondary methods, or that is left behind after primary depletion. EOR methods inject materials that normally are not part of the reservoir and aimed to alter the physicochemical behaviour of fluids in the reservoir to try to mobilise oil (Lake, 1989). Chemicals, steam and gases are injected to try to increase the oil recovery by: reduction of the oil-brine interfacial tension (IFT), reduction of capillary forces, reduction of the oil viscosity, or increasing the oil mobility.

In mixed-wetted systems, the remaining oil after primary depletion (subjected to EOR applications) would be mainly coating the surface grains of large pores and in small crevices. The larger pores remain oil-wet and smaller pores water wet. In this way, tertiary applications applied to mixed-wetted systems should not only address the problem of recovering oil by reducing the brine-oil IFT or increasing the oil mobility, but also to try to desorb the oil that is adhered in the larger pore walls (*i.e.* wettability alteration).

A number of experiments evaluating the effectiveness of natural and synthetic surfactants for EOR applications at Chicontepec have been analysed in the past (*e.g.* Hernandez-Gama *et al.*, 2013; Torres *et al.*, 2011; IMP, 2009a; IMP, 2009b). However, these have mainly been intended only to reduce brine-oil IFT and not for wettability reversal. Stimulation fluids employed in Chicontepec reservoirs should be specially designed for reverse wettability state from oil-wet (of the large pores) to water-wet. Injected fluids must have the property of desorbing crude-oil molecules from pore surfaces, thus altering wettability and increase oil recovery. Amongst the enhanced recovery mechanisms (Fig. 9.10), the chemical method seems to have the necessary characteristics to achieve tertiary oil recovery by wettability modification in the reservoirs of this study. Caustic solutions combined with surfactants have shown greater potential for such

purpose (*e.g.* Golabi *et al.*, 2012; Donaldson and Crocker, 1980; Leach *et al.*, 1962; Mungan, 1966; Anderson *et al.*, 2012).

Adhesion tests conducted during this study indicate that aged quartz surfaces change from strongly oil-wet to intermediate-wet when the surface mineral is flooded with a caustic solution at room temperature. Similarly, significant oil was recovered by spontaneous imbibition using the bio-surfactant *Rhamnolipid*. The extra oil produced was almost three times the average oil recovered from previous spontaneous imbibition experiments using synthetic brine and comparable rock samples. Although is not clear the mechanism of recovery improvement (*i.e.* whether it was produced by lowering the oil/brine IFT or wettability modification), the results are promising, and demonstrate the potential of the chemical method for enhancing oil recovery efficiencies in the Chicontepec reservoirs.

Adhesion tests described in Chapter 7 also indicate that aged-surface minerals tend to reduce their oil-wetness affinity as the temperature is raised and at greater brine concentrations. The greatest reduction of the oil's contact angle was observed in quartz surface at high temperature. Although no wetting modification was achieved at increasing temperatures in the calcite surface (*i.e.* this remained strongly oil-wet), the results indicate the potential of oil recovery by the thermal method. It is generally accepted that the wetting behaviour of a mineral surface is mainly dominated by the stability of the oil/brine/mineral film, which is function of variations in pH, brine type and composition, temperature, aging-time and crude-oil properties. Several distinct results of wettability modification by increasing temperature are then expected amongst different reservoir systems, a precaution that should be taken in the Chicontepec reservoirs due their variability in crude-oil composition.

The miscible method (Fig. 9.10) involves the injection of gas which dissolves in the oil, reducing its viscosity and allowing the oil to flow more easily towards the well. Gas injection may represent an efficient method of oil recovery in the Chicontepec reservoirs because their low-permeability fabric (*i.e.* gas is likely to reach larger surface areas than water). This method has been evaluated to be suitable for unconventional oil reservoirs (*e.g.* Xu and Hoffman, 2013). Previous analyses of miscible method in Chicontepec reservoirs (*e.g.* Abbaszadeh *et al.*, 2008) have concluded that large uncertainty exists in determining the minimum miscibility pressure, required to achieve gas miscibility in oil. This is due to large variations in reservoir oil characteristics normally observed in the reservoir units. Amongst the fluid mixtures evaluated by Abbaszadeh *et al*. (2008) in Chicontepec formations, the water alternating gas (WAG) method resulted with the best overall recovery factors, compared to CO_2, NGL, CH_4 and flue gas mixtures. Despite their apparent suitability to these reservoirs, only 0.25% of recovery

efficiency was simulated by tertiary gas injection in the Chicontepec reservoirs, after ten years of continuous WAG injection.

Cyclic CO_2 stimulation (regularly referred as 'huff-and-puff' CO_2) may be used as a single well operation (NIPER, 1986) and assists natural reservoir energy by thinning the oil so it will more easily move towards the well. CO_2 is injected into the reservoir, the well is then shut in for a time providing for a 'soak period', then is opened allowing the oil to flow. The extra oil is produced mainly because CO_2 causes the oil to swell and reduces its viscosity. This technique has given positive results in the Bakken tight-oil reservoirs (Yu *et al.*, 2014), although one of the main uncertainties of using this method is the difficulty in predicting the molecular diffusivity behaviour of CO_2 in small pore sizes.

Microbial enhanced oil recovery (MEOR) consists in injecting microbes into formation to ferment hydrocarbons and produce naturally occurring surfactant solutions and/or carbon dioxide that help to displace oil. Hernandez-Gama *et al*. (2013) studied indigenous microbial cultures collected from Chicontepec crude-oils. Even when they concluded that large amounts of CO_2 can be produced by these organisms at prevailing reservoir conditions (*i.e.* temperature and formation's water salinity), it was not clear whether this would be sufficient to mobilise oil. It seems that the microbial method potentially applied in Chicontepec reservoirs are largely regarded to their capacity of microbes to contact the areas where remaining oil may be located, and the existence of nutrients to favour incubation and proliferation. No field tests evaluating MEOR have been conducted in Chicontepec reservoirs.

Overall, the EOR applications planned to be applied in the Chicontepec reservoirs should evaluate two main factors: 1) the extreme reservoir heterogeneity, and 2) their non-homogeneous wetting characteristics. To accomplish the first, a careful sedimentary description of the reservoir combined with geostatistical tools may only provide with the likely distribution of rock properties, which may be used to infer sand connectivity. A more realistic approach to evaluate sand connectivity is integrating pressure interference tests or chemical/radioactive tracers. To achieve the second objective, the fluid mixtures intended to be injected should have the property of desorbing crude-oil molecules from pore surfaces, thus altering wettability and effectively mobilise oil and increase recovery. The chemical method, specially the combination of alkaline/surfactant flooding, seems to show interesting characteristics to achieve wettability reversal in the Chicontepec reservoirs.

9.8 Uncertainty in the *Sw* estimation

A word should be mentioned on the way the fluids content were estimated in the Chicontepec reservoirs. Although water saturation has little effect on oil production, the author thought necessary to highlight what it seems to be a controversial theme.

The water saturation estimated in this work has been determined using a resistivity-based method, the Dual-Water model (Clavier *et al.*, 1984). This model makes a correction for the electric contribution of clays by dividing the total pore water of the reservoir in two portions: the volume of water that is bound to the clay surface and in which conduction is assumed to take place and the remaining water volume that is in the pores and free of any clay-surface effects. This model was selected since it allows estimation of water saturations using variables (*e.g.* ρ_{cl}, *NeuCl*) that can be inferred by well-log data. However, the electric influence of clays in the reservoirs of this study has not been demonstrated by experimental studies (*e.g.* Co/Cw, CEC).

Moreover, the bulk electric flow behaviour of the Chicontepec reservoirs seems to be governed by a combination of microcracks and macropores, describing non-Archie trends. According to experimental data shown in this work (Fig. 9.13), the electrical conduction of fully-saturated Chicontepec rock samples appears to be more efficient at low-porosities and it seems to attenuate at higher-porosities. This behaviour, which has also been observed in the Mesaverde tight-gas reservoirs, has been attributed to the result of apparent electrically well-connected microfissures (*i.e.* microcracks/micropores) and electrically confined macropores.

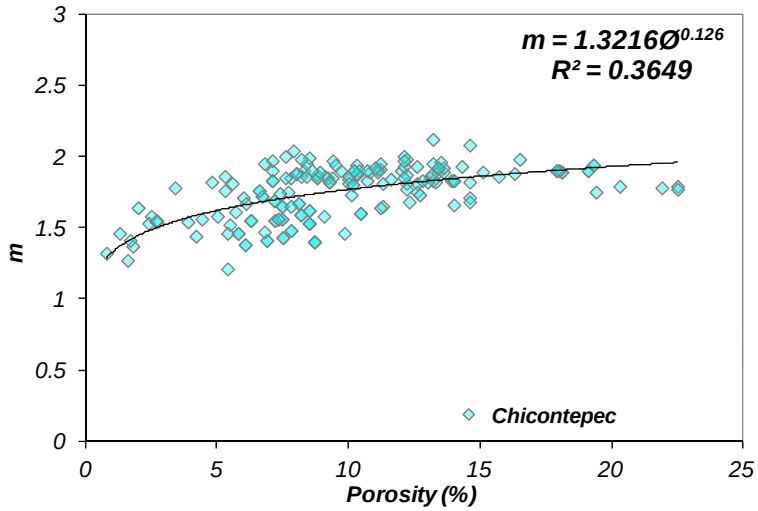

Figure 9.13 Archie's cementation factor measured from Chicontepec reservoir plugs. A porosity-based correlation was estimated (crossplot constructed using PEMEX databases and results obtained from this study)

All the resistivity-based algorithms to estimate water saturation and that are frequently used as industry standard (*e.g.* Simandoux, 1963; Poupon and Leveaux, 1971; Waxman and Smits, 1968; Juhasz, 1981) are based on the Archie equation (Archie, 1942). Although with distinctive modifications, mainly intended to take into consideration the electric flow of clays, these models have the following generic expression:

$$\frac{1}{R_t} = \frac{\emptyset^m}{a}\frac{Sw^n}{R_w}$$

where: *Ø* is the porosity, *Rw* is the formation water resistivity, *Rt* is the total resistivity of the rock and contained fluids, *m* and *n* are the cementation and saturation exponents, respectively, and *a* is the tortuosity factor (usually 1).

If the correlation obtained in Figure 9.13 were used to compute water saturations, this may result in significant inconsistencies. At low-porosities, for example, the Archie-based models would compute anomalous high-hydrocarbon saturations, in which it is known that most of the fluid in these pore systems will remain immobile by capillarity.

Similar electric behaviour was observed when the Archie's saturation exponent (*n*) is determined (Fig. 9.14). At low-porosities, the electric flow of Chicontepec samples seems to be more efficient. Moreover, the wetting characteristics of the rock may also exert an effect on the saturation exponent, as this partially controls the distribution of fluids (water or oil) in the pore space. No experimental data in aged-rock samples were produced in this study and the electric behaviour of Chicontepec samples by analysing their wetting characteristics is unknown.

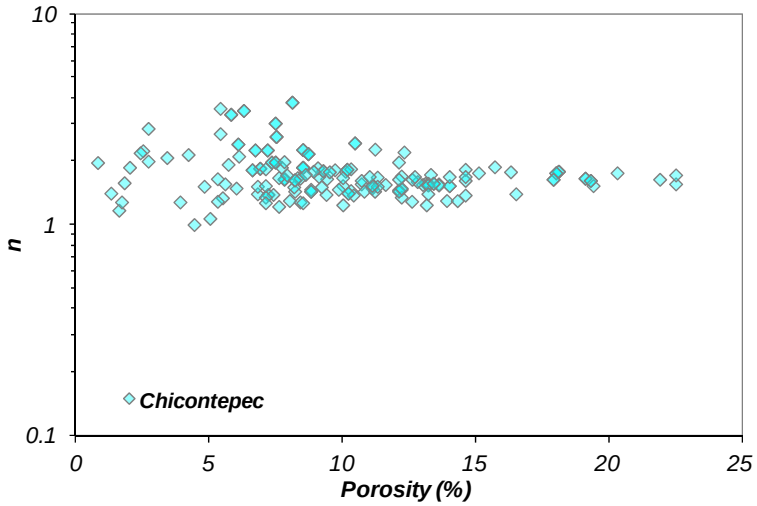

Figure 9.14 Archie's saturation exponent measured from Chicontepec reservoir plugs. High variation of *n* is observed at low porosities with a general tendency to decrease towards that direction (crossplot constructed using PEMEX databases and results obtained from this study)

Additionally, a number of rock samples used in this study were observed to have laminations, marks of bioturbation, and presence of conductive minerals (*e.g.* pyrite, ankerite). Examples of these features are shown in Figure 9.15, which according to Herrick and Kennedy (1996), these may exert electrical pathways which would also control the bulk electric flow behaviour.

Although the parameters employed to estimate water saturation (*i.e.* m= 1.85 and n= 2.2) were assumed to honour the overall electric behaviour of the reservoirs in this study, large uncertainties exist. This is due to the series of characteristics found in these rocks (Fig. 9.15) that may potentially influence the electric flow and that are not yet well understood. No experimental data to corroborate water saturation estimations, apart from MICP, were available. The latter is critical to produce more accurate and predictive saturation models for these reservoirs.

Overall, the bulk electric behaviour of the Chicontepec reservoirs describes non-Archie trends, thus the resistivity-based equations seem to be partially accurate in estimating water saturation. The degree of accuracy of the water saturation determined in this study is unknown. The electric flow of the Chicontepec formations may be the result of multiple conduction mechanisms that may include: a) clays, b) micro and macropores, c) laminations, d) conductive minerals different from clays (siderite, pyrite, etc.), e) wettability, and f) saturating fluids. Further investigation on this matter needs to be performed.

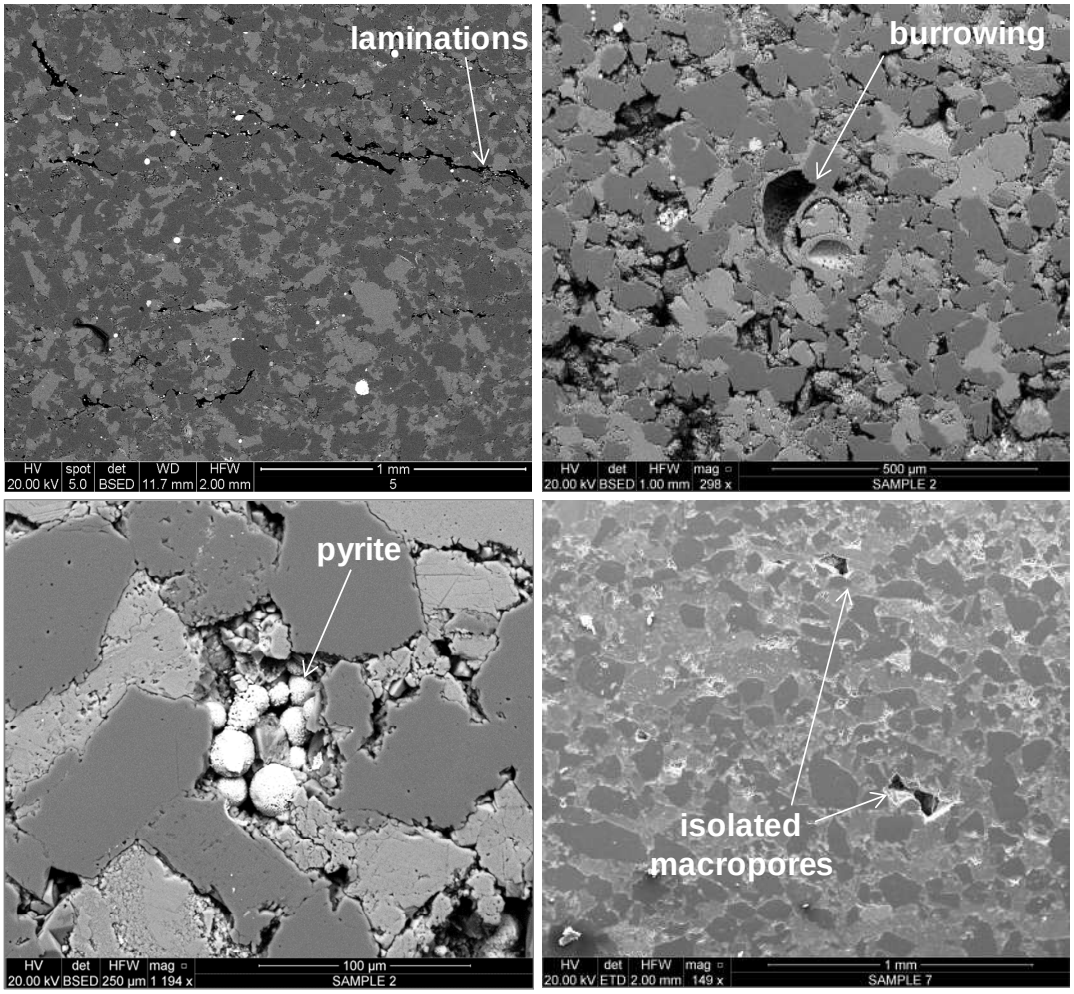

Figure 9.15 Features in Chicontepec rock samples that may influence electric flow conduction

Overall, the Chicontepec reservoirs integrate a number of characteristics that make them specially challenging and perhaps the content of the present research project may be useful to improve, in part, their understanding. This study integrated what it seems a comprehensive rock representation of these reservoirs. The core samples selected for conducting experimental work and comparisons to the rest of the oilfields were mineralogical and petrophysically representative of most pore/perm trend. It resulted clear that the low oil production in these is resulted from the combination of: 1) the low-transmissivity fabric of the reservoir rock, 2) the high spatial variation of their petrophysical properties, and 3) the limited capacity of their drive energy. Similarly, this work demonstrated that formation damage mechanisms potentially affecting these reservoirs seem to exert minimum control on oil production, at least during primary depletion. In the same way, the Chicontepec reservoirs show interesting potential on the following areas that seem worth to evaluate in the future: 1) improving their stimulation techniques by using horizontal drilling and multistage fracturing techniques, and 2) using the contemporary stress regime to try to stimulate greater reservoir volumes. Great potential is also

observed in improving the way the reservoir heterogeneity is evaluated. For achieving this, it seems necessary to incorporate dynamic, descriptive and geoestatistical approaches that combined with resolute seismic images, may provide a better understanding of the spatial connectivity of the sand units. The successful application of secondary and enhanced recovery projects may largely depend on the conceptualisation of the reservoir's heterogeneity. Amongst the enhanced methods for oil recovery, the chemical method (*e.g* alkaline/surfactant flooding) appears to accomplish the capacity to alter the wettability behaviour of Chicontepec reservoirs from mixed- to intermediate-wet.

A number of areas are still debatable in these reservoirs. For example, it would be interesting to explore the contribution of natural fractures on oil production. Perhaps the current scale of observation (*i.e.* seismic imaging) needs to be improved to highlight the presence, distribution, and geometry of natural fractures. The results so far suggest that natural fractures do not seem to contribute on oil production, probably as consequence of their apparent low connectivity; however, a detailed analysis should be conducted. Finally, this study produced a number of microscopic images and experiments that suggest that the electrical behaviour of the Chicontepec reservoirs is complex and needs to be analysed to improve the water saturation estimations. The electrical flow behaviour of these rocks appears to be governed by electrically-isolated macropores and electrically well-connected microfissures (*i.e.* microcracks/micropores). There is a great challenge to produce more predictive models of water saturation estimation in these reservoirs.

CHAPTER X.
CONCLUSIONS AND FURTHER WORK

The principal objective of this thesis is to improve the understanding of the Chicontepec reservoirs so as to increase their oil productivity and recovery. The objective has been addressed by combining descriptive, analytical, experimental and numerical approaches. The controls on oil production in the Chicontepec reservoirs have been analysed in this work by integrating:

1) descriptive studies of the reservoir rock to try to understand the origin of their low-permeability;
2) measured-rock attributes and well-log analysis to evaluate their petrophysical properties;
3) experimental tests to examine rock-fluid interactions and existence of formation damage;
4) reservoir modelling to assess heterogeneity; and
5) simulation case studies to investigate oil recovery efficiencies.

Beginning with the technical definitions of productivity, this work moved on to describe the experimental procedures conducted, where testing processes and the materials employed in this study were detailed. **Chapter 4** investigated the descriptive characteristics of the Chicontepec reservoir rock, paying special attention to their depositional and authigenic features. A sedimentary analysis of a specific reservoir was depicted, which was complemented with production data to evaluate reservoir compartmentalization, an important feature of these reservoirs. **Chapter 5** and **Chapter 6** examined the petrophysical characteristics of the Chicontepec reservoirs, based on the integration of measured rock properties and well-log analysis. The interpreted rock properties were used to build a number of petrophysical correlations. Well-log analysis results of 263 wells in the study area were then employed for reservoir modelling and simulation production scenarios. **Chapter 7** presented experimental results conducted to evaluate formation damage and rock-fluid interaction in these reservoirs. An evaluation of wettability was presented by integration of adhesion tests and experiments conducted in restored core plugs employing three different wettability methods. Wetting characteristics on oil-productivity were then assessed by continuous end-point relative permeability measurements to evaluate oil recovery efficiencies. Two experiments provided novelty in the study of these reservoirs: the evaluation of a biosurfactant in improving oil recovery by spontaneous imbibition; and the analysis of asphaltene precipitation from a crude-oil sample. **Chapter 8** analysed the low-oil production of the Chicontepec reservoirs by

integrating reservoir modelling of a specific sand unit in the study area, and simulation of oil production. Finally, **Chapter 9** discussed the analytical and experimental key results obtained from this work and their implications to oil productivity in Chicontepec reservoirs. In the following, further conclusions are presented.

The main conclusions that emerge from **Chapter 4** are:

- The Chicontepec reservoir rock is a fine to medium-grained litharenite with an average composition of $Q_{45}F_3L_{52}$. The lithic fraction is mainly constituted by limestone and igneous rocks. The calcite is the most common authigenic mineral, followed by the clay minerals and dolomite.
- Intergranular pores are generally observed in the reservoirs of this study, although secondary pores are sometimes present. Primary pores seem to control fluid-flow in these samples.
- Highly-variable sand distributions are observed in the S4 reservoir, which was likely produced by a submarine fan system. Amongst the interpreted sedimentary architectural elements associated to this, lobes (*i.e.* composite of overbank-levee deposits) seem to develop better and more continuous sand distributions than channels.
- Integration of dynamic data indicates that the S4 reservoir is highly compartmentalised. This response was interpreted as resulted from the combination of the reservoir's extreme heterogeneity and their low-permeability trend.
- The highly-variable sand distributions seem to be consistent in most Chicontepec sand units, and establish an important feature of these reservoirs.

Petrophysical assessment of Chicontepec reservoirs was conducted in **Chapter 5** and **Chapter 6**. The main conclusions emerged from these are:

- The Chicontepec reservoir rock has average rock properties normally regarded as tight-oil unconventional reservoirs. This mainly resulted from their fine-grained and poorly-sorted textures, and the widespread calcite cementation. Porosity, permeability and pore-radius trends of the reservoirs in this study are, respectively: $2<Ø<16$ %; $0.0001<k<10$ mD; $0.005<R<10$ µm.
- A correlation between the textural and mineral content in these reservoirs was found. Reservoir rock samples with silicate-to-carbonate ratios (or quartz-to-calcite ratios) greater than 1, combined with well-sorted, fine to medium sand grain sizes, generally are associated to greater k/Ø values.
- Electrical conduction experiments in rock samples of this study seem to describe a non-Archie rock trend. The electrical behaviour of these rocks seems to be governed by a

complex combination of electrically well-connected microfissures, isolated macropores, and relative contribution of large oil-wetted/small water-wetted pores.

- A correlation was found between the interpreted reservoir's mechanical characteristics and the oil recovered. In some wells of the study area, greater oil recoveries were observed as the brittleness index increases.

The main conclusions resulted from **Chapter 7**, which focuses on formation damage and wettability experiments are:

- The Chicontepec reservoir rock shows high sensitivity to the forced injection of fluids normally used for stimulation in the reservoirs of this study.
- The Chicontepec reservoir rock is water-sensitive at a critical brine concentration of 3.5%. Permeability reduction is possibly due to clay swelling. Partial mineral lixiviation was observed as the ionic-strength of the brine was reduced. The relative concentration of trace-elements in produced fluids behaves symmetrically with the ionic-strength of the brine, indicating a strong influence of the ion-concentration and the clay's stabilisation.
- Significant formation damage is produced by polymer-based gelling agents frequently used for fracturing treatments in the reservoirs of this study. The permeability reduction was attributed to polymer adsorption into rock surface and pore walls, demonstrating: 1) the importance of the flowback recovery efficiency in these reservoirs; and 2) alternate fracturing fluid systems should be evaluated.
- The Chicontepec restored-rock samples analysed in this project, describe non-uniform wettability behaviour. The term that best describes their wetting characteristics is the mixed-wet condition. This is an important input parameter to be considered for IOR/EOR applications in these reservoirs, due to the remaining oil will be preferentially located coating the surface grains of large pores and in small crevices.
- Oil recovery by spontaneous imbibition can be improved in aged-rock samples of this study by employing surface active compounds. Amongst the surfactants evaluated to be employed for chemical EOR applications, the biosurfactant (*Rhamnolipid*) shows promising results worth to be considered in the future.

Chapter 8 analyses the spatial distribution of rock properties in these reservoirs and their impact on oil productivity and recovery. The main conclusions emerging from **Chapter 8** are:

- The rock properties of the reservoirs in this study are spatially heterogeneous. This exerts an important control in fluid-flow efficiency and consequently on oil productivity and recovery.

- The wells in the study area have low drainage efficiencies. This signifies that most wells may be draining a significant lower area than that estimated in the current field's development plan.
- Stimulation efficiency (*i.e.* fracture propagation) also impacts on oil productivity, although no significant difference on oil recovery is observed by added metre of induced fracture. The combination of vertical drilling with conventional fracturing completions seems to offer a limited development option to exploit the Chicontepec reservoirs.
- Sensitivity analysis suggests that rock property heterogeneity plays a significant role in controlling the drainage efficiency and oil recovery in the reservoirs of this study. Permeable intervals do not form a continuous medium due to they describe disorganised distributions that make fluids to follow erratic flow patterns.

10.1 Recommendations for further work

The low-oil production of the Chicontepec reservoirs is likely resulted from the combination of: the low-permeability trend of its reservoir rock, the severe heterogeneity of their spatial components and the poor-recovery potential of the drive mechanism.

The author considers that the overall exploitation of the Chicontepec reservoirs may be substantially improved by increasing the level of understanding of the following four topics:

1) Improving the resolution of the descriptive approaches

The rock quality of the Chicontepec reservoirs is highly influenced by the sedimentary controls; thus a better definition of the sedimentary architectural elements may provide a powerful and predictive tool to potentially recognise prospective areas to guide the exploitation. The sedimentary facies definition conducted in this study included only three general classes (*i.e.* channel, lobe and mud) since these were observed to display characteristic rock properties in the S4 reservoir. However, a more exhaustive approach would not only provide with a better definition of the sedimentary components, which ultimately control the degree of heterogeneity in these reservoirs; but also it may serve as enhanced input data to model rock properties at finer detail.

The combination of comprehensive sedimentary models and geostatistically assisted tools may produce more robust reproductions of the degree of heterogeneity of the Chicontepec reservoirs. If these were also integrated with dynamic data (*e.g.* interference tests, chemical tracers), they would be useful for a variety of applications, such as: 1) well placement design (especially for horizontals), 2) production simulation, 3) reserves estimation, 4) production forecasts, 5) infill drilling, and 6) IOR/EOR applications.

2) Using alternate models to estimate water saturation

It has been discussed in this work that the electrical behaviour of the Chicontepec reservoirs seems to be the result of a complex combination of electrically well-connected microcracks and electrically insulator macropores, describing non-Archie trends. Additionally, the electrical contribution of clays in the reservoirs of this study is uncertain, due to the lack of laboratory data (*e.g.* CEC, Co/Cw). The resistivity-based method seems to be partially accurate in estimating water saturations in these reservoirs.

Alternate methods for water saturation estimation may be fundamental in these reservoirs, particularly because the volumetric method for reserves estimation (from which the Chicontepec reserves are evaluated) is entirely based on resistivity-based approaches. Core analyses such as

the Dean Stark method or capillary pressure data may provide with an alternate estimation of the water saturation. Although these methods are applied to core samples and significant lower resolution compared to well-logs may be produced, these may provide with an option to corroborate well-log computations.

The Dean Stark method collects the residual fluids in core samples. The sample is placed suspended above a flask containing toluene or any other solvent with a boiling point higher than water. The toluene is heated and the hot solvent vapour rises, surrounds the sample, the water vaporises, rises in a condensate tube together with toluene and falls into a graduated burette where it can be quantified. The process is repeated until constant water readings are obtained. When this information is combined with the estimated porosity of the sample, the volume of residual water can be converted to percent pore space (*Sw*). Although this method is clearly influenced by the degree of invasion of the drilling fluids, this may provide at least with a calibrating point of the water saturation. Since oil-based muds are generally used in the Chicontepec wells (*i.e.* no source of water contamination is expected), this technique may be valuable.

Capillary pressure data, such as that obtained from mercury injection, provides significant insight into the nature of pore geometry and distribution. An estimation of the water saturation in the sample can be obtained using MICP data. The procedure is explained in Chapter three and can be useful to improve the accuracy of water saturation distributions in the Chicontepec reservoirs. Although the procedure may be sensitive because a range of saturations can be obtained at different capillary pressure cut-offs, it provides an estimation of the water saturation that can be compared to well-log analyses.

3) Optimization of hydraulic fracturing

The combination of horizontal drilling and multi-stage hydraulic fracturing technologies (HD+MSHF), have allowed significant oil to be produced in tight-oil reservoirs. Recent examples in the Chicontepec reservoirs (*e.g.* Gutierrez *et al.*, 2014a) demonstrate that unconventional completions may be a key parameter to change the economic equation of these. The primary goal of this technique is to create a conductive path to contact the reservoir through multiple fractures along the horizontal section. In general, the tendency of hydraulic fracturing technologies at present is to create more complex fracture geometries by: changing the stress anisotropy (*e.g.* zipper frac; Rafie *et al.*, 2012) or decreasing the spacing between fracture stages (Rankin *et al.*, 2010). The treatment optimization is also a key parameter that is currently incorporated. An economic limit should be estimated above which the costs associated to horizontal drilling and number of fracture stages may not be feasible. The industry is also

moving in direction of using non-polymer based fluids (King, 2012) or environmentally friendly materials.

Polymer-free fracturing fluids such as viscous-elastic surfactants (VES) have given positive results to the Chicontepec reservoirs (*e.g.* Centurion *et al*., 2006). Higher propped-pack permeabilities and greater initial oil rates were obtained in Chicontepec wells fractured with VES, compared to conventional polymer-based mixtures. It is unclear why VES had not been massively used in the Chicontepec basin, possibly this may be due to an economical or operative reason. However, the use of non-damaging fluids in combination with unconventional completion technologies (HD+MSHF), seems an area of increasing interest worth to be evaluated.

4) Improving the understanding of rock/fluid interactions for EOR applications

The Chicontepec reservoirs are candidates for secondary/tertiary applications of oil recovery, especially because significant residual oil is left behind after natural depletion. IOR/EOR applications involve injecting foreign fluids into the reservoir aimed to alter the physicochemical behaviour of the rock/fluid system to try to mobilise oil.

The Chicontepec reservoir rock may show high sensitivity to the forced injection of low-ionic brines and polymer-based fluids, potentially developing formation damage. Clay swelling and polymer adhesion seem to be the main mechanisms of permeability impairment in these reservoirs. The selected fluids to be injected into these formations should be specially prepared trying to avoid permeability reductions that may eventually cause injectivity lost.

To guarantee that injected fluids are specifically designed to improve oil recovery, a careful screening selection should be conducted. This may include, for example, spontaneous imbibition experiments or adhesion tests, combined with critical salt/velocity tests. The experiments may include a wide range of variables to be evaluated, such as: fluid type and concentration, temperature, aging times, pH variations, crude-oil compositions, etc.

Since Chicontepec reservoirs produce crude-oils with variable compositions, it should be expected that these may exert different wetting tendencies. The rock sample conditioning (*i.e.* aging) to be used for EOR screening tests may represent the key stage to produce representative rock samples.

BIBLIOGRAPHY

Abbaszadeh, M.; Ohno, K.; Okano, H.; Morales, J.; and Riano-Caraza, J. 2008. Reservoir characterization and CO_2-EOR studies in Chicontepec turbidite reservoirs, Mexico. International Petroleum Technology Conference. IPTC-12637.

Abdassah, D.; Permadi, P.; Sumatri, Y. and Sumatri, R. 1996. Fractal modeling of thin-sections to determine saturation exponent for various wetting conditions. Society of Core Analysts no. 9622.

Aguilera, R. 2013. Flow units: from conventional to tight-gas to shale-gas to tight-oil to shale-oil reservoirs. Soc. Petr. Eng. SPE-165360.

Agrawal, A.; Danait, A. and Nanda, J. 2011. Investigation of solids flowback after hydraulic fracturing and remedial treatments. Soc. of Petroleum Engineers. SPE-143648.

Ahmed, T. 2006. Reservoir Engineering Handbook. Elsevier Publishing, third edition. 1360p.

Al-Aulaqi, T.; Grattoni, C.; Fisher, Q,; Musina, Z. and Al-Hinai, S. 2011. Effect of temperature, oil asphaltene content, and water salinity on wettability alteration. Soc. of Petroleum Engineers. SPE-149071-MS.

Ali, M. A. J. and Currie, P. K. 2005. Permeability damage due to water injection containing oil droplets and solid particles at residual oil saturation. Soc. of Petroleum Engineers. SPE-104608.

Al-Marhoon, N. O.; Grattoni, C. A.; Dawe, R. A., Carter, J. N. 1998. Formation Damage and near wellbore flow in reservoirs-An experimental study. Soc. of Petroleum Engineers. SPE-49499.

Al-Marooqi, *et al.* 2006. Pore-scale modelling of NMR relaxation for the characterization of wettability. Journal of Petroleum Science and Engineering, no. 52, 172-186 pp.

AlShaikh, M. and Mahadevan, J. 2014. Impact of brine composition on carbonate wettability: a sensitivity study. Soc. of Petroleum Engineers. SPE-172187-MS.

Amaefule, J. O.; Ajufo, A.; Peterson, E. and Durst, K. 1987. Understanding formation damage processes: an essential ingredient for improved measurement and interpretation of relative permeability data. Soc. of Petroleum Engineers. SPE-16232.

American Petroleum Institute. 2010. Hydraulic Fracturing: Unlocking America's Natural Gas Resources. American Petroleum Institute Report, Washington, D. C. July 19, 2010.

Amott, E. 1959. Observations relating to the wettability of porous rock. Trans AIME; 216, 156-62.

Anderson, E. 1951. The dynamics of faulting and dyke formation with applications to Britain. Edinburgh, Oliver and Boyd.

Anderson, G.; Delshad, M.; King, C.; Mohammadi, H. and Pope, G. 2012. Optimization of chemical flooding in a mixed-wet dolomite reservoir. Soc. of Petroleum Engineers. SPE-100082.

Anderson, W. G. 1986a. Wettability Literature Survey- Part 1: Rock/Oil/Brine Interactions and the Effects of Core Handling on Wettability. Journal of Petroleum Technology, 38(10), 1125-1144p.

Anderson, W. G. 1986b. Wettability Literature Survey- Part 2: Wettability Measurement. Journal of Petroleum Technology, November, 1986, 1246-1262p.

Anderson, W. G. 1987a. Wettability Literature Survey- Part 5: The effects of wettability on relative permeability. Journal of Petroleum Technology, 1453-1468p.

Anderson, W. G. 1987b. Wettability Literature Survey- Part 6: The effects of wettability on waterflooding. Journal of Petroleum Technology, 1605-1621p.

Andesina, F. A. S.; Olugbenga, F. and Samuel, A. 2010. Oilfield scale-induced permeability damage management during waterflooding. Soc. of Petroleum Engineers. SPE-126116.

Archie, G. 1942. The electrical resistivity log as an aid in determining some reservoir characteristics. Soc. Petr. Eng. SPE- 942054-G.

Arthur, D.; Bohm, B. and Layne, M. 2008. Hydraulic fracturing considerations for natural gas wells of the Marcellus Shale. Presented at the Ground Water Protection Council, Cincinnati, Ohio. September, 2008.

Asquith, G. and Krygowski, D. 2004. Chapter 7: Log interpretation. *In* AAPG Methods in Exploration, No. 16: Basic Well Log Analysis (Second Edition), 115-135p.

Ataei, M. 2012. Log facies evaluation and property modelling of a turbidite reservoir, The Gulf of Mexico. MSC Thesis. Norwegian University of Science and Technology, Department of Geology and Mineral Resources Engineering.

Audibert, A.; Argillier, J. F.; Ladva, H. K. and Way, P. W. 1999. Role of polymers on formation damage. Soc. of Petroleum Engineers. SPE-54767.

Austad, T. and Milter, J. 1997. Spontaneous Imbibition of Water Into Low Permeable Chalk at Different Wettabilities Using Surfactants. Soc. of Petroleum Engineers. SPE-37236-MS.

Balan, B.; Mohaghegh, S. and Ameri, S. 1995. State of the art in permeability determination from well-log data: Part 1 a comparative study, model development. Soc. of Petroleum Engineers. SPE-30978.

Mohaghegh, S.; Balan, B. and Ameri, S. 1995. State of the art in permeability determination from well-log data: Part 2 verifiable, accurate permeability predictions, the touch stone of all models. Soc. of Petroleum Engineers. SPE-30979.

Barree, R. D., Fisher, M. K. and Woodroof, R. A. 2002. A practical guide to hydraulic fracture diagnostic technologies. Soc. of Petroleum Engineers. SPE-77442.

Beaubouef, R.; Rossen, C.; Zelt, F.; Sullivan, M.; Mohrig, D. and Jennette, D. 1999. Deep-water sandstones, Brushy Canyon Formation, West Texas. American Association of Petroleum Geologists, Continuing Course Note Series no. 40, 62p.

Beauregard, M. 2014. El presente y futuro de las finanzas en Petróleos Mexicanos. ExpoForo PEMEX 2014.

Bennet, B.; Buckman, J. O.; Bowler, F. J. and Larter, S. R. 2004. Wettability alteration in petroleum systems: the role of polar non-hydrocarbons. Petroleum Geoscience, Geol. Soc. London, Vol. 10, pp. 271-277.

Bennion, D. B. and Thomas, F. B. 1992. Formation Damage due to mineral alteration and wettability changes during hot water and steam injection in clay-bearing sandstone reservoirs. Soc. of Petroleum Engineers. SPE-23783.

Bennion, D. B. and Thomas, F. B. 1994. Underbalanced drilling of horizontal wells: does it really eliminate formation damage? Soc. of Petroleum Engineers. SPE-27352.

Bennion, D. B.; Thomas, F. B.; Bennion, D. W. and Bietz, R. F. 1995. Mechanisms of formation damage and permeability impairment associated with the drilling, completion and production of low API gravity oil reservoirs. Soc. of Petroleum Engineers. SPE-30320.

Bennion, D.; Thomas, F. and Bietz, R. 1995. Low permeability gas reservoirs: problems, opportunities and solutions for drilling, completion, stimulation and production. Society of Petroleum Engineers Paper SPE-35577.

Bennion, D. B.; Bennion, D. W.; Thomas, F. B. and Bietz, R. F. 1998. Injection water quality – a key factor to successful waterflooding. Journal of Canadian Petroleum Technology, June, 1998. Vol. 37, No. 6.

Bennion, B. 1999. Formation Damage- the impairment of the invisible, by the inevitable and uncontrollable, resulting in an indeterminate reduction of the unquantifiable!. Journal of Canadian Petroleum Technology, February, 1999. Vol. 38, No. 2.

Bennion, D. B.; Thomas, F. B.; Jamaluddin, A. K. M. and Ma, T. 2000. Using underbalanced drilling to reduce invasive Formation Damage and improve well productivity – An update. Journal of Canadian Petroleum Technology, July, 2000. Vol. 39, No. 7.

Bennion, B. D. 2002. An overview of Formation damage mechanisms causing a reduction on the productivity and injectivity of oil and gas producing formations. Journal of Canadian Petroleum Technology, November, 2002. Vol. 41, No. 11.

Bennion, D. B.; Thomas, F. B.; Schulmeinster, B. and Romanova, U. G. 2006. Water and oil base fluid retention in low permeability porous media – an update. Canadian International Petroleum Conference, Calgary, Alberta, Canada, June 13-15, 2006. Paper no. 2006-136.

Berumen, S.; Gachuz, H.; Rodriguez, J.; Bovier-Lapierre, T. and Kaiser, P. 2004a. Hydraulic fracture mapping in treated well. Channelized reservoirs development optimization in Mexico. EAGE 66th Conference & Exhibition, Paris, France. 7-10 June.

Berumen, S.; Kaiser, P.; Gachuz, H.; de Swaan, A. and Rodriguez, J. 2004b. Fracturing microseismic response in turbidite reservoirs in Tajin Field. Soc. Petr. Eng. SPE- 92015.

Bhatia, K. And Chacko, L. 2011. Ni-Fe Nanoparticle: An innovative approach for recovery hydrates. Soc. of Petroleum Engineers. SPE-143159.

Birkle, P.; Pruess, K.; Xu, T.; Figueroa, R. and Diaz-Lopez, M. 2006. Using laboratory flow experiments and reactive chemical transport modeling for designing waterflooding of the Agua Fria reservoir, Poza Rica-Altamira Field, Mexico. Soc. of Petroleum Engineers. SPE-103869.

Bishop, S. R. 1997. The experimental investigation of formation damage due to the induced flocculation of clays within a sandstone pore structure by a high salinity brine. Soc. of Petroleum Engineers. SPE-38156.

Block, A. and Simms, B. 1967. Desorption and exchange of adsorbed octadecylamine and stearic acid on steel and glass. Journal of Colloid Interface Sci. Vol. 25: 514.

Bomar, R. M. and Dereniewski, E. 1997. Storage Formation Damage Mechanisms. Soc. of Petroleum Engineers. SPE-39221.

Bondino, I.; Doorwar, S.; Ellouz, R. and Hamon, G. 2013. Visual microscopic investigations about the role of pH, salinity and clay on oil adhesion and recovery. Society of Core Analysts, SCA2013-021.

Bottero, S.; Picioreanu, C.; Enzien, M.; Van Loosdrecht, M.; Bruining, H. and Heimovaara, T. 2010. Formation damage and impact on gas flow caused by biofilms growing with proppant packing used in hydraulic fracturing. Soc. of Petroleum Engineers. SPE-128066.

Brace, W.; Walsh, J. and Frangos, W. 1968. Permeability of granite under high pressure. Journal of Geophysical Research, vol. 73, no. 6, 2225‑2236p.

Bruno, M. S. 2002. Geomechanical and decision analyses for mitigating compaction-related casing damage. Soc. of Petroleum Engineers. SPE-79519.

Buckley, J.; Takamura, K.; and Morrow, N. 1989. Influence of electrical surface charges on the wetting properties of crude oils. SPE Reservoir Engineering, August 1989. SPE-16964.

Buckley, J. 1995. Asphaltene precipitation and crude oil wetting. Soc. of Petroleum Engineers. SPE-26675-MS.

Buckley, J. and Liu, Y. 1998. Some mechanisms of crude oil/brine/solid interactions. Journal of Petroleum Science and Engineering, 20: 155-160 pp.

Buckley, J. and Morrow, N. 1990. Characterization of Crude Oil Wetting Behavior by Adhesion Tests. Soc. of Petroleum Engineers. SPE-20263-MS.

Buckley, J. and Wang, J. 2002. Crude-oil and asphaltene characterization for prediction of wetting alteration. Journal of Petroleum Science and Eng., no. 33, 195-202p.

Buckley, J. and Fan, T. 2005. Crude-oil/brine interfacial tensions. Society of Core Analysts, SCA-2005-01.

Busch, D. and Govela, A. 1978. Stratigraphy and Structure of Chicontepec turbidites, Southeastern Tampico-Misantla basin, Mexico. AAPG Bull. V. 62, No. 2, p. 235-246.

Byrne, M.; Patey, I. and Green, J. 2007. A new tool for Exploration and Appraisal – Formation Damage Evaluation. Soc. of Petroleum Engineers. SPE-107557.

Cantu-Chapa, A. 2001. Paleocanyons in the subsurface of eastern Mexico: facts and uncertainties. *In* Bartolini, C. *et al*. 2001. The western Gulf of Mexico basin: Tectonics, sedimentary basins, and petroleum systems. AAPG Memoir 75, 421-430 p.

Centurion, S.; Rengifo, M.; Cortona, M.; Padilla, F. and Lavalle, A. 2006. Successful application of a novel fracturing fluid in the Chicontepec Basin, Mexico. Soc. of Petroleum Engineers. SPE-103879.

Chambers, R.; Yarus, J. and Hird, K. 2000. Petroleum geostatistics for nongeostatisticians: Part 1. Leading Edge, v. 19, p.474-479.

Cheatwood, C. and Guzman, A. 2002. Comparison of reservoir properties and development history: Spraberry trend field, West Texas and Chicontepec field, Mexico. Soc. of Petroleum Engineers. SPE-74407.

Chemical disclosure registry: //fracfocus.org/

Chen, Z.; Khaja, N.; Valencia, K. L. and Rahman, S. S. 2006. Formation damage induced by fracture fluids in coalbed methane reservoirs. Soc. of Petroleum Engineers. SPE-101127.

Chesapeake Energy. 2011. Hydraulic fracturing, fact sheet. September, 2011 (taken from www.hydraulicfracturing.com).

Chow, R. and Takamura, K. 1988. Electrophoretic mobilities of bitumen and conventional crude-in-water emulsions using the Laser Doppler Apparatus in the presence of multivalent cations. Jour. Colloid Interface Sci. 125, 212p.

Chowdiah, P. 1987. Laboratory measurements relevant to two-phase flow in a tight gas sand matrix. Soc. of Petroleum Engineers. SPE-16945-MS.

Cikes, M.; Vranjesevic, B.; Tomic, M. and Jamnicky, O. 1990. A successful treatment of formation damage caused by high-density brine. Soc. of Petroleum Engineers. SPE-18383-PA.

Cinco-Ley, H. and Samaniego, F. 1981. Transient pressure analysis: finite conductivity fracture case versus damaged fracture case. Soc. of Petroleum Engineers. SPE-10179.

Civan, F. 1996. Multipurpose Formation Damage Model. Soc. of Petroleum Engineers. SPE-31101.

Civan, F. 2007. Reservoir Formation Damage. Ed. Gulf Professional Publishing.

Civan, F. 2008. Correlation of permeability loss by thermally-induced compaction due to grain expansion. Petrophysics, Soc. of Petrophysics and Well Log Analysts, August, 2008.

Clavier, C.; Coates, G. and Dumanoir, J. 1984. Theoretical and experimental bases for the Dual-Water model for interpretation of shaly sands. Soc. Petr. Eng. SPE-6859-PA.

CNH (Comisión Nacional de Hidrocarburos), 2010. Proyecto Aceite Terciario del Golfo. Primera revisión y recomendaciones. Abril, 2010. Inedit.

CNH (Comisión Nacional de Hidrocarburos), 2014a. Seguimiento al Proyecto Aceite Terciario del Golfo. Monthly production reports available at: http://www.cnh.gob.mx/portal/Default.aspx?id=5100.

CNH (Comisión Nacional de Hidrocarburos), 2014b. Producción histórica de petróleo y gas mensual (1960-actual) y Pozos productores de petróleo y gas asociado mensual por campo (2001-actual). Monthly reports available at: http://www.cnh.gob.mx/portal/Default.aspx?id=5100.

Coates, G. and Denoo, S. 1981. The producibility answer product. The technical review. Schlumberger, vol. 29, no. 2.

Coates, G.; Xiao, L. and Prammer, M. 1999. NMR Logging, principles and applications. Halliburton Energy Services publication.

Committee on Energy and Commerce. 2011. Chemicals used in Hydraulic Fracturing. United States House of Representatives. Minority staff. April, 2011.

Cossey, S. 2007. Reservoir Facies, erosional channels and Mass transport complexes of the Chicontepec Formation, Eastern Mexico: Guidebook prepared to PEMEX Exploracion y Produccion.

Craig, F.F., 1971. The Reservoir Engineering Aspects of Waterflooding, Dallas, Texas.
Cronin, B. T. 1995. Structurally-controlled deep-sea channel courses: examples from the Miocene of south-east Spain and the Alboran Sea, south-west Mediterranean. *In* A. J. Hartley and D. J. Prosser, eds. Reservoir characterisation of deep water clastic systems: Geological Society of London Special Publication, 113–133p.

Cuiec, L., Longeron, D. and Pacsirszky, J. 1979. On the necessity of respecting reservoir conditions in laboratory displacement studies. Soc. of Petroleum Engineers. SPE-7785.

Da Motta, E. P. and Dos Santos, J. A. 1999. New fluosilicic acid system removes deep clay damage. Soc. of Petroleum Engineers. SPE-54729.

Davies, D. K. 1980. Reservoir stimulation of dirty sandstones. Fourth Symposium on Formation Damage Control. Soc. of Petroleum Engineers. SPE-8795-MS.

Ding, Y.; Herzhaft, B. and Renard, G. 2004. Near-wellbore formation damage effects on well performance – A comparison between underbalanced and overbalanced drilling. Soc. of Petroleum Engineers. SPE-86558.

Ding, D. Y. 2010. Modeling Formation Damage for flow simulations at reservoir scale. Soc. of Petroleum Engineers. SPE-121805.

Ding, D. Y.; Langouët, H. and Jeannin, L. 2012. Simulation of fracturing induced formation damage and gas production from fractured wells in tight gas reservoirs. Soc. of Petroleum Engineers. SPE-153255.

Division of Mineral Resources. 2009. Supplemental generic environmental impact statement on the oil, gas and solution mining regulatory program. Well permit issuance for horizontal drilling and high-volume hydraulic fracturing to develop the Marcellus Shale and other low permeability gas reservoirs. New York State Department of Environmental Conservation, United States. Draft.

Dixit, A.; McDougall, S. and Sorbie, K. 1998. Analysis of relative permeability hysteresis trends in mixed-wet porous media using network models. Soc. of Petroleum Engineers. SPE-39656.

Dixit, A.; Buckley, J.; McDougall, S. and Sorbie, K. 2000. Empirical measures of wettability in porous media and the relationship between them derived from pore-scale modelling. Transport in porous media, v. 40, 27-54p. Kluwer academic publishers.

Doane, R. D.; Bennion, D. B.; Thomas, F. B.; Bietz, R. and Bennion, D. W. 1999. Special core analysis designed to minimize formation damage associated with vertical/horizontal drilling applications. Journal of Canadian Petroleum Technology. Vol.38, No. 5, p. 35-45.

Donaldson, E. and Alam, W. 2008. Wettability. Gulf Publishing Company. 336 p.

Donaldson, E., Thomas, R. and Lorenz, P. 1969. Wettability determination and its effect on recovery efficiency. Soc. of Petroleum Engineers. SPE-2338-PA.

Donaldson, E. and Crocker, M. 1980. Characterization of the crude-oil polar compound extract. DOE/BETC/RI-80/5. National Tech. Info. Service, U.S. Dept. of Commerce, 27pp.

Donaldson, E. and Siddiqui, T. 1987. Relationship between the Archie saturation exponent and wettability. Soc. of Petroleum Engineers. SPE-16790.

Durand, C. and Rosenberg, E. 1998. Fluid distribution in kaolinite -or illite- bearing cores: cryo-SEM observations versus bulk measurements. Journal of Petroleum Science and Engineering, Vol. 19, p. 65-72.

Durham, L. S. 2011. 'Nano Balls' Prop shale fractures. AAPG Explorer magazine. December, 2011.

Ehrenberg, S. and Nadeau, P. 2005. Sandstone vs. Carbonate petroleum reservoirs: a global perspective on porosity-depth and porosity-permeability relationships. AAPG Bull. V. 89, no. 4, 435-445p.

El-Dessouky, H. and Ettouney, H. 2002. Fundamentals of salt water desalination. Elsevier, 690p.

England, K. 2004. Hydraulic fracturing method. United States Patent no. US 6,776,235B1. Date of Patent: August 17, 2004.

Environmental Protection Agency: http://www.epa.gov/

EPA, 2011. United States Environmental Protection Agency: http://www.epa.gov/

Erwin, M. D.; Pierson, C. R. and Bennion, D. B. 2006. Brine imbibition damage in the Alpine/Colville River Field, Alaska. Journal of Petroleum Science and Technology. Vol.45, No. 6, p. 33-40.

Eslinger, E. 1988. Clay minerals for Petroleum Geologists and Engineers. SEPM short course no. 22.

Estopier, M. 2009. Imágenes micro-resistivas de la pared del pozo HUMAPA-4004 en lodo base aceite. Schlumberger. PEMEX internal report.

Estrada, E.; Vielma, M.; Morales, J.; Estrada, J.; Tineo, F. and Gómez, G. 2010. Turbidite Chicontepec Formation, Channel Chicontepec, Mexico: A diagenetic and petrophysical study to optimize the completions Corralillo area. Soc. of Petroleum Engineers. SPE-139374.

Fan, T. and Buckley, J. 2002. Rapid and accurate SARA analysis of medium gravity crude oils. Energy & Fuels, no. 16, 1571-1575p.

Fang, X.; Wang, Q.; Bai, B.; Xi-Liu, X.; Tang, Y.; Shuler, P. and Goddard III, W. 2007. Engineering Rhamnolipid Biosurfactants as Agents for Microbial Enhanced Oil Recovery. Soc. of Petroleum Engineers. SPE-106048-MS.

Fleury, M. and Deflandre, F. 2003. Quantitative evaluation of porous media wettability using NMR relaxometry. Magnetic Resonance Imaging, vol. 21, 385-387 pp.

Folk, R. 1974. Petrology of Sedimentary rocks. Hemphill Publishing Company, Austin Texas.

Gachuz-Muro, H. 2009. Effective permeability vs. Drainage radius, correlation for the turbidites oil reservoirs – Chicontepec Paleochannel. Soc. of Petroleum Engineers. SPE-120267.

Gachuz-Muro, H. and Sellami, H. 2009. Analogous reservoirs to Chicontepec, alternatives of exploitation for this Mexican Oilfield. Soc. of Petroleum Engineers. SPE-120265.

Gama, C.; Gerez, D. and Babasick, P. 2009. Oriented perforation in dual completion wells: a real case in East Texas. Soc. of Petroleum Engineers. SPE-120508.

Gandossi, L. 2013. An overview of hydraulic fracturing and other formation stimulation technologies for shale gas production. Joint Research Centre, European Commission, Institute for Energy and Transport.

Gholami, V.; Moghadasi, J. and Abdi, R. 2008. Formation Damage through asphaltene precipitation resulting from CO2 gas injection in Iranian carbonate reservoirs. SPE Production & Operations, May 2008, 210-214 p.

Goddard, W.; Tang, Y.; Blanco, M.; Shuler, P. and Wu, Y. 2007. Cost effective surfactant formulations for improved oil recovery in carbonate reservoirs. California Institute of Technology Report. DOE Project: DE-FC26-04NT15521.

Golabi, E.; Seyedeyn, F.; Shahabuddin, S.; Nooroldine, S. and Dastanian, M. 2012. Experimental study of anionic and cationic surfactants effects on reduce of IFT and wettability alteration in carbonate rock. International Journal of Scientific and Engineering Research, vol. 3, issue 7.

Granados-Hernandez, J. C. and Fisher, Q. J. 2014. Textural and Mineralogical Characteristics of Chicontepec Reservoirs in Mexico; Keys to Understanding Oil Productivity. International Petroleum Technology Conference. Soc. Petr. Eng. SPE-17813-MS.

Granados, J. and Flores, F. 2013. Prueba tecnológica de estimulación de pozos petroleros mediante la tecnología ultrasónica (PU) en pozos del AIATG. Ingeniería Petrolera, vol. 53, no.1, 6-26p.

Gray, M.; Yeung, A.; Foght, J. and Yarranton, H. 2008. Potential microbial Enhanced Oil Recovery processes: a critical analysis. Soc. Petr. Eng. SPE-114676.

Green, D. and Willhite, P. 1998. Enhanced Oil Recovery. SPE Textbook Series Vol. 6.

Grieser, B. and Bray, J. 2007. Identification of production potential in unconventional reservoirs. Soc. Petr. Eng. SPE-106623.

Guan, H.; Brougham, D.; Sorbie, K. and Packer, K. 2002. Wettability effects in a sandstone reservoir and outcrop cores from NMR relaxation time distributions. Journal of Petroleum Science and Engineering, 34: 35-54 pp.

Gunter, W. D.; Zhou, Z. and Perkins, E. H. 1994. Modelling formation damage caused by kaolinite from 25 to 300°C in the Oil Sand Reservoirs of Alberta. Soc. of Petroleum Engineers. SPE-23786.

Gunter, G. W.; Finneran, J. M.; Hartmann, D. J. and Miller, J. D. 1997. Early determination of reservoir flow units using an integrated Petrophysical method. Soc. of Petroleum Engineers. SPE-38679.

Gunter, G. W.; Smart, C.; Miller, M. and Finneran, J. 1999. Saturation modeling at the well-log scale using petrophysical rock types and a classic non-resistivity based method. SPWLA 40th Annual Logging Simposium, May 30-June 3.

Gupta, D. and Bobier, F. 1998. The History and Success of Liquid CO2 and CO2/N2 Fracturing System. Soc. of Petroleum Engineers. SPE-40016.

Gupta, D.; Pierce, R. and Lift, N. 1997. Non-aqueous gelled alcohol fracturing fluid. Soc. of Petroleum Engineers. SPE-37229.

Gutierrez, G.; Sanchez, A.; Rios, A. and Arguello, L. 2010. Microseismic hydraulic fracture monitoring to determine the fracture geometry in Coyotes Field, Chicontepec. Soc. of Petroleum Engineers. SPE-139155.

Gutierrez, G.; Perazzo G.; Medina, E.; Sierra, J. and Henriquez, C. 2014a. Successful alternating sequential hydraulic multifrac in two parallel horizontal wells in a low-permeability turbidite oil reservoir. Soc. of Petroleum Engineers. SPE-167755.

Gutierrez, G.; Medina, E.; Perazzo G.; Sierra, J. and Henriquez, C. 2014b. Unconventional well completion generates significant production increase in lateral wells in Chicontepec Formation. Soc. of Petroleum Engineers. SPE-167756.

Gutierrez, G.; Ramirez, L.; Sierra, J.; Medina, E.; Gutierrez, L. and Salguero, J. 2014c. Improvements in multistage fracturing, Remolino Field, Mexico. Soc. of Petroleum Engineers. SPE-168576.

Hassler, G.; Brunner, E. and Deahl, T. 1944. The role of capillarity in oil production. Trans. AIME, vol. 155, 155-174p.

Hayatdavoudi, A. and Ghalambor, A. 1996a. A study of formation damage of selective clay and other minerals caused by bacterial plugging. Soc. of Petroleum Engineers. SPE-27006.

Hayatdavoudi, A. and Ghalambor, A. 1996b. Controlling formation damage caused by kaolinite clay minerals: Part I. Soc. of Petroleum Engineers. SPE-31118.

Hayatdavoudi, A. and Ghalambor, A. 1998. Controlling formation damage caused by kaolinite clay minerals: Part II. Soc. of Petroleum Engineers. SPE-39464.

Hernandez-Gama, R.; Munoz-Colunga, A.; Hernandez-Mendoza, E.; Torres, L. and Rojas-Avelizapa, N. 2013. Identification of carbon dioxide-producing microorganisms originating from Mexican oil Wells with potential application in oil recovery. Jour. Petr. Science Research, Vol. 2, Issue 1, January, 201 3.

Herrick, D. and Kennedy, W. 1996. Electrical properties of rocks: effects of secondary porosity, laminations, and thin beds. SPWLA 37th Annual Logging Symposium, June 16-19.

Holditch, S. 2009. Stimulation of tight-gas reservoirs worldwide. Soc. of Petroleum Engineers. SPE-20267.

Hovadik, J. and Larue, D. 2010. Stratigraphic and structural connectivity *In* Jolley, S.; Fisher, Q. and Ainsworth, R. 2010. Reservoir compartmentalization. Geological Society, London. Special publication v. 347. 219-242p.

Howell, D. and Normark, W. 1982. Sedimentology of Submarine Fans: Part 1. American Association of Petroleum Geologists, Memoir no. 31: Sandstone Depositional Environments.

Huang, T.; Evans, B. A.; Crews, J. B. and Belcher, C. K. 2010. Field case study on formation fines control with nanoparticles in offshore wells. Soc. of Petroleum Engineers. SPE-135088.

Hubbert, M. and Willis, D. 1957. Mechanics of hydraulic fracturing. Soc. Petr. Eng. SPE-686-G.

Hurtado, A.; Asadi, M.; Woodroof, R.; Casas, D. and Morales, R. 2005. Production enhancement for a northern Mexico field well resulting from flowback evaluations using chemical frac tracers: a case study. Soc. Petroleum Eng. SPE-95064.

Hutchinson, P. 1987. Morphology and evolution of a shale-filled paleochannel in the Wilcox Group (Paleocene-Eocene), southeast Texas. Gulf Coast Ass. Of Geological Soc. Trans. Vol XXXVII, 347-356 p.

Hydraulic Fracturing Facts: http://www.hydraulicfracturing.com/Pages/information.aspx

IMP (Instituto Mexicano del Petróleo), 2009a. Análisis de miscibilidad, desplazamiento y estabilidad de gas hidrocarburo, dióxido de carbono y metano, así como salmuera en aceite de la Formación Chicontepec. Proyecto F.47419. Dirección de Exploración y Producción. Elaborado por: Dra. Cecilia de los Ángeles Duran Valencia.

IMP (Instituto Mexicano del Petróleo), 2009b. Recuperación mejorada por inyección de químicos. Proyecto F.04REV06 PS-EP-04-01-01. Dirección Ejecutiva de Exploración y Producción. Dirección Regional Norte. Gerencia de Atención a Clientes.

Jensen, J.; Lake, L.; Corbett, P. and Goggin D. 1997. Statistics for petroleum engineers and geoscientists. Ed. Prentice-Hall.

Jiang, T.; Wang, Y.; Ding, Y.; Zhang, Y.; Xu, Z. and Zhang, H. 2005. The study of a new concept of low-damage fracturing technology in low-permeability exploration wells. International Petroleum Technology Conference, paper no. 10218.

Johnson, B.; Bossler, D. and Naummann, V. 1959. Calculations of relative permeability from displacement measurements. Trans. AIME 216, 370-372p.

Jolley, S.; Fisher, Q. and Ainsworth, R. 2010. Reservoir compartmentalization. Geological Society, London. Special publication v. 347.

Jones, F. and Owens, O. 1980. A laboratory study of low-permeability gas sands. Journal of Petroleum Technology, Soc. of Petroleum Engineers. SPE-7551-PA.

Jones, S. 1997. A technique for faster Pulse-Decay permeability measurements in tight-rocks. Journal of Formation Evaluation, Soc. of Petroleum Engineers. SPE-28450.

Juhasz, I. 1981. Normalised Qv – the key to chaly sand evaluation using the Waxman-Smits equation in the absence of core data. Trans. SPWLA 22nd Ann. Logging Symp., z1-36.

Kamath, J.1992. Evaluation of Accuracy of Estimating Air Permeability from Mercury Injection Data. SPEFE, 304-310p.

Keelan, D. K. and Koepf, E. H. 1977. The role of cores and core analysis in evaluation of formation damage. Journal of Petroleum Technology, Soc. of Petroleum Engineers. SPE-5696-PA.

Kenyon, W. 1992. Nuclear magnetic resonance as a petrophysical measurement. Nuclear Geophysics, vol. 6, no. 2.

Khilar, K. and Fogler, H. 1984. Water sensitivity in sandstones. Soc. Petroleum Eng. SPE-10103-PA.

King, G. E. 2012. Hydraulic Fracturing 101: What Every Representative, Environmentalist, Regulator, Reporter, Investor, University Researcher, Neighbor and Engineer Should Know About Estimating Frac Risk and Improving Frac Performance in Unconventional Gas and Oil Wells. Soc. of Petroleum Engineers. SPE-152596-MS.

Kolodzie, S., Jr. 1980. Analysis of pore throat size and use of the Waxman-Smits equation to determine OOIP in Spindle Field, Colorado. Soc. Petr. Eng. SPE-9382.

Kozeny J. 1927. Uber kapillare Leitung des Wassers im Boden (Aufstieg Versikerung und Anwendung auf die Bemasserung). Sitzungsber Akad., Wiss, Wein, Math- Naturwiss, KL, 1927; 136 (Ila): 271_306.

Lake, L. 1989. Enhanced oil recovery. Englewood Cliffs, New Jersey. Prentice Hall.

Law, J. 1944. Statistical approach to the interstitial heterogeneity of sand reservoirs. Trans. AIME, 155p.

Leas, W.; Jenks, L. and Russell, C. 1950. Relative permeability to gas. Trans. AIME, vol. 189, 65-72p.

Lebedeva, E.; Fogden, A.; Senden, T. and Knackstedt, M. 2010. Kaolinite wettability, the effect of salinity, pH and Calcium. Soc. Core Analysts, 2010, paper SCA2010-11, 12p.

Leontaritis, K.; Amaefule, J. and Charles, R. 1994. A systematic approach for the prevention and treatment of Formation Damage caused by asphaltene deposition. SPE Production & Facilities, August, 1994, 157-164p.

Li, X.; Wei, H.; Chen, B.; Liu, X.; Wang, C. and Zhao, X. 2008. Multi-stage fracturing stimulations improve well performance in tight-oil reservoirs of the Changqing Oilfield. Soc. Petroleum Eng. SPE-12303.

Loomis, A. and Crowell, D. 1972. Relative permeability studies: gas-oil and water-oil systems. United States Bureau of Mines, bulletin no. 599, 39p.

Luces, J.; Salguero, J.; Morales, J. and Riano, J. 2012. Hydraulic fracture geometry evolution and pressure during pumping; Chicontepec experiences indicate that natural fractures or fissures are not activated. Soc. Petroleum Eng. SPE-152396.

Mace, K.; Urbancic, T. and Baig, A. 2011. Fracture treatment optimization via points of diminishing return as determined by seismic moment tensor inversion. Soc. Petroleum Eng. SPE-147350.

MacDonald, R. and Chenery, D. 1988. The Damage discussion: its effect on well flow. Journal of Canadian Petroleum Technology, vol. 27, no. 4.

Ma, S.; Morrow, N.; Zhang, X. and Zhou, X. 1999. Characterization of wettability from spontaneous imbibition measurements. Journal of Canadian Petroleum Technology, vol. 38, no. 13.

Marchand, A.; Smalley, C.; Haszeldine, S. and Fallick, A. 2002. Note on the importance of hydrocarbon fill for reservoir quality prediction in sandstones. AAPG Bull. V. 86, No. 9, p. 1561-1571.

Masikewich, J. and Bennion, D. B. 1999. Fluid design to meet reservoir issues- a process. Journal of Canadian Petroleum Technology. Vol.38, No. 5, p. 61-71.
Mattax, C. and Kyte, J. 1962. Imbibition oil recovery from fractured water drive reservoirs. Trans. AIME 225, 177-184p.

Mayerhofer, M.; Richardson, M.; Walker, R.; Meehan, D.; Oehler, M. and Browning, R. 1997. Proppants? We don't need no proppants. Soc. Petroleum Eng. SPE-38611.

Mayerhofer, M.; Lolon, E.; Warpinski, N.; Cipolla, C.; Walser, D. and Rightmire, C. 2010. What is stimulated reservoir volume? Soc. Petroleum Eng. SPE-119890.

Mayol-Castillo, M. 2005. Caracterización geoquímica de los aceites de la Cuenca de Chicontepec. Tesis para obtener el grado de Maestra en Ciencias con Especialidad en Geología. Inedit.

McDougall, S. and Sorbie, K. 1995. The impact of wettability on waterflooding: pore-scale simulation. SPE Reservoir Engineering, August. 208-213p.

Moghadasi, J.; Kakavandi, M. and Kordestany, A. 2010. An experimental approach to investigate permeability alteration caused by underbalanced drilling in oil reservoirs. Soc. of Petroleum Engineers. SPE-127953.

Mohan, K. K. And Fogler, H. S. 1997. Colloidally induced smecticic fines migration: existence of microquakes. American Institute of of Chemical Engineers Journal, No. 43, March 1997, 565-576.

Mohan, K.; Vaidya, R.; Reed, M. and Fogler, H. 1993. Water sensitivity of sandstones containing swelling and non-swelling clays. Colloids and Surfaces A: Physicochemical and Engineering Aspects. 73 (1993) 231-254. Elsevier Science.

Montgomery, C. T. and Smith, M. B. 2010. Hydraulic Fracturing. History of an enduring technology. Journal of Petroleum Technology. December, 2010.

Morales-Gil, C. 2009. México halla histórica reserva de petróleo. El Universal, 17 de Febrero de 2009, primera plana.

Morrow, N. 1975. The Effects of Surface Roughness On Contact Angle: With Special Reference to Petroleum Recovery. Petroleum Society of Canada PETSOC-75-04-04.

Morrow, N. 1976. Capillary pressure for uniformly wetted porous media. J. Canadian Petroleum Tech. 49.

Morrow, N.; Lim, H. and Ward, J. 1986, Effect of crude-oil-induced wettability changes on oil recovery. Soc. Petr. Eng. SPE-13215-PA.

Morrow, N. 1990. Wettability and its effect on oil recovery. JPT, SPE Distinguished Author Series SPE-21621-PA.

Mullen, M.; Roundtree, R. and Barree, B. 2007. A composite determination of mechanical rock properties for stimulation design (What to do when you don't have a sonic log). Soc. Petr. Eng. SPE-108139.

Mungan, N. 1965. Permeability reduction through changes in pH and salinity. Journal of Petroleum Technology. SPE-1283.

Mungan, N. 1972. Relative permeability measurements using reservoir fluids. SPEJ Trans. AIME 253, 398-402p.

Nabipour, A.; Sarmadivaleh, M.; Asadi, M.; Sabogal, M. S. and Rasouli, V. 2010. A DEM study on perforation induced damaged zones and penetration length in sandstone reservoirs. American rock Mechanics Association, ARMA 10-248.

Narvaez, R.; Cetkovic, I.; Lopez, Ll.; Sandoval, G.; Tobias, H.; Hernandez, F.; Cobos, H. and Martinez, J. A. 2011. Real time lift monitoring and optimization solution applied at Chicontepec oilfield. Soc. of Petroleum Engineers. SPE-146096.

Narvaez, R. 2012. Yacimientos de aceite de baja permeabilidad. PEMEX internal presentation.

Nasiri, K. and Skauge, A. 2009. Use of enzymes to improve waterflood Performance. Proceedings of the 2009 International Symposium of the Society of Core Analysts.

Neasham, J. W. 1977. The morphology of dispersed clay in sandstone reservoirs and its effect on sandstone shaliness, pore space and fluid flow properties. Soc. of Petroleum Engineers. SPE-6858-MS.

Nelson, P. 2009. Pore-throat sizes in sandstones, tight sandstones, and shales. AAPG bull., v. 93, no. 3, 329-340p.

Nemirovich, G. and Islamgaliev, R. 2014. Horizontal drilling with multi-stage fracturing – access to challenged reserves of Tyumen Formation, Krasnoleninskoye Field. Soc. Petroleum Eng. SPE-171325-MS.

Neustaedter, R. 1968. Log evaluation of deep Ellenburger gas zones. Soc. Petr. Eng. SPE-2071.

Newberry, M. E. and Barker, K. M. 2000. Organic formation damage control and remediation. Soc. of Petroleum Engineers. SPE-58723.

Ning, X. and Olsen, T. 1995. The impact of fracturing-fluid cleanup and fracture-face damage on gas production. The Petroleum Society of CIM, paper no. 95-43.

NIPER (National Institute for Petroleum and Energy Research). 1986. Enhanced Oil Recovery Information. NIPER, Bartlesville, Oklahoma.

Nordgård Bolås, H. and Hermanrud, C. 2002. Rock stress in sedimentary basins –implications for trap integrity. *In* Hydrocarbon seal quantification, edited by Koestler, A. and Hunsdale, R. NPF Special publication 11, 17-35p. Elsevier.

Oshima, H, Healy, T. and White, L. 1983. Approximate analytic expressions for the electrophoretic mobility of spherical colloidal particles and the conductivity of their dilute suspensions. Jour. Colloid Sci. Faraday Trans. Series 2, 79, 1613-1628p.

Palisch, T.; Vincent, M. and Handren, P. 2008. Slickwater fracturing – food for thought. Soc. of Petroleum Engineers. SPE-115766.

Paxton, S. T.; Szabo, J. O.; Adjukiewicz, J. M. and Klimentidis, R. E. 2002. Construction of an intergranular volume compaction curve for evaluating and predicting compaction and porosity loss in rigid-grain sandstone reservoirs. American Association of Petroleum Geologists Buletin, v. 86, no. 12, pp. 2047-2067.

PEMEX, 1998. Estudio Regional Chicontepec. Internal report.

PEMEX, 2004. Estudio Regional de Plays Chicontepec del Terciario, Cuenca de Chicontepec Veracruz, Mexico. Prepared by The Scotia Group Inc. Internal report.
PEMEX, 2008. Estudio de Plays: Eoceno Inferior Chicontepec Turbiditas. Inedit.

PEMEX, 2009. Digitalización y actualización de la cartografía (Fase I y Fase II), Activo Chicontepec. GYMSA, Geoquímica y Perforación, S.A. de C.V. Internal report.

PEMEX, 2011. Perspectiva Estratégica de la Región Norte, Activo Integral Aceite Terciario Del Golfo. Internal report.

PEMEX, 2012a. Informe Anual 2012.
http://www.ri.pemex.com/index.cfm?action=content&sectionID=134&catID=12200

PEMEX, 2012b. Anuario Estadístico 2012.
http://www.ri.pemex.com/index.cfm?action=content&sectionID=134&catID=12200

PEMEX, 2013. Reservas de Hidrocarburos al 1 de Enero del 2013. PEMEX internal report.

PEMEX, 2013a. Presentación a Inversionistas, Noviembre 2013.

PEMEX, 2013b. Principales elementos del Plan de Negocios de PEMEX y sus Organismos subsidiarios 2014-2018. PEMEX internal report.

PEMEX, 2014. Presentación a Inversionistas, Abril 2014.

PEMEX, 2015. Las Reservas de Hidrocarburos de México, Evaluación al 1 de Enero de 2015.

Piro, G.; Canonico, L.; Galbariggi, G.; Bertero, L. and Carniani, C. 1996. Asphaltene adsorption onto formation rock: and approach to asphaltene formation damage prevention. SPE Production & Facilities, August 1996, 156-160p.

Pittman, E. 1989. Problems related to clay minerals in reservoir sandstones. AAPG Special Volume SG 28, Chapter 17, 237-244p.

Pittman, E., 1992. Relationship of porosity and permeability to various parameters derived from Mercury injection-capillary pressure curves for sandstone. AAPG Bull. V. 76, No. 2, p. 191-198.

Poupon, A. and Leveaux, J. 1971. Evaluation of water saturations in shaly formations. Trans. SPWLA 12th Ann. Logging Symp.

Porter, K. E. 1989. An Overview of Formation Damage. Journal of Petroleum Technology, August 1989, 780-786.

Pospisil, G.; Carpenter, C. and Pearson, C. 1995. Impacts of oriented perforating on fracture stimulation treatments: Kuparuk River Field, Alaska. Soc. of Petroleum Engineers. SPE-29645.

Purcell, W. 1949. Capillary pressures – their measurement using mercury and the calculation of permeability therefrom. Trans. AIME, no. 186, 39-48p.

Rabe, C. and Ortiz-Ramirez, J. 2010. Geomechanical analysis of the turbidite sandstone in the Soledad Field, Chicontepec basin, Mexico. Rock Mechanics in Civil and Environmental Engineering, Zhao, Labiouse, Dudt and Mathier (eds.). Taylor and Francis Group, London. ISBN 978-0-415-58654-2.

Ranking, R.; Thibodeau, M.; Vincent, M. and Palish, T. 2010. Improved production and profitability achieved with superior completions in horizontal wells: a Bakken/Three Forks case history. Soc. of Petroleum Engineers. SPE-134595.

Rae, P. and Di Lullo, G. 1996. Fracturing Fluids and Breaker Systems - A Review of the State-of-the-Art. Soc. of Petroleum Engineers. SPE-37359.

Reed, M. G. 1972. Stabilization of formation clays with Hydroxy-Aluminum solutions. Soc. of Petroleum Engineers. SPE-3694.

Reed, M. G. 1974. Formation permeability maintenance with Hydroxy-Aluminum Solutions. U.S. Patent number 3827500. August 6, 1974.

Reed, M. G. 1977. Formation permeability damage by mica alteration and carbonate dissolution. Soc. of Petroleum Engineers. SPE-6009.

Reinicke, A.; Blöcher, G.; Zimmermmann, G.; Huenges, E.; Dresen, G.; Stanchits, S.; Legarth, B.; and Makurat, A. 2011. Mechanically induced fracture face skin – insights from laboratory testing and numerical modelling. Soc. of Petroleum Engineers. SPE-144173.

Rezaian, A.; Kordestany, A.; Jamialahmadi, M. and Moghadasi, J. 2010. Modeling Formation Damage due to flocculated asphaltene deposition through dynamic displacement. Soc. of Petroleum Engineers. SPE-129583.

Ribeiro, L. and Sharma, M. 2011. Multi-phase fluid-loss properties and return permeability of energized fracturing fluids. Soc. of Petroleum Engineers. SPE-139622.

Ribeiro, L. and Sharma, M. 2013. Fluid selection for energized fracture treatments. Soc. of Petroleum Engineers. SPE-163867-MS.

Rickman, R.; Mullen, M.; Petre, E.; Grieser, B. and Kundert, D. 2008. A practical use of shale petrophysics for stimulation design optimization: all shale plays are not clones of the Barnett Shale. Soc. Petr. Eng. SPE-115258.

Rider, M. 2002. The Geological interpretation of well-logs. Whittles publishing, second edition, 280p.

Riese, W. C. and Riese, A. C. 1968. Prediction of Geochemical formation damage in the Vicksburg formation of South Texas. Soc. of Petroleum Engineers. SPE-18132.

Rivera, R. 2003. Mojabilidad de las rocas de Tajín y Agua Fría. PEMEX Exploracion y Produccion. Internal report. *In* Gachuz-Muro, H. 2009. Effective permeability vs. Drainage radius, correlation for the turbidites oil reservoirs – Chicontepec Paleochannel. Soc. of Petroleum Engineers. SPE-120267.

Rogers, W. F. 1963. Composition of oil well drilling fluids. Gulf Publishing Co. 2nd ed. Houston, Texas. 818 p.

Rühl, W., Schmid, C. and Wissman, W. 1963. Displacement tests with porous rock samples under reservoir conditions. 6th. World Petroleum Congress; Frankfurt. Sec. 2, paper 11, 467-481p.

Salathiel, R. 1973. Oil recovery by surface film drainage in mixed-wettability rocks. Jour. Petr. Tech., 1216-1224p.

Samuel, M.; Polson, D.; Graham, D.; Kordziel, W.; Waite, T.; Waters, G.; Vinod, P.; Fu, D. and Downey, R. 2000. Viscoelastic Surfactant Fracturing Fluids: Applications in Low Permeability Reservoirs. Soc. of Petroleum Engineers. SPE-60322-MS.

Sarkar, S. 2011. Depositional History and Reservoir Characteristics of Structurally Confined Foredeep Turbidites, Northern Chicontepec Basin, Mexico. PhD Dissertation.

Saavedra, T. D. 2009. Proyecto Aceite Terciario del Golfo (powerpoint presentation). PEMEX internal presentation.

Schembre, J. M. and Kovscek, A. R. 2004. Thermally induced fines mobilization: its relationship to wettability and formation damage. Soc. of Petroleum Engineers. SPE-86937.

Schlumberger, 2009. Log interpretation charts. Schlumberger edition 2009.

Schlumberger, 2009a. ECLIPSE Technical Description. Schlumberger edition 2009.2.

Schön, J. 2011. Physical properties of rocks, a workbook. Handbook of Petroleum Exploration and Production, Vol. 8. Elsevier.

Shepherd, M. 2009. Oil Field Production Geology. American Association of Petroleum Geologists Memoir no. 91, 350p.

Simandoux, P. 1963. Dielectric measurements on porous media: applications to the measurement of water saturations; study of the behaviour of arguilliceous formations. SPWLA Shaly sand reprint volume, 97-124p.

Skauge, A.; Vik, B. and Ottesen, B. 2003. Variation of special core analysis properties for intermediate wet sandstone material. Soc. Core Analysts, SCA2003-05.

SENER (Secretaria de Energía), 2014. Registro de Reservas Petroleras al 1 de enero de 2014. http://egob2.energia.gob.mx/SNIH/Reportes/

Sim, S.; Takabayashi, K.; Okatsu, K. And Fisher, D. 2005. Asphaltene-induced Formation Damage: effect of asphaltene particle size and core permeability. Soc. of Petroleum Engineers. SPE-95515.

Smith, C. 1973. Gas Well Fracturing Using Gelled Non-Aqueous Fluids. Soc. of Petroleum Engineers. SPE-4678-MS.

Smithson, T, 2012. How porosity is measured. Oilfield Review, Autumn 2012, 24, no. 3.

Soares, A. C. and Ferreira, F. H. 2002. An experimental study for mechanical formation damage. Soc. of Petroleum Engineers. SPE-73734.

Soares, A. C.; Ferreira, F. H. and Vargas, E. A. 2002. An experimental study for mechanical formation damage. Soc. of Petroleum Engineers. SPE-80614.

Soares, A. C.; Altoe, J. E.; Bedrikovetsky, P. and Ferreira, F. H. 2003. Formation damage due to pore collapse during pressure depletion. Soc. of Petroleum Engineers. SPE-82254.

Stadnes, D. and Austad, T. 2000. Wettability alteration in chalk 2. Mechanism for wettability alteration from oil-wet to water-wet using surfactants. Journal of Petroleum Science and Engineering, vol. 28, 123-143p.

Sun, H.; Stevens, D.; Cutler, J.; Wood, B. and Wheeler, R. 2010. A novel nondamaging friction reducer: development and successful slickwater frac applications. Soc. of Petroleum Engineers. SPE-136806.

Sun, H.; Wood, B.; Stevens, D. and Cutler, J. 2011. A nondamaging friction reducer for slickwater frac applications. Soc. of Petroleum Engineers. SPE-139480.

Swanson, B. 1981. A simple correlation between permeabilities and mercury capillary pressures. Journal of Petroleum Technology, 2498-2507p.

Takahashi, S.; Abbaszadeh, M.; Ohno, K.; Soto, H. and Cancino, L. 2006. Integrated reservoir modeling for evaluating field development options in Agua Fria, Coapechaca and Tajin Fields of Chicontepec basin. Soc. of Petroleum Engineers. SPE-103974.

Tang, G. and Morrow, N. 1999. Influence of brine composition and fines migration on crude oil/brine/rock interactions and oil recovery. Journal of Petroleum Science and Engineering, 24: 99-111 pp.

Tang, Z. and Morrow, N. 2005. Wettability control by adsorption from crude oil - aspects of temperature and increased water saturation. Proceedings of the 2005 International Symposium of the Society of Core Analysts.

Terracina, J.; Turner, J.; Collins, D. and Spillars, S. 2010. Proppant selection and its effect on the results of fracturing treatments performed in shale formations. Soc. of Petroleum Engineers. SPE-135502.

Thallak, S. G.; Holder, J.; and Gray, K. E. 1993. Deformation effects on formation damage during drilling and completion operations. Soc. of Petroleum Engineers. SPE-25430.

Thomeer, J. 1960. Introduction of a pore geometrical factor defined by the capillary pressure curve. Journal of Petroleum Technology, 73-77p.

Thompson, J. E. and DeVine, C. S. 1995. Fracturing fluid interactions with formation minerals and their subsequent effect on formation permeability. Soc. of Petroleum Engineers. SPE-29500.

Tiab, D. and Donaldson, E. 2012. Petrophysics: theory and practice of measuring reservoir rock and fluid transport properties. Third edition, Gulf Professional Publishing. 950 p.

Timur, A. 1968. An investigation of permeability, porosity, and residual water saturation relationships. SPWLA Transactions, 9th Annual Logging Symposium, New Orleans, USA.

Tissot, B. and Welte, H. 1984. Petroleum formation and ocurrence. Springer Verlag, New York. 699 p.

Tong, Z., Morrow, N. and Xie, X. 2002. Spontaneous imbibition for mixed-wettability states in sandstones induced by adsorption from crude-oil.

Torres, L.; Moctezuma, A.; Avendano, J.; Munoz, A. and Gracida, J. 2011. Comparison of bio- and synthetic surfactants for EOR. Jour. Petr. Science and Engineering, 76, 6-11p.

Tyler, N. and Finley, R. 1992. Architectural controls on the recovery of hydrocarbons from sandstone reservoirs. *In* The Three-Dimensional Facies Architecture of Terrigenous Clastic Sediments and Its Implications for Hydrocarbon Discovery and Recovery. Society for Sedimentary Geology (SEPM).

Tyler, N.; Gachuz-Muro, H.; Rivera, J.; Rodriguez, J.; Rivas-Gomez, S.; Tyler, R. and Nunez-Vegas, V. 2004. Integrated characterization of low permeability, submarine fan reservoirs for waterflooding implementation, Chicontepec fan system, Mexico. Soc. of Petroleum Engineers. SPE-92077.

Vasquez, R.; Cossey, S.; Niewenhuise, D.; Davis, J.; Castagna, J.; Morales, M. and Ramos, I. 2014. New insights into the stratigraphic framework and depositional history of the Paleocene and Eocene Chicontepec Formation, Onshore Eastern Mexico. AAPG Search and Discovery Article no. 30334.

Vessell, R. 2008. Modelo diagenético y caracterización de yacimiento areniscas de Chicontepec, Cuenca de Chicontepec, Veracruz. Inedit.

Volk, L. J.; Gall, B. L.; Raible, C. J. and Carroll, H. B. 1983. A method for evaluation of formation damage due to fracturing fluids. Soc. of Petroleum Engineers. SPE-11638.

Walker, R. 1978. Deep-Water sandstone facies and ancient submarine fans: models for exploration for stratigraphic traps. AAPG Bull. V. 62, no. 6, 932-966p.

Walls, J.D. and Amaefule, J.O. 1985. Capillary pressure and permeability relationships in tight gas sands. Soc. Petroleum Eng. SPE-13879.

Wang, X.; Brower, K. and Buckley, J. 1999. Advances in observation of asphaltene destabilization. Soc. of Petroleum Engineers. SPE-50575.

Wang, X. and Buckley, J. 2001. An experimental approach to prediction of asphaltene flocculation. Soc. of Petroleum Engineers. SPE-64994.

Wang, X. 2003. Development of a nonresidue polymer-based fracturing fluid. Soc. of Petroleum Engineers. SPE-80227.

Warpinski, N.; Kramm, R.; Heinze, J. and Waltman, C. 2005. Comparison of single- and dual-array microseismic mapping techniques in the Barnett Shale. Soc. of Petroleum Engineers. SPE-95568.

Watson, R. and Boukadl, F. 1991. The effects of clay matrix, carbonate cement and quartz overgrowth on wettability, porosity and residual oil saturation, tortuosity and rock surface area of Berea. Soc. of Petroleum Engineers. SPE-91-76.

Waxman, M. and Smits, L. 1968. Electrical conductivities in oil-bearing shaly sands. Soc. Pet. Engineers, j. 8, 107-122p.

Weimer, P. and Slatt, R. 2004. Petroleum Systems of deep-water settings: SEG/EAGE Distinguished Instructor Series 7, 465p.

Wilkinson, M.; Haszeldine, S. and Fallick, A. 2006. Hydrocarbon filling and leakage history of a deep geopressured sandstone, Fulmar formation, United Kingdom North Sea. AAPG Bull. V. 90, No. 12, p. 1945-1961.

Williams, N.; Kelly, P.; Berard, K.; Dore', E.; Emery, N.; Williams, C. and Mukhopadhyay, S. 2012. Fracturing fluid with low-polymer loading using a new set of Boron crosslinkers: laboratory and field studies. Soc. Petr. Eng. SPE-151715.

Worthington, P. 1985. The evolution of shaly sand concepts in reservoir evaluation. The Log Analysts.

Wu, Y.; Shuler, P.; Blanco, M.; Tang, Y. and Goddard, W. 2006. A Study of Wetting Behavior and Surfactant EOR in Carbonates With Model Compounds. Soc. of Petroleum Engineers. SPE-9612-MS.

Xie, X.; Weiss, W.; Tong, Z. and Morrow, N. 2004. Improved Oil Recovery from Carbonate Reservoirs by Chemical Stimulation. Soc. Petr. Eng. SPE-89424-MS.

Xu, T. and Hoffman, T. 2013. Hydraulic fracture orientation for miscible gas injection EOR in unconventional oil reservoirs. Soc. Petr. Eng. SPE-168774. Unconventional Resources Technology Conference URTeC-1580226.

Yang, L.; Wang, J.; Fan, T. and Buckley, J. 2003. Effect of crude-oil composition on wettability of mica. Society of Core Analysts, SCA-2003-01.

Yang, X. M. and Sharma, M. M. 1991. Formation Damage caused by cement filtrates in sandstone cores. Soc. of Petroleum Engineers. Production Engineering, November, 1991.

Yu, X. and Guo, B. 2011. How significant is the formation damage in multi-fractured horizontal wells? Soc. of Petroleum Engineers. SPE-125905.

Yu, M. and Nasr-El-Din, H. 2009. Quantitative analysis of viscoelastic surfactants. Soc. of Petroleum Engineers. SPE-121715-MS.

Yu, W.; Lashgari, H. and Sepehrnooni, K. 2014. Simulation study of CO_2 process in Bakken tight-oil reservoirs. Soc. of Petroleum Engineers. SPE-169575-MS.

Zhou, X.; Morrow, N. and Ma, S. 1996. Interrelationship of wettability, initial water saturation, aging time, and oil recovery by spontaneous imbibition and waterflooding. Soc. of Petroleum Engineers. SPE-35436-MS.

Zoback, M. 2007. Reservoir Geomechanics. Cambridge University Press. 449p.

Zongqiang, Z.; Lijun, M.; Xianwen, M.; Wen, Z.; Xiaodong, W.; Xiangqian, B.; Wenxiong, W. and Peng, P. 2012. Hybrid fracturing treatments unleash tight oil reservoirs consisting of sand shale sequences in the Changqing Oilfields. Soc. of Petroleum Engineers. SPE-156179.

APPENDICES

Appendix A. Eclipse®100 input Data File (HUM-4005 well, real case)

```
RUNSPEC
TITLE
Tight gas production
--       Number of cells
--      NX     NY     NZ
--      --     --     --
DIMENS
9       9      70   /

-- Phases
OIL
WATER
GAS
DISGAS

-- Units (distance in FT and pressure in PSI)
FIELD

-- Maximum well/connection/group values
--     #wells  #cons/w  #grps  #wells/grp
--     ------  -------  -----  ----------
WELLDIMS
1       100      1      1 /

-- Unified output files
UNIFOUT

-- Simulation start date
START

24 SEP 2011 /

NSTACK
40 /

NUPCOL
10 /

--================================================================
GRID

OLDTRANR

-- Size of each cell in X, Y and Z directions
DX
5670*0.16404199E+03  /

DY

5670*0.16404199E+03  /

DZ
 INCLUDE
```

```
‘HUM-4005_DZ.INC’

/

TOPS
INCLUDE
‘HUM-4005_TOPS.INC’

/

-- Permeability in X, Y and Z directions for each cell
PERMX
INCLUDE
‘HUM-4005_PERMX.INC’

/

COPY
PERMX PERMY /
PERMX PERMZ /

/

-- Porosity of each cell
PORO
INCLUDE
‘HUM-4005_PORO.INC’

/
-- Defining petrophysical values of the completed interval
EQUALS

PERMX 500 5 5 5 5 7 37  /
PERMY 500 /
PERMZ 500 /

PORO 0.01 5 5 5 5 7 37 /

/

-- Defining local grid refinement to represent hydraulic fracture (two fracture wins: LGR1 and
LGR2)
CARFIN
LGR1  5  5  3  4  7  37  20  2  31  /

NXFIN
20 /

HXFIN
2*0.482097  2*0.233660 4*0.116830 4*0.050583 4*0.116830 2*0.233660 2*0.482097    /

NYFIN
2*1 /

NZFIN
31*1 /

REFINE
LGR1  /
```

```
EQUALS

PERMX  0.85  1 9 1 2 1 31  /
PERMY  0.85  /
PERMZ  0.85  /

PERMX  10000   10 10 1 2 1 31  /
PERMY  10000   /
PERMZ  10000   /

PERMX  0.85  11 20 1 2 1 31  /
PERMY  0.85  /
PERMZ  0.85  /

/

ENDFIN

CARFIN
LGR2  5  5  6  7  7  37  20  2  31  /

NXFIN
20 /

HXFIN
2*0.482097  2*0.233660 4*0.116830 4*0.050583 4*0.116830 2*0.233660 2*0.482097    /

NYFIN
2*1 /

NZFIN
31*1 /

REFINE
LGR2  /

-- Defining permeability values of hydraulic fracture
EQUALS

PERMX  0.85  1 9 1 2 1 31  /
PERMY  0.85  /
PERMZ  0.85  /

PERMX  10000   10 10 1 2 1 31  /
PERMY  10000   /
PERMZ  10000   /
PERMX  0.85  11 20 1 2 1 31  /
PERMY  0.85  /
PERMZ  0.85  /

/

ENDFIN

INIT

--=================================================================
PROPS

-- Three phase relative permeabilities using SWOF and SGOF
```

```
--  SW     Krw   Krow   Pcow
--  ----   ----  ----   ----
SWOF
0.163     0.000     1.000     6.500
0.206     0.008     0.480     4.000
0.248     0.015     0.300     2.500
0.292     0.021     0.210     1.500
0.334     0.029     0.170     0.850
0.377     0.036     0.140     0.600
0.420     0.046     0.110     0.450
0.462     0.054     0.080     0.350
0.505     0.100     0.060     0.250
0.547     0.225     0.030     0.100
0.590     0.388     0.000     0.000  /

--  SG     Krg   Krog   Pcog
--  ----   ----  ----   ----
SGOF
0.000     0.000     1.000     0.000
0.056     0.038     0.930     0.025
0.111     0.075     0.800     0.055
0.167     0.113     0.650     0.125
0.222     0.163     0.480     0.250
0.278     0.225     0.300     0.400
0.334     0.288     0.180     0.600
0.389     0.375     0.100     0.900
0.445     0.563     0.050     1.350
0.501     1.000     0.000     2.000  /

-- PVT PROPERTIES OF WATER
--    Pressure  Bw    Cw (water compressibility)Muw   Viscosibility
--    -----     -----  -----                  -----    -----
PVTW
     3700      1.029    3.0E-6                0.89      0 /

-- ROCK COMPRESSIBILITY
--
--    REF. PRES   COMPRESSIBILITY
ROCK
       2500       7.0E-6         /

-- SURFACE DENSITIES OF RESERVOIR FLUIDS (IN LB/FT3)
--
--       OIL   WATER   GAS
DENSITY
       50.8   62.4   0.0749  /

-- PVT PROPERTIES OF LIVE OIL (WITH DISSOLVED GAS)
-- DATA OBTAINED FROM HUMAPA-1642 PVT ANALYSIS
--    Rs       Pb     Bo     Muo
--(Mscf/STB) (psi) (rb/STB) (cP)
-- -----  -----  -----  -----
PVTO
0.000006            14.7      1.048     3.014 /
0.005150            100       1.057     2.915 /
0.043454            300       1.078     2.267 /
0.084084            600       1.102     2.038 /
0.192255            1200      1.150     1.398 /
0.313069            2000      1.201     1.041 /
0.417034            2875      1.225     0.898
```

```
-- Subtable for undersaturated oil with Rs=0.4170 Mscf/STB
--   Po     Bo    Muo
--(psi) (rb/STB) (cP)
-- -----  -----  -----
3000      1.224     0.954
4000      1.215     1.164
5000      1.207     1.362
6000      1.199     1.620
7000      1.193     1.900
8000      1.186     2.133 /
/

-- PVT PROPERTIES OF DRY GAS (NO VAPOURISED OIL)
-- DATA OBTAINED FROM HUMAPA-1642 PVT ANALYSIS
--    Pg    Bg     Mug
-- (psi) (rb/Mscf) (cP)
--  -----  -----  -----
PVDG
14.7       216.704 0.0106
100        31.472   0.0119
300        10.330   0.0128
600        5.058     0.0135
1200      2.458     0.0146
2000      1.443     0.0167 /
--=====================================================================
SOLUTION
-- DATA FOR INITIALISING FLUIDS TO POTENTIAL EQUILIBRIUM
--
--   DATUM  DATUM   OWC    OWC    GOC    GOC    RSVD   RVVD   SOLN
--   DEPTH  PRESS  DEPTH   PCOW  DEPTH   PCOG  TABLE  TABLE   METH
EQUIL
     4790   3000   4950     0    4740    0      1      0       0  /

-- VARIATION OF INITIAL RS WITH DEPTH
--
--   DEPTH    RS
RSVD
4660  0.4170
4970  0.4171  /

--=====================================================================
SUMMARY

FOPR
FOPT
FGPR
FGPT
FPR
FWPR
FGOR
EXCEL
--=====================================================================
SCHEDULE

-- Output to Restart file for t>0 (.UNRST)
--     Restart file      Graphics
--      every step         only
--     ------------      --------
RPTRST
       BASIC=2          NORST=1 /
```

```
-- Location of wellhead and pressure gauge
--      Well  Well   Location   BHP    Pref.
--      name  group   I    J   datum   phase
--     -----  ----    -    -   -----   -----
WELSPECS
     HUM-4005   G1      5    5   3000    OIL  /
/

-- Completion interval
--      Well   Location  Interval  Status          Well
--      name    I    J    K1  K2   O or S          ID
--      ----    -    -    --  --   ------         --??----
COMPDAT
     HUM-4005   5    5    7   37   OPEN           1* 0.45 /

/

-- Maximum rate of increase of solution GOR
-- (in Mscf/stb/day)
DRSDT
  0.0003  /

-- Production control
--  Well  Status  Control   Oil   Wat   Gas    Liq  Resv   BHP
--  name          mode     rate  rate  rate   rate  rate  limit
--  ----  ------  ------    ----  ----  ----   ----  ----  -----
WCONPROD
   HUM-4005 OPEN    BHP      5*                    1 /
/

-- Number and size (days) of timesteps
TSTEP
50*0.001
100*0.01
200*0.1
250*1
--500*10
/

END
```

Appendix B. Experimental data generated in this study

The following tables display the core samples used for descriptive and experimental tests. See the text for reference.

Relation of the core samples and their petrophysical properties				
*Data provided by PEMEX **New data generated in this study				
Well Name	Sample Code	Depth (m)	Gas Ø (%)	Klinkenberg k (mD)
*COYULA-236	N1H2	1136.68	6.72	0.017
*COYULA-236	N1H3	1136.84	4.76	0.014
*COYULA-236	N1H7	1139.39	7.43	0.057
*COYULA-236	N1H8	1140.16	5.94	0.128
*COYULA-236	N1H9	1140.28	10.22	0.022
*COYULA-236	N1H10	1140.37	8.74	0.026
*COYULA-236	N1H11	1140.47	7.08	0.128
*COYULA-236	N1H12	1140.92	11.82	43.155
*COYULA-236	N1H13	1140.98	15.63	188.71
*COYULA-236	N1H14	1141.07	13.95	28.695
*COYULA-236	N1H15	1142.69	10.30	0.037
*COYULA-236	N1H16	1142.89	11.32	0.062
*COYULA-236	N1H17	1143.24	6.58	0.010
*COYULA-236	N1H19	1143.46	4.68	0.013
*COYULA-236	N1H20	1143.72	6.32	0.033
*COYULA-236	N1H21	1143.76	7.17	0.041
*COYULA-236	N3H3	1450.84	3.06	0.009
*COYULA-236	N3H8	1451.89	2.97	0.001
*COYULA-236	N4H3	1570.38	5.38	0.357
*COYULA-1019	N1H22	1673.39	1.41	0.001
*COYULA-1019	N1H27	1674.38	5.71	0.004
*COYULA-1019	N2H3	1680.02	4.17	0.001
*COYULA-1019	N2H12	1682.84	1.74	0.000
*COYULA-1024	N1H6	1326.61	0.35	0.001
*COYULA-1024	N1H21	1331.95	3.64	0.001
*COYULA-1024	N2H17	1372.2	9.16	0.401
*COYULA-1024	N2H25	1373.56	5.75	0.004
*COYULA-1024	N2H27	1374.35	6.11	0.008
*COYULA-1024	N2H29	1375.79	5.66	0.004
*COYULA-1024	N3H23	1602.54	3.93	0.026
*COYULA-1196	N1H27	1511.88	6.15	0.008
*COYULA-1196	N1H30	1512.5	5.90	0.013
*COYULA-1196	N1H31	1512.67	6.95	0.019
*COYULA-1196	N1H33	1513.56	5.15	0.010
*COYULA-1196	N2H4	1582.48	5.48	0.020
*COYULA-1196	N2H6	1582.71	2.81	0.226
*COYULA-1196	N2H8	1583.15	5.21	0.011
*COYULA-1196	N2H9	1583.47	3.96	0.364
*COYULA-1196	N2H12	1584.09	5.00	0.010
*COYULA-1196	N2H17	1585.4	1.17	0.001
*COYULA-1196	N2H23	1587.13	1.85	0.001
*COYULA-1196	N2H26	1587.62	6.55	0.016
*COYULA-1196	N2H27	1587.78	3.21	0.013
*HUMAPA-807	N1H4	1147.31	6.62	0.084
*HUMAPA-807	N1H18	1151.65	8.48	0.316
*HUMAPA-807	N1H27	1153.64	3.02	0.021
*HUMAPA-807	N2H3	1154.74	9.26	0.099
*HUMAPA-807	N2H5	1154.89	10.05	0.143
*HUMAPA-807	N2H15	1157.26	5.55	0.453

*HUMAPA-807	N2H23	1162.31	5.07	0.007
*HUMAPA-807	N2H27	1163	6.68	2.097
*HUMAPA-807	N3H2	1673.21	2.01	0.003
*HUMAPA-807	N3H9	1674.86	2.14	0.001
*HUMAPA-807	N4H3	1801.9	2.96	0.187
*HUMAPA-807	N4H14	1806.79	2.42	0.019
*HUMAPA-807	N4H15	1807.57	2.69	0.063
*HUMAPA-1643	N2H32	1524.35	2.94	0.099
*HUMAPA-1643	N3H14	1632.24	7.61	0.018
*HUMAPA-1643	N3H24	1634.48	5.04	0.262
*HUMAPA-1643	N3H37	1637.12	4.64	0.054
*HUMAPA-1643	N4H21	1641.97	2.24	0.338
*HUMAPA-4036	N1H6	1117.93	8.30	2.666
*HUMAPA-4036	N1H7	1118.19	8.34	2.287
*HUMAPA-4036	N1H8	1118.33	12.66	62.894
*HUMAPA-4036	N1H9	1118.39	6.78	0.170
*HUMAPA-4036	N1H17	1119.73	9.18	0.981
*HUMAPA-4036	N1H21	1120.25	11.44	1.513
*HUMAPA-4036	N1H26	1120.7	6.38	0.144
*HUMAPA-4036	N1H34	1122.25	12.63	2.746
*HUMAPA-4198	N3H1	1674.03	5.41	0.018
*HUMAPA-4198	N3H4	1674.75	3.89	0.010
*HUMAPA-4198	N3H8	1675.41	7.10	0.621
*HUMAPA-4198	N3H30	1680.71	7.45	0.673
**HUMAPA-4198	1	1449.75	4.12	0.0017
**HUMAPA-4198	2	1527.61	8.10	0.0025
**HUMAPA-4198	3	1680.05	6.35	0.0015
**HUMAPA-4036	4	1118.68	1.83	0.0002
**HUMAPA-4036	5	1352.71	4.41	0.0003
**HUMAPA-4036	6	1386.08	2.47	0.0005
**HUMAPA-4036	7	1387.6	4.29	0.0003
**HUMAPA-807	8	1152.18	3.79	0.0006
**HUMAPA-807	9	1155.47	3.48	0.0005
**HUMAPA-807	10	1673.82	2.21	0.0002
**HUMAPA-807	11	1802.06	2.41	0.0001
**HUMAPA-807	12	1804.13	2.20	0.0001
**HUMAPA-1643	13	1231	4.80	0.0006
**HUMAPA-1643	14	1522.08	2.49	0.0014
**HUMAPA-1643	15	1628.53	3.05	0.0003
**HUMAPA-1643	16	1639.52	2.99	0.0008
**COYULA-236	17	1422.23	2.87	0.0001
**COYULA-236	18	1450.75	1.14	0.0001
**COYULA-236	19	1570.69	2.88	0.0004
**COYULA-1196	20	1513.14	4.12	0.0003
**COYULA-1196	21	1583.89	2.00	0.0002
**COYULA-1196	22	1756.09	1.82	0.0003
**COYULA-1019	23	1674.26	4.53	0.0003
**COYULA-1019	24	1686.43	1.98	0.0001
**COYULA-1024	25	1325.57	3.60	0.0002
**COYULA-1024	26	1368.91	3.23	0.0003
**COYULA-1024	27	1370.24	7.76	0.0025
**COYULA-1024	28	1605.9	1.78	0.0001
**COYULA-236	29	1141.25	15.44	22.200
**HUMAPA-4036	30	1124.5	0.69	0.0004
**HUMAPA-1035	M1F30a	1711.68	13.33	40.846
**HUMAPA-1035	M1F30b	1711.68	12.57	63.163
**HUMAPA-1035	M3F26a	1712.56	12.57	20.160
**HUMAPA-1035	M3F26b	1712.56	12.78	22.381
**HUMAPA-1035	M4F22a	1713.56	13.64	24.097
**HUMAPA-1035	M4F22b	1713.56	13.72	63.861

***COYULA-236*	*S29a*	*1141.25*	*10.46*	*1.288*
***COYULA-236*	*S29a1*	*1141.25*	*15.39*	*10.035*
**HUMAPA-1708*	*N1H1*	*1388.1*	*4.80*	*0.020*
**HUMAPA-1708*	*N1H2*	*1388.6*	*3.69*	*0.022*
**HUMAPA-1708*	*N1H4*	*1389.12*	*2.59*	*n/a*
**HUMAPA-1708*	*N1H5*	*1389.62*	*3.34*	*0.024*
**HUMAPA-1708*	*N1H6*	*1390.43*	*3.56*	*0.006*
**HUMAPA-1708*	*N1H7*	*1390.48*	*2.00*	*n/a*
**HUMAPA-1708*	*N1H8*	*1390.6*	*5.34*	*0.020*
**HUMAPA-1708*	*N1H9*	*1391.13*	*5.47*	*0.146*
**HUMAPA-1708*	*N1H10*	*1391.26*	*5.30*	*0.101*
**HUMAPA-1708*	*N1H12*	*1391.71*	*3.53*	*0.013*
**HUMAPA-1708*	*N1H13*	*1391.88*	*6.24*	*0.026*
**HUMAPA-1708*	*N1H14*	*1392.35*	*3.35*	*0.012*
**HUMAPA-1708*	*N1H20*	*1393.32*	*5.01*	*0.012*
**HUMAPA-1708*	*N1H21*	*1393.66*	*9.27*	*3.430*
**HUMAPA-1708*	*N1H22*	*1393.73*	*4.25*	*0.014*
**HUMAPA-1708*	*N1H25*	*1394.27*	*6.93*	*0.013*
**HUMAPA-1708*	*N1H26*	*1394.47*	*4.13*	*0.019*
**HUMAPA-1708*	*N1H28*	*1395*	*3.81*	*0.016*
**HUMAPA-1708*	*N1H30*	*1395.28*	*8.47*	*0.039*
**HUMAPA-1708*	*N1H31*	*1395.85*	*3.36*	*0.033*
**HUMAPA-1708*	*N1H33*	*1396.19*	*1.99*	*n/a*
**HUMAPA-1708*	*N1H35*	*1396.81*	*7.10*	*0.030*
**HUMAPA-1708*	*N1H36*	*1396.97*	*9.76*	*0.114*
**HUMAPA-1708*	*N2H1*	*1578.03*	*2.35*	*0.524*
**HUMAPA-1708*	*N2H3*	*1578.31*	*3.25*	*0.016*
**HUMAPA-1708*	*N2H4*	*1578.72*	*3.42*	*0.020*
**HUMAPA-1708*	*N2H5*	*1579.03*	*4.13*	*0.023*
**HUMAPA-1708*	*N2H6*	*1579.8*	*2.05*	*n/a*
**HUMAPA-1708*	*N2H7*	*1580.05*	*2.41*	*0.011*
**HUMAPA-1708*	*N2H8*	*1580.63*	*3.06*	*0.018*
**HUMAPA-1708*	*N2H9*	*1580.78*	*2.33*	*0.011*
**HUMAPA-1708*	*N2H11*	*1581.31*	*5.58*	*0.041*
**HUMAPA-1708*	*N2H12*	*1581.48*	*4.77*	*0.067*
**HUMAPA-1708*	*N2H14*	*1581.93*	*2.39*	*0.017*
**HUMAPA-1708*	*N2H15*	*1582.21*	*5.62*	*0.050*
**HUMAPA-1708*	*N2H16*	*1583.03*	*1.58*	*0.009*
**HUMAPA-1708*	*N2H18*	*1583.56*	*2.49*	*0.014*
**HUMAPA-1708*	*N2H22*	*1585.02*	*2.40*	*0.009*
**HUMAPA-1708*	*N2H23*	*1585.91*	*5.35*	*0.044*
**HUMAPA-1708*	*N2H25*	*1586.83*	*2.40*	*0.020*
**HUMAPA-1708*	*N2H26*	*1587.06*	*5.12*	*0.054*
**HUMAPA-1708*	*N3H1*	*1653.32*	*5.00*	*0.026*
**HUMAPA-1708*	*N3H3*	*1653.84*	*2.04*	*0.012*
**HUMAPA-1708*	*N3H4*	*1655.97*	*1.79*	*0.007*
**HUMAPA-1708*	*N3H10*	*1659.93*	*1.85*	*0.016*
**HUMAPA-1708*	*N3H17*	*1660.59*	*5.98*	*0.059*
**HUMAPA-1708*	*N3H19*	*1661.25*	*4.63*	*0.040*
**HUMAPA-1708*	*N3H20*	*1661.54*	*3.51*	*0.022*
**HUMAPA-1708*	*N4H3*	*1738.98*	*7.22*	*2.077*
**HUMAPA-1708*	*N4H5*	*1740.11*	*10.10*	*6.065*
**HUMAPA-1708*	*N4H7*	*1740.55*	*6.44*	*0.155*
**HUMAPA-1708*	*N4H8*	*1740.98*	*4.99*	*0.039*
**HUMAPA-1708*	*N4H9*	*1741.42*	*3.14*	*0.018*
**HUMAPA-1708*	*N4H10*	*1741.61*	*14.80*	*473.76*
**HUMAPA-1708*	*N4H12*	*1742.16*	*7.82*	*1.517*
**HUMAPA-1708*	*N4H13*	*1742.97*	*5.30*	*0.057*
**HUMAPA-1708*	*N4H15*	*1743.71*	*4.25*	*0.039*
**HUMAPA-1708*	*N4H21*	*1745.78*	*3.42*	*0.050*

X-Ray Diffraction Mineralogy Results

*Data provided by PEMEX **New data generated in this study

***Q**: quartz; **F**: feldspar; **P**: plagioclase; **C**: calcite; **A**: ankerite; **D**: dolomite; **Py**: pyrite; **G**: gypsum; **Cl**: total clay; **I/M**: illite/mica; **K**: kaolinite; **Ch**: chlorite*

Well Name	Sample Code	Depth (m)	Bulk Fraction									Clay Fraction		
			Q	F	P	C	A	D	Py	G	Cl	I/M	K	Ch
*COYULA-236	N1H3	1136.8	35.6	0.6	5.2	42.9	0.0	1.3	0.9	0.0	13.5	10.1	1.0	2.4
*COYULA-236	N1H7	1139.4	36.9	0.7	7.3	36.2	0.0	1.8	1.3	0.0	15.8	13.2	0.9	1.7
*COYULA-236	N1H12	1140.9	50.2	0.5	5.0	32.9	1.1	2.0	0.5	0.0	7.8	4.8	2.1	0.9
*COYULA-236	N1H14	1141.1	48.6	0.4	5.1	34.6	0.8	1.8	0.6	0.0	8.1	5.4	1.9	0.8
*COYULA-236	N1H18	1143.4	35.4	0.9	4.3	48.4	0.3	2.0	0.5	0.0	8.2	5.8	0.9	1.5
*COYULA-236	N3H3	1450.8	21.5	1.8	12.8	45.1	1.5	3.0	0.4	0.0	13.9	8.5	4.5	0.9
*COYULA-236	N3H6	1451.4	47.1	1.1	7.3	33.3	0.6	2.1	1.5	0.0	7.0	4.3	1.2	1.5
*COYULA-236	N3H8	1451.9	31.7	1.0	12.2	37.0	1.1	3.0	0.8	0.0	13.2	8.2	2.5	2.5
*COYULA-236	N3H9	1452.4	42.1	0.9	6.7	38.1	1.8	2.6	0.4	0.0	7.4	4.5	1.5	1.4
*COYULA-236	N3H12	1452.9	32.3	1.7	9.2	45.6	1.6	1.7	0.6	0.0	7.3	4.5	1.9	0.9
*COYULA-236	N4H1	1570.2	45.6	0.6	7.5	34.5	0.3	2.9	1.3	0.3	7.0	3.8	2.1	1.1
*COYULA-236	N4H4	1570.8	37.5	0.3	3.1	48.8	0.7	1.6	0.6	0.0	7.4	5.5	0.6	1.3
*COYULA-236	N4H9	1573.8	35.9	0.9	9.5	30.9	0.5	2.3	1.2	0.0	18.8	12.5	2.0	4.3
*COYULA-1019	N1H6	1670.7	28.9	0.8	16.4	37.6	0.0	3.7	0.4	0.0	12.2	6.9	3.9	1.4
*COYULA-1019	N1H14	1672.3	28.5	0.9	17.1	36.3	0.0	2.8	0.3	0.0	14.1	9.0	3.6	1.5
*COYULA-1019	N1H22	1673.4	25.7	0.7	13.2	43.1	0.0	3.0	0.4	0.0	13.9	8.7	1.3	3.9
*COYULA-1019	N1H27	1674.4	30.2	0.6	15.8	35.1	0.0	3.4	0.8	0.0	14.1	8.1	4.0	2.0
*COYULA-1019	N1H31	1675.2	27.5	0.5	9.4	49.6	0.0	2.4	0.2	0.0	10.4	8.1	1.0	1.3
*COYULA-1019	N1H43	1678.6	16.7	1.2	13.1	50.4	0.0	3.0	0.3	0.0	15.3	13.4	0.7	1.2
*COYULA-1019	N2H3	1680.0	31.6	1.1	8.1	30.3	0.0	2.2	0.7	0.0	26.0	18.9	2.8	4.3
*COYULA-1019	N2H12	1682.8	36.6	1.8	8.3	30.0	0.0	2.3	0.6	0.0	20.4	14.9	2.0	3.5
*COYULA-1019	N2H18	1684.1	28.8	1.5	9.0	24.9	0.0	2.2	0.8	0.0	32.8	25.5	2.6	4.7
*COYULA-1019	N2H23	1686.5	38.7	0.6	3.2	47.0	0.0	2.1	0.5	0.0	7.9	5.4	0.9	1.6
*COYULA-1024	N1H6	1326.6	26.3	1.0	6.9	50.5	0.0	4.3	0.3	0.0	10.7	6.7	1.0	3.0
*COYULA-1024	N1H10	1327.4	34.1	0.9	9.3	35.0	0.0	4.0	0.5	0.0	16.2	11.7	1.1	3.4
*COYULA-1024	N1H12	1328.4	33.1	0.8	8.9	36.5	0.0	3.7	0.8	0.0	16.2	10.9	1.3	4.0
*COYULA-1024	N1H15	1329.0	27.7	0.6	7.9	45.5	0.0	4.2	0.3	0.0	13.8	9.1	1.2	3.5
*COYULA-1024	N1H21	1332.0	31.5	0.5	10.1	33.3	0.0	4.6	0.5	0.0	19.5	12.8	1.6	5.1
*COYULA-1024	N2H3	1368.2	38.3	0.4	3.1	47.7	0.0	1.6	0.7	0.0	8.2	5.6	1.2	1.4
*COYULA-1024	N2H8	1370.1	36.0	0.8	11.9	30.0	0.0	3.1	1.3	0.0	16.9	11.9	1.3	3.7
*COYULA-1024	N2H13	1371.5	38.2	0.7	5.5	39.7	2.6	2.5	0.6	0.0	10.2	7.3	1.6	1.3
*COYULA-1024	N2H18	1372.4	39.2	0.5	3.6	44.1	2.7	1.7	0.7	0.0	7.5	5.4	1.5	0.6
*COYULA-1024	N2H22	1372.8	40.2	0.4	4.3	46.7	0.8	1.4	0.6	0.0	5.6	4.0	0.6	1.0
*COYULA-1024	N3H4	1598.0	37.9	0.5	6.0	47.0	0.0	1.0	0.3	0.0	7.3	5.2	0.9	1.2
*COYULA-1024	N3H9	1599.8	26.5	0.4	4.4	58.6	0.0	1.9	0.5	0.0	7.7	5.8	0.8	1.1
*COYULA-1024	N3H15	1600.7	31.5	0.3	4.0	53.6	0.0	2.6	1.2	0.0	6.8	4.9	1.6	0.3
*COYULA-1024	N3H20	1602.1	32.2	0.7	3.7	55.1	0.0	1.3	0.4	0.0	6.6	5.0	0.5	1.1
*COYULA-1024	N3H23	1602.5	42.5	0.6	6.8	37.9	0.0	1.5	1.3	0.0	9.4	7.1	0.9	1.4
*COYULA-1024	N3H27	1604.9	29.1	0.8	7.4	30.0	18.5	5.3	0.4	0.0	8.5	6.5	0.8	1.2
*COYULA-1196	N1H11	1507.9	35.3	0.5	4.1	50.5	0.0	0.9	0.8	0.5	7.4	4.9	0.7	1.8
*COYULA-1196	N1H18	1509.4	32.1	1.5	8.6	48.8	0.0	1.4	0.3	0.0	7.3	4.7	1.9	0.7
*COYULA-1196	N1H23	1510.8	40.5	1.2	11.1	24.1	0.0	2.4	0.6	0.0	20.1	13.5	2.1	4.5
*COYULA-1196	N1H26	1511.7	34.0	1.1	5.3	50.5	0.0	1.3	0.4	0.0	7.4	4.9	1.1	1.4
*COYULA-1196	N1H30	1512.5	44.5	0.6	6.1	39.0	0.8	1.3	0.2	0.0	7.5	4.5	1.1	1.9
*COYULA-1196	N1H33	1513.6	33.8	0.7	12.7	37.8	0.0	2.6	0.4	0.0	12.0	5.7	4.3	2.0
*COYULA-1196	N2H6	1582.7	46.2	0.6	4.9	37.0	1.0	1.4	0.2	0.0	8.7	4.6	2.5	1.6
*COYULA-1196	N2H17	1585.4	41.7	0.5	3.5	45.7	0.0	1.1	0.7	0.0	6.8	4.0	0.9	1.9
*COYULA-1196	N2H21	1586.5	37.8	0.5	3.7	49.0	1.3	1.2	0.4	0.0	6.1	3.8	0.7	1.6
*COYULA-1196	N2H23	1587.1	43.6	0.4	4.1	42.8	0.6	1.9	0.5	0.0	6.1	3.7	1.3	1.1
*COYULA-1196	N2H28	1588.1	39.1	0.3	3.1	49.3	1.1	1.3	0.4	0.0	5.4	3.2	0.7	1.5
*COYULA-1196	N3H2	1754.3	46.3	0.4	4.3	40.2	0.8	1.0	0.4	0.0	6.6	4.2	1.7	0.7
*COYULA-1196	N3H5	1755.1	49.7	0.5	6.4	34.4	0.3	1.1	0.8	0.0	6.8	4.6	1.2	1.0
*COYULA-1196	N3H10	1756.2	41.6	0.5	3.4	45.9	0.0	1.9	0.3	0.0	6.4	4.3	0.8	1.3
*COYULA-1196	N3H22	1761.9	42.2	0.4	3.8	46.1	0.0	1.4	0.2	0.0	5.9	4.1	0.7	1.1
*COYULA-1196	N3H24	1762.4	46.9	0.3	5.7	38.4	0.0	1.5	0.3	0.0	6.9	4.5	0.9	1.5
*HUMAPA-807	N1H2	1146.2	34.9	0.5	7.9	47.4	0.0	0.9	0.2	0.0	8.2	6.0	0.6	1.6
*HUMAPA-807	N1H7	1148.5	28.6	1.4	18.6	34.4	0.0	2.1	0.7	0.0	14.2	8.7	1.4	4.1
*HUMAPA-807	N1H13	1150.0	37.6	1.0	9.5	40.3	0.0	1.7	0.3	0.0	9.6	5.5	0.9	3.2
*HUMAPA-807	N1H19	1152.0	33.2	1.3	12.7	35.7	2.4	3.4	0.5	0.0	10.8	7.2	1.5	2.1
*HUMAPA-807	N1H25	1152.9	29.2	1.4	12.1	40.4	0.3	2.0	0.7	0.0	13.9	10.2	0.9	2.8
*HUMAPA-807	N2H8	1155.3	28.3	1.6	10.3	46.2	0.6	2.3	0.6	0.0	10.1	7.0	0.6	2.5
*HUMAPA-807	N2H10	1155.7	23.1	1.4	8.5	55.0	0.8	2.2	0.5	0.0	8.5	5.4	0.7	2.4
*HUMAPA-807	N2H16	1157.4	44.9	0.7	9.7	33.4	0.0	1.3	0.2	0.0	9.8	5.4	1.2	3.2
*HUMAPA-807	N2H20	1162.0	32.7	1.0	7.9	47.8	0.0	1.1	0.3	0.0	9.2	5.5	0.7	3.0
*HUMAPA-807	N3H2	1673.2	14.9	0.5	2.4	67.5	0.4	2.2	2.2	0.0	9.9	7.1	1.0	1.8
*HUMAPA-807	N3H9	1674.9	25.6	0.4	6.3	54.0	0.8	3.1	0.9	0.0	8.9	5.6	2.4	0.9
*HUMAPA-807	N3H12	1675.2	17.1	0.2	2.8	70.8	0.4	1.9	1.1	0.0	5.7	3.6	0.7	1.4
*HUMAPA-807	N3H18	1675.9	16.8	0.3	2.2	71.1	0.5	2.3	1.6	0.0	5.2	3.5	0.6	1.1
*HUMAPA-807	N3H21	1678.4	21.4	0.9	8.4	28.1	0.4	1.6	0.9	0.0	38.3	28.0	2.4	7.9
*HUMAPA-807	N4H8	1803.2	34.4	0.4	11.8	42.3	0.0	2.3	0.3	0.0	8.5	4.5	2.4	1.6
*HUMAPA-807	N4H11	1805.6	34.6	0.3	9.5	42.9	0.5	4.3	0.2	0.0	7.7	4.1	1.9	1.7

*HUMAPA-807	N4H20	1808.9	17.9	0.3	3.7	65.9	0.0	2.3	1.9	1.7	6.3	4.2	1.5	0.6
*HUMAPA-1643	N2H4	1517.7	40.0	0.7	4.2	47.2	0.3	1.0	0.3	0.0	6.3	3.9	1.1	1.3
*HUMAPA-1643	N2H11	1519.6	41.3	0.5	3.6	45.4	1.1	1.6	0.4	0.0	6.1	3.9	1.0	1.2
*HUMAPA-1643	N2H24	1522.8	58.1	0.4	4.4	28.3	1.3	1.3	0.6	0.0	5.6	3.5	1.2	0.9
*HUMAPA-1643	N2H33	1524.6	42.7	0.5	5.1	43.0	0.0	1.9	0.3	0.0	6.5	4.6	0.8	1.1
*HUMAPA-1643	N3H6	1629.0	24.5	0.4	3.9	61.7	0.0	2.0	0.2	0.0	7.3	4.9	1.4	1.0
*HUMAPA-1643	N3H13	1631.8	50.5	0.7	2.9	37.6	1.6	2.3	0.3	0.0	4.1	2.8	0.9	0.4
*HUMAPA-1643	N3H18	1633.0	46.6	0.8	6.4	32.7	0.0	2.9	0.4	0.0	10.2	5.7	3.1	1.4
*HUMAPA-1643	N3H28	1635.0	30.4	0.5	3.6	48.5	5.4	3.0	0.2	0.0	8.4	5.0	2.4	1.0
*HUMAPA-1643	N3H32	1636.0	51.6	0.7	5.5	33.5	0.3	1.8	0.2	0.0	6.4	4.0	1.4	1.0
*HUMAPA-1643	N4H4	1638.7	23.9	0.4	4.1	57.2	1.2	3.2	0.5	0.0	9.5	5.4	2.9	1.2
*HUMAPA-1643	N4H9	1639.7	39.5	0.7	7.0	32.4	0.0	3.6	3.2	0.0	13.6	7.0	4.6	2.0
*HUMAPA-1643	N4H15	1641.0	22.5	0.6	3.6	54.6	4.6	3.3	0.5	0.0	10.3	5.0	3.6	1.7
*HUMAPA-1643	N4H21	1642.0	21.5	0.7	1.8	62.7	2.8	1.9	0.8	0.0	7.8	3.8	2.8	1.2
*HUMAPA-4036	N1H4	1117.7	39.4	0.6	8.0	38.2	0.0	2.3	0.4	0.0	11.1	7.1	2.3	1.7
*HUMAPA-4036	N1H8	1118.3	46.1	0.5	5.0	35.6	0.0	1.1	0.9	0.9	9.9	6.7	1.8	1.4
*HUMAPA-4036	N1H15	1119.3	42.3	0.6	6.6	39.5	0.0	2.1	0.3	0.0	8.6	5.4	2.2	1.0
*HUMAPA-4036	N1H29	1121.3	42.3	0.8	8.3	35.5	0.0	2.2	0.5	0.0	10.4	7.1	1.1	2.2
*HUMAPA-4036	N1H34	1122.3	41.8	0.7	9.3	34.7	0.0	2.1	0.4	0.0	11.0	7.5	1.9	1.6
*HUMAPA-4036	N2H3	1349.5	41.8	0.9	8.9	34.6	0.0	2.1	0.8	0.0	10.9	7.2	2.0	1.7
*HUMAPA-4036	N2H10	1352.2	32.8	1.0	12.1	39.0	0.0	3.6	0.3	0.0	11.2	7.7	1.9	1.6
*HUMAPA-4036	N2H15	1353.5	38.7	0.6	4.6	45.0	0.0	1.3	0.6	0.0	9.2	6.4	1.1	1.7
*HUMAPA-4036	N2H20	1354.9	37.9	0.7	5.1	46.5	0.0	1.1	0.3	0.0	8.4	5.7	1.5	1.2
*HUMAPA-4036	N2H25	1357.0	44.4	0.6	5.4	39.7	0.0	1.2	0.2	0.0	8.5	6.1	1.0	1.4
*HUMAPA-4036	N3H2	1379.9	38.4	0.5	5.6	43.8	0.0	1.4	0.5	0.0	9.8	6.5	1.9	1.4
*HUMAPA-4036	N3H8	1381.9	25.0	0.5	6.4	55.1	0.0	1.8	0.8	0.0	10.4	7.1	1.8	1.5
*HUMAPA-4036	N3H18	1383.8	44.6	0.5	6.2	39.2	0.0	2.0	0.6	0.0	6.9	4.5	0.9	1.5
*HUMAPA-4036	N3H25	1385.8	40.4	0.6	7.3	39.6	0.0	2.2	0.3	0.0	9.6	5.4	2.8	1.4
*HUMAPA-4036	N3H30	1386.6	45.9	0.4	4.0	40.3	2.2	1.4	0.2	0.0	5.6	3.5	0.7	1.4
*HUMAPA-4036	N3H34	1387.8	45.3	0.4	5.2	39.2	0.0	1.3	0.2	0.0	8.4	5.0	2.3	1.1
*HUMAPA-4198	N1H1	1449.1	48.6	0.5	8.3	25.4	0.0	2.1	1.0	0.0	14.1	9.2	2.9	2.0
*HUMAPA-4198	N1H4	1449.6	48.8	0.6	7.6	27.9	0.0	1.5	1.0	0.0	12.6	7.9	2.8	1.9
*HUMAPA-4198	N1H7	1450.6	41.3	0.5	4.9	41.1	0.0	1.2	0.6	0.0	10.4	6.4	2.4	1.6
*HUMAPA-4198	N1H13	1455.1	41.4	0.7	4.1	44.3	1.3	0.9	0.3	0.0	7.0	4.5	1.1	1.4
*HUMAPA-4198	N2H4	1525.6	50.1	0.6	7.9	24.7	0.0	2.4	2.3	0.4	11.6	8.3	1.0	2.3
*HUMAPA-4198	N2H9	1527.5	53.3	0.5	6.1	29.5	0.0	1.5	0.4	0.0	8.7	5.7	1.4	1.6
*HUMAPA-4198	N2H30	1532.4	49.4	0.6	10.1	23.6	0.0	2.2	0.6	0.0	13.5	9.2	2.4	1.9
*HUMAPA-4198	N2H35	1533.9	55.1	0.5	5.2	27.9	0.0	1.6	0.5	0.0	9.2	6.2	2.0	1.0
*HUMAPA-4198	N3H9	1675.5	58.1	0.6	6.2	24.7	0.0	1.3	0.4	0.0	8.7	5.5	2.4	0.8
*HUMAPA-4198	N3H10	1675.9	55.3	0.5	9.4	20.3	0.0	2.0	0.9	0.3	11.3	7.5	1.8	2.0
*HUMAPA-4198	N3H12	1676.5	48.2	0.8	8.0	29.2	0.0	1.4	0.5	0.2	11.7	8.0	1.6	2.1
*HUMAPA-4198	N3H25	1679.2	55.5	0.7	6.0	25.9	0.0	1.5	0.9	0.0	9.5	6.1	2.3	1.1
*HUMAPA-4198	N3H33	1681.5	53.1	0.8	6.1	28.8	0.0	1.3	0.4	0.0	9.5	6.2	1.9	1.4
**HUMAPA-4198	1	1449.8	37.5	0.0	5.7	49.7	0.0	0.0	0.7	0.0	6.4	1.6	2.1	2.6
**HUMAPA-4198	2	1527.6	51.7	0.0	10.7	27.6	0.0	2.2	1.0	0.0	6.7	4.3	2.4	0.0
**HUMAPA-4198	3	1680.1	47.9	0.0	9.6	30.4	0.0	1.6	0.7	0.0	9.8	3.7	1.8	4.4
**HUMAPA-4036	4	1118.7	31.6	0.0	3.4	54.8	0.0	7.2	0.8	0.0	2.3	2.3	0.0	0.0
**HUMAPA-4036	5	1352.7	43.7	0.0	13.1	26.0	0.0	1.8	1.2	0.0	14.2	8.0	6.1	0.0
**HUMAPA-4036	6	1386.1	40.3	0.0	5.2	49.5	0.0	2.6	0.3	0.0	2.1	0.6	1.5	0.0
**HUMAPA-4036	7	1387.6	47.6	0.0	7.7	39.1	0.0	1.2	0.3	0.0	4.0	4.0	0.0	0.0
**HUMAPA-807	8	1152.2	26.2	0.0	13.2	54.1	0.0	2.6	0.4	0.0	3.6	0.8	2.8	0.0
**HUMAPA-807	9	1155.5	23.4	0.0	10.7	59.4	0.0	1.4	0.7	0.0	4.4	1.7	2.7	0.0
**HUMAPA-807	10	1673.8	17.9	0.0	6.3	70.6	0.0	0.0	0.6	0.0	4.6	1.4	3.2	0.0
**HUMAPA-807	11	1802.1	25.8	0.0	10.3	52.4	0.0	2.7	0.4	0.0	8.4	4.2	4.2	0.0
**HUMAPA-807	12	1804.1	37.0	0.0	9.7	43.0	0.0	2.9	0.8	0.0	6.6	2.7	3.8	0.0
**HUMAPA-1643	13	1231.0	30.9	0.0	11.5	45.4	0.0	3.3	0.6	0.0	8.4	2.4	6.0	0.0
**HUMAPA-1643	14	1522.1	36.6	0.0	4.3	55.2	0.0	1.0	0.6	0.0	2.2	0.8	1.4	0.0
**HUMAPA-1643	15	1628.5	26.9	0.0	7.9	54.0	0.0	3.2	0.6	0.0	7.5	2.0	5.4	0.0
**HUMAPA-1643	16	1639.5	33.1	0.0	6.0	53.5	0.0	2.1	0.5	0.0	4.8	1.4	3.4	0.0
**COYULA-236	17	1422.2	27.8	0.0	12.7	45.8	0.0	3.4	0.7	0.0	9.5	1.4	8.1	0.0
**COYULA-236	18	1450.8	25.0	0.0	15.5	42.5	0.0	3.8	0.6	0.0	12.7	6.3	6.4	0.0
**COYULA-236	19	1570.7	35.8	0.0	10.4	42.5	0.0	1.8	0.6	0.0	8.9	4.0	4.9	0.0
**COYULA-1196	20	1513.1	36.8	0.0	10.6	42.3	0.0	1.3	0.6	0.0	8.3	2.8	5.6	0.0
**COYULA-1196	21	1583.9	38.8	0.0	6.1	50.5	0.0	1.6	0.7	0.0	2.2	0.5	1.7	0.0
**COYULA-1196	22	1756.1	38.7	0.0	4.9	52.1	0.0	1.3	0.4	0.0	2.5	0.2	2.2	0.0
**COYULA-1019	23	1674.3	25.3	0.0	16.7	45.0	0.0	2.2	0.5	0.0	10.2	3.4	6.9	0.0
**COYULA-1019	24	1686.4	42.4	0.0	5.0	45.2	0.0	1.8	0.9	0.0	4.6	3.0	1.6	0.0
**COYULA-1024	25	1325.6	30.4	0.0	11.4	34.0	0.0	4.5	0.8	0.0	18.9	11.7	7.2	0.0
**COYULA-1024	26	1368.9	41.1	0.0	14.0	28.5	0.0	2.5	1.2	0.0	12.8	6.7	6.1	0.0
**COYULA-1024	27	1370.2	43.4	0.0	10.3	38.7	0.0	1.3	1.2	0.0	5.1	0.0	5.1	0.0
**COYULA-1024	28	1605.9	29.9	0.0	16.3	43.3	0.0	3.0	0.8	0.0	6.7	2.8	3.9	0.0
**COYULA-236	29	1141.3	49.4	2.2	7.9	29.9	0.0	1.2	0.0	0.0	9.5	4.3	1.8	3.5
**HUMAPA-4036	30	1124.5	38.8	0.0	4.6	47.2	0.0	1.2	0.0	0.0	8.2	5.3	2.8	0.0
**HUMAPA-1035	M1F30	1711.7	31.3	0.0	3.5	47.4	0.0	1.8	0.0	0.0	16.0	13.6	1.4	1.0
**HUMAPA-1035	M3F26	1712.6	32.2	0.0	4.4	48.2	0.0	1.8	1.0	0.0	12.4	9.0	2.7	0.7
**HUMAPA-1035	M4F22	1713.6	29.3	0.0	3.8	49.6	0.0	1.1	0.8	0.0	15.4	12.5	1.9	1.0

Critical Salt Concentration Results

PV	Brine strength (%)	Core Samples used					
		KCl (N1H21)		$CaCl_2$ (N1H8)		NaCl (N1H34a)	
		k brine (mD)	%	k brine (mD)	%	k brine (mD)	%
0	3.5	7.676	100	22.323	100	0.693	100
10	2.5	7.063	92	21.834	98	0.662	96
20	1.5	6.923	90	21.391	96	0.661	95
30	0.5	6.790	88	20.972	94	0.583	84
40	DW*	5.887	77	17.813	80	0.502	72
50	0.5	6.790	88	20.972	94	0.720	104
60	1.5	6.923	90	21.391	96	0.801	116
70	2.5	7.063	92	21.834	98	0.802	116
80	3.5	7.225	94	22.323	100	0.801	116

*DW is de-ionised water

Extended Critical Salt Concentration Results

		Sample M4F22a				ICP trace element results (mg/l)				
PV	Brine (%)	pH injected	pH effluent	k (mD)	%	Al	Ca	Fe	K	Mg
0	3.5	7.92	8.02	10.559	100	-0.006	14.080	0.005	3.628	1.892
10	3.0	7.16	8.55	8.359	79	-0.003	8.180	0.014	3.703	0.728
20	2.5	7.07	8.53	6.131	58	-0.005	7.942	0.054	4.395	0.700
30	2.0	7.34	8.94	5.845	55	0.000	7.550	0.007	4.237	0.410
40	1.5	7.44	9.01	5.402	51	-0.004	8.312	0.011	4.404	0.450
50	1.0	7.80	9.04	5.348	51	0.002	9.393	0.015	4.903	0.511
60	0.5	7.03	9.18	3.975	38	0.010	8.197	0.045	5.731	0.757
70	DW	6.12	10.20	3.151	30	0.143	1.413	0.021	1.427	0.124
80	0.5	7.09	8.67	3.533	33	0.019	43.430	0.037	10.300	3.225
90	1.0	7.12	8.38	2.139	20	0.005	33.770	0.011	4.238	2.154
100	1.5	7.30	8.47	2.614	25	0.000	17.540	0.073	4.743	1.584
110	2.0	7.12	8.73	3.410	32	-0.002	9.917	0.004	6.334	0.668
120	2.5	6.97	8.83	3.593	34	-0.001	7.519	0.005	3.031	0.450
130	3.0	7.04	8.94	3.635	34	-0.004	6.229	0.005	3.138	0.372
140	3.5	6.43	8.91	3.674	35	-0.002	4.692	0.012	1.831	0.363

*DW is de-ionised water

Critical Velocity Test Results

Sample	Increasing flow rates (ml/min) and resulted permeability (mD)																	
	0.1	0.3	0.5	0.7	0.9	1.1	1.3	1.5	1.7	1.9	2.1	2.3	2.5	2.7	2.9	3.1	3.3	3.5
N1H34a	0.742	0.747	0.759	0.769	0.744	0.750	0.763	0.780	0.793	0.815	0.815	0.815	0.817	0.840	0.843	0.853	0.858	0.862
N1H8	10.15	14.88	15.26	15.43	15.84	15.85	16.07	16.45	16.56	16.65	16.88	16.93	17.10	17.13	17.04	17.17	17.09	16.92
N1H21	7.978	8.062	8.079	8.707	9.100	9.369	9.565	9.714	9.831	9.925	10.00	10.06	10.12	10.41	10.43	10.46	10.48	10.69
	Decreasing flow rates (ml/min) and resulted permeability (mD)																	
	3.5	3.3	3.1	2.9	2.7	2.5	2.3	2.1	1.9	1.7	1.5	1.3	1.1	0.9	0.7	0.5	0.3	0.1
N1H34a	0.862	0.869	0.843	0.817	0.792	0.763	0.733	0.712	0.685	0.658	0.617	0.580	0.555	0.522	0.507	0.482	0.476	0.477
N1H8	16.92	16.89	16.75	16.48	16.30	16.21	15.86	15.59	15.27	14.90	14.45	14.08	13.60	12.96	12.32	11.61	10.64	10.15
N1H21	10.69	10.69	10.46	10.43	10.41	10.38	10.06	10.30	10.25	9.831	9.714	9.565	9.369	9.100	8.707	8.503	8.062	7.978

Extended Critical Velocity Test Results (sample M4F22a)					
PV	***Flow Rate (ml/min)***	***k (mD)***	***Permeability change (%)***	***Interstitial Velocity (cm/min)***	***Effluent pH***
0	*1*	*3.521*	*100*	*0.668*	*8.97*
16	*1.5*	*3.961*	*113*	*1.002*	*9.24*
26	*2*	*4.225*	*120*	*1.336*	*9.32*
34	*2.5*	*4.543*	*129*	*1.670*	*9.60*
42	*3*	*4.783*	*136*	*2.004*	*9.62*
50	*3.5*	*4.929*	*140*	*2.338*	*9.59*
59	*4*	*5.160*	*147*	*2.672*	*9.70*
68	*4.5*	*5.244*	*149*	*3.005*	*9.62*
77	*5*	*5.451*	*155*	*3.339*	*9.64*

Fracturing Fluid Experiment (sample M3F26b)			
Pore Volumes Pumped (pv)	***Fluid Pumped***	***Average Differential Pressure (psi)***	***Resulted permeability k (mD)***
14	*3.5% NaCl*	*7.665*	*8.146*
31	*2.0% KCl*	*7.340*	*8.503*
254	*3.5% NaCl*	*297.839*	*0.211*

Spontaneous Imbibition and Forced Displacement Results				
Sample	**After Spontaneous imbibition**		**After Forced Displacement**	
	Sw (%pv)	***Oil Recovered (%OOIP)***	***Sor (%pv)***	***Oil Recovered (%OOIP)***
M1F30a	*9.14*	*3.5*	*56.2*	*40.3*
M1F30b	*20.1*	*1.3*	*54.5*	*32.7*
S29a1	*7.7*	*2.8*	*66.5*	*30.0*
S29a	*13.7*	*6.8*	*49.2*	*46.8*
Berea 1	*46.1*	*25.8*	*44.6*	*38.8*
Berea 2	*56.7*	*47*	*43.3*	*47*

Amott-Harvey Wettability results					
Sample	**Brine**		**Oil**		**Amott-Harvey Index**
	Spontaneous imbibition (cm^3)	***Forced displacement (cm^3)***	***Spontaneous imbibition (cm^3)***	***Forced displacement (cm^3)***	
M1F30a	*0.2*	*2.6*	*1.04*	*1.28*	*-0.4*
M1F30b	*0.06*	*1.5*	*1.23*	*0.7*	*-0.6*
S29a1	*0.1*	*0.96*	*0.4*	*0.57*	*-0.3*
S29a	*0.15*	*0.91*	*0.66*	*0.25*	*-0.6*
Berea 1	*1.95*	*0.95*	*0.02*	*2.11*	*0.7*
Berea 2	*3.85*	*0*	*0.05*	*3.4*	*1.0*

Adhesion Tests Results

Non-aged Surface Minerals

	Advancing Contact Angles of Oil in Brine					
	Temp. (°C)	***3.5% NaCl***	***2.5% NaCl***	***1.5% NaCl***	***0.5% NaCl***	***DW***
Calcite	*21°C*	*30*	*30*	*30*	*35*	*30*
	40°C	*33*	*30*	*30*	*35*	*33*
	60°C	*30*	*25*	*25*	*25*	*25*
	Advancing Contact Angles of Oil in Brine					
	Temp. (°C)	***3.5% NaCl***	***2.5% NaCl***	***1.5% NaCl***	***0.5% NaCl***	***DW***
	21°C	*40*	*30*	*30*	*30*	*40*
	60°C	*35*	*30*	*30*	*35*	*30*
Quartz	***Advancing Contact Angles of Oil in Brine @ 21°C***					
	pH	***3.5% NaCl***	***2.5% NaCl***	***1.5% NaCl***	***0.5% NaCl***	***DW***
	pH 9	*50*	*55*	*50*	*50*	*50*
	pH 7	*40*	*30*	*30*	*30*	*40*
	pH 5	*30*	*35*	*35*	*60*	*60*

Aged Surface Minerals

	Advancing Contact Angles of Oil in Brine					
	Temp. (°C)	***3.5% NaCl***	***2.5% NaCl***	***1.5% NaCl***	***0.5% NaCl***	***DW***
Calcite	*21°C*	*160*	*165*	*170*	*170*	*175*
	40°C	*160*	*165*	*165*	*170*	*170*
	60°C	*145*	*150*	*155*	*155*	*160*
	Advancing Contact Angles of Oil in Brine					
	Temp. (°C)	***3.5% NaCl***	***2.5% NaCl***	***1.5% NaCl***	***0.5% NaCl***	***DW***
	21°C	*135*	*130*	*135*	*140*	*145*
	60°C	*70*	*80*	*80*	*80*	*85*
Quartz	***Advancing Contact Angles of Oil in Brine @ 21°C***					
	pH	***3.5% NaCl***	***2.5% NaCl***	***1.5% NaCl***	***0.5% NaCl***	***DW***
	pH 9	*100*	*93*	*100*	*100*	*100*
	pH 7	*135*	*130*	*135*	*140*	*145*
	pH 5	*100*	*80*	*150*	*150*	*156*

NMR-Index Wettability results

Sample	***Irreducible Water Saturation***		***Residual Oil Saturation***		***NMR Wettability Index***
	Swi (%pv)	***NMR $T2_{LM}$ (msec)***	***Sor (%pv)***	***NMR $T2_{LM}$ (msec)***	
M1F30a	*5.9*	*89.6*	*56.2*	*185.8*	*-0.51*
M1F30b	*19.1*	*86.1*	*54.5*	*171*	*-0.49*
S29a1	*5.0*	*29.7*	*66.5*	*60.83*	*-0.51*
S29a	*7.5*	*27.8*	*49.2*	*45.3*	*-0.38*
Berea 1	*27.3*	*114.8*	*44.6*	*101.7*	*0.12*
Berea 2	*18.3*	*109.7*	*43.2*	*98.1*	*0.11*

Continuous End-point Relative Permeability					
Berea 1			***M1F30a***		
Sw (%pv)	*fraction of kro@Swi*		***Sw (%pv)***	*fraction of kro@Swi*	
	kro	***krw***		***kro***	***krw***
32.5	*1.000*	*0*	*13.6*	*1.000*	*0*
35.1	*0.550*	*0.003*	*17.2*	*0.480*	*0.006*
37.6	*0.370*	*0.007*	*20.7*	*0.300*	*0.012*
40.2	*0.250*	*0.010*	*24.3*	*0.210*	*0.017*
42.7	*0.180*	*0.013*	*27.8*	*0.170*	*0.023*
45.3	*0.140*	*0.016*	*31.4*	*0.140*	*0.029*
47.8	*0.100*	*0.019*	*35.0*	*0.110*	*0.037*
50.35	*0.080*	*0.023*	*38.5*	*0.080*	*0.043*
52.9	*0.050*	*0.030*	*42.1*	*0.060*	*0.080*
55.45	*0.025*	*0.040*	*45.6*	*0.030*	*0.180*
58	*0*	*0.140*	*49.2*	*0*	*0.310*

Asphaltene onset test results					
Flask number	**n-heptane (%)**	**AT (%)**	**$1/(T2_{LM})^2$**	**Mass of precipitate (g)**	**RI**
13	*90*	*10*	*4.82E-07*	*0.005*	*1.395*
14	*80*	*20*	*3.97E-07*	*0.013*	*1.405*
15	*70*	*30*	*3.63E-07*	*0.018*	*1.419*
16	*60*	*40*	*4.32E-07*	*0.024*	*1.437*
17	*50*	*50*	*6.70E-07*	*0.024*	*1.448*
18	*40*	*60*	*9.85E-07*	*0.03*	*1.456*